NASA/CP—2005-213431

18th Space Photovoltaic Research and Technology Conference

April 2005

The NASA STI Program Office . . . in Profile

Since its founding, NASA has been dedicated to the advancement of aeronautics and space science. The NASA Scientific and Technical Information (STI) Program Office plays a key part in helping NASA maintain this important role.

The NASA STI Program Office is operated by Langley Research Center, the Lead Center for NASA's scientific and technical information. The NASA STI Program Office provides access to the NASA STI Database, the largest collection of aeronautical and space science STI in the world. The Program Office is also NASA's institutional mechanism for disseminating the results of its research and development activities. These results are published by NASA in the NASA STI Report Series, which includes the following report types:

- TECHNICAL PUBLICATION. Reports of completed research or a major significant phase of research that present the results of NASA programs and include extensive data or theoretical analysis. Includes compilations of significant scientific and technical data and information deemed to be of continuing reference value. NASA's counterpart of peer-reviewed formal professional papers but has less stringent limitations on manuscript length and extent of graphic presentations.

- TECHNICAL MEMORANDUM. Scientific and technical findings that are preliminary or of specialized interest, e.g., quick release reports, working papers, and bibliographies that contain minimal annotation. Does not contain extensive analysis.

- CONTRACTOR REPORT. Scientific and technical findings by NASA-sponsored contractors and grantees.

- CONFERENCE PUBLICATION. Collected papers from scientific and technical conferences, symposia, seminars, or other meetings sponsored or cosponsored by NASA.

- SPECIAL PUBLICATION. Scientific, technical, or historical information from NASA programs, projects, and missions, often concerned with subjects having substantial public interest.

- TECHNICAL TRANSLATION. English-language translations of foreign scientific and technical material pertinent to NASA's mission.

Specialized services that complement the STI Program Office's diverse offerings include creating custom thesauri, building customized databases, organizing and publishing research results . . . even providing videos.

For more information about the NASA STI Program Office, see the following:

- Access the NASA STI Program Home Page at ***http://www.sti.nasa.gov***

- E-mail your question via the Internet to help@sti.nasa.gov

- Fax your question to the NASA Access Help Desk at 301–621–0134

- Telephone the NASA Access Help Desk at 301–621–0390

- Write to:
  NASA Access Help Desk
  NASA Center for AeroSpace Information
  7121 Standard Drive
  Hanover, MD 21076

NASA/CP—2005-213431

18th Space Photovoltaic Research and Technology Conference

Proceedings of a conference
held at Ohio Aerospace Institute
and sponsored by NASA Glenn Research Center
Brook Park, Ohio, September 16–18, 2003

National Aeronautics and
Space Administration

Glenn Research Center

April 2005

This report is a formal draft or working paper, intended to solicit comments and ideas from a technical peer group.

This report contains preliminary findings, subject to revision as analysis proceeds.

Available from

NASA Center for Aerospace Information
7121 Standard Drive
Hanover, MD 21076

National Technical Information Service
5285 Port Royal Road
Springfield, VA 22100

Available electronically at http://gltrs.grc.nasa.gov

Foreword

The 18th Space Photovoltaic Research and Technology Conference, SPRAT XVIII, was held from September 16 to 18, 2003. The purpose of the SPRAT conference is to bring members of the space solar cell community together to discuss the recent developments in solar cell technology and future directions of the field. The SPRAT conference is convened roughly every 2 years. The venue for SPRAT XVIII was the Ohio Aerospace Institute (OAI), located just outside the gate of the NASA Glenn Research Center at Lewis Field. SPRAT is sponsored by the Photovoltaic and Space Environmental Effects Branch at the NASA Glenn Research Center. The conference organizers were all NASA and OAI staff. They did an outstanding job and it was my pleasure to serve as chairman.

Representatives of industry, government, and universities presented topical papers on space solar cell and array technology. The SPRAT conference also holds a series of half-day workshops on current issues in space photovoltaics. The papers and workshop summaries are included in the SPRAT proceedings.

As the SPRAT XVIII chairman, I had the pleasure of awarding the Irving Weinberg Award to a researcher who has made significant contributions to space solar cell research and technology. The SPRAT XVIII Irving Weinberg Award went to Dr. Bruce Anspaugh of the Jet Propulsion Laboratory. He made significant contributions in the field of solar cell calibration and radiation damage. Dr. Anspaugh retired from JPL this year. I wish Bruce well and hope he has a long and happy life.

Phillip Jenkins
Chairman of the 18th Space Photovoltaic Research and Technology Conference

Contents

Workshops

TOWARDS REALIZING SUPER-HIGH-EFFICIENCY AND RADIATION RESISTANT MULTI-JUNCTION SOLAR CELLS

Masafumi Yamaguchi,
Toyota Technological Institute, Nagoya 468-8511, Japan

Tatsuya Takamoto,
Sharp Corporation, Nara 639-2198, Japan

Aurangzeb Khan
University of South Alabama, Mobile 36688, USA

Mitsuru Imaizumi
NASDA, Tsukuba 305-8505, Japan

Sumio Matsuda
NASDA, Tsukuba 305-8505, Japan

Nicholas J. Ekins-Daukes
Toyota Technological Institute, Nagoya 468-8511, Japan

1 INTRODUCTION

The idea that a multi-junction solar cell can achieve high efficiency has a long history, dating back to 1957 [1]. However the actual realization of efficient multi-junction solar cells that demonstrate the advantages predicted by the early papers, has taken approximately 30 years. Currently there is cause for optimism, as the InGaP/GaAs/Ge solar cell has begun to penetrate the space market and considerable efforts are underway to bring highly efficient multi-junction solar cells to terrestrial concentrator systems. This paper will provide an overview of important developments over the last decade or so, with particular emphasis on work performed in Japan.

2 KEY ISSUES FOR REALIZING HIGH-EFFICIENCY MULTI-JUNCTION SOLAR CELLS

A key point in the development of Japanese multi-junction solar cells was the Super-High Efficiency Solar Cell project, that started in the fiscal year 1990. The programme marked a long term commitment to develop a 40% efficient solar cell and faced considerable technical challenges. The multi-junction approach was, and still is, the only realistic means of attaining such high efficiency in the medium term.

Table 1 summarises the past, present and anticipated future trends of high efficiency multi-junction solar cells. In the 1980's much effort was invested in the monolithic AlGaAs/GaAs tandem solar cell, but progress was slowed by oxygen contamination of the AlGaAs. Extremely low surface recombination velocities were observed in the more oxygen tolerant InGaP material [2] and it soon became the material of choice for multi-junction solar cells, leading to a number of notable achievements using the InGaP/GaAs tandem structure and mechanical stack designs. A study to optimise the InGaP top cell showed that the lowest surface recombination was obtained using an AlInP window layer and the longest minority lifetime obtained with a buffer layer and optimised growth temperature [3]. This resulted in a record efficiency 18.5% InGaP solar cell.

The tunnel junction forms another important aspect of the multi-junction structure. It should be optically transparent and connect the component cells in the multi-junction structure with the minimum of electrical resistance. The optical absorption in the tunnel junction can be minimised by using thin layers of wide band-gap material, although care must be exercised as the tunnelling current decreases exponentially with increasing band-gap energy. A double heterostructure (DH) was initially proposed for AlGaAs/GaAs tandem cells with the DH layers blocking dopant diffusion [4]. Similar advantages were found when

Table 1: Key issues for realizing high-efficiency multi-junction solar cells

Key Issue	Past	Present	Future
Top Cell	AlGaAs	InGaP	AlInGaP
3rd Layer	None	Ge	GaInNAs etc...
Substrate	GaAs	Ge	Si
Tunnel Junction	DH-GaAs	DH InGaP	DH wide/narrow Eg
Lattice Matching	GaAs	$In_{0.01}GaAs$	Lattice Mismatch
Carrier Confinement	InGaP BSF	AlInP BSF	Widegap BSF
Photon Confinement	None	None	Bragg reflector etc..

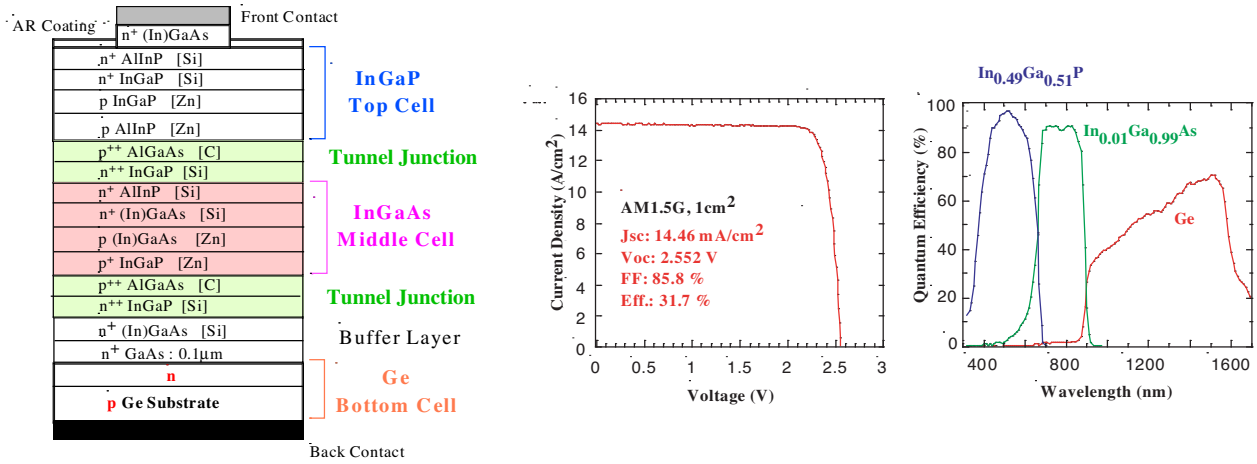

Fig. 1. Schematic structure, light-IV and spectral response for the high efficiency InGaP/InGaAs/Ge 3-junction cell fabricated on a Ge substrate. (From Ref. [8])

the DH tunnel junction was applied to the InGaP/GaAs tandem solar cell. Compared to a plain InGaP tunnel junction, the DH tunnel junction with AlInP barriers achieved a peak tunneling current of $2A/cm^2$ while the plain InGaP tunnel junction achieved a peak tunnelling current of only $5mA/cm^2$. This improvement is due to the lower diffusion coefficient of Zn in the AlInP and InGaP materials [5]. An additional benefit of the DH tunnel junction is the provision of a back-surface-field and window layer for the adjacent p/n junctions.

By growing the InGaP/GaAs device on a Ge substrate it is possible to create a third junction, thereby marginally increasing the voltage of the multi-junction device. A further improvement can be made by paying careful attention to the lattice parameter of the Ge substrate. It is commonly assumed that the 0.08% lattice mismatch between GaAs and Ge is negligibly small, but it is still sufficient to introduce misfit dislocations when a thick GaAs epilayer is grown. By replacing the GaAs with $In_{0.01}GaAs$, a fully lattice-matched cell can be made with a negligible misfit dislocation density. A further advantage of the $In_{0.01}GaAs$ layer is a marginal increase in short-circuit current over the GaAs, on account of the lower band-gap of the $In_{0.01}GaAs$ [6,7].

3 HIGH EFFICIENCY & RADIATION RESISTANT InGaP/GaAs/Ge 3-JUNCTION SOLAR CELLS

The most recent InGaP/GaAs/Ge solar cell design uses a C-doped AlGaAs/ Si-doped InGaP heterostructure tunnel junction [9] with DH AlInP barriers, described previously. A schematic of the device is shown in figure 1 together with light-IV and quantum efficiency results from a $1cm^2$ device. Such solar cells have achieved efficiencies of 31.7% (1cm x 1cm) and 31.2% (5cm x 5cm) under 1 sun AM1.5G and were fabricated by Japan Energy Co. [8]. Under AM0, a 29.2% efficient $2x2cm^2$ device has been demonstrated; the light-IV is shown in figure 2.

Other notable cells include:

– InGaP/GaAs/InGaAs mechanical stack that achieved a world record 33.3% efficiency under AM1.5G, following joint work by Japan Energy Co., Sumitomo Electric Co. and Toyota Tech. Inst. [10], shown in figure 3.
– AlGaAs/GaAs monolithic tandem cell with a 1 sun AM1.5 efficiency of 27.6% by Hitachi Cable Co [11].

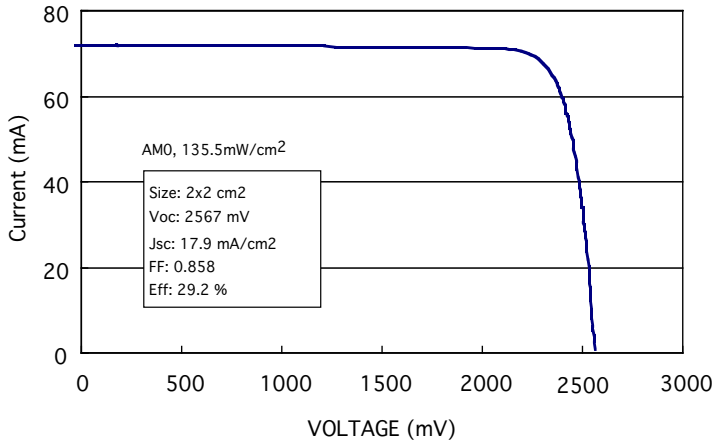

Fig. 2. Light-IV curve for the InGaP/GaAs/Ge 3-junction cell under AM0 illumination.

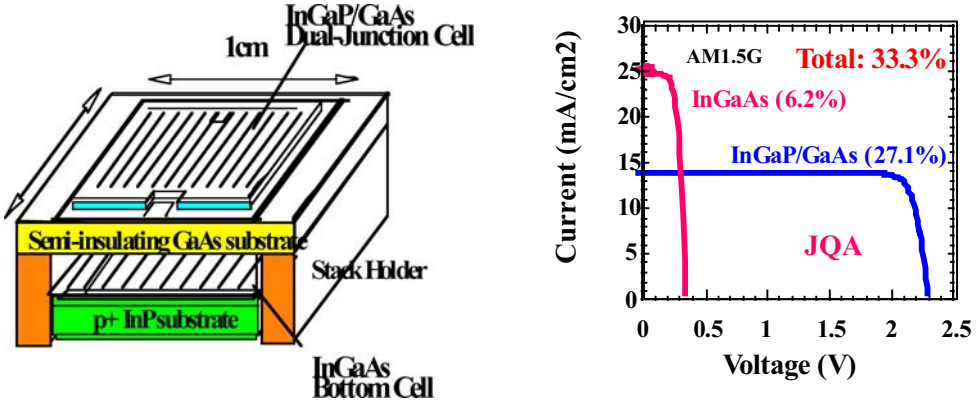

Fig. 3. Schematic structure for the InGaP/GaAs/InGaAs mechanically stacked 3-junction solar cell and light-IV curve showing the world-record efficiency under 1 sun AM1.5G. (From Ref. [10]

– GaAs/GaInAsP mechanical stack tandem cell with a 1 sun AM1.5 efficiency of 31.1% by Sumitomo Electric Co. [12].
– InGaP/GaAs/Ge concentrator cell with an efficiency in excess of 36% for concentrations from 100-500 suns [13]; the increase in efficiency under concentration is shown in figure 4.

Due to the series connection in the multi-junction solar cell, the radiation resistance of the cell as a whole will be dominated by the worst performing layer. Figure 5 shows the degradation in both Voc and Isc for the sub-cells of a InGaP/GaAs/Ge multi-junction cell under 1MeV electron irradiation. The effect of radiation damage is first a reduction in the minority carrier diffusion length followed by majority carrier removal under heavy irradiation [14,15]. It is clear that the InGaP is reasonably radiation hard, maintaining a high Isc, while the Ge and GaAs junctions fall quite quickly. However, as the Ge junction is current rich, its effect on the overall multi-junction cell radiation performance is small. It is then the degradation of the GaAs junction that dominates the degradation of the multi-junction cell under irradiation. Various schemes such as thinning the emitter and base layers and field assisted collection can be employed to improve the radiation response of each sub-cell in a multi-junction device. When considering the multi-junction cell as a whole, the standard means for maintaining high efficiency is to design the solar cell such that the GaAs junction is current rich at the beginning of life (BOL) and becomes current matched to the InGaP at the end of life (EOL), as shown in figure 6. Nevertheless, this compromises the BOL efficiency, so it is desirable to replace the GaAs junction with a more radiation resistant material, such as InGaAsP [16].

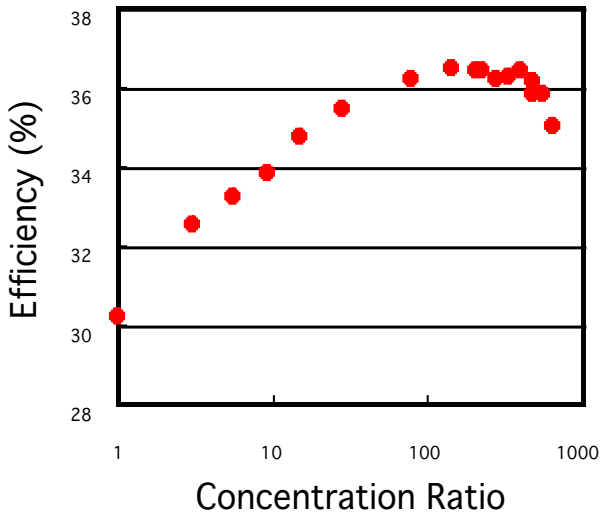

Fig. 4. Efficiency of the 3J concentrator cell shown as a function of solar concentration. (From Ref. [13])

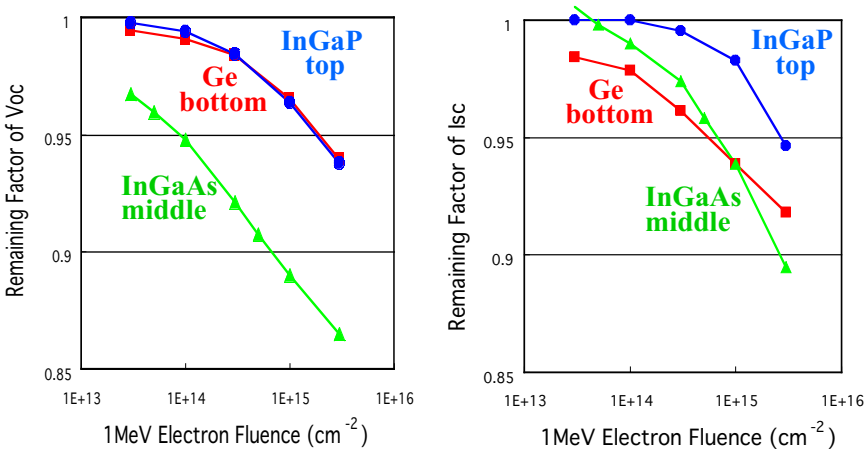

Fig. 5. Radiation resistance of sub cells in a triple-junction cell. (From Ref. [13])

4 SHORT & LONG TERM TARGETS

It is worth noting that the triple junction concentrator solar cell is an important driving force in Japanese R&D on multi-junction solar cells. A consortium supported by NEDO and comprised of Sharp Co., Daido Steel Co. and Daido Metal Co. are working to demonstrate a 40% efficient solar cell under 500 suns illumination by the end of March 2006. As shown in figure 4, efficiencies in excess of 36% were recently demonstrated from an InGaP/InGaAs/Ge concentrator solar cell [13]. It is very likely that advances achieved under this programme will bring improvements to the AM0 multi-junction space solar cell, as there are many shared problems which we now will discuss with reference to table 1.

The InGaP/GaAs band-gap combination is not ideally suited to the AM0 solar spectrum, the InGaP being current rich and the GaAs current poor. In the past, the situation has been helped by thinning the top cell, allowing unabsorbed sunlight to penetrate to the lower junction [17]. This raises the current in the lower junction and thus the overall current in the multi-junction cell, but the top cell open-circuit voltage is compromised. A preferable, but more challenging approach is to find a higher band-gap material to replace the InGaP material, thereby increasing the photocurrent in the lower junction and increasing

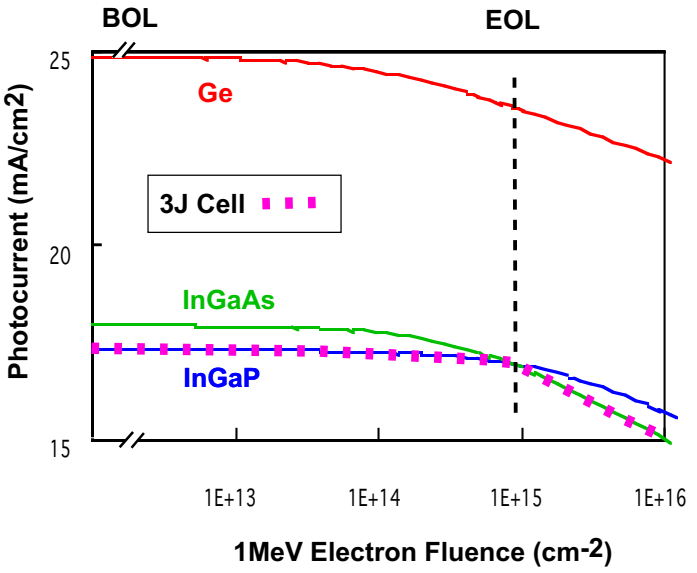

Fig. 6. Photogenerated current in each sub cell as a function of 1MeV electron fluence; the overall triple junction cell current is shown by the broken line. (From Ref. [13])

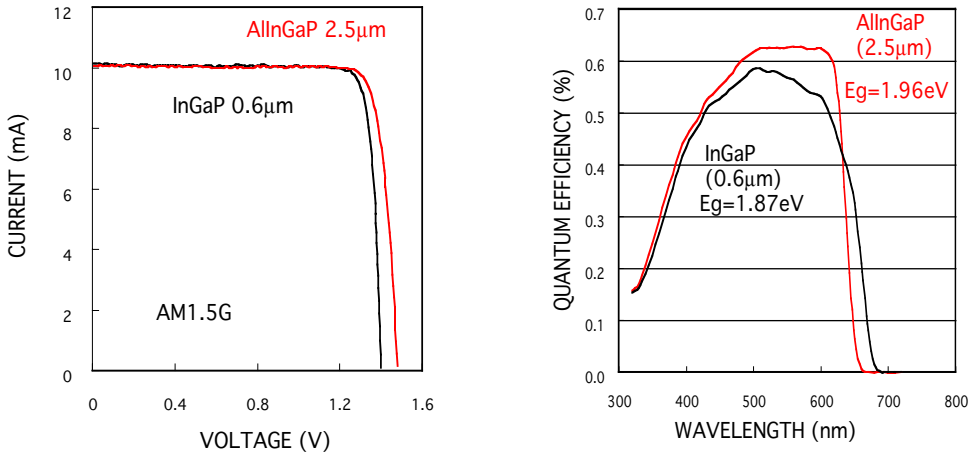

Fig. 7. Light-IV and QE curves for a thick AlGaInP cell and a thin GaInP cell under AM1.5G with no AR coating. (From Ref. [13])

the top-cell open-circuit voltage. A recent demonstration of this is shown in figure 7, comparing a thick 1.96eV AlInGaP device to a thin 1.87eV InGaP device. The short-circuit currents are identical but the AlInGaP device yields a higher open-circuit voltage [13]. It is anticipated that this improvement alone will raise the multi-junction AM0 efficiency from 29% to almost 31%.

The Ge junction provides a fairly robust substrate for the multi-junction cell, but its properties as a third junction are far from ideal. The band-gap is too low for efficient conversion of the sub-GaAs photon flux and it would be preferable to use a material with a band-gap of around 1eV. Considerable effort has been invested in dilute nitride materials such as GaInNAs for this purpose and although results to date have been poor on account of low minority carrier diffusion lengths [18], a greater understanding of the material and its defects is emerging [19]. Recent progress in growing high-quality lattice mismatched materials may offer a shorter term solution, to the problem of a 1eV junction. While the efficiencies of lattice-matched devices

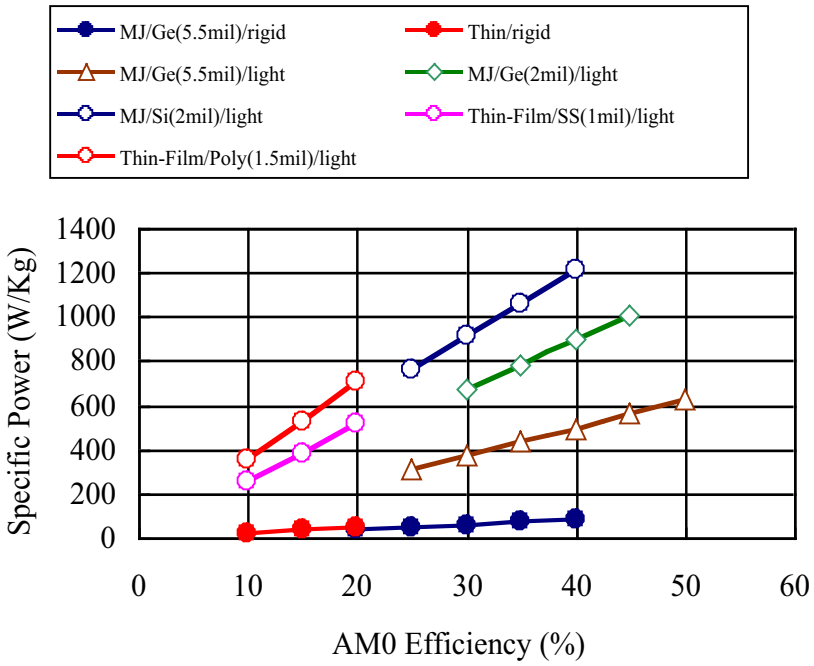

Fig. 8. Specific power vs BOL AM0 efficiency for complete space panels. The filled circles represent conventional rigid panels, while the open symbols represent a light-weight panel technology where the cell weight is the dominant factor.

still exceed those of lattice-mismatch devices, the flexibility offered by the lattice mismatch approach is very attractive. For example, encouraging results on an ambitious 5-junction lattice-mismatched device were recently reported [20].

The substrate material also plays an important role. Traditionally, the choice of GaAs and Ge substrates have constrained the multi-junction solar cell to a limited range of materials, due to the usual requirement for lattice matching. However, the recent progress in growing high quality lattice mismatched materials noted above, frees the choice of substrate to some extent. While Ge provides a more robust substrate than GaAs, further gains could be made by replacing the Ge substrate with a Si. For space, the mechanical strength of Si combined with the high-efficiency and radiation tolerance of the III-V cells would give a highly attractive power to weight ratio when combined with a light-weight panel structure. This is illustrated in figure 8 where the specific power for a complete panel is plotted as a function of BOL AM0 efficiency. The current rigid panel technology is indicated by the filled circles, for both multi-junction cells on thick (5.5mil) Ge substrates and thin devices (e.g. 3mil Si). In this case, the area of the rigid panel dominates the specific power, so multi-junction cells outperform the thin devices [21]. However, if a lightweight panel technology is developed, then the overall specific power becomes dominated by the cell's specific power. Here the choice of substrate for the multi-junction solar cell becomes critical and a move to lighter substrates, such as 2mil Si, is required for the multi-junction cells to maintain superior specific power over the less efficient thin-film devices.

In the longer term, it is worth considering if the multi-junction cell is the only means for achieving high efficiency solar cells. In this respect, the next generation of high-efficiency solar cells is likely to draw from breakthroughs in semiconductor materials. If a material were found where a third (intermediate) band exists in addition to the usual conduction and valance band, then it would be possible to surpass the efficiency of a 2 junction solar cell [22,23]. Various hot carrier approaches have been suggested, some maintaining a high voltage by sustaining the hot carrier population for longer than the carrier collection time [24] with others yielding a high current through impact ionization [25]. The physics of these hot carrier proposals are closely related [26] and yield identical limiting efficiencies. It is interesting to note that some of these concepts were proposed almost simultaneously to the multi-junction solar cell [27], so while developments in compound semiconductor technology have lead to the InGaP/GaAs/Ge multi-junction cell, so it is hoped that advanced semiconductor materials may lead to a practical implementation of these photovoltaic concepts.

5 SUMMARY

Recent progress in high-efficiency multi-junction solar cells has been reviewed, together with the technological improvements that have led to InGaP/InGaAs/Ge multi-junction solar cells with efficiencies of 29.2% under AM0 and 31.7% under AM1.5G. In a mechanical stack configuration, a GaInP/GaAs/InGaAs device holds the world record efficiency of 33.3% under 1 sun AM1.5G. Under concentrated light, efficiencies in excess of 36% have been demonstrated between 100-500X. Near term improvements include the use of an AlInGaP top cell which is projected to raise the AM0 efficiency to 31%.

REFERENCES

[1] Masafumi Yamaguchi. Super-high efficiency III-V tandem and multijunction cells. *Clean electricity from photovoltaics*, 1:347–375, 2001.

[2] J.M. Olson, R.K. Ahrenkiel, D.J. Dunlavy, B. Keyes, and A.E. Kibbler. Ultralow recombination velocity at $Ga_{0.5}In_{0.5}P$/GaAs heterointerfaces. *Appl.Phys.Lett*, 55(12):1208–1210, 1989.

[3] M-J. Yang, M. Yamaguchi, T. Takamoto, E. Ikeda, H. Kurita, and M. Ohmori. Photoluminescence analysis of InGaP top cells for high-efficiency multi-junction solar cells. *Solar Energy Materials and Solar Cells*, 45:331–339, 1997.

[4] H. Sugiura, C. Amano, A. Yamamoto, and M. Yamaguchi. Double heterostructure GaAs tunnel junction for AlGaAs/GaAs tandem solar cell. *Jpn.J.Appl.Phys*, 27:269, 1998.

[5] T. Takamoto, M. Yamaguchi, E. Ikeda, T. Agui, H. Kurita, and M. Al-Jassim. Mechanism of Zn and Si diffusion from a highly doped tunnel junction for InGaP/GaAs tandem solar cells. *J.Appl.Phys.*, 85(3):1481, 1998.

[6] T. Takamoto, T. Agui, E. Ikeda, and H. Kurita. High efficiency InGaP/$In_{0.01}Ga_{0.99}$As tandem solar cells lattice matched to Ge substrates. *Solar Energy Materials & Solar Cells*, 66:511–516, 2001.

[7] T Takamoto. Lattice matched solar cell and method for manufacturing the same. *U.S. Patent*, 6,300,558, 2001.

[8] T. Takamoto, T. Agui, E. Ikeda, and H. Kurita. High efficiency InGaP/InGaAs tandem solar cells on Ge substrates. In *Proc. 28th IEEE PV Specialists Conference*, pages 976–981, USA, 2000. IEEE.

[9] D. Jung, C. A. Parker, J. Ramdani, and S. M. Bedair. AlGaAs/GaInP heterojunction tunnel diode for cascade solar cell application. *J. Appl. Phys.*, 74(3):2090–2093, 1993.

[10] T. Takamoto, E. Ikeda, H. Kurita, T. Tanabe, S. Tanaka, H. Matsubara, Y. Mine, S Takagishi, and M. Yamaguchi. InGaP/GaAs and InGaAs mechanically stacked triple-junction solar cells. In *Proc. 26th PV Specialists Conference*. IEEE, 1997.

[11] K Takahashi, S. Yamada, Y. Minagawa, and T. Unno. Characteristics of $Al_{0.36}$GaAs/GaAs tandem solar cells with pp^-n^-n structural AlGaAs solar cells. *Solar Energy Materials and Solar Cells*, 66:517, 2001.

[12] T. Yamada, A. Moto and S.Tanaka, T.Tanabe and S.Takagishi. to be published.

[13] T. Takamoto, T. Agui, K. Kamimura, M. Kaneiwa, M. Imaizumi, S. Matsuda, and M. Yamaguchi. Multi-junction solar cell technologies - high efficiency, radiation resistance and concentrator applications. In *Proc. 3rd World Conference and Exhibition on Photovoltaic Energy Conversion*, 2003.

[14] Aurangzeb Khan, Masafumi Yamaguchi, Jaques C. Bourgoin, and Tatsuya Takamoto. Thermal annealing study of 1MeV electron-irradiation induced defects in n^+p InGaP diodes and solar cells. *J.Appl.Phys*, 91(4):2391–2397, 2002.

[15] Nethaij Dharmarasu, A. Khan, Masafumi Yamaguchi, Tatsuya Takamoto, Takeshi Ohshima, Hisayoshi Itoh, Mitsuru Imaizumi, and Sumio Matsuda. Effects of proton irradiation on n^+p InGaP solar cells. *J.Appl.Phys.*, 91(5):3306–3311, 2002.

[16] Nethaij Dharmarasu, Masafumi Yamaguchi, Aurangzeb Khan, Takashi Yamada, Tatsuya Tanabe, Shigenori Takagishi, Tatsuya Takamoto, Takeshi Ohshima, Hisayoshi Itoh, Mitsuru Imaizumi, and Sumio Matsuda. High radiation-resistant InGaP, InGaAsP and InGaAs solar cells for multijunction solar cells. *Appl.Phys.Lett.*, 79(15):2399–2401, 2001.

[17] S.R. Kurtz, P. Faine, and J.M. Olson. Modeling of 2-junction, series-connected tandem solar-cells using top-cell thickness as an adjustable-parameter. *J. Appl. Phys.*, 68(4):1890–1895, 1990.

[18] J.F. Geisz and D.J. Friedman. III-N-V semiconductors for solar photovoltaic applications. *Semicond. Sci. Technol.*, 17:769–777, 2002.

[19] S.B. Zhang and S. Wei. Nitrogen solubility and induced defect complexes in epitaxial GaAs:N. *Phys.Rev.Lett.*, 86(9):1789–1793, 2001.

[20] F. Dimroth, C. Baur, M Meusel, S. van Riesen, and A.W. Bett. Multi-junction III-V solar cells for space applications. In *Proc. 3rd World Conference and Exhibition on Photovoltaic Energy Conversion*, 2003.

[21] Navid S. Fatemi, Howard E. Pollard, Hong Q. Hou, and Paul R. Sharps. Solar array trades between very high-efficency multi-junction and Si space solar cells. In *Proc. 28th IEEE PV Specialists Conference*, pages 1083–804, USA, 2000. IEEE.

[22] A. Luque and A. Martí. Increasing the efficiency of ideal solar cells by photon induced transitions at intermediate levels. *Phys.Rev.Lett.*, 78(26):5014–5017, 1997.

[23] P. Würfel. Improvement of solar cell efficiencies by impurity transitions. *Sol. Energy Mater. Sol. Cells*, 79(1):153–161, 2003.

[24] Robert T. Ross and Arthur J. Nozik. Efficiency of hot-carrier solar energy converters. *J.Appl.Phys*, 53:3813–3818, 1982.

[25] P. Würfel. Solar energy conversion with hot electrons from impact ionisation. *Sol. Energy Mater. Sol. Cells*, 46(1):43–52, 1997.

[26] Jenny Nelson. *The physics of solar cells*. Imperial College Press, London, U.K., 2003.

[27] M. Wolf. Limitations and possibilities for improvement of photovoltaic solar energy convertors. *Proc. IRE*, 48:1246–1263, 1960.

MULTI-JUNCTION GaAs PHOTOVOLTAIC ASSEMBLY TECHNOLOGY FOR VERY SEVERE LEO ENVIRONMENT MISSIONS

A. Caon, C. Signorini
ESA/ESTEC, Noordwijk, The Netherlands, 2200AG

A. Bals, K. Dettlaff
EADS Astrium, Munich, Germany, 81663

Abstract

The paper reports the results of a development and testing programme dedicated to photovoltaic assembly technology, based on multi-junction GaAs/Ge solar cells, for the very severe low earth orbit environments typical of some earth observation missions.
The selection of material, components and technologies are discussed, with respect to the environmental requirements:

- a combination of high number of thermal cycles (about 25,000) and extreme thermal conditions (between +160°C and -170°C);
- all parts and materials had to be ATOX (Atomic Oxygen) resistant or had to get an ATOX protection.

In particular, the paper reports about the optimisation of the welding process on two types of ATOX resistant solar cell interconnectors, gold (Au) and silver plated molybdenum (MoAg) and the evaluation of an ATOX protection process for the panel structure front side (Kapton face sheet).
Finally, the cell characterization and the extensive environmental tests performed at cell, SCA (Solar Cell Assembly) and coupon level are described.
The results of the evaluation show how the MoAg interconnector passed all tests successfully, while the Au-interconnector requires further optimisation for very severe LEO environments

1. INTRODUCTION

For orbits below 650 km the density of Atomic Oxygen is such, that ATOX sensitive parts and materials of the solar array must be either replaced by ATOX resistant materials or they have to be protected by an ATOX resistant coating. As far as EADS Astrium solar arrays are concerned, special care has to be taken for the insulating 50 µm Kapton top-layer of the panel substrate and for the solar cell interconnectors and bus bars which are made of silver (Ag) for all Geostationary Earth Orbit (GEO) applications and all Low Earth Orbit (LEO) applications in orbits higher than 650 km.
In this R&D activity, as a reference, it was considered an orbit characterized by an altitude of 250km, an inclination of 96.5° and an Atomic Oxygen fluence of 10^{23} cm^{-2} per year; a mission lifetime of about 3 years was taken into account.
In addition to the ATOX environment, the solar array components have to withstand a high number of thermal cycles (up to 25.000) in a temperature range which goes up to +160°C / -170°C.
In the following, some design solutions, compatible with the very sensitive GaAs Triple Junction solar cells, are presented. The design was tested on several coupons with different panel substrates, which were submitted to thermal cycling.

2. PROCESSES AND MATERIALS

2.1 ATOX Protection of Kapton

There are ATOX resistant Kapton foils on the market, however it was decided to use a standard Kapton foil and to protect it with an ATOX resistant silicone adhesive; this process is very flexible because it allows the use of a standard panel skin. A homogeneous layer of siliconic adhesive was obtained using a glass fibre sheet of the same thickness (100µm) and bonding it with the siliconic resin on the Kapton layer by means of a complex curing process; this adhesive (RTV S 691 from WACKER) is used for the solar cell lay-down and is very well known. This additional layer of glass fiber and adhesive has an additional positive effect: it helps to decouple the sensitive solar cells from possible stresses caused by the panel structure.

2.2 ATOX resistant solar cell interconnectors and bus bars

The standard interconnector used at EADS Astrium is a 12.5 µm thick Ag interconnector which is produced (punching and stress relief bending) out of a silver ribbon by a fully automated solar cell - interconnector welding machine. The most cost effective solution, which is considered, consists of replacing the ATOX sensitive silver by ATOX resistant gold and to keep the interconnector manufacturing process unchanged. These Au interconnectors were successfully tested and used in the past on 200 µm thick Silicon solar cells and 200 µm thick single junction GaAs/Ge cells for temperature ranges of +100°C / -100°C and up to 25000 thermal cycles. However, there were indications that with the much more severe temperature range in combination with the 160 µm thick GaAs Triple Junction cells the Au interconnectors with the actual design might go over there limit.
A more expensive solution is a MoAg interconnector, which has already been used on the HUBBLE SPACE TELESCOPE solar array and on several other Silicon (Si) solar arrays for LEO missions. This interconnector consists of 15 µm Mo and a 5µm Ag plating on each side; the silver plating is necessary to make the interconnector weldable. After welding and lay-down of the solar cells the weld area is protected by the RTV laydown adhesive while the exposed Ag will be eroded by the ATOX and will flake away; for missions with very sensitive optical instruments which do not allow this flaking, it is possible to get the interconnectors with the Ag etched away in areas which are not used for welding.
These robust MoAg interconnectors had never been used before on the much more sensitive 160 µm GaAs/Ge Triple Junction cells. To reach a good yield for the interconnector welding operation, it was necessary to optimise the weld electrodes as well as the weld parameters (electrodes pressure, weld duration and energy).
The test hardware has been equipped with both Au and MoAg interconnectors.
At the solar cell string ends in the standard design for high LEO and GEO, a 50 µm thick, ATOX sensitive, Ag bus bar with stress relief loops is used as an interface to the string cabling.
As an alternative a 50µm Au bus bar with the same design as the standard Ag bus bar was selected and tested.

2.3 Type of tested solar cells

The welding optimisation activity was focused on different solar cells:

- The GaInP2/GaAs/Ge Triple Junction cells named GAGET1 from RWE Space, which were based on an EMCORE epitaxy and which had an integral protection diode which is protecting the adjacent cell.
- The GaInP/GaAs/Ge Triple Junction cells named GAGET 2 ID 2 cells from RWE Space, which were based on a Spectrolab epitaxy.

The several coupons which were submitted to long term thermal cycles were equipped with the GaInP/GaAs/Ge Triple Junction cells named GAGET 2 ID cells from RWE Space, which were based on a Spectrolab epitaxy.
One additional coupon equipped with GaInP/GaAs/Ge Triple Junction cells named ATJ solar cells, from EMCORE and characterized by a monolithic Schottky protection diodes was added in the thermal cycling test.

3. TESTING AND PRE-QUALIFICATION OF CELLS, SCA'S AND COUPONS

3.1 **Testing of cells and SCA's**

The purpose of this task was to verify the optimisation of the parallel gap resistance welding process applied to the above mentioned Triple Junction GaAs based solar cells and the Gold and Silver plated Molybdenum interconnectors. Several iterations, based on the adjustments of the welding process including the electrode design and the verification testing, were done to achieve a fine tuning of the existing welding process to the multi-junction solar cells.
The subsequent validation of the complete solar cell assembly process was performed on the basis of the following test plan:

- Visual Inspection of welded solar cell and SCA
- Electrical Performance measurements of cell and diode
- SAM (Scanning Acoustic Microscope) investigation of weld spots
- Pull test at Beginning of Test (BOT) on cells and SCAs
- Pull test at End of Test (EOT) on cells and SCAs
- Up to 7500 thermal cycles –100°C / 160°C

The Test Articles were 10 GAGET 1 solar cells integrated with Au interconnectors (see Fig.1) and 20 GAGET 2 ID solar cells integrated both with Au and with MoAg interconnectors (see Fig.2); the used coverglasses were the CMX100 μm for the GAGET 1 solar cells and the CMO 100 μm for the GAGET 2 solar cells. The size of the cells was 40 mm x 80 mm with cropped corners.
The results of the testing activity showed the optimization of the welding processes both for the Au and MoAg interconnectors. In particular, the visual inspection and the electrical performance measurements of the cells highlighted the welding process and the thermal loads derived from the thermal cycling do not cause any degradation of the cells, neither mechanical (e.g. cracks) nor electrical. Furthermore, the SAM pictures demonstrated the excellent repeatability of the welding and the non degradation of the welding joints in the thermal environment; finally, the pull force values (4N for Au interconnectors at 90° and 10N for MoAg at 0° with respect to the solar cell plane) showed the good quality of the joints and the non degradation of them in the thermal environment.

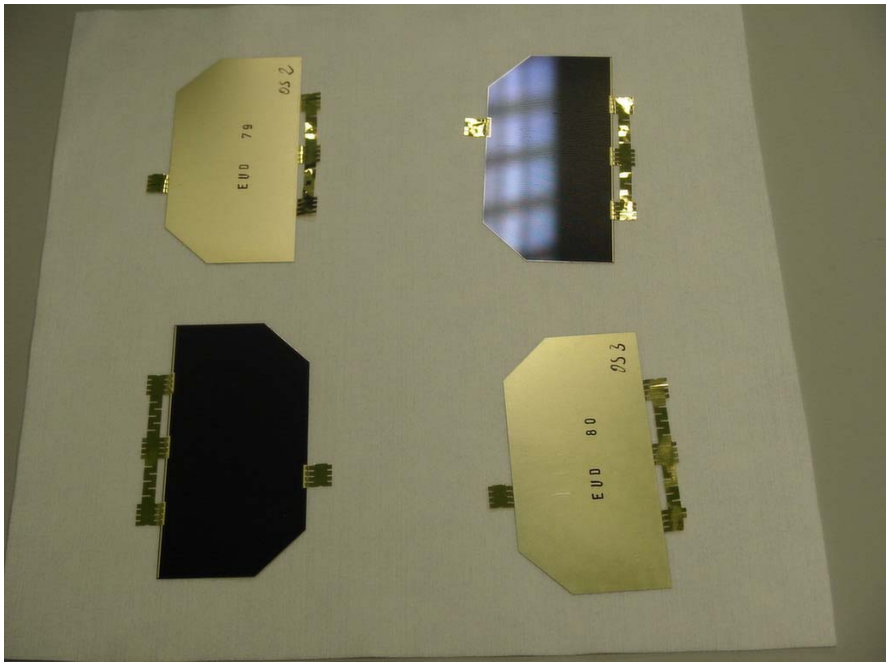

FIG.1: GAGET 1 SCA with Au interconnector

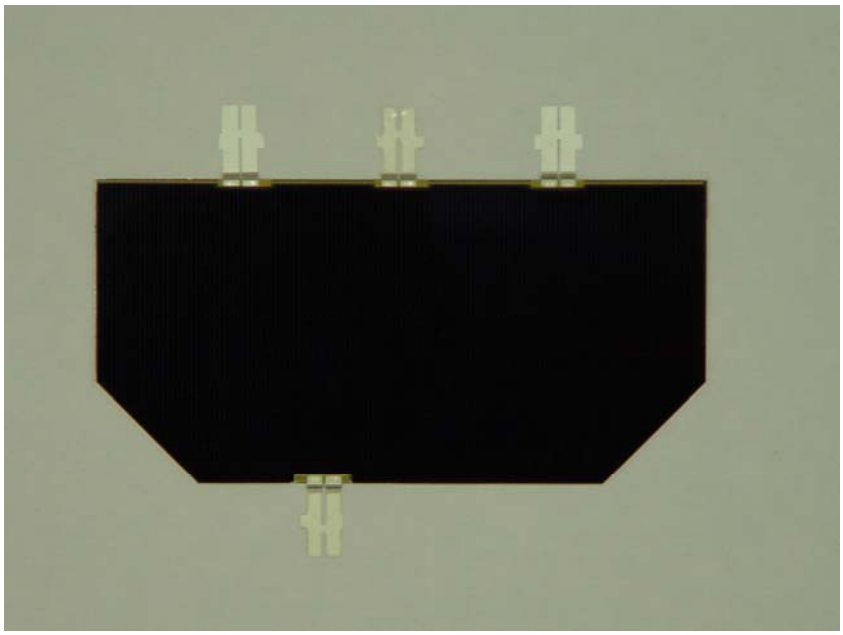

FIG. 2: GAGET 2 ID with MoAg interconnector

3.2 Test of Coupons

3.2.1 Pre-Testing

In a first pre-test step, 4 coupons characterized by different sizes, substrate and interconnector types have been build and tested. The aim of this test was to check the capability of all components and processes (including the demonstration of SCA and bus bar repair) to withstand a thermal environment characterized by 6,030 thermal cycles (30 cycles +160°C/-170°C, 6000 cycles +160°C/-100°C) and to verify their electrical and mechanical behaviour. Coupons 1 & 4 have been submitted to additional 9000 cycles reaching the 15000 cycles.

The test coupons were equipped as follows:

FRONT SIDE

- GaAs Solar Cells RWE (GAGET I) (80 mm x 40 mm, 160 µm, with integrated diode, cropped corner)
- GaAs Solar Cells RWE (GAGET II) (80 mm x 40 mm, 160 µm, with integrated diode, cropped corner)
- One diode strip per coupon
- Coverglass from Thales Space Technology (TST) CMO 100 AR
- Gluing spot for solar cells to structure,
- Cell Interconnectors 12,5 µm gold and 25 µm MoAg
- Bus bars 50 µm gold
- Kapton insulated wire type
- APL (Atox Protection Layer) consisting of RTV-S 691 and glass filament
- The front side layout was characterized by one complete string of 14 cells (Coupon 1,4), 1 cell (Coupon 2)

and 8 cells (Coupon 3)

- The strings of the Coupons 1-3 and the Coupon 4 (String B+C) were manufactured with 12.5µm gold cell interconnector and 50µm gold bus bars while the string A of the Coupon 4 was realised with 25µm MoAg cell interconnector

REAR SIDE

- Kapton insulated wire type AWG 20 and 22
- Blocking Diode 1N5417
- Bleed Resistor RWR 89 2,8 kΩ
- LRB (Line Reduction Board)
- Cable clamps with conductive gluing spots

After thermal cycling the ATOX Test (Atomic Oxygen Exposure) was performed on Coupon 2 (Au interconnector). The aim of the test was to determine if there would be any degradation in the materials on the surface of the array after exposure to a reduced atomic oxygen fluence of approximately $2x10^{20}$ atoms cm $^{-2}$. The average beam velocity during the exposure was 7.4 ± 0.4 kms^{-1}, the background pressure was approximately 5 x 10^{-5}mbar and the temperature of the sample plate was 23±3°C.
Using high resolution optical imaging and scanning electron microscopy, no discernible degradation of the exposed materials due to atomic oxygen erosion could be detected at the magnifications used (see Fig.3).
The ATOX resistivity of the MoAg interconnector was already demonstrated in previous programs.

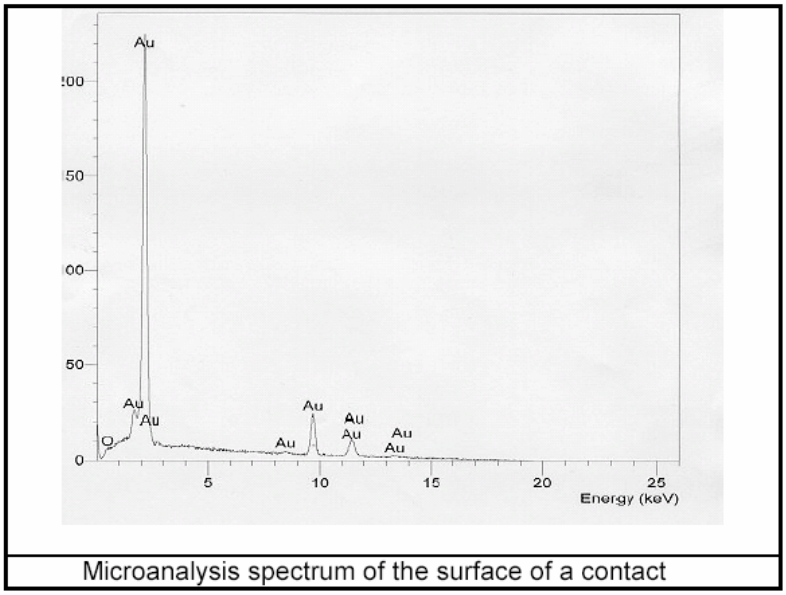

Fig. 3 Microanalysis spectrum of the surface of an Au-contact

After completion of all testing, the electrical performance did not change more than 3% at operational voltage, (except for the strings with gold interconnectors on coupon 4 showing some cracks on some interconnector fingers). All parts, except the Au interconnector on the coupons have passed the pre-test program successfully.

3.2.2 Pre-Qualification Testing with Coupons 5 & 6

The aim of this test was to demonstrate the capability of all components, processes (including the demonstration of SCA repair) to withstand a thermal environment extended up to 22,545 thermal cycles of which 45 cycles with extreme high/low temperature of +160°C/-170°C and 22,500 cycles with a temperature range tailored for a specific mission (1800 cycles +160/-100°C, 7200 cycles +150°C/-100°C, 900 cycles +160°C/-80°C, 3600 cycles +150/-80°C, 1800 cycles +160/-0°C, 7200 cycles +150/-0°C).

The 2 coupons represented a flight panel especially designed for high temperatures with flight parts, processes and electrical connection that could be used for future LEO solar array. The front side of the coupon 5 (see Fig.4) was covered with RWE GaAs Triple Junction (GAGET II) solar cell assemblies and for the coupon 6 EMCORE Triple Junction cells have been used (see Fig.5). On both coupons, the SCAs had both Au interconnectors and MoAg interconnectors (see pictures below).

The cell lay down was divided into two strings. The string 1 was manufactured with Au interconnector while the string 2 with MoAg interconnector; the termination tabs to the string ends were made of Au.

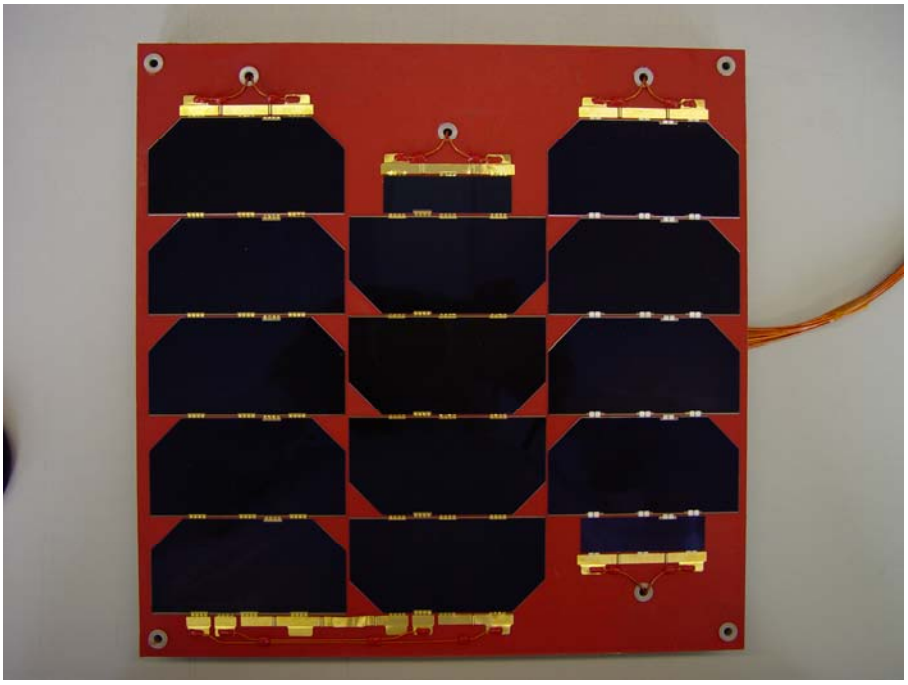

Fig.4: Front side of Coupon 5

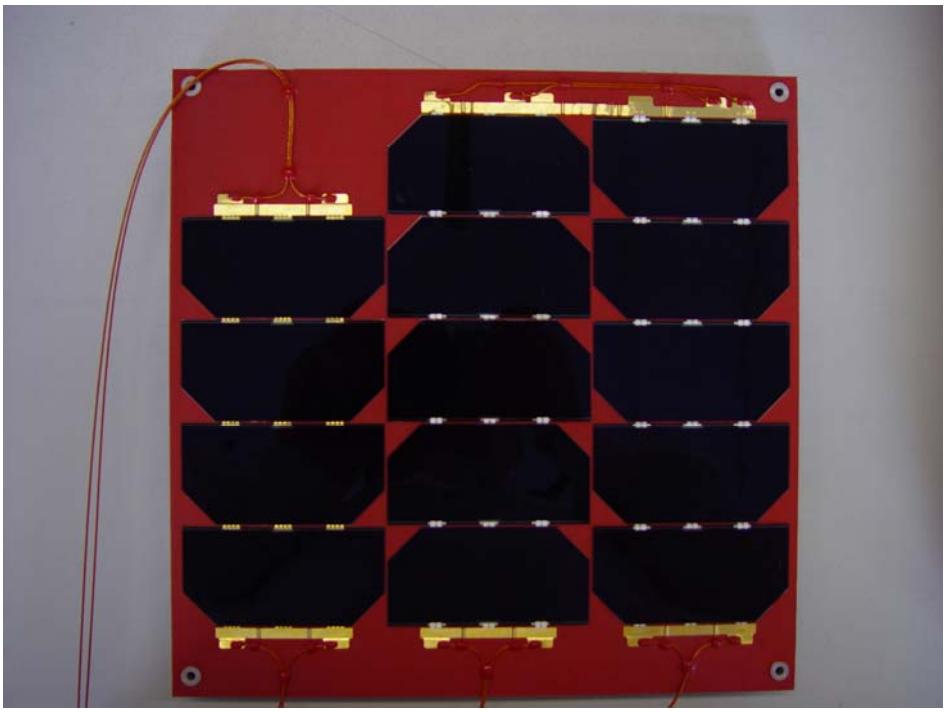

Fig.5: Front side of Coupon 6

The rear side of coupon 5 (see Fig.6) was covered with harness, diode, resistor, LRB and cable clamps.

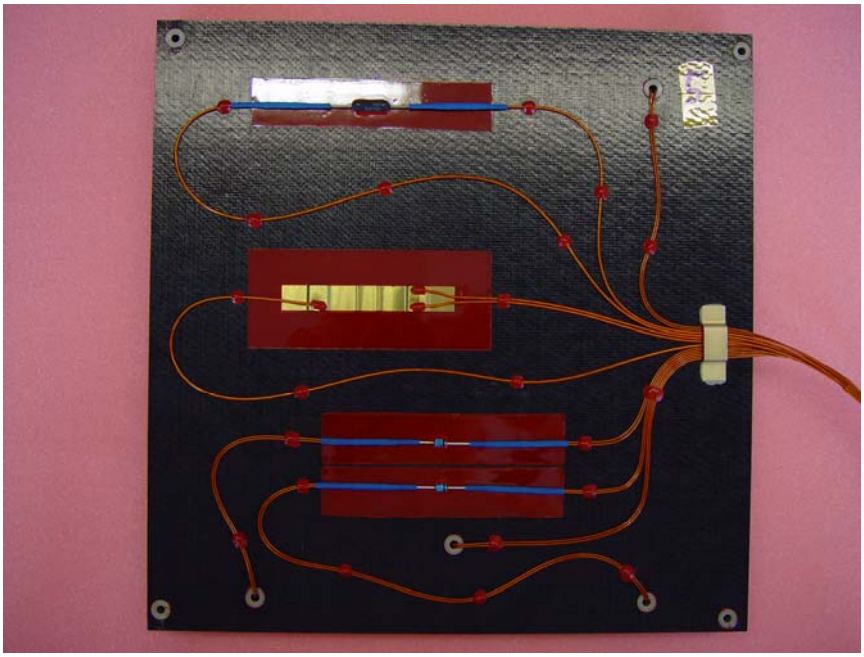

Fig.6: Rear side of Coupon 5

The detailed list of the components of the two coupons is reported here below:

FRONT SIDE

- 13 GaAs Solar Cells GAGET II RWE/SPL, 40 mmx80 mm, 160 µm with cropped corner, BOL Efficiency (Eff.) of 26.8% at 28°C with integrated diode on Coupon 5
- 2 diode strip on Coupon 5
- 14 GaAs Solar Cells ATJ Emcore, 40 mmx80 mm, 160 µm, with cropped corner, BOL Eff. 27.0% at 28°C with monolithic Schottky diode
- Coverglass TST CMO 100 AR (40.15 mm x 80.15 mm, 100 µm, with cropped corner)
- Gluing spot for solar cells to structure**,** thickness 80 µm
- Interconnector Au 12.5 µm
- Interconnector MoAg 25 µm
- Bus bars Au
- Kapton insulated wire type AWG 24 (SPL 10-24), 22 (SPL 10-22)
- ATOX protection layer (RTV S691 + glasfilament)

REAR SIDE

- The rear side cable harness was manufactured with different size of American Wire Gauge (AWG 20/22 connected to the diode (welded) resistor (welded), LRB (welded) and cable clamps in welding and crimping version (for testing leads only).
- Kapton insulated wire type AWG 20 (SPC 10-20) and 22 (SPL 10-22)
- Blocking Diode 1N5417
- Cable clamps with conductive gluing spots
- Resistor RWR 89 2.8 kΩ
- LRB

The coupons have been submitted to the following tests:

- Inspections and electrical performance measurements
- Insulation measurements & continuity measurements
- 5 Thermal vacuum cycles –170°C / 160°C (before and the thermal cycling)
- 45 Thermal cycles –170°C / 160°C
- 22500 Thermal cycles up to–100°C / 160°C

The main results are summarized here below:

After completion of all testing the electrical performance measurement did meet the requirement only for the MoAg string; the value changed for the string with Au-interconnector more than 3% at operational voltage due to some cracks on some interconnector fingers.

A new replacement method for SCAs with MoAg interconnector was included and passed the pre-qualification successfully.

One cell hairline crack has been detected, which had no impact on the electrical performance.
All parts, except the Au-interconnectors, on the coupons (front and rear side) have passed the pre-qualification program successfully.

4. Conclusions

The test performed at the end of the development programme demonstrated that the assembly technology applied to the multi-junction GaAs/Ge solar cells has reached an excellent level of confidence, for very demanding low earth orbit environment.
The welding process has been optimised for the Triple Junction GaAs solar cells with both Au and MoAg interconnectors.
The design of the MoAg interconnector has withstood without any failure or degradation the thermal fatigue derived from the considered LEO environment testing.
The actual design of the Au interconnector has shown a limit of applicability with respect to the chosen cell thickness and panel substrate configurations, in combination with the considered LEO environment; on the basis of these results, further optimisation of the Au interconnector design should be considered in the future R&D activities, in order to extend its potential use for these types of solar array and missions.
The ATOX protection process applied to the kapton insulation layer of the panel front side has been successfully tested. This method is very flexible because it allows the use of a standard panel skin and provides an additional positive effect because it helps to decouple the sensitive solar cells from the possible stresses caused by the panel structure.
Finally, it is important to underline that the selected Multi-Junction solar cells and photovoltaic assembly processes have been demonstrated to be compatible with the chosen panel structures in a very demanding LEO environment.

CURRENT STATUS OF PHOTOVOLTAIC DEVELOPMENT AT AFRL

John Merrill, Paul Hausgen, Donna Senft, and Pawel Tlomak
Air Force Research Laboratory, Space Vehicles Directorate
Kirtland AFB, NM USA 87117-5776

ABSTRACT: Advances in design and manufacturing technology of crystalline multijunction solar cells have continued to push efficiencies higher. Triple junction cells with 28% efficiency are now available to the user and 30 % prototype cells have been demonstrated. Development of thin-film solar cell arrays is being aggressively funded for next-generation high power space platforms. Initial modules of thin-film photovoltaics comprised of amorphous silicon and $Cu(In,Ga)Se_2$ devices have been demonstrated. Space-compatible technologies for thin-film cell integration, contacts, and protective coatings are being developed. Cell-level development efforts aimed at increasing performance are continuing and progress is being made toward a 15% efficiency goal for cells on lightweight, flexible substrates. High temperature polymer substrates for $Cu(In,Ga)Se_2$ cells have been demonstrated. Thin-film solar arrays are promising for 3-5 times reductions in specific power (W/kg), array cost ($/W), and stowed volume ($W/m^3$) compared to state-of-the-art rigid panel solar arrays. A proposed thin-film solar cell flight experiment is also discussed.

1. INTRODUCTION

Rigid panel arrays populated with crystalline solar cells are currently the only practicable power generation option for earth orbit missions, with multijunction crystalline solar cells the primary option for DoD and most commercial spacecraft. Air Force Research Lab (AFRL) multijunction solar cell programs continue to increase the efficiency of these cells at a steady rate. Multijunction solar cells can be directly retrofitted into existing arrays and offer increased power, mass, and fairing volume budgets for spacecraft designers. Triple junction cells with 28 % efficiency [1] are now commercially available. Impact of efficiency increase is specific to a given mission/spacecraft design, but one recent study showed a 30 % increase in efficiency (27 to 35 %) would result in ~ 70 % increase in power available to the payload.

FTFPV (Flexible Thin-Film Photovoltaics) have been touted as the next-generation technology for space power [2,3] for their advantages over crystalline multijunction cells. With launch costs exceeding $10,000/kg to LEO, the specific power of the solar array is often a critical metric. Current solar arrays comprised of multijunction solar cells grown on single crystal wafers, mounted on Al honeycomb panels, and protected with a relatively heavy cover glass have specific power levels of less than 100 W/kg. In addition, multijunction solar cell arrays can create problems in terms of stowage volume for high power spacecraft (8-13 kW/m^3). Thin-film photovoltaic arrays, where the photovoltaic materials are deposited on flexible, lightweight metal foils or polymers, are capable of an EOL specific power of 235 W/kg or greater. Thin-film arrays are ultimately projected to have efficiencies of 15% and a stowed volume on the order of 45-60 kW/m^3.

FTFPV technology has advantages over state-of-the-art technology in terms of cost and radiation resistance in addition to mass and stowage volume. Thin-film deposition processes are low-cost and have been developed for the terrestrial market, where the long-term cost target is $1/W. The two major types of thin-film solar cells are amorphous silicon (a-Si) and polycrystalline $Cu(Ga,In)Se_2$ (CIGS). Space-qualified adaptations of these terrestrial products are more expensive than their terrestrial counterparts, but costs are not expected to exceed $100/W for FTFPV arrays. Multijunction panel costs typically exceed $400-500/W. CIGS solar cells in particular have been found to be radiation resistant, with post-irradiation results that compare to InP.

Lightweight FTFPV arrays will be enabling for certain classes of high power satellites and microsatellites. A microsatellite having a total mass of less than 100 kg and a power requirement of 650 W, for example, will need to allocate 14% of its total mass to the solar array using a crystalline multijunction array. A thin-film array with a conservative specific power of 255 W/kg could reduce the requirement for the solar array to 2.5% of the total mass. For a very large 100 kW system, a thin-film solar array would reduce the mass by over 1700 kg and the stowage volume by over 8 m^3; this mass and volume could be reallocated to the payload.

To realize the full advantages from FTFPV technology, first the technology to construct space qualified modules from thin-film cells must be developed. Second, specialized lightweight array support structures must be designed and developed. Finally, attention must be paid to the issues of space environmental effects on thin-film photovoltaics and the protective layers necessary to ensure long-term reliable operation.

2. MULTIJUNCTION SOLAR CELL DEVELOPMENT

State-of-the-art multijunction solar cells are now commercially available from EMCORE Corp. and Spectrolab, Inc. with nominal efficiencies of 28%. Prototype triple junction cells (4 cm^2), also with the GaInP/GaAs/Ge device structure, have been demonstrated at efficiencies of up to 30%. AFRL programs are pursuing multiple technical approaches to increase cell efficiency beyond 30%. Lattice-mismatch GaInp/GaInAs/Ge solar cells have been demonstrated at 28.8% efficiency with an ultimate practical efficiency of 31.5% predicted. The second technical approach involves the addition of a 1.0 eV-bandgap nitride-material junction. Previously, AFRL programs have focused on developing InGaAsN material to be used in a 4 junction device. The material has proven to be current limiting in the 4-junction cell design due to defects in the material, which has prevented the 4-junction design from reaching the predicted performance levels. A 5-junction approach (GaInP/GaInP/GaAs/GaInNAs/Ge) splits the top junction into two separate junctions, yielding a higher open circuit voltage, while reducing the current to levels capable of being produced by the InGaAsN junction. The overall effect is higher efficiency, with projections of >34 % and an open circuit voltage of 4.7 V.

3. THIN-FILM ARRAY DEVELOPMENT AND SPACE QUALIFICATION

The goal of AFRL thin-film solar cell programs is the development of the technology necessary to achieve reliable operation of thin-film arrays in space. There is still significantly more work to do to demonstrate a space qualifiable array based on thin-film photovoltaics. Multijunction solar cell development yields a drop-in replacement using existing solar array designs; to take advantage of the benefits of thin-film solar cells, new solar arrays must be developed which are lightweight but have the stiffness necessary for array pointing and maneuvering. The challenges to accomplishing this goal are three-fold: 1) improvements in cell technology on lightweight substrates compatible with space use, 2) integration of cells into modules and the design of arrays, and 3) space qualification of the array blankets. AFRL has ongoing thin-film solar cell and module development programs focused on these objectives. The initial progress in the three areas of FTFPV blanket development and plans for future work are detailed below.

3.1 Cell Development

In contrast to crystalline wafer solar cells that were developed initially for space and eventually adapted to terrestrial applications, the thrust behind the development of thin-film solar cells has come from the terrestrial market, primarily because of the potential for lower production costs. As a result, some commonly used thin-film substrates and materials are unsuitable for space applications. For example, CIGS modules with efficiencies of 12% are commercially available with 3.2 mm-thick glass substrates. Less fragile substrates such as metal foils and Kapton films are more suitable for space. EVA and other polymeric encapsulants have been developed to protect thin-film cells from the effects of weather, but are insufficient for shielding arrays from the space environment.

AFRL-funded cell development programs are intended to make changes in cell technology geared to space application by increasing cell specific power via tilting performance/cost tradeoffs towards higher efficiencies and supporting the development of cell production processes with lightweight substrates such as metal foils and polyimide. A summary of the cell development programs for the two most promising thin-film technologies, a-Si and CIGS alloys, is listed in Table I.

For a-Si, the more mature technology of the two, the challenges have been to increase efficiencies above the 10% threshold, to integrate cells into modules, and to use lightweight substrates. United Solar Systems (USS) has increased the efficiency of their product to 9.8% for 929 cm^2 (1 ft^2) cells and to 12% for small cells by the addition of an internal reflector layer to their triple junction cells and by reducing the a-Si deposition rates.[4] At the same time, USS has decreased the weight of their terrestrial product by thinning the 127 μm stainless steel substrate to 25 μm. These improvements have increased the specific power at the cell level to 680 W/kg. Similar efficiencies have been demonstrated on polymer substrates at the research and development level. These polymer substrate cells have a cell level specific power >1000 W/kg.

CIGS technology, while being less developed than a-Si, has the advantage of higher efficiencies than a-Si with the promise of further increases. The main challenge has been to develop a high efficiency CIGS cell on metal foil substrates. Since high temperature processing (>500 ºC) is currently necessary to yield the optimal efficiencies in CIGS, our efforts have concentrated on metal foil substrates. Efforts are also underway to develop high temperature polymer films that can withstand the (>500 ºC) processing temperature.

International Solar Electric Technologies (ISET) has successfully achieved efficiencies of 10.2% for 10 cm^2 cells on Mo foil substrates using a non-vacuum process. DayStar Technologies has achieved efficiencies of 15.2% for 1.1 cm^2 cells and >11% for the larger 24 cm^2 cells using batch evaporation processing. ITN Energy Systems, using a roll-to-roll evaporation production line has achieved efficiencies of 11% for sample sizes of 0.68 cm^2 and 7% for 58 cm^2 samples.

3.2 Cell Integration and Array Design

Integration and array design involves producing a prototype thin-film array from individual cells, including cell layout, electrical contacts and interconnects, wire harnesses, and method of array deployment. A lightweight thin-film array support structure is being designed under the AFRL PowerSail program. Under this program, special attention is being paid to array dynamics and deployment mechanisms that will enable >20 kW arrays. Under the PowerSail FTFPV blanket qualification program (Table I), a prototype thin-film blanket as shown in Fig. 1 was fabricated. CIGS cells from ISET and a-Si cells from USS on 25 μm-thick metal foil substrates were spot-welded together to form the blanket without the use of a separate blanket support material. Hinges were developed so that the blanket can be stowed in a Z-fold configuration. During the initial round of blanket development, the cells were tested for adhesion using tape tests and under thermal cycling conditions for GEO orbits. Additional designs for a roll-out array are being constructed.

More extensive array blanket development programs are continuing under Dual Use Science and Technology (DUS&T) programs. These two 3-year programs with Lockheed Martin and Boeing Satellite Systems involve 50-50% cost sharing between industry and government and will focus on the design and development of FTFPV modules.

The Lockheed Martin DUS&T program, with sub-contractors ISET and USS, has identified 5 kW, 10 kW, and larger thin-film array designs using stabilized 10-15% efficient cells. The module electrical architectures have been optimized and include an appropriate number of bypass and blocking diodes. The program is working to optimize cells for space, and has generated specifications for module strength and structural support requirements. The effort has resulted in the technology to construct a 32 ft^2 module comprised of 30 USS a-Si solar cells. Smaller 3-cell modules have also been fabricated. A 3-cell module and individual cells have been cycled from -175 °C to +120 °C for 100 cycles and 1100 cycles, respectively. Cell efficiencies after thermal cycling were within 97% of pre-test values.

The Boeing DUS&T program has identified 1kW, 20 kW, and 50 kW arrays suitable for thin-film blankets. The Boeing program is also developing modules, their electrical architectures, and structural support requirements. Sub-contractors on the Boeing program are USS, and ITN Energy Systems. The program has produced a comprehensive requirements document covering all aspects of the thin-film blanket, array and interconnect design.

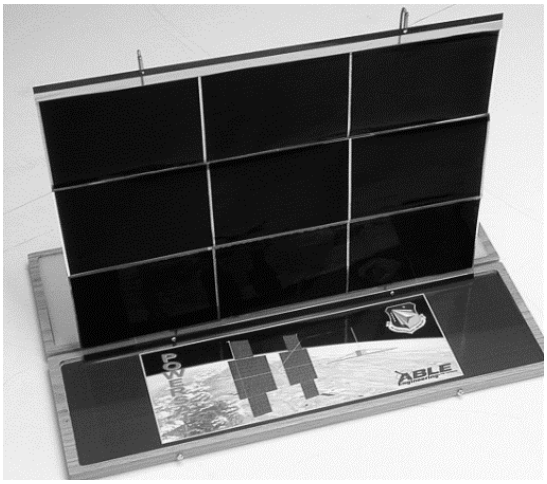

Figure 1: Prototype for the FTFPV module design under the PowerSail blanket qualification program.

3.3 Space Qualification of FTFPV

Despite some limited flight tests of thin-film solar cells, including space qualification of USS cells by Fokker and KVANT [5], more rigorous and comprehensive testing of FTFPV cells and modules is needed to provide design data for degradation rates and to uncover any potential failure mechanisms. Crystalline multijunction solar cells are typically covered with glass that protects the cells against low energy protons, atomic oxygen, and micrometeorite damage. Thin-film cells, to maintain their flexibility and avoid the weight penalty of the glass will be protected with a multi-purpose protective coating, the development of which is discussed below. Space qualification will involve testing of this encapsulant along with the modules it covers.

One concern is that the integrated cells withstand thermal cycling. Steep thermal gradients can cause buckling in PV blankets, and interconnect strength must withstand the strain. Thermal cycling has also been responsible for the delamination of cells from substrates and degradation in electrical contact materials, particularly conductor-filled epoxies.

Although thin-film solar cells have been shown to be more radiation-resistant than crystalline cells and radiation damage has been found to anneal from a-Si cells at 70-80 ºC, comprehensive tests to measure and model the radiation response of both a-Si and CIGS [6,7] materials are needed. Previous radiation testing has shown that the radiation resistance of CIGS exceeds that of a-Si.[8] In addition, both thermal and light-induced annealing rates have been quantified for CIGS cells on glass substrates.[8]

As part of space qualification, the AFRL has an on-going program for the evaluation of radiation hardness of FTFPV solar cells. The goal of this program is to develop a predictive model and to demonstrate survivability in the different space environments defined for given missions. The model is expected to be able to predict the end-of-life performance of FTFPV solar cells for a given orbit. Planned experiments will expose both a-Si and CIGS solar cells to both electrons and protons at different energy levels and fluences. Experimental conditions are based on 1.) potential orbit environments, and 2.) data needed to support model development. Experiments will measure rates of annealing, light assisted annealing, and combined affects. Uncoated CIGS and a-Si cells from a variety of manufacturers have been irradiated by electrons and protons of several different energies. Irradiation experiments will be repeated for coated cells, using cells coated by two or more materials/processes. Results of the radiation and annealing tests are expected to be published in 2004. In addition to solar cell behavior under irradiation, coatings being developed for FTFPV for environmental protection and thermal management (as discussed in the next section), will be subjected to similar radiation conditions.

Additional space qualification tests for thin-film modules will measure their mechanical durability, resistance to ultraviolet light and atomic oxygen, high temperature performance, and response to micrometeorite bombardment. The module performance will depend upon the quality of the protective coating. The protective layer for the modules must shield against

low energy protons, have high emissivity in order to reduce operating temperatures, have high optical transparency, and be resistant to micrometeorite damage and atomic oxygen. In addition, thin-film arrays will operate at >100 V in order to reduce wiring mass. The coating will be required to be pinhole-free and possess a high dielectric constant to eliminate high voltage arcing.

3.4 Coatings Development

State-of-practice crystalline solar cell technology employs a cover glass to protect cells from on-orbit radiation environments, arcing, and atomic oxygen. This cover glass adds mass to the solar array and increases costs. One of the advantages of thin-film solar cells is that they are relatively resistant to radiation and thus do not require a thick cover glass. However, these technologies do require development of flexible, lightweight protective coatings that would provide thermal management and environmental protection in the space environment. Emphasis on thermal management is necessary due to the high absorption and low emissivity characteristic of materials used for FTFPV. The key to controlling the temperature of FTFPV is the spectral separation between the solar power input and the thermal emission in the infrared range. Specifically, more than 95% of the Air Mass Zero (AM0) solar spectrum lies between 0.3 – 2.5 microns, whereas more than 95% of the energy radiated by a blackbody lies between 3.5 – 35 microns. Consequently, a coating with maximum transparency in the visible/NIR range while having maximum absorption in the IR range will significantly and effectively lower the operating temperature of the FTFPV acting as a passive thermal control system.

To reach these goals, a comprehensive coatings development program, establishing a scientific base for modeling and fabrication of thin-film multifunctional protective coatings, industrial scale-up, and concurrent qualification testing, has been initiated. The coating development program emphasizes the multifunctional role of FTFPV protective coatings. The key elements of the program are: (1) Design of coatings that are multifunctional in nature, i.e. simultaneously provide environmental protection, maintain high optical transmission, provide thermal management, and prevent charging, (2) Selection of suitable, low-temperature coating deposition techniques with high deposition rates, (3) qualification testing, and (4) scalability and ability to tailor to specific mission needs. Currently, three different coating processes using SiO_x and Al_2O_3 materials are being developed. The processes are based on proprietary sputtering and/or hybrid methods. Both single layer and multilayer, multi-component coatings are being investigated.

The initial results of the coating programs will be used to downselect a coating process which will then be scaled up for large area deposition and production. Initial coatings have achieved target emissivity and optical performance goals. Environmental tests of coated solar cells, including thermal cycling, mechanical durability, and high voltage plasma are scheduled to begin in 2003.

3.5 Proposed flight experiment for FTFPV

One of the obstacles to acceptance of FTFPV is developing flight heritage. While some thin-film cells have been flown in space [5] more comprehensive data is needed to instill confidence in the technology and understand combined effects. These tests along with ground testing have given us a promising view of the performance of these cells in a space environment, but combined effects cannot easily be fully explored in ground testing. In addition, while conceptual thin-film array deployment structures have been built and tested using offloading to simulate zero-g environments, no actual tests of these large structures has occurred in space. In order to mitigate these concerns, a relatively large space experiment involving FTFPV has long been desired.

The AFRL Advanced Power Group is collaborating with the PowerSail program on a proposed flight experiment that will incorporate a relatively large area (~130 m^2, or the equivalent of a 15 kW array using 8.5% efficient solar cells) thin-film array in a large deployable structures experiment (DSX). The array will include thin-film solar cells from as many as five different vendors as shown in Figure 2. The array is not intended to be fully populated, but will demonstrate power levels greater than 3 kW. The array will have two areas of high voltage (100V and 300V) to test breakdown and arcing, and the proposed orbit will include high radiation levels. The array cells will be coated using the technology being developed as discussed in section 3.4. This flight will be the first large scale demonstration of FTFPV in space, and should pave the way for routine use of FTFPV arrays for space applications. Successful development and demonstration of FTFPV technologies will enable a new generation of lightweight high-power spacecraft.

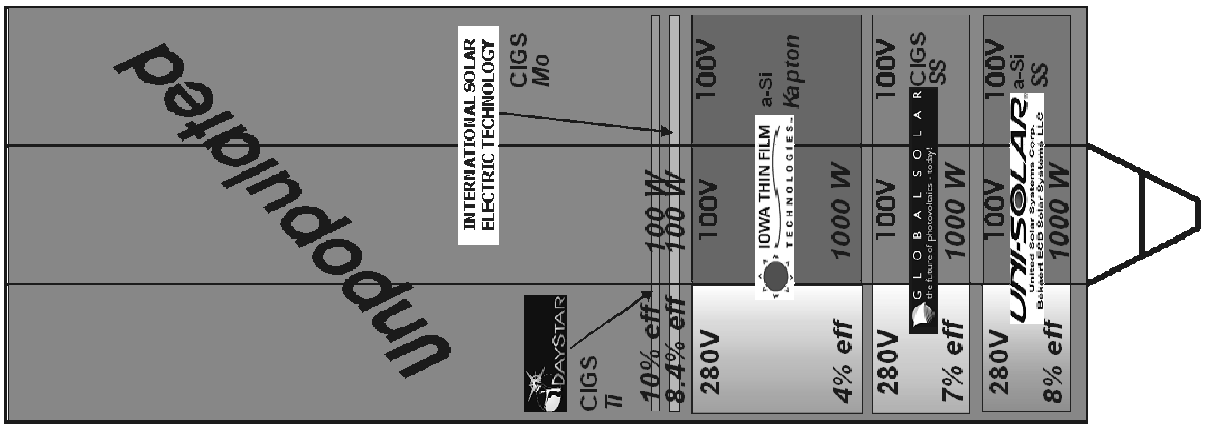

Figure 2: Proposed DSX (Deployed Structures Experiment) lightweight thin-film array showing layout of thin-film solar cell experiment.

4. CHALLENGES FOR THE FUTURE

With AFRL programs in-place for increased efficiency of multijunction crystalline solar cells, future direction will be geared to "quantum leap" type technologies with significantly higher specific power, Watts/m^3, and/or efficiency. One approach to achieve the quantum-leap goals is to devise a method for the low cost deposition of crystalline high efficiency cells onto flexible, lightweight blankets. Other approaches include polymer solar cells and spectrum alteration.

For thin-film solar cells, further improvements in specific power from efficiency increases, lighter substrates, and monolithic integration of cells are all challenges. Efficiency increases are expected to arise primarily from CIGS technology where efforts to increase the bandgap and the research into multijunction cells are underway in several laboratories. Further thinning of metal foils and a switch to lower density metals may also produce further increases in specific power density due to mass reduction. Progress is also being made in polymeric substrates for both a-Si and CIGS. Monolithic integration is expected to reduce solar blanket production costs while decreasing areal losses, wiring mass, and complexity of cell interconnections. Monolithic integration requires either a dielectric substrate such as polyimide or an insulating layer on a metal foil. Large-scale pinhole-free coatings on metal foils at low cost have been problematic in the past, but AFRL programs are making headway. Monolithically integrated a-Si is currently being produced on 1 mil polyimide at Iowa Thin Film Technologies (ITFT). ITFT sub-modules have AM0 efficiencies of 4-5% for 0.93 m^2 (10 ft^2) areas. Under an AFRL-funded program, ITFT is developing a higher efficiency product with a target goal of 10%. The development of high temperature polymers promises to enable monolithic integration for CIGS cells on flexible substrates.

References and notes:

[1] All quoted solar cell efficiency values are as measured with the Air Mass Zero or AM0 solar spectrum.
[2] J.W. Tringe, "Trends in Thin Film PV Technology Development"
[3] J. Tringe, J. Merrill, and K. Reinhardt, IEEE Photovoltaic Specialists Conference, 2000, 28, pp. 1242-1245.
[4] K.C. Palinginis, J.D. Cohen, S. Guha, J.C. Yang, Phys. Rev. 63, 2001, 201203.
[5] M. Kagan, V. Nadorov, S. Guha, J. Yang, and A. Banerjee, IEEE Photovoltaic Specialists Conference, 2000, 28, pp. 1261-1264.
[6] U. Rau, A. Jasenek, H.W. Schock, et al, IEEE Photovoltaic Specialists Conference, 2000, 28, pp. 1032-1037.
[7] A. Boden, D. Bräunig, J. Klaer et al, IEEE Photovoltaic Specialists Conference, 2000, 28, pp. 1038-1041.
[8] A. Jasenek, U. Rau, H. Weinert, H.W. Schock, and J.H. Werner, 3rd WCPEC Proceedings, 2003.

Table I: Thin-film cell development and module/array development efforts funded by the AFRL as part of the space FTFPV array development program.

Company or Program Name	Program	Technology	Substrate
Blanket Qualification for PowerSail	FTFPV Array Development	a-Si and CIGS	Metal foils
Boeing Satellite Systems	FTFPV Module Development	a-Si and CIGS	Metal foils
Lockheed Martin	FTFPV Module Development	a-Si and CIGS	Metal foils
United Solar Systems	Performance enhancements & monolithic integration on polyimide	a-Si	Stainless steel and polyimide
ITN Energy Systems	Sputtered fabrication process	CIGS	Stainless steel
Iowa Thin Film Technologies (ITFT)	Monolithic integration and efficiency improvements	a-Si	Polyimide
International Solar Electric Technologies (ISET)	Non-vacuum painted-on process & lightweight substrates	CIGS	Polymer
Florida Solar Energy Company (FSEC)	Increased bandgap and decreased temperature coefficient	CIGSS	Metal foil
Foster-Miller ITN Energy Systems	High temperature polymer substrates	CIGS	Polymers
Triton Sommer Materials	Dielectric coatings to enable monolithic integration	CIGS	Metal foil
ITN Energy Systems	Tandem CIGS cells	CIGS	Metal foil
Encapsulant Development	Multi-functional protective coating development	a-Si and CIGS	Metal foils and polymers
Grain Boundary Orientation Studies	Study effect of grain boundary size and orientation	CIGS	Metal foils
Radiation Testing	Measure and model effects of radiation on thin-film cells	a-Si and CIGS	Metal foils

RESULTS OF FLIGHT DEMONSTRATION OF TERRESTRIAL SOLAR CELLS BY MDS-1 IN GTO

Mitsuru Imaizumi, Taishi Sumita, Shirou Kawakita, Osamu Anzawa, and Sumio Matsuda
National Space Development Agency of Japan (NASDA)*, Tsukuba, Ibaraki, Japan
*Current name: Japan Aerospace Exploration Agency (JAXA)

INTRODUCTION

It is very costly to develop special electronic devices for space use, and the market for such devices is not sufficiently large for business. As a result, semiconductor industries are less aggressive in developing space devices. Therefore, application of commercial electronic devices that should be robust against the space environment has been considered recently for space applications.

Mission Demonstration-test Satellite No. 1 (MDS-1) was developed to test and demonstrate state-of-the-art technologies in space. One of the MDS-1 missions is to evaluate advanced terrestrial semiconductor devices in space environment in order to clarify their possibilities or capabilities as space applications.

MDS-1 was launched on February 4, 2002, by NASDA's new launch vehicle H2A. The satellite was placed in a geostationary transfer orbit (GTO) with apogee of 500km, perigee of 36,000km, inclination angle of 28.5º, and period of 10 h 45 min. The orbit cuts across the inner and the outer Van Allen Belts so that the satellite is exposed to a very severe radiation environment compared to satellites in low Earth orbit (LEO) or geostationary orbit (GEO). Figure 1 schematically illustrates the MDS-1 orbit.

The mission duration was supposed to be one year, and the observation of cell degradation in space has been completed successfully in February 2003. This study presents the degradation flight data of the terrestrial solar cells and describes results of comparative analysis of the flight data and ground irradiation test results using the JPL [1, 2] and NRL [3] methodologies.

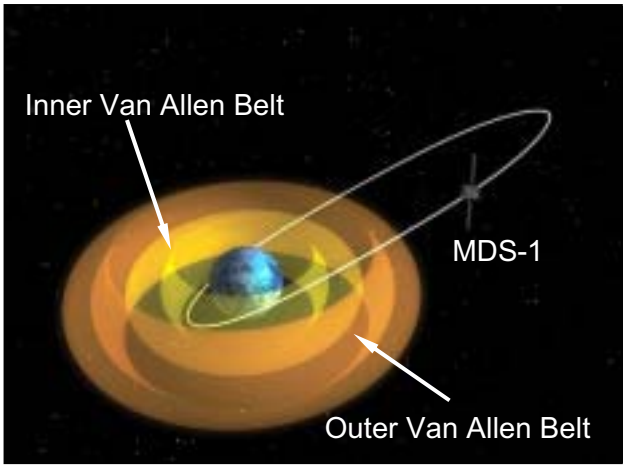

Fig. 1 Schematic orbit of MDS-1. The orbit cuts across the inner and the outer Van Allen Belts.

TERRESTRIAL SOLAR CELL TEST BOARD

MDS-1 is equipped with a test board of solar cells developed for terrestrial use and called the "terrestrial solar cell test board" (TSC). Six kinds of terrestrial cells with different structures, materials, or manufacturing techniques (see Table I) were attached on the TSC. Two of each type of cell were prepared, and 500μm and 100μm thick coverglasses were attached on the cells. In addition, two kinds of space solar cells, Si and GaAs, were mounted on the TSC for comparison. The combination of the GaAs single junction cell and a 300 μm–thick coverglass is the same to the cells on the solar paddles of the satellite. Figure 2 shows the TSC board under light irradiation from an AM0 solar simulator.

The TSC was fitted on top of the satellite (see Fig. 3) and kept facing the sun at all times in orbit with an average angle of 10 degrees (MET < 15 days after launch) or 30 degrees (MET ≥ 15 days after launch). Five

Table 1 List of Solar Cells on the TSC board

Cell Type	Cover-glass Thickness (μm)	Note
U-type bulk poly-crystalline silicon	100/500	Cast
Bulk poly-crystalline silicon	100/500	Cast
N-type base single crystal silicon	100/500	Thin Emitter
InGaP/GaAs dual-junction tandem	100/500	MOCVD
Large-area $Cu(In,Ga)Se_2$ poly-crystalline thin film	100/500	Wet-chemical deposition
High-efficiency $Cu(In,Ga)Se_2$ poly-crystalline thin film	100/500	Dry-physical deposition
Bulk single crystal silicon (Base resistivity = 10 Ωcm)	100/500	Space cell (reference)
Bulk single crystal silicon (Base resistivity = 2 Ωcm)	100/500	Space cell (reference)
GaAs single crystal thin film on Ge sub.	300/300	Space cell on satellite paddle

sensors monitored the TSC temperature; the average measured temperature, except during eclipse, is about 70 ºC.

In order to obtain the cell performance, 16 points on the current-voltage (I-V) curve, including open-circuit voltage (Voc) and short-circuit current (Isc), of each cell were collected from the TSC using 16 loads with different resistances. The measured I-V data were packed with the temperature values and sent to a ground site via telemetry signals. The voltage and current values were corrected for temperature, angle to the sun, and solar irradiance (distance between the sun and the satellite) automatically at the ground site.

Maximum power (Pmax) values were not obtained directly, but can be estimated from the I-V data. First, the point of greatest power and adjacent two points on an I-V curve are selected from among the 16 power values (i.e., products of current and voltage values). A fitting equation is then obtained. Finally, the maximum power is determined from the fitting curve. However, it is impossible to calculate conversion efficiency because the solar irradiance is not monitored on orbit. In this report, therefore, we will focus on the degradation of Isc and Voc.

The initial I-V curves measured on orbit (MET=4 days after launch) showed good agreement with the I-V curves measured in our laboratory using an AM0 solar simulator after the correction. This means that the cells, as well as the measurement system, were not damaged during the launch.

The radiation environment on orbit is also measured by dose monitors (standard dose monitor: SDOM) as another mission. The SDOM produces the energy flux of the radiation electrons and protons detected by the loaded multi channel monitors (12 channels for protons, 5 channels for electrons).

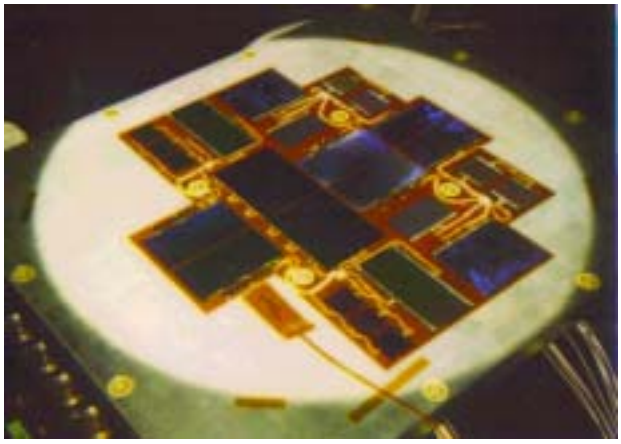

Fig. 2 TSC test board under light illumination from an AM0 solar simulator.

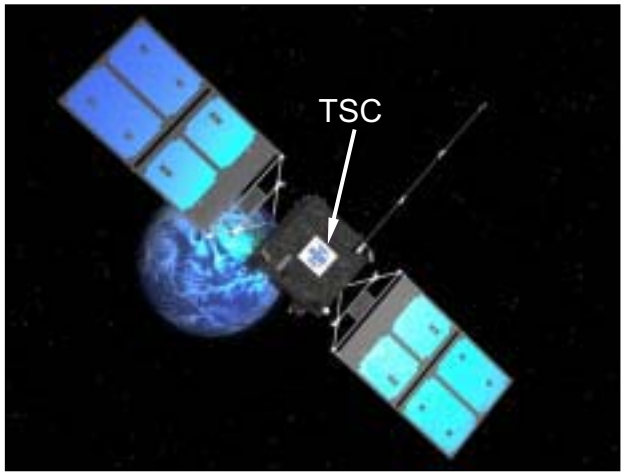

Fig. 3 Image of MDS-1 and TSC test board on orbit.

FLIGHT DATA

Prior to the launch, ground irradiation tests for the mounted cells were carried out at the Japan Atomic Energy Research Institute (JAERI). In the ground tests the cells were irradiated with unidirectional radiation beams without coverglass. The results demonstrated that the CIGS cells have excellent radiation tolerance, while the *n*-type base single-crystal silicon cells have the lowest one. Other test results have been described elsewhere [4].

Figure 4 depicts the Isc and Voc of eight types of solar cells on the TSC up to MET of about 400 days after launch, expressed as remaining factor. The data on MET=4 days after launch were used as the initial values. Each data point is the average of a date.

The reference space silicon cell data (Figs. 4(g) and 4(h)) indicate that the remaining factor of Voc is higher for the lower resistivity (2 Ωcm) cells, while that of Isc is higher for the higher resistivity (10 Ωcm) cells. This tendency was expected from the ground test results as well as from experience with Si space cells, and the flight data confirmed it. Therefore, the flight data are not considered to express irregular degradation. Note that the degradation rate changes around MET=50 days after launch. Figure 6 presents the day fluence rate for a typical channel of dose monitors for protons (ch. 2: 1.08-1.46 MeV) and electrons (ch.4: 6.36-10.0 MeV) in SDOM system. According to the environmental data, the fluence rate of both electrons and protons increased by more than one order of magnitude at this time. The radiation fluence increase around MET=50 days is attributed to a solar flare and is thought to have increased the degradation rate of the TSC cells.

The poly-crystalline silicon cells (Figs. 4(a) and 4(b)) exhibit radiation tolerance comparable to space single-crystal silicon cells, supposedly due to their relatively low initial performance. However, this type of cell could be acceptable for low-power, low-cost space missions.

The *n*-type base single-crystal silicon terrestrial cells exhibit the greatest degradation (Fig.4(c)), which also coincides with the ground test results. This is believed to be not due to its structure but the material. The radiation damage in an *n*-type single crystal silicon cell is known to greatly decrease the minority-carrier lifetime due to generated recombination centers.

The InGaP/GaAs dual-junction tandem cells exhibit good radiation tolerance (Fig. 4(d)), in spite of being designed without consideration for radiation damage. This radiation tolerance is thought to be mainly due to its dual-junction (DJ) tandem structure. The superior radiation tolerance of the InGaP top cell [5] is thought to contribute the tolerance although the bottom GaAs cell is current limiting in the DJ cell. The results imply that the cell can be applied without any modification to space missions for which the radiation environment is not severe.

Almost no degradation on orbit was observed in the CIGS cell (Figs. 4(e) and 4(f)), especially with regard to Isc. This agrees with the ground test results, verifying the super radiation tolerance in space. Another study by the authors previously reported that radiation-induced damage in CIGS cells can be annealed out quickly at relatively low temperature [6]. According to the study described in ref. [6], an average temperature of 70ºC of the TSC is high enough to recover most of radiation damage.

Table 2 Equivalent 1 MeV electron fluence for TSC cells at MET=400 days after launch

Cell Type	Remaining Factor of Isc/Voc (100μm Coverglass Cell)	Equivalent 1MeV e^- Fluence (cm^{-2})
U-type bulk poly-crystalline silicon	0.79 / 0.83	6E14 / 5E15
Bulk poly-crystalline silicon	0.80 / 0.86	6E14 / 4E15
N-type base single crystal silicon	0.67 / 0.70	1E14 / 4E15
InGaP/GaAs dual-junction tandem	0.87 / 0.91	2E14 / 2E15
Large-area Cu(In,Ga)Se_2 poly-crystalline thin film	1.00 / 0.97	--- / 1E17
High-efficiency Cu(In,Ga)Se_2 poly-crystalline thin film	0.96 / 0.92	--- / 1E17
Bulk single crystal silicon (Base resistivity = 10 Ωcm)	0.89 / 0.74	1E15 / 1E16
Bulk single crystal silicon (Base resistivity = 2 Ωcm)	0.83 / 0.80	6E14 / 7E15

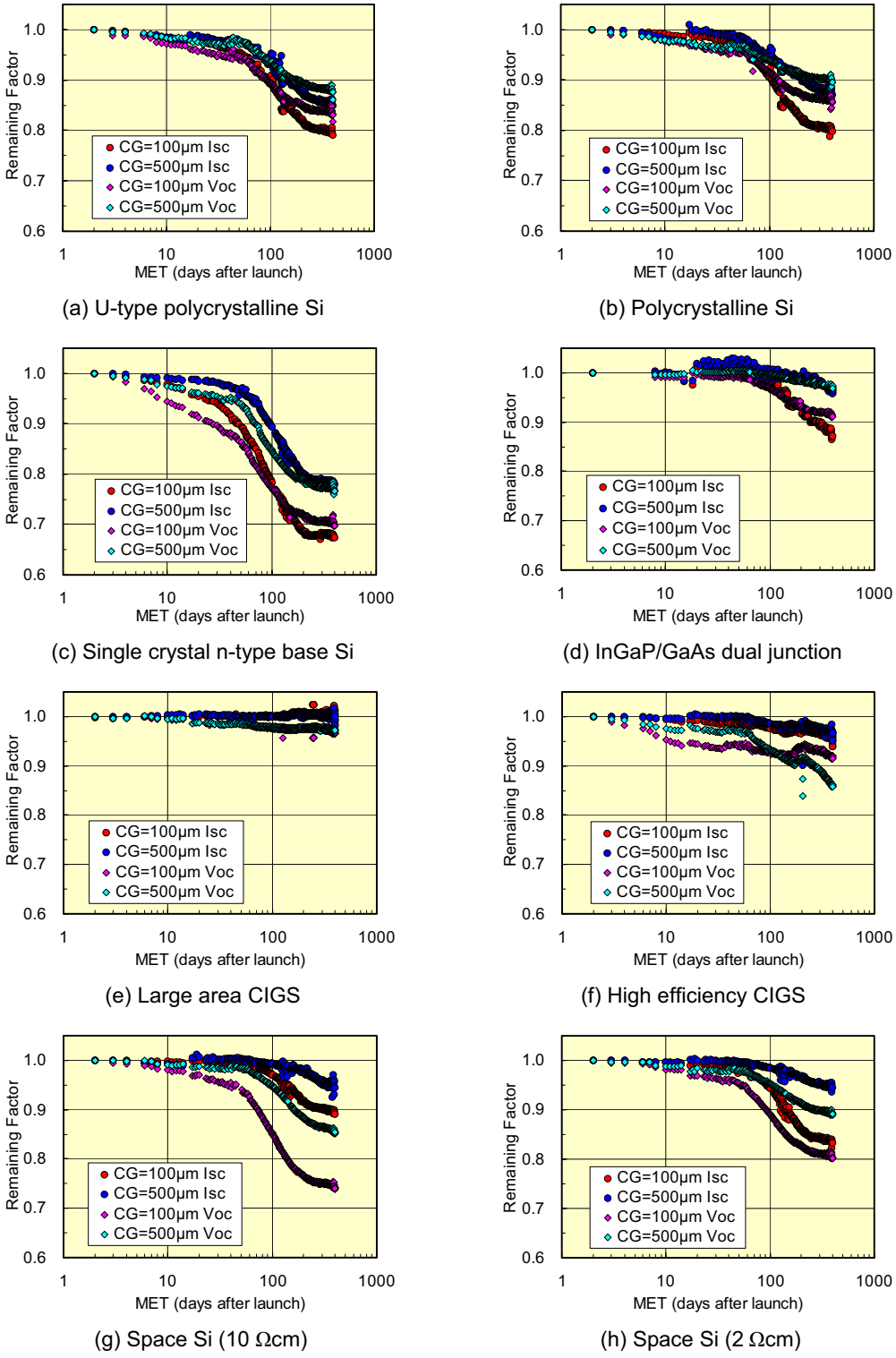

Fig. 4 Flight degradation data of Voc and Isc of solar cells on TSC.

DATA ANALYSIS

Ground-based experiments of proton and electron irradiation on the TSC cells were performed prior to the launch. In particular, radiation response of the single crystal silicon space cells was investigated in detail and derived relative damage coefficients (RDC) for the cells since the cells are reference. As a result, the RDC agreed with the values exhibited in Solar Cell Radiation Handbook [1].

The equivalent 1 MeV electron fluence based on JPL methodology for degradation of each cell at MET=400 days after launch is presented in Table 2. These values were obtained by comparing flight data of 100μm-thick cover-glass cells with the ground irradiation test data of bare cells [4]. According to the Monte Carlo simulation, 1MeV electrons pass through the 100μm-thick cover-glass with almost no energy loss. Therefore, a shielding effect for incident electrons does not have to be considered in this case and the fluence values obtained are considered to be significant. Note that the equivalent fluence of Voc is generally about an order of magnitude higher than that of Isc. This might be due to differences in irradiated particles: One MeV electrons were irradiated for the ground test, while protons with various energies are major particles in the flight environment. Thus, damage in the shallow region of the cells including the space charge region due to especially low energy protons is likely to a reason of the difference.

Cell degradation data from TSC and the ground tests were converted to the function of displacement damage dose (Dd), using the non-ionizing energy loss (NIEL) values for each cell material (Si, III-Vs, and CIGS) [7]. The NIEL value of GaAs has been used for InGaP/GaAs dual-junction cells because GaAs damage usually determines multi-junction cell degradation [8] and also the GaAs NIEL value is close to that of InGaP.

Figure 5 shows the differential proton fluence spectra corresponding to the total incident protons at 400 days after launch obtained from the SDOM. The diamond symbols correspond to the proton fluence detected by the 12 channels of the proton dose monitor. To account for the coverglass shielding effect, the transmitted proton fluence spectra were calculated by the model described by Haffner [9]. The calculated spectra are indicated in Fig. 5 with the coverglass thickness. The amount of Dd can be determined by summing the product of the differential spectrum with the NIEL values of the cells.

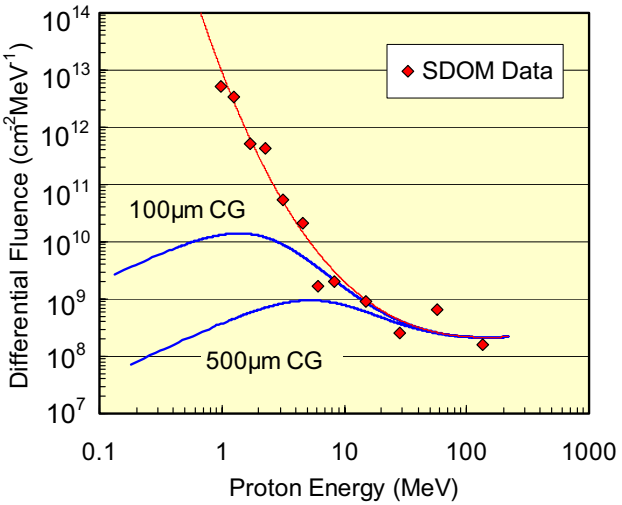

Fig. 5 Differential incident proton dose spectra on orbit and the transmitted spectra after passing through 100μm and 500μm-thick coverglasses.

Figure 6 presents the flight data and the ground test results of Isc and Voc of representative terrestrial cells on TSC as a function of Dd. The ground irradiation tests were carried out with 1MeV electrons and 380keV, 3MeV, and 10MeV protons [4]. However, in the case of the large-area CIGS cell, the ground test result of 1MeV electron irradiation was not plotted since no degradation was observed in ground tests even in the high fluence region (~10^{17}cm^{-2}). In addition, Dd value of electrons for the flight data was not included since the degradation was supposed to be mainly due to protons according to the observed environment. In this figure, degradation curves from flight data for 100μm and 500μm coverglass are identical, confirming that the calculation of transmitted proton energy spectrum was successful.

Generally, degradation tendency of the flight data and that of ground test results for both Isc and Voc of all the cells show good agreement even for the large-area CIGS cell which exhibited almost no degradation in space. Especially for Isc, degradation curves are almost identical. This confirms the validity of the ground test method/conditions adopted in this study.

From the results of the Dd analysis, it is possible to predict EOL performance on orbit. For example, in the case of the CIGS cell, the total Dd required to cause 10% degradation in Isc is estimated to be appropriately 1.4×10^{12} MeV/g from Fig. 6(d). This is 650 times of the Dd value on orbit at MET=400 days after launch for a cell with a 100μm coverglass and 6700 times for a cell with a 500μm coverglass! These values imply that CIGS cells have practically infinite lifetime in space as far as remaining factor is concerned.

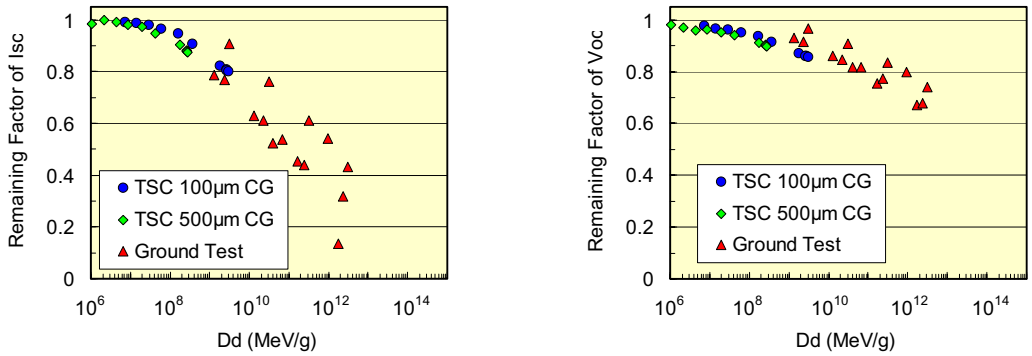

(a) Polycrystalline Si

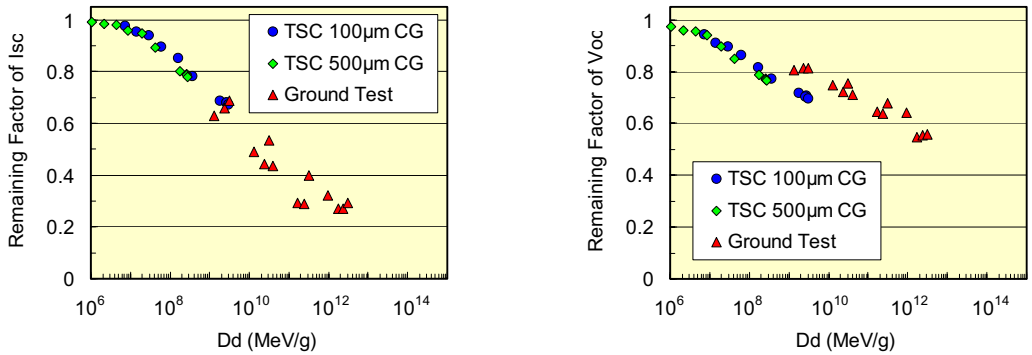

(b) Single crystal n-type base Si

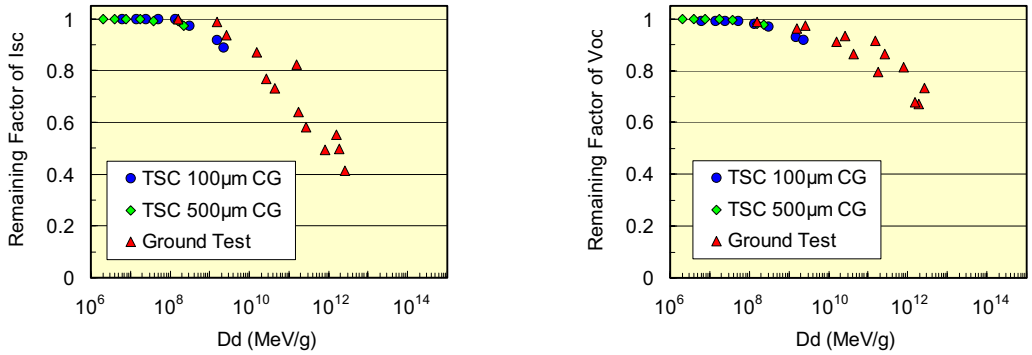

(c) InGaP/GaAs dual junction

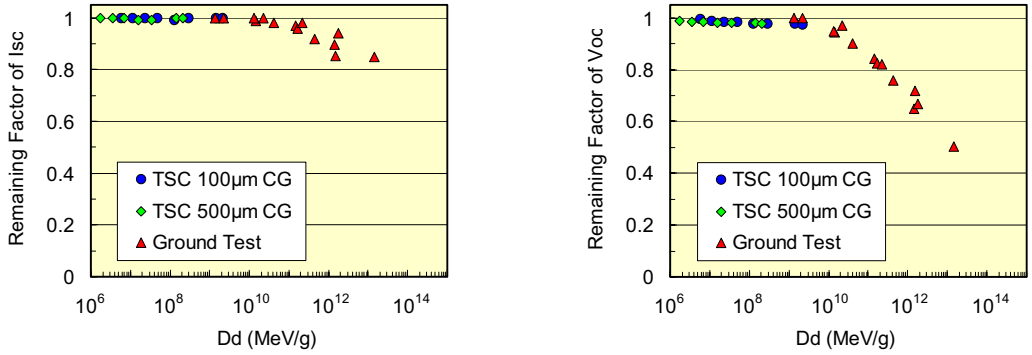

(d) Large area CIGS

Fig. 6 Comparison of flight and ground test results for Isc and Voc as a function of Dd

However, for silicon cells (Figs. 6(a) and 6(b)), degradation of Voc on orbit exhibits slightly lower tolerance compared with the ground test degradation curve. It is likely because Dd for electrons on orbit was not included. If the Dd of incident electrons, which is calculated to be about 1×10^9 MeV/g for MET=400 days after launch, is taken into account, the Voc degradation roughly corresponds with the ground test results. This fact suggests that degradation in Voc of silicon cells might involve an additional effect which has to be considered for NIEL analysis. Otherwise, some modification should be required in the NIEL calculation.

SUMMARY

MDS-1 successfully monitored degradation tendencies of six types of terrestrial solar cells by flying in a severe radiation environment for more than a year. An increase in degradation rate of Voc and Isc was observed at MET~50 days after launch, which is due to an increase in the fluence rate of high energy electrons and protons caused by solar flare. Super-radiation tolerance of CIGS cells observed in ground irradiation tests was verified in actual space. Also, InGaP/GaAs tandem cells exhibited sufficient radiation tolerance, and poly-crystalline silicon cells, reasonable radiation tolerance. The results indicate the possibility and capability of the terrestrial cells for space application.

The equivalent 1MeV electron fluence of Voc estimated at MET=400 days after launch was generally higher than that of Isc, indicating that degradation in Voc involves an additional effect that does not affect Isc degradation. According to the results of NIEL/Dd analysis, degradation tendency of the flight data and that of ground test results agree very well. This confirms the validity of the ground test method/conditions adopted in this study.

ACKNOWLEDGEMENTS

The authors would like to express their sincere appreciation to the New Energy and Industrial Technology Development Organization (NEDO) for their kind cooperation to this mission. They would also like to thank Dr. T. Hisamatsu of SHARP Corporation for fruitful discussion.

REFERENCES

[1] H. Y. Tada, "*Solar Cell Radiation Handbook, Third Edition"* (JPL Publication, 1982)
[2] B. E. Anspaugh, "*GaAs solar Cell Radiation Handbook*" (JPL Publication, 1996)
[3] G.P Summers et al. Proceedings of the 1st World conference of Photovoltaic Energy Conversion, (1994) 2068
[4] T. Aburaya, T. Hisamatsu, and S. Matsuda, Proceedings of 2nd World Conference and Exhibition on Photovoltaic Solar Energy Conversion, (1998) 3568
[5] N. Dharmarasu, M. Yamaguchi, A. Khan, T. Yamada, T. Tanabe, S. Takagishi, T. Takamoto, T. Ohshima, H. Ito, M. Imaizumi, and S. Matsuda, *Appl. Phys. Letters*, **79** (2001) 2399
[6] S. Kawakita, M. Imaizumi, M. Yamaguchi, K. Kushiya, T. Ohshima, H. Itoh, and S. Matsuda, *Jpn. J. Appl. Phys.*, **41** (2002) L797
[7] S. R. Messenger, G. P. Summers, E. A. Burke, R. J. Walters and M.A.Xapsos, *Progress in Photovol*taics, **9** (2001) 103
[8] T. Sumita, M. Imaizumi, S. Matsuda, T. Ohshima, A. Ohi and H. Itoh, Nucl. Instr. Meth. Phys. Res. B **206** (2003) 448
[9] J.W.Haffner, "*Radiation and Shielding in Space"* (Academic, New York, 1967)

SOLAR ARRAY VERIFICATION AND ANALYSIS TOOL (SAVANT) ANALYSIS OF THE MICROELECTRONICS AND PHOTONICS TESTBED (MPTB) SPACE SOLAR CELL DATA

R. J. Walters and G. P. Summers
US Naval Research Laboratory, Code 6818

S. R. Messenger
SFA, Inc.

T. L. Morton
Ohio Aerospace Institute

1. Introduction

The United States Naval Research Laboratory (NRL), in collaboration with the Ohio Aerospace Institute (OAI) and NASA Glenn Research Center (GRC), have developed an improved space solar cell radiation response analysis capability and produced a computer modeling tool which implements the analysis. This was accomplished, in part, through analysis of data taken from the solar panel that powers the Micro-electronics and Photonics Test Bed (MPTB) experiment. This project was funded by the NASA Living with a Star Space Environments Testbed, NRA8-3. This project specifically addresses issues related to rapid technological change in the area of solar cells for space applications in order to enhance system performance, decrease risk and reduce cost for future missions. In this paper, an analysis of MPTB solar panel flight data is presented. The analysis focuses on the data for the photo-generated current from the MPTB solar array that was telemetered to the ground from the spacecraft. The concept of displacement damage dose (Dd) has been used to characterize the radiation-induced degradation of the solar array output, employing the methodology developed at NRL. The computer code Solar Array Verification and Analysis Tool (SAVANT) being developed by OAI under contract to GRC, was used to predict the solar array output as a function of time in orbit. The ultimate goal of this work was to validate the SAVANT code against the measured space data and to develop SAVANT into a user-friendly executable program that can be widely distributed.

2. MPTB Solar Array Data

The solar array under study in this project is mounted on the host spacecraft and is dedicated to providing power to the MPTB experiment. The array operates at a fixed voltage of 31.2 V, but the current is not controlled. Therefore, any changes in the photocurrent of the array can be measured and analyzed. The array consists of 27 strings of cells with 54 cells in each string. The solar cell technology is Spectrolab (SPL) 8 mil single-junction (SJ) GaAs/Ge. The solar array consists of a ¾ inch think honeycomb Al substrate with 10 mil graphite epoxy face-sheets. A schematic diagram of the solar array structure is shown in **Figure 1**.

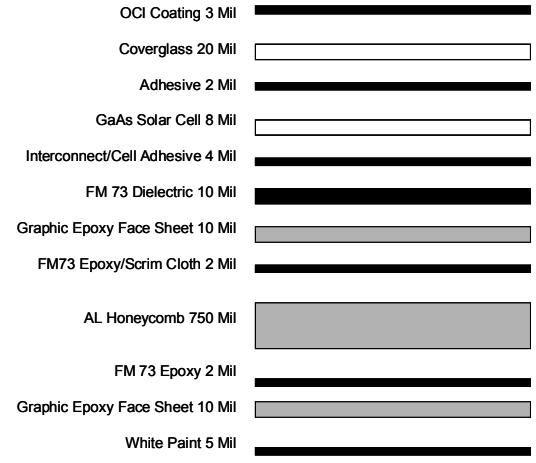

Figure 1: A schematic diagram of the MPTB solar array.

The spacecraft telemetry data includes both the solar array temperature and current (**Figure 2**). To minimize earth albedo effects, only the data taken near apogee were analyzed. The backside solar array temperature varied from about 32 to 49°C. There is about an 11.1°C temperature increase from the rear to the front face of the array. Using temperature coefficient data from reference [1], the on-orbit current data was corrected to 28°C to match ground measurements. The solar array current data were also corrected for seasonal variations where it was assumed that the spacecraft was collocated with the Earth. The Sun-Earth separation was calculated as a function of time using Kepler's equations [2]. Since the photocurrent of the solar array varies linearly with solar intensity and since the solar intensity varies with the inverse square of distance, the seasonal variations could be normalized to the data measured at the average Sun-Earth distance, 1 A.U..

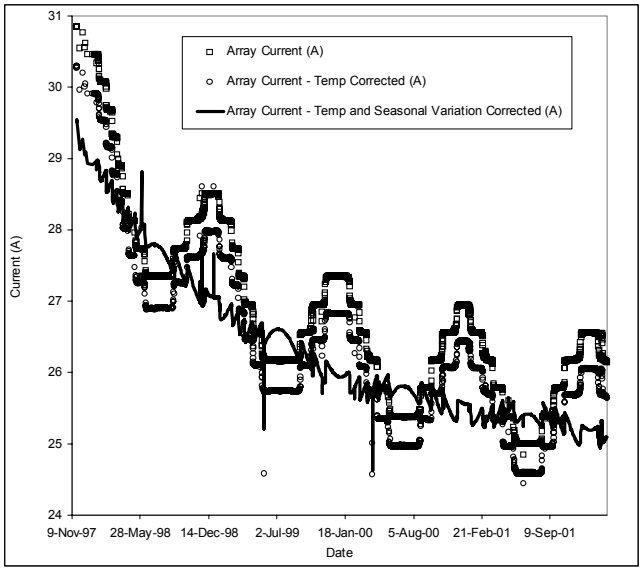

Figure 2: The MPTB on-orbit solar array data. The raw telemetered data are shown along with the data after temperature correction and correction for seasonal variations.

As can be seen in **Figure 2**, the seasonal correction produced the desired effect of smoothing out the periodic oscillations in the measured data. The roughly saw-tooth pattern visible in the data occurs because the original data has a distinct stair-step pattern and the plateaus at each perihelion and aphelion are due to the limited resolution of the analog to digital (A/D) converter onboard the spacecraft.

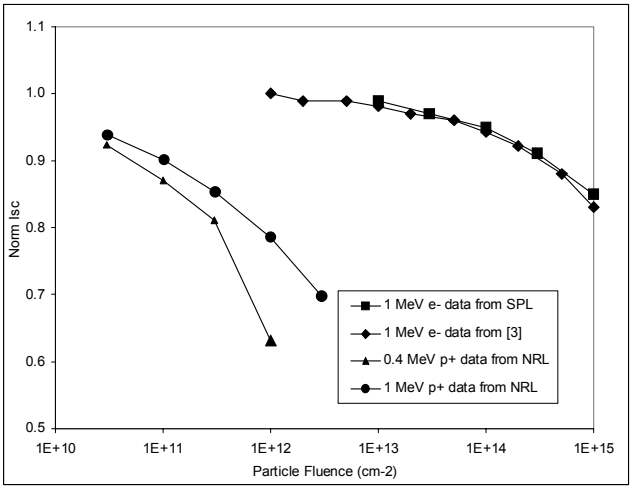

Figure 3: Short circuit data measured in SPL SJ GaAs/Ge solar cells after proton and electron irradiation. The data have been normalized to the pre-irradiation values.

3. Ground Test Data

The prediction of the performance of a solar cell in orbit is based on measurements of the cell output made on the ground. In this section, the ground test data reduction and analysis will be described. SPL supplied NRL with a set of ground test data consisting of the current vs. voltage (IV) parameters depicted in **Figure 3** measured after irradiation with incrementally larger fluences of 1 MeV electrons. A second dataset measured after 1 MeV electron irradiation was taken from [3]. In a separate project funded by SPL, NRL measured 0.4 and 1 MeV proton irradiation data on SPL SJ GaAs/Ge solar cells. The Isc data from these various sources are plotted in **Figure 3**.

Under typical operational conditions, a solar array operates at a fixed voltage, so the individual solar cells operate at a fixed load point characterized by a load current and voltage. The data telemetered from the MPTB spacecraft is the solar array load current. Therefore, we must determine if the radiation response of the solar array load current is accurately modeled by the ground test parameters. The array consists of 27 strings of 54 solar cells in each string. Single junction GaAs solar cells have an open circuit voltage of about 1.02 V. The array open circuit voltage is therefore expected to be 54 x 1.02 = 55.9 V. The MPTB solar array voltage is held constant at 31.2 V. Therefore, the array load point is

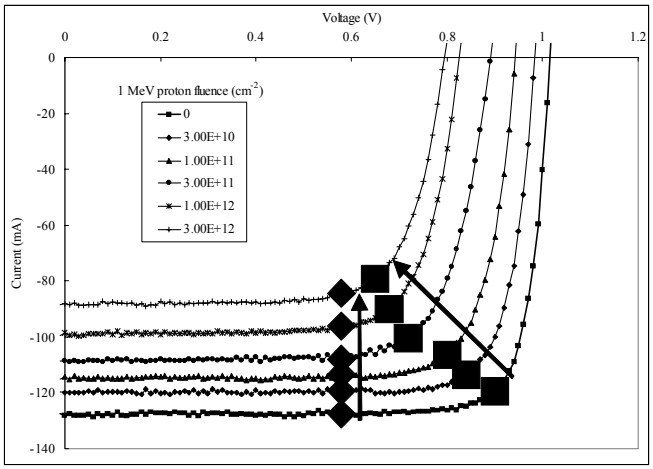

Figure 4: IV curves measured on SJ GaAs solar cells that are representative of the cells on the MPTB array. Each curve represents the cell output after irradiation by 1 MeV protons up to the fluence level given in the legend. The squares indicate the maximum power point, and the diamonds indicate the load point.

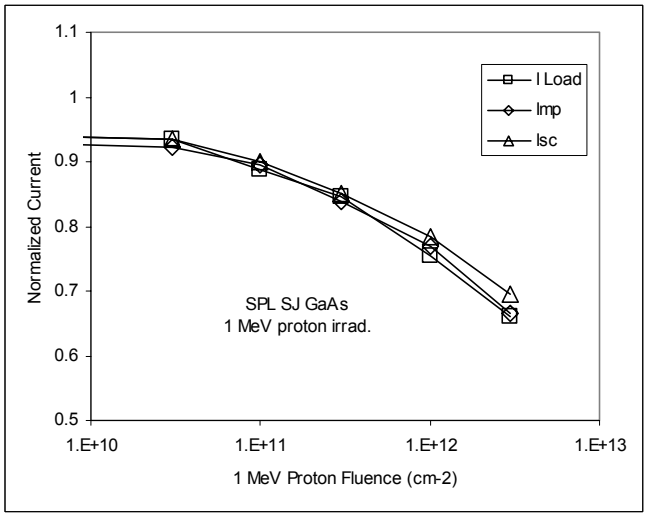

Figure 5: Current data taken from **Figure 4**. These data show that the three parameters show similar degradation characteristics, but Imp is a better description of I-load than Isc.

approximately 56.8% of Voc. Using this value, we can estimate the load voltage for an individual cell to be 56.8% of Voc or 0.578 V. With this information, we may now track the radiation degradation of the solar cell current at this load point (I-load).

Using 1 MeV proton irradiation ground test data, we generated the graph in **Figure 4**. The maximum power point and the load point on each curve are highlighted in the graph. The two different points are seen to follow different tracks through the current-voltage space with increasing fluence, but since the slope of the IV curve is very small up to the maximum power point, the change in I-load with increasing fluence is essentially the same as that of the Imp. This is shown explicitly in where the I-load, Imp, and Isc have been normalized to their pre-irradiation values and plotted as a function of fluence. These data suggest that I-load tracks Imp closely, so we will use the data for Imp in the calculations that follow.

4. Ground Test Data Reduction and Analysis

The analysis of the ground test data performed here employs the displacement damage dose (Dd) methodology developed by NRL [4,5]. In the Dd methodology, the data measured after irradiation by different particles at different energies are reduced to a common degradation curve by converting the particle fluence to an equivalent value of Dd. The Dd is calculated through the following expression:

$$Dd(E) = \Phi(E) \bullet S(E) \left[\frac{S(E)}{S(E_{ref})} \right]^{n-1} \qquad \text{Equation 1}$$

The quantity Φ(E) is the particle fluence. The quantity, S(E), is the calculated nonionizing energy loss (NIEL) at incident particle energy E. Values of NIEL for electrons and protons incident on GaAs have been calculated and are tabulated in [5]. The symbol Eref refers to an arbitrary reference energy, and n is an empirically determined parameter. For proton irradiation of GaAs and a wide array of other semiconductor materials, n has been found to be unity indicating a linear dependence of the proton damage coefficients on NIEL [5]. In the case of electron irradiation, however, n has been found to vary between 1 and 2 depending on the material and dopant species. For p/n GaAs solar cells like those used on MPTB, n has been determined to be 1.7 [5]. To keep consistency with previous studies, the reference energy is set to 1 MeV for the electron irradiation data. The radiation degradation data for Imp corresponding to the data sets given in **Figure 3** are plotted as a function of Dd in **Figure 6**.

Figure 6 shows that the data measured after irradiation by different particles at different energies collapse to a single curve when plotted as a function of Dd. This curve is therefore characteristic for this technology and be

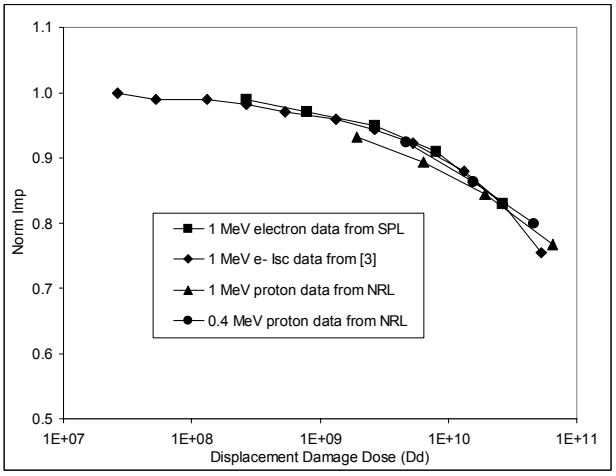

Figure 6: GaAs/Ge solar cell Imp data plotted as a function of Dd. The data are seen to follow the same curve, which is characteristic for this technology and can be used to describe the cell response in any radiation environment. Imp data were not available in [3], so Isc data are shown.

used to describe or predict the cell response in any proton or electron radiation environment. This is the foundation of the NRL method. By analyzing the data in terms of Dd, data from a variety of different radiations can be readily reduced to a common curve. Moreover, since the NIEL is a calculated quantity, the characteristic curve can be determined from a single proton data set. In the case of electrons, at least two data sets are required to enable a determination of the n parameter. From a practical standpoint, this represents a significant advance because it greatly reduces the amount of radiation data required to fully characterize the radiation response of a solar cell technology. The Dd method frees resources that can be used to generate more data points at each specific energy, thereby specifying the characteristic curve more precisely and producing a more accurate predictive capability at a lower cost. Also, the Dd analysis allows a full characterization for new technologies even though there may be very little radiation data available.

The next step in the data analysis is to parameterize the characteristic curve. This is typically done by fitting the data to the following semi-empirical equation:

$$\mathrm{Imp}/\mathrm{Imp}_0 = 1 - C\log\left[1+\frac{\mathrm{Dd}}{\mathrm{Dx}}\right] \quad \text{Equation 2}$$

The terms C and Dx are the fitting parameters and Imp/Imp0 refers to the value of Imp measured after irradiation and normalized to the pre-irradiation value. This is essentially the equation presented in [3] except that the particle fluence has been replaced by Dd. Similar expressions can be written for the other PV parameters. Because the nonlinear dependence of the electron Dd on NIEL, the characteristic curve for the electron data does not typically align with that from the proton data without further manipulation. Therefore, in the analysis, the electron and proton data are typically fit separately. The separation of the proton and electron is not very evident in **Figure 6** because the separation for the Imp data is typically small, while larger differences are often observed for the other PV parameters. The electron and proton data are fit such that each is described by a common value of C and a separate value of Dx. The proton Dx is designated by Dxp and the electron by Dxe. The ratio of Dxe to Dxp is referred to as the Rep factor, which is used to convert an electron Dd value to an equivalent proton Dd value. The fit parameters determined for each of the photovoltaic parameters are given in **Table 1**.

Table 1: The parameters determined from fitting each of the GaAs PV parameter datasets to Equation 2. The columns identified as dC, dDxp, etc. are the uncertainty associated with the calculated parameter. The Dxp and Dxe parameters are in units of MeV/g, which is the unit of Dd.

	C	dC	Dxp	dDxp	Dxe	dDxe	Rep
Isc	0.153	0.002	2.36E+09	6E+07	3E+09	1E+09	1.3
Voc	0.112	0.002	1.81E+09	9E+07	2E+09	1E+09	1.1
Imp	0.236	0.004	5.2E+09	2E+08	6E+09	2E+09	1.2
Vmp	0.128	0.002	1.9E+09	1E+08	3E+09	2E+09	1.6
Pmp	0.261	0.003	1.57E+09	8E+07	2.7E+09	7E+08	1.7

5. SAVANT CALCULATIONS

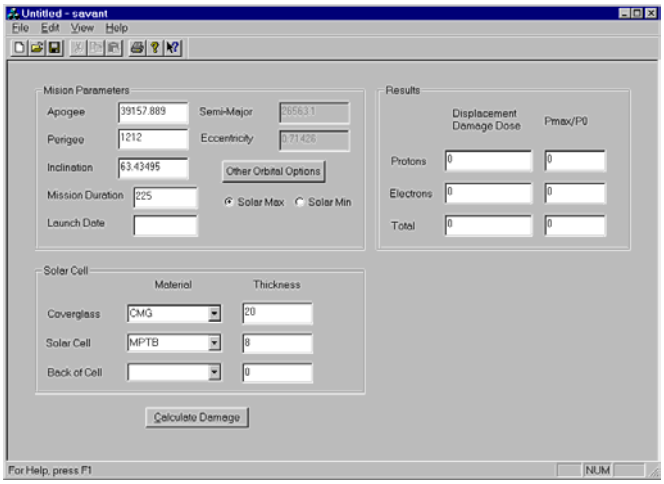

Figure 7: The input screen for the SAVANT GUI.

In this section, we will describe the process by which the SAVANT code produces a prediction of the solar array output as a function of time in orbit. An image of the program interface is shown in **Figure 7**. The SAVANT program is being developed into a user-friendly, distributed program, and it is presently being distributed for beta-version testing [6]. The procedure begins with a determination and specification of the spacecraft orbit. However, the actual orbit for the MPTB spacecraft is not available for general use. Based on the published report of Dyer, et al. [7], an orbit consisting of 39,158 x 1,212 km 63.43^{o} inclination for 225 days, and then at 38,868 x 1,502 km 63.43^{o} inclination for the remainder of the mission was assumed. A detailed description of the actual ephemeris data was also obtained. The SAVANT code was run for both of these orbits. As will be seen in the results to be presented, there is only a small difference between these two calculations in terms of the calculated solar cell degradation. This result gives us confidence in our original choice of orbit.

Once the orbit has been defined, the SAVANT code implements a model to account for geomagnetic shielding and then calls on the NASA AP8 and AE8 computer codes to calculate the proton and electron radiation environments, respectively. This is important because the degradation predictions will only be as accurate as the environment calculations. This research has given insight into the accuracy of the environment calculations [8]. Both the AP8 and AE8 programs "advertise" an inherent factor of two uncertainty due to scatter in the original space data. Also, AP8 and AE8 are static models that have not been updated since their release (1976 for AP-8, and 1991 for AE-8). They are based on satellite data taken between 1963 and 1970, and 1970 was the lowest solar max period of the space age. Therefore, the accuracy of the environment models is taken as a factor of two at best.

With the radiation environment calculated, SAVANT performs an analysis of the shielding effects of materials in contact with the solar cells. In this procedure, the radiation spectrum incident directly upon the cell active region must be determined since the ground based solar cell measurements are performed on unshielded solar cells. This is done in SAVANT by the application of the continuous slowing-down approximation to the incident spectrum using slab geometry. The result is the slowed-down, omnidirectional, differential spectrum that emerges from the shielding material and is incident directly upon the solar cell active region [4, 9].

Typically, solar cells are shielded on the front by a coverglass and on the back by the solar array substrate. A schematic diagram of the MPTB solar array structure is shown in **Figure 1**. The shielding properties of each of the layers and the coverglass are included in SAVANT by reducing the multi-layer stack to an equivalent thickness of solar cell coverglass using the densities of the materials. This is summarized in **Table 2** for the solar array itself, and it is seen that the rear-side shielding is equivalent to 31.25 mils of CMG coverglass. Examples of the calculated incident proton spectrum and associated slowed-down spectra are shown in **Figure 8**.

As is evident from **Figure 8** for the case of protons, the resultant radiation environment impinging on the solar cells is complex, consisting of protons and electrons with energies extending continuously over a large range. Because the ground test data are taken with unidirectional, monoenergetic radiation, a correlation method is required. With the NRL Dd method, the correlation is achieved by reducing the particle spectrum to an equivalent value of Dd. This is accomplished by integrating the product of slowed-down differential spectrum with the NIEL as a function of energy. The functional form of the integral comes from Equation 1 where the

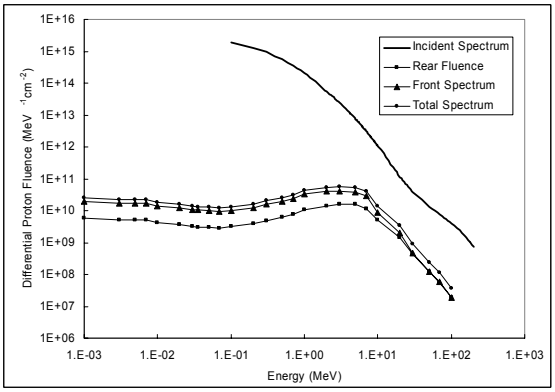

Figure 8: These are SAVANT calculations of the proton environment for the MPTB mission. Shown are the incident proton spectrum and the proton spectrum emerging from the front and rear shielding. The total spectrum is that incident upon the solar cells.

Table 2: Table of thickness and density of the layers comprising the MPTB solar array. The values are reduced to an equivalent thickness of coverglass material at the bottom of the table. These data are used to determine the radiation shielding of the MPTB solar cells on orbit.

	Thickness (mils)	Density (g/cm3)	Equiv. thickness (mil g/cm3)
Adhesive/Interconnect	4	0.64	2.56
FM 73 dielectric	10	1.16	11.6
Graphite Epoxy Face Sheet	10	1.65	16.5
FM 73 dielectric	2	1.16	2.32
Al honeycomb	750	0.032	24
FM 73 dielectric	2	1.16	2.32
Graphite Epoxy Face Sheet	10	1.65	16.5
White Paint	5	0.8	4
Total Equivalent thickness			79.8
Density of Coverglass (g/cm^3)			2.554
Total/CMG = equiv coverglass (mils)			***31.25***

monoenergetic particle fluence is replaced by the differential fluence spectrum. The electron and proton contributions are calculated separately and then summed using the Rep factor as shown in Equation 3:

$$Dd_{Eqiv} = \int \frac{d\Phi_p(E)}{dE} \bullet S_p(E)\,dE + Rep \int \frac{d\Phi_e(E)}{dE} \bullet S_e(E) \left[\frac{S_e(E)}{S_e(1MeV)} \right]^{0.7} \qquad \text{Equation 3}$$

In Equation 3, the "p" and "e" subscripts refer to the proton and electron cases, respectively. The value of n has been set to 1.7. The value of the Rep factor is given in **Table 1**.

The SAVANT code performs this integral iteratively over time at a user defined time interval. For the MPTB mission, the accumulated Dd was calculated once per day. The results are shown in **Figure 9**. Results are shown for the two descriptions of the MPTB orbit given above. Up to about April 2000, the two orbits result in essentially the same accumulated Dd. After that date, the orbit determined from the orbital ephemeris data results in a lower accumulated Dd, but the difference is small.

With the equivalent Dd values calculated, the performance of the MPTB solar cells as a function of time in orbit can be predicted. This is done by inserting the equivalent Dd values from **Figure 9** into the solar cell characteristic degradation curve (Equation 1). The resultant data are shown in Fig. 11. In these calculations, the ephemeris data were used for the orbit, and the Imp parameters were used in the solar cell degradation calculations.

The predictions are seen to underestimate the measured solar cell degradation. A second calculation is shown by the dashed curve assuming twice the estimated orbital value of Dd. Up to about August of 2000, the data

calculated assuming twice the Dd seem to agree with the measured data very well. After that date, however, there appears to be a reduction in the degradation rate in the measured data. We have performed an investigation in an attempt to resolve this apparent discrepancy. This investigation made use of the onboard dosimeter data as well as an analysis of the effect of solar proton events, as will be described in the next sections.

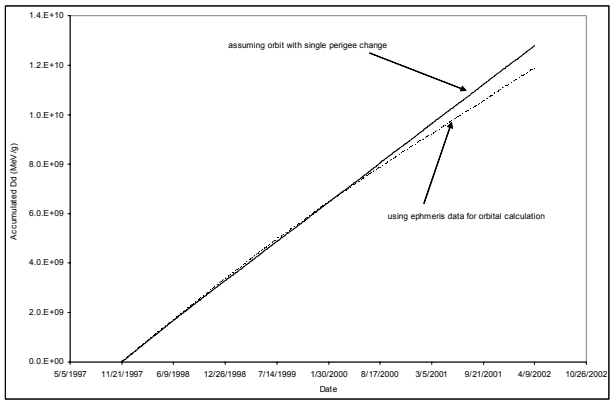

Figure 10: Equivalent Dd values accumulated by the MPTB solar cells calculated for each day in orbit. Calculations for the two descriptions of the MPTB orbits are shown.

6. Onboard Dosimeter Analysis

The MPTB experiment included the CREDO experiment [7] that measures the total fluence of protons with energy above 38 MeV per orbit. Some of the CREDO data are plotted in . As a comparison, SAVANT was used to predict the total fluence of protons with energies greater than 40 MeV received per orbit, and these data are also shown in Figure 12. Note that the data are shown as lines connecting the individual data points, and the lines appear to have a thickness. This is due to the fact that the even and odd orbits of MPTB alternatively pass through the South Atlantic Anomaly (SAA), so each orbit delivers different amounts of radiation to the spacecraft. Initially, SAVANT underpredicts the measured data by about a factor of 2. This is in agreement with the apparent factor of 2 under prediction of the solar array degradation seen in Figure 10.

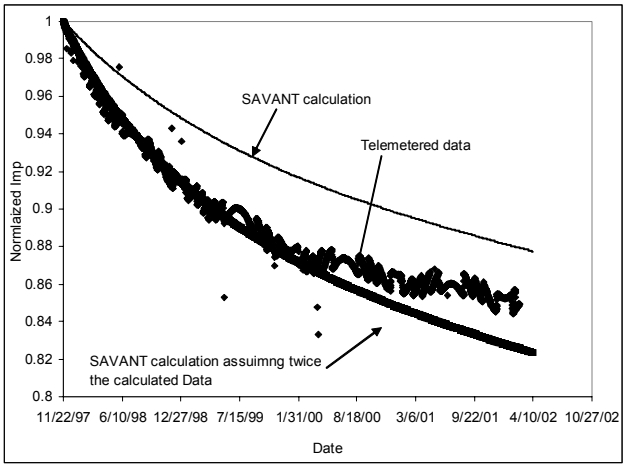

Figure 10: These are the predicted solar array data from SAVANT compared to the measured data. The ephemeris data were used to generate the Dd values, and the degradation characteristics of Imp we used in the solar cell calculations. For discussion purposes, predictions assuming twice the amount of Dd appear to match the measured data more closely.

It is interesting to note that the CREDO data shows a decrease in the total proton fluence absorbed after about 3/15/00 indicating a change in the radiation environment. This roughly coincides with the decrease in the degradation rate of the MPTB solar array output highlighted in Figure 10. The cause for this change is not currently known.

7. Solar Event Analysis

The CREDO data have been used to quantify the proton fluence incident on the MPTB spacecraft due to solar events. The CREDO data are shown in two forms in **Figure 12**. One curve in **Figure 12** represents the total number of protons measured the CREDO instrument. The other curve is a subset of the CREDO data that represents the proton fluence measured while the spacecraft was outside of the trapped proton belts. The spikes in the data measured outside the proton belts correspond to solar proton events. Viewing the data in this fashion shows that while the solar events do produce large fluxes of protons for a short time, the vast majority of the protons incident on the spacecraft come from the trapped proton belts. The additional protons produced by solar proton events are relatively small in number.

The data in **Figure 12** suggest that the effect of the solar event protons will be minimal on the MPTB solar arrays. To quantify this result, a SAVANT calculation was made with a solar proton spectrum based on the July

14, 2000, and the equivalent proton Dd was determined to be 1.9×10^6 MeV/g. This is equivalent to about ten days in the MPTB orbit. Given that the mission spans thousands of days, this is not significant and will not noticeably change the slope of the solar cell damage curves.

8. Discussion

The data in Figure 10 represent the best effort at predicting the on-orbit solar array data. The predictions are accurate to within a factor of about two in terms of accumulated Dd. While this result is within the stated uncertainties of the environment models [8], previous analyses have produced better agreement between the SAVANT estimates and measured on-orbit data [9,10]. One difference with MPTB is that it is, by far, the longest mission to be considered. There are over four years of MPTB data as compared to less than 2 years for the next longest mission. This means the predictions are especially sensitive to temporal variations in the radiation environment since such variations are not accounted for in the AP8 model. In addition, the solar cells on MPTB have a 20 mil thick coverglass, which is more than three times the thickness of the thickest coverglass analyzed in the past. This means that the portion of the proton spectrum under consideration is at much higher energies than in past studies.

Another point to note is that in the MPTB orbit, the spacecraft experiences higher electron fluences than analyzed in the past. All of previous missions analyzed using SAVANT were almost exclusively proton environments, so the model has yet been fully validated in such a mixed environment. Research is currently underway to study solar cell response in a mixed electron and proton environment.

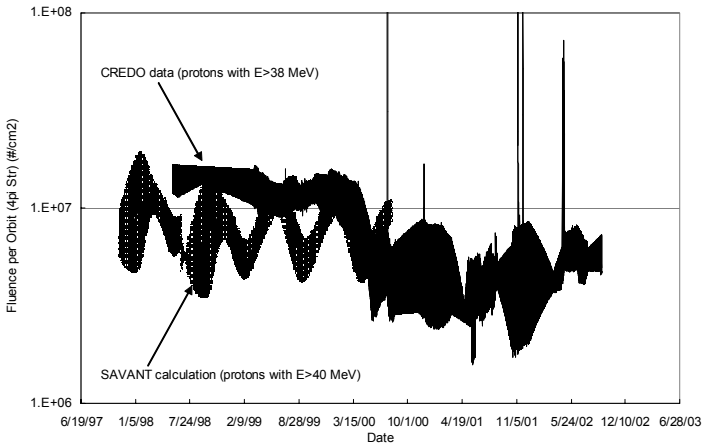

Figure 12: Values of total fluence of protons with energies above 38 MeV absorbed each orbit by the CREDO experiment on MPTB along with similar data predicted by the SAVANT code.

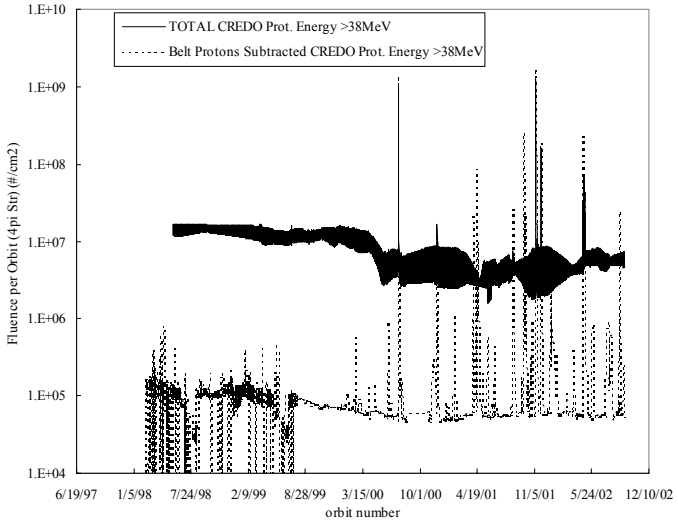

Figure 12: Another plot of the CREDO data. The solid curve represents that total CREDO data that shown in Figure 12. The dashed curve represents the amount of proton fluence measured by the CREDO instrument when the spacecraft was outside of the trapped proton belts. The spikes in the remaining data correspond to solar proton events.

While the points highlighted above suggest areas where the accuracy of the SAVANT calculations may be improved, the primary area of uncertainty in the present calculations lies in our knowledge of the radiation environment. Considering as an example only the higher energy proton of the incident proton spectrum, the CREDO data suggests that AP8 underestimates the proton flux by a factor of 2. Increasing the SAVANT predicted Dd values by this amount brings the predicted solar array output into very close agreement with the measured data at least up to 3/00. Beyond this date, there appears to have been a change in the radiation environment of the spacecraft. This factor of 2 discrepancy between the measured data and AP8 calculations is in agreement with the CRRES dosimeter

measurements that indicate that AP8 under predicts the flux for energies > 10 MeV and overpredicts the flux for lower energies [11]. Since only protons with incident energies greater than ~8 MeV can pass through the 20 mil coverglass on the MPTB solar cells, the MPTB solar cell degradation is expected to track the higher energy portion of the spectrum. Therefore, it may be concluded that the calculated results presented here are in good agreement with the measured values, where the primary cause of uncertainty lies in the environment models.

9. References

[1] M. R. Brown, C. A. Garcia, G. S. Goodelle, J. S. Powe, and J. A. Schwartz, "Characterization Testing of Measat GaAs/Ge Solar Cell Assemblies", Prog. In Photovoltaics: Res. and App., 4, 129 (1996)

[2] J. B. Marion, Classical Dynamics, Academic Press, NY 1970

[3] B. E. Anspaugh, "GaAs Solar Cell Radiation Handbook", JPL Publication 96-9, July 1, 1966.

[4] G. P. Summers, S. R. Messenger, E. A. Burke, M. A. Xapsos, and R. J. Walters, "Low Energy Proton-Induced Displacement Damage in Shielded GaAs Solar Cells in Space", Appl. Phys. Lett., 71, 832 (1997)

[5] G.P. Summers, E.A. Burke, P. Shapiro, S.R. Messenger, and R.J. Walters, "Damage Correlations in Semiconductors Exposed to Gamma, Electron, and Proton Radiations", IEEE Trans. Nucl. Sci., vol. 40, pp. 1372-1379, December 1993.

[6] For a copy of the Beta-version, contact the authors: phone (202) 767-2533, Email: Robert.Walters@nrl.navy.mil

[7] C. S. Dyer, P. R. Truscott, C. Sanderson, C. Watson, C. L. Peerless, P. Knight, R. Mugford, T. Cousins, and R. Noulty, IEEE Trans. Nuc. Sci., 47, 2208, Dec 2000

[8] T. L. Morton, Proc. 5th International Workshop on Radiation Effects on Semiconductor Devices for Space Applications, page 7, Oct 9-11, 2002,

[9] S. R. Messenger, R. J. Walters, G. P. Summers, T. Morton, G. La Roche, C. Signorini, O. Anzawa, and S. Matsuda, "A Displacement Damage Dose Analysis of the COMETS AND EQUATOR-S Space Solar Cell Flight Experiments", Proc. 16th European Photovoltaic Solar Energy Conference and Exhibition, Glasgow, Scotland, May 2000

[10] T. L. Morton, R. Chock, K. Long, S. Bailey, S. R. Messenger, R. J. Walters, and G. P. Summers, Technical Digest of the International PVSEC-11, Sapporo Hokkaido, Japan, 1999.

[11] M. S. Gussenhoven, E. G. Mullen, and D. H. Brautigam, Trans. Nuc. Sci., 46, 353 (1995)

RECENT PROGRESS ON THE STRETCHED LENS ARRAY (*SLA*)

Mark O'Neill and A.J. McDanal, ENTECH, Inc., Keller, TX 76248

Michael Piszczor and Patrick George, NASA Glenn Research Center, Cleveland, OH 44135

Michael Eskenazi and Matthew Botke, ABLE Engineering Company, Goleta, CA 93117

David Edwards and David Hoppe, NASA Marshall Space Flight Center, Huntsville, AL 35812

Henry Brandhorst, Auburn University, Auburn, AL 36849

ABSTRACT

At the last Space Photovoltaic Research and Technology Conference, SPRAT XVII, held during the fateful week of 9/11/01, our team presented a paper on the early developments related to the new Stretched Lens Array (*SLA*), including its evolution from the successful *SCARLET* array on the NASA/JPL Deep Space 1 spacecraft. Within the past two years, the *SLA* team has made significant progress in the *SLA* technology, including the successful fabrication and testing of a complete four-panel prototype solar array wing (Fig. 1). The prototype wing verified the mechanical and structural design of the rigid-panel *SLA* approach, including multiple successful demonstrations of automatic wing deployment. One panel in the prototype wing included four fully functional photovoltaic receivers, employing triple-junction solar cells. These receivers were fully encapsulated to enable high-voltage operation in space plasma, and the receivers all passed 500 V wet hi-pot testing. Complete lens/receiver units were accurately tested for performance using a large-area pulsed solar simulator (LAPSS), calibrated with reference cells flown by NASA Glenn on their Lear Jet photovoltaic test facility. The best lens/receiver unit achieved 27.5% net efficiency at 28C cell temperature under AM0 sunlight. The measured mass and performance of the prototype wing accurately matched predictions. The same performance and mass model shows that a 7 kW wing, using the same rigid-panel technology demonstrated on the prototype wing, will achieve these unprecedented performance metrics at beginning of life (BOL) on geostationary orbit (GEO, with 75C cell temperature):

- >180 W/kg specific power
- >300 W/m^2 areal power density
- >300 V operational voltage
- >9 kW/m^3 stowed power at launch
- >85% savings in cell area (cm^2/W), cell mass (g/W), and cell-related cost ($/W) compared to planar arrays

In addition to making rapid progress on the rigid-panel version of *SLA*, the *SLA* team has also made significant advances over the past two years in the flexible-blanket version of *SLA*. By integrating *SLA* with ABLE's new ***SquareRigger*** deployment and support platform, truly transformational improvements in performance metrics are achievable for very large arrays (50 kW to MW class).

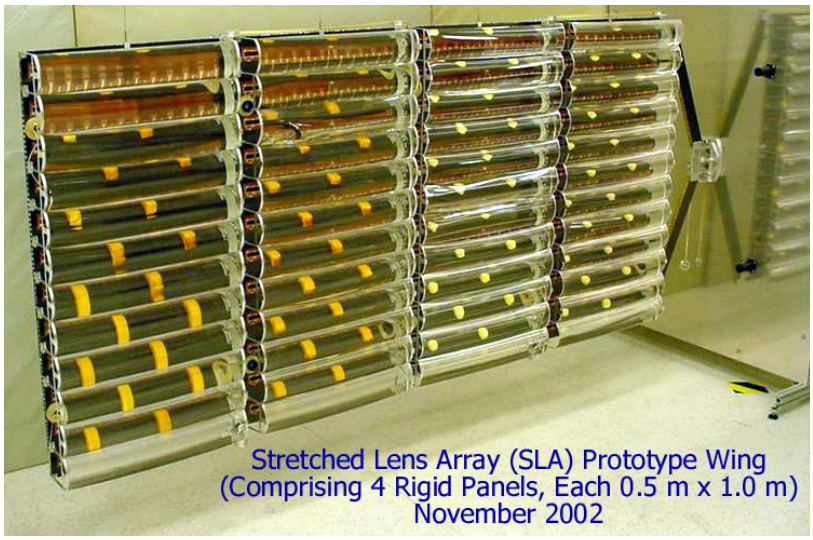

Figure 1 – Stretched Lens Array (*SLA*)

The following paragraphs present further details related to these recent developments on both versions of *SLA*.

INTRODUCTION

Fig. 2 shows the basic concept of the Stretched Lens Array (*SLA*) in an early functional prototype. Thin (140 micron), flexible, line-focus Fresnel lenses, made from a space-qualified silicone polymer (Dow Corning DC93-500), are deployed and supported by end arches, which tension the lenses in their lengthwise direction forming a stressed membrane optical element. These stretched lenses collect space sunlight and focus it onto narrow state-of-the-art multi-junction photovoltaic (PV) cell receivers, which are mounted to thin (125 micron) carbon composite sheet radiators for waste heat rejection to deep space.

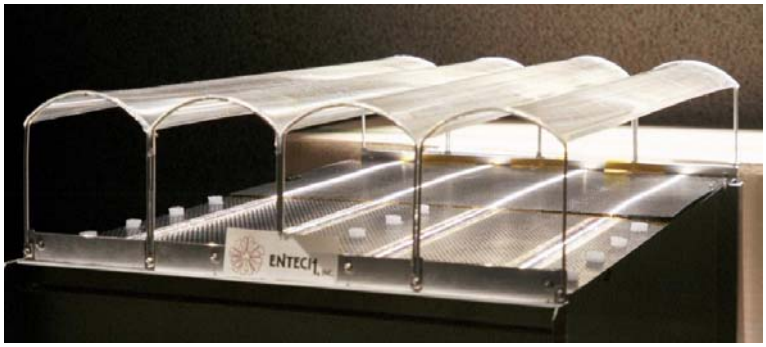

Figure 2 – Stretched Lens Array (*SLA*) with Four Lenses and Receivers

The arched-shaped lenses are each 8.5 cm wide, and focus sunlight onto PV cells which are 1.0 cm wide, for a geometric concentration ratio of 8.5X. This 8.5X concentration ratio was selected to provide ± 2 degrees of sun-pointing tolerance without appreciable power loss. Compared to conventional planar one-sun photovoltaic arrays, *SLA*'s principal and inherent advantages include a significantly lower mass (kg/m^2) and a substantially lower cost ($/W). *SLA*'s weight advantage is due to the simple fact that the lens, radiator, and narrow photovoltaic receiver assembly, all taken together, weigh about half as much per square meter as a one-sun solar cell assembly by itself. *SLA*'s cost advantage is due to the use of 85% less of the expensive photovoltaic cell material per Watt of power produced. In addition, *SLA* offers better electrical performance (W/m^2) than conventional planar one-sun photovoltaic arrays, due to the normal gain in cell conversion efficiency with concentration. The small size of the photovoltaic receiver in *SLA* enables super-encapsulation of the photovoltaic circuit with very little mass penalty. Such super-encapsulation can be tailored to enable high-voltage operation in space plasma and/or to provide radiation hardness for space missions in high charged-particle radiation environments.

Since a stressed membrane support method will never provide a near-perfect shape for the optical element, the lens is engineered to be extremely shape-error tolerant. This shape error tolerance is obtained by configuring the lens to a unique arch shape, wherein each prism comprising the lens symmetrically refracts the solar ray passing through it. As shown in Fig. 3, for each prism in the lens, the solar ray angle of incidence at the smooth outer surface is equal to the solar ray angle of emergence at the prismatic inner surface. This symmetrical refraction condition,

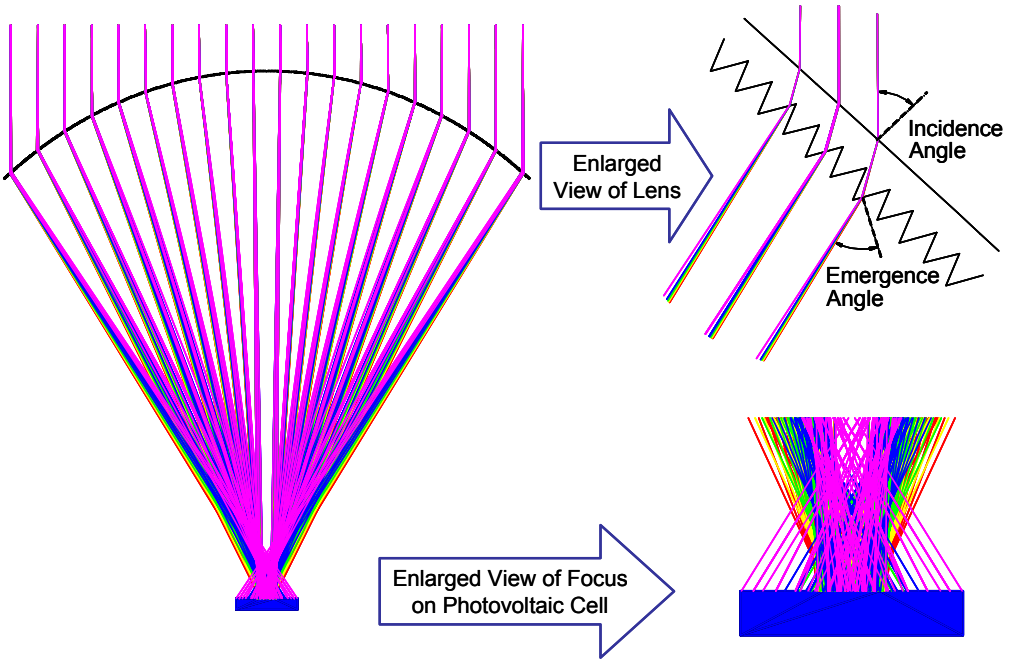

Figure 3 – Symmetrical Refraction Lens with False-Color Rays Showing Wavelengths in the Photovoltaic Cell Response Range (0.36 µm to 1.80 µm for All Three Junctions of a Triple-Junction GaInP/GaAs/Ge Cell)

combined with the refractive index of the lens material, fully defines the lens shape and prismatic pattern, and implies that each prism is oriented at its minimum-deviation condition. The symmetrical refraction lens has two key optical benefits: minimum total reflection loss at the two lens/vacuum interfaces (thereby maximizing throughput transmittance) and a unique and remarkable slope error tolerance. Compared to a reflective concentrator of any kind or to a conventional flat Fresnel lens, the slope error tolerance of the symmetrical refraction lens is more than 100 times better, as further discussed in later sections of this paper. This shape error tolerance is critical to the excellent optical performance of the *SLA* and of its predecessor solar concentrator arrays which also used the symmetrical refraction lens approach. The following section compares the symmetrical refraction lens approach with reflective concentrator arrays which have recently experienced highly publicized problems on communication satellites.

FRESNEL LENS VERSUS MIRROR SOLAR CONCENTRATORS: VASTLY DIFFERENT

In the past two years, significant problems with large reflective concentrator arrays on six GEO communication satellites have been highly publicized [1-3]. These reflective concentrator arrays use vastly different technology than the stretched lens array (*SLA*), which is the subject of this paper. The reflective concentrator arrays use 60-degree tilted mirrors on both sides of planar photovoltaic panels to increase the solar flux on these panels, an approach which has also been attempted in large terrestrial solar arrays, which also suffered from significant problems [4]. The basic concept of using tilted mirrors to augment the solar flux on planar photovoltaic panels is shown in the left sketch of Fig. 4. If such mirrors could be made and maintained in a perfect optically flat configuration, the reflected solar flux would be uniform over the planar photovoltaic panel, nearly doubling the total solar flux on the panel. Unfortunately, shape errors in these mirrors can cause significant losses and non-uniformity of the reflected solar flux on the planar photovoltaic panel, as shown in the right sketch of Fig. 4. If the mirror errors lead to concavity, the reflected flux can have spikes and voids. If the mirror errors lead to convexity, the reflected flux can be reduced by significant reflected ray losses. Both types of mirror errors are shown in the right sketch of Fig. 4, for an example value of the maximum slope error of 10 degrees at the edges of the mirrors.

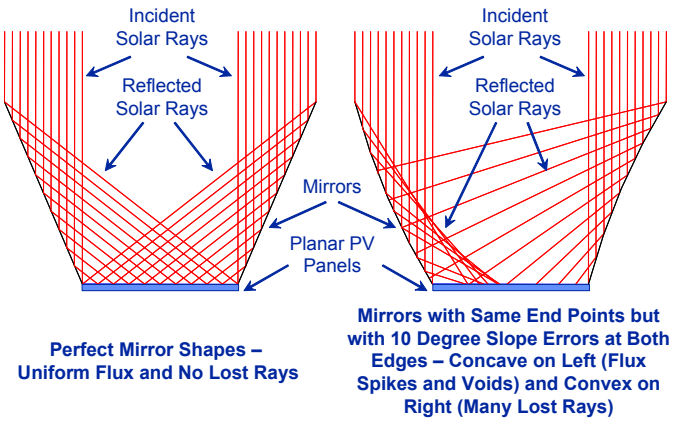

Figure 4 – Ray Traces for 60° Tilted Mirrors for Perfect Mirrors (Left) and for Mirrors with Shape Errors (Right)

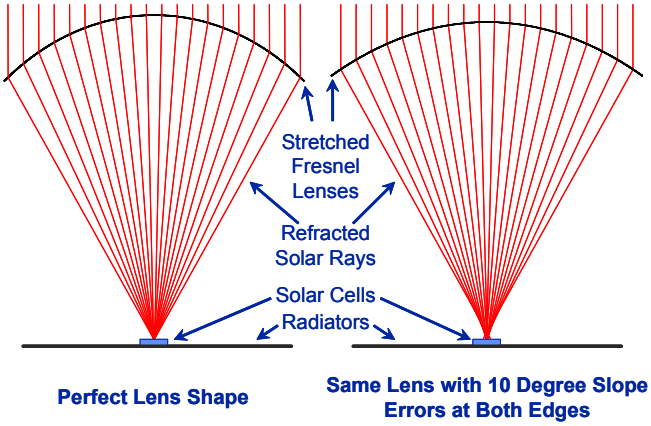

Figure 5 – Ray Traces for Symmetrical-Refraction Lens for a Perfect Lens Shape (Left) and for a Lens with Shape Errors (Right)

In contrast to reflective optics, the stretched lens array (*SLA*) uses a symmetrical-refraction Fresnel lens, described in the previous section, which is by far the most error-tolerant optical concentrator yet developed [5,6]. The symmetrical-refraction lens concentrator approach is shown in the left sketch of Fig. 5. The right sketch shows a ray trace for the same symmetrical-refraction lens with its shape distorted by a similar amount as for the mirrors in Fig. 4, i.e., with 10 degree slope errors at both edges. Note that the lens still focuses almost perfectly despite these large slope errors. This unique error tolerance has been fully described in previous publications about the symmetrical-refraction lens, which is more than 100 times as tolerant of shape errors as any reflective concentrator [6]. A direct comparison of the right sketches of Figs. 4 and 5 shows why shape errors are the most critical optical problem for reflective concentrators of all types, while shape errors are not even a significant concern for the symmetrical refraction lens.

Item	Planar Array	2X Mirror-Augmented Array (Reflective Trough Array)	8.5X Stretched Lens Array (SLA)
Cell Savings vs. Planar Array: Area, Mass, and Cost per Watt	0%	50%	85%
Space Flight Heritage and Experience	Numerous Successful Programs	Significant Performance Problems on 6 Boeing 702 Comsats (and Geometry Is Conducive to Outgassing/Photofixing)	Extremely Successful: PASP+ and SCARLET on Deep Space 1 (and Geometry Discourages Photofixing)
Terrestrial Experience for Similar Technology	Numerous Successful Programs	Significant Performance Problems for Reflective Systems (e.g., ARCO Solar 5 MW System at Carissa Plains – Mirrors Reduced Power)	Several Successful Programs (e.g., Best Performance of All 20 kW PVUSA Arrays for 10 Years)
Optics – Inherent Shape Error Problems	N/A	Significant Problem (Efficiency and/or Flux Uniformity)	Negligible Problem (200X Advantage Over Mirrors)
Predictable, Same, Unchanging Photon Flux on Each Solar Cell in Each Source Circuit	Yes	No – Reflective Optics Are Inherently Sensitive to Minuscule Shape Errors (e.g., Hubble Telescope Primary)	Yes – ENTECH's Error-Tolerant Refractive Optics
Cell Operating Temperature on GEO	50-60C	120-130C	75-80C
Super-Encapsulation of Cells for High-Voltage and/or High-Radiation Missions	Difficult and Heavy	Relatively Difficult and Relatively Heavy	Simple and Lightweight – Auburn Micrometeoroid Tests with Cells at 1,000 V

Table 1 – Fundamental Comparison of Different High-Efficiency Space Solar Arrays

While the shape error tolerance of the symmetrical-refraction lens (Fig. 5) is its most dramatic advantage over reflective concentrators (Fig. 4), a more complete comparison of these two concentrator approaches is provided in Table 1 (on the following page). A conventional planar array is also included in this comparison as the point of departure for both concentrator designs. The primary reason for using concentrators instead of planar arrays is to save cell area, mass, and cost, and the higher concentration of *SLA* leads to much higher savings than for the reflective concentrator. The space flight heritage of the Fresnel lens concentrators has been excellent, in contrast to the reflective approach. Boeing has diagnosed the problems on the 702 communication satellite arrays, and believes that outgassing products from the hot photovoltaic panels caused deposits on the mirrors, which were within the line-of-sight of the panel outgassing source. This deposition of outgassing products on the mirrors was enabled by a "photofixing" process made possible by the direct solar flux on the mirrors [3]. The material deposited on the mirrors could then itself outgas and cause deposits on the photovoltaic panels, which were within the line-of-sight of the mirror outgassing source. The deposition of outgassing products on the photovoltaic panels was enabled by the "photofixing" process made possible by the direct solar flux on the cells [3]. *SLA*'s geometry inherently discourages this complex process, since only the outer lens surface is exposed to direct solar flux. *SLA*'s predecessor, the *SCARLET* (**S**olar **C**oncentrator **A**rray using **L**inear **E**lement **T**echnology) array, which performed flawlessly for 38 months on Deep Space 1, did not experience any of the unexpected power degradation problems experienced by the Boeing 702 communication satellite arrays.

As summarized in Table 1, the terrestrial experience for both reflective and refractive concentrator approaches has also been problematic for the mirrors, and successful for the lenses. In fact, a 5 MW installation of 2X mirror-augmented silicon photovoltaic panels was installed by ARCO Solar in the middle 1980's, and degraded rapidly in power output [4]. In fact, when the system was being dismantled in the early 1990's, tests were run on array segments with and then without the mirrors in place, and more power was measured with the mirrors removed than with them in place [4]. In stark contrast, the line-focus Fresnel lens array at the U.S. Department of Energy-sponsored Photovoltaics for Utility Scale Applications (PVUSA) test site in Davis, California, outperformed all of the other photovoltaic technologies in an independent, side-by-side field test throughout the whole decade of the 1990's [7].

The inherent shape-error tolerance of the symmetrical-refraction lens enables the concentrated solar flux profile over the solar cell to be tailored by design and then accurately produced and maintained over the operational life of the system. In contrast, minute shape errors in reflective concentrators cause substantial variations in the concentrated solar flux profile, not only over an individual solar cell, but also from cell-to-cell in a series string of cells forming a source circuit. These photon flux variations from cell-to-cell in a source circuit, and the cell current variations they produce, are the Achilles' heel of reflective concentrator optics, since they can substantially degrade the source circuit power output.

As summarized in Table 1, an additional problem for the mirror-augmented panel (reflective trough) is the high cell operating temperature caused by the increased solar flux without a corresponding increase in heat rejection area. *SLA* does not suffer from this problem, since its heat rejection area equals its sunlight-collecting aperture area, just like a one-sun planar array. Furthermore, the *SLA*'s small individual lens size was selected based on radiator heat conduction from the line-focus solar cell receiver laterally outward into the surrounding radiator area. For the selected 8.5 cm aperture width, only a 125 micron thick graphite cloth radiator is needed to efficiently spread the waste heat laterally into the radiator. Thus, the operating cell temperature for *SLA* is about 50°C cooler than for the reflective trough.

Finally, the *SLA* enables super-encapsulation of the photovoltaic cell circuit with very little mass penalty, due to the small size of the cells compared to the aperture area of the array. Such super-encapsulation enables high-voltage operation of the *SLA* in the space plasma, reducing cabling size and mass, and minimizing the need for voltage-boosting electronics for high-voltage loads such as electronic thrusters. Such super-encapsulation can also provide radiation hardness for the solar cells, especially for high-radiation missions or military missions. Such super-encapsulation is heavy and expensive for lower concentration arrays or planar arrays, due to the much larger cell area per unit power output.

In summary, the technologies for mirror-augmented photovoltaic panels and Fresnel lens photovoltaic concentrators are vastly different. The track records of these two competing concentrator approaches have also been completely different, both in space and on the ground. Clearly, experiences, good or bad, for either one of these two technologies do not apply to the other.

The following paragraphs further describe the Fresnel lens photovoltaic concentrator array technology.

BACKGROUND

Since 1986, ENTECH and NASA have been developing and refining space photovoltaic arrays using refractive concentrator technology [8]. As discussed above, unlike reflective concentrators, these refractive Fresnel lens concentrators are configured to minimize the effects of shape errors, enabling straightforward manufacture, assembly, and operation on orbit. By using a unique arch shape, these Fresnel lenses provide more than two orders of magnitude better shape error tolerance than reflective concentrators or conventional flat Fresnel lens concentrators [6].

In the early 1990's, the first refractive concentrator array was developed and flown on the PASP Plus mission, which included a number of small advanced arrays [9]. The refractive concentrator array used ENTECH mini-dome lenses over Boeing mechanically stacked multi-junction (MJ) cells (GaAs over GaSb). The mini-dome lenses were made by ENTECH from space-qualified silicone (DC 93-500), and coated by Boeing and OCLI to provide protection against space ultraviolet (UV) radiation and atomic oxygen (AO). This array performed extremely well throughout the year-long mission in a high-radiation, 70-degree inclination, 363 km by 2550 km elliptical orbit, validating both the high performance and radiation hardness of the refractive concentrator approach [9]. In addition, in high-voltage space plasma interaction experiments, the refractive concentrator array was able to withstand cell voltage excursions to 500 V relative to the plasma with minimal environmental interaction [9].

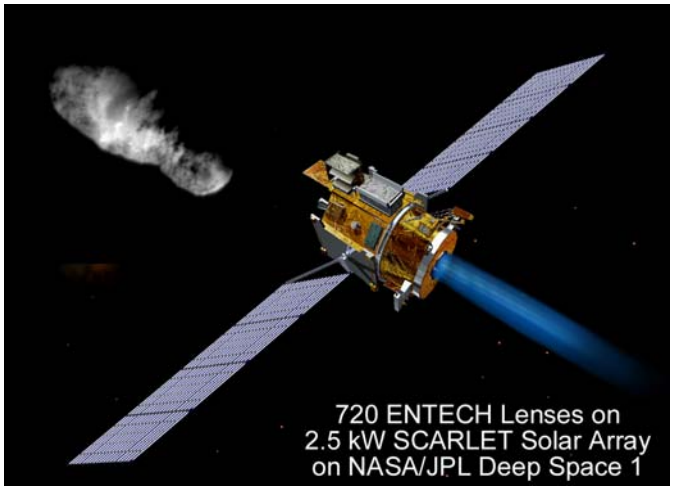

Figure 6 – *SCARLET* Array on Deep Space 1

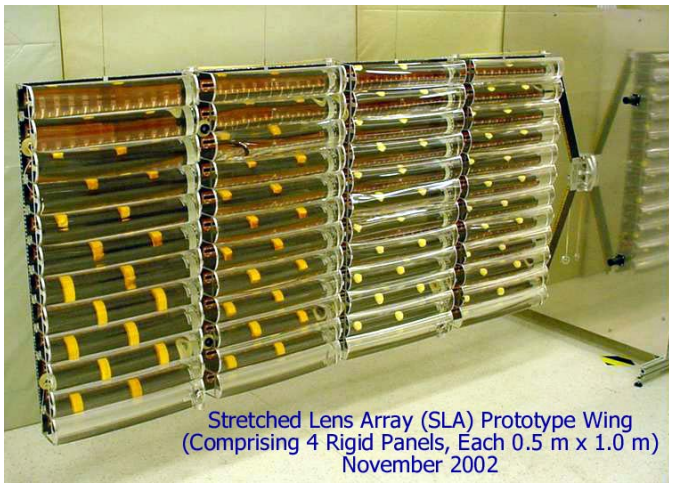

Figure 7 – Stretched Lens Array (*SLA*) Wing

In the middle 1990's, ENTECH and NASA developed a new line-focus Fresnel lens concentrator, which is easier to make and more cost-effective than the mini-dome lens concentrator. Using a continuous roll-to-roll process, 3M can now rapidly mass-produce the line-focus silicone lens material in any desired quantity. In 1994, ABLE joined the refractive concentrator team and led the development of the *SCARLET* solar array [10]. *SCARLET* (Fig. 6) used a small (8.5 cm wide aperture) silicone Fresnel lens to focus sunlight at 8X concentration onto radiatively cooled triple-junction cells. Launched in October 1998, the 2.5 kW *SCARLET* array powered both the spacecraft and the ion engine on the NASA/JPL Deep Space 1 probe, shown in Fig. 6.

SCARLET achieved over 200 W/m^2 areal power density and over 45 W/kg specific power, the best performance metrics up to that time [11]. With *SCARLET* working flawlessly, Deep Space 1 had a spectacularly successful rendezvous with the comet, Borrelly, in September 2001, capturing the highest-resolution images of a comet to date and other unprecedented comet data. At the end of the 38-month extended mission, in December 2001, *SCARLET*'s power was still within $\pm$ 2% of predictions.

Over the past four years, the team, now including Auburn University, has developed an evolved version of the flight-proven *SCARLET* array, called the Stretched Lens Array (*SLA*), with much better performance metrics [12-17]. A prototype *SLA* wing is shown in Fig. 7, and the new *SLA* approach is described in the following section.

STRETCHED LENS ARRAY (*SLA*) DESCRIPTION

The Stretched Lens Array (*SLA*) is an evolved version of *SCARLET*, retaining the essential power-generating elements (the silicone Fresnel lens, the multi-junction solar cells, and the composite radiator sheet) while discarding the non-power-generating elements (the lens glass arch superstrates, the lens support frames, the photovoltaic receiver support bars, and most of the honeycomb and back face sheet material in the panels). The defining feature of *SLA* (Fig. 7) that enables the elimination of so many elements of the *SCARLET* array is the stretched lens optical concentrator (Fig. 8). By using end arches to stretch the silicone Fresnel lens in the lengthwise direction only, these lenses become self-supporting stressed membranes. *SCARLET*'s glass arches are thus no longer needed, eliminating their complexity, fragility, expense, and mass in the new, patented *SLA* [13]. With this substantial lens-related mass reduction, the supporting panel structural

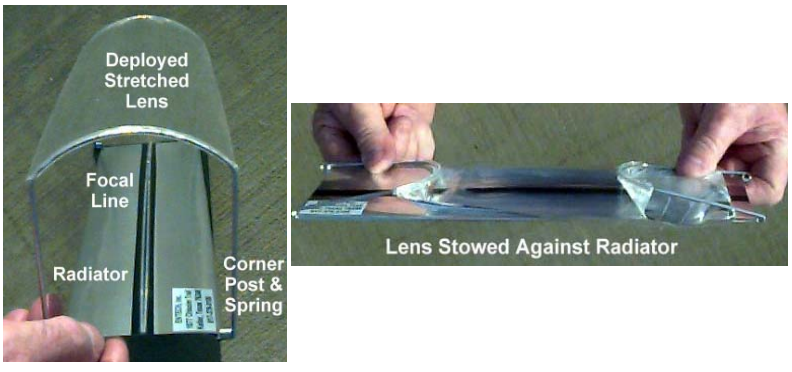

Figure 8 – Model Showing Basic Stretched Lens Approach

loads are reduced, making ultra-light panels practical for *SLA*. This cascading mass-reducing effect of the stretched lenses continues throughout the *SLA* wing structure, resulting in unprecedented performance metrics.

HARDWARE DEVELOPMENT AND TESTING

In the past year, the *SLA* team has fabricated and successfully evaluated a subscale four-panel array (Fig. 7), including 48 stretched lenses and 4 fully functional photovoltaic receivers, each containing 14 series-connected solar cells (Fig. 9). The four receivers included two using triple-junction (GaInP/GaAs/Ge) cells from Spectrolab and two using triple-junction cells from EMCORE. Two of the receivers used prism covers over the cells to eliminate gridline shadowing losses and two used more conventional ceria-doped microsheet covers. The receivers were assembled as flex circuits, including both cells and bypass diodes, and were fully encapsulated to enable high-voltage operation. To verify high-voltage operation, each of the receivers was wet hi-pot tested, with 500 V applied between the cell string and the composite panel, while distilled water was sprayed onto the receiver and panel. The water simulated space plasma, which can lead to leakage currents or arcs from photovoltaic circuits to the panel structure for conventional cell circuits exposed to high voltage operation. None of the four circuits had more than 1 micro-Amp leakage current during the test. Similar wet hi-pot testing has been used in the past to verify the encapsulation on *SLA* photovoltaic receiver coupons which were successfully tested at 1,000 V in simulated space plasma while being subjected to simulated micrometeoroid impacts [15]. These latest results extend the earlier single-cell coupon high-voltage test results to more flight-like 0.5-meter-long *SLA* receivers.

Figure 9 – Photovoltaic Receivers Undergoing 500 V Wet Hi-Pot Testing

The four *SLA* receivers were performance-tested for one-sun performance in ABLE's Large Area Pulsed Solar Simulator (LAPSS), using NASA-Glenn-Lear-Jet-flown triple-junction reference cells from the same production lots, in addition to individual reference cells of each of the three junction types. Then the panel was equipped with stretched lenses, and the receivers were again LAPSS-tested for *SLA* performance. Fig. 10 shows the measured results (AM0, 20°C) for the two receivers using Spectrolab cells with and without the lenses installed. The solid curves represent the receiver with prism covers over the cells, while the dashed curves represent the receiver with ceria-doped microsheet over the cells. Note that the one-sun efficiency of the prism-covered-cell receiver was approximately 29%, while the net lens/receiver efficiency for the same prism-covered-cell receiver was approximately 28%. When these results were corrected to the standard reporting temperature of 28°C, the net lens/receiver efficiency for the prism-covered-cell receiver was 27.5%. As expected, the net lens/receiver efficiency for the microsheet-covered-cell receiver was slightly lower at 26.1% at 28C.

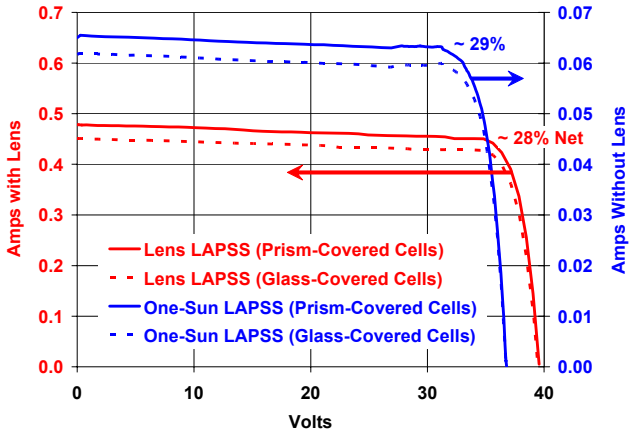

Figure 10 – Measured Performance Results (Air Mass Zero, 20°C)

The measured performance results of the 0.5-meter-long lenses and receivers extend the earlier results for single lens/cell units which were flown by NASA Glenn on their Lear jet test platform for AM0 current calibration, and then LAPSS-tested for AM0 performance. These lens/cell units also had over 27% net lens/cell efficiency (AM0, 25°C), using prism-covered cells from either Spectrolab or EMCORE [14,15]. All of these results are also in close agreement with individual lens optical efficiency measurements and prism-covered solar cell conversion efficiency measurements. The stretched lens provides 90% ± 2% net optical efficiency in collecting photons and placing them onto the triple-junction solar cells. This excellent lens performance is due in large part to the unique color-mixing design of the lens, which eliminates chromatic aberration losses in the multi-junction cells [17]. The prism-covered multi-junction cells are over 30% efficient (8 suns AM0, 28°C) in converting sunlight into electricity [16,18]. This excellent cell performance is due in large part to the gain in efficiency with concentration, an 11% relative improvement for the Spectrolab triple-junction cells [16,18].

The mass of every element in the prototype four-panel wing of Fig. 7 was carefully measured, and ABLE used these results to accurately estimate the mass of the prototype wing if it had been fully populated with 48 photovoltaic receivers under 48 stretched lenses. The result of this mass estimate is 6.46 kg for a fully populated four-panel wing of the prototype's size (2.06 m^2 total wing area). ABLE also estimated the on-orbit beginning-of-life (BOL) power output of this prototype wing, including the power reduction at the GEO operating temperature of 75°C compared to the standard test temperature of 28°C and all other normal array losses (e.g., packing factors, cabling and blocking diode losses, etc.). The result of this performance estimate is 629 W for a fully populated wing of the prototype's size. Ratios of these values provide the prototype wing's key performance metrics of 305 W/m^2 areal power density and 97 W/kg specific power. The areal power density goal for a near-term *SLA* was 300 W/m^2, which has been met. The wing-level specific power value also falls right on the predicted curve of *SLA* specific power versus wing power level (Fig. 11). Note also that NASA's target value for future lightweight solar arrays of 175 W/kg for a 7 kW wing, as detailed in the recent New Millennium Program Space Technology 8 (NMP ST8) procurement is exceeded by *SLA*.

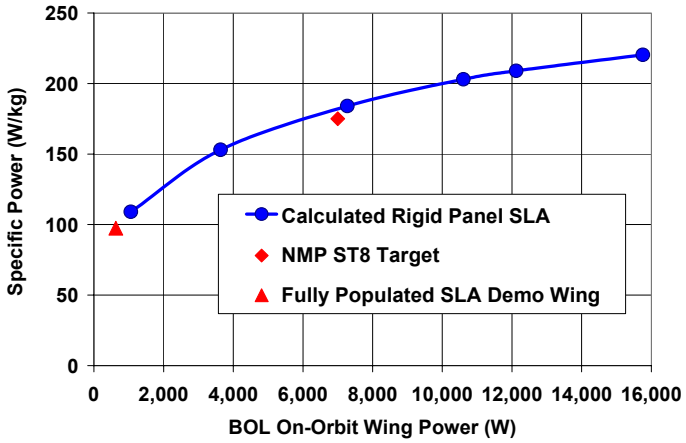

Figure 11 – *SLA* Specific Power vs. Wing Power on Geostationary (GEO) Orbit at Beginning of Life (BOL)

In addition to verifying the performance and mass estimates for *SLA*, the prototype four-panel wing of Fig. 7 also validated, via numerous deployments, the basic *SLA* mechanical approaches for deploying the four panels and the 12 lenses on each panel (Fig. 12).

The following section describes a point design of an *SLA* solar array wing rated at 7 kW of output power, a wing size typical of today's communication satellites.

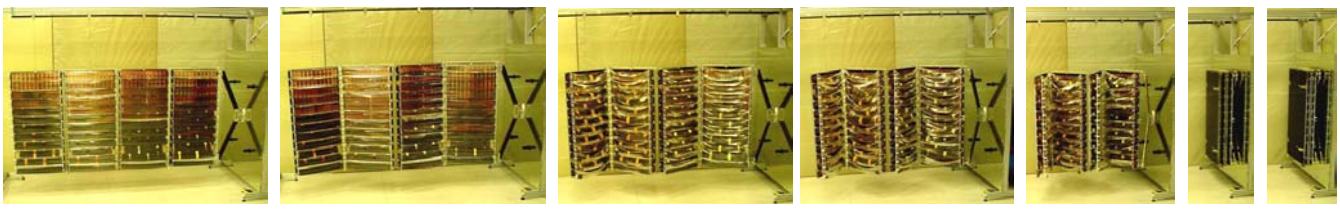

Figure 12 – *SLA* Prototype Wing Deployment

POINT DESIGN OF A 7 KW *SLA* WING

As shown in Fig. 11, the performance advantages of *SLA* increase rapidly with increasing wing size, with the specific power reaching more than 180 W/kg at the important wing size of 7 kW. Since this wing size is typical of the latest generation of GEO communication satellites, the *SLA* team has generated a detailed point design for a 7 kW wing, as shown in the sketch and table below (Fig. 13). This wing design is conventional and conservative in configuration and components, with robust structural stiffness parameters. The beginning-of-life (BOL) areal power density is slightly lower than already demonstrated on the prototype hardware described above. Future multi-junction cells will no doubt eclipse the demonstrated values, providing even higher performance metrics than those shown in Fig. 13. While cost values are not presented, the *SLA* team has analyzed costs in detail, and due to more than 85% savings in cell area and cost compared to a planar multi-junction array, the *SLA* wing will cost 50% less than a planar wing of equal power.

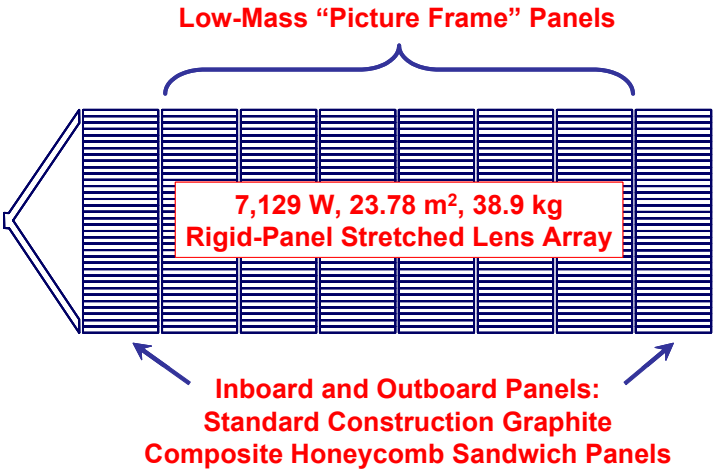

Feature	Value or Characteristic
Point Design Basis	7,129 Watts (BOL)
SLA Implementation	Pop-up lenses
Base Platform Design Maturity	Most components flight proven on DS1
Specific Power	183 W/kg
Stowed Volume	0.11 m^3/kW
Stowed Stiffness	40 Hz
Deployed Stiffness	0.1 Hz
Stowed Power	Easily implemented on outer panel
Ease of Adding Planar Panel	Easily implemented on outer panel
Flatness & Warping	Well understood flat stable platform
Deployment Testing	Can use existing off-loaders
Power Testing	Pop-up lenses allow each panel to be tested as a complete assembly before wing integration
Commercial Appeal	Easier to integrate on commercial spacecraft. Readily accepted configuration.
Self Shadowing	No self shadowing

Figure 13 – Point Design for 7 kW *SLA* Wing

RELATED WORK

The *SLA* team is also performing space environmental effects testing of key *SLA* components [19,20]. This ongoing testing includes solar ultraviolet and charged particle radiation exposure of stretched lenses, and micrometeoroid impact testing of lenses and photovoltaic receivers at high voltage in simulated space plasma. In addition, the *SLA* team has analyzed additional *SLA* performance metrics for a wide variety of different missions, and in each case, *SLA* provides excellent advantages over the planar array competition [21].

ALTERNATE VERSIONS OF *SLA*

While the rigid-panel wing, described in previous paragraphs, is the near-term, conservative embodiment of *SLA* for near-term missions, alternate flexible-blanket versions of *SLA* are also under development. These versions use lenses and photovoltaic receiver/radiator elements that accordion fold for compact launch stow volume, and then deploy as an end-tensioned dual-blanket (stretched lenses on top and stretched radiator sheets with photovoltaic receivers on bottom) array on orbit. In fact, Fig. 2 shows a small model of the flexible-blanket *SLA*.

One of the most attractive approaches for deploying and supporting the flexible-blanket version of *SLA* on orbit is ABLE Engineering's *SquareRigger* platform, originally developed for the Air Force Research Laboratory. *SLA* on *SquareRigger* could provide very large power arrays (50 kW to MW class) for a variety of future space missions. Fig. 14 (on the following page) shows a schematic of the *SLA*/*SquareRigger* array. The stowed package of *SquareRigger* is a tight bundle of structural tubes with the flexible blanket elements (flexible silicone lenses and composite radiator sheets with photovoltaic receivers mounted to the sheets) folded tightly between tubes. The tubes deploy first to form initially empty rectangular bays.

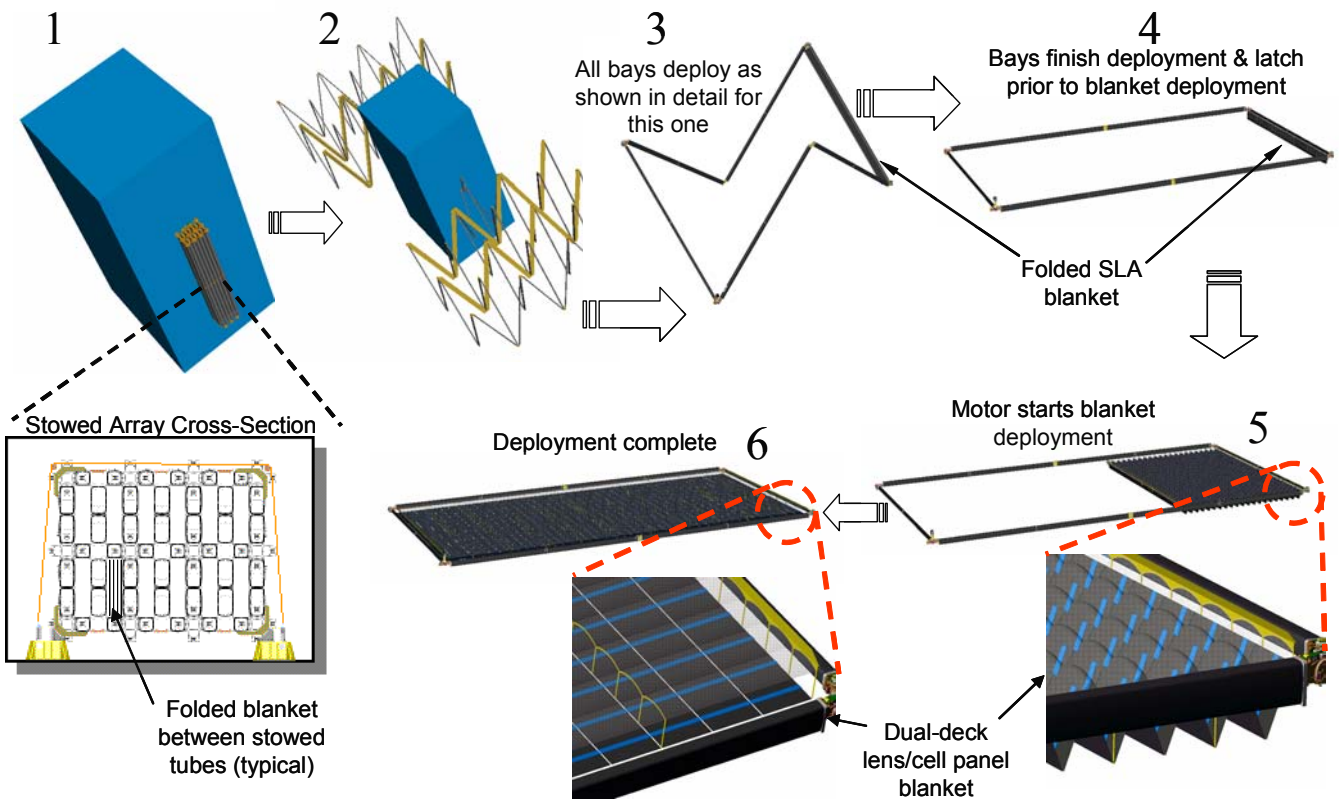

Figure 14 – Stretched Lens Array (*SLA*) on *SquareRigger* Platform

As shown in Fig. 14, after tube deployment is complete, a motor automatically unfolds the flexible blanket photovoltaic array from one end to the other until the bay is fully populated. While *SquareRigger* was initially envisioned as a thin-film photovoltaic blanket platform, it is ideally suited to the more efficient *SLA* technology. The combination of *SLA* and *SquareRigger* provides an unmatched set of performance metrics for large-capacity space power arrays, as summarized in Table 2.

Time Frame	< 5 Years	5-10 Years
Power Capability (kW)	100	1,000
BOL Specific Power (W/kg)	330	500
Stowed Power (kW/m^3)	80	120
Voltage	1,000	TBD

Table 2 – Performance Attributes of *SLA* on ABLE's *SquareRigger* Platform

ABLE Engineering has recently completed a NASA Phase I SBIR contract related to the integration of *SLA* with *SquareRigger*, including fabrication of a small demonstration unit. The results of this contract have confirmed the expected advantages of marrying *SLA* to *SquareRigger*, as discussed in another paper at this SPRAT XVIII Conference.

In addition to space applications, the combination of color-mixing symmetrical-refraction Fresnel lenses and multi-junction photovoltaic cells should have spin-off applications in the terrestrial solar energy marketplace. Developments are already underway on terrestrial versions of these high-performance photovoltaic concentrators. Indeed, numerous outdoor performance tests of a space-optimized *SLA* mini-concentrator module have demonstrated over 30% net-aperture-area solar-to-electric conversion efficiency. These results are believed to represent the first time that the 30% efficiency threshold has ever been broken by any type of solar energy converter tested outdoors under natural terrestrial sunlight [15].

CONCLUSIONS

A new type of space solar power system is being developed with unprecedented performance and mass properties. The Stretched Lens Array (*SLA*) uses ultra-thin refractive optical elements to collect and focus sunlight onto narrow state-of-the-art multi-junction photovoltaic cells, which are mounted to ultra-thin composite radiator sheets. *SLA* is being developed in two versions:

- A rigid-panel *SLA*, which uses a conventional and low-risk approach to deployment and support on orbit. This version of *SLA* offers substantially improved performance metrics for near-term solar array wings up to 20 kW.
- A flexible-blanket *SLA*, which uses more advanced and higher performance approaches to deployment and support on orbit. This version offers transformational performance metrics for longer-term solar array wings in the 50 kW to MW class.

Hardware developments to date have verified the performance, mass, and cost advantages of the new *SLA* technology.

ACKNOWLEDGMENT

The authors gratefully acknowledge NASA's support of the work presented in this paper.

REFERENCES

1. P.B. deSelding, "Power Problems Threaten On-Orbit Satellites," *Space News*, September 27, 2001.
2. P.B. deSelding, "Space Insurance Continues to Be Seen as Risky Market," *Space News*, January 14, 2003.
3. M. Bodeau, "Root-Cause of the 702 Concentrator Array Anomaly," Presentation at the 2003 Space Power Workshop, Redondo Beach, April 2003.
4. H.J. Wenger et al., "Decline of the Carissa Plains PV Power Plant: The Impact of Concentrating Sunlight on Flat Plates," 22nd IEEE-PVSC, 1991.
5. M.J. O'Neill, "Solar Concentrator and Energy Collection System," U.S. Patent 4,069,812, 1978.
6. M.J. O'Neill, "Silicon Low-Concentration, Line-Focus, Terrestrial Modules," Chapter 10 in *Solar Cells and Their Applications*, John Wiley & Sons, 1995.
7. PVUSA Project Team, "1998 PVUSA Progress Report," USDOE Contract No. DE-FC04-96AL89774, 1999.
8. M.F. Piszczor and M.J. O'Neill, "Development of a Dome Fresnel Lens/GaAs Photovoltaic Concentrator for Space Applications," 19th IEEE-PVSC, 1987.
9. H. Curtis and D. Marvin, "Final Results from the PASP Plus Flight Experiment," 25th IEEE-PVSC, 1996.
10. P.A. Jones et al., "The *SCARLET* Light Concentrating Solar Array," 25th IEEE-PVSC, 1996.
11. D.M. Murphy, "The *SCARLET* Solar Array: Technology Validation and Flight Results," Deep Space 1 Technology Validation Symposium, Pasadena, 2000.
12. M.J. O'Neill, "Stretched Fresnel Lens Solar Concentrator for Space Power," U.S. Patent 6,075,200, 2000.
13. M.J. O'Neill et al., "Development of the Ultra-Light Stretched Lens Array," 29th IEEE-PVSC, 2002.
14. M.J. O'Neill et al., "The Stretched Lens Array (*SLA*): A Low-Risk, Cost-Effective Concentrator Array Offering Wing-Level Performance of 180 W/kg and 300 W/m^2 at 300 VDC," 37th IECEC, 2002.
15. M.J. O'Neill et al., "The Stretched Lens Array (*SLA*)," IEEE Aerospace and Electronic Systems Magazine, Vol. 18, No. 1, January 2003.
16. M.F. Piszczor et al., "Stretched Lens Array (*SLA*) Photovoltaic Concentrator Hardware Development & Testing," Third World Conference on Photovoltaic Energy Conversion, Osaka, 2003.
17. M.J. O'Neill, "Color-Mixing Lens for Solar Concentrator System and Methods of Manufacture and Operation Thereof," U.S. Patent 6,031,179, 2000.
18. A. Stavrides et al., "Fabrication of High-Efficiency III-V Multi-Junction Solar Cells for Space Concentrators," 29th IEEE-PVSC, 2002.
19. H.W. Brandhorst et al., "Hypervelocity Impact Testing of Stretched Lens Array Modules," Sixth European Space Power Conference, Oporto, Portugal, 2002.
20. D.L. Edwards et al., "Optical Analysis of Transparent Polymeric Material Exposed to Ultraviolet Radiation," 8th International Symposium on Materials in a Space Environment, Arcachon, France, 2000.
21. H.W. Brandhorst et al., "Photovoltaic Options for Increased Satellite Power at Lower Cost," Third World Conference on Photovoltaic Energy Conversion, Osaka, 2003.

Materials on the International Space Station - Forward Technology Solar Cell Experiment

R. J. Walters, J. C. Garner, S. N. Lam, J. A. Vazquez, W. R. Braun, and R. E. Ruth
US Naval Research Laboratory, Washington, DC 20375

J. R. Lorentzen
SFA Inc.

Cdr R. Bruninga (Ret.)
US Naval Academy, Annapolis, MD 21402

P. P. Jenkins
Ohio Aerospace Institute, Cleveland, OH 44135

J. M. Flatico
QSS, Cleveland, OH 44135

D. M. Wilt, M. F. Piszczor, L. C. Greer, and M. J. Krasowski
NASA Glenn Research Center, Cleveland, OH 44135

INTRODUCTION

This paper describes a space solar cell experiment currently being built by the Naval Research Laboratory (NRL) in collaboration with NASA Glenn Research Center (GRC), and the US Naval Academy (USNA). The experiment has been named the Forward Technology Solar Cell Experiment (FTSCE), and the purpose is to rapidly put current and future generation space solar cells on orbit and provide validation data for these technologies. The FTSCE is being fielded in response to recent on-orbit and ground test anomalies associated with space solar arrays that have raised concern over the survivability of new solar technologies in the space environment and the validity of present ground test protocols. The FTSCE is being built as part of the Fifth Materials on the International Space Station (MISSE) Experiment (MISSE-5), which is a NASA program to characterize the performance of new prospective spacecraft materials when subjected to the synergistic effects of the space environment. Telemetry, command, control, and communication (TNC) for the FTSCE will be achieved through the Amateur Satellite Service using the PCSat2 system, which is an Amateur Radio system designed and built by the USNA. In addition to providing an off-the-shelf solution for FTSCE TNC, PCSat2 will provide a communications node for the Amateur Radio satellite system. The FTSCE and PCSat2 will be housed within the passive experiment container (PEC), which is an approximately 2ft x2ft x 4in metal container built by NASA Langley Research Center (NASA LaRC) as part of the MISSE-5 program. NASA LaRC has also supplied a thin film materials experiment that will fly on the exterior of the thermal blanket covering the PCSat2. The PEC is planned to be transported to the ISS on a Shuttle flight. The PEC will be mounted on the exterior of the ISS by an astronaut during an extravehicular activity (EVA). After nominally one year, the PEC will be retrieved and returned to Earth. At the time of writing this paper, the subsystems of the experiment are being integrated at NRL, and we are preparing to commence environmental testing.

The Space Test Program (STP) is responsible for the integration of MISSE-5 with the Shuttle and the launch of MISSE-5. All public release of information concerning the Spaceflight of the MISSE5 payload will be coordinated and approved by STP and NRL. This includes the release of any information associated with MISSE-5 space flight experiment integration or operations.

MATERIALS ON THE INTERNATIONAL SPACE STATION EXPERIMENTS

The Materials on the International Space Station Experiments (MISSE) is a NASA program designed to provide access to space for new materials and devices being considered for use in space (http://misse5.larc.nasa.gov/index.html). This is accomplished by placing experiments into the Passive Experiment Container (PEC) which is a metal box approximately 2 ft x 2ft x 4 inches fabricated by NASA Langley Research Center (Figure 1). As shown in Figure 1, the experiments are mounted on custom designed trays that mount within the PEC. When closed, the PEC provides the container for the experiments for launch and transfer to the ISS on the Shuttle. For deployment, the PEC is clamped to a handrail on the exterior of the ISS by an astronaut who then opens the PEC to expose the experiments (Figure 2). The FTSCE will be the primary experiment on the 5th MISSE project.

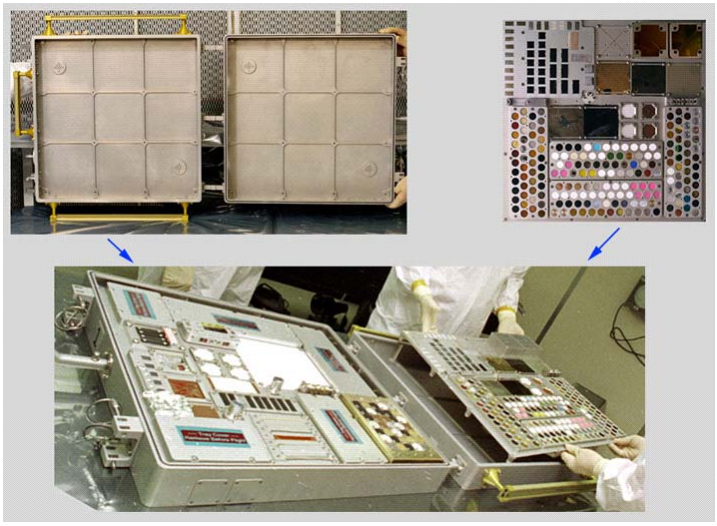

Figure 1: This is a photograph of a Passive Experiment Container (PEC). The PEC is built by NASA and is designed to hold experiments mounted on trays as shown. The PEC is closed to protect the experimental samples during transport on the Shuttle and deployment on the ISS. Once deployed, the PEC is opened to expose the experiments to the space environment. At the end of the mission, the PEC is closed and returned to Earth.

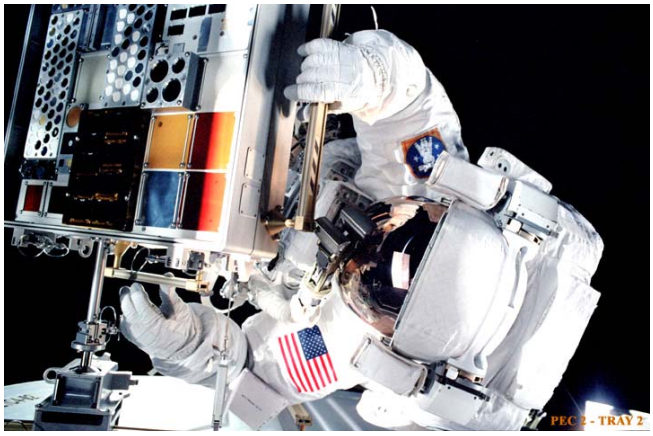

Figure 2: This is a photograph of an astronaut deploying the second PEC onto the exterior of the ISS.

DESCRIPTION OF THE FTSCE EXPERIMENTS

A total of 39 solar cells are included in the FTSCE. The technologies include state-of-the-art and next generation multijunction InGaP/GaAs/Ge, heteroepitaxial GaAs/GeSi/Ge, and amorphous Si and CuIn(Ga)Se_2 thin film solar cells. A photograph of the deck that holds the experiments is shown in Figure 3. This deck is designed as a heat shield to help keep the interior of the PEC warm and is referred to as the Thermal Deck. The experiments are identified in Table 1. The primary experiments are the triple-junction (3J) InGaP/GaAs/Ge based technologies from Spectrolab (SPL) and Emcore. In each case, the current state-of-the-art technology (ITJ for SPL and ATJM for Emcore) and the next generation technology (UTJ for SPL and BTJ for Emcore) are included. In addition, the Emcore ATJM devices include the new monolithic bypass diode. The SPL panel includes two DJ InGaP/GaAs/Ge solar cells that serve as control cells. The Emcore and SPL experiments were assembled by the manufacturer according to their standard practices on aluminum honeycomb rigid array substrates.

Laboratory development technologies are also included in the FTSCE. There are several single-junction (SJ) GaAs solar cells grown on Si substrates that are representative of the GaAs/SiGe/Si technology being developed jointly by NASA GRC, Ohio State University (OSU), and Massachusetts Institute of Technology (MIT). These cells, along with GaAs/Ge control cells, are mounted on a rigid Al honeycomb substrate. There are four 3J InGaP/InGaAs/Ge solar cells supplied by SPL. These are the metamorphic cells that employ a stoichometry that results in a slightly lattice mismatched semiconductor stack, which, in turn, results in a bandgap combination more closely optimized for the air mass zero (AM0) spectrum. These solar cells are mounted on the SPL panel.

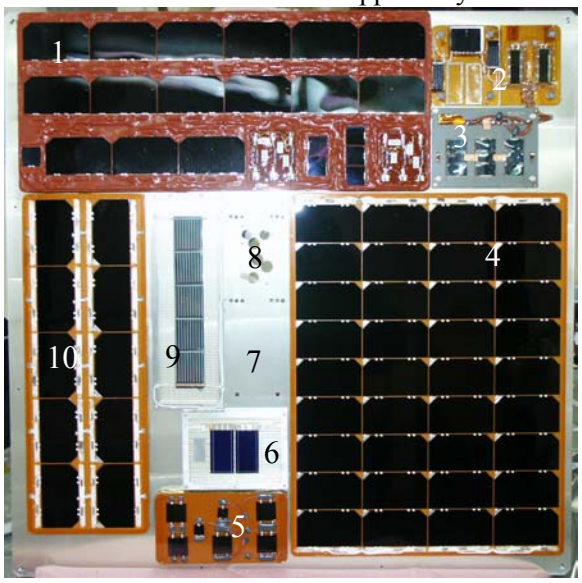

Figure 3: This is a photograph of the FTSCE experiment deck to be placed into the MISSE5 PEC. The experiments are numbered in the picture and described in **Table 1**. Note that the contamination monitor (6) and sun sensors (7) are not in this picture.

The FTSCE also includes flexible, thin-film solar cell (TFSC) technologies. Because the flexible TFSC experiments represent not only a shift in solar cell technology but also a potential dramatic change in future solar blanket and array technology designs, the FTSCE TFSC experiments were fabricated to mimic as closely as possible functional "first-generation" thin-film blanket technology. Each experiment includes multiple, interconnected cells mounted on a light weight array substrate. Two of the experiments incorporate amorphous silicon (a-Si) photovoltaic technology. One a-Si sample utilizes monolithically-interconnected cells grown by Iowa Thin Film (ITF) on a Kapton substrate. This unit was provided by Lockheed Martin and the Aerospace Corporation and represents a variety of interconnect, laydown and coating techniques developed for their thin-film program. The other a-Si experiment consists of a-Si material from UniSolar grown on a stainless steel (SS) substrate using their commercial production process. The cells for this experiment were integrated by AEC-Able Engineering using an adaptation of their UltraFlex blanket design and represents a near-term attempt to "space-qualify" thin-film cell technology when integrated into a viable light weight solar array design. This sample consists of two interconnected a-Si on SS cells affixed to a Vectran gore weave, which simulates the deployed conditions on the UltraFlex array design. It will test cell-to-cell interconnects, cell-to-array attachments and coating technology under long-term space environmental conditions. AEC-Able/NASA Glenn also supplied a $CuIn(Ga)Se_2$ (CIGS) experiment integrated into the same UltraFlex blanket design as described above. This experiment consists of five CIGS cells interconnected in series using a "shingled" approach. The CIGS cells were provided by ITN/Global Solar. It is important to note that the three FTSCE thin film experiments are primarily thin-film blanket technology durability tests. As noted in Table 1, the efficiency of some of the thin-film devices being flown do not represent the current achievable performance of that technology and were selected because of availability or adaptability to specific thin-film blanket technologies.

The FTSCE includes an experiment to test the environmental durability and long-term transmittance of silicone materials. Certain silicones, such as DC 93-500 that is currently used as a transparent adhesive to affix a coverglass to crystalline solar cells, are being considered for use as concentrator lens materials or coatings for advanced photovoltaic devices. It is critical to quantitatively understand the long-term performance of these materials, specifically optical transmittance degradation due to UV darkening, for such applications. The Silicone Degradation Experiment consists of films of silicone (DC 93-500) attached to two different solar cell coverglasses. These two samples are placed over multijunction solar cells so that optical transmission (relative to the response of the MJ cells) can be monitored throughout the duration of the flight experiment. Two other bare

silicone samples are being flown as passive experiments and will be evaluated upon return to earth at the completion of the mission.

A passive contamination monitor will fly on the FTSCE. The monitor consists of a piece of CMX coverglass mounted such that a large surface area of the glass is exposed to the space environment. Transmission and reflectance measurements were made on the glass prior to integration, and these measurements will be repeated upon return to Earth. Comparison of the pre- and post-flight data will enable an evaluation of the effect of contamination on the output of the experimental solar cells. The theory is that any loss in transmission due to contamination will be observed in the coverglass data, and assuming uniform contamination of the FTSCE surface, this will translate into a decrease in photocurrent of all of the experimental cells.

DESCRIPTION OF THE THIN FILM MATERIALS EXPERIMENT

As described more fully below, one half of the MISSE 5 PEC will hold the PCSat2 system which is the RF communications subsystem. This half of the PEC is covered by a thermal blanket, and the PEC will be oriented on orbit so that this side is always facing away from the sun. The NASA Langley team has transformed the outer layer of the thermal blanket into a three and one half ounce experiment to evaluate the in space survivability of 200 advanced materials that are being developed to enable future US space missions. The survivability of these materials will be established by comparing pre and post flight characterization test data. The exposure conditions anticipated for this experiment are unprecedented in previous space exposure experiments. Since these specimens will be facing the anti-solar direction when mounted on the ISS, they will receive no UV radiation that can rupture chemical bonds and provide reactive free-radical sites. They will be subjected to thermal cycling, particulate radiation and atomic oxygen bombardment. With no UV exposure, all reactions that do occur will be essentially chemically driven oxidation. A photograph of the experiment package is shown in Figure 4.

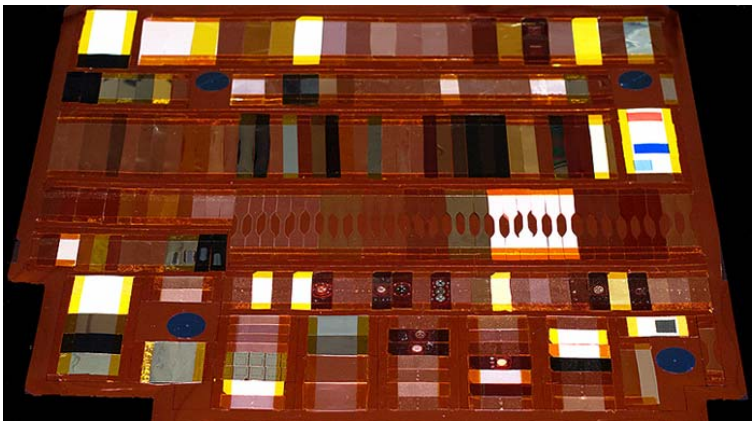

Figure 4: This is the Thin Film Materials Experiment fielded by NASA Langley Research Center. This 3 & 1/2 ounce experiment will evaluate in-space survivability of 200 advanced space materials. Specimens are attached to thermal blanket outer layer. Specimen survivability determined from comparisons of pre and post flight laboratory characterization tests data

DATA ACQUISITION ELECTRONICS AND SOFTWARE

The data acquisition electronics were designed and built by the NASA GRC team. A photograph of the electronics is shown in Figure 6. In Figure 6, the electronics are shown mounted to the deck (named the Electronics Deck) that will hold the boards within the PEC. The Thermal Deck holding the solar cell experiments (Figure 3) is mounted on stand-offs on the opposite side of the Electronics Deck. The two layer unit will be mounted in one half of the PEC. The electronics consists of one “main” microprocessor board and nine data acquisition (DAC) boards. The main microprocessor board provides the communications link with the TNC of PCSat2, serves as the command interpreter, and controls the DAC boards. In addition, the main microprocessor includes dual redundant flash memory so that not only is data transmitted to ground, but is also archived on board. Upon return to Earth, and in the event of communication downlink failure, the mission will still have data available.

Each DAC board is approximately 4x6 in^2 and is capable of measuring a 32 point IV curve on four individual solar cells, making two temperature measurements using AD590 temperature sensors, and taking data from one sun angle sensor. The two temperature channels on a board can be combined to measure temperature using a resistance temperature device (RTD), which provides a wider operating range than the AD590. A single temperature channel on a board can also be configured to make a single IV point measurement on a cell. The IV curve is created by using a FET as a variable resistor and thereby sweeping the load resistance while measuring the solar cell current and cell voltage. Considering that most solar cell experiments employ a bank of switched load resistors for making the IV measurement, which requires much more space and weight, these measurement boards are a significant improvement. A comparison of data measured by one of the DAC boards on a 3J InGaP/GaAs/Ge solar cell under illumination by the X-25 solar simulator in the NRL Solar Cell Characterization Laboratory with data measured by laboratory equipment under illumination by the same simulator is shown in Figure 6, and the agreement can be seen to be excellent.

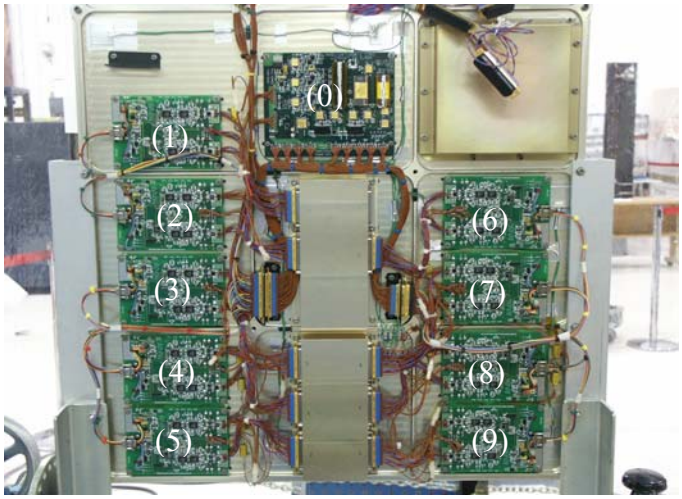

Figure 6: This is a photograph of the data acquisition electronics mounted on the electronics deck. There is a single "main" microprocessor board (0) that controls nine "daughter" boards (1-9), which measure the IV curve, temperature, and sun angle data. The metal box in the upper right of the photograph is the power control unit (PCU). The metal boxes in the center are feed-throughs that route the wires from the solar cells that are mounted on the opposite side. These boxes serve to maintain a Faraday cage around the measurement electronics.

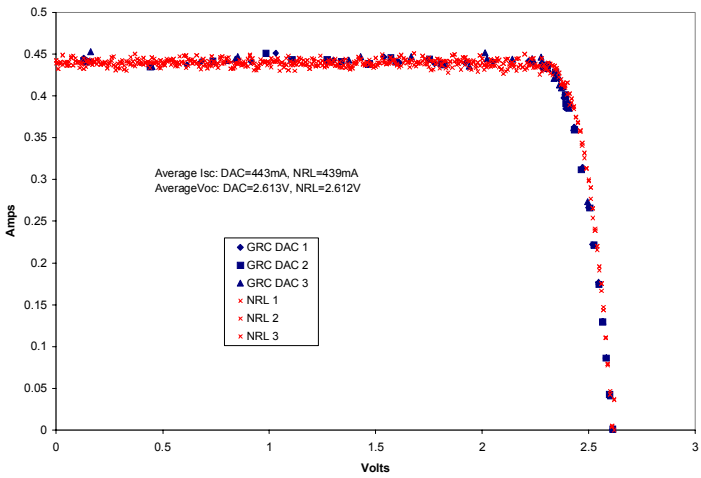

Figure 6: This graph compares IV data measured on one of the FTSCE 3J InGaP/GaAs/Ge solar cells by a flight DAC board and flight software compared to data measured on the same cell by laboratory equipment. In each case, three data sets were measured in succession, and the three curves are shown. All measurements were made under the same X-25 solar simulator in the NRL Solar Cell Characterization Laboratory.

The data acquisition software was also designed and written by the NASA GRC team. Portions of the software reside on each of the DAC boards and the main microprocessor. The DAC board software is responsible for taking commands from the main microprocessor, returning data to the main microprocessor, and performing the IV curve, temperature, and sun angle measurements. The software is designed to autonomously take data when user defined conditions of sun angle and temperature are met. Also, the experiment can be commanded to measure on demand. In addition, each DAC board can be commanded individually with a specific set of measurement criteria. This grants the scientists on the ground flexibility in creating experimental data sets. For example, the DAC boards can be commanded to measure data once the sun angle is below a set threshold, which allows IV data vs angle of incidence data to be generated. Alternatively, the DAC boards can be commanded to

measure once the temperature has exceeded a set threshold value, which allows IV data vs. temperature to be generated.

The software resident on the main microprocessor board is responsible for receiving command from the TNC of PCSat2, decoding the commands, and passing the appropriate commands to the DAC boards. The main microprocessor software must also take the data from the 9 DAC boards, translate it into printable ASCII characters and pass it to the TNC for down-linking by PCSat2. The main microprocessor software must also "oversee" the autonomous operation of the experiment, which consists of periodically recording readings from all of the temperature sensors to give a temperature profile for the PEC during each orbit and monitoring the temperature and sun angle data and determining if the measurement conditions have been reached.

POWER SUBSYSTEM

In sunlight the experiment is powered by an array of 4 strings of Emcore ATJ solar cells (the power array is pictured in Figure 3). Each string has 9 cells wired electrically in series to produce an open circuit voltage (Voc) of approximately 23.09 Volts. Power from the 4 strings is fed into the Power Control Unit (PCU). The PCU distributes power to the GRC data acquisition electronics and the PCSat2 communications system and regulates charge current to the battery. When the experiment power array is shadowed, by either the ISS itself or normal orbit eclipses, the experiment is powered by 4 high capacity (55 A-hr) prismatic Lithium Ion (Li-ion) batteries. This will be the first flight of this battery technology and one of the first flights of a Li-Ion battery system in a low Earth orbit (LEO) space environment. Lithion of Pawcatuck, Connecticut, manufactured the battery cells. The cells are wired together in series to provide a bus voltage of 12.0 to 16.0 volts. The PCU uses a shunt regulator to reduce the charge current to the battery when the battery voltage reaches 16.0 volts. The thin film shunt resistors are taped to the inside of the PEC. An under-voltage detection circuit sheds all non-critical loads when the battery voltage drops below 11.5 volts.

It was determined that RF emissions from the PCSat2 transmitters could cause electromagnetic interference with the astronauts' EVA suit, so a multiple inhibit scheme has been implemented to prevent RF transmission when the astronauts are in the vicinity of the PEC. The power system is inactive for launch and EVA transportation to the experiment site on the ISS. Solar array power and battery connection to the experiment are only enabled after an astronaut installs a turn-on plug and toggles a power switch. Power to the transmitters, however, remains delayed by an 8 hour timer circuit to allow sufficient time for the astronauts to exit the area around the PEC.

PCSAT2 – RF COMMUNICATIONS SUBSYSTEM

The RF communications subsystem is called PCSat2. PCSat2 is an Amateur Satellite Communications system similar to what it is flying on PCsat as an external Amateur Radio on the ISS (ARISS) payload. The PCSat2 subsystem will operate in the ITU Amateur Satellite Service in cooperation with ARISS and provide a PSK-31 multi-user transponder, an FM voice repeater for possible use with ISS Crew communications and an AX.25 packet system for use as a UI digipeater and for telemetry, command, control. PCSAT2 will use the same dual redundant AX.25 command and control system as used on PCsat (NO-44) offering 8 on/off commands, 5 telemetry channels and a serial port for the solar cell experiment telemetry. It also supports the Digital Comms Relay support of the PCsat2/APRS mission. The packet uplink is on 145.825 MHz and the default downlinks are in the 435 MHz band to avoid any possible interference with existing ARISS missions. PCSAT2 will have quad redundant transmit inhibits for EVA safety issues, thus, it is also easy to turn off to avoid any issues with other UHF ARISS experiments that may be activated in the future.

One of the key issues with any Amateur Radio experiments on ISS is the requirement to avoid any mutual interference between systems. For this reason, ARISS will need to eventually move all uplinks and downlinks into separate bands. This is so that multiple uplinks and multiple downlinks can be going on simultaneously. As it is, with both uplinks and downlinks on 2m, that band cannot be shared without mutual interference. Thus

PCSat2 is designed as mode J to avoid transmitting on 2m, even though mode B (downlinks on 2m) is far superior to reaching schools and low-tech stations and meeting our mission objectives. There is much UHF equipment being planned for ISS, but until it is operational and ARISS has a long range plan, mode J must be used.

DEPLOYMENT ON ISS

In the MISSE Program, experiments are packaged inside a PEC which is then transported to the ISS via the Shuttle. Once aboard the ISS, the PEC is taken outside the Station by an astronaut during an EVA and clamped onto an external handrail. For MISSE-5, the requirement for favorable sun exposure for the experiments and for power generation made the choice of the location of the PEC critical. After several iterations of lighting, thermal, and power budget analysis, the P4 trunion handrail was chosen. This handrail is located on the port-side solar array truss section between the solar arrays. This section of the ISS is scheduled to be installed on ISS Mission 12A.1/STS Flight 116, and MISSE-5 was scheduled to be installed at the same time. The original STS-116 launch date was July 14, 2003, but the loss of the Space Shuttle Columbia has delayed this date. In an effort to be deployed sooner, alternate locations are being investigated. In particular, a handrail on the crew airlock, which is the current site of MISSE-2, has been identified as a viable alternative. Another possible alternative is on the P6 truss section between the existing solar arrays. The important point gained from the analysis of possible locations is that the amount of sun that the experiment will see during a given orbit and the incident solar angle will vary significantly over the duration of the mission depending on the ISS orbital attitude. Furthermore, certain locations may experience extended periods of shadow during Shuttle docking. This proved to be the major driver in the design of our thermal management system, power subsystem, and experimental data acquisition protocols.

CONCEPT OF OPERATIONS

The plan is for MISSE-5 to remain on orbit for one year. At the end of the mission, the PEC will be closed and returned to Earth. Once returned, the FTSCE will be disassembled to allow for full characterization of the individual experiments. While on orbit, the FTSCE will experience the LEO orbital environment of the ISS. The orbit has a 90 minute period with typically 60 minutes of sunlight and a thirty minute eclipse. The experiment is designed to track the illumination conditions on the face of the FTSCE and the temperature. As the illumination and temperature approach the user-defined set points, the main microprocessor board energizes the DAC boards. When the measurement conditions have been met, the main microprocessor initiates the data measurement, and the DAC boards measure all 36 IV curves within one minute. When complete, the DAC boards pass the data to the main microprocessor, which, in turn converts the data into Automatic Position Reporting System (APRS) format and passes it to the TNC via a serial port. PCSat2 telemeters the data to the ground as AX.25 packets at 9600 bps. To maximize probability of reception, the data is transmitted as a beacon, repeating approximately every 3 minutes. The primary ground station is the USNA where the data will be received and transferred to NRL for analysis. The back-up ground station is NASA GRC. In addition, the data can be received by any amateur radio station operating in AX.25 mode. Once received, the data is placed on the Internet from which it will be received by NRL.

Table 1: This table identifies and gives a brief description of the individual solar cell technologies included in the FTSCE . The approximate solar cell size is given and the number of individual cells is given in parentheses. The beginning of life (BOL) efficiency is the average of the data measured by the responsible organization and given to NRL with the experiments. * - Denotes atypical cell efficiency due to available selection/modification of cells for flight experiment.

#	Experiment Name	Responsible Organization	Description	BOL Eff (%)
1	ITJ	Spectrolab	3J commercial ITJ cells, 26.6 cm^2 (10)	27.0
	UTJ	Spectrolab	3J commercial UTJ cells, 26.6 cm^2 (5)	28.6
	Metamorphic	Spectrolab	3J lattice-mismatched cells, 4 cm^2 (4)	28.5
	Control	Spectrolab	DJ InGaP/GaAs/Ge control cells, 27 cm^2 (2)	22.9
2	Si Degradation	NASA GRC/Entech	Films of DC 93-500 silicone mounted on coverglass superstrate over MJ cell to measure the transmittance degradation of silicone material, 4 cm^2, (2 active, 2 passive)	N/A
	USNA Solar Cells	USNA/NASA GRC	Commercial-off-the-shelf terrestrial solar cells, passive experiment, 2 are ~3.5 cm^2 and the third is ~7.75cm^2, (3)	7.0*
3	Amorphous Si on Kapton	NASA GRC/LM/Iowa Thin Films	Blanket-level test of interconnected thin film amorphous silicon cells on Kapton substrate (3 monolithically-interconnected cells for 1 active sample, 2 passive samples)	0.24*
4	Power Panel	Emcore	Primary power panel for mission, ATJ cells	N/A
5	GaAs on Si	NASA GRC/OSU/MIT	SJ GaAs cells grown on SiGe/Si substrates with one GaAs/GaAs control, 1 & 4 cm^2, (7)	12.2
6	Amorphous Si on Stainless Steel	NASA GRC/AEC Able/UniSolar	Blanket-level test of interconnected thin film amorphous silicon cells on stainless steel substrate affixed to a Vectran gore sheet (simulating UltraFlex array design), ~20.5cm^2 (2 series-interconnected cells)	10.4
7	Contamination Monitor	NRL	Thales 5 mil CMX coverglass, passive witness plate for contamination effects, Not shown in figure	N/A
8	Sun Angle Sensors	NRL	Two orthogonal sun angle sensors. Not shown in figure	N/A
9	CIGS	NASA GRC/AEC-Able/ITN	Blanket-level test of interconnected CIGS cells on stainless steel affixed to a Vectran gore sheet simulating UltraFlex array, ~20cm^2 (5 series-connected cells)	~3.5*
10	ATJM	Emcore	3J commercial ATJM cells, includes monolithic bypass diode, 26.6cm^2 (5)	27.1
	BTJ	Emcore	3J commercial BTJ cells, 26.6cm^2 (5)	27.8

PROMISING RESULTS FROM THREE NASA SBIR SOLAR ARRAY TECHNOLOGY DEVELOPMENT PROGRAMS

Mike Eskenazi, Steve White, Brian Spence, Mark Douglas, Mike Glick, Ariel Pavlick, and David Murphy
ABLE Engineering, Goleta, CA 93117

Mark O'Neill and A.J. McDanal
ENTECH Inc., Keller, TX 76248

Michael Piszczor
NASA Glenn Research Center, Cleveland, OH 44135

ABSTRACT

Results from three NASA SBIR solar array technology programs are presented. The programs discussed are the 1) Thin Film Photovoltaic UltraFlex Solar Array; 2) Low Cost/Mass Electrostatically Clean Solar Array (ESCA); and 3) Stretched Lens Array SquareRigger (SLASR). The purpose of the Thin Film UltraFlex (TFUF) Program is to mature and validate the use of advanced flexible thin film photovoltaics blankets as the electrical subsystem element within an UltraFlex solar array structural system. In this program operational prototype flexible array segments, using United Solar amorphous silicon cells, are being manufactured and tested for the flight qualified UltraFlex structure. In addition, large size (e.g. 10 kW GEO) TFUF wing systems are being designed and analyzed. Thermal cycle and electrical test and analysis results from the TFUF program are presented. The purpose of the second program entitled, "Low Cost/Mass Electrostatically Clean Solar Array (ESCA) System," is to develop an Electrostatically Clean Solar Array meeting NASA's design requirements and ready this technology for commercialization and use on the NASA MMS and GED missions. The ESCA designs developed use flight proven materials and processes to create a ESCA system that yields low cost, low mass, high reliability, high power density, and is adaptable to any cell type and coverglass thickness. All program objectives, which included developing specifications, creating ESCA concepts, concept analysis and trade studies, producing detailed designs of the most promising ESCA treatments, manufacturing ESCA demonstration panels, and LEO (2,000 cycles) and GEO (1,350 cycles) thermal cycling testing of the down-selected designs were successfully achieved. The purpose of the third program entitled, "High Power Platform for the Stretched Lens Array," is to develop an extremely lightweight, high efficiency, high power, high voltage, and low stowed volume solar array suitable for very high power (multi-kW to MW) applications. These objectives are achieved by combining two cutting edge technologies, the SquareRigger solar array structure and the Stretched Lens Array (SLA). The SLA SquareRigger solar array is termed SLASR. All program objectives, which included developing specifications, creating preliminary designs for a near-term SLASR, detailed structural, mass, power, and sizing analyses, fabrication and power testing of a functional flight-like SLASR solar blanket, were successfully achieved.

1. NASA SBIR PHASE 2 THIN FILM PV ULTRAFLEX PROGRAM

1.1 INTRODUCTION

As flexible thin film photovoltaic (FTFPV) cell technology is developed for space applications, integration into a viable solar array structure that optimizes the attributes of this cell technology is critical. An advanced version of the ABLE Engineering, Inc. (ABLE) UltraFlex solar array platform represents a near-term, low-risk approach to demonstrating outstanding array performance with the implementation of FTFPV technology. Recent studies indicate that an advanced UltraFlex solar array populated with 15% efficient thin film cells can achieve over 250 W/kg BOL.

ABLE, in collaboration with the NASA Glenn Research Center (GRC), is currently executing a NASA Phase 2 Small Business Innovation Research (SBIR) program to implement and validate the integration of FTFPV technology within an advanced UltraFlex solar array [1]. The primary objectives of the Phase 2 SBIR program are to mature and validate the use of advanced FTFPV blankets as the electrical subsystem element within an advanced UltraFlex solar array structural system. Program objectives to mature and validate the use of FTFPV blankets in the UltraFlex solar array platform are being met though the implementation of a hardware oriented development and test approach (at the coupon and engineering model level).

As has been recognized in recent array system level studies [2], integration of a FTFPV electrical subsystem into an advanced UltraFlex solar array structural system allows realization of the full potential of FTFPV technologies to increase solar array specific power and significantly reduce cost. While the prior research focus has been aimed at the FTFPV device level in an effort to improve BOL/EOL efficiencies, reduce weight, and enhance space environmental survivability [2, 3], the development, implementation and validation of these technologies within a viable lightweight array system (including the "real world" effects on specific power performance from array wiring, structures and deployment mechanisms) has been only superficially addressed prior to this Thin-Film UltraFlex SBIR study. Validating the successful combination of a structurally/mechanically efficient advanced UltraFlex solar array platform with the unique properties of FTFPV technology is a key step in maturing these technologies and readying their space commercialization.

During this NASA Phase 2 SBIR program preliminary design/analysis activities have been performed for a high performance thin film PV UltraFlex solar array system configured for a 10kW EOL GEO application. Feasible design solutions for high voltage operability, scalability, optical characteristics, high thermal performance, and radiation survivability have been identified. Coupon development and hardware tests have been performed on flight-like FTFPV gore/blanket assemblies to validate concept/design feasibly. Larger scale flight-like engineering model hardware has been built to further validate design manufacturing, packaging and deployment feasibility at the wing system level.

1.2 TECHNOLOGY OVERVIEW

The UltraFlex solar array, shown in Figure 1, combines structural performance and the highest available specific power with a very low stowed volume and footprint [3]. The UltraFlex achieves its deployed strength and stiffness from lightweight composite radial spar members that allow tensioning of a flexible blanket populated with photovoltaic. This unique structural system allows the use of a flexible blanket without requiring massive secondary structure to deploy and tension the wing as is common in other flexible substrate solar array systems. UltraFlex is an excellent platform to demonstrate maximum specific power performance gains from high areal mass-efficient thin-film photovoltaics because of its superior areal structural mass efficiency that is up to 3.5X better than a conventional rigid planar array.

Figure 1. UltraFlex Solar Array for the Mars 01-Lander Program

The UltraFlex is an accordion-fan-fold flexible solar array composed of ten interconnected isosceles triangular shaped lightweight substrates (gores). The fan-fold geometry sequences the gore blanket assemblies during deployment. Each interconnected triangular shaped substrate/gore unfolds to form a tensioned ten-sided polygon structure when fully deployed. Radial spar elements attached to each substrate are elastically deflected to form a tension-preloaded concave paraboloid, providing high-deployed strength and stiffness. A layout of the deployed UltraFlex depicting its major components is shown in Figure 2.

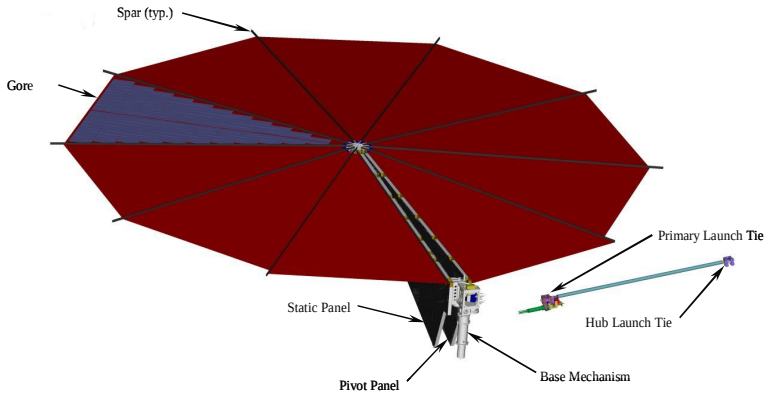

Figure 2. UltraFlex Wing Components

When stowed, the UltraFlex occupies a triangular space that is approximately 20% the stowed volume of conventional planar arrays, which enables spacecraft to maximize launch volume for critical payloads. The honeycomb-composite static and pivot panels sandwich and preload the folded solar array blanket under pressure in the stowed configuration. In a standard crystalline photovoltaic-based design, the UltraFlex wing's solar cells are protected from damage in the launch environment by foam interleaved in the folded blanket assembly. The stowed and compressed wing assembly is held to the space vehicle at three releasable launch tie points. Figure 3 shows the stowed UltraFlex configuration.

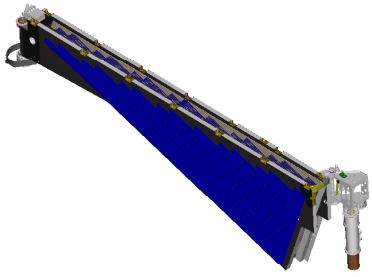

Figure 3. UltraFlex Stowed Configuration

1.3 FLEXIBLE THIN FILM PV (FTFPV)

The primary suppliers and technologies under consideration during this program included United Solar Systems' (USS) amorphous silicon (α-Si) FTFPV, and ITN Energy Systems' CIGS FTFPV technology. At program commencement, due to limited funding, only the USS α-Si technology was selected for implementation and test. Additional funding was obtained later in the program, and ITN Energy Systems CIGS will be included in similar coupon-level and engineering model level development tests to be performed in early 2004.

The baseline α-Si FTFPV technology utilized for this program was USS "Q" solar cell. The "Q" cells are produced on a 25 micron (0.001-inch) thick stainless steel substrate, have a Ag/ZnO back reflector, a top side Indium-Tin-Oxide (ITO) coating, and are tuned to the 1AM0 solar spectrum. The top surface conductive grid consists of a series of longitudinally oriented small diameter compression-bonded copper wires. The wires are terminated/connected to a silver coated copper bus that is used for cell-to-cell series interconnection. The cells measure approximately 4-cm X 17.8-cm and have an active area of 64.30 cm^2. The measured mass of each solar cell assembly is approximately 2.37 g (areal density of 0.37 kg/m2). A picture of the a-Si USS solar cell assembly is shown in Figure 4.

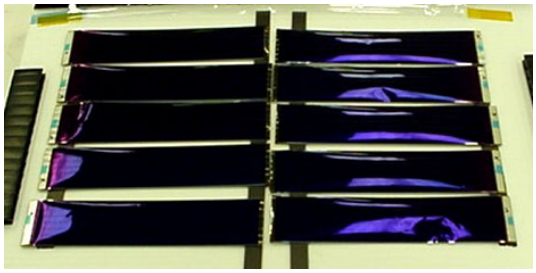

Figure 4. USS a-Si FTFPV ("Q"-cell)

The baseline copper indium gallium diselenide (CIGS) FTFPV technology to be investigated during this program is the ITN Energy Systems Inc. (ITN) space-application solar cell mounted on 1 mil. stainless-steel substrates. ITN Energy Systems has developed a technology that adapts the cell material obtained from Global Solar Energy Inc. (GSE) into a product capable of surviving in a space environment. This is accomplished by adding AM0 optimized space grids, thermal coatings to reduce on-orbit operating temperature and electrostatic discharge layers (ESD) for operation in a plasma environment to the basic cell material obtained from GSE. Additionally, the cells provided by ITN for this program will include ITN's bonded interconnect technology that will allow integrated solar arrays for space applications to be implemented. As previously mentioned, validation of the ITN CIGS technology is currently underway with results anticipated for early 2004.

1.4 THIN FILM ULTRAFLEX HARDWARE DEVELOPMENT & TESTING

1.4.1 Structural Optimization

During this program many of the standard UltraFlex array's structural design features were weight-optimized to take advantage of the FTFPV's significantly lighter weight and robustness versus classical crystalline PV technologies. Because FTFPV technologies are projected to be almost four times lighter than the state-of-the art crystalline multi-junction cells on a weight per unit area basis, and are not subject to cracking or damage from vibratory motion, the method of tightly preloading the folded gore stack between layers of foam does not appear to be necessary with this technology. This allows the UltraFlex static and pivot panels (nominally of honeycomb-composite construction) to be further weight-optimized for use as stowed protective covers and deployed structural members, without the considerable stiffness and strength required to apply a uniformly-distributed preload over the stowed stack area, which is necessary for crystalline PV applications. ABLE has developed a concept for a lightweight iso-grid static and pivot panel construction that allows the panel stiffness to be tailored specifically for a low mass stowed FTFPV blanket stack. This panel construction saves significant weight (20-40%), especially when scaling UltraFlex to the larger sizes (>4m diameter) required when implementing lower efficiency FTFPV.

An alternate approach to reduce the weight of the static and pivot panel structure on large FTFPV UltraFlex wing configurations is to increase the number of launch tie locations so that the panels do not have to be as stiff and strong to apply preload to the stowed blanket stack. This concept requires the implementation of a weight-optimized launch tie assembly. The baseline UltraFlex launch tie is based on the heritage ABLE launch release that uses high-output paraffin actuators to release a tensioned cable. This design has extensive flight heritage and works well for applications requiring three or less tie-down release points, but would add unnecessary weight if applied at multiple (>4) launch tie points. For a larger-diameter FTFPV UltraFlex application requiring more launch tie locations, ABLE has initiated development of a next-generation launch tie release that utilizes small lightweight discrete bolt-separation actuators at each tiedown location. During this Phase 2 SBIR program, such a weight optimized launch tie release was considered in the FTFPV UltraFlex array sizing trades, with results indicating they have the potential to significantly reduce mass versus the existing launch tie technology, as well as reducing the necessity for ultra-stiff (and massive) structural panels.

Additionally, the radial spar elements can be structurally optimized for FTFPV applications. With lightweight FTFPV technology the spar structures do not need to support as much weight when deploying or in the fully deployed configuration (under 1-G ground-test conditions). The standard UltraFlex design utilizes a flat rectangular composite spar construction with the lay-up optimized to support deployment loads under 1-G with minimal external support. A FTFPV array, with significantly larger wing area required for the same power output,

will require an external ground support structure to allow deployment under earth gravity. A rectangular spar applied to such a large wing could be susceptible to torsional instability and could buckle even when supported under 1-G unless it becomes very large and heavy. The design of a large TFTPV wing required re-assessment of the spar's design to provide the most weight-optimal cross section that can still be packaged in the stowed configuration. ABLE has investigated concepts for deployable "lenticular" spar sections that stow in a flat package but expand out when deployed to form a very lightweight, torsionally stiff beam section that is less susceptible to lateral/torsional instability.

1.4.2 Interconnect Development and Testing

Previous solar array system studies suggest that a monolithically interconnected FTFPV blanket assembly is needed to truly realize the cost and mass benefits potential of this technology [1]. Because monolithic interconnection of FTFPV is still in development this technology was not available to implement on this program. Instead, the FTFPV interconnection technologies developed during this program focused on classical welding and soldering approaches.

Because the UltraFlex blanket/gore assemblies are stowed face-to-face it is desirable to employ an interconnect that exhibits very low profile. To satisfy this need two interconnect approaches were ultimately pursued, a folded-flexible type that provided large stress relief and an in-plane type. A representative folded flexible interconnect prototype mock-up was made and tested for flexibility in two directions. The interconnect consisted of a folded copper strip that was welded to the top and bottom of adjacent cells. The fold in the copper strip allows the interconnect to flex during expansion and contraction of the circuit during thermal cycling. The folded interconnect testing successfully demonstrated the durability and flexibility of the design concept. A picture of the mechanical fold interconnect mock-up is shown in Figure 5. A prototype in-plane interconnect was also made and evaluated by ABLE and USS. The in-plane interconnect consisted of a straight copper strip that was welded to the top and bottom of adjacent cells using multiple welds. The in-plane interconnect testing successfully demonstrated the durability of this design. The results of this interconnect development effort indicated that either in-plane or stress-relief interconnects were suitable for UltraFlex and should be evaluated at the flight-like coupon level using the α-Si FTFPV.

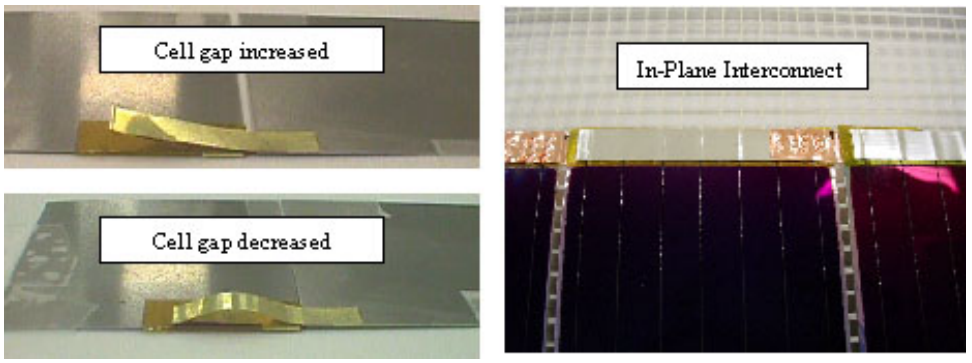

Figure 5. Folded-Flexible Interconnect Detail (Left) and In-Plane Interconnect Detail (Right)

The ITN CIGS cells will be interconnected using an adhesive bonding interconnect technology that combines the strength of a mechanical bond (to carry the CTE mismatch induced stress) with the electrical conductivity of a conductive bond. This interconnect design will be tested by ITN and ABLE to demonstrate the thermal-cycle durability of the design.

1.4.3 Circuit/Laydown Development & Test

To maintain blanket design commonality with previously qualified crystalline PV UltraFlex systems the FTFPV blanket/gore approach is comprised of a mesh substrate to which the interconnected cells are bonded. The amount of cell-to-gore mesh bond area can be significantly reduced, because the lightweight FTFPV will have less of a propensity to de-bond under its own accelerated mass.

An ultra-lightweight method for cell-to-gore mesh attachment was developed that utilized Kapton “dots” bonded directly to the cell backside and the UltraFlex gore/substrate, as shown in Figure 6. This feature resulted in an 80% savings in cell-to-gore adhesive mass over the crystalline UltraFlex design. This low-cost method also provides a significant reduction in laydown assembly time compared to the standard UltraFlex cell attachment method. Engineering development tests were performed on a prototype incorporating this laydown approach to demonstrate concept feasibility. A localized proof load using a small vacuum suction cup was applied to each bonded cell to determine acceptable bond strength. Test results indicate that no bond degradation occurred under the normal load application.

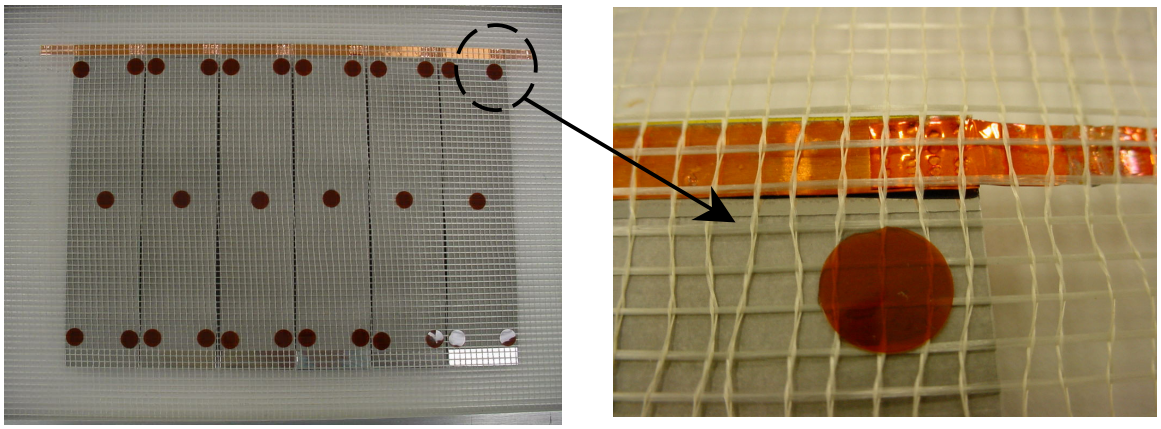

Figure 6. Lightweight Cell-to-Gore Attachment Using Kapton Dots

To further validate the cell/circuit interconnect approach, and circuit laydown, a flight-like engineering mock-up was fabricated. The engineering circuits incorporated the folded flexible interconnect design as well as the baseline in-plane welded interconnect and were mounted to a tensioned UltraFlex blanket/gore segment. The hardware employed the following three circuits: Circuit-1 consisted of three 25-micron-thick dummy cells with straight 100-micron-thick copper strip soldered interconnects, Circuit-2 consisted of two 125-micron-thick cells with a soldered flexure interconnect and improved grid wire terminations, and Circuit-3 consisted of two 125 micron-thick cells with a soldered flexure interconnect and improved (segmented) grid wire termination. The original design for the grid wire terminations consisted of a layer of Kapton tape above and below the grid wires, and this double-layer termination method exhibited significant peeling following limited thermal cycles. An improved approach was developed that utilized a single layer of Kapton tape compression-bonded over the grid wires and to the cell edge surface. Additionally, this grid wire termination tape was segmented into three shorter sections on one of the samples in an effort to reduce thermal stresses and distortion. A photograph of the development circuit hardware is shown in Figure 7. Thermal cycle testing of the engineering gore segment was performed to determine any degradation and validate grid wire termination, cell/substrate attachment, and interconnect integrity/performance. The hardware was thermal cycled for a total of 266 cycles between –175C to +100 C at a rate of 2.5 cycles/hr. Visual inspections and interconnect resistance measurements were made at 55, 104, and 266 cycles. Test results indicated no visible degradation of the straight and flexible interconnect configurations, no change in interconnect resistance, and the cell/substrate attachment was unaffected based on pull test measurements. The improved single layer grid wire termination (segmented and un-segmented) had no visible degradation following 266 thermal cycles. As a result of this testing the improved, segmented approach has been baselined.

`

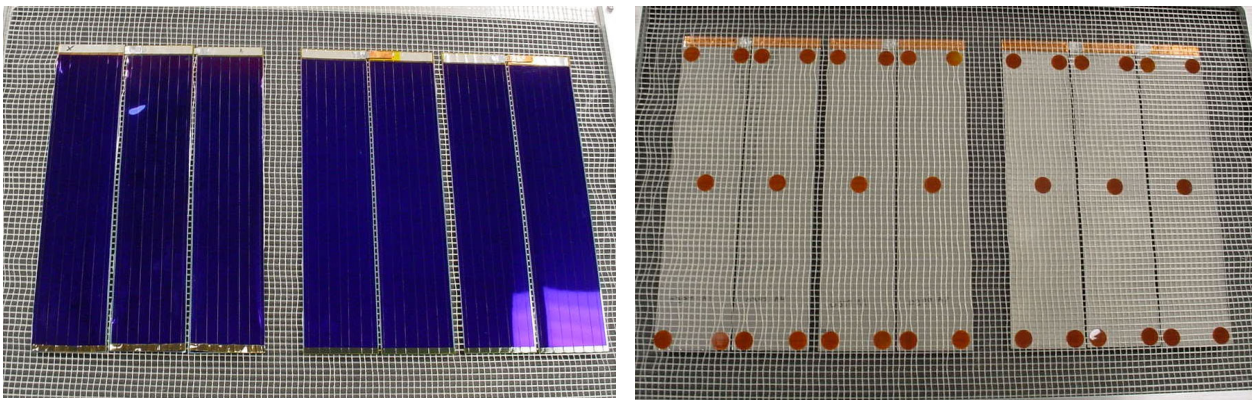

Figure 7. Development Circuits (Front and Back Views)

1.4.4 Thin-Film UltraFlex Engineering Circuit (E-Board) Testing

To further validate FTFPV interconnection and laydown onto UltraFlex, two flight-like engineering circuits (E-Boards) were fabricated. Each circuit consisted of a 6-cell series interconnected a-Si FTFPV assembly bonded to the UltraFlex gore/substrate. Cell thickness was 25 microns (0.001 inch). Each circuit utilized a different interconnect method; the baseline in-plane welded tab design and the folded flexure design. The engineering circuits were inspected and tested with ABLE's Large Area Pulsed Solar Simulator (LAPSS), and then mounted on two separate sections of tensioned UltraFlex gore/blanket using the previously verified Kapton "dot" attachment method. A pre-test electrical LAPSS performance evaluation was performed for the completed assembly. Pictures of the small flight-like E-Boards are shown in Figure 8.

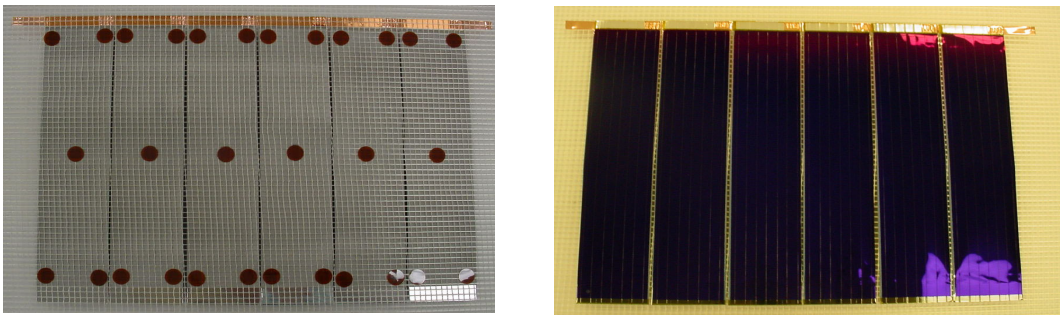

Figure 8. E-Board Circuit on UltraFlex Gore/Substrate

The completed E-boards were then mounted within a thermal chamber and were subjected to 500 thermal cycles at temperatures from -175°C to +100°C. Periodic inspections and continuity monitoring during the thermal cycle tests indicated no apparent degradation/failures of either circuit. Final post-test inspection and LAPSS verification of the circuits were performed, showing both circuits in good condition with only minimal localized physical degradation.

Post-thermal LAPSS testing of the two circuits demonstrated no measurable degradation in cell performance when compared to the pre-thermal LAPSS data. The observed local separation of the Kapton tape and the rear contact on the flexible copper interconnect circuits did not affect the circuit performance. Pull tests on the cell-to-gore/substrate bonds demonstrated that the cell attachment was unaffected by thermal cycling.

The following conclusions were made from the fabrication and testing of the two E-Board circuits:

1) The circuit electrical performance was unchanged by the thermal cycle testing.
2) The straight welded interconnect is generally a good match with the UltraFlex gore/substrate and local attachment of the cell. No interconnect failure resulted from the thermal expansion and contraction of the cells relative to the UltraFlex gore/substrate. The flexible interconnect is probably not required when the cells are attached to the UltraFlex gore/substrate.
3) The number of welds used to attach the rear copper contact to the stainless substrate may need to be increased to prevent the observed separation of the contact from the stainless substrate.
4) The separation of the Kapton tape from the top ohmic points to a required change in surface preparation, tape adhesive, tape type, or material configuration when the cell is required to operate at the tested thermal environment.
5) The cell attachment was generally unaffected by the thermal environment.

1.4.5 Face-to-Face Survivability

An investigation into the surface durability of the α-Si FTFPV modules was performed. This is an area of particular concern for the UltraFlex application because in the nominal stowed configuration, FTFPV cells are in direct face-to-face contact. A number of tests were performed initially to assess the relative durability of the (unprotected) α-Si FTFPV surface, as shown in Table 1. The tested FTFPV cells did not have any anti-reflective or oxide coatings on their front surface. Initial test results indicate that an unprotected front surface of the α-Si FTFPV is highly susceptible to damage from cell-to-cell contact and handling.

Table 1. Surface Durability Test Results of Un-coated FTFPV

Test Description	Test Result
Two cells were placed face-to-face under 0.1 psi pressure	No cell damage
Rounded edge of paperclip placed in contact with cell surface and lightly translated across cell	Cell completely shunted
Two cells were placed face-to-face. Light pressure was applied to top cell and top cell moved relative to bottom cell (displacement ~ .05 in., duration ~ 3 sec).	Cell completely shunted
Two cells were placed face-to-face. Foam was placed over top cell and weights applied to exert 0.1 psi pressure. The assembly was repeatedly moved on granite table (displacement ~ .05 in., duration ~ 3 sec.)	Cell completely shunted

The effectiveness in improving FTFPV durability by employing various thickness SiO_2 coatings applied to the PV front surface was investigated. A number of 4.7" x 14" terrestrial α-Si cells were obtained from USS for use in determining optimal coatings to enhance cell front surface durability. The cells were coated with SiO_2 of thickness varying from 0.1 μm to 3 μm, as shown in Table 2. Additionally, a 0.06 thick ITO layer was applied to the front surface of the cells. The reason for the ITO layer was to eliminate the potential for charge buildup on the SiO_2 surface on orbit. Subsequent discharge from the cell surface may damage the circuit.

Table 2. Matrix of ITO Coating Thickness Applied to Durability Test Cells

Designation	SiO_2 Thickness (μm)	ITO Thickness (μm)
A	0.1	0.06
B	1.0	0.06
C	3.0	0.06

After coating, the electrical performance of the test cells was measured and the durability of the cells was evaluated. One cell was placed on a smooth granite surface with the PV side facing upward. The second cell was positioned so that the PV surface of the second cell contacted the PV surface of the first cell. A foam-covered plate was placed over the assembly and weights were applied to the aluminum plate in order to achieve a particular contact pressure. The top cell was then moved relative to the bottom cell with a displacement of approximately 0.05 inches along the direction of the gridlines for a period of 20 seconds. The process was repeated with the displacement direction perpendicular to the gridlines. The electrical performance of the test cell was then determined. The contact pressure was then increased and the durability test repeated. Three contact pressures (0.1, 0.2 and 0.3 psi) were studied. Two different contact surfaces (PV to PV and PV to ohmic) were evaluated. The durability test matrix is shown in Table 3.

Table 3. Durability Test Matrix

Sample No.	Contacting Surfaces	SiO2 Thickness (μm)	Pressure (psi)	Duration (sec)
1000A1	PV to PV	0.1	0.1, 0.2, 0.3	20/20,20/20,20/20*
1000A2	PV to PV	0.1	0.1, 0.2, 0.3	20/20,20/20,20/20*
1000A3	PV to Ohmic	0.1	0.1, 0.2, 0.3	20/20,20/20,20/20*
1000A4	PV to Ohmic	0.1	0.1, 0.2, 0.3	20/20,20/20,20/20*
10000B1	PV to PV	1.0	0.1, 0.2, 0.3	20/20,20/20,20/20*
10000B2	PV to PV	1.0	0.1, 0.2, 0.3	20/20,20/20,20/20*
10000B3	PV to Ohmic	1.0	0.1, 0.2, 0.3	20/20,20/20,20/20*
10000B4	PV to Ohmic	1.0	0.1, 0.2, 0.3	20/20,20/20,20/20*
30000C1	PV to PV	3.0	0.1, 0.2, 0.3	20/20,20/20,20/20*
30000C2	PV to PV	3.0	0.1, 0.2, 0.3	20/20,20/20,20/20*
30000C3	PV to Ohmic	3.0	0.1, 0.2, 0.3	20/20,20/20,20/20*
30000C4	PV to Ohmic	3.0	0.1, 0.2, 0.3	20/20,20/20,20/20*

* Duration: Test cell in contact with adjacent cell under specified pressure. Test cell moved relative to static adjacent cell (20 seconds along direction of gridlines, 20 seconds across direction of gridlines).

The post-test LAPSS data showed that the cells with the 1.0 μm and 3.0 μm SiO_2 coatings had no measurable degradation in performance following the durability testing at the three contact pressure levels. The cells with the thinnest SiO_2 coating (0.1 μm) showed a significant drop in peak power (10 -11 %). The results of these tests indicated that a 10000A-thick SiO_2 coating to the front surface prevented the cell shunting failure mode caused by direct face-to-face contact as would be seen in a Thin Film UltraFlex application. Even with significant abrasion pressures (well above those expected in an UltraFlex application), damage was limited to minimal power degradation (< 2% reduction in P_{MAX}) in the SiO_2-coated cells. Further tests, including vibration, are planned as part of this study to more thoroughly validate the coatings.

In addition to the protective SiO_2 coating, several interleave options were evaluated in order to protect the cells within the stowed UltraFlex stack. The first interleave option studied was a layer of Tedlar film that rolls up via a lightweight constant force spring as the stowed array stack separates. The roll of interleave film would be located adjacent to the spar when the array was deployed. An engineering model was produced and used to verify the functionality of this interleave concept. This interleave method does add significant complexity to the array deployment.

The second interleave option studied was a static layer of open-weave gore/substrate that covers the front side of the cells. Although this concept is relatively easy to implement, the gore/substrate produces a minimum power loss of approximately 5% over an uncovered cell. The thermal effects of the gore/substrate on array operating temperature need to be evaluated. The SiO_2 coating is the best cell protective option investigated to date.

1.4.6 Large Engineering Gore Circuit

A flight-like engineering gore/blanket circuit of the α-Si FTFPV technology was fabricated that incorporated many of the lessons learned from the previous development/validation tests. A picture of this circuit is shown in

Figure 9. The circuit was laid-down to the UltraFlex substrate/gore and then will be integrated into ABLE's 1st generation IR&D qualification wing, as shown in Figure 10. Wing system level tests will then be performed to further validate the implementation of the α-Si FTFPV technology within the UltraFlex platform.

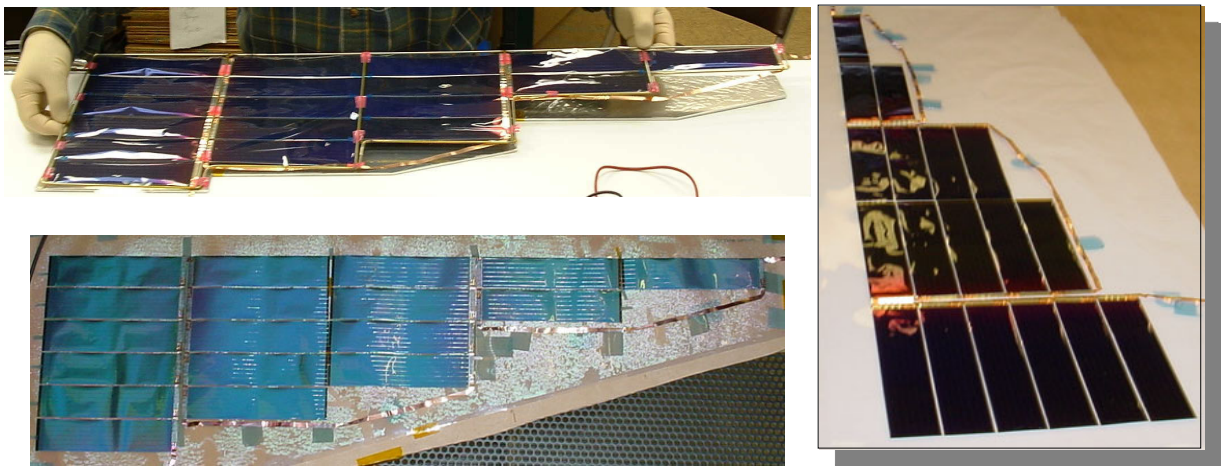

Figure 9. Engineering Gore/Blanket Circuit

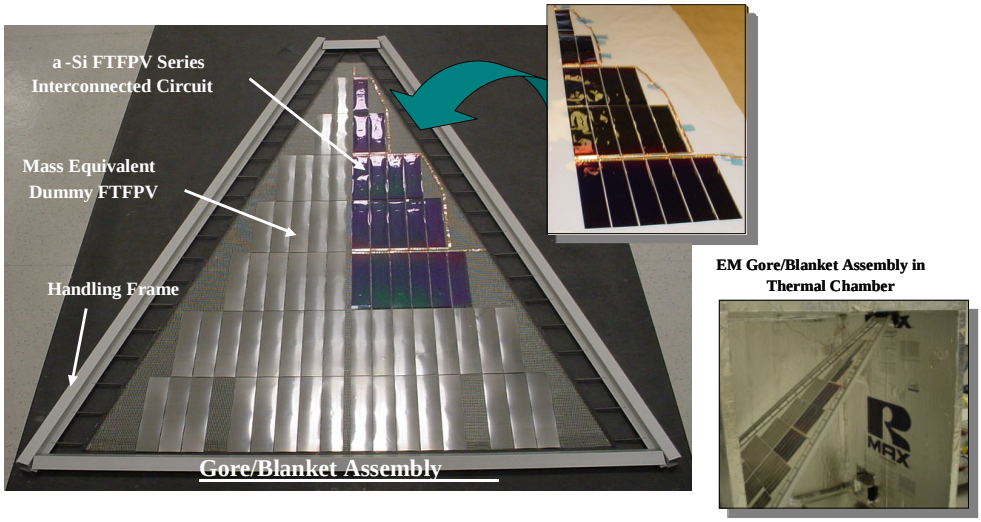

Figure 10. EM Gore Circuit Integrated into Prototype UltraFlex Substrate Gore

The 18-cell USS circuit mounted to the EM gore was coated with 1 μm SiO_2 and 60 nm of ITO. LAPSS tests were performed on the circuit both before and after the coating operation. The preliminary results of the LAPSS tests performed on the circuit after coating indicated a 34% power reduction from the pre-coated circuit, as shown in Figure 11.

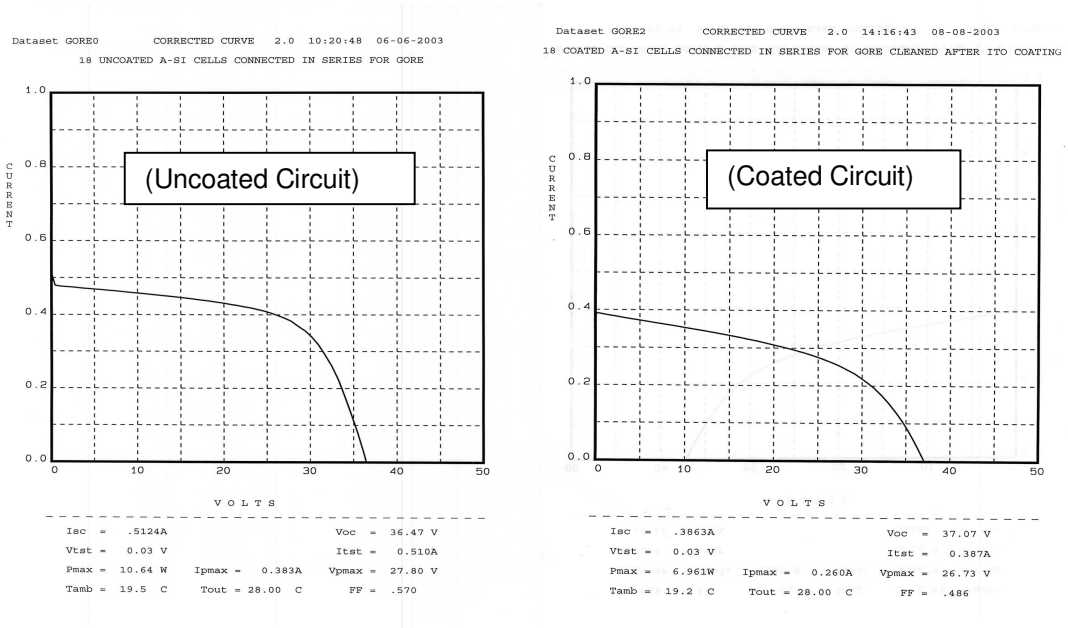

Figure 11. Pre and Post-Coating LAPSS Test Results for 18-cell EM Circuit

Because of the observed degradation in power as a result of the coating, an investigation was initiated to evaluate the cause of the power reduction. The investigation indicated that the shorting between the conductive ITO coating and the cell front photovoltaic surface was occurring through pinholes in the SiO_2. Currently, United Solar is researching suitable front-surface space-rated conductive coatings and application methods to eliminate this problem. Cells to be subsequently tested will be coated with 1 μm SiO_2 only (no ITO).

1.4.7 MISSE Flight Experiment Coupons

Flight experiment coupons of the thin film UltraFlex designs were produced for the Materials of the International Space Station Experiment–5 program (MISSE-5). The purpose of the Materials International Space Station Experiment (MISSE) is to characterize the performance of new prospective aerospace materials when subjected to the effects of the space environment. Two FTFPV UltraFlex flight experiment coupons were produced, each with a different FTFPV technology. The first experiment employed USS α-Si FTFPV, while the second experiment used ITN Energy's CIGS. Both experiments were laid down to a dedicated UltraFlex gore/blanket assembly. The USS α-Si circuit consisted of two AM0 cells with Al/ZnO back reflector on 1-mil stainless steel substrate with single layer side "B" Kapton tape termination. A redundantly welded copper interconnect was used to connect the two cells. Cell to cell interconnection, I-V performance, and operating temperature will be assessed during this experiment. Pictures of the MISSE-5 flight experiment coupons are shown in Figure 12.

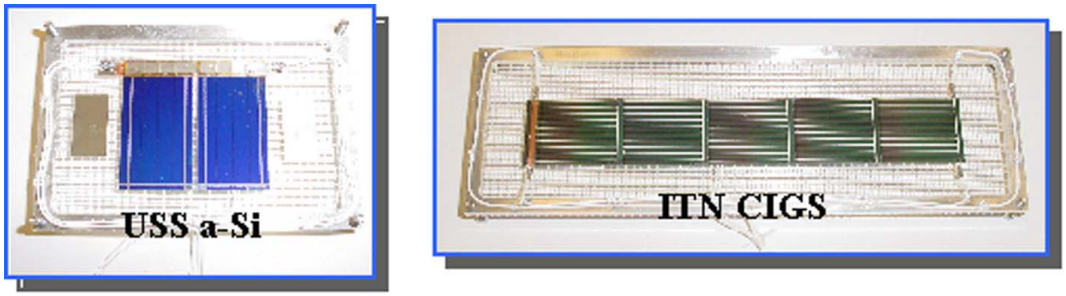

Figure 12. MISSE-5 FTFPV UltraFlex Flight Experiment Coupons

1.5 ACKNOWLEDGMENT

This work was administered though the NASA Glenn Research Center and funded by the NASA SBIR Phase 2 program under contract #NAS3-02078.

1.6 THIN FILM ULTRAFLEX PROGRAM SUMMARY

The initial results of this program indicate that advanced FTFPV can be successfully integrated to a lightweight optimize UltraFlex solar array to produce a system that exhibits very high specific power. This program has provided an important foundation towards validating through hardware development cell-to-cell interconnection, electrical circuitry, circuit laydown and blanket/gore construction, survivability (thermal life cycling and face-to-face contact) and wing/array system level aspects. Future work will involve a series of wing system-level integration and validation activities that will further demonstrate concept feasibility, and more detailed hardware approach to assess face-to-face survivability of the FTFPV under a vibration environment. Additionally, an advanced UltraFlex incorporating the alternative ITN CIGS thin film technology will be developed and validated

2. NASA SBIR PHASE 1 LOW COST/MASS ELECTROSTATICALLY CLEAN SOLAR ARRAY (ESCA) PROGRAM

2.1 INTRODUCTION

Electrostatic interaction of solar arrays in a space plasma environment is of great concern as differential charging across panel portions can lead to high electric fields, charge loss to plasma, and arcing between critical components, which may disrupt scientific measurements of fields or particles [4]. The objective of this program is to develop a low cost and low mass Electrostatically Clean Solar Array (ESCA) which will not interfere with sensitive spacecraft instruments/measurements and ready this technology for commercialization and use on NASA and commercial programs such as the NASA MMS and GED missions. Previous developed ESCA designs are shown in references [5, 6, & 7].

Solar array electrostatic cleanliness is achieved when circuitry is sealed to prevent exchange of charge with the plasma, or unintentionally between cell/string components, and all exterior surfaces are sufficiently conductive to prevent charge differentials on the panels. In meeting this objective, two innovative ESCA solutions have successfully been developed and tested. These are shown in Figure 13 (Zone 1 and Zone 2). The first design uses conductive adhesive grout, which is grounded to the panel core, to electrically connect the ITO coated coverglass on the front of the cells and create an external ground plane. The second design uses conductive tape grounded to the panel core to seal circuitry, electrically connect the ITO coverglass, and create an external ground plane. In both designs, the front-side solar cell circuitry is fully encapsulated in non-conductive adhesive for electrical isolation prior to the application of the conductive exterior ESCA treatment. On the panel backside layers of non-conductive natural Kapton film and conductive polymer films are used for circuit sealing and conductivity. The ESCA designs use flight proven materials and processes to create ESCA systems that yields low cost, low mass, high reliability, high power density, and adaptability to any cell type and coverglass thickness.

2.2 REQUIREMENTS

The NASA requirements and goals specified in Table 4 form the basis of the ESCA design solutions. All requirements and goals shown in Table 4 are met by ABLE's ESCA designs.

2.3 ANALYSIS

2.3.1 Mass Analysis

Mass calculation summaries for the conductive grout and conductive tape ESCA treatments are presented in Table 5. Mass was calculated on a per Cell-Interconnected-Cover (CIC) basis so that the relative magnitude of the mass could be easily determined and so that the calculation would be independent of panel type. The results show that the mass added by either ESCA treatment compared to the CIC's is < 8% and compared to a typical solar panel assembly < 3%, on a per unit area basis. However, the mass of an ESCA solar array also increases by approximately another 10% on a kg/W basis because of the increased panel area required due to the ESCA treatment reducing the total illumination area. The mass of the conductive tape treatment was found to be

significantly lighter than the conductive grout treatment. Both treatments meet the NASA specification for mass increase (<20%).

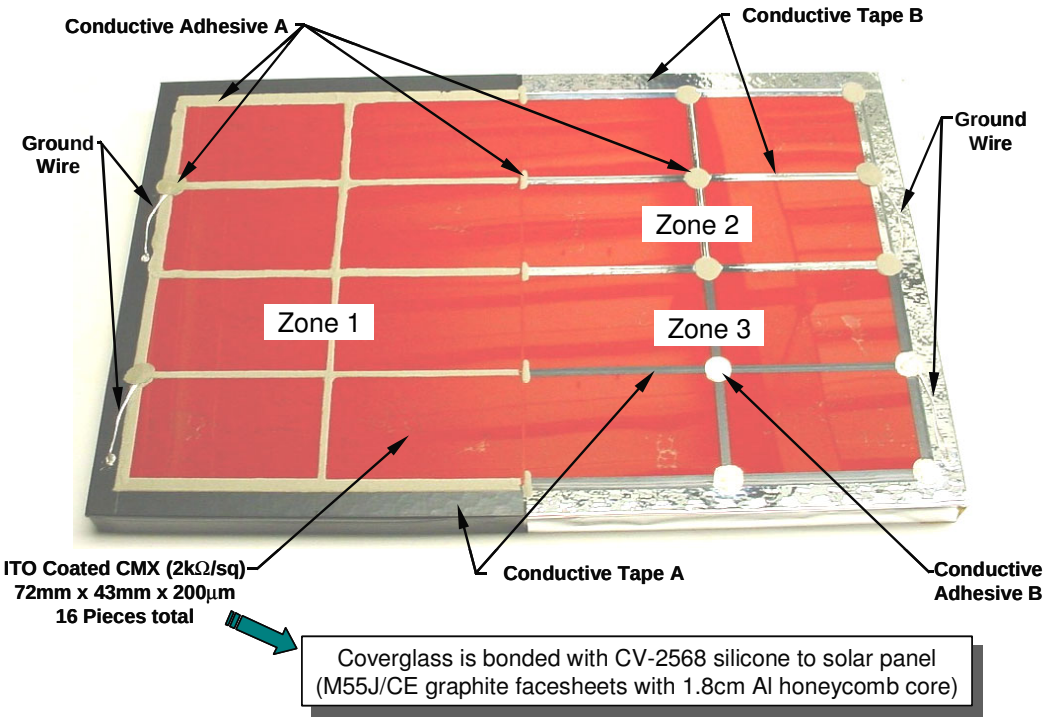

Figure 13. Phase I ESCA demonstration panel that was successfully thermal cycled 2,000 times between -90°C to 100°C (LEO) and 1,350 times from –175°C to 75°C (GEO)

Table 4. NASA ESCA System Requirements/Goals

#	NASA Requirement/Goal Description
1	Regardless of size, there shall be no more than 100 millivolts between any two points on a given panel's surface, even in the presence of a current of 0.1 microampere per square centimeter caused by the ambient plasma
2	The ESCA system shall not induce an electric potential greater than 0.1 volts, at a distance of 0.1 cm or greater from the panel surface, compared with a perfectly conductive surface grounded to the spacecraft structure
3	There shall be no exposed insulator on the panel's front or rear surfaces to the charged particle environment
4	The ESCA system shall be capable of having its quasi-equipotential surface connected to the spacecraft through a connector
5	The proposed method to achieve electrostatic cleanliness shall be compatible with cover thicknesses from .004 inches to .060 inches
6	The proposed method to achieve electrostatic cleanliness shall be compatible with any type of solar cell typically used on spacecraft solar arrays including single crystal silicon, GaAs/Ge, and multi-junction solar cells
7	The ESCA design shall only use materials that exhibit no more than 1.0- percent total mass loss and no more than 0.1 percent-collected volatile condensable materials from outgassing in a vacuum
8	The methods to achieve electrostatic cleanliness shall be compatible with typical spacecraft solar array materials and assembly processes
9	The ESCA design shall use no magnetic parts
10	The ESCA design shall lend itself to easy cell removal and replacement
11	The method to achieve electrostatic cleanliness shall not increase array cost ($/W) by more than 20%
12	The method to achieve electrostatic cleanliness shall not increase array mass (W/kg) by more than 20%
13	The method to achieve electrostatic cleanliness shall not significantly decrease the reliability of the solar array
14	The method to achieve electrostatic cleanliness shall be applicable to multi-AU missions

Table 5. Mass Summary for ESCA Treatments

Mass Calculation Summary for Conductive Grout ESCA Treatment

Cell Length (cm)	3.76
Cell Width (cm)	7.61
Cell-to-Cell Gap (cm)	0.0762
Grout Overlap on Cell (cm)	0.0508
Grout Thickness (cm)	0.0381
Grout Volume per CIC (cc)	0.077
Grout Density (g/cc)	3.4
Grout Mass per CIC (g)	0.262
Measured CIC Mass, 100µm cover (g)	3.34
Grout as a percentage of CIC mass	7.8%
Typical CIC mass fraction of solar panel	36.0%
Deduced grout mass fraction of solar panel	**2.8%**

Mass Calculation Summary for Aluminized Tape ESCA Treatment

Cell Length (cm)	3.76
Cell Width (cm)	7.61
Cell-to-Cell Gap (cm)	0.0762
Tape Overlap on Cell (cm)	0.0508
Tape Thickness (cm)	0.00635
Tape Volume per CIC (cc)	0.013
Tape Average Density (g/cc)	1.4
Tape Mass per CIC (g)	0.018
Conductive Adhesive Corner Dots per CIC (g)	0.055
Total ESCA mass per CIC	0.073
Measured CIC Mass, 100µm cover (g)	3.34
ESCA as a percentage of CIC mass	2.2%
Typical CIC mass fraction of solar panel	36.0%
Deduced ESCA mass fraction of solar panel	**0.8%**

2.3.2 Power Analysis

ESCA treatments reduce power by blocking sunlight that would normally hit the edges of the cell and because ITO coated coverglass has lower transmittance compared to AR coated coverglass. The reduction in transmittance for ITO coated glass compared to standard MgF_2 AR coated glass for the $GaInP_2$ (top) junction of a triple-junction solar cell calculated from the manufacturer's data is shown in Figure 14. The calculated power reduction for the conductive grout and conductive tape ESCA treatments are presented in Table 6. The total power reduction for both treatments is about 8%, of which 5% is due to light blockage and 3% due to reduced transmittance through the ITO. The power reduction can be reduced slightly by using oversize cover glass so that less or none of the cell is blocked by the conductive grout or tape.

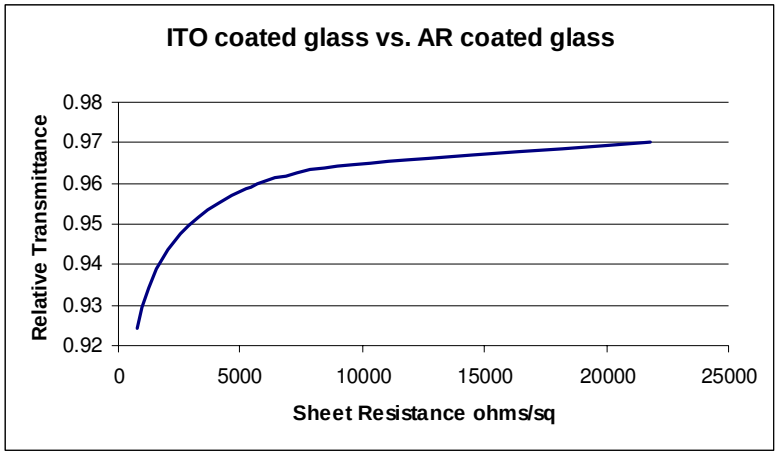

Figure 14. Relative Reduction in Solar Cell Current for ITO Coated Glass

Table 6. Power Reduction for ESCA Treatments

ESCA Power Adjustment Factors Summary
Conductive Grout Treatment

Cell Length (cm)	3.76
Cell Width (cm)	7.61
Cell Area (cm^2)	28.6
Overlap Along Edges (cm)	0.051
Covererd Area (cm^2)	1.14
Average Blocked Light %	4.0%
Cell-to-Cell Variation in Blocked Light %	1.0%
Worse Case Blocked Light %	5.0%
ITO Coverglass Transmittance Loss (%)	3.0%
Total	**8.0%**

ESCA Power Adjustment Factors Summary
Aluminized Kapton Treatment

Cell Length (cm)	3.76
Cell Width (cm)	7.61
Cell Area (cm^2)	28.6
Overlap Along Edges (cm)	0.051
Covererd Area Edges (cm^2)	1.14
Covered Area Dots (cm^2)	0.14
Average Blocked Light %	4.5%
Cell-to-Cell Variation in Blocked Light %	1.0%
Worse Case Blocked Light %	5.5%
ITO Coverglass Transmittance Loss (%)	3.0%
Total	**8.5%**

2.3.3 Cost Analysis

The material cost in both the conductive grout and conductive tape ESCA treatments are relatively low. Most of the cost associated with both methods is due to labor. The estimated recurring cost for the ESCA treatments are presented in Table 7. The treatments are relatively inexpensive comprising only about 5% of the solar panel cost based on an area basis. However, more panel area (~8%) is required to obtain a given power level compared to an untreated panel. Thus, in terms of $/W the increase in cost is approximately (1.05)(1.08) = 1.134. Both ESCA treatments meet the NASA requirement for cost (<20% cost increase). These cost estimates do not include any non-recurring engineering, which would be required for a 1st of a kind array.

Table 7. Estimated Recurring Cost for ESCA Treatments

ESCA Cost Summary
Conductive Grout Treatment

Materials	
CV2-2646 $/Gram	5
Installed Grams/CIC	0.26
Waste Factor	1
Waste (g)	0.26
Total Grams/CIC	0.52
CV2-2646 Cost/CIC	**$2.62**
Labor	
Time Per Task (minutes)	
Inspection	3
Masking	2
Grouting	3
Clean-up	3
Inspection	2
Rework	2
Misc	5
Total Labor (min)	**20**
Assumed Labor Rate $/min	$1.00
Labor Cost per CIC	**$20.00**
Material Cost per CIC	$2.62
ESCA Treatment Total	**$22.62**
Typical 3J CIC Cost	$450.00
ESCA Cost/CIC Cost	**5.0%**

ESCA Cost Summary
Aluminized Tape Treatment

Materials	
Aluminized Kapton ($/$cm^2$)	0.78
Installed Area (cm^2/CIC)	2.02
Waste Factor	1
Waste (cm^2/CIC)	2.02
Total cm^2/CIC	4.04
CV2-2646 Cost/CIC	**$3.15**
Labor	
Time Per Task (minutes)	
Inspection	1
Taping	2
Adhsive Dots	2
Inspection	2
Rework	2
Misc	5
Total Labor (min)	**14**
Assumed Labor Rate $/min	$1.00
Labor Cost per CIC	**$14.00**
Material Cost per CIC	$3.15
ESCA Treatment Total	**$17.15**
Typical 3J CIC Cost	$450.00
ESCA Cost/CIC Cost	**3.8%**

2.4 DEMONSTRATION HARDWARE AND TEST RESULTS

Based on the results of pathfinder coupon tests, the Phase 1 ESCA engineering model, shown in Figure 15, was fabricated using the most promising conductive adhesive and conductive tape treatments. T he engineering model contained sixteen pieces of ITO coated coverglass (72mm x 43mm x 200microns). The engineering model was thermal cycled 2,000 times in a LEO environment and 1,350 times in a GEO environment. Visual inspections and resistance measurements were made prior to and after thermal cycling. The visual inspection results and resistance measurements are shown in Figures 16. The conductive adhesive (zone 1) and conductive tape B (zone 2) passed both the mechanical and electrical test criteria. The conductive tape A treatment (zone 3) failed both mechanically and electrically.

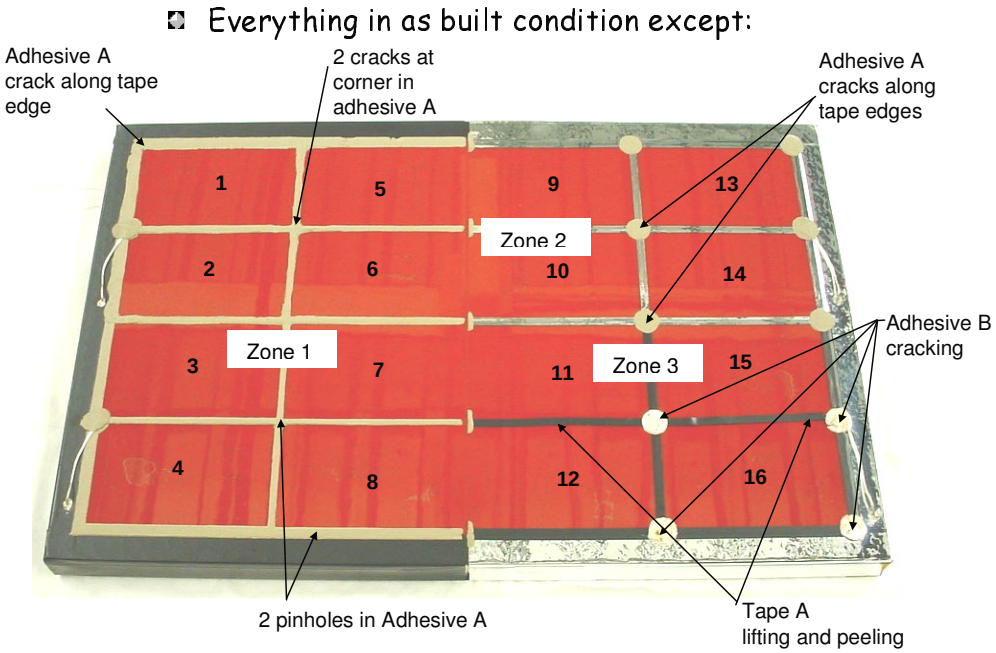

Figure 15. Visual Inspection Results for Engineering Model After 2,000 LEO Cycles and 1,350 GEO Cylces Between –175°C and 75°C

Glass	Treatment	Ground Resistance (kΩ)*		Comment
		Pre Test	Post Test	
1	Conductive Adhesive	1.0	1.1	Pass Mechanical and Electrical
2	Conductive Adhesive	1.5	1.6	Pass Mechanical and Electrical
3	Conductive Adhesive	1.5	1.2	Pass Mechanical and Electrical
4	Conductive Adhesive	1.5	1.3	Pass Mechanical and Electrical
5	Conductive Adhesive	1.0	1.0	Pass Mechanical and Electrical
6	Conductive Adhesive	2.2	1.5	Pass Mechanical and Electrical
7	Conductive Adhesive	3.0	1.2	Pass Mechanical and Electrical
8	Conductive Adhesive	1.4	1.1	Pass Mechanical and Electrical
9	Conductive Tape B	1.6	1.8	Pass Mechanical and Electrical
10	Conductive Tape B	1.6	2.7	Pass Mechanical and Electrical
13	Conductive Tape B	2.3	2.4	Pass Mechanical and Electrical
14	Conductive Tape B	6.3	8.5	Pass Mechanical and Electrical
11	Conductive Tape A	2.0	1.8	Fail, Tape Peeling, Adhesive Cracking
12	Conductive Tape A	2.0	3.3	Fail, Tape Peeling, Adhesive Cracking
15	Conductive Tape A	2.6	3.8	Fail, Tape Peeling, Adhesive Cracking
16	Conductive Tape A	6.0	OVLD	Fail, Tape Peeling, Adhesive Cracking

*Less than 30kohm required to meet ESCA requirement of 0.1V maximum
2,000 LEO Thermal Cycle from -90℃ to +100℃
1,350 GEO Thermal Cycles from -175℃ to +75℃

Figure 16. Coverglass Ground Resistance Results for Engineering Model After 2,000 LEO Cycles and 1,350 GEO GEO Cylces.

2.5 ELECTRICALLY ACTIVE ESCA PANEL

An electrically active engineering model of the conductive tape ESCA treatment containing nine TECSTAR TEC1 3J solar cells (Donated by EMCORE) wired in series was fabricated and is shown in Figure 17. The power of the electrically active engineering model was measured before and after application of the ESCA treatments to measure the effect on power. The results, which are shown in Figure 18 show a decrease in current (Isc) of 4.6% and a decrease in power (P_{max}) of 6.3% which is in good agreement with the predicted light blockage of 5.5% calculated in Table 6.

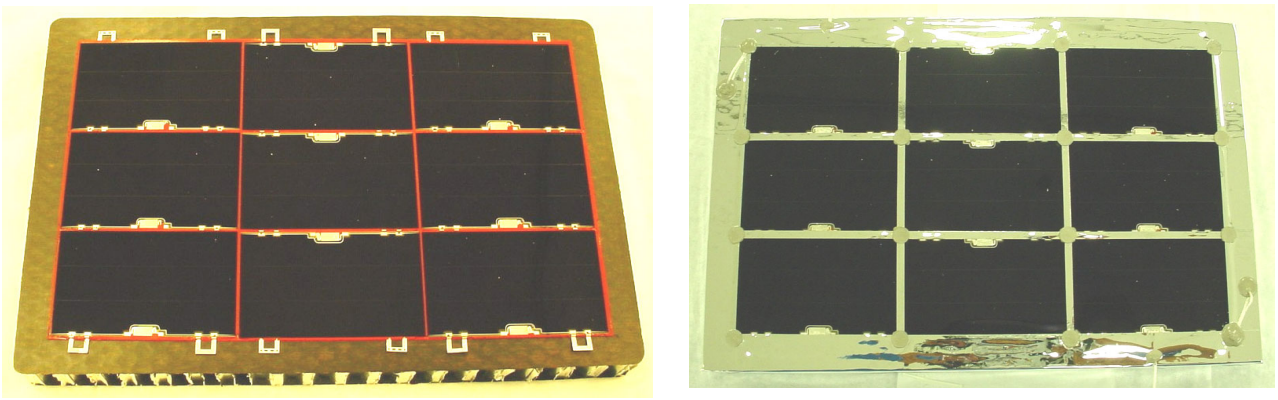

Figure 17. Electrically Active Prototype Before and After ESCA Treatment

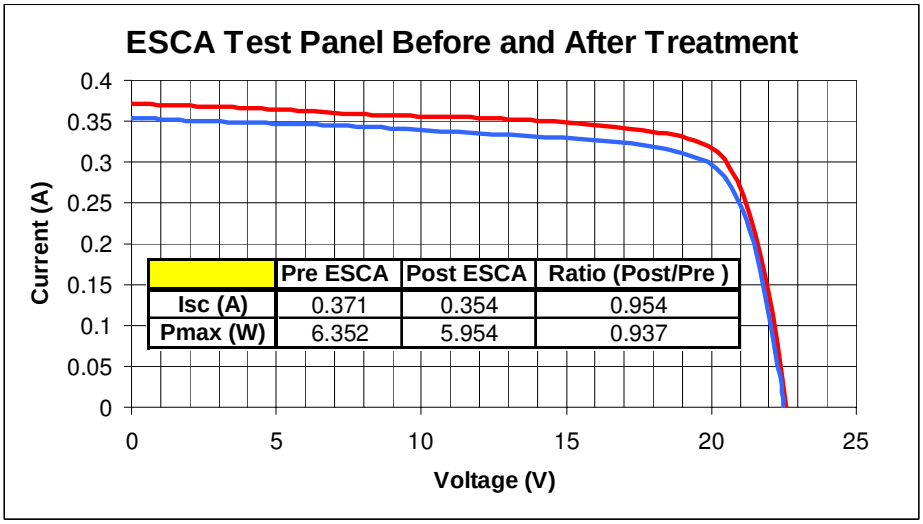

Figure 18. LAPSS Results for Active ESCA Test Panel

2.6 ACKNOWLEDGMENT

This work was administered though the NASA Goddard Space Flight Center and funded by the NASA SBIR Phase 1 program under contract #NAS5-03030.

2.7 ESCA SUMMARY

Electrostatically Clean Solar Array (ESCA) technologies meeting NASA's design requirements have been developed in preparation for commercialization and use on the NASA MMS and GED missions. The ESCA designs developed use flight proven materials and processes to create ESCA systems that yields low cost, low mass, high reliability, high power density, and is adaptable to any cell type and coverglass thickness. All Phase 1

objectives, which included developing specifications, creating ESCA concepts, concept analysis and trade studies, producing detailed designs of the most promising ESCA treatments, manufacturing ESCA demonstration panels and LEO (2,000 cycles) and GEO (1,350 cycles) thermal cycling testing of the down-selected designs were successfully achieved. It is hoped that these exceptional Phase 1 results and the high payoff of this technology to NASA GSFC's planned MMS and GED missions result in a Phase 2 continuation of this program.

3. NASA PHASE 1 SBIR HIGH POWER PLATFORM FOR THE STRETCHED LENS ARRAY

3.1 INTRODUCTION

The purpose of this program is to develop an extremely lightweight, high efficiency, high power, high voltage, and low stowed volume solar array suitable for very high power (multi-kW to MW) applications. This is achieved by integrating a Stretched Lens Array (SLA) blanket into the SquareRigger (SR) solar array structure. The resulting solar array is termed Stretched Lens Array SquareRigger (SLASR).

SLASR uses SquareRigger, which is a well demonstrated structural approach for deploying extremely large photovoltaic blankets in terms of low mass, low stowed volume, and high stiffness and the SLA Fresnel concentrator, which is believed to be the best-demonstrated photovoltaic system in terms of the desirable combination of low cost, high efficiency (30%), ultra-low mass (>500 W/kg blanket), and high voltage (>1000V). The proposed SLA concentrator elements are highly optimized versions of the extremely successful Deep Space 1 SCARLET solar array lenses [8]. An electrically active, flight-like, SLASR demonstration blanket was successfully fabricated and tested during Phase 1 and is shown in Figure 19. The excellent optical alignment achieved by the prototype SLASR blanket is shown in Figure 19 where the focus of natural sunlight on to the solar cells is demonstrated by the gossamer structure.

The predicted near-term (<5 years) BOL performance for a 100 kW SLA SquareRigger array system is a specific power of 320 W/kg, a power per unit area of 310 W/m^2, and a stowed power per unit volume of 70 kW/m^3 *using the existing designs and demonstrated triple-junction solar cell technology*. These characteristics of the SLA SquareRigger solar array, which are based on detailed models, make it an ideal candidate for meeting civil, military and commercial future power generation needs.

Figure 19. SLASR Demonstration Blanket Built During Phase 1
(Precise Optical Alignment of Prototype SLASR Demonstrated in Sunlight)

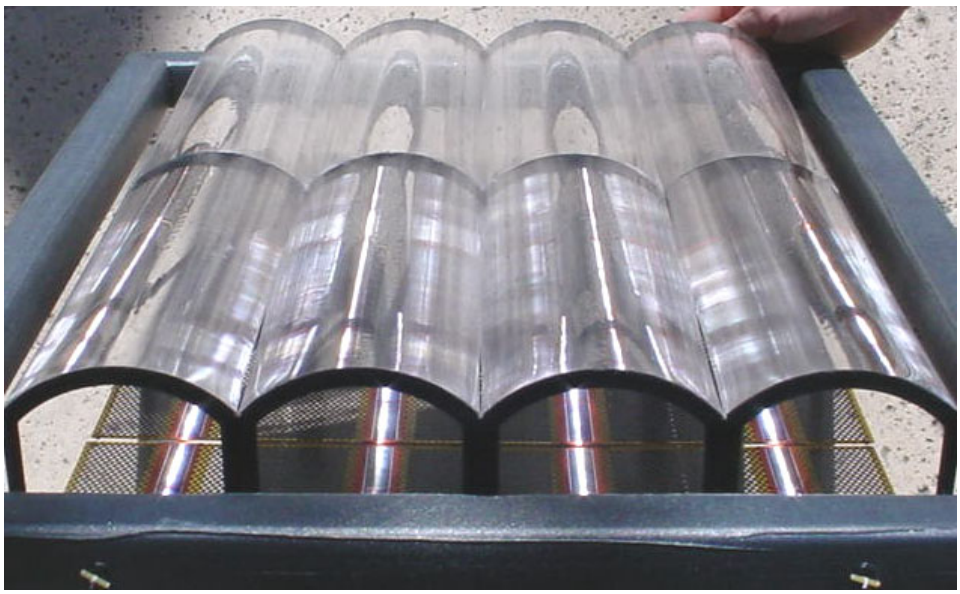

3.2 BACKGROUND

The SquareRigger solar array structure (Figure 20) was developed by ABLE for the Air Force Research Laboratory (AFRL) to deploy and structurally support very large thin film solar array blankets for future high power Air Force missions. The key features of SquareRigger (using a hypothetical 0.2 kg/m^2 thin film photovoltaic blanket made from 15% efficient CIGS) are very high power capability, low cost ($/W), low mass (>200 W/kg), and compact stowage for launch (>40 kW/m^3) [1]. These highly desirable characteristics may also enable numerous future NASA missions including Space Solar Power (SSP), high-power deep space SEP probes, Solar Electric Propulsion (SEP) tugs and large earth-orbiting science satellites.

While the SquareRigger structure development has progressed rapidly, with all elements of 2nd generation hardware recently demonstrated at full scale as shown in Figure 21, the high efficiency (>15% AM0 & 0.2 kg/m^2) thin film photovoltaic blanket needed to complete this extremely lightweight, low cost, and high power solar array is currently not available. Additionally, there are many experts in the photovoltaic community who are concerned that the timeframe to develop a space-qualified, high efficiency, thin film blanket may be much longer than currently projected and that the attained performance will be lower than anticipated and the cost higher than expected. Thus, it is very desirable to develop alternative low cost and low mass photovoltaic blanket technologies for SquareRigger in case thin film photovoltaics are unavailable when needed. It is also highly desirable to develop a much more efficient photovoltaic system compared to thin films to greatly reduce the deployed area and the launch volume of the SquareRigger array. The Stretched Lens Array (SLA) blanket, under development for SquareRigger in this program, fits these requirements perfectly.

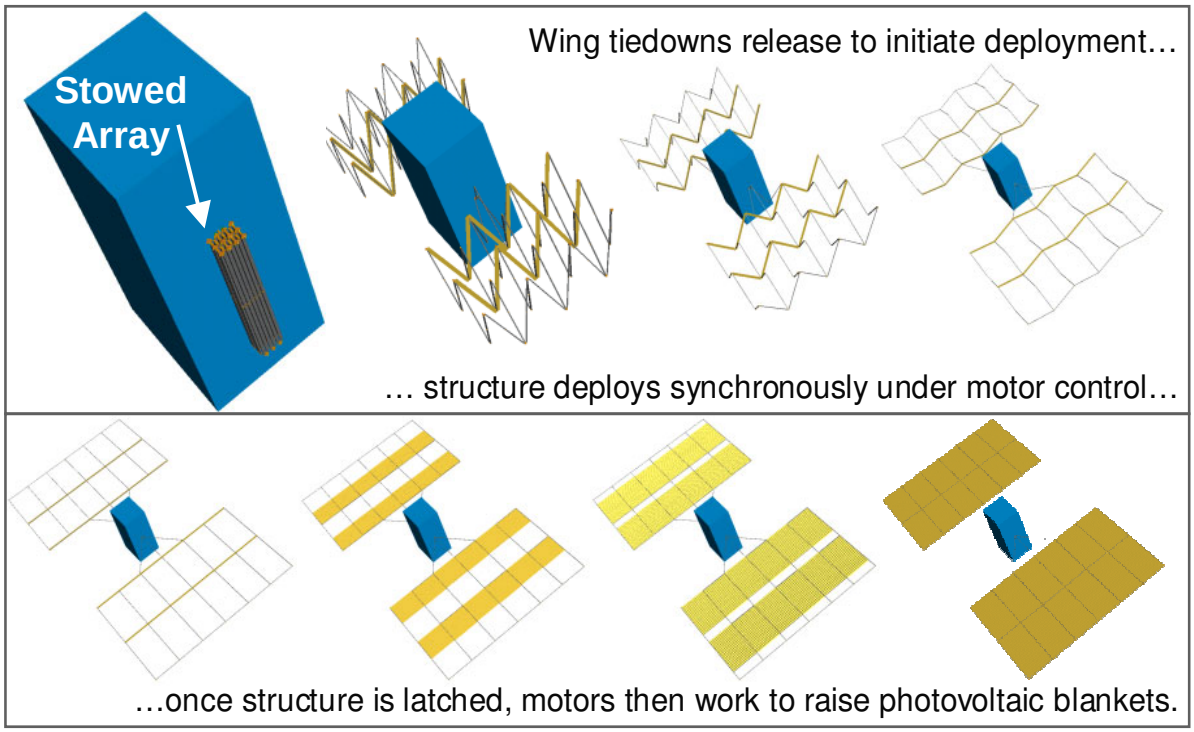

Figure 20. SquareRigger Structure and Blanket Deployment

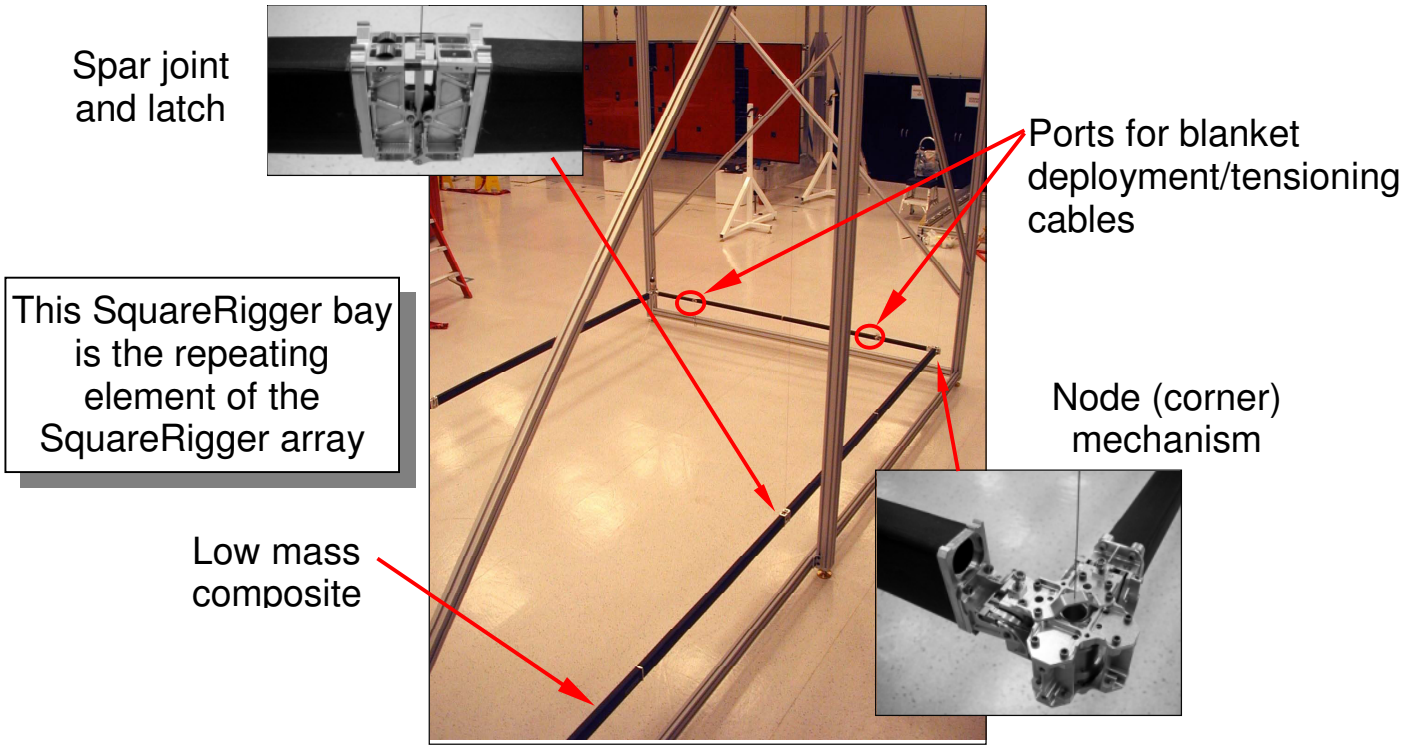

Figure 21. Full-Scale SquareRigger Bay after Successful Ground Deployment

The Stretched Lens Array (SLA) [9] is a low mass/low cost *high efficiency* photovoltaic system that uses gossamer line-focus Fresnel lenses to focus sunlight at approximately 8.5X concentration on to spaced rows of high performance crystalline solar cells. The current embodiment of SLA on optimized rigid panels is well suited for lower power level spacecraft, offering a robust 180 W/kg, but not as well suited as SLA SquareRigger for high power applications (>15 kW wings). This is because SquareRigger was developed to specifically to overcome scale-up problems inherent in rigid panel platforms and provide lower mass and stowed volume.

The SquareRigger platform can accommodate nearly any photovoltaic blanket technology. The AFRL is leading the development of thin films for space applications and the SquareRigger is a leading structural platform candidate. ABLE recently completed an AFRL funded program developing a thin film SquareRigger solar array system and also a crystalline (standard multi-junction cell) blanket as a backup technology to thin films, as this offers lower risk in the near term but much higher cost and mass. Alternatively, SLA technology adapted to SquareRigger simultaneously provides small deployed wing area and stowed volume (due to the use of high efficiency multi-junction cells), and low cost and low mass (enabled by a 70% to 80% reduction in cell area) approaching/surpassing the best thin film projections.

Typical components of a SLA blanket, which can directly replace the thin film solar cell blanket in SquareRigger, are shown in Figure 22. The early version of the SLA photovoltaic blanket, also shown in Figure 22, was developed as part of the SSP program for use in a lower performing, earlier generation, “Space Station” style blanket array platform known as Aurora. Though built in 2000, this fully functional demonstration blanket was measured by NASA Glenn Research Center to have an output of greater than 375 W/m^2 at 20°C equating to a lens efficiency of 92%, a cell efficiency of 30.0%, and over 400 W/kg [4]. The SLA blanket developed for SquareRigger is an optimized version of this early concept.

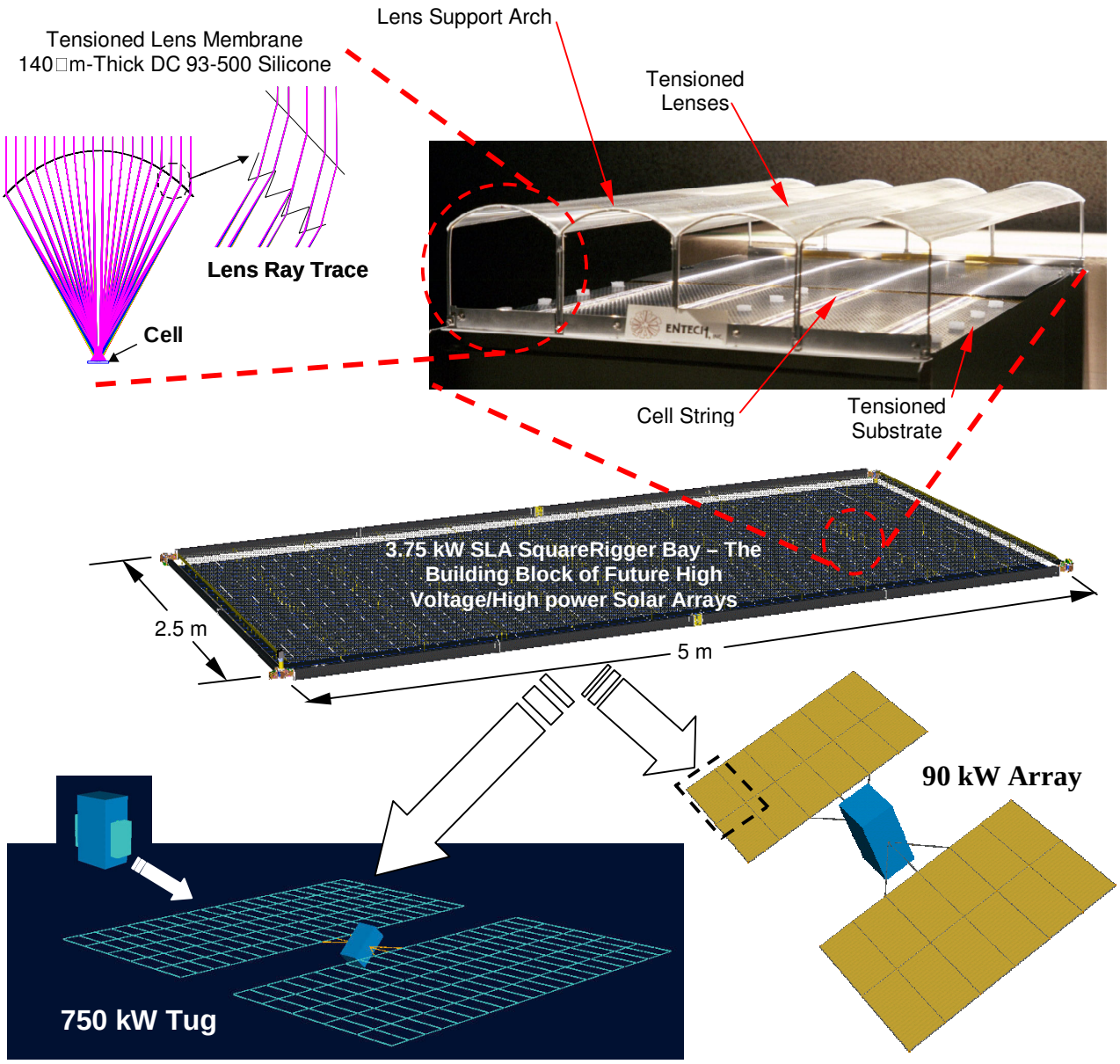

Figure 22. Stretched Lens SquareRigger (SLASR) Array

3.3 SLASR System Requirements and Goals

At the start of the Phase 1 program requirements/goals were developed for SLASR for both the near-term (2008) and mid-term (2013). These requirements, which are shown in Table 8, specify the performance metrics for the system (e.g. W/kg, W/m2, $/W etc.) and also define the launch and on-orbit environmental durability. These performance metrics were aggressively set to vastly improve the state of art in cost, mass, and stowed power density. The environmental durability requirements are representative of typical space solar array industry requirements and are based on ABLE's broad experience in manufacturing solar arrays for commercial, NASA and military missions. These requirements were reviewed by NASA personnel and modified as required based on NASA's input. All detailed design, analysis and testing performed during Phase 1 support the attainment (or very near) of all the requirements/goals as is shown in later sections. For the cases where projected performance, based on Phase 1 results, is now slightly less than the original goals it is shown in parenthesis.

Technical specifications specific to the SLA blanket were then derived from the system requirements and the structural characteristics and capabilities of SquareRigger. These blanket specifications, which are shown in Table 9, were used as the design guideline for the SLA blanket during Phase 1.

Table 8. Original Requirements/Goals Developed for SLA SquareRigger System

Characteristic	When?	Near-Term Requirement (2008)	Mid-Term Requirement (2013)
Missions		LEO, MEO, GEO & Interplanetary	
Deployed Power (kW)	EOL	10 to 100	
Stowed Power (kW)	BOL	0	
Recurring Production Cost ($/ W)	BOL	250	125 (150)
Specific Mass (W/kg)	BOL	330 (320)	500
Deployed Power Density (W/m^2)	BOL	300	390
Stowed Volume (kW/m^3)	BOL	80 (70)	120 (110)
Voltage (V)	EOL	100 to 1000	
Radiation Degradation (e^-, p^+, UV)	EOL	Comparable to multi-junction planar array	
Contamination Degradation	EOL	Comparable to multi-junction planar array	
Thermal Cycling Degradation	EOL	Comparable to multi-junction planar array	
Micrometeoroid Degradation	EOL	Comparable to multi-junction planar array	
Quasi Static Acceleration	Launch	22 g's in each axis	
Acoustic Vibration	Launch	146 dB OASPL for 120 seconds	
Stowed Stiffness (fn Hz)	Launch	> 30 Hz	
Deployed Stiffness (fn Hz)	On-Orbit	> 0.1 Hz for 10kW , > 0.01 Hz for 100kW	
Deployed Accelerations	On-Orbit	0.001g's	
Grounding, ESD	On-Orbit	No sustained arcs or degradation, minimize trigger arcs	
System Reliability	EOL	0.99	
Deployment Torque Margin	On-Orbit	200% (3 to 1)	
Deployment Time	On-Orbit	1 hour total, 30 min structure, 30 min blanket	
Ground Test Capability	Pre-Launch	LAPSS test at the bay level (5m x 2.5m section)	
Assumed Cell Efficiency (8AM0, 28°C)	BOL	30%	40%
Pointing Accuracy at Base	On-Orbit	+/- 1 degrees	

3.4 SLASR BLANKET DESIGN

The primary components of the dual-deck lens and cell panel blanket are shown in Figures 23, 24, 25, and 26. The ultra-thin Fresnel lenses used in the dual-deck SLA blanket, which are made of electron, proton, and UV radiation resistant DC 93-500 silicone, are 0.14-µm-thick and are spaced approximately 9 cm from the solar cells. The flexible lenses are tensioned over arches, with approximately one meter of span of lens between arches, to produce a curved shape that significantly increases shape-error tolerance and off-pointing performance compared to flat Fresnel lenses. The solar cells are mounted to thin (130micron or less) graphite-composite panels optimized for high stiffness and efficient waste heat removal via high thermal conductivity and emissivity. Both the lens film and composite panels are tensioned end-to-end between the struts of the SquareRigger structure when the array is deployed. The demonstrated tension to achieve precise lens shape and alignment is only 1.1 Newton (0.25 lbf) per lens.

Lateral lens-to-cell alignment is critical. Very accurate alignment is achieved by attaching the lens guides and panels to small diameter Kevlar cords tensioned straight between spreader bars, which are attached to the SquareRigger end struts. These primary support cords run continuously between the end interfaces under moderate tension and, therefore, form a near perfect datum for aligning the lens guides and panels. The support cord also doubles as the hinges between panels.

Table 9. Derived Technical Specification the for SLA SquareRigger Blanket

Characteristic	When?	Blanket Specification
Deployed Dimensions		2.54 m wide x 5.08 m long (100 in x 200 in)
Stowed Dimensions	Launch	13.2 cm x 3.3 cm x 2.54 m (5.27 in x 1.35 in x 100 in)
Power	BOL	3.75 kW (290 W/m^2)
Mass		8.25 kg maximum (0.64 kg/m^2)
Operational Voltage	EOL	100 V to 1000 V
Deployed Lens- to-Cell Spacing	On-Orbit	9.22 ± 0.05 cm (3.63 ± 0.02 in) from top of lens arch to face of cell
Deployed Tension (Radiator + Lens)	On-Orbit	44.5 N (10lb) Maximum
Deployment Force	On-Orbit	66.8 N (15lb) Maximum
Cell-to-cell centerline alignment (all cells)	On-Orbit	± 0.025 cm (± 0.010 in) = 0.16 degrees error
Cell-to-lens centerline alignment (all cells)	BOL	± 0.050 cm (± 0.020 in) = 0.31 degrees error
Radiation Degradation (e^-, p^+, UV)	EOL	Comparable to multi-junction planar array
Contamination Degradation	EOL	Comparable to multi-junction planar array
Thermal Cycling Degradation	EOL	Comparable to multi-junction planar array
Micrometeoroid Degradation	EOL	Comparable to multi-junction planar array
Quasi Static Acceleration	Launch	22 g's in each axis
Acoustic Vibration	Launch	146 dB OASPL for 120 seconds
Grounding, ESD	On-Orbit	No sustained arcs or degradation, minimize trigger arcs
Storage	Ground	Meets all requirements after 1 year of stowage (20±5°C, <50%RH)
Deployment Time	On-Orbit	< 30 minutes
Assumed Cell Efficiency (8AM0, 28°C)	BOL	30%
Required Pointing Accuracy (α)	On-Orbit	+/- 1.5 degrees
Required Pointing Accuracy (β)	On-Orbit	+/- 10 degrees

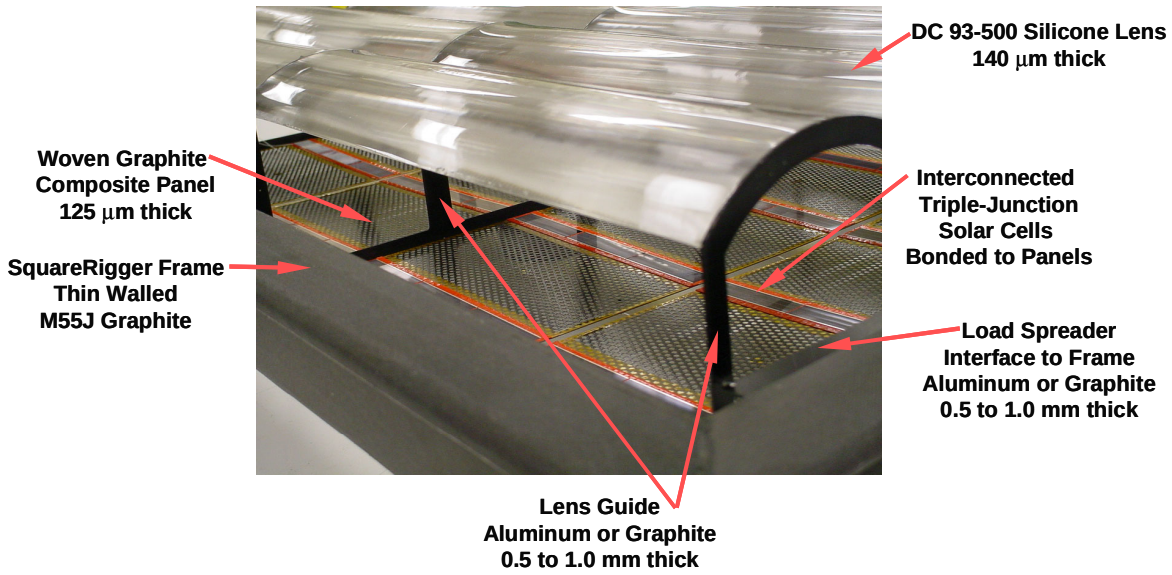

Figure 23. Lens Blanket Components Shown on the Phase 1 Demonstrator

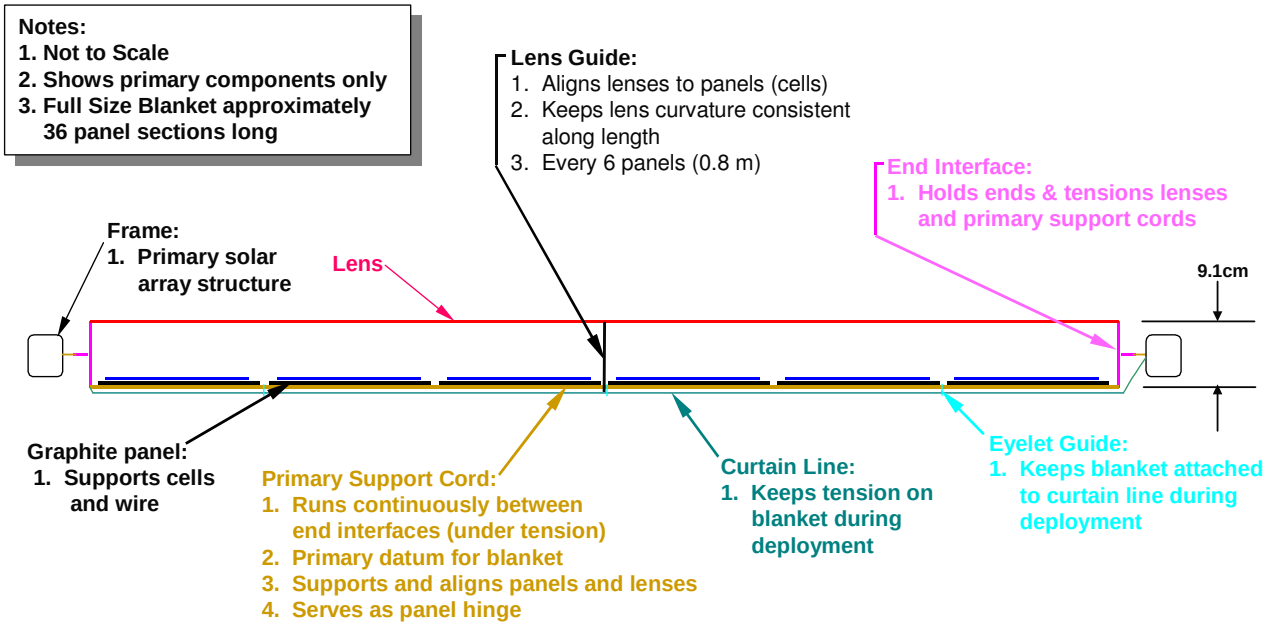

Figure 24. SLA SquareRigger Blanket Primary Components

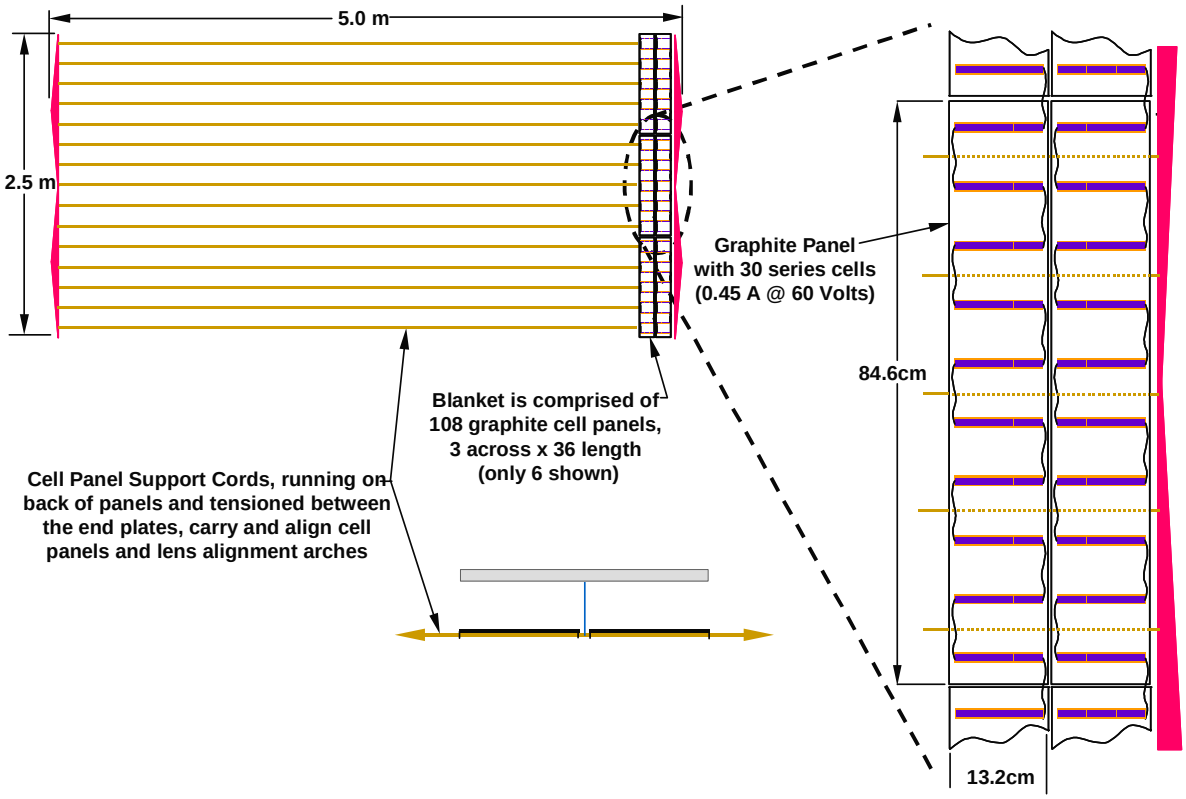

Figure 25. SLA SquareRigger Cell Panel Blanket

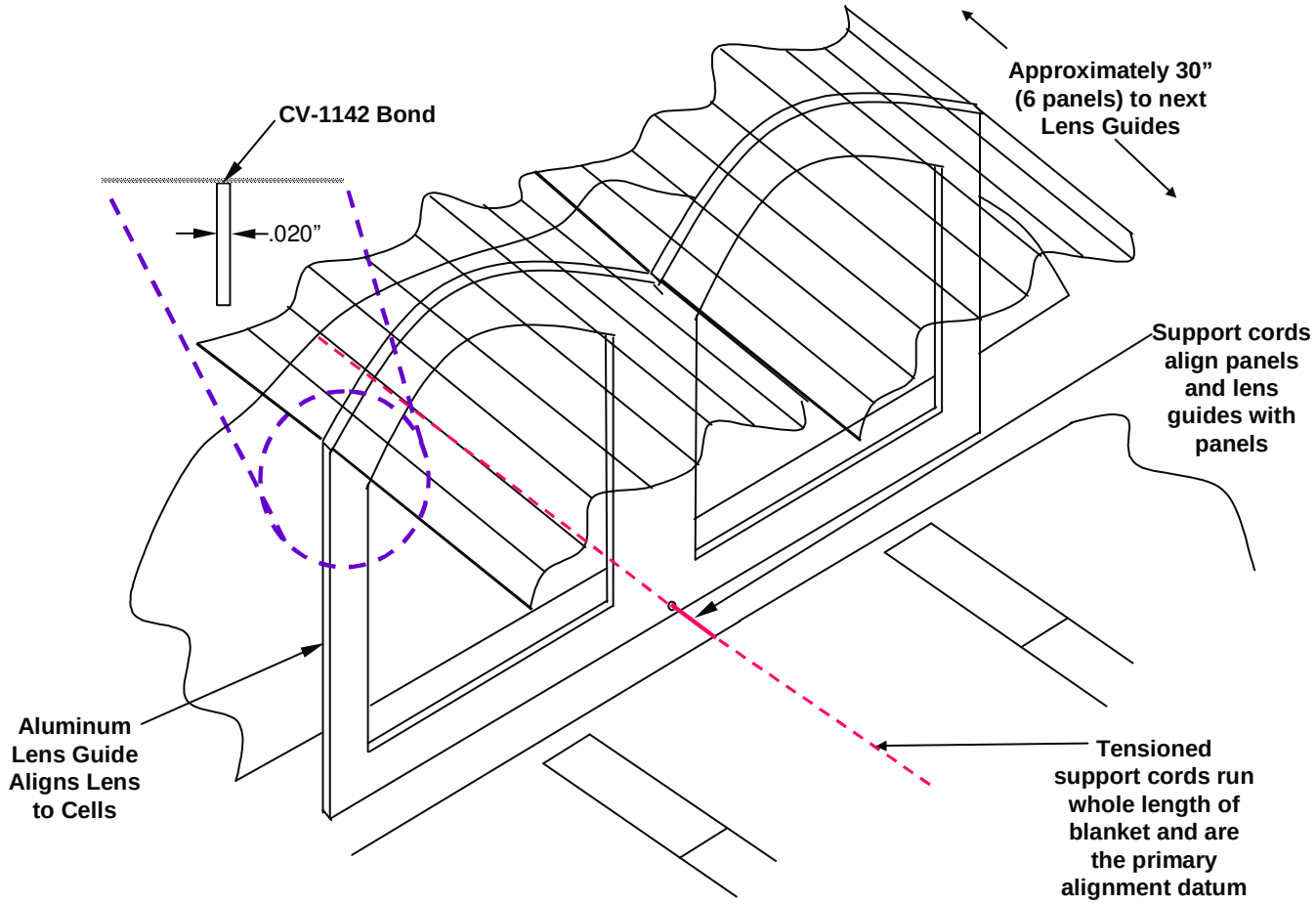

Figure 26. Lens Guide Alignment

A typical deployment sequence for SLA SquareRigger is shown in Figure 27. During launch the dual-deck lens and cell blanket is stowed in a compressed stack in the cavity that exists between the SquareRigger struts and spars to protect them from vibration damage. As shown in Figure 28 and Table 10, the lenses are folded between the cell panels when stowed providing a compact blanket stack, 5.65cm (2.23 in.) tall, which is highly damped. The folded panels and lenses are deployed accordion style pulled by the same motor that unfolded the SquareRigger structural elements. Low spring rate tensioners are used to attach the lens/cell panel blanket to the SquareRigger frame to minimize the effect of thermally induced length change on lens and/or panel tension and to enhance structural stability. These designs for SLA blanket stowage and deployment are derived from the original thin film blanket stowage and deployment concepts.

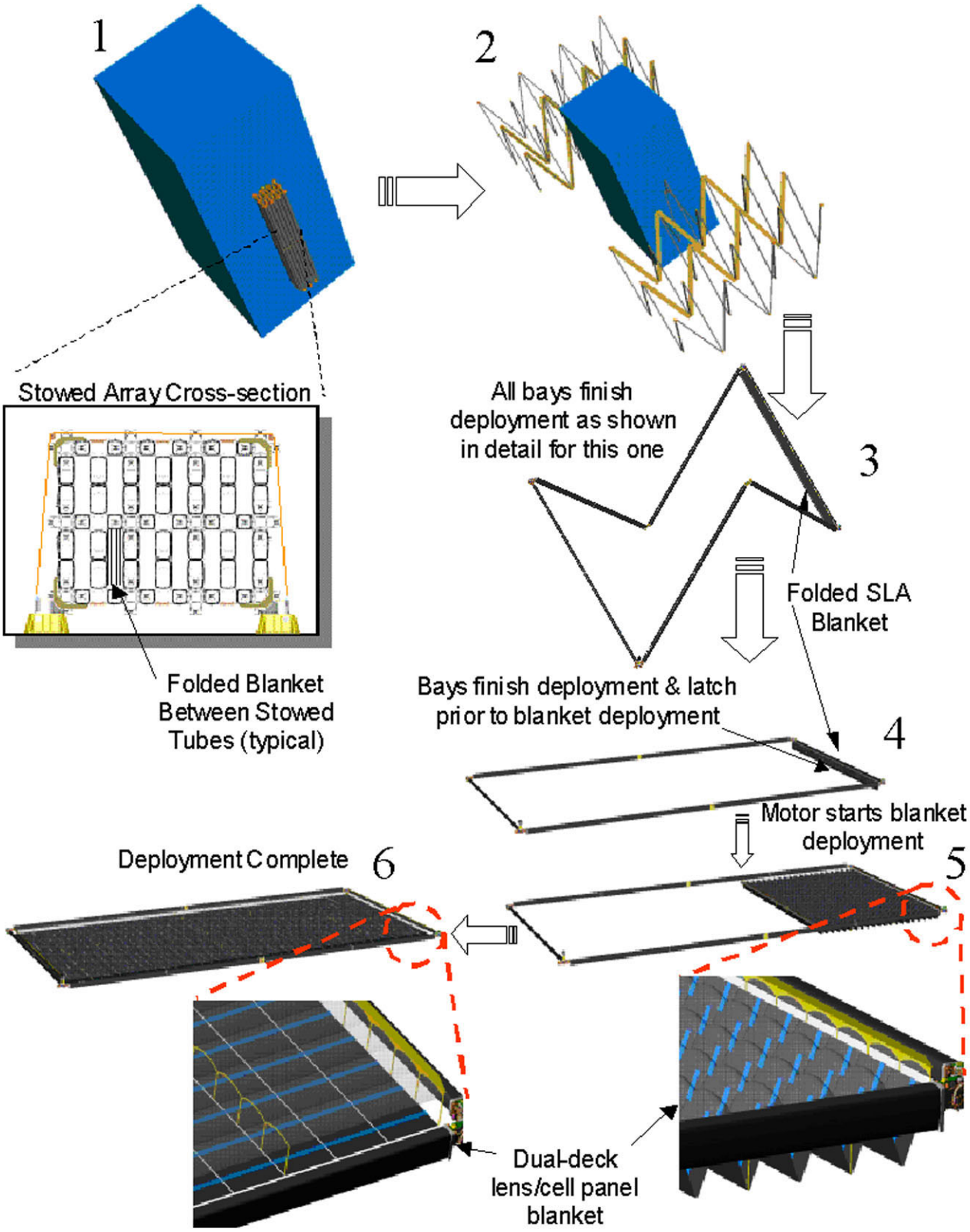

Figure 27. SLASR Stowage and Deployment

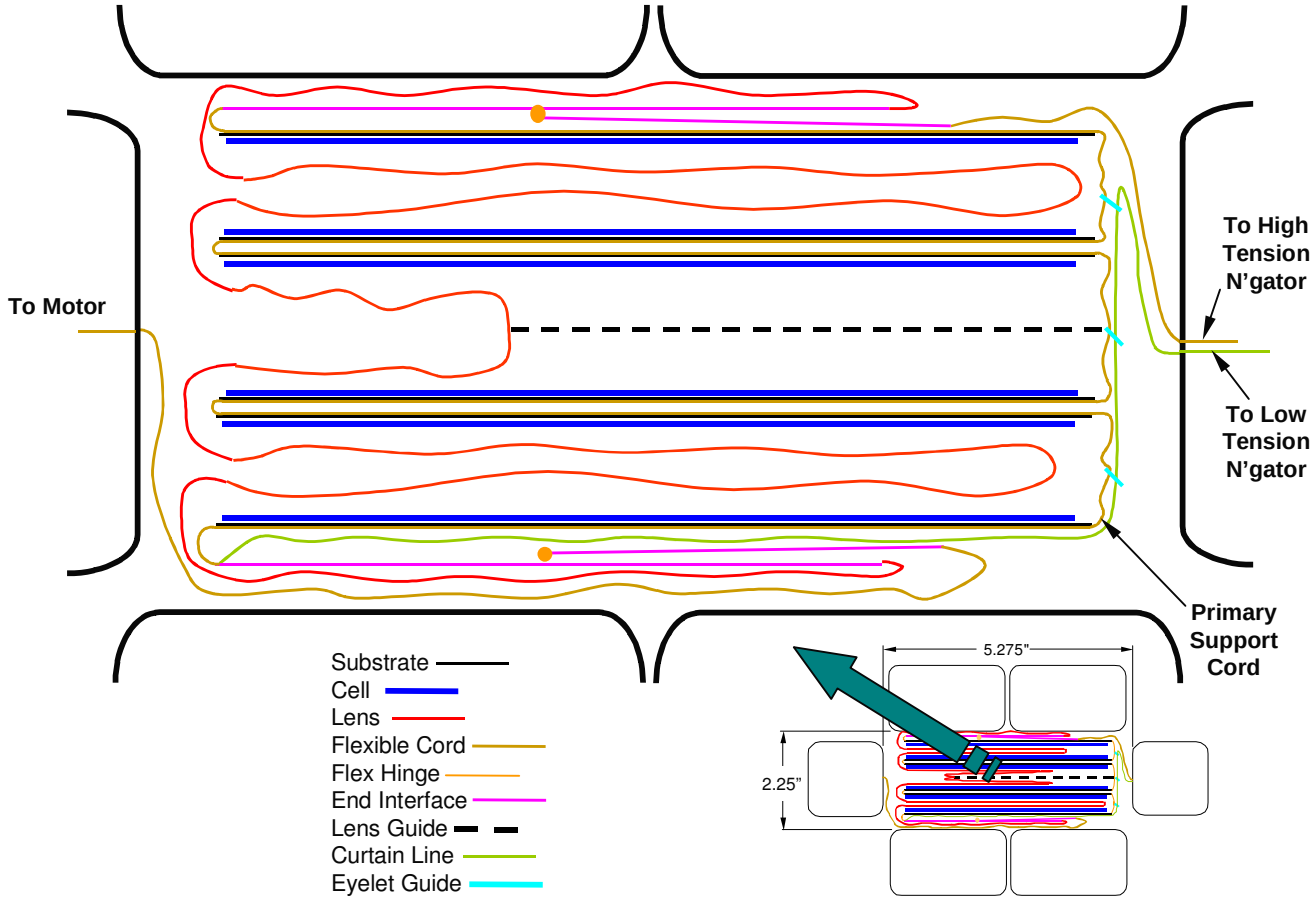

Figure 28. SLASR Blanket Stowage

Table 10. Stowed Blanket Thickness Calcuation

Stowed Blanket Thickness (Inches)				
Component	**Thickness**	**Quantity**	**Total**	**Fraction**
1/2 Cords on Back	0.005	36	0.180	8.9%
Substrate	0.005	36	0.180	8.9%
Flex Bond	0.000	36	0.000	0.0%
Flex Circuit	0.004	36	0.144	7.1%
Cell Bond	0.004	36	0.144	7.1%
Cell	0.006	36	0.216	10.7%
Glass Bond	0.002	36	0.072	3.6%
Glass	0.003	36	0.108	5.3%
Lens	0.008	36	0.288	14.2%
1/2 Lens Fold	0.012	36	0.432	21.3%
Sub Total	0.044	36	1.764	
End Interface Plate	0.04	4	0.160	7.9%
Lens Guide	0.02	5	0.100	4.9%
Nominal Total			**2.024**	**100%**
Contingency			**0.2024**	**10%**
Total with Contingency			**2.226**	

3.5 SYSTEM ANALYSES

3.5.1 Sizing Model

Development of an Excel spreadsheet to rapidly size and predict all key SLASR metrics was completed during the Phase 1 program. The model allows an analyst to quickly and accurately predict SLASR array size, power and mass for any reasonable configuration of bay size, quantity and arrangement. The model contains 22 detailed worksheets addressing the various details of the design such as mass properties, strength, stiffness, power, environmental degradation and packaging in a single Excel file.

The model performs a detailed power analysis. On-Orbit EOL electrical performance is calculated from:

- Measured BOL cell performance
- Detailed radiation dose calculation
- Operating temperature
- Harness Losses
- On-orbit degradation
- Radiation, contamination, UV, micrometeorites, thermal cycling etc.

The detailed mass analysis is based on prototype SquareRigger and SLA hardware as available. The model contains a complete parts list and there is a mass breakout and contingency for each component based on its maturity. Harness mass is determined by wire count and length. A mass contingency, which is currently running at about 5% at the system level, is included in all reported metrics and is calculated for each component based on the following criteria:

- 2% for actual or PRO/E designed part
- 10% for calculated
- 15% for estimated

The model also includes approximate structure strength and stiffness calculations to ensure that these very important features are consistent with the stated requirements. The key metrics of mass (W/kg) and stowed power (kw/m^3) calculated from the sizing model for already demonstrated 30% efficient concentrator cell efficiency is shown in Figure 28. A typical mass breakdown is also shown in Figure 29. A summary of a typical power analysis performed for a high power 15 year GEO mission is shown in Figure 30.

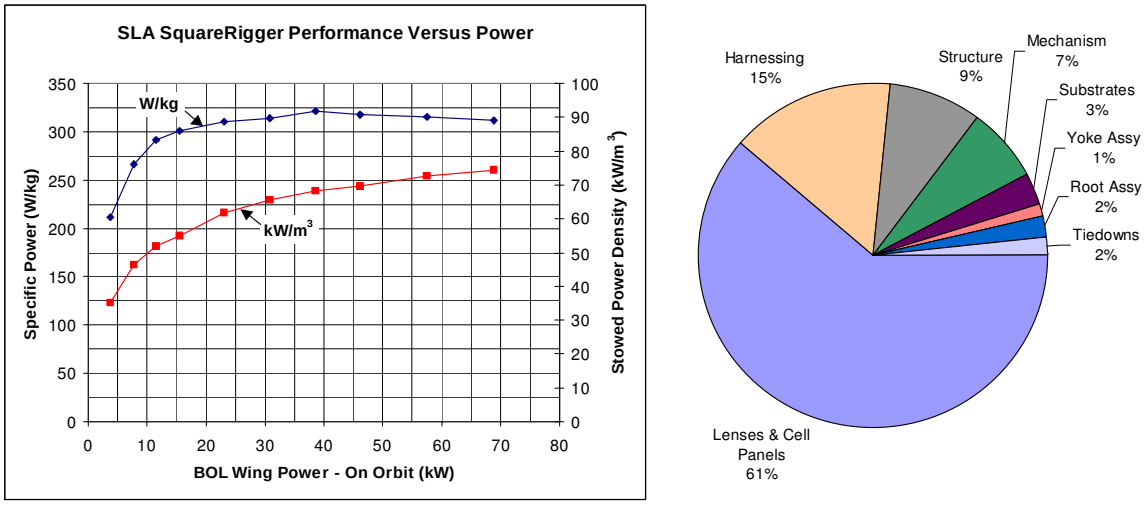

Figure 29. Calculated SLASR Mass and Stowed Power Density and Typcical Mass Breakdown

SLA Triple Junction Cell Data at 1 AM0 and 28 °C	Isc	Imp	Vmp	Voc	Pmp	Efficiency
	Amps/cm^2		Volts			
Bare Cell Performance, BOL 28 °C	0.0177	0.0170	2.389	2.714	0.0406	30.00%
Temperature Coeffcients °C^{-1}	1.00E-05	7.00E-06	-0.0065	-0.0059	-9.37E-05	-0.0693%

15yr GEO Mission

Cell Length (cm)	3.50
Cell Active Width (cm)	1.00
Lens Width (cm)	8.50
Geometric Concentration Ratio	8.50
Lens Gap or Blocking at Edges (cm)	0.076
Lens Optical Efficiency	0.92
Effective Optical Concentration Ratio	7.68
Net Optical Efficiency	0.904
Effective Cell Area (cm^2)	26.88
Concentration Voltage Boost Factor	1.09

	Reference Value	Loss Factor	Isc	Imp	Vmp	Voc	Pmp	System Efficiency
Cell Under Lens @ 28°C			0.476	0.457	2.604	2.958	1.19	29.54%
LAPSS Calibration to AM0		1.000	0.476	0.457				
CIC Assembly Voltage Loss		0.995			2.591	2.943		
CIC Glassing Loss		0.995	0.473	0.454				
Sun Distance	1.0000 AU	1.000	0.473	0.454				
Alpha Off-Pointing		1.000	0.473	0.454				
Beta Pointing (Cosine)	3.00 deg	0.999	0.473	0.454				
Beta Pointing (Shadowing)		1.000	0.473	0.454				
UV degradation, Lens		0.980	0.463	0.445				
UV degradation, Cell Cover		0.980	0.454	0.436				
Micro-Meteoroid and Debris		0.990	0.449	0.432				
Contamination on Lens and Cell		0.980	0.440	0.423				
Isc Radiation Degradation	4.20E+14 1MeVe/sqcm	0.990	0.436					
Imp Radiation Degradation	5.20E+14 1MeVe/sqcm	0.978		0.414				
Vmp Radiation Degradation	5.20E+14 1MeVe/sqcm	0.899			2.330			
Voc Radiation Degradation	5.93E+14 1MeVe/sqcm	0.897				2.639		
CIC Operating Temperature	85.6°C							
Isc Temperature Correction	10.0 uA/sqcm/C	0.0155 A	0.451					
Imp Temperature Correction	7.0 uA/sqcm/C	0.0108 A		0.425				
Vmp Temperature Correction	-6.5 mV/°C	-0.3744 V			1.956			
Voc Temperature Correction	-5.9 mV/°C	-0.3398 V				2.299		
Cell-to-Cell Interconnect Voltage Drop	0.01 ohms	-0.0042 V			1.952			
EOL CIC Performance			0.451	0.425	1.956	2.299	0.83	20.63%
Series Cells Per Module	4	4	0.451	0.425	7.824	9.196		
Module-Module IC Voltage Drop	0.01 ohms	-0.0042 V			7.819			
Cell Module Performance			0.451	0.425	7.819	9.196	3.32	20.62%
Thermal Cycle Current Loss		0.995	0.449	0.422				
Thermal Cycle Voltage Loss		0.995			7.780	9.150		
Cell/Module Stringing Mismatch		0.99		0.418				
Lens Stringing Mismatch		0.99		0.414				
Number of Series Modules per String		15			116.704	137.256		
String Performance on Panel			0.449	0.414	116.704	137.256	48.32	20.01%
Blocking Diode Voltage Drop		0.7000 V			116.004			
Panel Harness Voltage Drop	0.28 ohms	0.1139 V			115.891			
Strings per Power Circuit	**6**							
Wing Harness Voltage Drop	0.95 ohms	2.3563 V			113.534			
String Performance at SADA/Spacecraft Connector			0.449	0.414	113.534	137.256	47.01	19.46%

Input to Array IV curve calculator

Number of Strings = 1188

Voc	Isc	Vmp	Imp	Pmp	FF
137.26	533.60	113.53	491.87	55843.7	0.76

Performance at Load Voltage

Volts	Amps	Watts
100.00	514.07	51406.7
110.00	**503.48**	**55382.3**
113.53	491.87	55843.7

Power at Selected Load Points

Peak Power

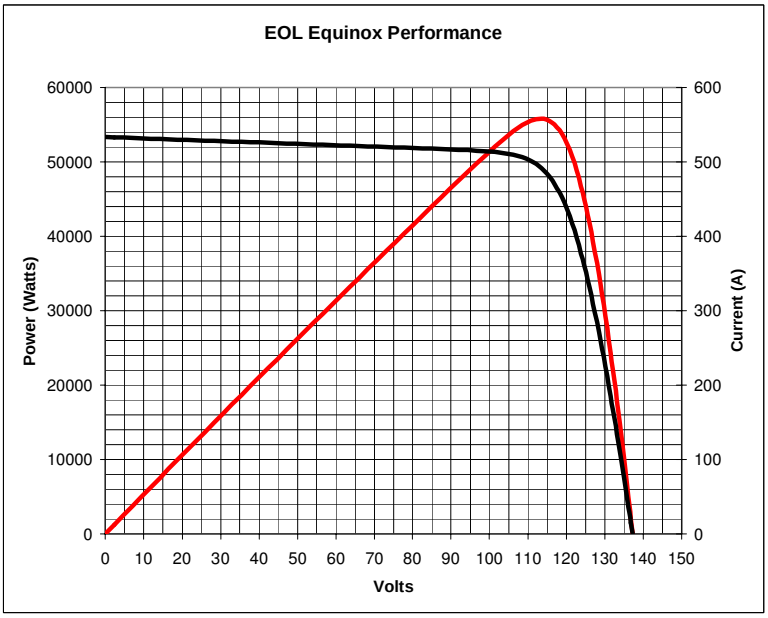

Figure 30. SLASR EOL Power Analysis Example for 56kW 15-year GEO Mission

3.5.2 Detailed Structural Analysis

ANSYS Finite Element models were developed for 14 kW, 42 kW and 56 kW wings to calculate natural frequency and deflection due to acceleration. It was determined that the baseline SquareRigger structure (tube cross-section and thickness), originally developed to support a thin film photovoltaic blanket, meets the SLASR stiffness requirements (frequency > 0.1 Hz for 10 kW Array - 2 Wings, frequency > 0.01 Hz for 100 kW Array - 2 Wings, and maximum a rotation < 1 Degree @ 0.01 g). Results of the finite element calculations are shown in Figure 31.

3.6 MID-TERM (10 YEAR) TECHNOLOGY ROADMAP

All near-term analysis and performance projections are based on the existing designs and current technology capabilities, the most important of which is cell efficiency. Thus, a SLASR array constructed from existing components will achieve the near-term performance given in Table 11. Over the next ten years significant improvements are forecast for many key SLASR technologies. For example *mass produced* crystalline solar cells for space have achieved an average improvement of approximately 1% per year between 1995 (19% SJ GaAs) and 2003 (27.5% ATJ $GaInP_2$/GaAs/Ge) based on the production of over 1.5 million cells and this trend is expected to continue. The key improvements in SLASR technology are listed in Table 11 along with the corresponding impact on the key metrics of efficiency (W/m^2), cost ($/W), mass (W/kg) and stowed power density (kW/m^3).

Table 11. Mid-Term (10 year) Technology Roadmap for SLASR

				Improvement			
Component Improvement	**Current Performance**	**Projected Performance**	**Basis**	**W/m^2**	**W/kg**	**$/W**	**kW/m^3**
Cell Efficiency	30% Efficiency	40% Efficiency	EMCORE and SPL Technology Roadmap Trends	1.33	1.33	1.33	1.33
Solar Cell Module Mass	2.51 grams (4cells)	1.51 grams (4 cells)	Use 1/2 thickness cell being developed by EMCORE. Interconnect Cells without copper flex circuit. Co-cure kapton to panel.	1.00	1.09	1.00	1.05
Lens Mass & Cost	140 μm thick	115 μm thick	Improved processing and materials	1.00	1.03	1.10	1.02
Panel Mass	100 μm thick	75 μm thick	Higher conductivity graphite fibers including carbon nanotubes	1.00	1.05	1.00	1.02
Mechanism Mass		75% reduction from current	Design and material optimization	1.00	1.02	1.05	1.00
Structural Size & Mass		75% reduction from current	Higher modulus graphite fibers including carbon nanotubes	1.00	1.02	1.10	1.10
			Total Improvement Factor	1.33	1.64	1.69	1.60
			Current Performance	300	320	250	70
			10 Year Performance	**400**	**523**	**148**	**112**

3.7 DEMONSTRATION HARDWARE AND TESTING

Based on the full scale SLASR design concepts developed, detailed drawings for the Phase 1 SLA SquareRigger prototype were prepared. As shown in Figures 32 through 35, the demonstration blanket contains four 12.7cm (5.0") x 34.0cm (13.4") woven graphite panels, four approximately 53.3cm (21")-long lenses that are supported by a lightweight graphite SquareRigger frame. The lenses were manufactured and bonded to the aluminum lens guides by ENTECH. The lens and cell panel blankets are tensioned to approximately 4.5 Newtons (1lbf) each and this equates to approximately 4% stretch of the lenses. Left over (scrap) two-junction $GainP_2$/GaAs/Ge TECSTAR cells from the DS1 SCARLET program were installed on the panels to enhance the quality of the demonstrator. Two strings, of 3 cells in series, were installed and interconnected on one of the panels for electrical performance testing. The optical alignment and flatness of the prototype was exceptional as proven by the ease at which all cells can be simultaneously brought into focus as shown in Figure 36.

The blanket deployment concept was successfully verified by manually tensioning the blanket draw cords simulating tensioning of the cords by an electric motor as shown in Figure 37. The power production of the two 3-cell strings was measured using ABLE's Large Area Pulsed Solar Simulator (LAPSS) with and without the lenses installed to record system efficiency. The data from string 1 is shown in Figure 38. The increase in power and current from the lenses was as expected with a measured lens efficiency of 90%. The power and current increase for string 2 was similar to string 1, though it was noted that one of the cells in the strings was damaged, resulting in string 2 having low voltage compared to string 1.

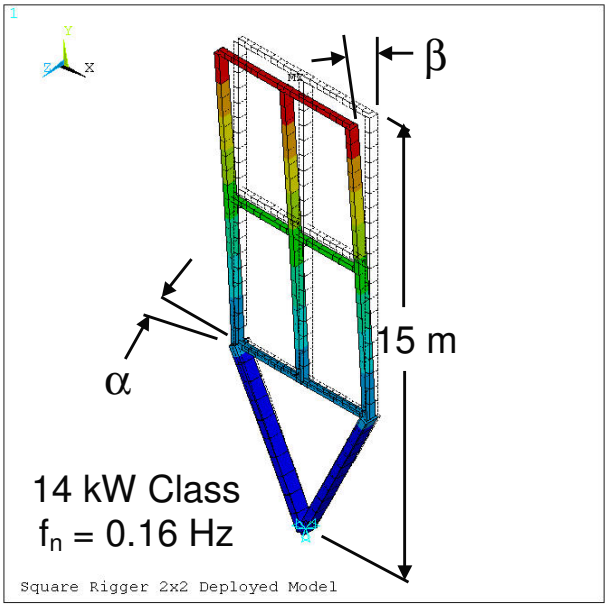

Maximum Rotation at 0.01 g
α = 0.11 deg
β = 0.79 deg

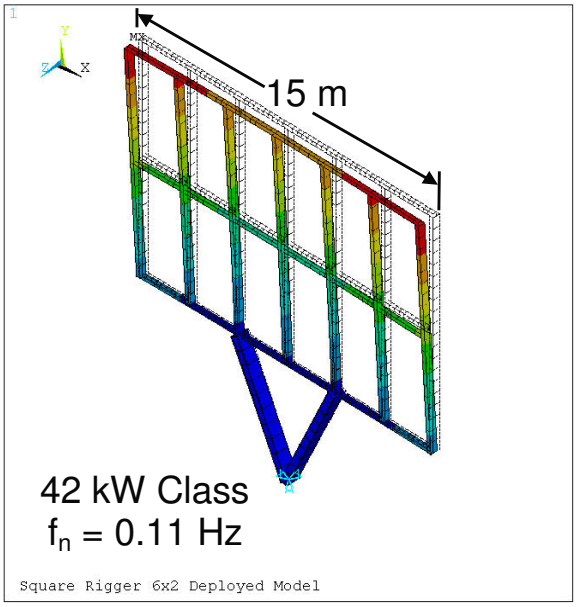

Maximum Rotation at 0.01 g
α = 0.57 deg
β = 1.43 deg

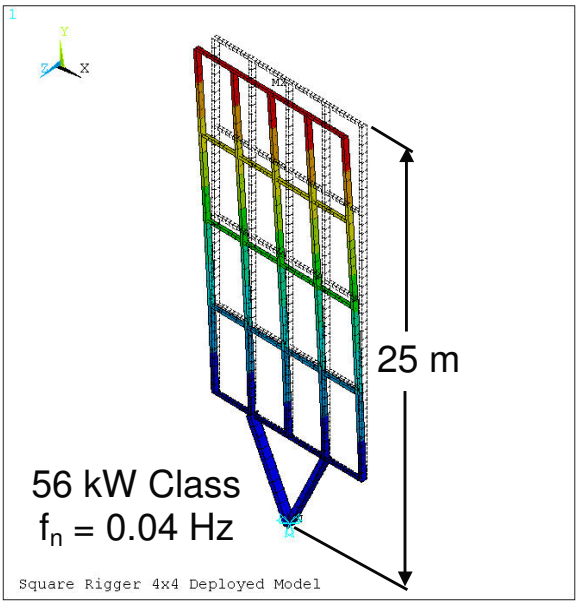

Maximum Rotation at 0.01 g
α = 0.64 deg
β = 5.69 deg

Requirements

- Frequency > 0.1 Hz (10 kW Array= 2 Wings)
- Frequency > 0.01 Hz (100 kW Array = 2 Wings)
- Maximum a rotation < 1 Degree @ 0.01 g

Figure 31. SLASR FEA Stiffness Calculations for Several Configurations Showing Compliance to Requirements

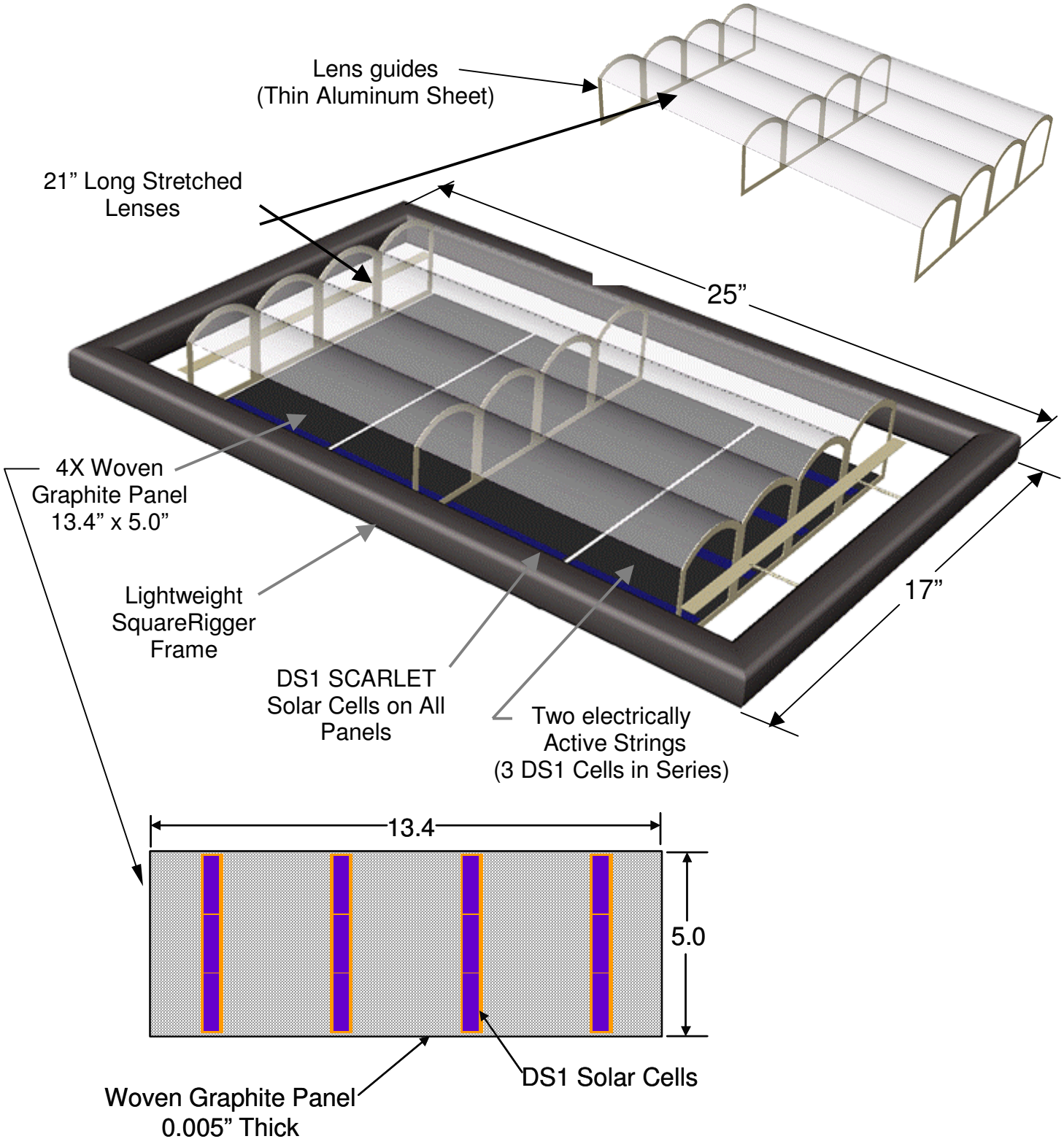

Figure 32. SLA SquareRigger Demonstration Blanket Components

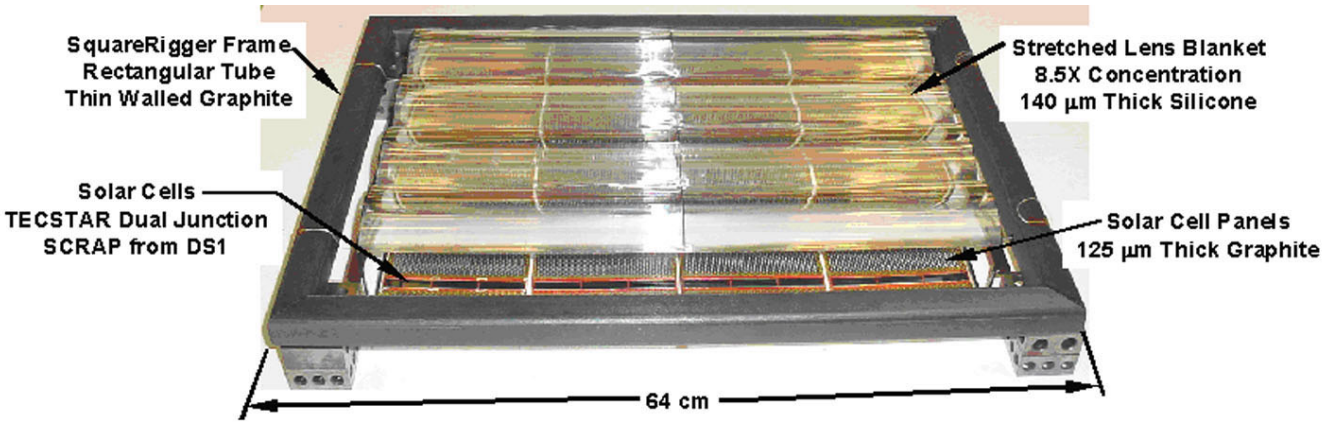

Figure 33. Phase 1 SLASR Prototype Top View

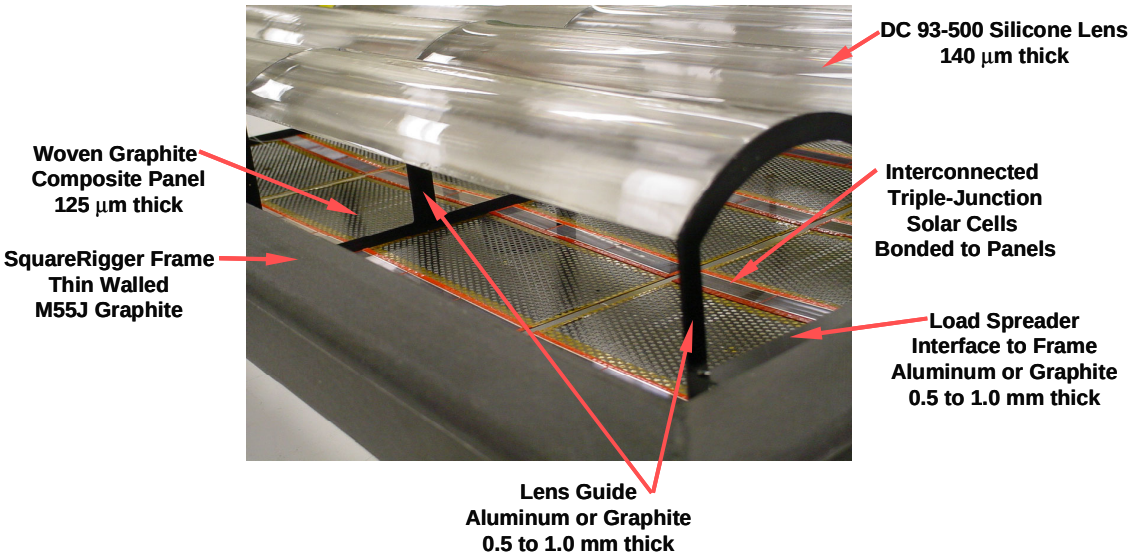

Figure 34. Phase 1 SLASR Prototype Oblique View

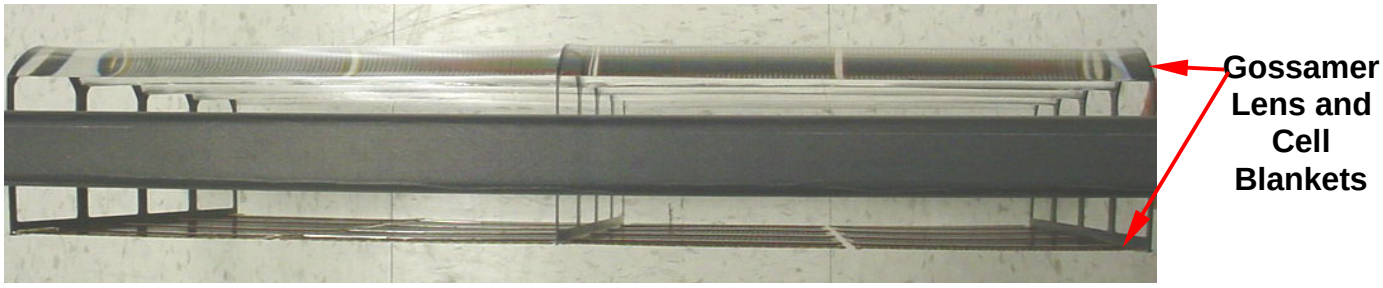

Figure 35. Phase 1 SLASR Prototype Side View

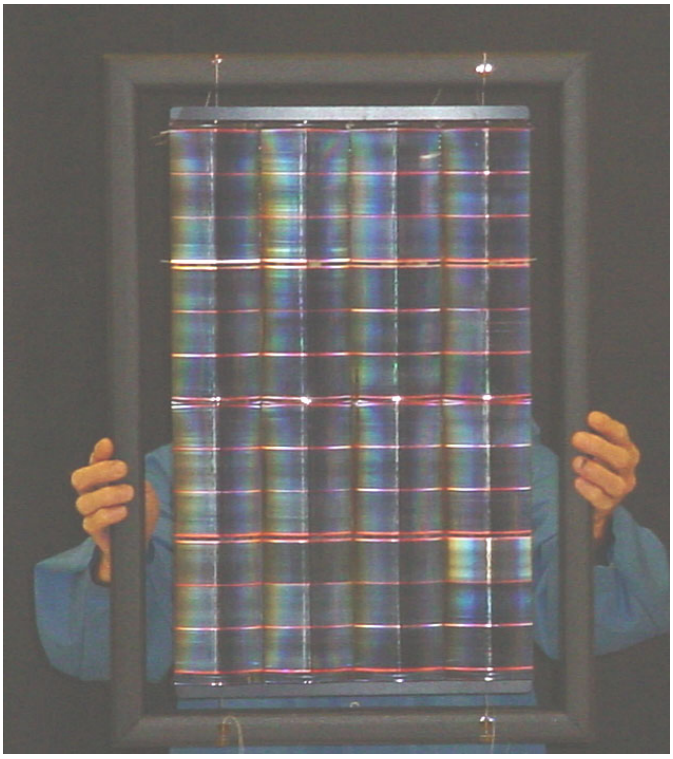

Lenses perfectly image cells verifying optical alignment and flatness

Lenses perfectly focus sunlight on cells verifying optical alignment and flatness

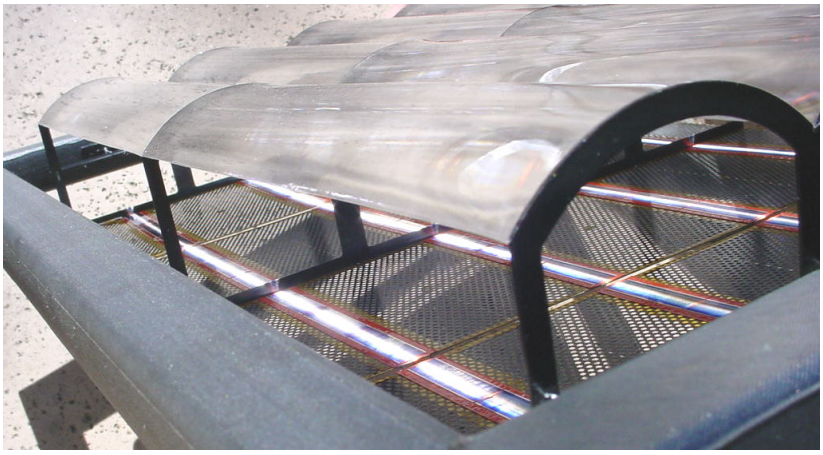

Figure 36. Optical Verification of Phase 1 SLASR Demonstration Blanket

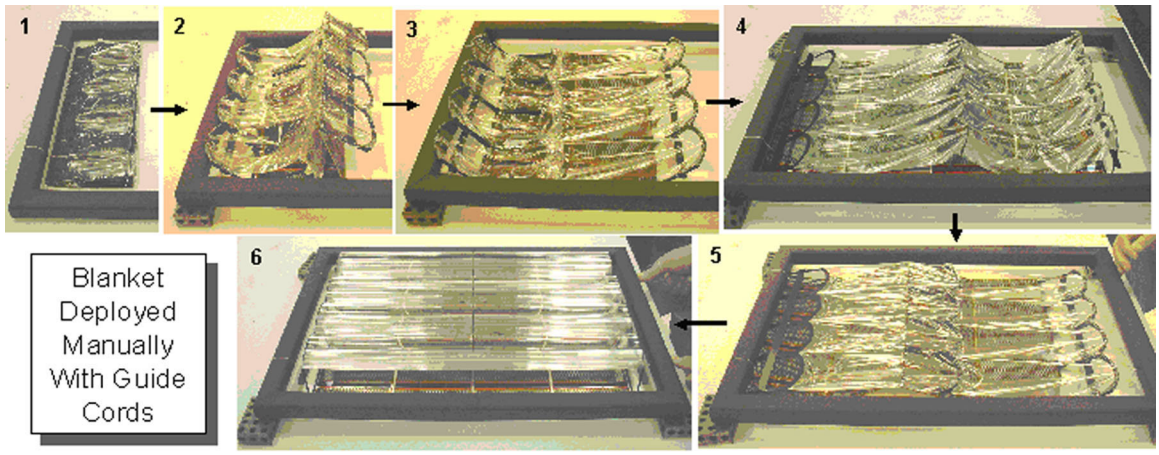

Figure 37. Phase 1 SLASR Demonstration Blanket Deployment

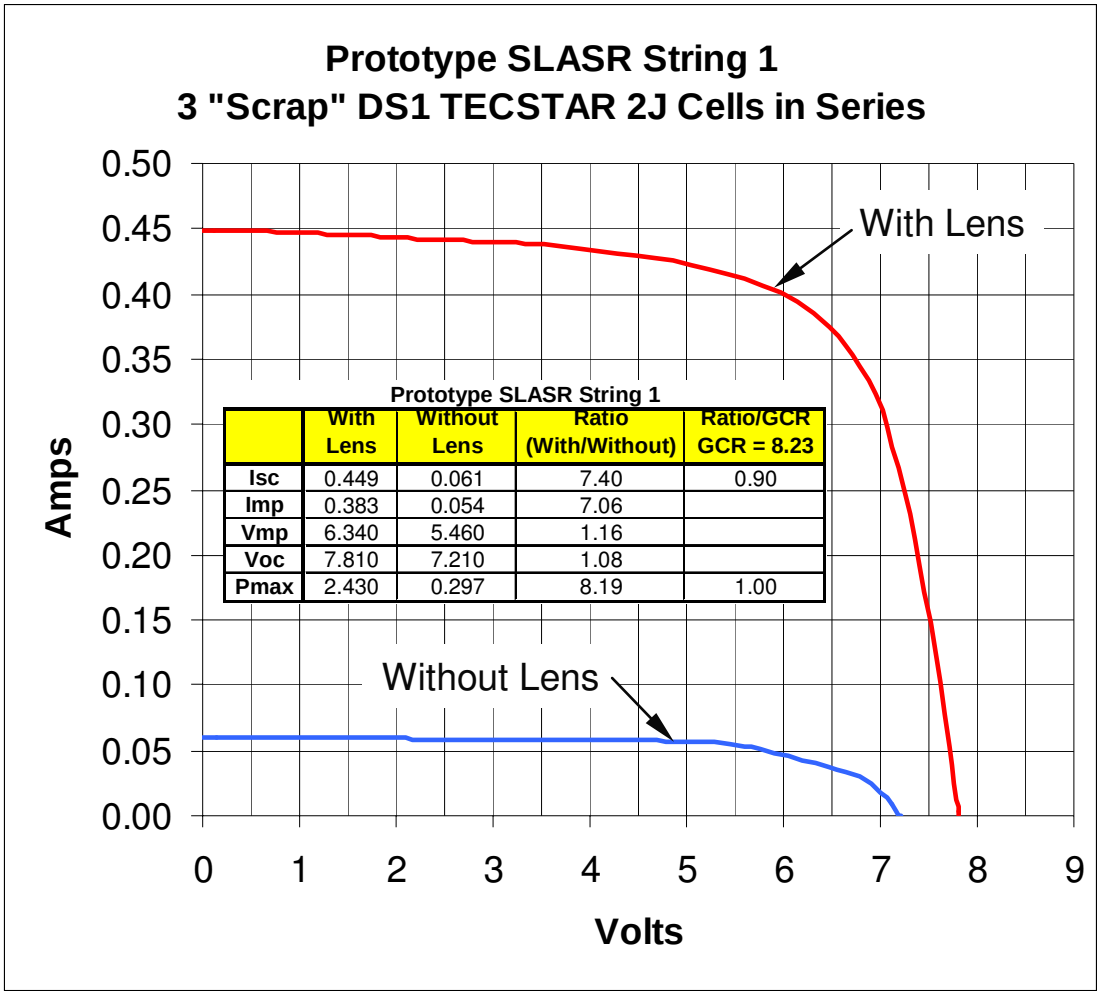

Figure 38. Phase I SLASR Demonstration Blanket LAPSS Data

3.8 ACKNOWLEDGMENT

This work was administered though the NASA Glenn Research Center and funded by the NASA SBIR Phase 1 program under contract #NAS3-03017.

3.9 SLASR SUMMARY

Excellent progress has been made in integrating a Stretched Lens Array photovoltaic blanket into the SquareRigger solar array structure. The result is an extremely lightweight, high efficiency, high power, high voltage, and low stowed volume solar array that may enable numerous future NASA missions such as Space Solar Power (SSP), high-power deep space SEP probes, Solar Electric Propulsion (SEP) tugs and large earth-orbiting science satellites.

REFERENCES:

1) S. White, M. Douglas, B. Spence, P. Jones and M. Piszczor, "Development of an UltraFlex-Based Thin Film Solar Array for Space Applications", 3rd WCPEC, May 2003 with, and of GRC.

2) D. Murphy, M. Eskenazi, B. Spence & P. Jones, "Thin Film & Crystalline Solar Cell Array Performance Comparisons, IEEE Conference, 2002.

3) P. Jones, J. Harvey, S. White & B. Smith, "A High Specific Power Solar Array for Low to Mid Power Spacecraft", SPRAT Conference, 1994.

4) D. B. Snyder, "Dynamic Interactions Between Ionospheric Plasma and Spacecraft," 75th Anniversary U.R.S.I. Symposium, Brussels, Belgium, 26-27 April 1995.

5) M. Kruer and J. Lyons, "The FAST Solar Array: Challenging Requirements, Novel Design," 1st World Conference on Photovoltaic Energy Conversion, December 5-9, 1994.

6) S. Davis, R. Stillwell, W. Andiario, D. Snyder, and I. Katz, "EOS-AM Solar Array Arc Mitigation Design," 1999 Intersociety Energy Conversion Engineering Conference, Vancouver, BC Canada, August 2-6, 1999.

7) T.G. Stern, et. al., "Development of an Electrostatically Clean Solar Array Panel", IEEE Conference, 2002.

8) B. Spence, D. Murphy, P. Jones, and M. Eskenazi, "The SCARLET Array for High Power GEO Satellites, 26th IEEE Photovoltaic Specialists Conference, September 1997.

9) O'Neill, M., et al, The Stretched Lens Array (SLA): A Low-Risk, Cost-Effective Concentrator Array Offering Wing-Level Performance of 180 W/kg and 300 W/m^2 at 300 VDC, Proceedings of the 37th Intersociety Energy Conversion Engineering Conference, July 29–31, 2002, Washington, DC IECEC 2002 Paper No. 20115.

DEVELOPMENT OF A HIGH EFFICIENCY MECHANICALLY STACKED MULTI-JUNCTION SOLAR CELL

Daniel Aiken, Paul Sharps, Mark Stan
Emcore Photovoltaics, Albuquerque, NM 87123

Harry Atwater, Anna Fontcuberta i Morral, James Zahler,
California Institute of Technology, Pasadena, CA 91125

Mark Wanlass
National Renewable Energy Laboratory, Golden, CO 80401

INTRODUCTION

Monolithic, 2-terminal, epitaxially grown multi-junctions represent the state-of-the-art in high efficiency photovoltaic space power. Their *in-situ* monolithic integration results in an elegant device structure with high efficiency, relatively high specific power, and a simple fabrication process. The monolithic, epitaxially grown nature of these devices also imposes materials and design restrictions which impede the march to significantly higher performance. These devices presently require lattice matched epitaxial templates (substrates) which limits the materials choices for integration. The barriers to producing high photovoltaic quality epitaxial materials on lattice mismatched templates have not been easy to surmount, despite extensive effort in the research community. Also, series interconnection of subcells is by far the most applicable connectivity approach for these monolithic devices, which further limits the connectivity design space.

In comparison, the mechanically stacked approach is advantageous because it relaxes or completely removes the material and design restrictions inherent in monolithic approaches. Device designers can conceivably integrate subcells of a chosen bandgap regardless of their lattice parameter, and in any connectivity arrangement. The benefits of alternative connectivity arrangements have been demonstrated [1].

In contrast to the elegance of monolithically integrated solar cells, mechanically stacked solar cells can be described as the “brute force” approach to higher performance. Mechanically stacked approaches have been investigated for over 25 years, but have been deployed in space only on small-scale experimental testbeds. Mechanically stacked approaches have historically been limited by several barriers. The cost associated with integrating devices on multiple substrates has been economically prohibitive. The substrates used as templates for III-V epitaxial solar cell structures comprise a very large fraction of the total cell cost. Techniques such as the CLEFT process [2] or epitaxial lift-off [3] have been developed to allow substrate removal and re-use, but they are difficult to implement cost-effectively in a production environment. *Ex-situ* integration is another barrier which increases the processing complexity and cost, and also results in performance losses associated with parasitic losses inherent to common interconnect schemes. Excessive weight also limits the practicality of these devices for space applications because of the multiple substrates and/or fixturing hardware used to stack the subcells together.

Here we present results of work performed on a new mechanically stacked solar cell approach for achieving very high efficiency and high specific power for space concentrator applications. This work addresses some of the cost and practicality limitations present in many historical mechanically stacked approaches, and is being funded by the NASA Office of Space Science through the Advanced Cross-Enterprise Technology Development Program. The goal of this project is to demonstrate the critical technology elements necessary for producing a 40% efficient, lightweight solar cell for concentrator arrays. A specific power of 1kW/kg is projected at the cell level.

DEVICE CONCEPT

The device structure being developed is shown in Figure 1. A high bandgap tandem based on the well-understood InGaP/GaAs materials combination is grown on an inactive GaAs or germanium substrate. By similarity, this tandem device structure capitalizes on the highly refined triple junction device structure already in high volume production at Emcore. Subsequent glass encapsulation provides a superstrate for mechanical support of the active solar cell, and a substrate selective removal process is used to decrease the weight of this high bandgap tandem.

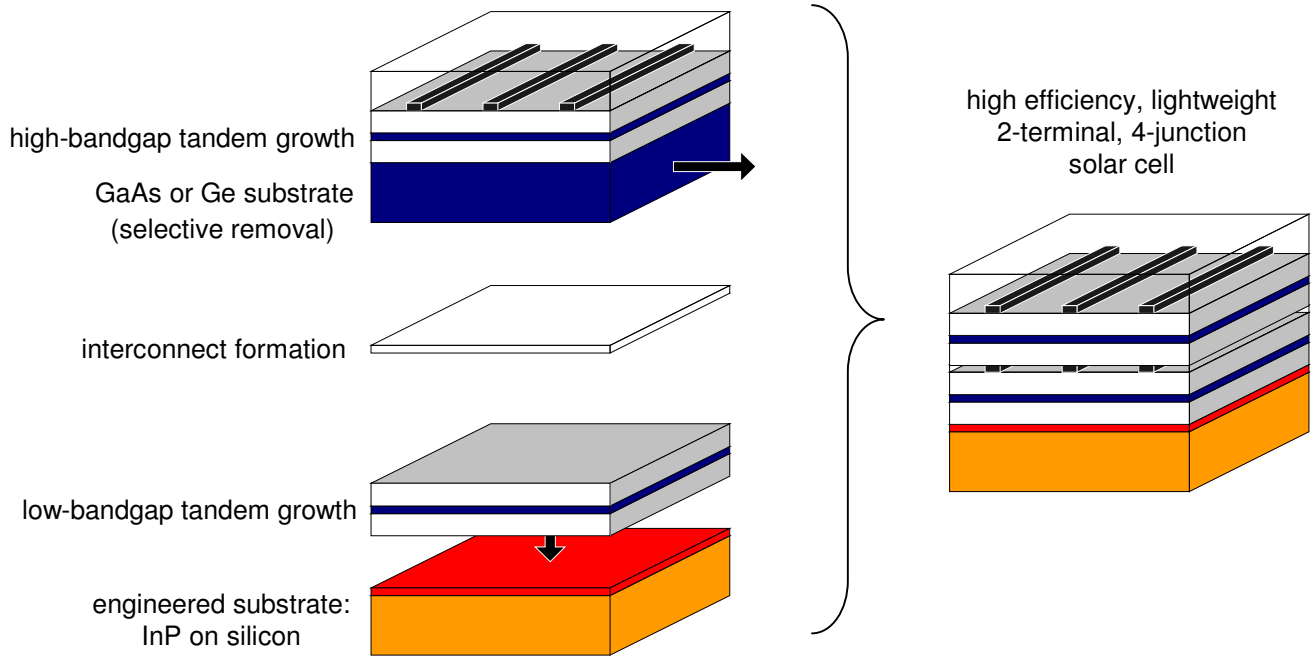

Figure 1 A schematic of the mechanically stacked 4-junction device integration scheme under development

Growth and processing of a low bandgap 1 eV InGaAsP / 0.74 eV InGaAs tandem is performed independently of the top tandem on an engineered InP-on-silicon substrate. The engineered substrate in this application is designed to provide an epitaxial template for active layers lattice matched to InP, while also benefiting from the lower weight, lower cost, and superior mechanical stability of silicon as compared to InP. Silicon's mass density is less than half that of InP, and the superior mechanical strength of silicon permits the use of thinner substrates. A thinner, lower density substrate allows a much higher power to weight ratio than would be possible with an InP substrate. A thin InP film, shown in red in Figure 1, is transferred to a silicon host substrate from a re-useable InP source wafer using a process that will be described in the next section.

A number of different schemes for mechanical and electrical interconnection of the two independently grown and processed devices are being considered. As shown in Figure 2, this combination of bandgaps is nearly ideal for a four junction series interconnected solar cell. This combination of bandgaps is therefore very compatible with two terminal, series interconnected integration, provided that the tandem interconnect is sufficiently transparent so as to transmit a near-theoretical spectral content to the bottom tandem. Achieving a highly transparent interconnect while also maintaining both a low electrical specific resistivity and good mechanical stability at the interconnection is critical to the success of this two terminal approach. Here we note that transmission loss through the tandem interconnect can be partially compensated for by reducing the thickness of the top tandem, thereby decreasing the fundamental, above-gap absorption in the top tandem.

ENGINEERED SUBSTRATES

The InP-on-silicon engineered substrate is being developed at Cal Tech using the Smart-cut process originally developed by Bruel *et al.* for silicon-on-insulator applications [4]. The process is illustrated schematically in Figure 3. An InP wafer is implanted with hydrogen ions to a controllable projected range. The implanted side of the InP

wafer is then bonded to the silicon host substrate using modern direct wafer bonding methods [5]. The InP/Si wafer pair is annealed in a controlled ambient at elevated pressure and temperature. The anneal simultaneously strengthens the direct bond and perforates the InP wafer at the implanted region. The released InP substrate can then be re-polished and repeatedly used in the layer transfer process. The engineered substrate can then in principle be used to grow a high quality low bandgap tandem solar cell.

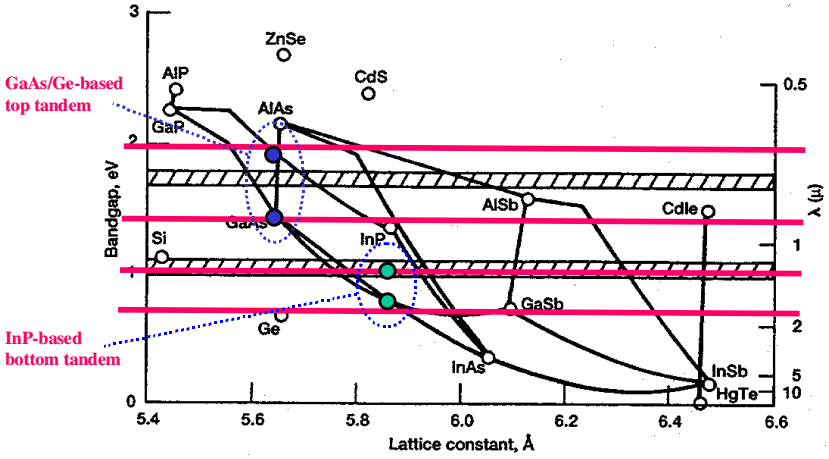

Figure 2 Bandgap versus lattice constant for the common compound semiconductor materials. Red lines indicate the ideal bandgaps for a four junction series interconnected solar cell under the AM0 spectrum at 25ºC. Dotted lines indicate the bandgap combinations being investigated in this work.

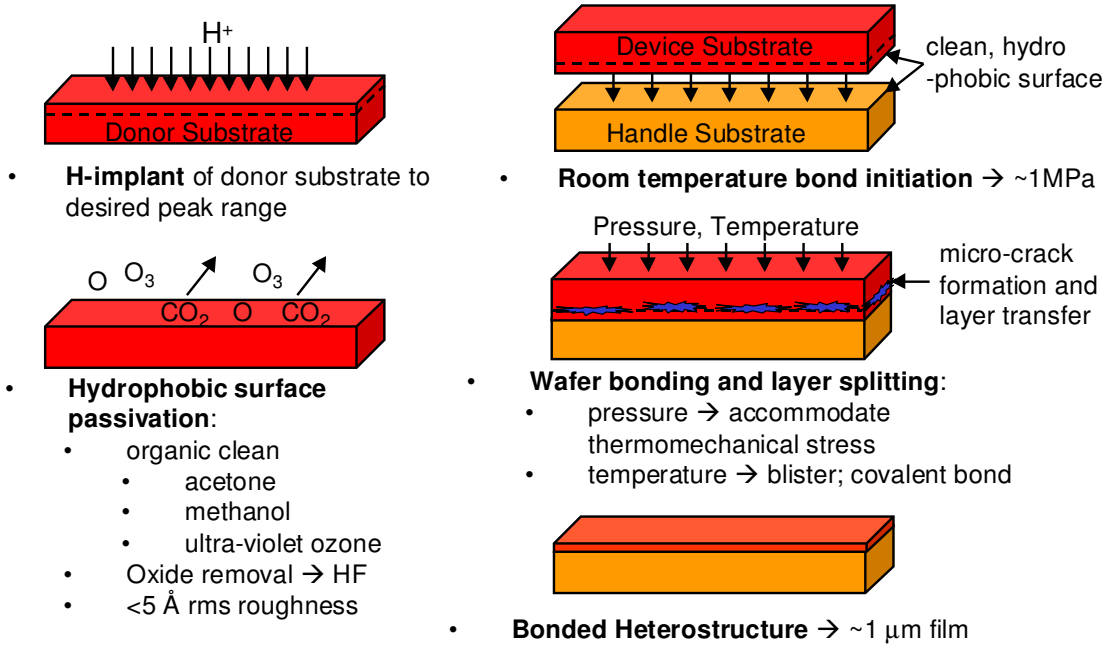

- **H-implant** of donor substrate to desired peak range
- **Room temperature bond initiation** → ~1MPa
- **Hydrophobic surface passivation**:
  - organic clean
    - acetone
    - methanol
    - ultra-violet ozone
  - Oxide removal → HF
  - <5 Å rms roughness
- **Wafer bonding and layer splitting**:
  - pressure → accommodate thermomechanical stress
  - temperature → blister; covalent bond
- **Bonded Heterostructure** → ~1 μm film

Figure 3 A process for producing InP-on-silicon engineered substrates based on the Smart-cut technology.

Much of the work at Cal Tech has focused on perfecting the Smart-cut process for InP/Si and developing an engineered substrate that is epi-ready. This requires a surface which is both free of dislocations that might propagate into the epitaxial film, and has a characteristic surface roughness similar to that of epi-ready polished InP.

Double heterostructures grown on as-transferred InP/Si engineered substrates have produced much lower photoluminescence intensity as compared to control samples grown on thick InP substrates. One potential cause of the presumed lower material quality on InP/Si is due to the presence of a region of highly defective InP at the surface of the engineered substrate, presumably caused by the ion implantation and layer transfer process. Figure 4 shows cross-sectional TEM images of the InP/Si pair, clearly showing an area of defective material at the exposed surface. More importantly, InP near the bonded interface appears to be less defective than the surface region. Polishing processes such as plasma etching, chemo-mechanical polishing, and wet chemical polishing etches are being investigated as means for removing the surface damage, thereby creating a surface more conducive to high quality epitaxial growth.

High resolution TEM images have revealed the presence of an oxide at the InP/Si interface. This interface layer is formed during the anneal in a nitrogen ambient, presumably resulting from residual water at the clean interfaces just prior to bonding. Despite the presence of this interfacial oxide layer, through-the-film current voltage measurements indicate an ohmic, low resistance behavior. The specific resistivity of the interface is less than 0.1 Ω-cm^2.

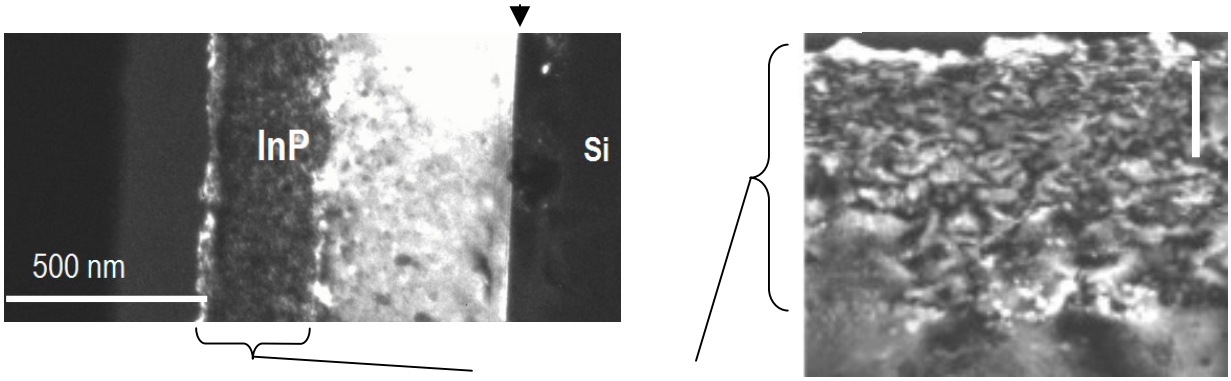

Figure 4 Cross-sectional TEM micrographs of an InP/Si engineered substrate. The images suggest a region of damaged, highly defective material near the implanted region of the InP.

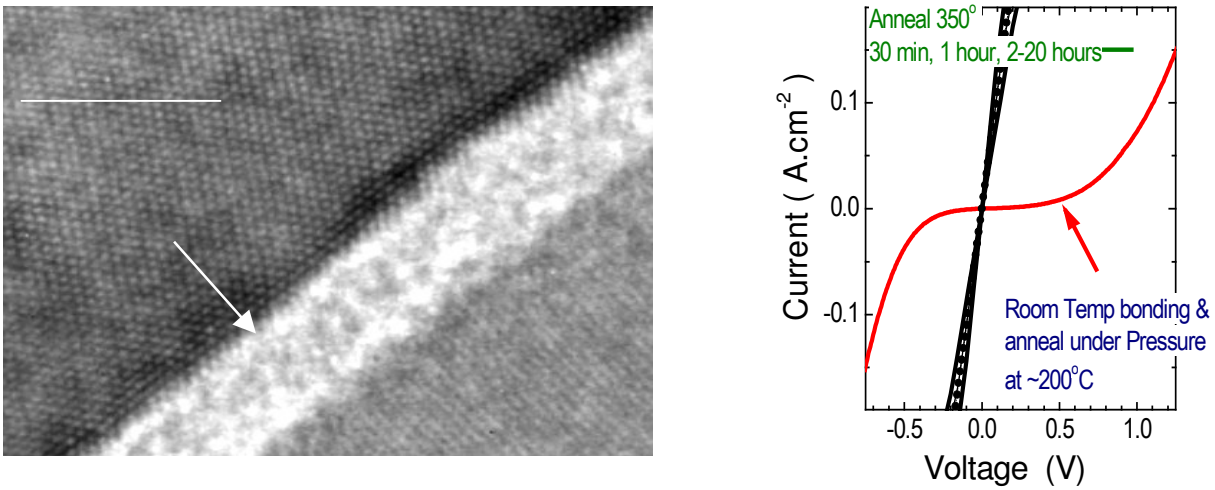

(a) (b)

Figure 5 (a) A high resolution TEM image indicating the presence of an interfacial oxide. (b) Through-the-film current-voltage characteristics of an InP/Si pair, suggesting less than 0.1 ohm-cm^2 specific resistivity.

TANDEM INTERCONNECTION

One of the tandem interconnect approaches being evaluated is a eutectic metal bond at the interface between two perpendicularly oriented metallic grids, as depicted in Figure 6(a). Advantages of this approach include the absence of a fixturing jig to hold the two cells optically in series, the absence of a peripherally formed interconnect which otherwise complicates the fabrication procedure, and the elimination of the need for pattern alignment in joining the two grids. Gold-germanium melts at a eutectic temperature of 356ºC. Grid fingers coated with a gold-germanium alloy can therefore be bonded together at low temperatures using moderate pressure. The eutectic metal bond approach is being experimentally evaluated using test structures such as that shown in Figure 6(b). Gridded germanium wafers have been bonded together to test the mechanical stability and electrical conductivity of the resulting interconnect. Figure 7(a) suggests intimate contact between the grid finger and germanium substrate. The resulting test structures are mechanically robust and produce an interconnect with very low specific resistivities of 0.024 Ω-cm^2 and 0.014 Ω-cm^2 for 1600 µm and 800 µm grid spacings, respectively. This type of interconnect scheme results in a modest 2-4% transmission loss due to grid shading.

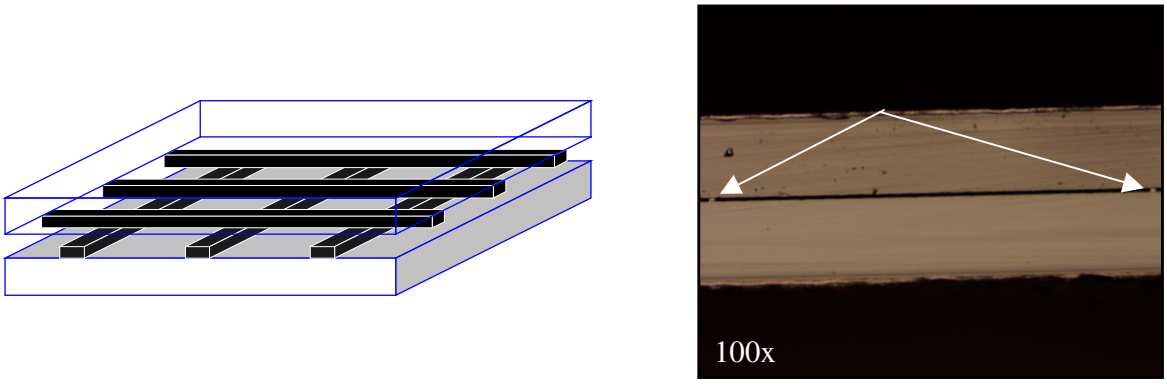

(a) (b)

Figure 6 (a) A conceptual schematic of the gridded interconnect scheme being evaluated. (b) A cross-sectional optical micrograph (100x) showing a metallic grid successfully bonded to two germanium wafers.

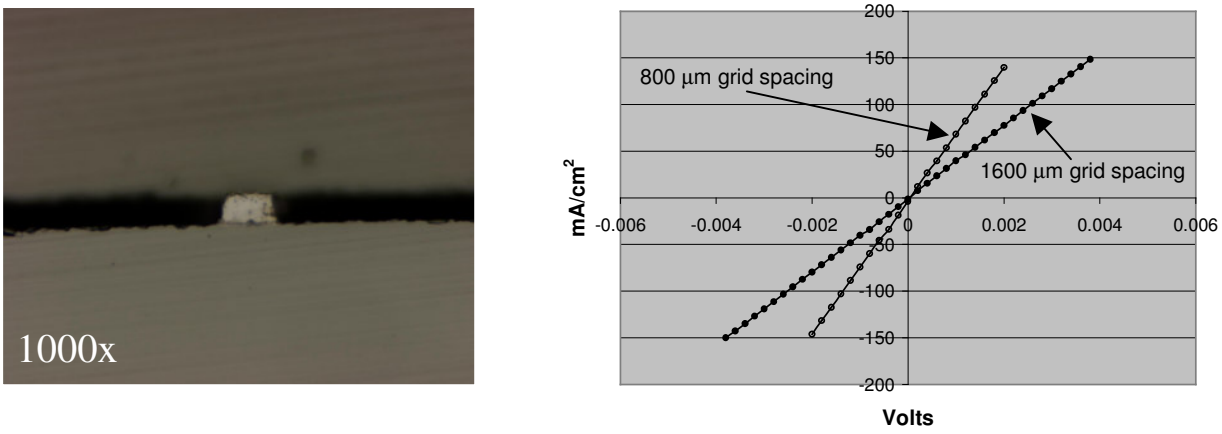

(a) (b)

Figure 7 (a) A cross-sectional optical micrograph (1000x) showing metallic grid successfully bonded to two germanium wafers. (b) Through-the-film current voltage characteristics of germanium wafers with a gridded, bonded interface.

BOTTOM TANDEM DEVELOPMENT

Prototype lattice matched bottom tandems consisting of 1eV InGaAsP, a low bandgap tunnel diode, and 0.74 eV InGaAs are being grown and processed on InP. The performance of these devices serves as a benchmark for devices to be grown on the InP/Si engineered substrates. The bottom tandem is projected to contribute 9-10% absolute to the overall device efficiency at ~10 suns AM0. Devices grown and processed at NREL have reached 6.1% efficiency without AR coating at 1 sun AM0, as shown in Figure 8. These 0.108 cm^2 devices were measured under a simulated AM0 spectrum filtered by a low resistivity GaAs wafer coated on both sides with an AR coating.

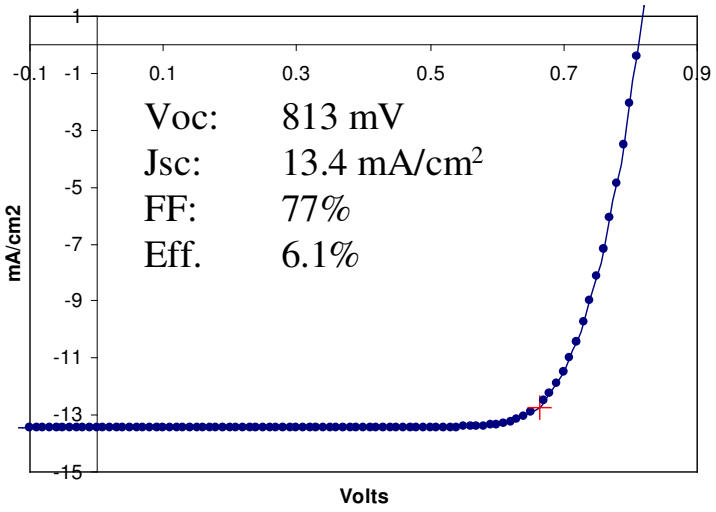

Figure 8 Current density-voltage characteristics of a 1.0 eV InGaAsP, 0.74 eV InGaAs prototype tandem on InP, measured under a fintered AM0 spectrum at 25ºC.

ANTI-REFLECTION COATING DEVELOPMENT

The 4-junction, nominally current matched solar cell being developed here can achieve an unprecedented AM0 efficiency of 40%, which is near the theoretical limits of a 4-junction device. This is made possible by the highly efficient utilization of photons over an extremely broad spectral range (300–1700 nm). Achieving a performance near the theoretical limits requires near-unity quantum efficiency for all subcells in the solar cell structure. This places requirements on AR coating performance that have previously not been necessary. The AR coating transmission band of the top tandem must be much broader that is currently necessary for production triple junction solar cells.

With the realization that the standard AR coating used for production triple junction solar cells would result in substantial loss in a 4-junction cell, we have designed an improved AR coating using methods presented in earlier work [6]. Anti-reflection coating design is accomplished here with optical modeling software which both optically and electrically models device performance as a function of the AR coating structure. A new AR coating design as presented in Figure 9 results in a modeled 1% absolute efficiency gain over the standard dual layer AR coating. Table I summarizes the relevant modeled device parameters.

SUMMARY

An affinity for high performance solar cells in the space market, as well as the development of new engineered substrate technology, has warranted a re-consideration of mechanically stacked solar cell technologies. Mechanically stacked approaches result in a wider materials and interconnectivity design space compared to monolithic approaches. We are investigating the Smart-cut technology to produce InP/Si engineered substrates. Successful transfer of InP films to a silicon substrate has been demonstrated, and the resulting structure is

mechanically stable after MOCVD growth. The electrical resistivity of the bonded interface is low, despite the presence of a very thin interfacial oxide. Work continues in regard to producing an epi-ready surface for the subsequent growth of high quality MOCVD layers. Tandem cell interconnectivity approaches are being investigated which can result in minimal parasitic loss and are also simple to process. Bottom tandem prototype cells have been fabricated on InP, with encouraging results. New AR coatings have also been designed to improve the optical coupling to these extremely wide-band solar cells.

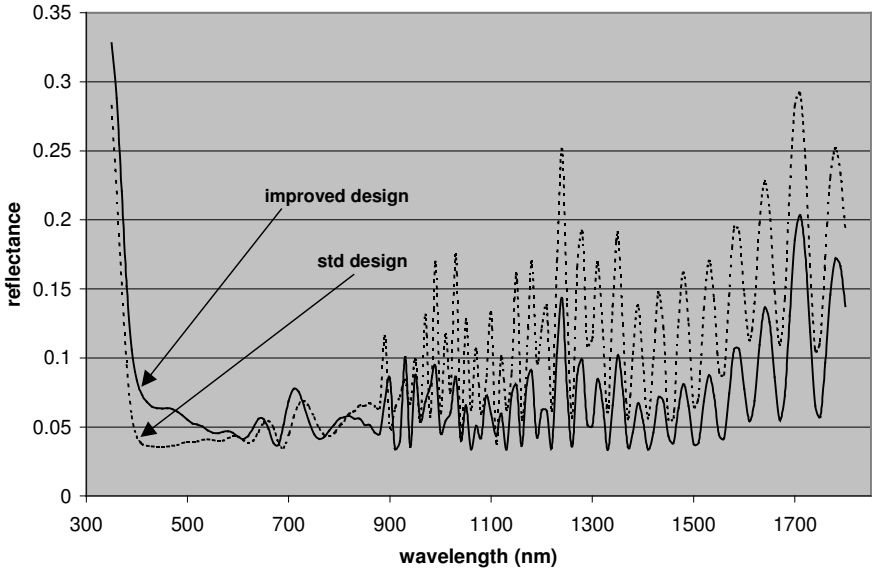

Figure 9 Modeled reflectance of a top tandem solar cell. A new AR coating design is compared to Emcore's standard AR coating structure.

Table I Predicted performance metrics for a 4-junction cell, nominally current matched, using the reflectance design modeled in Figure 9.

	std. design	new design
modeled efficiency (%)	34.23	35.67
maximum Jsc (mA/cm^2)	17.86	17.86
achieved Jsc (mA/cm^2)	15.54	16.65
weighted transmission (%)	87.03	93.21

REFERENCES

[1] L. Fraas, J. Avery, D. Scheiman, "AM0 calibration of 34% efficient mechanically stacked GaInP/GaAs-GaSb Circuits", Proceedings of the 29th IEEE Photovoltaics Specialists Conference, 2002, pp. 912-915.

[2] R.W. McClelland, C.O. Bozler, J.C.C. Fan, "A technique for producing epitaxial films on reuseable substrates", Appl. Phys. Lett., vol 37, no. 6, September 1980, pp. 560-562.

[3] E. Yablonovitch, T. Gmitter, J.P. Harbison, R. Bhat, "Extreme selectivity in the lift-off of epitaxial GaAs films", Appl. Phys. Lett., vol. 51, no. 26, December 1987, pp. 2222-2224.

[4] M. Bruel, B. Aspar, A.J. Auberton-Herve, "Smart-cut: A new silicon on insulator material technology based on hydrogen implantation and wafer bonding", Jpn. J. Appl. Phys., vol. 36, 1997, p. 1636.

[5] Q.-Y. Tong, U. Gösele, "Semiconductor Wafer Bonding", John Wiley & Sons, 1999.

[6] D. J. Aiken, "High performance anti-reflection coatings for broadband multi-junction solar cells", Solar Energy Materials and Solar Cells, vol. 64, 2000, pp. 393-404

RECENT ADVANCES IN HIGH EFFICIENCY III-V MULTIJUNCTION SOLAR CELLS FOR SPACE APPLICATIONS: ULTRA TRIPLE JUNCTION QUALIFICATION

Hojun Yoon, Jennifer E. Granata, Peter Hebert, Richard R. King, Christopher M. Fetzer, Peter C. Colter, Kenneth M. Edmondson, Daniel Law, Geoffrey S. Kinsey, Dmitri D. Krut, James H. Ermer, Mark S. Gillanders, and Nasser H. Karam
Spectrolab, Inc., Sylmar, California

INTRODUCTION

The performance of GaInP/GaAs/Ge-based multijunction (MJ) space solar cells has continually advanced in the past several years, satisfying the ever-increasing power requirements of satellites. The first commercial satellite that employed this technology was launched in 1997 (HS 601HP), which used solar arrays populated with Spectrolab's dual junction (DJ) GaInP/GaAs/Ge cells, with beginning of life (BOL) efficiency of 21-22% [1]. Building on this DJ benchmark, triple junction cells based on the same materials system have improved the performance to a new level. For example, Spectrolab's Improved Triple Junction (ITJ) cells which have been in production for the past 3 years, have BOL efficiency of greater than 26.5%, providing ~20-25% more power than the DJ cells [2]. Today, there are more than 225 kW of multijunction arrays on orbit that are performing to predict, a clear demonstration of the heritage and technology soundness of Spectrolab's MJ cells.

Spectrolab's latest triple junction production space solar cell – Ultra Triple Junction (UTJ) – exhibits key performance advances over the ITJ cell, and pushes the performance of triple junction cells to yet a higher level [3]. The UTJ cell has a BOL average efficiency at maximum power of 28.0% (AM0, 28ºC, 135.3 mW/cm^2) and P/P_o = 0.86 for 1 MeV electrons after 1E15 e/cm^2 fluence. More importantly, the efficiency at an operating temperature of 60ºC after 15 years in GEO environment is predicted to be 22.6%, which is higher by 5.5% relative than the ITJ cell. The purpose of this report is to describe some of the UTJ cell features as well as some of the key BOL and end of life (EOL) performance results stemming from the most comprehensive to date space-qualification program. The details of the qualification program, which includes electrical, mechanical, radiation, and environmental tests, have been described previously [3].

CELL DESIGN

Device Structure

Figure 1 shows a schematic cross-section of a baseline triple junction cell structure, upon which the UTJ cell is based. It comprises of lattice matched (LM) GaInP and GaAs based subcells grown epitaxially on a p-type Ge substrate using metal organic vapor phase epitaxy (MOVPE) process. The precise lattice-matching of the epilayers to the Ge lattice constant promotes the growth of high crystallinity materials, and is one of the key factors in the resulting high performance device. Details of the cell development efforts, including optimization for EOL performance, that led to the final UTJ device structure have been described previously [4, 5].

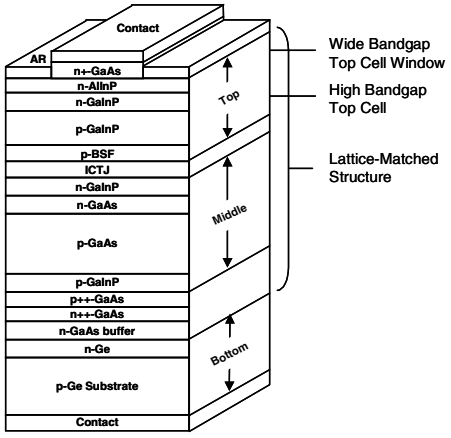

Fig. 1. Cross section of a baseline triple junction GaInP/GaAs/Ge solar cell, highlighting some of the key features of the UTJ cell.

While the GaAs-based middle cell of the UTJ cell is unchanged from that of the ITJ cell, the GaInP top cell has been modified to enhance its performance. First, the GaInP top cell is grown disordered, resulting in a higher bandgap material, and hence a higher cell voltage. The ordering refers to the atomic arrangement of the group-III sublattice sites by the Ga and In atoms. In a disordered GaInP material, the Ga and In atoms occupy the group-III sites in a random manner, whereas in an ordered GaInP material, they are arranged in a systematic manner. Second the AlInP top cell window material has been made more optically transmissive, providing a greater amount of incident light into the cell. The resulting UTJ structure has a higher cell load voltage by 80 mV, while maintaining the same current density compared to the ITJ cell. Consequently, the UTJ cell has an efficiency at load = 27.7%. A comparison of the light IV curves (AM0, 28ºC, 135.3 mW/cm^2) of a typical UTJ and ITJ cell is shown in Fig. 2.

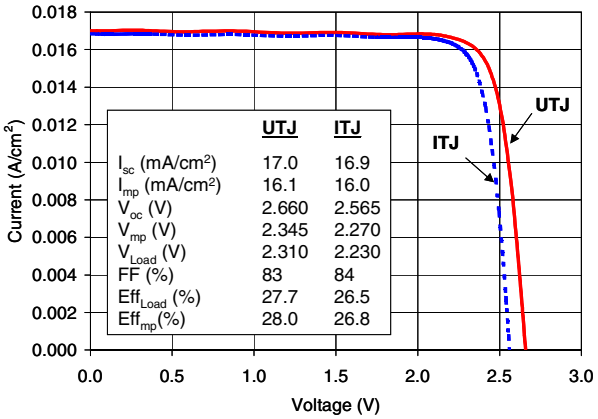

Fig. 2. Comparison of light IV curves (AM0, 28ºC, 135.3 mW/cm2) of a typical UTJ and ITJ cell, highlighting the higher voltage and efficiency of the UTJ cell.

Minority carrier lifetime is an important parameter that strongly influences the solar cell device performance, and the disordered GaInP material has been measured to exhibit long lifetimes, in the tens of nanosecond range as measured by time resolved photoluminescence [4], nearly approaching the values measured on ordered GaInP material. These values translate to minority carrier diffusion lengths that are many times the cell base thickness, which is desired for high cell performance.

Cell-Interconnect-Coverglass (CIC) Assembly

In addition to the improved device structure, the UTJ cell uses a 20% thinner (140 micron) Ge substrate compared to a standard ITJ cell, enhancing the power-to-weight ratio. All joints including the interconnects and the diode assembly onto the cell are welded for improved manufacturability. Two interconnects are welded on the cell front side and redundant “H-tab” diode assembly welded on the back side, with double-stick Kapton tape used for attachment and isolation of the diode assembly to the back side of the cell. The interconnects and the H-tabs are both made from silver-clad Kovar material. A photograph showing both the front and back sides of the UTJ CIC assembly is presented in Fig. 3.

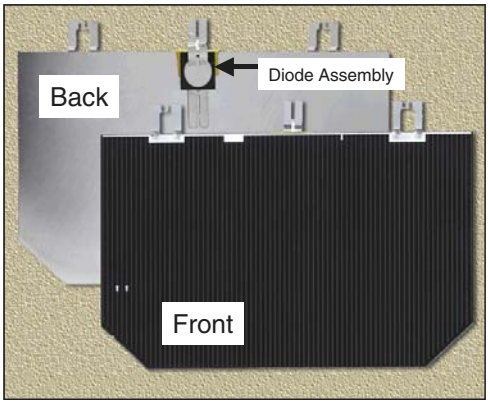

Fig. 3. Photograph of UTJ CIC assembly.

BOL PERFORMANCE

The efficiency at load (Eff$_{Load}$) distribution of more than 1,000 large area (26.41 cm^2) UTJ bare cells from the qualification build is shown in Fig. 4. All measurements were performed using Spectrolab’s X-25 solar simulator (AM0, 28ºC, 135.3 mW/cm^2), calibrated using balloon flight-traceable standards. The average Eff$_{Load}$ of this population is 28.1%, while the average efficiency at maximum power (Eff$_{mp}$) is 28.3%. The highest Eff$_{mp}$ measured to be 29.4%. Table 1 summarizes all the photovoltaic parameters for this population. As previously discussed, the improved performance stems primarily from the voltage increase – the load voltage for the UTJ cell has been increased by 80 mV (~3.5% increase) over the ITJ cell, while the current density remains approximately the same. The resulting efficiency makes the UTJ cell the highest efficiency space solar cell available today.

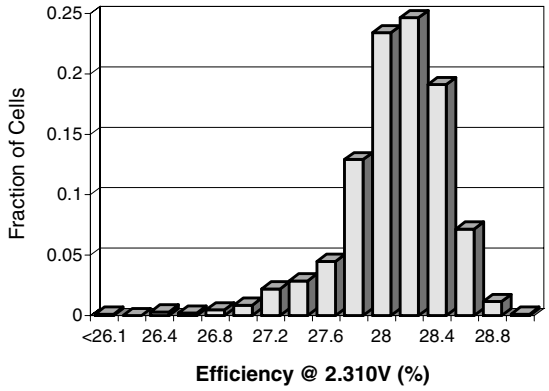

Fig. 4. Efficiency at load (2.310 V) distribution of 1,045 large area UTJ bare cells tested under AM0, 28ºC, 135.3 mW/cm^2 condition. The average Eff_{Load} = 28.1%.

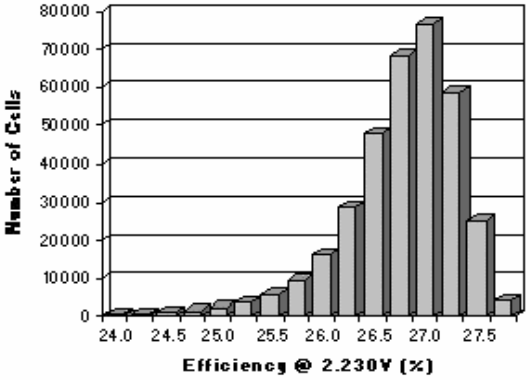

Fig. 5. Efficiency at load (2.230 V) distribution of 351,024 large area ITJ bare cells tested under AM0, 28ºC, 135.3 mW/cm^2 condition. The average Eff_{Load} = 26.7%.

The high efficiency performance of the UTJ cells builds upon the heritage of the ITJ cells which have been in production at Spectrolab since 2000. Figure 5 shows the Eff_{Load} distribution of more than 350,000 large area ITJ bare cells, with average Eff_{Load} = 26.7%. Compared to this value, the UTJ qualification average is 5% higher, at Eff_{Load} of 28.1%.

Table 1. Average BOL photovoltaic parameters for large area UTJ bare cells.

	Parameter							
	J_{sc} (mA/cm^2)	J_{mp} (mA/cm^2)	V_{oc} (V)	V_{mp} (V)	$J_{Load\ (2.31V)}$ (mA/cm^2)	$Eff_{Load\ (2.31V)}$ (%)	Eff_{mp} (%)	FF (%)
Qual Avg. (1045 cells)	17.09	16.26	2.669	2.352	16.44	28.1	28.3	83.7
Target/Spec	17.00	16.16	2.660	2.345	16.22	27.7	28.0	83.0

EOL PERFORMANCE

All space cell designs must take into account EOL performance in order to meet the spacecraft power needs throughout a typical mission life of 15 years. The key parameters that are necessary to predict on-orbit power performance at EOL are radiation resistance and temperature coefficients. Various electron and proton radiation energies present in space induce varying degrees of degradation to the solar cell. Taking these effects into account for a typical 15-year GEO mission, a 1 MeV electron equivalent fluence can be calculated in order to provide a single radiation degradation factor for EOL performance. This value has been determined for the UTJ cell to be approximately 6E14 e/cm^2, similar to Spectrolab's other MJ solar cells.

1 MeV Electron Radiation

Results of 1 MeV electron radiation effects on UTJ cell performance are summarized in Fig. 6, which plots the normalized degradation of the current (NI_{sc}, NI_{mp}), voltage (NV_{oc}, NV_{mp}), and power (NP_{mp}) as a function of fluence. Five fluences ranging from 3E13 to 3E15 e/cm^2 were used, with 15 cells (2 cm x 2 cm) tested at each fluence. Similar to other MJ cells, the voltage generally degrades faster than the

current, but the overall NP_{mp} after 1E15 e/cm^2 fluence has improved to 0.86, highest value achieved to date among all MJ cells. At 6E14 e/cm^2 (1 MeV electron equivalent fluence at EOL for a 15-year GEO mission), the NP_{mp} is 0.89.

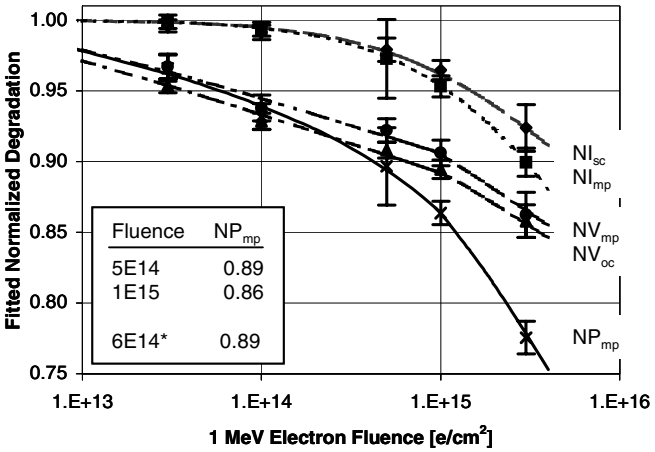

Fig. 6. Effects of 1 MeV electron radiation on UTJ cell performance. *6E14 e/cm^2 is the 1 MeV equivalent fluence after a 15-year GEO mission.

Temperature Coefficients

It is well known that with increasing temperature, the efficiency of the solar cell decreases as a result of the competing effect between the voltage and current. The voltage decreases largely due to the increase in the saturation current and also due to a shift in the bandgap. The current increases due to a shift in the bandgap as well as a general increase in the carrier lifetime. The combined effects cause the cell efficiency to decrease with increasing temperature because the voltage drop is higher than the current gain. In MJ cells where the current produced by the entire stack is limited by the lowest current-generating subcell, the current balance among the subcells can also influence the measured current temperature coefficients.

Temperature coefficients have been measured on UTJ cells after subjecting them to various 1 MeV electron fluences. Figure 7 plots the cell efficiency at maximum power measured as a function of temperature in the range 15-75ºC. The temperature coefficients (absolute % efficiency per ºC) do not vary significantly as a function of fluence, ranging from -0.076%/ºC for BOL condition to -0.065%/ºC for 3E15 e/cm^2 fluence. At 6E14 e/cm^2 (1 MeV electron equivalent fluence at EOL for a 15-year GEO mission), the efficiency temperature coefficient is -0.070%/ºC.

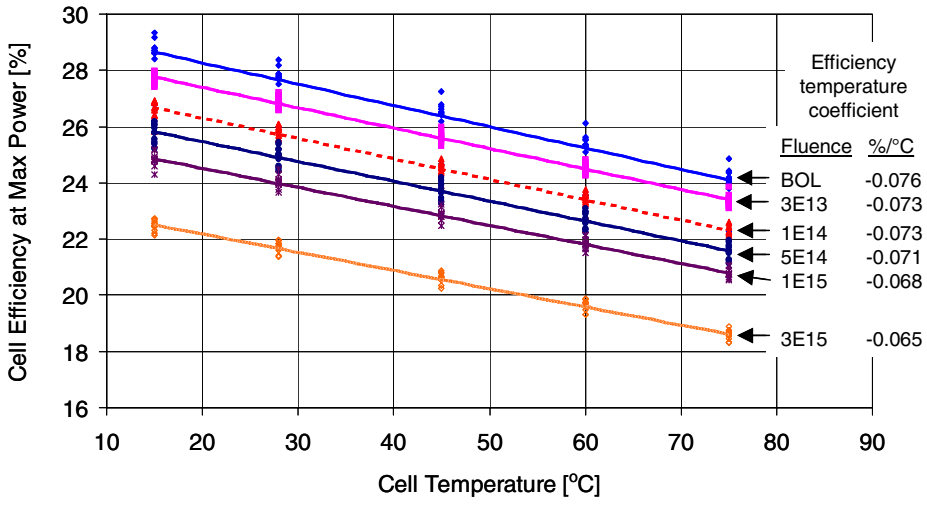

Fig. 7. UTJ cell efficiency at maximum power measured as a function of temperature, for various 1 MeV electron fluences. The temperature coefficient values are noted in terms of absolute % efficiency per ºC.

EOL Power Estimate

Using the 1 MeV electron radiation data for the UTJ cells, the remaining power after a 15-year GEO mission can be estimated. In addition, the temperature coefficients determined for various 1 MeV

electron fluences can be used to approximate the remaining power at an operating temperature. Table 2 provides these estimates, in comparison to the ITJ, TJ, and DJ cells, using 60ºC as an operating temperature. At EOL (60ºC), the UTJ cell is projected to provide 5.5% more power than the ITJ and 25% more power than the DJ cell. The higher performance of the UTJ cell is attributed to an increase in the BOL efficiency as well as an improvement in the radiation resistance.

Table 2. Power estimate for UTJ cells, compared to ITJ, TJ, and DJ cells. EOL condition assumes 15-year GEO mission and 1 MeV electron equivalence of 6E14 e/cm^2. Operating temperature of 60ºC is assumed.

	UTJ 2003	ITJ 2000	TJ 1999	DJ 1997
Eff_{mp} at BOL, AM0, 28ºC	**28.0%**	26.9%	25.1	21.7%
P/P_o (6E14 e/cm^2, 1 MeV)	**0.89**	0.87	0.87	0.88
Temp. Coeff. at EOL, AM0	**-0.070%/ºC**	-0.063%/ºC	-0.053%/ºC	-0.031%/ºC
Eff_{mp} at EOL, AM0, 28ºC	**24.9%**	23.4%	21.8%	19.1%
Eff_{mp} at EOL, AM0, 60ºC	**22.6%**	21.4%	20.1%	18.1%

SUMMARY

Key performance results stemming from the Ultra Triple Junction cell qualification program have been described. The BOL average efficiency at maximum power for UTJ cells is 28.0% (AM0, 28ºC, 135.3 mW/cm^2), while the P/P_o = 0.86 for 1 MeV electrons after 1E15 e/cm^2 fluence. These results combined with temperature coefficient measurements, translate to an efficiency of 22.6% at an operating temperature of 60ºC after a 15-year GEO mission. This represents a 5.5% relative higher efficiency at EOL compared to the previous generation ITJ cells, providing the highest power of any previously available space cell technology. Along with the improved bare cell performance, the UTJ CIC technology has been improved to provide enhanced manufacturability at the assembly level, adding to the many benefits of the latest production UTJ space solar cell technology. To date, the UTJ bare cell qualification tests have been completed, meeting all pass/fail criteria. The CIC assembly qualification is expected to be completed in October 2003.

Despite the impressive efficiency increases achieved from the GaInP/GaAs/Ge based triple junction cells in the past few years, there remain opportunities for further improvements. Spectrolab has identified these opportunities and is pursuing the next generation cell, the XTJ space solar cell, which is expected to provide 30% efficiency at BOL. As always, EOL performance will be emphasized as well as manufacturability in order to provide the highest value product at a lowest possible cost.

REFERENCES

[1] M.R. Brown, L.J. Goldhammer, G.S. Goodelle, C.U. Lortz, J.N. Perron, J.S. Powe, J.A. Schwartz, B.T. Cavicchi, M.S. Gillanders, and D.D. Krut, "Characterization Testing of Dual Junction $GaInP_2$/GaAs/Ge Solar Cell Assemblies," *Proc. 26th IEEE Photovoltaic Specialists Conf.* (IEEE, New York, 1997), p. 805.

[2] J.E. Granata, J.H. Ermer, P. Hebert, M. Haddad, R.R. King, D.D. Krut, M.S. Gillanders, N.H. Karam, and B.T. Cavicchi, "Advancements in $GaInP_2$/GaAs/Ge Solar Cells – Production Status, Qualification Results and Operational Benefits," *Proc. 29th IEEE Photovoltaic Specialists Conf.* (IEEE, New York, 2002), p. 824.

[3] J.E. Granata, C. Fetzer, J.H. Ermer, R.R. King, K. Edmondson, A. Stavrides, P. Hebert, P. Colter, G.S. Kinsey, H. Yoon, M.S. Gillanders, N. Beze, K. Bui, J. Hanley, N.H. Karam, and B.T. Cavicchi, "Ultra Triple Junction $GaInP_2$/GaAs/Ge Solar Cells – Cell Design and Qualification Status," *presented at the 3rd World Conf. On Photovoltaic Solar Energy Conversion, Osaka, Japan, May 2003.*

[4] R.R. King, C.M. Fetzer, P.C. Colter, K.M. Edmondson, J.H. Ermer, H.L. Cotal, H. Yoon, A.P. Stavrides, G. Kinsey, D.D. Krut, and N.H. Karam, "High-Efficiency Space and Terrestrial Multijunction Solar Cells Through Bandgap Control in Cell Structures," *Proc. 29th IEEE Photovoltaic Specialists Conf.* (IEEE, New York, 2002), p. 776.

[5] G.S. Kinsey, R.R. King, K.M. Edmondson, A.P. Stavrides, H. Yoon, C.M. Fetzer, P.C. Colter, J.H. Ermer, M.S. Gillanders, P. Hebert, J.E. Granata, and N.H. Karam, "Ultra Triple-Junction High-Efficiency Solar Cells*," IEEE AESS Systems Magazine*, March 2003, p. 8.

HIGH EFFICIENCY, MULTI-JUNCTION CELLS WITH MONOLITHIC BYPASS DIODES

P. R. Sharps, M. A. Stan, D. J. Aiken,
B. Clevenger, J. S. Hills, and N. S. Fatemi
EMCORE Photovoltaics, Albuquerque, NM

INTRODUCTION

The manufacture of solar panels for both space and terrestrial applications involves stringing cells together such that they are connected electrically in series. If a solar cell in a series connected string is shaded, with the remaining cells still in the light, the cell is forced into reverse bias breakdown so that it can conduct the current of the string. The reverse biasing of the cell into breakdown, particularly for III-V multi-junction solar cells, will permanently damage the cell. To protect the cells from breakdown, discrete silicon bypass diodes are electrically connected in parallel to the cell, but with opposite polarity. If a cell is shaded, the diode is forward biased, and the string current safely passes through the diode. Several different approaches to attaching a discrete diode to the solar cell have been proposed and are in use, including front mounted, corner mounted (in-plane with the cell), and back mounted diodes [1].

The connection of the discrete silicon diode to the cell is done during the CIC (coverglass-interconnect) operation, and involves front and back interconnects to both the diode and the cell. Automation of the CICing process is complicated because of the number of parts involved, i.e., the cell, the diode, and the front and the back interconnects for the diode.

A monolithic bypass diode, integral to the solar cell and not a discrete part, has the advantage of reducing the number of parts required during the CICing operation. However, there are several design criteria that the monolithic bypass diode must meet. First, it has to protect the cell, i.e., it has to be able to pass the string current without causing the cell to go into reverse bias breakdown. Secondly, it has to be reliable. The diode has to be stable in a space environment, as well as perform repeatedly without failure. Finally, it has to be simple. The inclusion of the diode must not add growth or processing complexity such that the reduction in CICing costs are outweighed by the cost of the monolithic diode.

DIODE DESIGN

The dark electrical schematic of the cell and diode is shown in Figure 1. As can be seen, the diode and the multi-junction cell are electrically parallel. We have looked at two different approaches for the monolithic bypass diode, a Schottky junction approach and an epitaxially grown p-n junction approach. For performance and reliability reasons we have chosen the epitaxially grown p-n junction approach.

For the Schottky diode approach, the diode can be located within the cell structure. What is required is a semiconductor layer that, when the appropriate metal is deposited on it, will create a Schottky junction with polarity opposite to that of the multi-junction cell. Figure 2 is a schematic of one Schottky junction approach, where the junction is created using one of the semiconductor buffer layers. In Figure 2 the Schottky diode is placed in the buffer layers, above the Ge junction, but beneath the epitaxially grown III-V layers. However, the Schottky diode could just as easily be placed on top of the III-V epitaxially grown layers. It is important to remember that the actual junction is at the metal semiconductor interface. During processing, the semiconductor layer has to be exposed (through appropriate etching), and the necessary metal deposited. A mesa etch also has to be done to electrically isolate the diode area from the rest of the cell.

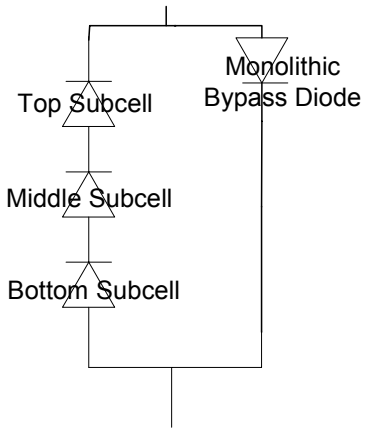

Figure 1. Electrical schematic of the monolithic bypass diode, under dark conditions.

Figure 2 also shows "metal shorts", necessary to short out the junction underneath the Schottky diode. If these "metal shorts" are not included, the Schottky diode is in series with another junction underneath of opposite polarity. For the Schottky diode to protect the cell, the junction underneath of opposite polarity has to be forced into reverse breakdown to allow the current to be conducted. The "metal short" resolves this issue by providing an electrical short around the opposite polarity junction underneath the Schottky diode. The "metal shorts" also remove the necessity of including welded straps or "C-clamps" for completing the electrical circuit. The usual interconnect tab welded to the top of the Schottky diode and the cell bus pads completes the circuit. Emcore has both US and international patents pending on the "metal shorts" approach.

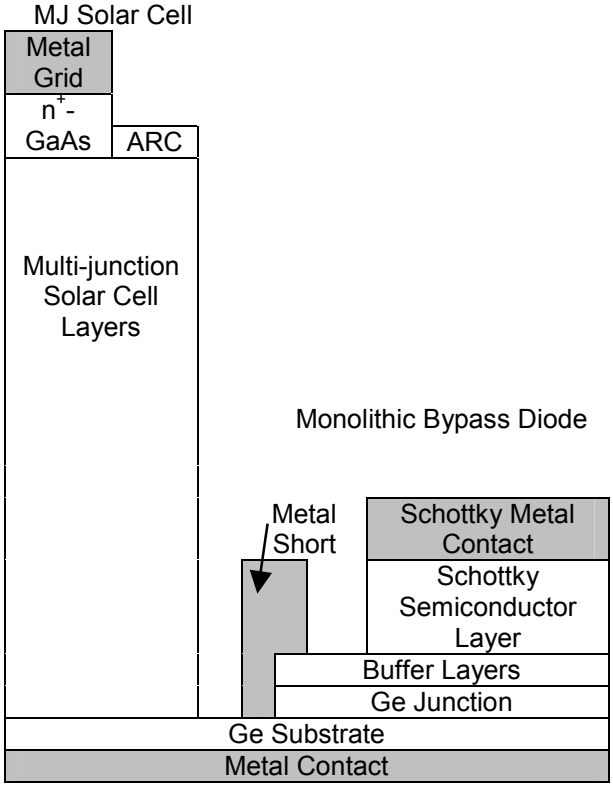

Figure 2. Schematic of the Schottky diode approach. Note that neither the horizontal nor the vertical distances are to scale. The monolithic bypass diode area covers a much smaller portion of the cell (e.g., 4 mm^2 for the diode versus 30 cm^2 for the cell) than depicted here.

Figure 3 shows a schematic of the epitaxially grown p-n junction approach. In this approach the bypass diode is grown on top of the multi-junction cell. The complete diode is epitaxially grown, and is of opposite polarity to the multi-junction device. The diode layers are removed from the areas above the multi-junction cell, and a mesa etch isolates the bypass diode area from the cell. As with the Schottky diode approach, a "metal shorts" approach is again used to short out the multi-junction cell layers underneath the bypass diode. The amount of processing required for either the Schottky or epitaxial diode approach are nearly identical.

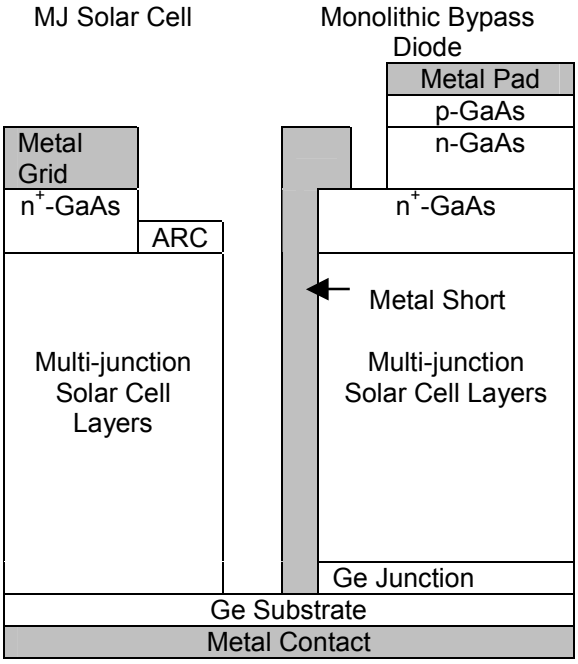

Figure 3. Schematic of the epitaxial p/n diode approach. The same comments regarding scales and areas mentioned for Figure 2 apply for this Figure.

In terms of electrical performance, the key diode parameters are the reverse bias leakage current (I_{RB}) (measured at a value close to the cell load voltage, i.e., ~2.5 volts), the forward bias turn on voltage (V_{FB}) (approximately how much voltage is required to pass the load current), and the diode series resistance (R_S) (which is a measure of how much I^2R losses occur in the diode). Because the bypass diode is electrically parallel to the cell, any diode reverse bias leakage current reduces the total current through the cell/diode combination when the cell is at load. Hence, minimizing the bypass diode reverse leakage is critical to having a high efficiency cell/diode combination.

DIODE PERFORMANCE

We have found that the performance of the epitaxially grown p-n bypass diode is better than that of the Schottky diode. The reason for this is straight forward. Since the Schottky junction occurs at the metal/semiconductor interface, any variability in processing or contamination of the semiconductor surface will have an effect on the performance of the diode. Schottky diodes are very dependent on the surface conditions of the semiconductor prior to deposition of the metal. Since etching is required to expose the semiconductor surface, chemical residue can be left behind on that surface. Also, as the surface is exposed to air, an oxide layer will be created on the semiconductor surface, the thickness of which is time dependent. These varying conditions, inherent during processing of the diode, will alter the metal/semiconductor barrier height, and will in turn effect both the leakage current and forward bias turn on voltage. In addition, during the welding of the interconnect to the Schottky diode, the interconnect tab is actually welded to the metal part of the Schottky junction. The heat and pressure from the weld can affect the metal/semiconductor interface, further changing the properties of the junction.

The epitaxial p/n junction approach has several advantages over the Schottky approach, one of which is that the junction interface can be precisely controlled during the MOCVD growth. The thickness and doping levels of the

p- and n-layers are precisely controlled, and the junction is also made in a tightly controlled environment (purified H_2 in the MOCVD reactor), similar to the epitaxial growth of the solar cell. Hence, the manufacturing repeatability issues associated with the Schottky diode are avoided. In addition, welding to the epitaxial p-n diode is identical to welding to contact pads on the solar cell. A cap layer is included on top of the p-n junction, and the junction is removed from the metal to which the interconnect is welded.

Testing of the diode in reverse bias indicates a considerable amount about a diode's robustness. Because the bypass diode is in the reverse biased condition when the cell is at load (at approximately 2.3 volts), not only does the leakage current thorough the diode have to be minimal, it also has to be stable. Since these bypass diodes may operate for up to 15 to 20 years in space, there cannot be pre-mature failures.

As part of the design phase of developing a monolithic bypass diode, we have taken both the Schottky and p/n diodes into far reverse bias to determine where breakdown occurs, what kind of breakdown mechanisms are involved, and how stable the breakdown is. We looked at two different types of p/n junctions, which we refer to as Design 1 and Design 2. Because of U.S. and International patents pending, we cannot discuss the details of Design 1 and 2.

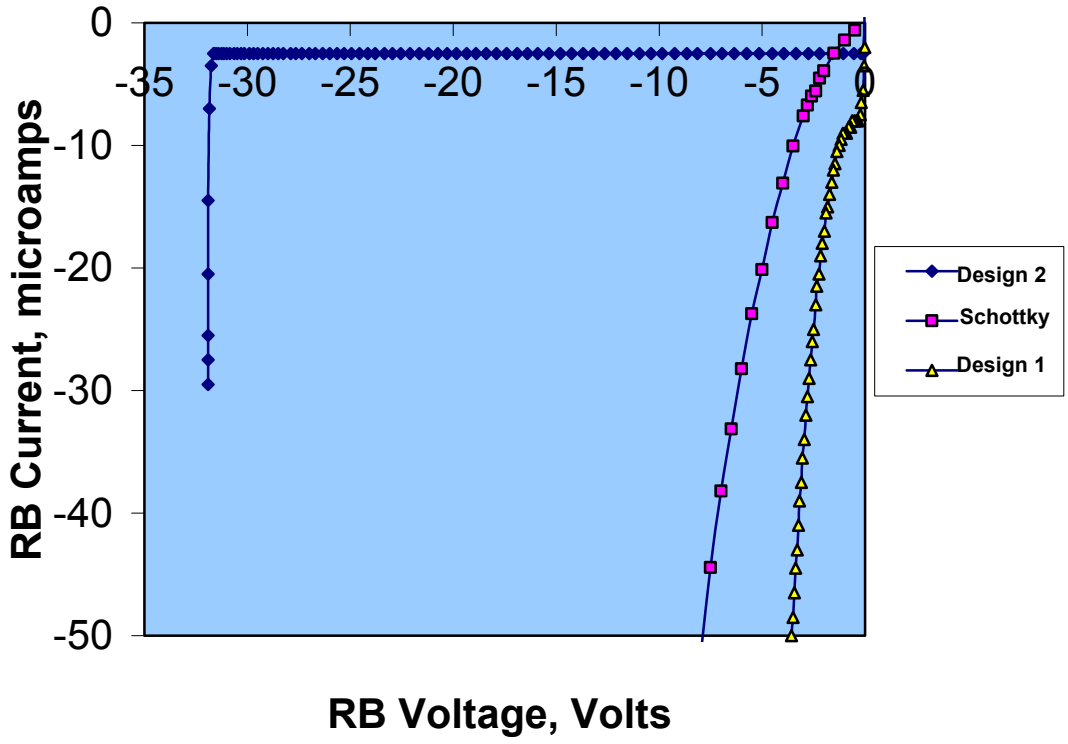

Figure 4. Reverse bias I-V curves for Schottky, Design 1, and Design 2 monolithic bypass diodes. Note the qualitative difference between the Schottky and Design 1 diodes and the Design 2 diode. See text for further discussion.

The results of the reverse bias tests are shown in Figure 4. The vertical axis on the graph is in micro-amps. Testing the cells in reverse bias at these currents is a sensitive measure of the type of breakdown that is occurring. Note the qualitative difference between the breakdown characteristics between p/n diode Design 2 and the other two diodes, the Schottky diode and p/n diode Design 1. Design 1 and the Schottky design show "microplasma" breakdown, associated with crystalline imperfections [2]. In the case of Design 1 and the Schottky design, we have been able to see the current pulses associated with the microplasmas on a curve tracer. The reverse bias I-V curves for the Schottky and Design 1 diodes will literally "flicker" as the microplasmas turn on and off. Because of the association of the microplasmas with crystalline defects and ensuing concerns about on orbit

device reliability, both the Schottky approach and the Design 1 approach are deemed undesirable. However, the reverse bias characteristic of Design 2 is clearly different, and indicates that it can support significant reverse bias voltage before breaking down.

The breakdown seen in Design 2 in Figure 4 is consistent with the avalanche breakdown mechanism. Avalanche breakdown has a well defined, abrupt breakdown knee, while other types of breakdown (Zener and crystalline imperfection breakdowns), have a softer breakdown knee. In looking at the curve in Figure 4 for Design 2, the breakdown is abrupt, indicating that avalanche breakdown is the dominant mechanism. In addition, with avalanche breakdown, the breakdown voltage increases with increasing temperature. For Zener and crystalline imperfection breakdown, the breakdown voltage decreases with increasing temperature. To confirm that avalanche breakdown was controlling the Design 2 diode, the reverse bias characteristics of the diode were examined as a function of temperature. The results are shown in Figure 5.

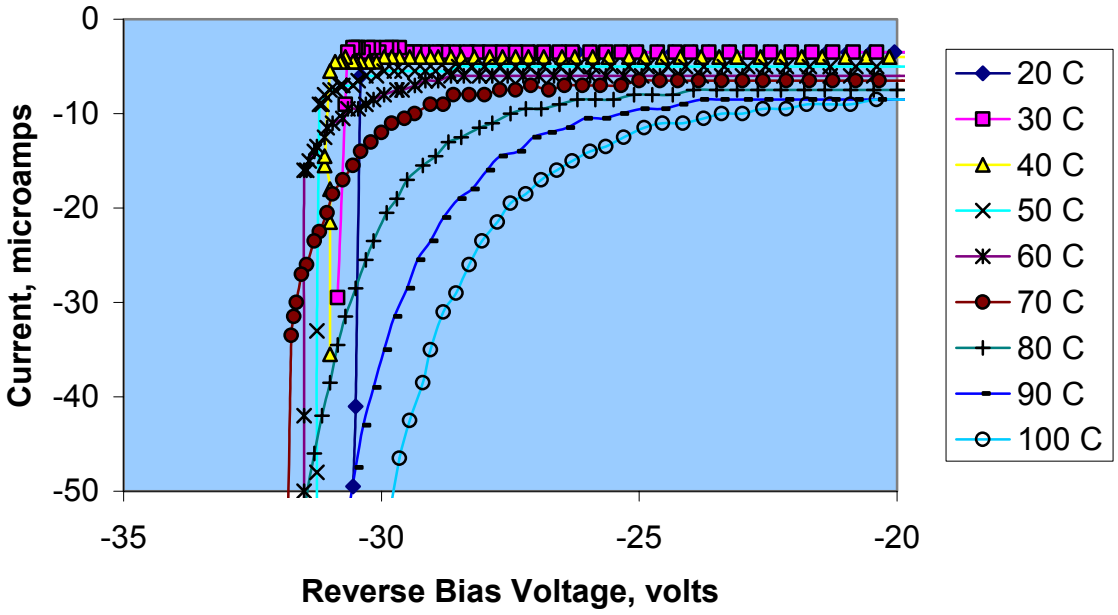

Figure 5. Current-voltage curves as a function of reverse bias voltage, for various temperatures, for one of the epitaxially grown p-n junctions.

Taking 30 microamps as a point to demarcate the onset of breakdown, it can be seen from Figure 5 that as the temperature increases from 20 ºC to 70 ºC, the voltage for the onset of breakdown increases in magnitude. After 70 ºC, the breakdown voltage decreases in magnitude with increasing temperature. In addition, the breakdown knee starts to soften around 60 ºC. The conclusion is that up to 60 ºC, the breakdown is through the avalanche mechanism, but as the temperature increases above this another mechanism controls the breakdown. Zener breakdown is associated with heavy doping on each side of the junction, and a thin depletion region. Since that is not the case in the Design 2 diode, it is thought that a localized crystalline imperfection starts to control the breakdown at higher temperatures. During the breakdown/temperature measurement it was noted that reverse biases of greater than 20 volts were still required to breakdown the Design 2 diode when the diode was at 150 ºC. The Design 2 diode is robust and able to withstand temperatures of up to 150 ºC without having any deleterious effect on solar cell operation.

DIODE QUALIFICATION

For use in space, the monolithic bypass diode has to pass several qualification steps. These include a welding test, a high temperature reverse bias soak, a high temperature forward bias soak, a high temperature cycling test, and performance comparisons before and after exposure to particle radiation. Since the standard diode

incorporated into the cells is 4 mm^2 in area, all of the diode qualification tests were done on Design 2 diodes of this size. Several tests were also done on the Schottky type diodes.

The welding test was of particular concern for the Schottky diode approach. Since the junction in the Schottky diode actually occurs at the metal/semiconductor interface, any high temperature welding to the contact metal always had the possibility of altering that interface. We have found that the Schottky junction can be particularly sensitive to welds, with an increase in the reverse bias leakage current at 2.5 volts (I_{RB}) due to the welding. The p/n junctions, both Designs 1 and 2, were much less sensitive to the welding process, since the actual junction is completely within the semiconductor. One result of the welding study was the institution of the criteria for a successful weld. The I_{RB} before and after the weld process cannot change by more than 30 microamps. We found that it was much more difficult for the Schottky diodes to pass this bench mark.

The reverse bias soak, the forward bias soak, and the cycling tests were all done under ambient atmosphere at a chamber temperature of 120 °C. The reverse bias soak involved holding the diode at 2.5 volts reverse bias for 1,000 hours. During the forward bias soak, 650 mA was passed through the diode for 250 hours. For the cycling test, the diodes were switched between 2.5 volts reverse bias and 650 mA over 100,000 times. The dwells at each of the biases were 1 second, with an approximately 1 milli-second switching time. For all of the tests, the diode performance was measured before and after. The particle irradiation involved exposure to both 1 MeV electrons, and 10 MeV protons. For 1 MeV electrons, the diodes were exposed to a fluence of 1 x 10^{15} e/cm^2, while for 10 MeV protons, the diodes were exposed to a fluence of 1 x 10^{12} p/cm^2.

The results of the diode qualification tests for the Design 2 diode are shown in Table 1. As can be seen, all of the tests were passed.

Table 1. Summary of space qualification tests on the monolithic bypass diode Design 2, with 4 mm^2 area. I_{RB} was measured at 2.5 volts reverse bias, and ΔV_{FB} refers to the change in the forward bias voltage needed to pass 500 mA through the diode before and after the particular test. See text for further discussion.

Test Item	Requirement	Results	Status
Reverse Bias	I_{RB} < 30 μA ΔV_{FB}<10%	I_{RB} < 1 μA ΔV_{FB}=1.6%	Pass
Forward Bias	I_{RB} < 30 μA ΔV_{FB}<10%	I_{RB} < 1 μA ΔV_{FB}=0.4%	Pass
Diode Cycling	I_{RB} < 30 μA ΔV_{FB}<10%	I_{RB} < 1 μA ΔV_{FB}=0.2%	Pass
Irradiation: Electrons Protons	I_{RB} < 30 μA ΔV_{FB}<10%	Electrons: I_{RB} < 1 μA ΔV_{FB}<1% Protons: I_{RB} < 1 μA ΔV_{FB}<1%	Pass

To further characterize the diode, the temperature of the diode was measured during forward biasing of the diode. The cell and diode were under ambient atmosphere in a chamber with a temperature of 120 ºC. Vary small thermocouples were placed on the cell, 5 mm away from the diode, and also on the diode itself. The diode was forward biased to 650 mA, and the temperature of the cell and diode brought to a steady state. The cell temperature and the ambient chamber temperature were 120 ºC, while the diode temperature rose to 133 ºC. The implications of this are that the diodes tested above actually were at 133 ºC, not at the ambient 120 ºC. The I^2R heating of the diode is generating some heat, which is being dissipated through the diode and into the cell. Further diode temperature measurements are underway in a simulated space environment, with cells mounted on substrates, and the measurements being done in a vacuum of less than 10^{-5} torr.

CELL PLUS DIODE PERFORMANCE

We have made a number of cells with the monolithic bypass diode. Figure 6 shows the I-V curve for one of these cells, along with the device performance parameters. Figure 7 shows a histogram of the performance of 2,000 large area (>30 cm^2) devices. The average efficiency for this group of cells is 27.5% (135.3 mW/cm^2). In addition, we are working to increase the average lot efficiency to 28.5%. Figure 8 is a histogram of some recent data for some higher efficiency lots.

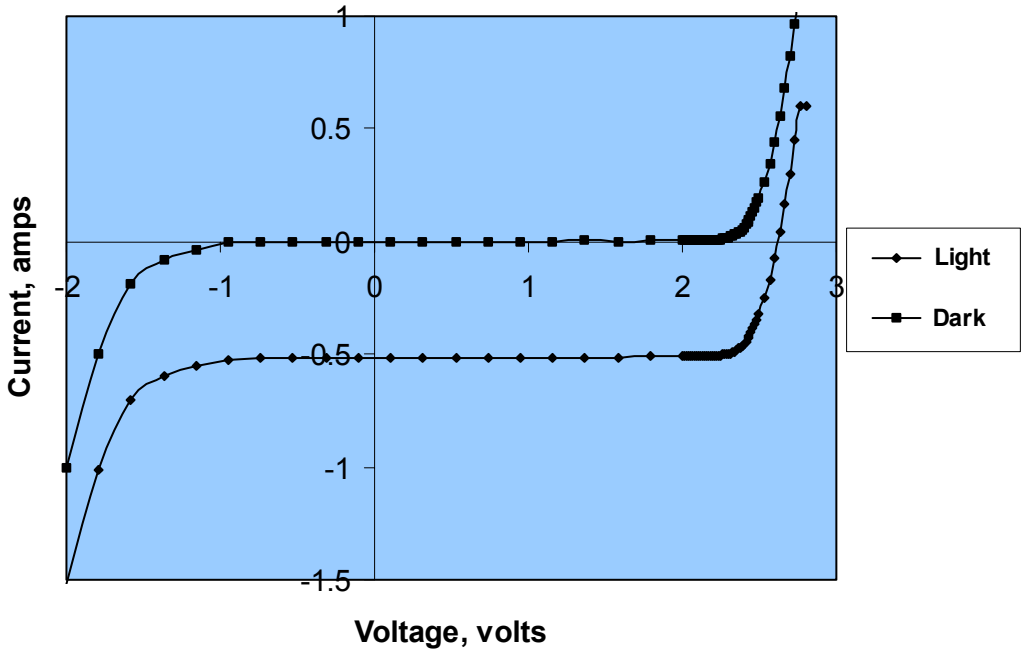

Figure 6. I-V curve for a 30.2 cm^2 multi-junction solar cell with a Design 2 monolithic bypass diode. The cell Voc, Isc, ff, and efficiency are 2621 mV, 517 mA, 84.5%, and 28%, respectively, under 135.3 mW/cm^2.

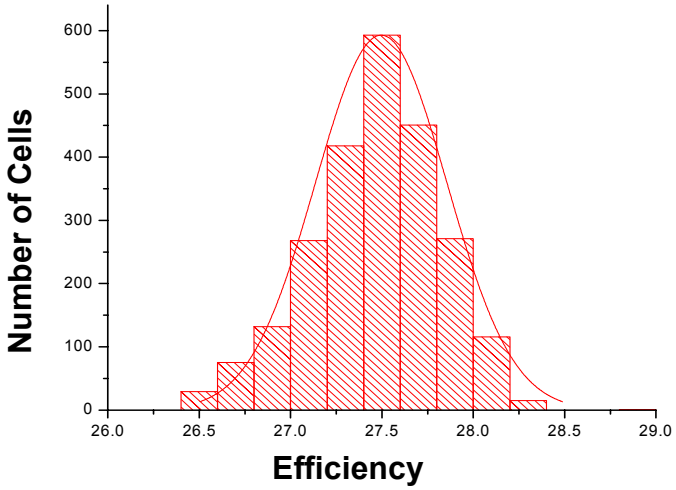

Figure 7. Histogram for over 2,000 multi-junction cells grown with monolithic bypass diodes. All of these cells were 30 cm^2 in area or larger. The average efficiency is 27.5%, under 135.3 mW/cm^2.

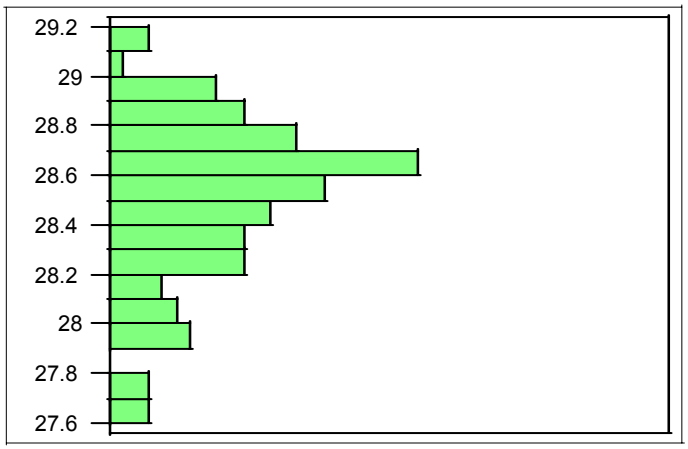

Figure 8. Histogram for over 200 higher efficiency cells. The average cell efficiency is 28.5%, under 135.3 mW/cm^2.

CONCLUSIONS

We have been able to demonstrate a monolithic bypass diode that meets the design criteria mentioned in the Introduction. The diode performs as intended as it prevents the cell from being reverse biased into breakdown. It is robust and reliable, as demonstrated by the qualifications tests. Finally, it is simple in design and does not add significant complexity during growth and processing.

REFERENCES

[1] See, for example, U.S. Patents 6,326,540 and 6,103,970
[2] M. S. Tyagi, Introduction to Semiconductor Materials and Devices, (John Wiley & Sons, New York, 1991) pp. 214-235.

DENDRITE GROWTH AND DEGRADATION IN MULTI-JUNCTION SOLAR CELLS

Dr. Donna Speckman
Dr. Dean Marvin
John Nocerino
The Aerospace Corporation, Los Angeles, CA

Contact Author
Dr. Donna Speckman
The Aerospace Corporation
PO Box 92957 MS M2/244
Los Angeles, CA 90009
Donna.m.speckman@aero.org
310 336 9399

ABSTRACT

Silver dendrites have been shown to be responsible for shunting of p/n multijunction solar cell assemblies with silver plated interconnects. A variety of cell and interconnect designs has been studied in order to identify the key factors that result in silver dendrite formation and subsequent cell shunting. The experimental results suggest that in this case the shunting was due to the particular polarity of the cell and design of the interconnect that placed it in close proximity to the cell edge. As a result, mitigation strategies are readily available.

INTRODUCTION

Silver coated interconnects have historically been used for many years on single junction (SJ) solar cells for space applications, with no apparent difficulties. However, with the recent introduction of high efficiency, multi-junction solar cells with higher operation voltages for space-based solar array applications, some problems have arisen that appear to be related to the use of silver based interconnects. Solar panels constructed using p/n dual junction (DJ) cascade cells showed a severe degradation in performance upon long-term storage in room light and normal humidity conditions. Destructive analysis of solar cells removed from this panel revealed that the edges of the solar cells were highly decorated with silver dendrite growths, but the mechanism and conditions required for dendrite growth were not elucidated. Furthermore, identical solar cell assemblies that had not been mounted on a panel, but instead were stored in room air with occasional exposure to light, also were covered with dendrites along the cell edge. The performance degradation in the stored panels is believed to be due to the growth of dendrites that formed shunt paths across the cell junction. Although metal migration is well known in the printed circuit board industry[1], this is the first instance known to us of the phenomenon affecting solar cells.

The formation of silver dendrites in the junction region of a solar cell edge is a multi-step process. Since there is no silver inherently present in this region of the cell, silver ions must first be generated elsewhere. These ions must then be transported to the junction region, where they are reduced to silver metal. If enough silver metal is present to bridge the solar cell junction, a highly conductive shunt can be formed. There are several cell features that could contribute to the formation of dendrites. These include: a) cell voltage (to ionize silver, transport the ions to the cell edge, and reduce the ions at the cell junction), b) cell polarity (to transport silver ions towards the junction), c) amount of exposed silver in close proximity to the cell edge (interconnect design, presence of a crossbar, bus bar and solder pad locations), and d) presence of electrolytes on the cell surface to aid in ion transport (solder flux, contamination, moisture, solvents). In order to understand the mechanism of dendrite growth, and to identify the conditions that lead to this phenomenon, we have carried out a series of experiments to assess the influence of each of these features on the growth of dendrites and subsequent cell shunting.

EXPERIMENTAL SECTION

A variety of glassed solar cells with different polarities, cell voltages, interconnect designs, and interconnect attachment methods were obtained from vendors for comparison in our studies. Single junction p/n cells (Air Mass Zero open circuit voltage of as-received cells ~ 1.0v) were evaluated, as were several types of multi-junction cells (Air Mass Zero open circuit voltage of as-received cells ~ 2.4v). Multi-junction cells with p/n polarity were compared with n/p multi-junction cells, and two interconnect designs were assessed: a "Z-bend" interconnect, which wraps closely around the solar cell edge and has the option of having a crossbar lying directly over the cell edge, and an "out-of-plane stress relief" interconnect, which does not contain a crossbar and does not conform closely to the cell edge. The influence of electrolytes from solder flux was evaluated by comparing interconnects attached to the cells either by soldering (using no-clean solder flux) or by welding. Interconnected solar cell assemblies obtained for testing included 1) p/n dual junction GaInP/GaAs/Ge (Tecstar) cells with soldered Z-bend interconnects with crossbars, 2) n/p dual junction GaInP/GaAs/Ge (Spectrolab) cells with soldered Z-bend interconnects with crossbars, 3) p/n dual junction GaInP/GaAs/Ge (Tecstar) cells with welded, out-of-plane stress relief interconnects with no crossbars, and 4) p/n single junction GaAs/Ge (Tecstar) cells with soldered Z-bend interconnects with no crossbars.

For our experiments, each interconnected cell assembly was suspended in a Petri dish above a fluid whose vapor might be in contact with a solar panel during storage, such as water, ketoxime (a cure product of the cell/substrate adhesive), or a mixture of both solvents. A control sample, in which no solvent was added to the Petri dish (room humidity exposure only), was also included for each set of samples studied. The assemblies were illuminated with quartz halogen lamps (approximately 0.2 suns) to achieve an approximate open circuit cell voltage while exposed to the solvent vapors (Figure 1). The open circuit voltages (V_{oc}) of these samples were monitored continuously during the test. Solar cell assemblies that demonstrated a significant and permanent drop in V_{oc} were removed from the test apparatus, and examined by scanning electron microscopy (SEM). I-V curves were also obtained for these degraded samples using an X-25 solar simulator as the illumination source. In all cases, I-V curves and SEM photos were obtained for the samples prior to testing, so that these could be used for comparison with the post-test results. All initial I-V curves showed good fill factors, and no dendrites were observed on any cell edges prior to testing.

RESULTS AND DISCUSSION

Open circuit voltage data as a function of time for the p/n dual junction Tecstar cascade cell assemblies with soldered Z-bend interconnects are shown in Figures 2a-c. These solar cell assemblies are the same design as those on the degraded solar panel array, with slight process differences. Five samples were initially placed under test (SN 112, 034, 053, 063, 008). All of these

assemblies were exposed to the vapor of a 50:50 mixture of water and ketoxime during illumination. One of these five samples (SN 034) was also treated with additional solder flux, applied to the underside of the crossbar of the Z-bend interconnect before testing. This solder flux-treated sample and one of the untreated solar cell assemblies (SN 112) exhibited a rapid and significant V_{oc} degradation within 24 hours of being placed under test (Figure 2a), after which, the V_{oc} values remained relatively stable. After 12 days on test, these solar cell assemblies were removed for I-V measurements and SEM analysis. The final V_{oc} value for the solder flux-treated sample was about 1.3 volts and the non-treated sample had a final V_{oc} of approximately 0.9 volts. The I-V curves for these two degraded samples are shown in Figure 3. Both solar cell assemblies exhibited a V_{oc} recovery upon illumination with the X-25 solar simulator. However, the fill factors for both of the samples were degraded compared to pre-test conditions. SEM analysis of the solder flux-treated sample (SN 034) shows extensive dendrite growth along the cell edge at what appears to be the cell junction region, as shown in Figure 4a. The untreated sample (SN 112) shows large silver crystals apparently growing upwards from the top edge of the cell towards the overhanging interconnect crossbar (Figure 4b). There are also silver crystals growing downwards from the crossbar. It is possible that these crystals once formed a continuous bridge between the interconnect crossbar and the cell edge and served as electrical shunts, but that these were broken prior to SEM analysis. Since the SEM pictures were obtained after the I-V measurements were made, they also reflect the solar cell assembly conditions following V_{oc} recovery. A recovery in V_{oc} suggests that some shunts were destroyed during the I-V measurement, possibly by current overloading of the shunts produced by the greater light intensity from the X-25 simulator.

Following removal of these two degraded samples from testing, two more interconnected solar cell assemblies were added to the illumination test in their place. One of these was another p/n dual junction cascade cell with soldered Z-bend interconnects (SN 069), which was placed into a Petri dish with no added water or ketoxime, to serve as a DJ cascade control. The second sample added was a single junction p/n GaAs/Ge cell (Tecstar) with soldered Z-bend interconnect with no crossbar (SN T-50), which was also placed in a Petri dish without added solvent. This sample was intended to serve as a SJ control. The DJ "control" sample began to show evidence of shunting within 24 hours on test, as indicated by a gradual and "noisy" loss in V_{oc} (Figure 2b). The V_{oc} of this cascade cell assembly appeared to stabilize at about 1.5 volts, and then partially recovered to a value of 2 volts after 22 days on test (Figure 2c). Three days later, the V_{oc} of the cascade "control" assembly dropped again, this time to about 1 volt, and eventually stabilized at approximately 0.9v. These data demonstrate that shunt formation can occur in p/n cascade cell assemblies, even in the absence of high humidity or other solvent vapors, and that these shunts can occasionally be spontaneously reversed, resulting in partial cell recovery. However, degradation eventually results in cell failure.

After three months of continuous illumination, two of the remaining three original p/n cascade solar cell assemblies had severely degraded (SN 063 and SN 008) and the last cascade assembly (SN 053) had begun to show slight signs of V_{oc} degradation (which may be attributable to halogen lamp aging). In contrast, the single junction cell assembly remained stable throughout. The degraded V_{oc} values for all of the p/n cascade solar cell assemblies were found to stabilize at one of two values: V_{oc} ~ 1.3-1.5v or V_{oc} ~0.9v. These V_{oc} values are consistent with the loss of either one of the two junctions in these solar cells. The degraded p/n DJ cascade samples and the SJ control sample remaining on test were removed from the test apparatus and their I-V curves were measured under illumination with the X-25 simulator. In order to determine whether or not the high current generated by the X-25 was destroying some of the dendritic shunts in the degraded solar cell assemblies, V_{oc} values were monitored as a function of time as the X-25 shutter was opened. The results of these measurements are shown in Figure 5. For each of the severely degraded cascade samples, the V_{oc} value is seen to initially rise to its last test value, and then continue to rise as the shutter is opened. These observations are consistent with the hypothesis that high current destroys some of the dendritic shunts. In contrast, the V_{oc} for the stable SJ cell assembly immediately rises to its final V_{oc} test value and remains stable. The one cascade cell assembly that did not exhibit severe degradation (SN 053) also rose rapidly to its final test V_{oc} value. The I-V

curves for the degraded cascade samples (SN 069, SN 063, SN 008) were found to be similar to those observed for SN 112 and SN 034. The fill factors for each of the degraded p/n cascade cell assemblies are significantly reduced compared to their pre-test values, and the depressed "knee" in the I-V curve is consistent with shunting in these cells. A representative I-V curve (SN 008) is shown in Figure 6.

SEM pictures of the degraded p/n cascade cells SN 069, SN 063, and SN 008 are shown in Figure 7a-c. In all cases, silver dendrites and/or silver crystallites were found to have formed along the cell edges and between the cell and the overhanging crossbar of the Z-bend interconnect, which supports they hypothesis that cell degradation is due to shunting via these new growths.

Three n/p dual junction solar cell assemblies with soldered Z-bend interconnects (same overall configuration as the p/n Tecstar cascade assemblies, but with a reverse cell polarity) were then placed in the Aerospace test apparatus under similar test conditions as the p/n cascade samples. Two solar cell assemblies were suspended in Petri dishes over 50:50 mixtures of water and ketoxime, and one assembly was suspended in room air only. The SJ control sample remained on test for comparison. After two months on test, none of the n/p DJ solar cell assemblies showed any signs of degradation. These data suggest that reversing the cell polarity mitigates the problems of dendrite growth and subsequent shunting, possibly by transporting any silver ions that are formed away from the solar cell junction region, instead of towards it.

The last set of interconnected solar cell samples to be subjected to the Aerospace illumination testing consisted of three p/n dual junction cells with a welded out-of-plane stress relief interconnects. These assemblies were exposed to similar test conditions as the previous n/p DJ samples. One solar cell assembly was exposed to water vapor, one was exposed to ketoxime vapor, and one was exposed only to room air. Surprisingly, this last set of samples did not exhibit any V_{oc} degradation after two months on test, despite the apparent undesirable polarity of the solar cells. This lack of degradation might be accounted for by the difference in interconnect design (no crossbar present, interconnect tabs are further away from the cell edge, and the silver weld pads are smaller than the Z-bend solder pads), or it might be explained by the lack of solder flux (which can serve as an electrolyte for silver ion migration). In an effort to differentiate between these two effects, solder flux was added to the backside of the welded interconnects on two of these solar cell assemblies (those exposed to excess solvent vapor), and all three samples were placed back on test. After more than 3 weeks of illumination testing following this change, no degradation has been observed. It may be that more time is required before an effect of the solder flux is seen, or it may be that the interconnect design prevents silver migration and subsequent degradation. These experiments are still ongoing.

Finally, it is significant that the single junction p/n "control" sample did not show any signs of degradation, even after more than seven months on test, and SEM analysis shows no evidence of dendrite growth. This lack of degradation in the single junction solar cell assembly may be due to the low operating voltage of the SJ cell, but the use of a Z-bend interconnect without a crossbar may also contribute to the robustness of this assembly.

SUMMARY

The results of the Aerospace illumination experiments indicate that cell polarity and interconnect design play significant roles in controlling multi-junction cell dendrite growth and subsequent degradation in solar cell assemblies with silver-coated interconnects. The use of an out-of-plane stress relief interconnect appears to minimize dendrite formation, as does using an n/p cell polarity cell design. These results should aid in the design of robust multi-junction solar cell assemblies for future space applications.

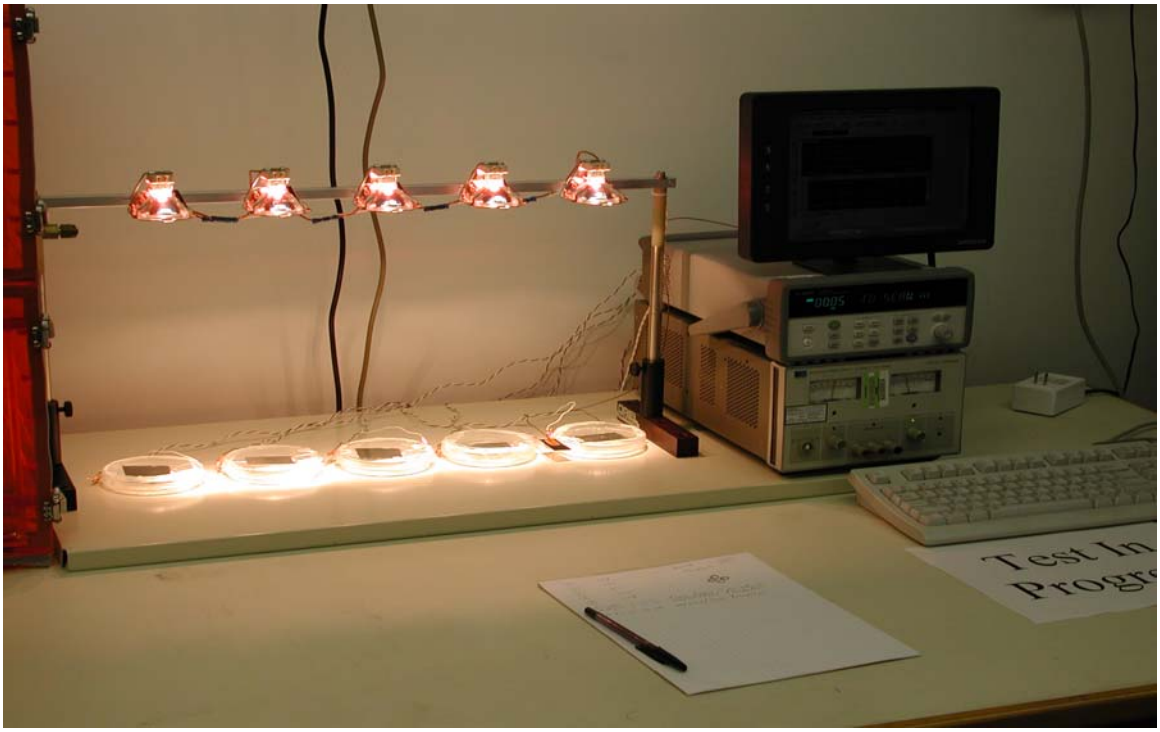

Figure 1. Experimental apparatus for illumination testing

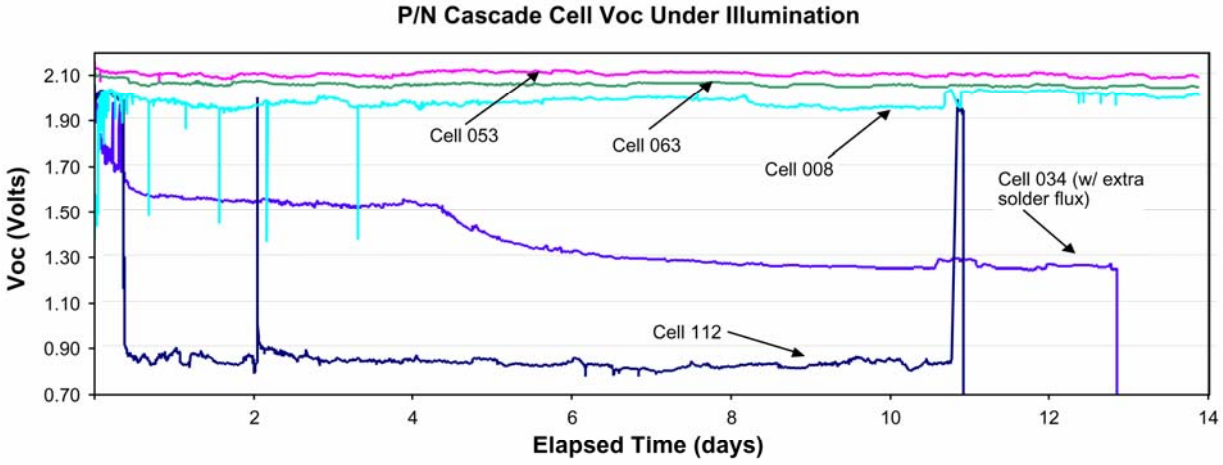

2a) Five new p/n cascade assemblies placed on test (SN 112, SN 034, SN 053, SN 063, SN 008)

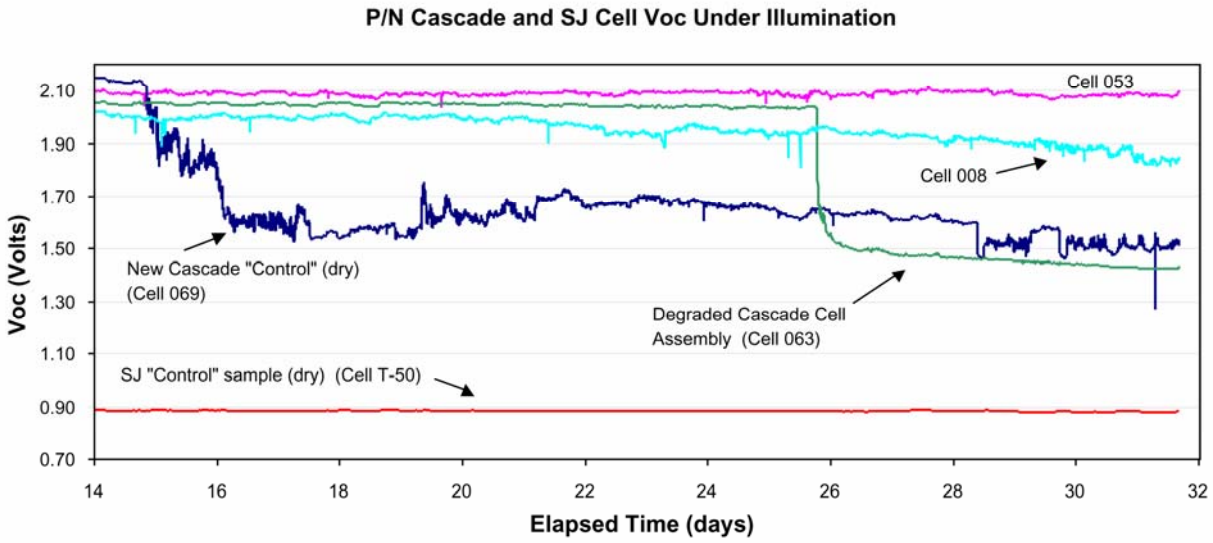

2b) One new cascade cell assembly (SN 069) and one single junction cell assembly (SN T-50) replace SN 112 and SN 034 on test. SN 069 begins to show immediate, noisy degradation; SN 063 degrades abruptly after 25 days on test.

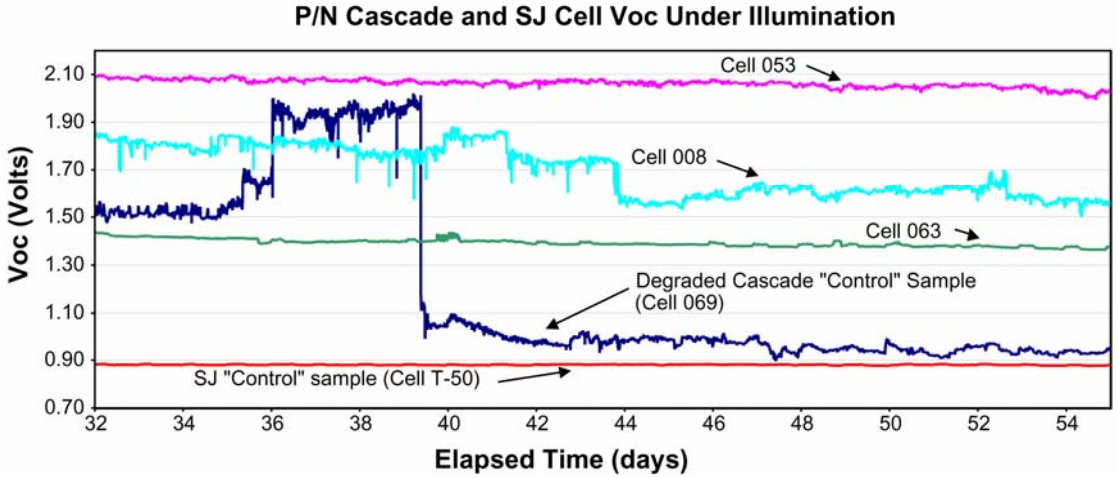

2c) SN 069 shows partial recovery followed by degradation; SN 008 gradually degrades

Figure 2. Open circuit voltage as a function of illumination time for p/n dual junction and single junction solar cell assemblies with soldered, Z-bend interconnects.

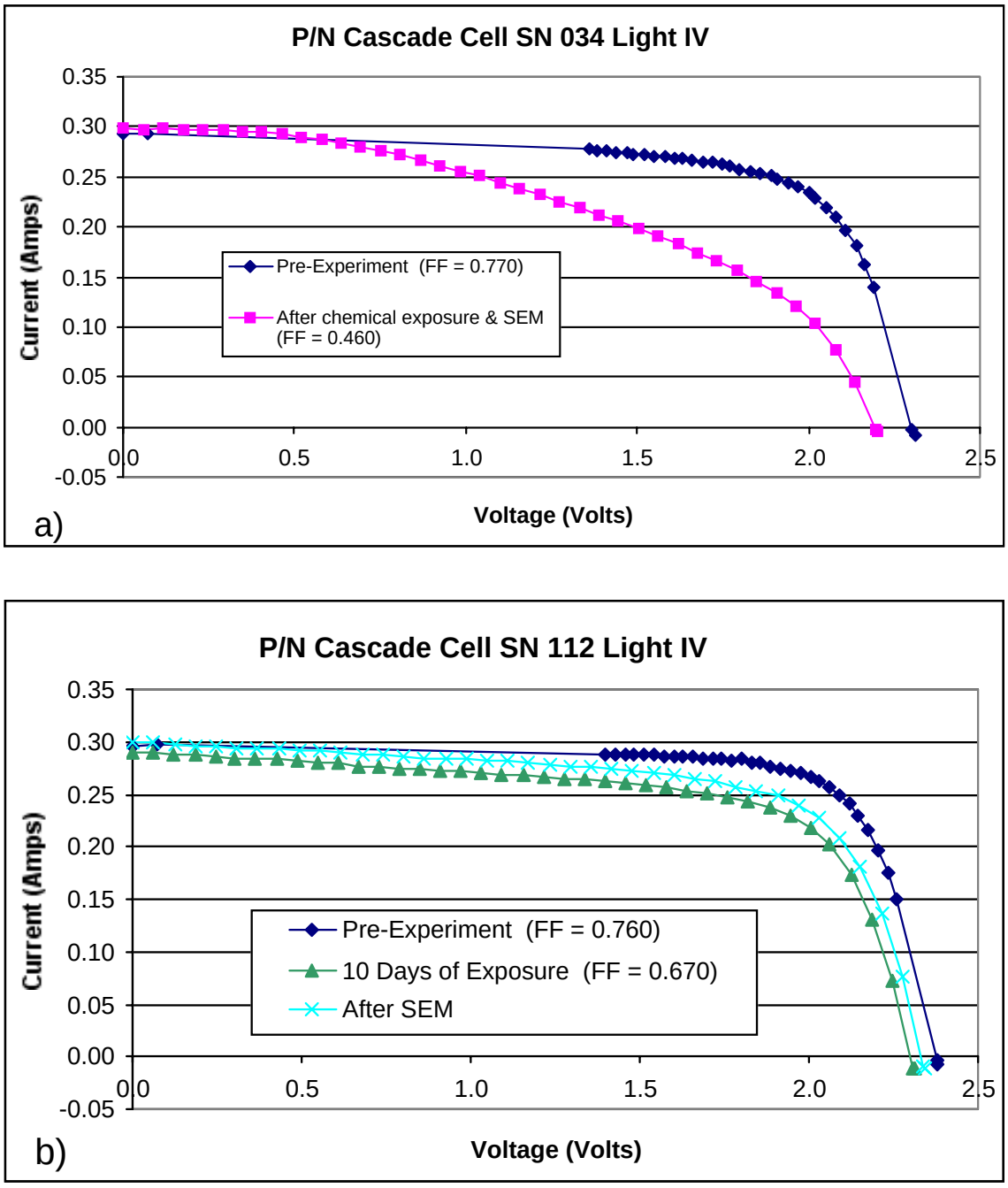

Figure 3. I-V curves for degraded p/n dual junction solar cell assemblies with soldered Z-bend interconnects. a) SN 034 (with added solder flux), and b) SN 112

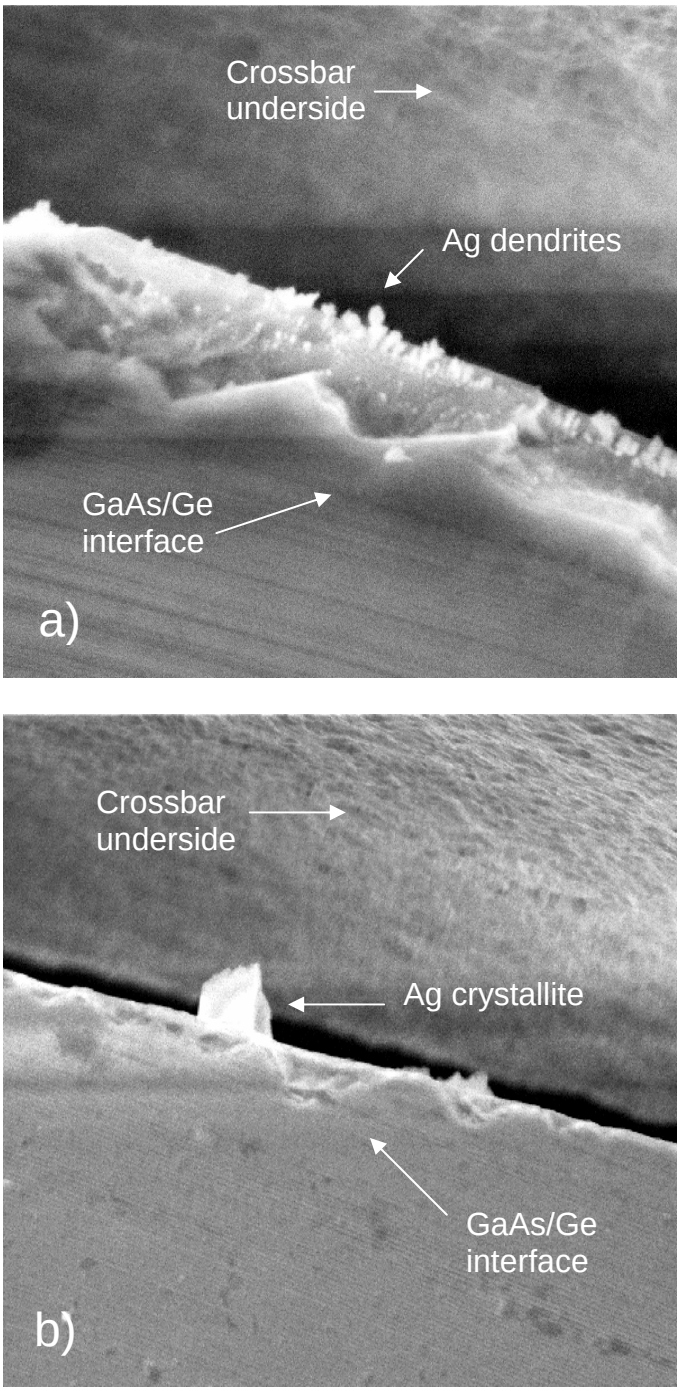

Figure 4. SEM images of cell edges for degraded p/n dual junction solar cell assemblies, located under Z-bend crossbar. a) Cell edge of SN 034 (added solder flux), and b) Cell edge of SN 112

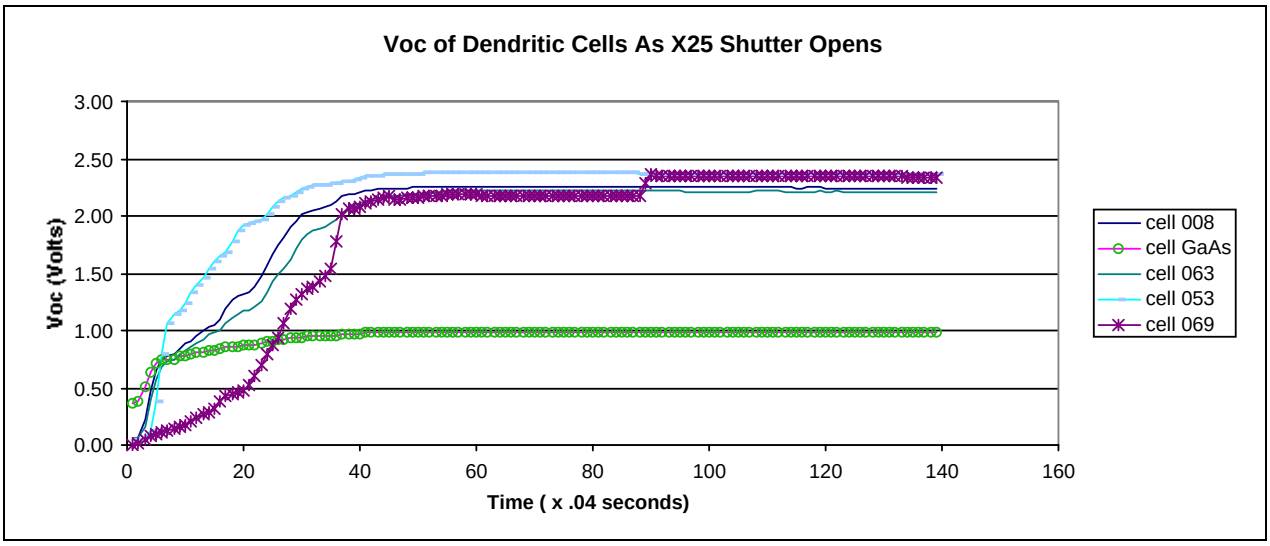

Figure 5. Open circuit voltage of degraded and non-degraded solar cell assemblies as X25 solar simulator shutter opens

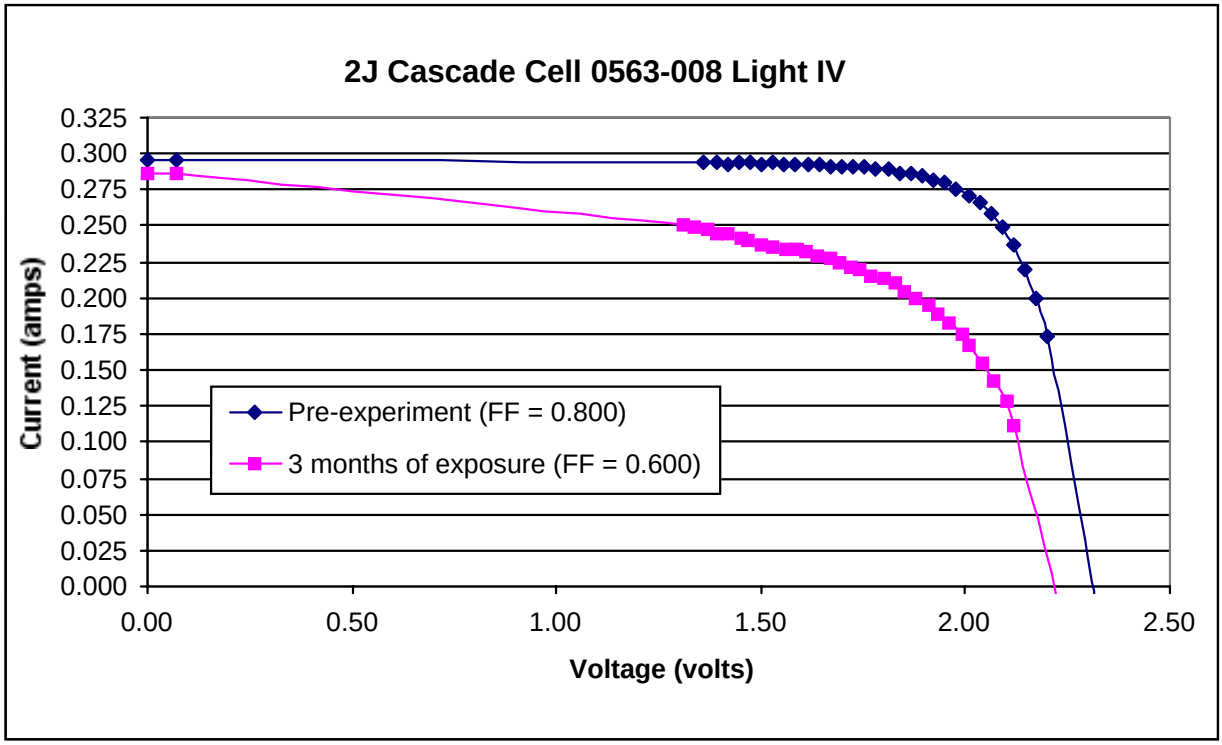

Figure 6. I-V curve for degraded p/n cascade cell SN 008 with soldered Z-bend interconnects, after several months on test.

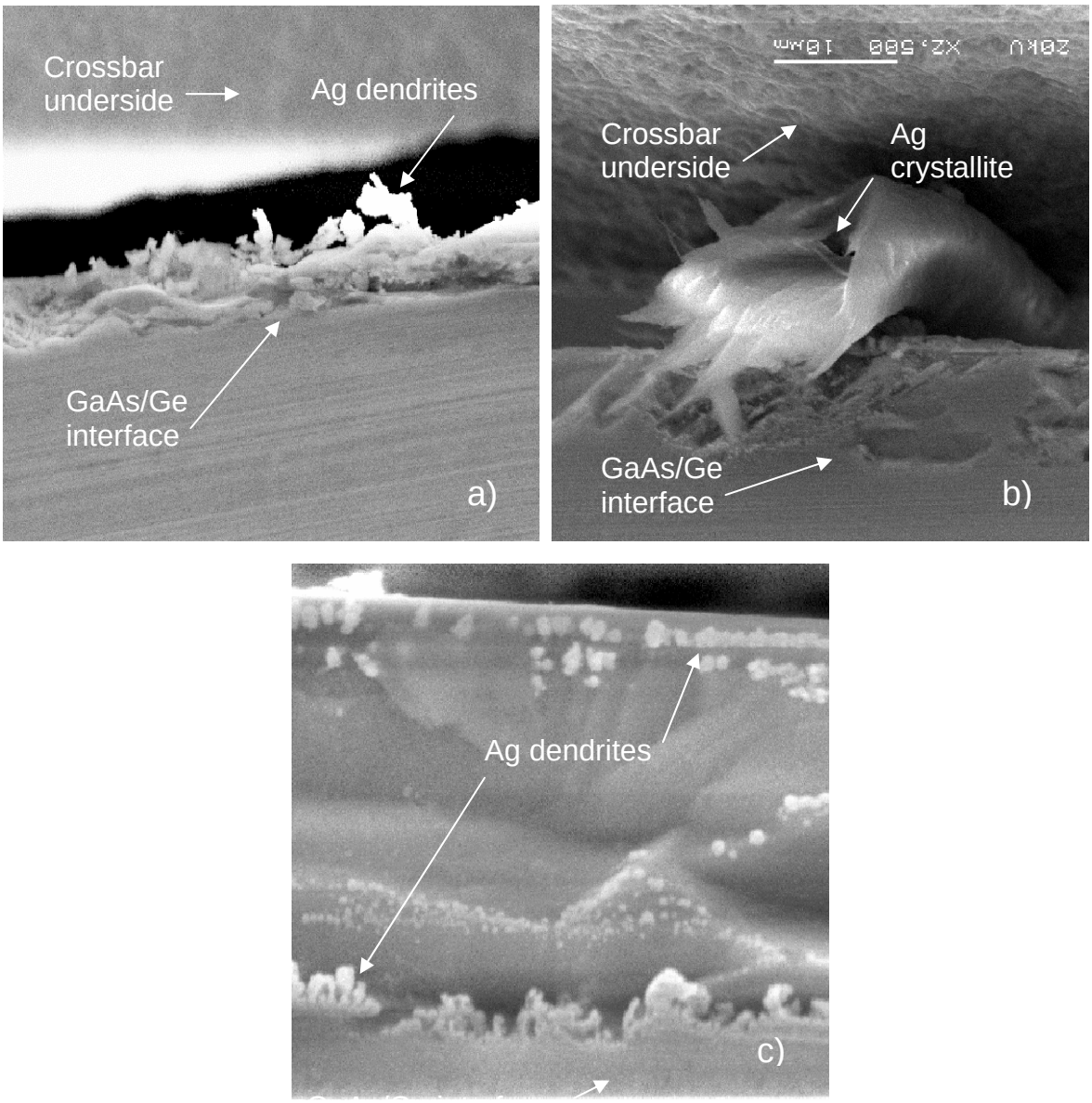

Figure 7. SEM images of cell edges for degraded p/n cascade solar cell assemblies, located under Z-bend crossbar a) SN 069 (DJ "control" sample, b) SN 063, and c) SN 008

[1] Michalkiewicz R, Green J, and Opperhauser S. "Surface Insulation Resistance Testing of Soldering Pastes and Fluxes," Proceedings of the Pan Pacific Microelectroinics Symposium. Kauai Hawaii. February 2001.

INDIUM PHOSPHIDE WINDOW LAYERS FOR INDIUM GALLIUM ARSENIDE SOLAR CELLS

Raj K. Jain*
NASA Lewis (now Glenn) Research Center, Cleveland, OH 44135

Window layers help in reducing the surface recombination at the emitter surface of the solar cells resulting in significant improvement in energy conversion efficiency. Indium gallium arsenide ($In_xGa_{1-x}As$) and related materials based solar cells are quite promising for photovoltaic and thermophotovoltaic applications. The flexibility of the change in the bandgap energy and the growth of InGaAs on different substrates make this material very attractive for multi-bandgap energy, multi-junction solar cell approaches. The high efficiency and better radiation performance of the solar cell structures based on InGaAs make them suitable for space power applications. This work investigates the suitability of indium phosphide (InP) window layers for lattice-matched $In_{0.53}Ga_{0.47}As$ (bandgap energy 0.74 eV) solar cells. We present the first data on the effects of the p-type InP window layer on p-on-n lattice-matched InGaAs solar cells. The modeled quantum efficiency results show a significant improvement in the blue region with the InP window. The bare InGaAs solar cell performance suffers due to high surface recombination velocity (10^7 cm/s). The large band discontinuity at the InP/InGaAs heterojunction offers a great potential barrier to minority carriers. The calculated results demonstrate that the InP window layer effectively passivates the solar cell front surface, hence resulting in reduced surface recombination and therefore, significantly improving the performance of the InGaAs solar cell.

INTRODUCTION

Window layers are quite important in improving the solar cell energy conversion efficiency. They help in effectively reducing the surface recombination at the emitter surface of the solar cell without absorbing the useful light required for the device. Unlike silicon, solar cells based on III-V compound semiconductors and related materials suffer from the lack of native passivating oxides and/or wide choice of suitable large bandgap energy window materials. Various window layer materials have been investigated for III-V compound semiconductor based solar cells [1]. Further optimization work on the existing choices of windows and more development work on new window materials are required. It is also important to understand the physics of the window-emitter hetero-interface as well as growth related issues.

Indium gallium arsenide ($In_xGa_{1-x}As$) material has been used widely in several state-of-the-art electronic and optoelectronic devices. $In_xGa_{1-x}As$ and related materials based solar cells are quite promising for photovoltaic (PV) [2] and thermophotovoltaic (TPV) applications [3]. $In_xGa_{1-x}As$ is a ternary semiconductor whose bandgap energy can be varied between 1.42 eV (of GaAs) and 0.36 eV (of InAs) by changing the In/Ga ratio (see Fig. 1). The flexibility of the change in the bandgap energy and the growth of InGaAs on different substrates (Si, Ge, GaAs, InP, InAs) make this material very attractive for various devices. InGaAs solar cells grown on gallium arsenide (GaAs) substrates were developed twenty years ago [4]. The 1.15 eV and 1.35 eV bandgap energy InGaAs on GaAs cells

*Presently employed at Space Systems/Loral, 3825 Fabian Way, M/S Z-51, Palo Alto, CA 95014

demonstrated efficiencies in excess of 24% at 400-sun concentration [5]. These developments were intended for the use of InGaAs cells in multi-bandgap energy, multi-junction solar cell approaches. Two-junction monolithic InP/InGaAs tandem cells grown on InP substrates have demonstrated AM0 1-sun efficiencies over 22% [6].

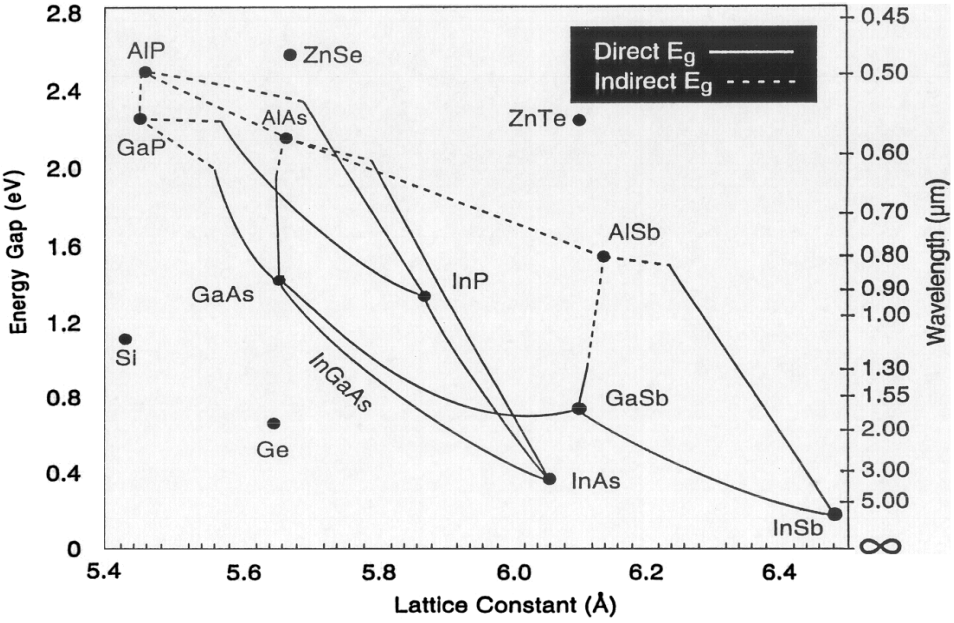

Figure 1. Bandgap energy of indium gallium arsenide and related materials as a function of lattice constant.

Record efficiency n-on-p and p-on-n lattice-matched InGaAs (0.74 eV bandgap energy) solar cells grown on InP were reported [7,8]. Lower bandgap energy (0.74 eV and below) InGaAs cells grown on InP substrates offer high efficiencies [9] for thermophotovoltaic applications and have been developed [8]. InGaAs based solar cells also find use in quantum well, operation under monochromatic light, and related applications. The demonstration of high PV and TPV efficiencies and better radiation performance [10] of the solar cell structures based on InGaAs solar cells make them attractive for space power applications. InGaAs and related materials based solar cells grown on GaAs substrates for applications in tandem cells are getting renewed interest and are under investigation. The InGaAs based cell technologies on GaAs substrates could easily be adopted later on germanium (Ge) substrates [2], similar to high efficiency GaInP/GaAs/Ge dual or triple-junction cells grown on Ge substrates.

InGaAs solar cells have been fabricated with or without window layers but no quantitative theoretical or experimental data on the effects of window materials are available in the literature. This work investigates the suitability of indium phosphide (InP) window layers for lattice-matched $In_{0.53}Ga_{0.47}As$ (bandgap energy 0.74 eV) solar cells. We present the data on the effects of the p-type InP window layer on p-on-n lattice-matched InGaAs solar cells. p-on-n structure was selected for further investigation and development as it offered better optical and electrical properties than n-on-p structure. The calculated quantum efficiency results demonstrate the suitability of the InP window in effectively reducing the surface recombination at the front surface of the InGaAs cell resulting in significant improvements in the blue response. The large band discontinuities at the heterojunction provide a great potential barrier for the minority carriers. PC1D computer code [11] was used in performing the numerical calculations.

MODELING APPROACH

InGaAs Material Parameters

The InGaAs solar cell modeling requires an accurate knowledge about the various physical parameters. Little or no experimental information is available about the various physical parameters of lattice-matched or mismatched InGaAs material. The optical absorption coefficient and the intrinsic carrier concentration are very important parameters, which greatly influence the solar cell current and voltage respectively. Jain et al. [12,9] provided the first estimated and calculated data on these two important parameters based on available information. Figure 2 shows the optical absorption coefficient versus wavelength for the lattice-matched 0.74 eV bandgap energy InGaAs at 300 K.

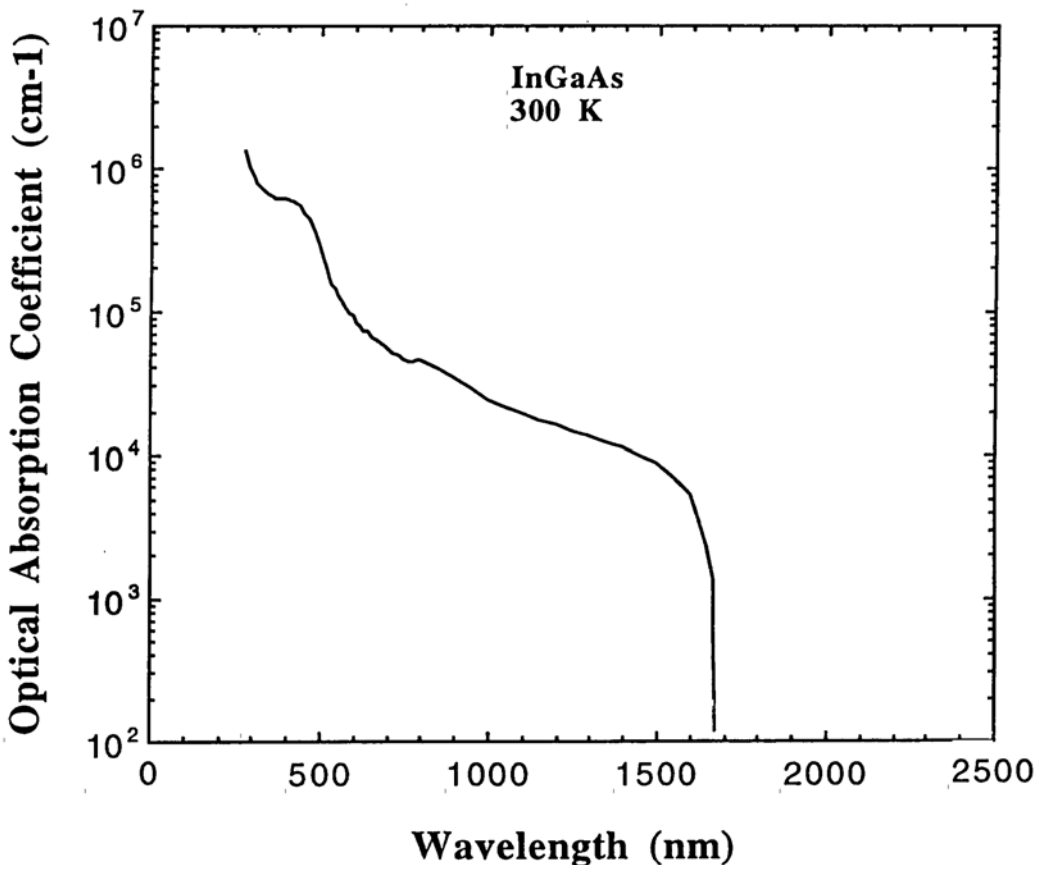

Figure 2. Optical absorption coefficient of lattice-matched InGaAs (0.74 eV bandgap energy) versus wavelength at 300 K.

The intrinsic carrier concentration, n_i for InGaAs was calculated by using the scaling relation described by Jain et al. [12],

$$n_i\,(\text{InGaAs}) = n_i\,(\text{GaAs})\,\exp\{-\bullet E_G/(2kT)\} \qquad (1)$$

where $\bullet E_G$ is the bandgap difference, k is the Boltzman's constant, and T is the temperature in K. Figure 3 shows the plot of the intrinsic carrier concentration vs. InGaAs bandgap energy at 300 K. An n_i value of 2.59×10^6 cm^{-3} for GaAs at 300 K was used. As the bandgap energy of InGaAs decreases (with increase in In/Ga ratio), the n_i value increases and correspondingly the open-circuit voltage of the InGaAs solar cell decreases. The absorption coefficient versus wavelength values (Fig. 2) and the n_i value at 0.74 eV (Fig. 3) were used in modeling the performance of the lattice-matched InGaAs solar cell. Similarly, the various physical parameters for the InP window material were used from the literature.

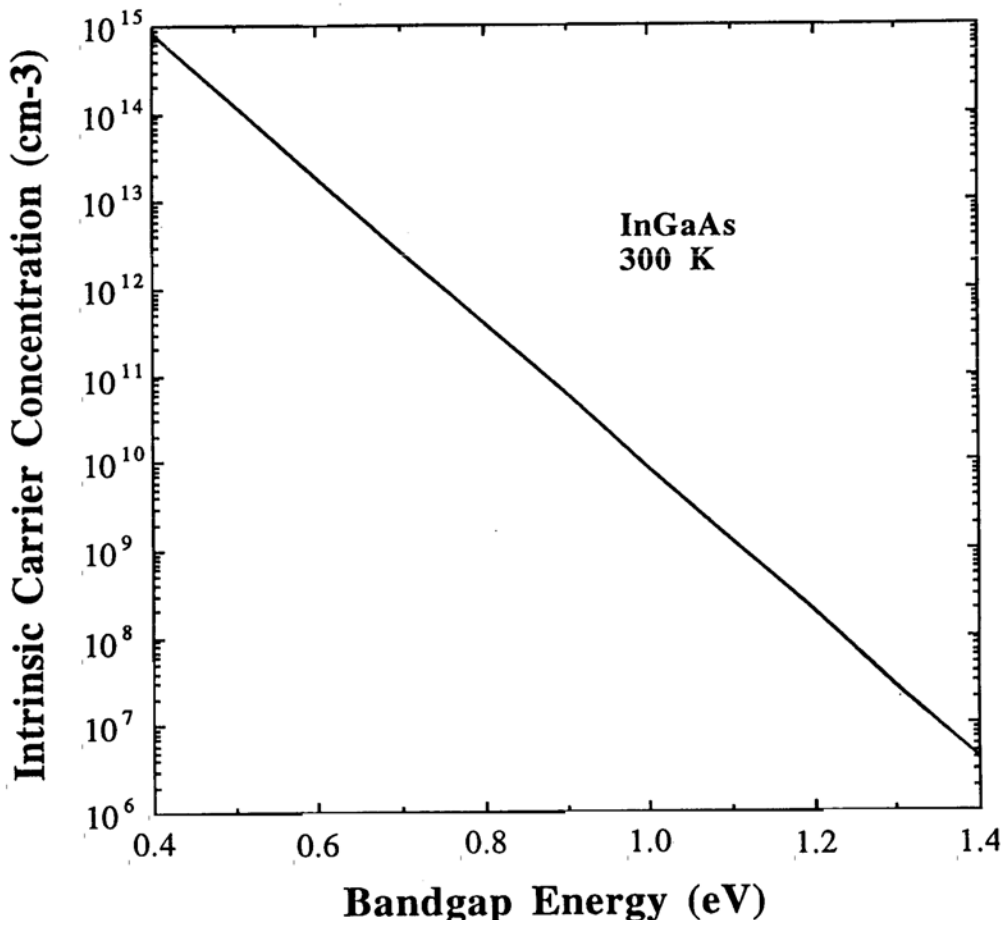

Figure 3. Plot of the intrinsic carrier concentration versus InGaAs bandgap energy at 300 K.

InP/InGaAs Interface Band Structure

InP forms a heterojunction with InGaAs and the InP/InGaAs interface plays an important role in controlling the performance of the devices based on these materials. The bandgap energy difference between the two materials causes the mis-alignment of the conduction and valence bands resulting into band discontinuities. The band offsets in InP/InGaAs heterojunction structures have been studied experimentally and theoretically. Reference 13 describes the various values for the conduction band and the valence band discontinuities ($\bullet E_c$ and $\bullet E_v$) measured and calculated by several research groups.

We have used average experimental values of 0.23 eV and 0.37 eV for $\bullet E_C$ and $\bullet E_V$ respectively in this work. Figure 4 shows our calculated band structure diagram for the p-InP/p-InGaAs heterojunction. These results have been discussed in detail in the next section.

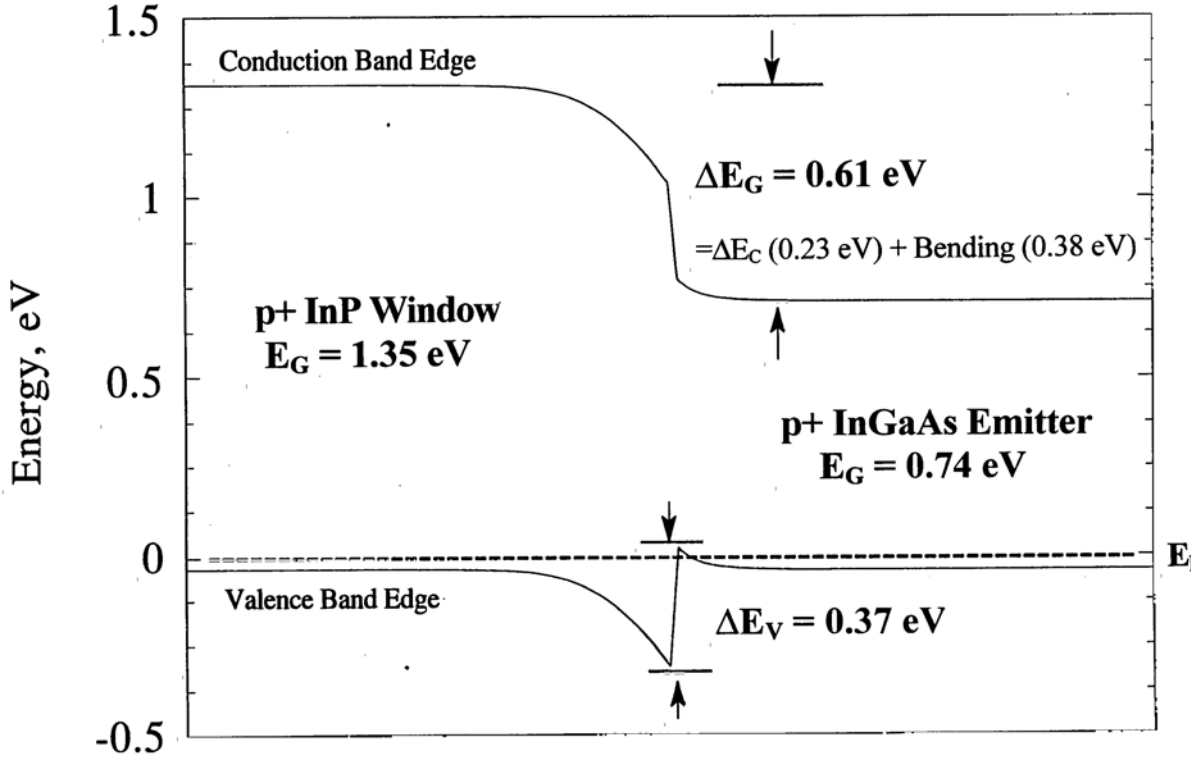

Figure 4. Band structure diagram of p-InP/p-$In_{0.53}Ga_{0.47}As$ (window/emitter) heterojunction interface.

RESULTS AND DISCUSSION

For the past several years, we have been using a numerical code PC1D for silicon and III-V compound semiconductor based (GaAs, InP, InGaAs, GaInP, etc.) solar cell modeling and simulation of the measured cell performance to understand and provide feedback for further improvements to produce state-of-the-art devices. This work has resulted in several publications and a US patent [14]. NASA Lewis (now Glenn) Research Center has been continuing the pioneering work on the development of InGaAs based solar cells [15-17] and has reported record cell efficiencies [7,8].

In this work we have considered a p-on-n lattice-matched InGaAs solar cell grown on InP substrate. Figure 5 shows the cell structure considered. The emitter and base thickness and doping concentration were 0.3 μm, $2x10^{18}$ cm^{-3} and 4 μm, $1x10^{17}$ cm^{-3} respectively. The p InP window layer doping concentration was $2x10^{18}$ cm^{-3}, same as in the emitter. No antireflection coatings were considered to separate the effects of the window layer on the performance of the InGaAs solar cell. Minority carrier diffusion lengths of 0.5, 1, and 4 μm have been assumed in the window, emitter and base layers. The front, interface and the back surface recombination velocities were assumed to be 10^7, 10^7, and 10^4 cm/s. These values are typical of the current state-of-the art in p-on-n InGaAs solar cells. The heterojunction band structure parameters were used in modeling calculations.

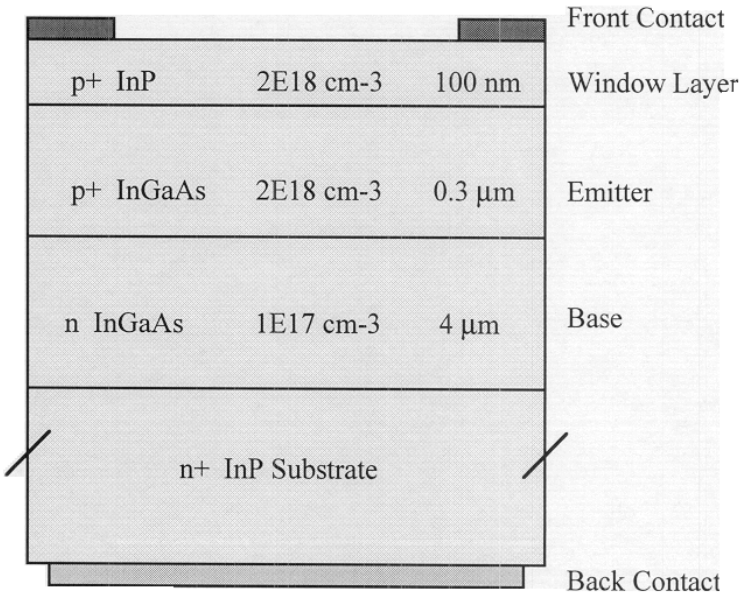

Figure 5. Structure of an InP/$In_{0.53}Ga_{0.47}As$ p-on-n solar cell.

Figure 6 shows the calculated internal quantum efficiency response for the InGaAs solar cell with and without InP window layer. A 100 nm thick window layer was considered. Calculations were

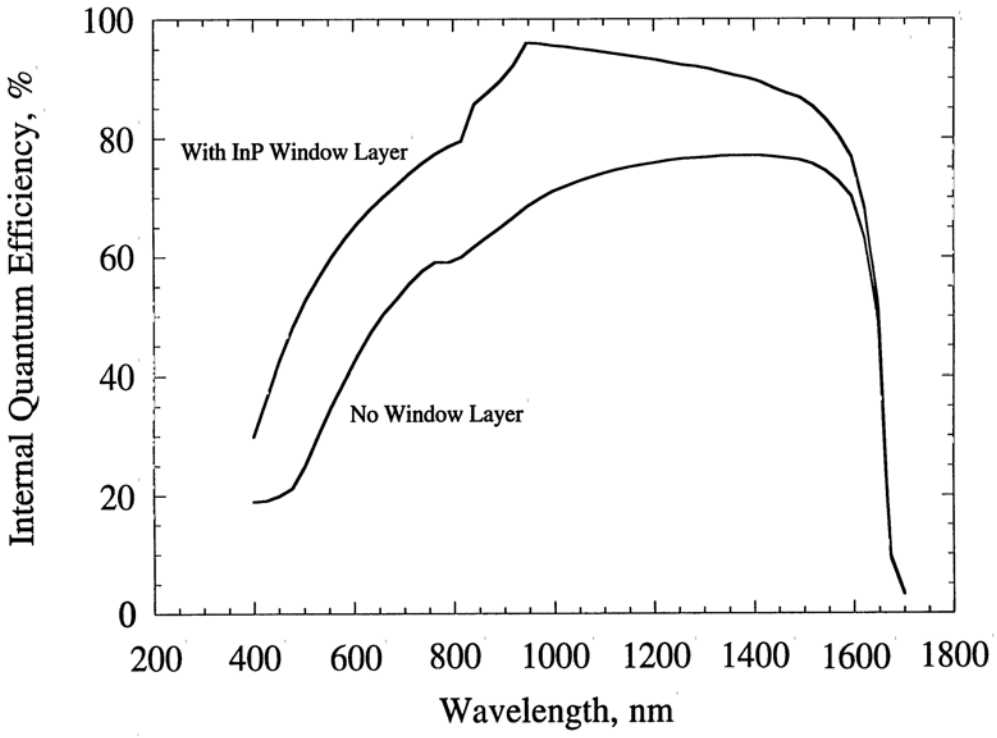

Figure 6. Plot of the internal quantum efficiency versus wavelength of p-on-n InGaAs solar cell with and without InP window layer.

performed by varying the window layer thickness and no significant difference in results was observed. This suggests that the wide-bandgap 1.35 eV InP window layer material does not absorb the light useful to InGaAs solar cell. There is a significant improvement in internal quantum efficiency, especially in the blue region, with window layer as shown in Figure 6. These results can be explained by the large conduction band discontinuity as shown in Figure 4. This discontinuity of 0.61 eV {= $\bullet E_c$ (0.23 eV) + Band bending (0.38 eV)} acts as an effective potential barrier for the minority carriers (electrons) of the p-on-n InGaAs cell, thereby stopping them from recombining at the surface. We have also calculated the effect of InP as a back surface passivation layer for InGaAs solar cells and found that the red response increases significantly. Detailed results will be published elsewhere.

CONCLUSIONS

The modeling results demonstrate the suitability of InP window layer material for lattice-matched InGaAs p-on-n solar cells. The internal quantum efficiency response significantly improves with window layer. These results can be explained by the large conduction band offset which acts as a potential barrier to minority carriers. Hence, InP reduces the surface recombination and effectively passivates the InGaAs surface. InGaAs based solar cells have been developed in single and multijunction structures for space photovoltaic and thermophotovoltaic applications. The current work and future developments should benefit from the results reported in this paper.

Acknowledgments

This work was done when the author was working at the NASA Lewis (now Glenn) Research Center, Cleveland, Ohio and supported by National Research Council-NASA Research Associate Program. Helpful discussions with David M. Wilt, Dr. Geoffrey Landis, Dr. Dennis J. Flood, and several other NASA colleagues are greatly appreciated.

REFERENCES

[1] J. Lammasniemi, R. K. Jain, M. Pessa, “Status of Window Layers for III-V Semiconductor Cells”, *Proceedings 14th European Photovoltaic Solar Energy Conference* (1997) p. 1767.

[2] R. R. King, C. M. Fetzer, P. C. Colter, K. M. Edmondson, J. H. Ermer, H. L. Cotal, H. Yoon, A. P. Stavrides, G. Kinsey, D. D. Krut and N. H. Karam, “High-Efficiency Space and Terrestrial Multijunction Solar Cells Through Bandgap Control in Cell Structures”, *Proceedings of the 29th Photovoltaic Specialists Conference*, (IEEE, New York, 2002) p. 776.

[3] R. J. Wehrer, M. W. Wanlass, B. Wernsman, J. J. Carapella, S. P. Ahrenkiel, D. M. Wilt and C. S. Murray, “0.74/0.55-eV GaxIn1-xAs/InAsyP1-y Monolithic, Tandem, MIM TPV Converters: Design, Growth, Processing and Performance”, *Proceedings of the 29th Photovoltaic Specialists Conference*, (IEEE, New York, 2002) p. 884.

[4] M. J. Ludowise, W. T. Dietze, R. Boettcher and N. Kaminar, “High-Efficiency (21.4%) Ga0.75In0.26As/GaAs (Eg=1.15 eV) Concentrator Solar Cells and the Influence of Lattice Mismatched on Performance”, *Appl. Phys. Lett.*, Vol. 43, p. 468 (1983).

[5] J. G. Werthen, B. A. Arau, C. W. Ford, N. R. Kaminar, M. S. Kuryla, M. L. Ristow, C. R. Lewis, H. F. MacMillan, G. F. Virshup and J. M. Jee, “Recent Advances in High Efficiency InGaAs Concentrator

Cells", *Proceedings of the 20th IEEE Photovoltaic Specialists Conference* (IEEE, New York, 1988) p. 640.

[6] M. W. Wanlass, J. S. Ward, K. A. Emery, A. Duda, T. J. Coutts, *Proceedings First World Conference on Photovoltaic Energy Conversion* (IEEE, New York, 1994) p. 1717.

[7] D. M. Wilt, N. S. Fatemi, R. W. Hoffman, P. P. Jenkins, D. J. Brinker, D. Scheiman, R. Lowe, R. K. Jain, "High Efficiency Indium Gallium Arsenide Photovoltaic Devices for Thermophotovoltaic Power Systems", *Appl. Phys. Lett*., Vol. 64, p. 2415 (1994).

[8] D. M. Wilt, N. S. Fatemi, P. P. Jenkins, V. G. Weizer, R. W. Hoffman, R. K. Jain, C. S. Murray, D. R. Riley, "Electrical and Optical Performance Characteristics of 0.74 eV p/n InGaAs Monolithic Interconnected Modules", *Proceedings 3rd NREL Conference on Thermophotovoltaic Generation of Electricity* (American Institute of Physics 1997) p. 237.

[9] R. K. Jain, D. M. Wilt, R. Jain, G. A. Landis, D. J. Flood, "Lattice-Matched and Strained InGaAs Solar Cells for Thermophotovoltaic Use", *Proceedings 2nd NREL Conference on Thermophotovoltaic Generation of Electricity* (American Institute of Physics 1995) p. 375.

[10] I. Weinberg, R. K. Jain, C. Vargas, D. M. Wilt, D. A. Scheiman, Performance of Ga0.47In0.53As Solar Cells Over a Range of Proton Energies", *Proceedings First World Conference on Photovoltaic Energy Conversion* (IEEE, New York 1994) p. 2173.

[11] P. A. Basore, "PC-1D Version 3: Improved Speed and Convergence", *Proceedings of the 22nd Photovoltaic Specialists Conference* (IEEE, New York, 1991) p. 299.

[12] R. K. Jain, D. M. Wilt, G. A. Landis, R. Jain, I. Weinberg, D. J. Flood, Modeling of Low Bandgap Solar Cells for Thermophotovoltaic Applications", *Proceedings 1st NREL Conference on Thermophotovoltaic Generation of Electricity* (American Institute of Physics 1994) p. 202.

[13] Properties of Lattice-Matched and Strained Indium Gallium Arsenide, INSPEC (1993) p. 86.

[14] R. K. Jain and G. A. Landis, "InP Solar Cell with Window Layer", US Patent Number 5,322,573, June 21, 1994

[15] D. M. Wilt, et al., "Lattice-Mismatched InGaAs PV Devices for TPV Power Systems", *Proceedings First World Conference on Photovoltaic Energy Conversion* (IEEE, New York, 1994) p. 1738.

[16] D. M. Wilt, et al., "Monolithically Interconnected InGaAs TPV Module Development", *Proceedings of the 25th Photovoltaic Specialists Conference*, (IEEE, New York, 1996) p. 43.

[17] D. M. Wilt, et al., "0.55 eV n/p/n MIM TPV Cell Development", *Proceedings of the 28th Photovoltaic Specialists Conference*, (IEEE, New York, 2000) p. 1024.

DESIGN AND PERFORMANCE OF A TRIPLE SOURCE AIR MASS ZERO SOLAR SIMULATOR

Phillip Jenkins
Ohio Aerospace Institute, Brook Park, OH 44142
David Scheiman
Ohio Aerospace Institute, Brook Park, OH 44142
David Snyder
NASA Glenn Research Center, Cleveland, OH 44135

Simulating the sun in a laboratory for the purpose of measuring solar cells has long been a challenge for engineers and scientists.[1,2,3] Multi-junction cells demand higher fidelity of a solar simulator than do single junction cells, due to a need for close spectral matching as well as AM0 intensity. A GaInP/GaAs/Ge solar cell for example, requires spectral matching in three distinct spectral bands (**figure 1**). A commercial single source high-pressure xenon arc solar simulator such as the Spectrolab X-25 at NASA Glenn Research Center, can match the top two junctions of a GaInP/GaAs/Ge cell to within 1.3% mismatch, with the GaAs cell receiving slightly more current than required. The Ge bottom cell however, is mismatched +8.8%. Multi source simulators are designed to match the current for all junctions but typically have small illuminated areas, less uniformity and less beam collimation compared to an X-25 simulator. It was our intent when designing a multi source simulator to preserve as many aspects of the X-25 while adding multi-source capability.

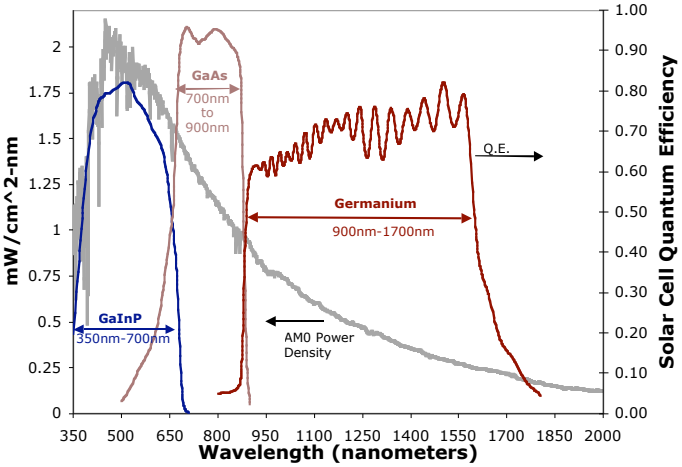

Figure 1) The quantum efficiency of a GaInP/ GaAs/Ge solar cell plotted with the AM0 spectrum.

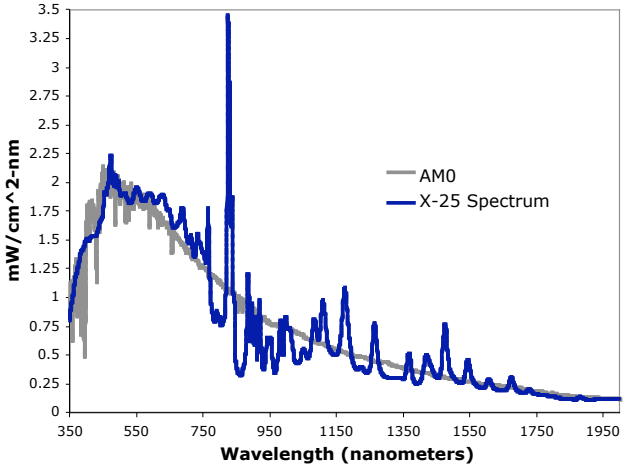

Figure 2) Spectrum of the Spectrolab X-25 solar simulator5 compared to AM0.

The X-25 faithfully reproduces the AM0 spectrum from approximately 350-nm to 750-nm but beyond that region the spectrum quickly diverges from AM0 (**figure 2**). This multi-source simulator takes advantage of this property and uses the X-25 to provide the bulk of the UV and visible light. A non-absorbing dichroic mirror (designed and fabricated by Displays and Optical Technologies, of Round Rock, Texas) is used as a beam splitter to reflect the blue portion of the spectrum and transmit the infrared. The transmission and reflection curves of the filter (**figure 3**) show that there is a fairly good cutoff transition at 700-nm but that the reflection band pass is limited to approximately one octave and begins to transmit excessively at wavelengths shorter than 450nm. This behavior

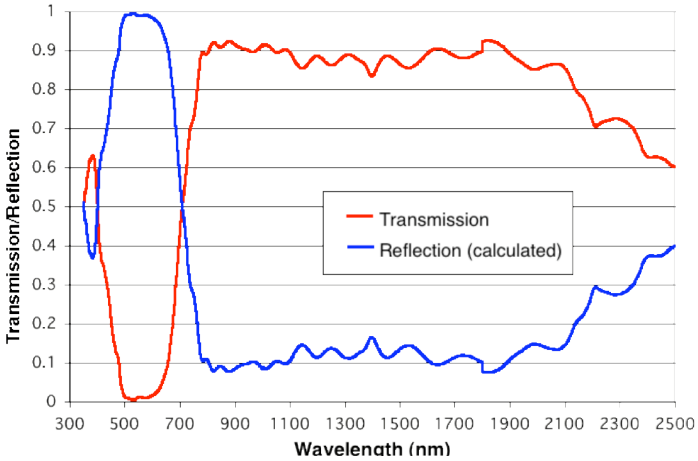

Figure 3) Transmission and reflection of dichroic mirror.

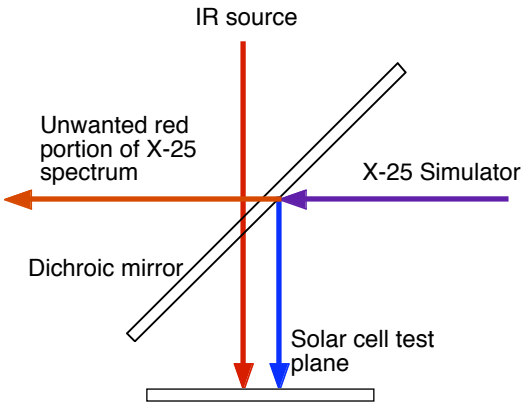

Figure 4) Optical path for combining the IR source with the X-25 beam.

is typical for high efficiency, thin-film dielectric stack filters. Although not ideal, the filtered beam provides sufficient UV and visible light for solar cells and excellent IR transmission for adding in the balance of the AM0 spectrum. With the cell test plane and the X-25 simulator mounted 90° to each other, the dichroic mirror is mounted at a 45° angle to reflect the blue portion of the X-25 beam onto the cell and allow for additional lights sources from above the cell plane (**figure 4**).

The initial design strategy for the IR source was to pack as many lamps into as small an area as possible and mount the lamps as far from the test plane as practical. This philosophy (in principle) will yield the best collimation angle and beam uniformity. The lamps used are tungsten filament bulbs mounted in a gold reflector. The lamps operate at 12 Volts with an output of 75 Watts and have an average life expectancy of 4,000 hours. The vendor is Gilway Technical Lamp in Woburn, MA. The reflector has a nominal beam angle of 14°. The attempt to pack as many lamps into as small a space as possible, was a rectangular array of 40 lamps. Although a round lamp should pack more tightly in a hexagonal pattern, the lamp holders have a rectangular base and thus the best packing is achieved using a rectangular pattern. This lamp arrangement had one major shortcoming; it required that each lamp have two degrees of pointing control in order to achieve acceptable uniformity. Without this control, the beam had a significant center hot spot. A second design, which capitalizes on the natural radial symmetry of the beam pattern, was designed. Here, the lamps required only one degree of freedom of pointing to achieve acceptable beam uniformity. In this design, 36 lamps are oriented in a radial pattern and each lamp can be pointed along a line that sweeps from center to edge along a radius of the beam. Pointing of each lamp is achieved by mounting the lamp holder to a aluminum block with four spring-loaded screws. The blocks are fastened normal to the lamp mounting plate. The four screws can be adjusted to tilt the lamp housing approximately ±5°. This is enough movement to sweep the beam from center to the outside edge of the test plane. **Figure 5** shows the mounting arrangement for a single lamp. In practice, all the lamps are splayed away from the center to decrease the center beam hot spot.

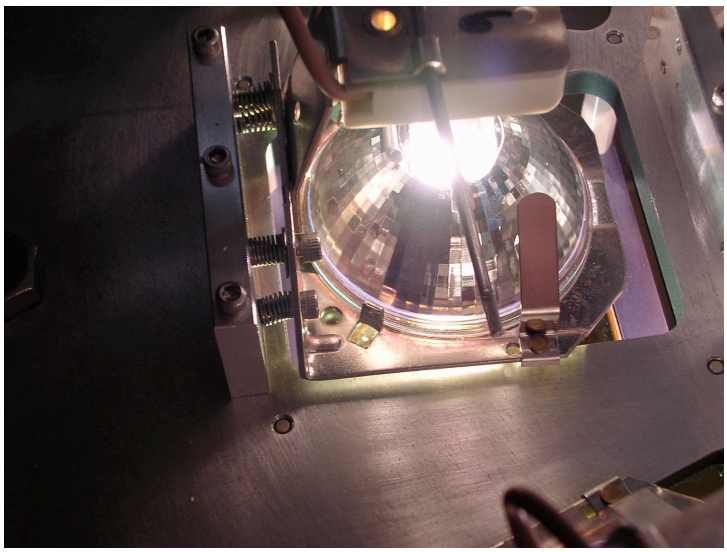

Figure 5) Each IR lamp is mounted on an aluminum block with 4 spring-loaded adjustment screws.

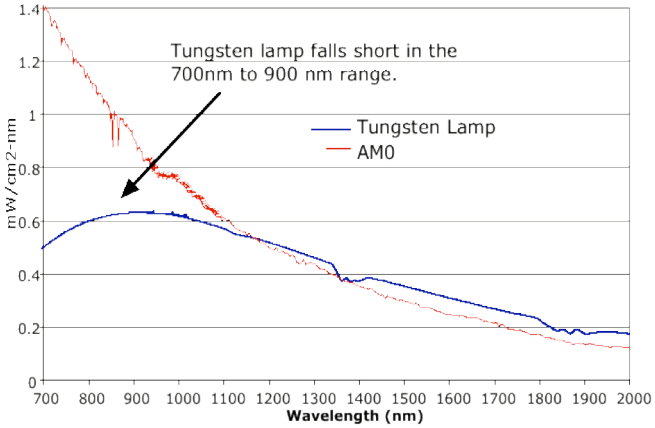

Figure 6) Spectrum of the tungsten lamp compared to AM0.

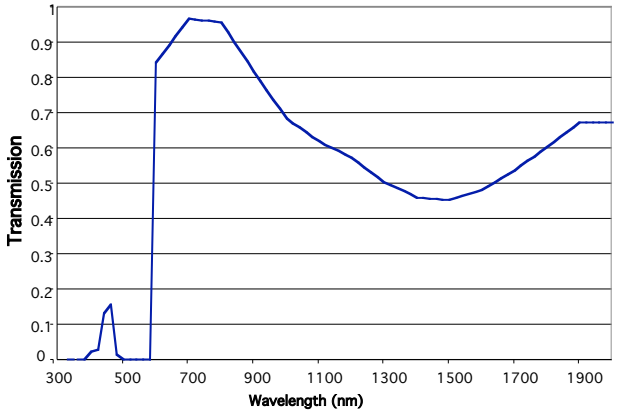

Figure 7) Design of the filter to shape the IR lamp spectrum to match AM0.

The spectrum of an unfiltered tungsten lamp does not adequately simulate the IR portion of AM0. **Figure 6** shows the spectrum of an unfiltered tungsten lamp versus AM0 in the infrared. Note that below 1000-nm the power density of the tungsten lamp drops compared to AM0. This is a critical region of the spectrum for the GaAs junction of a GaAlnP/GaAs/Ge cell. When the intensity of the tungsten lamps is raised to match the GaAs middle cell current, then the Ge cell has 40% excess current! Another filter was designed to shape the tungsten lamps to match AM0. **Figure 7** shows the (calculated) transmission of this filter. The filter is placed between the tungsten lamps and the dichroic mirror. The resulting spectrum is close to AM0, but still needs an additional degree of freedom to perfectly match all three junctions.

A third light source was created by filtering a subset of the 36 tungsten lamps. A non-absorbing filter was designed to transmit only in the region of 700-900-nm. This filtration is optimized for adjusting the current of a GaAs middle cell separate from the germanium or GaInP cell. The filters are placed in front of 6-12 lamps depending on the amount of spectral mismatch of a particular cell (**figure 8**). The filtered lamps are put on a separate power supply and their intensity is controlled independently of the 24 remaining lamps. For the 12 700-900-nm filtered lamps, the lamps are connected as 4 parallel strings of 3 lamps each for a nominal operating voltage of 36 Vdc at 25 Amps. The remaining 24 lamps are wired as 4 parallel strings of 6 lamps, and operate at 72 Vdc at 25 Amps. Using all three light sources, the short circuit current of each reference cell of a GaInP/GaAs/Ge multijunction cell, can be simultaneously matched to their reference values to better than 0.5% in less than 30 minutes set up time. The spectrum of the simulator is shown in **figure 9**.

Figure 8) Photograph showing the 12 filtered lamps of the 36 lamp IR source.

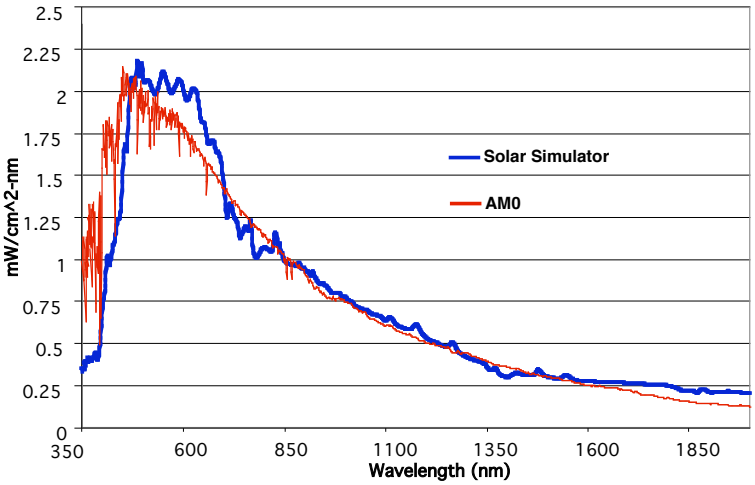

Figure 9) Spectrum of the solar simulator when all three junctions of a GaInP/GaAs/Ge solar cell are properly illuminate, compared to AM0.

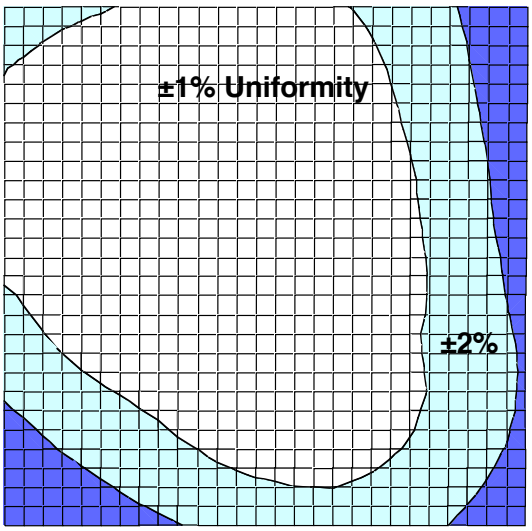

Figure 10) Uniformity of the long IR light source over a 20-cm x 20-cm area. The light blue contour represents the additional area where the uniformity is at least ±2%.

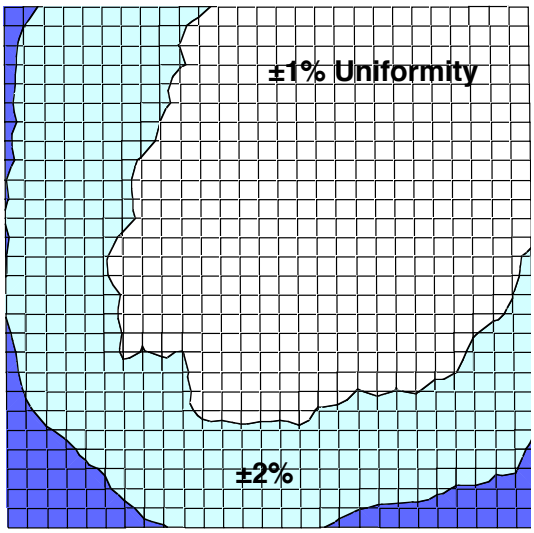

Figure 11) Uniformity of the X-25 Simulator over a 20-cm x 20-cm area.

The collimation half-angle is determined by the angle formed by the radius of the IR lamp cluster and the distance the lamps are located above the test plane. This angle is 7.6 degrees. The uniformity of light intensity in the test plane is most strongly affected by the number of individual lamps that can be articulated to reduce “hot or cold” spots in the beam. All of the lamps contribute to the 700-900-nm portion of the spectrum and therefore the number of lamps is effectively 36 in the 700-900-nm region. The intensity changes made with the 700-900-nm filtered lamps are small (<5%) compared to the overall intensity in the 700-900-nm range and have little affect on the uniformity. In the long IR region (900-1700-nm) the number of lamps is effectively 24. The intensity uniformity of these lamps is ±1% over a large area of a 20-cm X 20-cm test plane as shown in **figure 10**. The uniformity of the X-25 is similar to the IR lamps and is shown in **figure 11**. The intensity maps were made using an X-Y plotter fitted with a photodiode. The method is similar to that used by Spectrolab to characterize the X-25 (X-25 documentation) and at other labs such as National Renewable Energy Laboratory (NREL). The stability of the lamps has not been quantitatively characterized at this time but after an initial 30 minute warm-up period there is no perceptible drift while making measurements over a 4 hour period. The IR lamps are also flicker free, due to the nature of the IR lamp optics and the DC power used.

A schematic figure of the entire system is shown in **figure 12**. For many applications the single source X-25 is all that is required. In such cases, the system can be quickly reconfigured by exchanging the dichroic mirror for a simple aluminized first surface mirror. This also helped preserve the X-25 capability while the new system was being built.

The cost of all the hardware (excluding the X-25 simulator) was 25,000 USD (in 2002). Operating the simulator offers many challenges. There are a number ways to set up the intensity and spectrum of a multi-source simulator. The easiest method is to have separate calibrated reference cells for each sub junction of the test cell. If such cells are not available, then one must either apply spectral correction to existing reference cells that are close in spectral response, or calculate the required spectral intensity from measurements of the spectral response of the test cell and measurements of the simulator’s spectral intensity.

We have successfully converted a Spectrolab X-25 solar simulator into a multi-source simulator capable of precisely matching the required currents in a triple junction GaInP/GaAs/Ge solar cell. The system is relatively inexpensive to impliment and preserves the original functionality of the X-25 as well. It has excellent uniformity as well as good stability and a collimation angle better than ±8°. Future plans for improving the performance, include the addition of another xenon light filtered to provide a boost in the blue region of the spectrum to more closely match AM0.

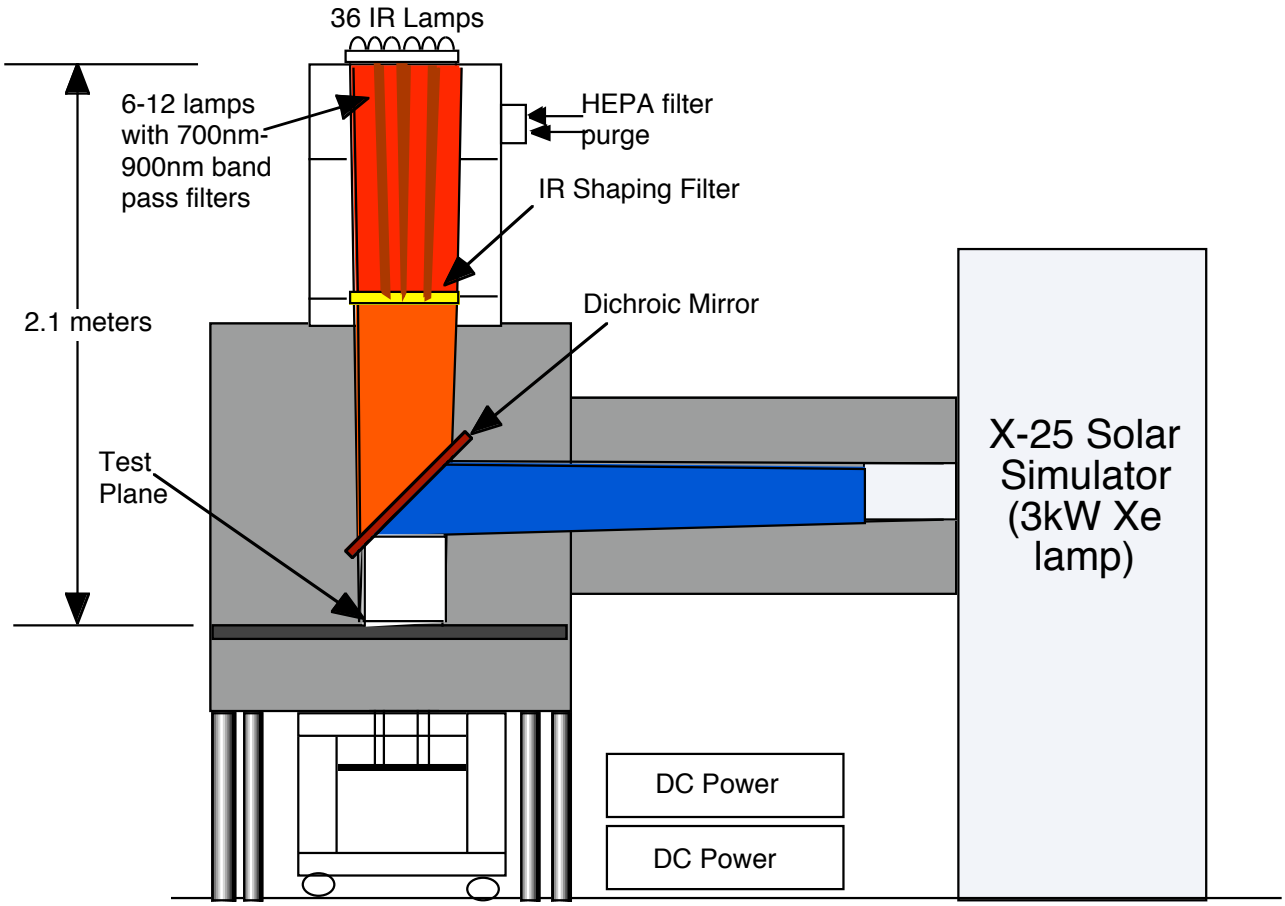

Figure 12) Schematic representation of the multi-source simulator.

References

[1] Solar Cell Standards Group, Energy Conversion Task Group, West Coast Solid State Devices, "Photovoltaic Solar Simulator Specification, American Institute of Electrical Engineers, June 7, 1961, Revised September 5, 1961.

[2] D.B. Bickler, "The Hoffman Solar Simulator," Proceedings of the Solar Working Group Conference (2nd PVSC), Volume II, 6-1 to 6-21, Held, in Washington D.C., Feb. 27 and 28, 1962.

[3] Joseph H. Apfel and Alfred J. Thelen, "A Solar Simulator," Proceedings of the Solar Working Group Conference (2nd PVSC), Volume II, 7-1 to 7-21, PIC-SOL 209/2.1, Held, in Washington D.C., Feb. 27 and 28, 1962.

MEASUREMENT AND CHARACTERIZATION OF CONCENTRATOR SOLAR CELLS II

Dave Scheiman[1], Bernard L. Sater[2], Donald Chubb[3], Phillip Jenkins[1], Dave Snyder[3]
[1]OAI, 22800 CedarPoint Rd, Brookpark, OH 44142
[2]PhotoVolt, Inc., 21282 Woodview Circle,Strongsville, OH 44149
[3]NASA GRC, 21000 Brookpark Rd, Cleveland, OH 44135

Concentrator solar cells are continuing to get more consideration for use in power systems. This interest is because concentrator systems can have a net lower cost per watt in solar cell materials plus ongoing improvements in sun-tracking technology. Quantitatively measuring the efficiency of solar cells under concentration is difficult. Traditionally, the light concentration on solar cells has been determined by using a ratio of the measured solar cell's short circuit current to that at one sun, this assumes that current changes proportionally with light intensity. This works well with low to moderate (<20 suns) concentration levels on "well-behaved" linear cells but does not apply when cells respond superlinearly, current increases faster than intensity, or sublinearly, current increases more slowly than intensity. This paper continues work on using view factors to determine the concentration level and linearity of the solar cell with mathematical view factor analysis and experimental results [1].

INTRODUCTION

Solar cells are designed to convert photon energy directly into electrical energy. The amount of natural sunlight incident on a solar cell is considered the 1 sun power density. Higher than 1 sun power densities achieved using lens or reflectors are concentrated sunlight. The increase in power density or ratio of power density to the 1 sun power density is the concentration level. Efficiency measurement of concentrator solar cells has always been a difficult task due to the lack of equipment available to measure the light power intensity. Most laboratory measurements are done using a Large Area Pulse Solar Simulator (LAPSS) with data being taken in 1-2 milliseconds. Measuring the power density/flux under these conditions requires a very fast thermopile or pyroelectric device, if any exist. Consequently, determining the power density or light concentration ratio on a solar cell is the ratio of the measured short circuit current (I_{SC}) to the short circuit current at 1 sun. This process can be inaccurate for solar cells that do not behave linearly with power density.

One way to obtain power density/flux is by using radiative energy transfer equations and calculating the view factor between the source and the test sample. Energy radiating from a source incident on a surface at some fixed distance away can be characterized by the view factor between the source and the surface. Knowing the shape of the source and the incident surface and using numerical integration, the view factor can be calculated. The view factor has always been used in determining the efficiency of thermophotovoltaic energy conversion systems [2]. The view factor ratio between a location with a known power density and some other location can be used to determine the concentration (change in power density) by ratio of the view factors. When dealing with a point source, the view factor varies as $1/r^2$ where r is the distance between the source and the surface. The sun is modeled as a point source because of its distance from the earth, closer objects can't use this approximation.

THE VIEW FACTOR

The view factor is the fraction of the total energy emitted by one surface, the source, that is directly incident on another surface. As the source and surface move farther apart or off-axis from each other, the view factor becomes smaller. A point source with the incident surface forming a full hemisphere surrounding that source has a view factor of 1 because the total energy from the source is incident on the surface. Additionally, the view factor between a point source and the target surface decreases proportionally with the square of the distance between them. Calculating the view factor between two finite shaped surfaces requires numerical integration of both surfaces. The general form of the view factor calculation is defined by the following equation [3]:

$$\text{View Factor} \quad F_{AA'} = \frac{1}{\pi A'} \int_A dA \int_{A'} \frac{\cos\theta \cos\theta}{s^2} dA'$$

Where A and A' are the two surfaces, s is the distance between the two surfaces and ø are the respective angles between a point on surface A and a point on surface A' and vice versa. Generating and solving this equation for specific surface geometries is beyond the scope of this paper.

View Factor Solution for LAPSS

For the case described here, the source is the Spectrolab LAPSS100, and the incident surface is a planar solar cell. The source in the LAPSS is a Xenon arc lamp that generates a pair of 15 cm. arcs as shown in figure 1. To simplify the view factor calculation, the light source is modeled as a rectangle with a finite length and width, assumed to be uniform and isotropic. The LAPSS system contains two identical arc lamps which fire simultaneously. By placing the solar cell (incident surface) symmetrically centered between the two lamps only one view factor is calculated, and the resulting view factor for both lamps is simply twice that of the single lamp.

Using this model, a drawing of the test geometry is made as shown in figure 2. There are two identical sources, offset from the center line of the test solar cell. Because of the symmetry of the test setup, only one lamp needs to be used to calculate the view factor which is identical for the second lamp. These two view factors can be added to get the actual view factor. The lamp source is surface A_1 in the xy plane, the solar cell surface is A_2 in the □□ plane. The distance between the two planes is z and the distance between points the two surfaces is s with angles □ $_{1,2}$ between them. Based on this model, discrete coordinates of the rectangular endpoints can be obtained for the view factor calculation. The actual view factor calculation is shown in appendix A, it is derived from two parallel and perpendicular rectangular finite surfaces.

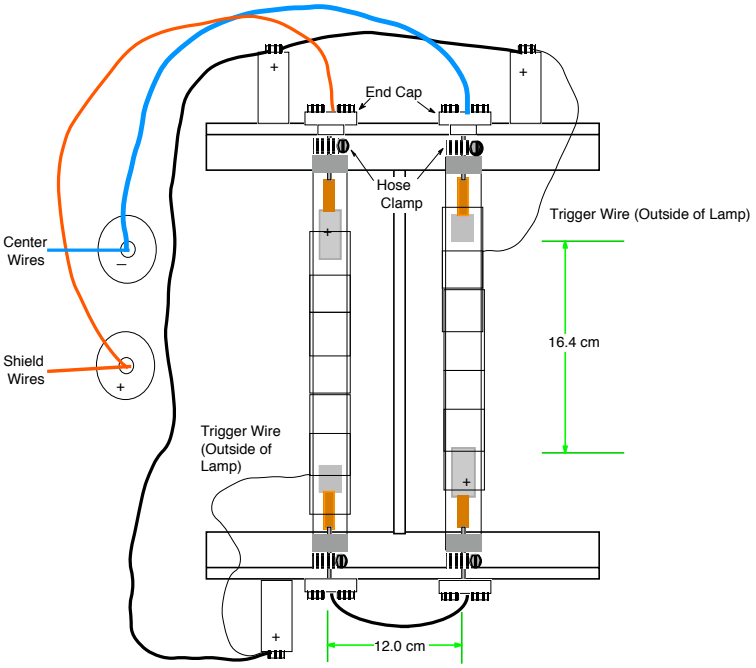

Figure 1 LAPSS lamp setup

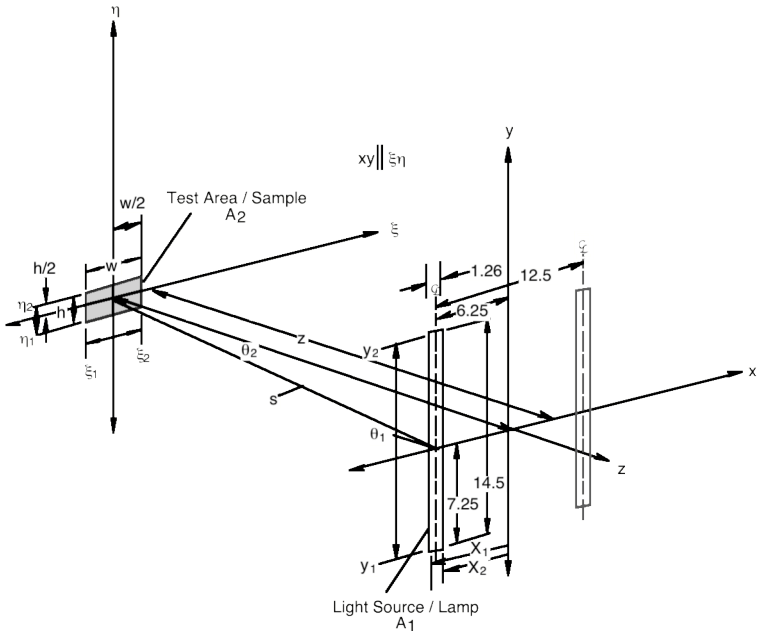

Figure 2 LAPSS test geometry

The viewfactor is calculated for a range of distances z from the source using the numerical summation from appendix A [4]. By plotting the ratio of the view factor at the farthest distance to shorter distances a graphical representation of this calculation is compared to a $1/r^2$ and shown in Figure 3. The concentration level of light on the solar cell is obtained by the following steps:

STEP 1: Measure the solar cell performance under a known or calibrated light source at 1 sun (this can be done in a solar simulator other than the LAPSS with a standard cell). Light level of the simulator is adjusted using a calibrated primary or secondary reference cell.

STEP 2: Set up a coordinate system for the cell and the LAPSS or concentrating light source, select a distance z between the two surfaces farthest away as a 1 sun starting point. The coordinate system is based on figure 2.

STEP 3: Using the coordinates in step 2 calculate a range of View Factors from z and shorter, ratio these view factors to the view factor at z to get the concentration level. A computer program can be written for this step.

STEP 4: Set up the solar cell at distance z from the light source(s), measure and adjust the light source to obtain the 1 sun numbers from Step 1.

STEP 5: Using the data from step 3, move the solar cell closer to the light source to various distances as denoted in Step 3, these measurements are at the calculated concentration levels.

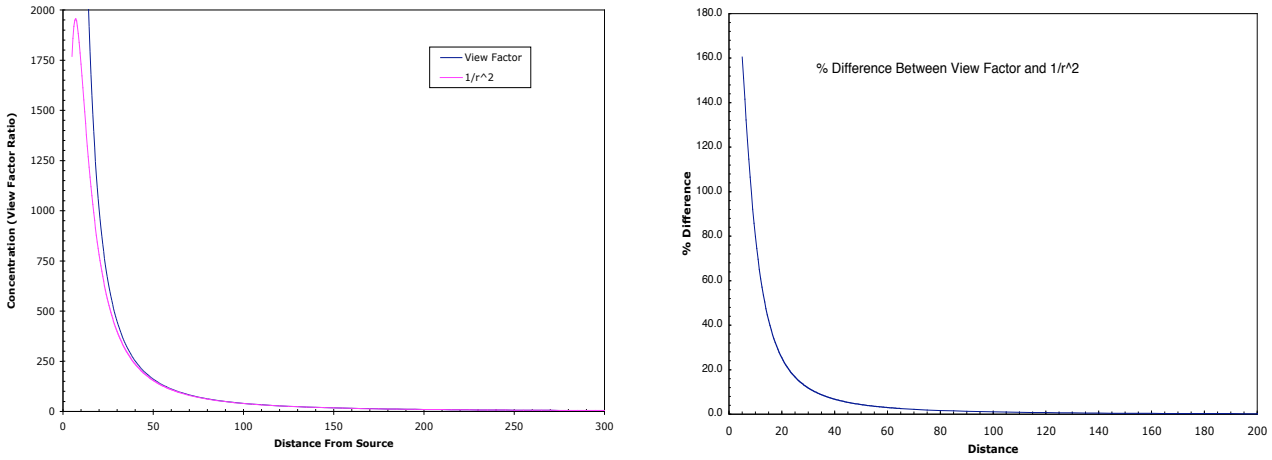

Figure 3. Concentration by View Factor Ratio

The data used in figure 3 was for a 2 x 2 cm. solar cell, the light source is the Spectrolab LAPSS and the 1 sun measurement was made at a distance of 635 cm. The view factor was calculated every 5 cm. going into the source.

THE ARC LAMP

The arc lamp is the most optimum single source solar simulator because of its close temperature match to the solar spectrum. The disadvantages are that the arc lamp's spectrum has many spikes due to the emission lines of the gas in the lamp. The Spectrolab LAPSS system was designed to minimize the spikes and maintain good uniformity at a 2 m x 2 m 1-sun plane within ±2%[5]. In order for the view factor calculation to be accurate, the light source is assumed to be uniform and isotropic. The uniformity of the lamp can be generated from knowledge of the plasma characteristics of the arc itself [6]. Arc lamps tend to be cooler near the electrodes but have relatively constant temperature across the arc. To minimize this temperature effect, the lamps were baffled 1 cm. above and below the electrodes. As can be seen in the photos, the arc completely fills the interior area of glass between the electrodes, this is a result of electrode design, and insures ionization of all of the gas, resulting in uniform light generation. The source is also isotropic, emitting light equally in all directions, however half of the lamp diameter is not used. Any reflective optics or lenses used on this lamp would enhance the light intensity but also complicate the view factor calculation.

High speed photographs of the lamp during a flash are shown in figure 4. As can be seen from these photographs, the arc fully saturates the glass housing and decays to a thin line. The solar cell performance is only obtained during the full light portion of the arc with the best uniformity. This full light section of the arc also has the flattest intensity and can last a few milliseconds. It is during these few milliseconds that the solar cell is characterized, a monitor cell is also used to adjust for slight intensity variations within the flash and between consecutive flashes. Typically, intensity between flashes of the arc lamp are controlled to be less than .25% which is needed for measuring the cell at different positions or concentration levels.

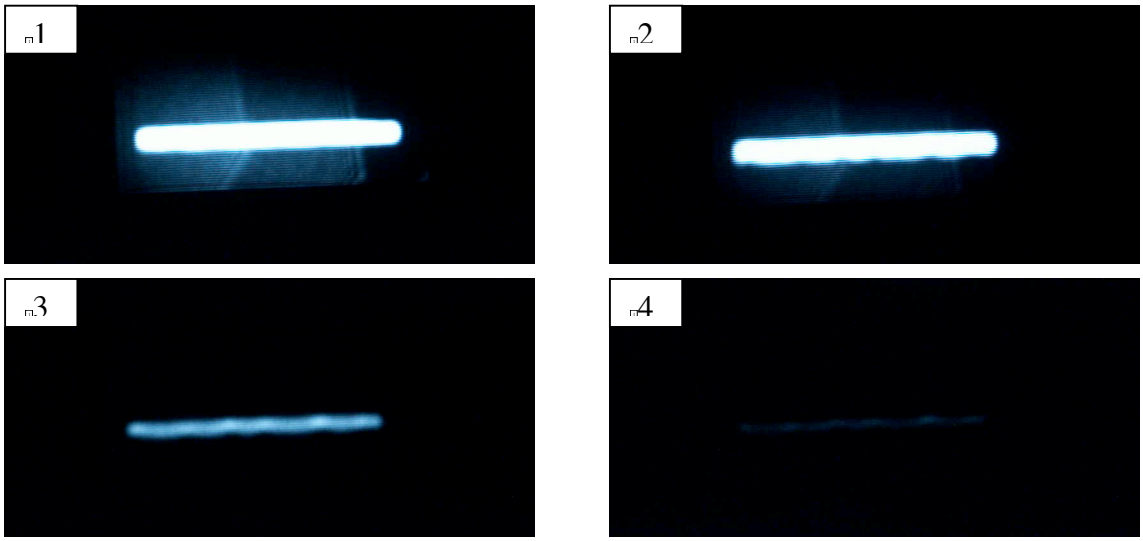

Figure 4 Arc Lamp Sequence (2000 frames/sec) frames 57,60, 61, & 62.

TEST

Several cells were measured at 1 Sun AM0 in a solar simulator using a calibrated reference cell. A LAPSS100 was used for a light source, assumed to be uniform and isotropic. The LAPSS light intensity was adjusted for 1 sun intensity at a fixed distance. Using the view factor ratio, the cells' current-voltage characteristics were measured at a variety of concentrations. Arc lamps exhibit uniformity in the center portion of the arc away from the electrodes which tend to be cooler. Therefore the lamps were baffled 1 cm. from either electrode. No additional optics were used with the lamps which would affect the view factor calculation. Based on the mathematical analysis defined in section 2, a test was set up. Four different solar cells were selected to cover a range of performance characteristics; Triple Junction InGaP/GaAs/Ge 1 cm. x 4 cm. from two different vendors. These cells were designed as space concentrator cells to operate at <20 suns. Each of these cells were characterized at 1 Sun AM0 using an appropriate reference standard.

All tests were performed at NASA Glenn Research Center. The Spectrolab LAPSS100 system performs IV curves on solar cells/arrays in 1-2 milliseconds. It has a 12-bit A/D measuring cell voltage, current, and monitor cell current simultaneously. IV curves consist of from 20 to 100 data points. The monitor cell was placed in a fixed position within the beam path, its location was selected to monitor flash intensity and not interfere with the test set up.

Test Setup

Before the test could be performed, several modifications had to be made to the existing LAPSS facility to minimize any measurement errors. The LAPSS data acquisition system was calibrated with special consideration for the scale range change accuracy. The lab was painted black with additional black cloth and drapes added to eliminate any stray light. A rail system was added on the centerline between the two lamps. A metric ruler was attached to the rail as an indicator of the distance from the lamps to the solar cell test plate. The solar cell test plate was suspended from the rail so that its center was aligned to the center of the lamps. These changes are shown in figures 5 and 6.

Test Procedure

The solar cell area was measured and its dimensions were used to calculate the view factor over a range of distances from the lamp. The lamps were fired 20 times with one minute wait intervals between flashes to warm up the electronics and lamps.

The solar cells were mounted to the test plate and set at a distance of 635 cm. Distances are estimated to be within 1 mm. Lamp intensity (pulse network voltage) on the LAPSS was adjusted until the solar cell I_{SC} matched the 1 sun AM0 measured previously. The monitor cell nominal current was recorded and used for a

correction to normalize the intensity variation. This test was repeated 5 times with the monitor cell correction less than 0.25% for each of the IV curves to eliminate subtle variations due to lamp intensity and repeatability.

After the 1 sun measurement, the test plate was moved to the ~2 sun position and the tests were repeated 5

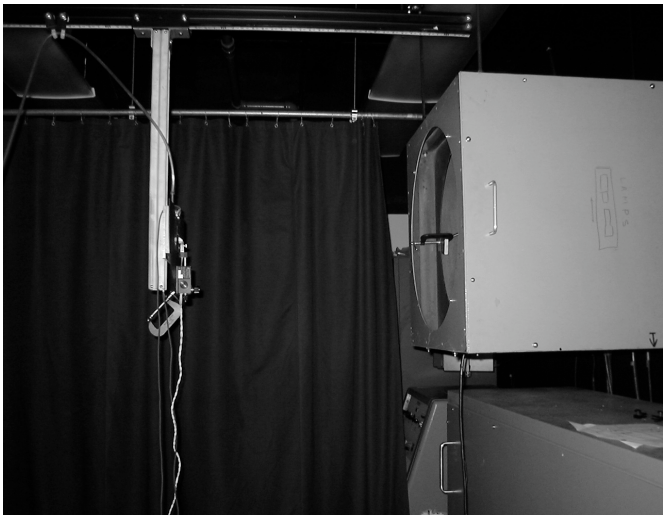

Figure 5. LAPSS test set up

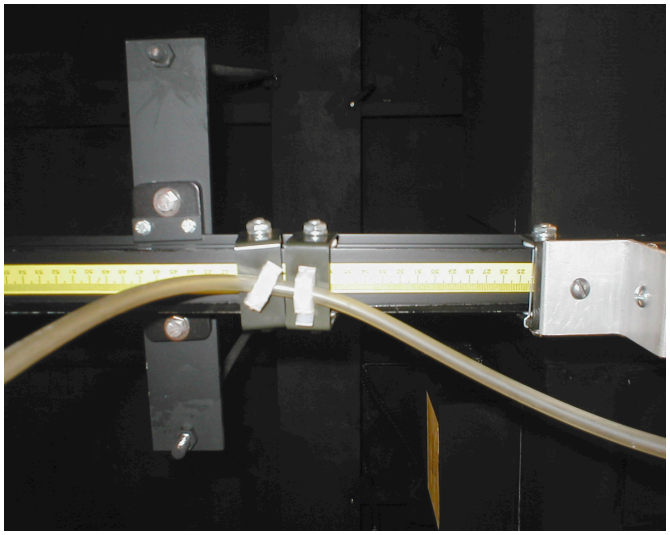

Figure 6. Test plate rail system

times as before. No adjustments were made beyond the original settings. The test plate was then moved in to a 5 sun position and the IV curves were measured. Testing was continued at other concentration levels. With this setup, a maximum ~62 suns is just outside the face of the lamp housing.

Test Results

The I_{SC} of a solar cell is used for setting the light intensity and calibration. The 5 sets of data points at each

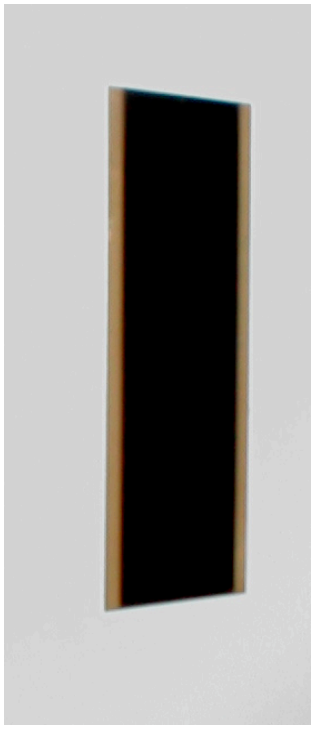

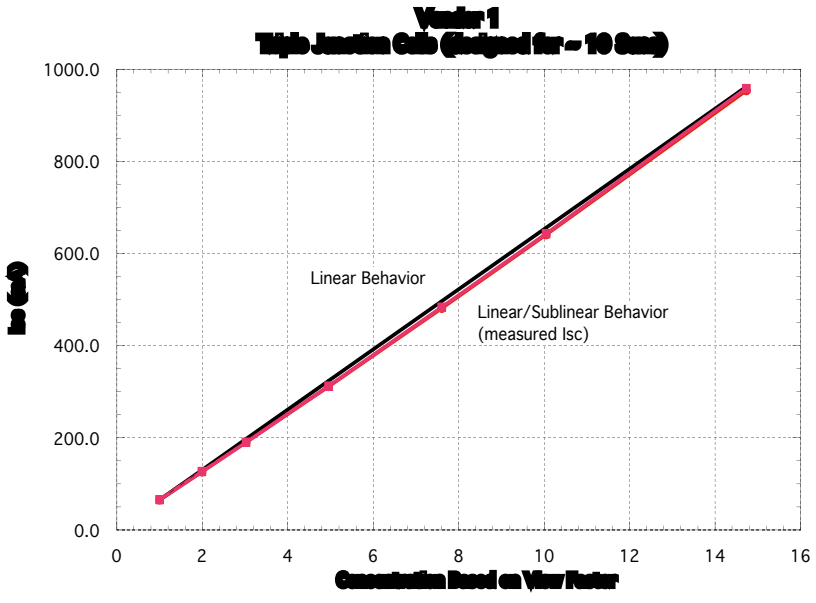

Figure 7 Vendor 1 Solar Cell Data

concentration level were averaged and then the I_{SC} is plotted as a function of the concentration level. The test results are shown in figures 7-8. A black line is added to the plot to depict a “linear” behavior of the I_{SC} as commonly used in concentrator measurements. None of the cells exhibited a true ‘linear“ response.

The cells plots shown depict either slightly superlinear or sublinear behavior with concentration. Other performance parameters such as Fill Factor, Maximum Power, and Open Circuit Voltage (V_{OC}) all increased as expected with increases in intensity. Details of the cell performance are not presented here as these test are primarily for proof-of-concept.

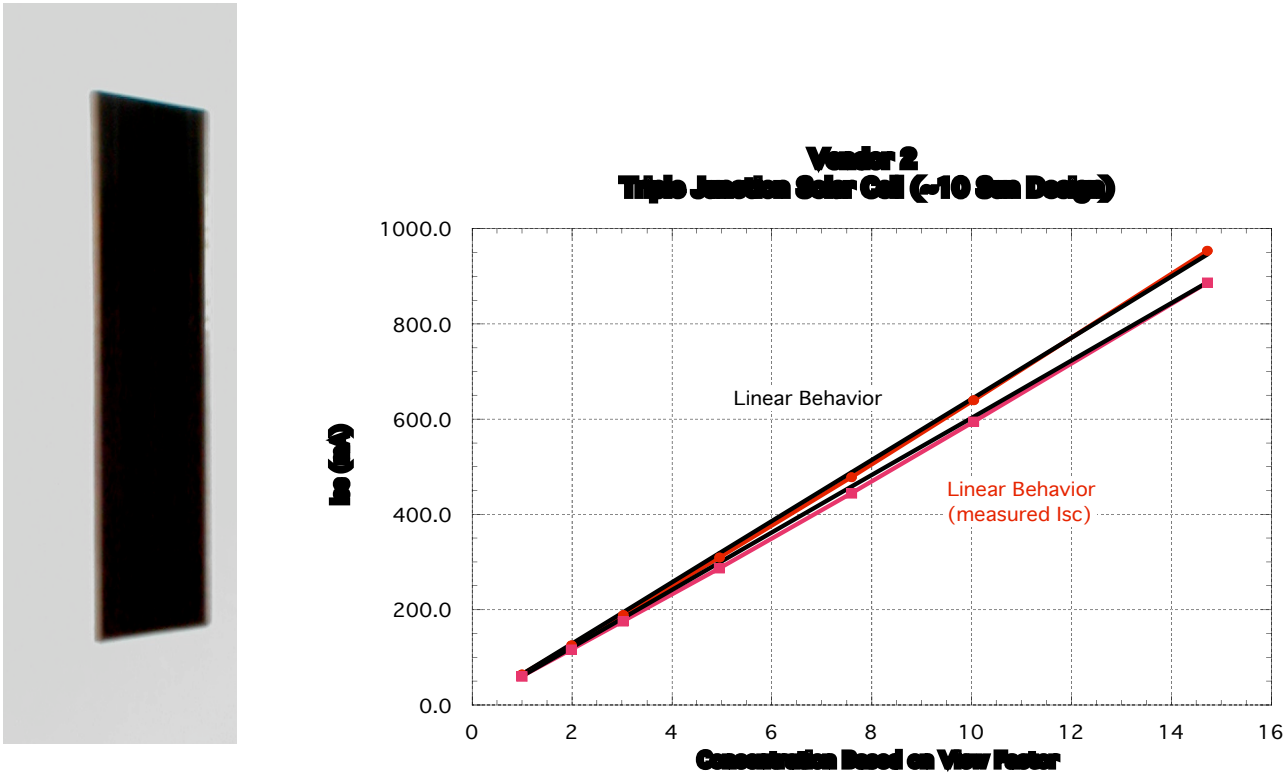

Figure 8 Vendor 2 Cell Data

CONCLUSION

This paper is the second publication of this method. It is intended to provide a simple means of calculating the view factor for a given source and sample and account for variations in light intensity at a given distance from the light source(s). The mathematical calculations include the derivation and integration required to solve for the view factor, its solution, and a way of applying that calculation to test systems. Knowledge of the light source is not required. Once the view factor calculation is applied, the value was used to determine the intensity at a given distance from the source. 4 solar cells were measured at a variety of intensities. The results show that this method is viable for measuring and calibrating concentrator cells. Solar cells have been tested to concentrations in excess of 500 suns.

These tests indicate that most solar cells do not exhibit a proportional 1:1 short circuit current behavior with intensity. Solar cells and arrays measured under concentration determined by the ratio of I_{SC} are suspect to the accuracy of the concentration level. Multi-junction cells with inherent current limiting due to spectral separation and current mismatch of junctions can exhibit even greater variation in linearity. This test eliminates the errors

associated with determining the concentration by using mathematical analysis. Errors introduced with this method include assumptions about the uniformity and geometry of the source, and positioning of the test cells.

A need for this measurement technique has arisen from the fact that Vertical Multi-Junction (VMJ) Cells exhibit a superlinear behavior, having poor performance at 1 sun [7]. Other cells designed for high intensity also experience this non-linearity. There are also no known reliable standards for calibration of solar cells at high intensity, it is hard to assume that the current of a cell remains linear over many orders of magnitude in concentration especially when series resistance, minority carrier lifetimes, and recombination centers change with intensity.

Refinement of this method can be implemented for better accuracy at higher concentrations if so desired. The model of the arc lamp as a rectangular source could be changed to reflect the actual shape of the lamp, all depending on how far the modeler wants to go. Dimensional accuracy of the test plate could also be improved, high precision optical rails with fine positioning can help to avoid errors at high-intensity. Positioning errors tend to increase with higher concentration levels, at 60 suns a 1 cm. difference in position changes the intensity by nearly two suns.

It is the intention of this paper to provide a demonstration of a method to calibrate concentrator cells. NASA GRC facility is available for testing of cells/arrays with the limitations of the 50 Volts and 20 Amps.

REFERENCES

[1] D. Scheiman, B. L. Sater, D. Chubb, P. Jenkins, “Measurement and Characterization of Concentrator Solar Cells”, 3P-C3-76, 3rd World Conference on Photovoltaic Energy Conversion, May 2003.

[2] B. Good and D. Chubb, “Effects of Geometry on the Efficiency of TPV Energy Conversion”, Thermophotovoltaic Generation of Electricity, Third NREL Conference, 487 (AIP, 1997)

[3] R. Siegel and J. Howell, “Thermal Radiation Heat Transfer”, 2nd Edition, (McGraw-Hill, 1980)

[4] J.R. Ehlert and T.F. Smith, “View Factors for Perpendicular and Parallel Rectangular Plates”, Journal of Thermophysics, Volume 7, No. 1: Technical Notes, p173-175, March 1992.

[5] R.L. Mueller, “The Large Area Pulsed Solar Simulator (LAPSS), JPL Publication 93-22, Rev A. , July, 1994

[6] S. C. Haydon, “An Introduction to Discharge and Plasma Physics”, 217-226, Department of University Extension, University of New England, 1964 (Armidale, N.S.W., Australia).

[7] B. Sater and N. Sater, “High Voltage Silicon VMJ Solar Cells for up to 1000 Suns Intensities”, 29th IEEE Photovoltaics Specialists Conference, 1019,

APPENDIX A : View Factor (Rectangle to Rectangle)

A view factor is defined as the fraction of area in the total field of view (180° hemisphere) of one surface as seen from another surface, its value is a maximum of 1. The general equation for the view factor between two finite areas is;

$$F_{1\to 2} = \frac{1}{A_1} \int_{A_2} \int_{A_1} \frac{\cos\theta_1 \cos\theta_2}{\pi s^2} dA_1 dA_2 \qquad 1$$

where F_{1-2} is the view factor from finite surface A_1 to finite surface A_2. Angles θ_1 and θ_2 are the angles between the two surfaces from a point dA_1 to dA_2 and vice versa. Applying the general equation 1 to two surfaces which are parallel rectangles of different size and not coaxial (see figure 1), the following substitutions can be made from this graphical layout.

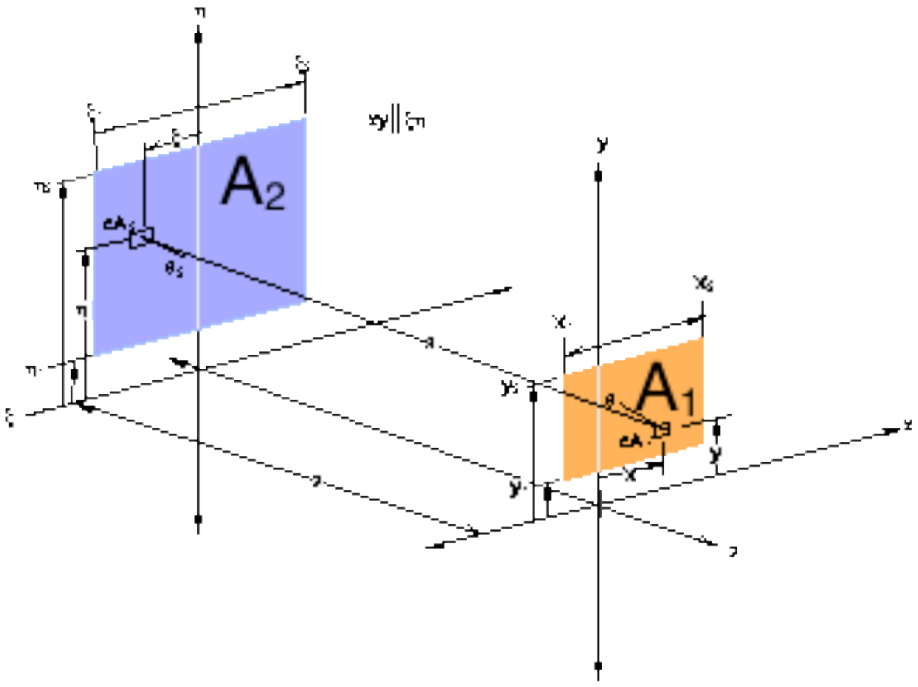

$$s^2 = z^2 + (x - \xi)^2 + (y - \eta)^2 \qquad \cos\theta_1 = \cos\theta_2 = z/s \qquad 2$$

by substituting the above, equation 1 can be re-written to the following integral based on the four corner coordinate terms (x, y) for the source rectangle A_1, and (ξ, η) for the rectangle A_2. The integral is in the following form:

$$G(x,y,\xi,\eta) = \frac{z^2}{\pi} \int_{\xi} \int_{\eta} \int_{y} \int_{x} \frac{x\eta}{\left[z^2 + (x-\xi)^2 + (y-\eta)^2\right]^2} dx dy d\xi d\eta \qquad 3$$

and solving equation 3 using symbolic mathematics, the final solution becomes a series of summations based on the corner coordinates (x_1,y_1; x_1,y_2; x_2,y_1; x_2,y_2) for A_1 and (ξ_1, η_1; ξ_1, η_2; ξ_2, η_1; ξ_2, η_2) for A_2 of the parallel rectangles. The location of the axis for either coordinate system is random, as long as both rectangles are parallel to each other and their relative positions do not change. This solution is shown below;

$$F_{1\to 2} = \frac{1}{(x_2 - x_1)(y_2 - y_1)} \sum_{i=1}^{2}\sum_{j=1}^{2}\sum_{k=1}^{2}\sum_{l=1}^{2} (-1)^{(i+j+k+l)} G(x_i, y_j, \zeta_k, \eta_l) \qquad 4$$

where

$$\text{G(x,y,}\zeta\text{,}\eta\text{) is : } G = \frac{1}{2\pi}\left\{ \begin{array}{l} (y_j - \eta_k)\left[(x_i - \zeta_l)^2 + z^2\right]^{1/2} \tan^{-1}\left[\dfrac{y_j - \eta_k}{\left[(x_i - \zeta_l)^2 + z^2\right]^{1/2}}\right] \\ + (x_i - \zeta_l)\left[(y_j - \eta_k)^2 + z^2\right]^{1/2} \tan^{-1}\left[\dfrac{x_i - \zeta_l}{\left[(y_j - \eta_k)^2 + z^2\right]^{1/2}}\right] \\ - \dfrac{z^2}{2}\ln\left[(x_i - \zeta_l)^2 + (y_j - \eta_k)^2 + z^2\right] \end{array}\right\} \qquad 5$$

A computer program can be written to calculate the view factor. Please note that double precision numbers should be used to avoid errors, large numbers are added and subtracted with small differences in the lower digits, single precision does not have the resolution to retain these small differences.

Example:

Rectangle A_1 has corners located at coordinates **(-2,1), (-2,10), (4,1), (4,10)**
Rectangle A_2 has corners located at coordinates **(-3,2), (-3,11), (3,2), (3,11)**
They are the same 6 x 9 size except offset by 1 unit in both axes.

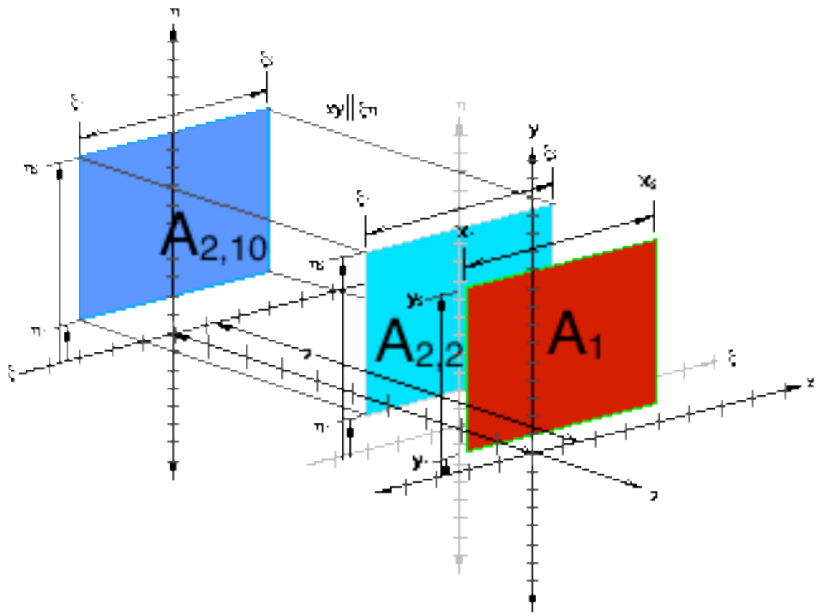

Calculate the view factor if they are separated by 2 and 10 units, **z = 2, 10**

Plugging the coordinates into the view factor calculation equations 4 and 5 and performing the summation results in the view factors: **$F_{1\text{-}2}$ (z=2) = .54926 and $F_{1\text{-}2}$ (z=10) = .12407**

HIGH-ALTITUDE AIR MASS ZERO CALIBRATION OF SOLAR CELLS[1]

James R. Woodyard
Wayne State University, Detroit, Michigan

David B. Snyder, NASA Glenn Research Center
Cleveland, Ohio

ABSTRACT

Air mass zero calibration of solar cells has been carried out for several years by NASA Glenn Research Center using a Lear-25 aircraft and Langley plots. The calibration flights are carried out during early fall and late winter when the tropopause is at the lowest altitude. Measurements are made starting at about 50,000 feet and continue down to the tropopause. A joint NASA/Wayne State University program called Suntracker is underway to explore the use of weather balloon and communication technologies to characterize solar cells at elevations up to about 100 kft. The balloon flights are low-cost and can be carried out any time of the year. AM0 solar cell characterization employing the mountaintop, aircraft and balloon methods are reviewed. Results of cell characterization with the Suntracker are reported and compared with the NASA Glenn Research Center aircraft method.

INTRODUCTION

It is important in characterizing solar cells for use in space-power applications that the spectral irradiance of the calibration-light source is within a percent of the spectral irradiance of air mass zero conditions (AM0). Spectral irradiance differences greater than a few percent can result in calibration errors; the magnitude of the errors depends on the structure of the solar cell. In the case of single-junction cells, the current-voltage characteristics are not very sensitive to small differences in the spectral irradiances of calibration-light sources because the spectral response is not sensitive to spectral irradiance. The current in a single-junction solar cell under AM0 normal incidence operating at a voltage V is given by

$$I_o(V) = \int_{\lambda 1}^{\lambda 2} S_o(\lambda) R(\lambda, V) d\lambda \tag{1}$$

where $S_o(\lambda)$ is the absolute AM0 spectral irradiance of sunlight and $R(\lambda, V)$ is the spectral response of the cell at wavelength λ and voltage V. In the ideal case, the spectral response is independent of the irradiance of the light source. The spectral response depends on the opto-electronic properties of the materials used in the fabrication of the cell that include, but are not limited to, the wavelength dependence of the optical absorption coefficient; optical band gap, material thickness, doping, temperature and quality; and carrier mobility and lifetime. $\lambda 1$ and $\lambda 2$ are the lower and upper cut-off wavelength values where the spectral response no longer contributes to cell current.

The spectral irradiance of laboratory-based solar simulators is different than the AM0 spectral irradiance. The simulator is set to “AM0” intensity by adjusting the intensity to produce the short-circuit current in a standard cell,

[1] This work was supported in part under NASA Grant NAG3-2801.

i.e., a cell calibrated under AM0 conditions. This approach may be used because the spectral response of single-junction solar cells is somewhat insensitive to spectral irradiance. Adjusting the intensity of the simulator will compensate for spectral irradiance differences when compared to AM0 over the range of the spectral response of the cell. The adjustment produces a spectral irradiance that is larger than AM0 in some regions of the spectrum and smaller than AM0 in other regions of the spectrum. Following adjustment of the simulator intensity, cells may be characterized under "AM0" conditions. This method may be used as long as two conditions are met. First, it is necessary that the simulator is stable, meaning that spectral irradiance remains constant during the measurements on the standard cell and the cells to be characterized. Second, the voltage dependence of the spectral responses of the standard cell and cells to be characterized must be the same and not influenced by differences in the spectral irradiances of the solar simulator and AM0. The method requires stable standard cells for each of the types of single-junction cells to be characterized. Laboratory-based "AM0"characterization of single-junction solar cells has been carried out for many years with good results using this method.

The evolution of solar-cell technology for space applications has resulted in "state-of-the-art" cells with four and five junctions in series. Each junction is designed with a spectral response matched to one region of the spectral irradiance of AM0 in order to optimize the efficiency of solar cells. The current in a four-junction solar cell operating at a given voltage is given by:

$$I_o(V) = \int_{\lambda 1}^{\lambda 8} S_o(\lambda) R(\lambda, V) d\lambda \text{ and} \tag{2}$$

$$I_o(V) = \int_{\lambda 1}^{\lambda 2} S_o(\lambda) R_1(\lambda, V_1) d\lambda = \int_{\lambda 3}^{\lambda 4} S_o(\lambda) R_2(\lambda, V_2) d\lambda = \int_{\lambda 5}^{\lambda 6} S_o(\lambda) R_3(\lambda, V_3) d\lambda = \int_{\lambda 7}^{\lambda 8} S_o(\lambda) R_4(\lambda, V_4) d\lambda \tag{3}$$

where the variables in Equation 2 are the same as in Equation 1 except $\lambda 1$ and $\lambda 8$ are the lower and upper cut-off wavelength values, above and below which the spectral response is negligible and no longer contributes to cell current. The spectral response in Equation 2 characterizes the overall operation of the four junctions in optical absorption and carrier transport. However, the spectral responses and voltages in Equation 3, $R_i(\lambda, V_i)$ and V_i respectively, are subscripted to show that they are different for each of the four junctions. The voltage across the cell is equal to the sum of the voltages across each of the four junctions, namely, $V = \sum_{i=1}^{i=4} V_i$. The wavelength ranges on each of the integrals, in the most general case, will overlap since it is not possible to fabricate materials with sharp wavelength cut-offs. Equation 3 shows the series nature of the current in multi-junction solar cells, namely, the current is the same in each of the junctions.

The sensitivity of a four-junction solar cell to spectral irradiance can be illustrated with an example. Consider a cell that has been optimally designed for AM0 is to be characterized with a solar simulator. Assume the solar simulator has a spectral irradiance that is less than AM0 in the $\lambda 1$ and $\lambda 2$ wavelength range and the same as AM0 in the other three wavelength ranges shown in Equation 3. The lower spectral irradiance will result in less current in the junction optimized for the $\lambda 1$ and $\lambda 2$ wavelength range which in turn will limit the current in the cell due to the series nature of the four junctions. Equation 3 shows that the current reduction in the four junctions must be accomplished through changes in spectral responses of the other three junctions; this is the case because the spectral irradiances in the other three wavelength ranges are assumed to be the same as AM0. The collective interaction of the four junctions will result in redistribution of the cell voltage across the four junctions, which in turn changes the spectral responses of the four junctions and the cell current.

The role of the interaction of four junctions in the operation of a multi-junction solar cell, as compared to a single-junction cell, can be illustrated with an example. Assume the average spectral irradiance and the average spectral response are the same in the four wavelength regions in Equation 3. A one percent decrease in the spectral irradiance relative to AM0 over the $\lambda 1$ and $\lambda 2$ wavelength range will result in about a one percent decrease in the cell short-circuit current. A single-junction junction solar cell that responds in a similar fashion

over the $\lambda 1$ to $\lambda 8$ wavelength range will experience only a 0.25 % decrease in short-circuit current. The reason is a one percent decrease in the integrated spectral irradiance over the $\lambda 1$ and $\lambda 2$ wavelength range in the multi-junction cell corresponds to a 0.25 % decrease in the integrated spectral irradiance over the $\lambda 1$ to $\lambda 8$ wavelength range in the single-junction cell

A calibration procedure for multi-junction solar cells that uses a standard cell to set a solar simulator to "AM0" intensity may result in data that are not useful in optimizing the design of a test cell for space power generation. Assuming the voltage dependence of the spectral responses of each of the junctions in the standard and test cells are the same under the simulator "AM0" conditions, the junctions may be operating under conditions that are vastly different than AM0 conditions. It is possible that the test cell current-voltage characteristics measured under "AM0" conditions may not be useful in optimizing the cell design to improve efficiencies at the one percent level. Moreover, the complex nature of the interaction of the junctions does not lend itself to the use of an optical technique to compensate for the deficiencies in the "AM0" spectral irradiance.

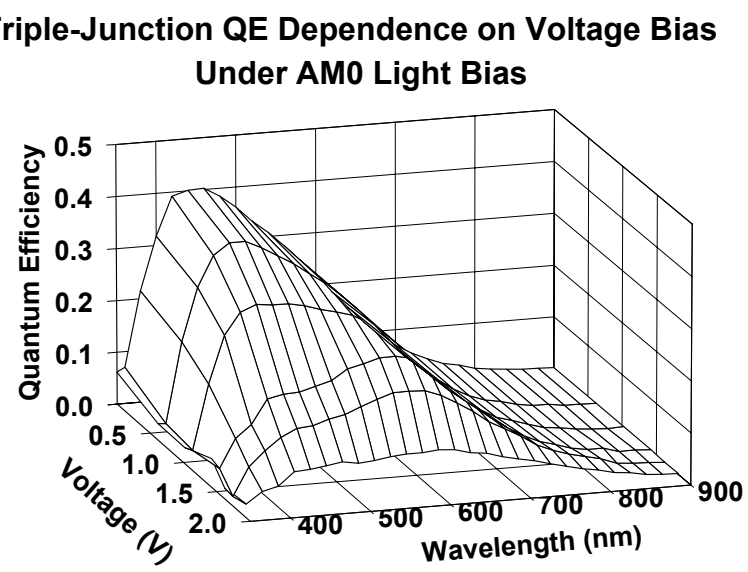

Figure 1. Dependence of quantum efficiency of an a-Si:H alloy-based triple-junction thin-film solar cell on forward bias [1]

The differences in the "AM0" and AM0 spectral irradiances are more problematic at the maximum power point than short-circuit conditions. The reason is the electrostatic potential barriers in each of the junctions are relatively small at the maximum power point as compared to short-circuit current conditions. Redistribution of voltages across the junctions can produce relatively large changes in the electrostatic potential barriers and produce major changes in the spectral responses of the junctions. Figure 1 shows the effect of forward bias on the quantum efficiency of a solar cell [1]. The solar cell is a triple-junction a-Si:H alloy-based thin-film solar cell that was illuminated with a solar simulator with an AM0 spectral irradiance. The spectral irradiance was within one percent of AM0 in the wavelength range where the spectral response contributed to cell current. The figure shows the maximum quantum efficiency is at a wavelength of about 450 nm, serving as evidence that the top junction in this particular cell was limiting the current of the cell under short-circuit conditions. The maximum in the quantum efficiency shifted from 450 to 600 nm as the forward bias approached the maximum-power point showing that the middle and bottom junctions limited the cell current. The quantum efficiency of the cell changed markedly when the spectral irradiance of the simulator was altered [1]. A history of particle irradiation can also have a large effect on the dependence of the quantum efficiency of multi-junction cells on forward bias thereby further complicating the optimization of design of cells for space power generation in radiation environments.

It is clear that the voltage dependence of the spectral responses of multi-junction solar cells complicates optimization of cell design. While there are characterization methods that make it possible to use solar simulators in advancing the multi-junction solar cell technology, the series nature of the cells places more demands on the need for standard cells characterized under AM0 conditions. AM0 conditions are available only in space; near AM0 conditions can be achieved at altitudes in excess of 100,000 ft. The demand for greater access to AM0, and the costs associated with AM0 calibration, has generated interest in exploring lost-cost methods for AM0 solar cell calibration. The NASA supported Suntracker program is an attempt to meet this challenge.

AM0 SOLAR CELL CALIBRATION MEHTODS

Efforts to develop new methods for AM0 calibration of solar cells should be founded in an awareness of current calibration methods, a knowledge of fundamental principles, and possible shortcomings of existing methods. Reviewing analyses of data collected by various methods is also an instructive way to gain a better understanding of the methods. Mountaintop, aircraft and balloon-based methods for AM0 calibration of solar cells are reported in the literature. While there have been a number of satellite-based measurements, no space calibration method has emerged that is available to the photovoltaic community for producing solar cell standards. A photovoltaic engineering test bed facility for use on the International Space Station has been designed but not implemented [2]. This section will review the mountaintop, aircraft and balloon-based methods used in AM0 calibration of solar cells.

Mountaintop method

Laboratory-based solar simulators have been used since solar cells became attractive for space-power applications. However, it was recognized by Zoutendyk that sunlight should be used " to diminish uncertainty in the design of space solar cell power systems" [3]. He was one of the first investigators to attempt to correct for the effects of the atmosphere on the spectral irradiance of sunlight. A review of his work with silicon single-junction solar cells serves as a basis for understanding some of the challenges associated with AM0 calibration methods.

Zoutendyk assumed the spectral irradiance at a given air mass $S_m(\lambda)$ is given by:

$$S_m(\lambda) = S_o(\lambda)e^{-\alpha(\lambda)m} \tag{4}$$

where $\alpha(\lambda)$ is the monochromatic atmospheric absorption coefficient per unit air mass and m is the geometric air mass. He defined the geometric air mass as the ratio of the path length of the sunlight through the atmosphere at a zenith angle θ to the path length for the sunlight when the sun is overhead and the zenith angle is zero. The geometric air mass was taken as the secant of the zenith angle, namely, $m = \sec(\theta)$. The sea-level irradiance at a given air mass is:

$$S_m = \int_{\circ}^{\infty} S_o(\lambda)e^{-\alpha(\lambda)m}d\lambda \,. \tag{5}$$

The monochromatic short-circuit current at a given air mass was assumed to be given by:

$$I_{scm}(\lambda) = I_{sc0}(\lambda)e^{-\alpha(\lambda)m} \quad \text{where} \quad I_{sco}(\lambda) = R(\lambda)S_o(\lambda) \tag{6}$$

where $I_{sco}(\lambda)$ is the monochromatic short-circuit current under AM0 conditions. The short-circuit current of a single-junction cell over $\lambda 1$ to $\lambda 2$ wavelength range where the spectral response contributes to the current is:

$$I_{scm} = \int_{\lambda 1}^{\lambda 2} R(\lambda)S_o(\lambda)e^{-\alpha(\lambda)m}d\lambda = \int_{\lambda 2}^{\lambda 2} I_{sc0}(\lambda)e^{-\alpha(\lambda)m}d\lambda \,. \tag{7}$$

Equation 7 serves as the basis for the use of Langley plots to characterize solar cells. The exponential term may be factored out of the integral if $\alpha(\lambda)$ is assumed to be constant over the $\lambda 1$ and $\lambda 2$ wavelength range. The short-circuit current for a given air mass can then be written as:

$$I_{scm} = e^{-\alpha m} \int_{\lambda 1}^{\lambda 2} I_{sco}(\lambda) d\lambda = e^{-\alpha m} I_{sco} \tag{8}$$

where I_{sco} is the AM0 cell short-circuit current. Taking the Log_{10} of both sides of Equation 8 gives:

$$Log_{10} I_{scm} = -0.4343 \alpha m + Log_{10} I_{sco} \tag{9}$$

which is the theoretical equation used to determine the short-circuit current of solar cells under AM0 conditions. The logarithm of the short-circuit current is plotted on the ordinate of a semi-log graph and the air mass on the abscissa. The graph is referred to as a Langley plot. The data are fitted to a straight line using a least-squared method and the line extrapolated to $m = 0$. The intercept of the straight line with the ordinate is taken as the short-circuit current under AM0 conditions. The slope of the graph is -0.4343α and may be used to determine the atmospheric optical absorption coefficient. It is important to emphasize the constancy of the atmospheric optical absorption coefficient and the use of the "air mass" concept implies the following:

1. The optical absorption coefficient must be constant with respect to wavelength over the range of wavelengths where the solar cell spectral response contributes to cell current. If it is not constant, using Equation 9 to analyze data will produce errors in the extrapolated AM0 short-circuit current.

2. The concentration of optically absorbing atomic and molecular species in the atmosphere and their altitude dependence must not change for the duration of the short-circuit current as a function of air mass measurements. If the concentrations are changing during the measurements as a result of weather fronts, turbulence in the atmospheric, solar heating of the atmosphere etc., Equation 9 may not be linear and linear extrapolation of the short-circuit current to zero air mass may be in error.

3. The optical absorption coefficient must not be large enough to totally absorb the AM0 spectral irradiance at any air mass over the range of wavelengths where the solar cell spectral response contributes to cell current. If there are regions of the spectral irradiance where the sunlight is totally absorbed as it travels through the air mass, then the use of the Langley method to determine the AM0 short circuit will produce erroneous results.

4. Only normally incident sunlight must contribute to the short-circuit current. Scattered sunlight, referred to as "sky radiation" by Zoutendyk, must not contribute to the short-circuit current. Additionally, the presence of reflected light, or light produced by any other mechanisms, may introduce errors in the determination of the AM0 short-circuit current.

Zoutendyk set up a tracking system with silicon single-junction solar cells at an elevation of 7.4 kft on a mountaintop and carried out diurnal measurements of cell short-circuit current and temperature as a function of the zenith angle as the sun moved across the sky. The cell short-circuit current was defined at the current through a 1.000 Ω precision resistor in series with the cell. The sea level geometric air mass was calculated using $m = \sec(\theta)$. The data were analyzed using a Langley plot to arrive at cell AM0 short-circuit currents. The short-circuit current was corrected for cell temperature, precision resistor temperature and the earth-sun distance. The cells were then flown on the Ranger III spacecraft and cell data downlinked. The agreement between the AM0 short-circuit current measurements on the mountaintop and space was reported to be $\pm 2\%$ [3].

It is noteworthy to evaluate the constancy of the atmospheric optical absorption coefficient in mountaintop work to understand the utility of Langley plots. Equations 8 and 9 show that the exponential term is assumed to be constant over the $\lambda 1$ and $\lambda 2$ wavelength range in order to permit factoring it out of the integral. The cut off wavelength of Zoutendyk's solar cell at low wavelengths was $\lambda 1 = 450\ nm$ because of the optical properties of the cover glass on the cells. The high wavelength cut off was about $\lambda 2 = 1200\ nm$ due to the band gap of the silicon material used in the solar cells. Analyses were carried out using values of the atmospheric optical

absorption coefficients in the $450 - 1100\ nm$ wavelength range that were reported by Moon [4]. The coefficients ranged between 0.05 and 0.96 per air mass. The spectral response of the solar cells peaked at about $850\ nm$ where the atmospheric optical absorption was about 0.1 per air mass. The geometrical air masses used by Zoutendyk must be multiplied by 0.7 to correct for the 7.4 kft altitude [5]. For $\alpha = 0.1$ per air mass and $m = 0.7$, the exponential term in Equation 8, has a value of about 0.93. At the largest and smallest values of the optical absorption coefficient, 0.96 and 0.05 per air mass, the values of the exponential term will be 0.51 and 0.96, respectively. Clearly the exponential term varies with wavelength when Moon's atmospheric optical absorption coefficients are used in Equation 8. However, as shown in Equation 7, the exponential term is convoluted with the cell spectral response. The spectral response is always less than one; it decreases from a maximum value at $850\ nm$ to approximately zero at the cut off wavelengths. The effect of convolution of the spectral response with the exponential term in Equation 7 is to decrease the weighting of the exponential term in the integral. A non-constant exponential term in Equation 7 will produce a concave up feature in Langley plots [4]. There is no evidence of a concave up feature in the Langley plots in Zoutendyk's work. This suggests variations in the atmospheric optical absorption coefficients were small enough so as to not invalidate the use of Langley plots to determine solar cell AM0 short-circuit currents.

It is surprising the extrapolated AM0 short-circuit currents agree with the space measurements to within 2 %. It may be the case that the optical absorption coefficients used by Zoutendyk are not appropriate for the conditions under which the mountaintop measurements were carried out. There are three reasons for this conjecture.

1. The ratios of Zoutendyk's measured and calculated short-circuit currents as a function of air mass differ considerably. He used Equation 7 to calculate short-circuit currents along with a standard AM0 spectral irradiance [5], the spectral response of the cells and atmospheric optical absorption coefficients [6]. In every case, the calculated short-circuit currents are smaller than the ones measured, suggesting the atmospheric optical absorption coefficients used are larger than the effective optical absorption coefficients at 7,400 ft.

2. The irradiances measured as a function of air mass are also considerably larger than the irradiances calculated using Equation 5. Zoutendyk plotted measured irradiance as a function of air mass on semi-log plots. The curves are clearly concave up providing convincing evidence of the effect of non-constant atmospheric optical absorption coefficients. In the case of the irradiance curves, Equation 5 shows the integral extends over a larger wavelength range and is not convoluted with the cell spectral response. The larger wavelength range and absence of the convolution both lead to the full effect of the atmospheric optical absorption coefficients on the transmitted sunlight and a concave up feature in irradiance plots.

3. An analysis of Zoutendyk's data in six Langley plots yields atmospheric optical absorption coefficients ranging between 0.079 and 0.101 per unit air mass; the average is 0.087 per unit air mass. The average value of Moon's optical absorption coefficients is about 0.15 per unit air mass in the 700 to $900\ nm$ range where the solar cell spectral response is the largest. The fact that the average slope is about 60 % of Moon's optical absorption coefficients suggests either Moon's coefficients are too large to be used in predicting AM0 short- circuit currents or the atmospheric conditions that prevailed during Zoutendyk's measurements are different than the conditions under which Moon's coefficients were determined. Additionally, the variation in the slopes of the Langley plots measured from day-to-day suggests changing atmospheric conditions may have played a role in the mountaintop measurements.

Ritchie recognized the problems associated with using Moon's atmospheric optical absorption coefficients to correct solar cell short-circuit currents. He employed measurements on a mountaintop to produce secondary standards [7] that did not employ Langley plots. The secondary standards were based on the use of primary standards calibrated with the balloon method and the following equation:

$$I^{s}_{sco} = \frac{I^{p}_{sco}}{I^{p}_{scm}} \times I^{s}_{scm} \tag{10}$$

where I^{s}_{sco} and I^{p}_{sco} are the calculated secondary and measured primary standard AM0 short-circuit currents, respectively; I^{s}_{scm} and I^{p}_{scm} are the secondary and primary standard short-circuit currents, respectively, measured at the same time on a mountaintop. The balloon method was used to measure I^{p}_{sco}. Following the mountaintop measurements, the secondary standards were flown on a balloon flight and the AM0 short-circuit currents measured; the currents agreed to within 0.5% with the currents predicted using the mountaintop measurements based on Equation 10. It is important to note that the spectral responses of the primary and secondary standards must be the same when using a primary balloon standard, Equation 10 and mountaintop measurements to produce secondary standards.

Aircraft method

The use of an aircraft to carry out high-altitude solar cell measurements at altitudes between 47 kft and 6 kft and air masses in the 0.180 – 0.862 range was first reported by Brandhorst [8]. It was suggested that the aircraft method is attractive when compared to the mountaintop method for three reasons. First, measurements are made at lower values of air mass than the mountaintop method resulting in shorter extrapolations of the short-circuit current on Langley plots. It is expected that the more accurate values of the AM0 short-circuit currents will be obtained if the extrapolation is over a smaller range of air masses. Second, the atmosphere should be less prone to compositional changes during the relatively short time of the aircraft measurements as compared to diurnal mountaintop measurements, i.e., minutes versus hours. Third, the measurements are made at altitudes that are above ground haze and low-altitude atmospheric disturbances.

The aircraft method employed a 4.5” diameter windowless collimator with a collimation ratio of 4:1 that was mounted inside the aircraft and extended through a hole in the side of the tail section [9]. The collimator was designed to over-fill the cell holder so that the cells were uniformly illuminated even when the orientation of the aircraft resulted in a $\pm$2-degree error in the pointing of the collimator. The collimator angle was set before each flight to the zenith angle of the sun during the measurements. The tail section was not pressurized and the cells were exposed to the low pressure and temperature environment that is characteristic of the altitudes at which the measurements were carried out. Single-junction silicon solar cells were mounted on a heated stage and the cell temperature maintained between 15 and 30 ^{o}C with a variation of less than 4 ^{o}C. The cell short-circuit current was taken as the current through a 1.000 Ω precision resistor that was placed in series with the cell, as was done by Zoutendyk. The aircraft altimeter was used to measure pressure to an accuracy of 75 ft. The pilot used a sight tube mounted next to the controls in the cockpit to orient the aircraft and control the pitch, roll and yaw so as to point the collimator at the sun with a pointing accuracy of better than $\pm$ 2 degrees. Altitude, cell short-circuit current and cell holder temperature were measured at altitude intervals of 5 kft during descent from 47 to 6 kft.

A standard atmospheric model was used to convert the altitude measurements to pressure [5]. The air mass was calculated using:

$$m = \left(P / P_o\right)\sec\theta \tag{11}$$

where P is the pressure at which the cell short-circuit current was measured and P_o is the sea-level pressure. Langley plots were produced and extrapolations carried out to determine the AM0 short-circuit current of the single-junction silicon solar cells. The AM0 short-circuit currents were corrected for cell temperature, precision resistor temperature, ozone absorption and the earth-sun distance. The extrapolated AM0 short-circuit current was corrected for ozone absorption using the cell spectral response; ozone absorption coefficients in the $400 - 700\ nm$ wavelength range [10]; ozone altitude profile [11]; and the percent of the total column ozone above the aircraft during measurements. The effect of ozone absorption on the short-circuit current of single-junction Si and GaAr solar cells was estimated to be 1.04 and 1.23 %, respectively. Brandhorst reported that

all the Langley plots were straight lines [8,9]. However, there were differences in the slopes of the Langley plots from flight-to-flight suggesting atmospheric conditions, while perhaps constant during a flight, changed from flight-to-flight. The atmospheric optical absorption coefficients, as determined from the slopes of the Langley plots in the publications, ranged between 0.09 and 0.30 per air mass. The change in the slopes suggests there were variations in the concentration of optically absorbing atomic and molecular species in the atmosphere from flight-to-flight. The agreement in the AM0 short-circuit currents, measured by the aircraft method and the mountaintop method that used Equation 10, was $\pm$ 0.9 %. The AM0 short-circuit currents measured during three separate flights were reproducible within $\pm$ 1 % even though the slopes of the Langley plots, and therefore the atmospheric conditions, were different.

Hadley analyzed data from three single-junction silicon cells. Two were balloon calibrated primary standards and one was a secondary standard calibrated using mountaintop measurements with Equation 10. All three of the cells were characterized with the aircraft method. He found that the cell AM0 short-circuit currents measured by the aircraft method were consistently about 1.6 % lower [12]. Hadley pointed out that the Langley plots for different days had different slopes and some of the plots appeared to be concave up . While there was a need to make spectral corrections because the spectral responses of the cells were slightly different, it was not possible since the different slopes for different days "indicate that there cannot be a unique value of the spectral correction factor." The effect of Hadley's work was to suggest that while it was agreed that the use of the Langley plots in the mountaintop method was faulted, there was evidence that there were also problems in using Langley plots to analyze data from the aircraft method.

Subsequently, the aircraft method was used to measure silicon single-junction solar cell short-circuit currents versus altitude. The measurements resulted in Langley plots that exhibited an anomalous behavior. [13]. The plots had a curve with two linear regions, each of which had a different slope. There was a "break" in the curve where the linear segments met. It was determined that the "break" occurred at an air mass that corresponded to the altitude of the tropopause. The short-circuit currents measured at altitudes above the tropopause produced a linear plot with a larger slope than the slope of the currents measured at altitudes below the tropopause. Extrapolation of each of the linear segments produced different AM0 short-circuit currents. The Langley plots for data collected at altitudes above the tropopause extrapolated to larger AM0 short-circuit currents than the plots for data collected at altitudes below the tropopause. The slopes of the Langley plots for data collected above the tropopause were the same on a month-to-month basis while the slopes for data collected below the tropopause were different on a month-to-month basis. The observation that the slope above the tropopause was constant on a month-to-month basis suggests the concentrations of the optically absorbing atomic and molecular species are the same on month-to-month basis for species that absorb in the region of the solar spectrum that contributes to cell current [13]. The atmospheric optical absorption coefficient determined from one of the Langley plots for the data collected above the tropopause was about 0.20 per air mass. On the other hand, the fact that the slopes below the tropopause changed on a month-to-month basis suggests concentrations of the absorbing atomic and molecular species are different below the tropopause on a month-to-month basis. The atmospheric optical absorption coefficient determined from one of the Langley plots for the data collected below the tropopause was about 0.09 per air mass.

A comparison was made of AM0 short-circuit currents of five silicon single-junction solar cells measured with the balloon and aircraft methods [13]. The accuracy of the balloon measurements was estimated at $\pm$ 0.9 %. Only aircraft data collected above the tropopause were used. Differences in the AM0 short-circuit currents measured by the two methods ranged from 0.3 to 1.2 % with an average of 0.7 %. The AM0 short-circuit currents measured with the aircraft method were always larger than those measured with the balloon method. It was concluded that the measurements "show excellent agreement", and the aircraft method must be used above the tropopause in order to produce good results.

Brandhorst carried out a series of experiments with the aircraft method to determine the wavelength region of the anomalous effect [14]. Optical filters were placed over solar cells and data collected both above and below the tropopause. The Langley plots had straight lines for data collected with filters that transmitted red and green light; an anomalous plot with a "break" was produced with data collected with a filter that transmitted blue light. The measurements suggested the anomalous effect was due to an atomic or molecular species that absorbed in the blue wavelength region of the solar spectrum, and that the species existed primarily above the tropopause.

The anomalous Langley plot can be understood by modifying Equations 7, 8 and 9 to include the effect of two atmospheric optical absorption coefficients. The atmospheric optical absorption coefficient for an optically absorbing species that exists primarily above the tropopause is taken as $\alpha 1$ for a range of wavelengths from $\lambda 1$ to $\lambda 2$, the wavelength range where the spectral response contributes to the cell current. The optical absorption coefficient in the same wavelength range is $\alpha 2$ for a different species that exists primarily below the tropopause in the same range of wavelengths. Equations 7, 8 and 9 above the tropopause become:

$$I_{scm} = e^{-\alpha 1 m} \int_{\lambda 1}^{\lambda 2} R(\lambda) S_o(\lambda) d\lambda = e^{-\alpha 1 m} I_{sco} \quad \text{and}$$

$$Log_{10} I_{scm} = -0.4343 \alpha 1 m + Log_{10} I_{sco} . \tag{12}$$

The slope of the Langley plot above the tropopause is $-0.4343\alpha 1m$ and the extrapolated AM0 short-circuit current is I_{sco}. Below the tropopause:

$$I_{scm} = e^{-\alpha 2 m} \int_{\lambda 1}^{\lambda 2} R(\lambda) S_{ot}(\lambda) d\lambda = e^{-\alpha 2 m} I_{s\cot} \quad \text{and}$$

$$Log_{10} I_{scm} = -0.4343 \alpha 2 m + Log_{10} I_{s\cot} \tag{13}$$

where $S_{ot}(\lambda)$ is the solar spectral irradiance just below the tropopause; it is corrected for absorption due to the optically absorbing species above the tropopause. $I_{s\cot}$ is the short-circuit current due to the convolution of $S_{ot}(\lambda)$ with $R(\lambda)$. The slope of the Langley plot below the tropopause is $-0.4343\alpha 2m$ and the extrapolated AM0 short-circuit current is $I_{s\cot}$. The "break" in the straight line segments on the Langley plot defines two regions of air mass where the data have linear characteristics, namely, a straight line segment with a larger slope at lower air masses and a straight line segment with a smaller slope at larger air masses. It follows that $\alpha 1$ in the region of lower air is greater than $\alpha 2$ in the region of larger air masses. Hence, the anomalous plots may be explained by assuming the atmospheric optical absorption coefficients are different above and below the tropopause.

The aircraft method has been developed over the years by investigators at NASA Glenn Research Center [15,16]. A large body of calibration data has been collected and AM0 standards provided to the PV community. The aircraft has been replaced twice and the method improved. The current aircraft is a Lear 25 that houses the instrumentation and collimator in a pressurized and temperature controlled compartment. Photographs of the Lear 25 aircraft, collimation tube and test cell may be viewed on the NASA Glenn Research Center Web site [17]. The ratio of the collimation has been increased to 1:4.5. The method was upgraded to carry out measurements every nine seconds during a 6E-4 air mass per second rate of descent from 50 kft down to the tropopause. Sources of random error were estimated to be about 0.04 % and agrees with measurements. The difference in the average of measurements on a single-junction cell carried out over a twenty-year period and a recent measurement was at the 0.05 % level. Systematic errors were estimated to be at the one percent level. Space shuttle AM0 short-circuit current measurements on two cells were compared with the aircraft method. The aircraft measurements were less than the shuttle measurements by 1.0 and 0.8 % for the two cells; the errors were consistent with the estimated systematic errors.

The role of ozone on the solar cell AM0 short-circuit current measured with the aircraft method has been investigated by Snyder and collaborators [18]. The extrapolated AM0 short-circuit current was corrected using an ozone correction factor. The correction factor was determined using a calculated AM0 short-circuit current

and a calculated short-circuit current that included the effects of ozone absorption. The WMO solar spectral irradiance [19] and solar cell spectral response were convoluted using Equation 1 to calculate the AMO short-circuit current I^x_{scoc} where x corresponds to Si, GaAs and InGaP single-junction solar cells. The short-circuit current I^x_{scdu} was calculated using Equation 7 and the WMO solar spectral irradiance, solar cell spectral response, ozone absorption coefficients [20] and total column ozone value T_{co}. The ozone correction factor F^x_o for each of the types of solar cells was found using:

$$F^x_o = \left(\frac{I^x_{scoc} - I^x_{scdu}}{I^x_{scdu} T_{oc}} \right) \tag{14}$$

where the units of T_{co} are Dobson units, d.u. The correction factors were found to be insensitive, at the 5 % level, to the value of the total column ozone, different sets of spectral response data, and the resolution of the spectral response data used in the calculations. The ozone correction factor was reported to increase with an increase in the optical band gap of the materials used in the solar cells.

The ozone correction method consisted of employing a Langley plot to first determine the extrapolated AM0 short-circuit current I^x_{scol}. Then the current was corrected for optical absorption in the ozone column on the day of the flight. The sun zenith angle, total column ozone on the day of the flight and the ozone correction factor were used in the following equation to determine the AM0 short-circuit current for the various types of cells:

$$I^x_{sco} = I^x_{scol} + 0.83 F^x_o T_{oc} \sec\theta \,. \tag{15}$$

The 0.83 factor results from assuming that 83 % of the total column ozone was above the aircraft during the measurements. The correction method was used to analyze Si solar cell data collected during 20 flights. The correction resulted in an increase of 0.52 % in the Si AM0 short-circuit current as compared to the earlier one percent correction method introduced by Brandhorst [9]. Applying Equation 15 to the earlier aircraft measurements also reduced the differences noted by Hadley in currents determined with the aircraft and balloon methods [12]. The percentage standard deviation of the ozone corrected currents decreased from 0.49 % with the earlier correction method to 0.28 %, thereby suggesting the importance of using Equation 15 to correct for the effect of ozone.

Applying the correction method to a GaAs solar cell, which has a larger band gap than Si, resulted in AM0 short-circuits that were different from flight-to-flight. The corrected currents increased with increases in total column ozone suggesting that the method was sensitive to the band gap of the cell. The correction method was revised in an effort to eliminate the dependence of currents on total column ozone [21]. The revised method called for first correcting the short-circuit current measured at each altitude for ozone absorption, then plotting the data and extrapolating to air mass zero. The approach requires the column ozone at each of the altitudes at which the cell current is measured. The TOMS standard ozone profiles were used to calculate column ozone as function of altitude [22]. Figure 2 shows the TOM ozone profiles used in calculating the column ozone. The average ozone density in the figure is plotted at the midpoint of each Umkehr layer [23], starting at layer zero corresponding to an altitude of 9 kft, through layer 9 at 143 kft. The density shown in

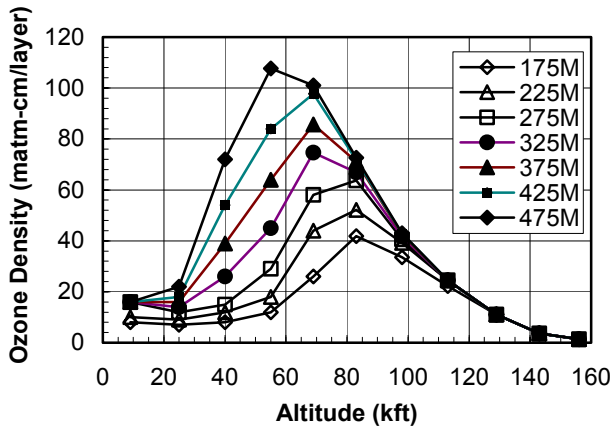

Figure 2. TOMS ozone profiles as function of altitude and total column ozone at mid latitudes [22] .

the figure at 156 kft includes the ozone above 156 kft. The profiles in the figure are for mid latitudes and total column ozone values ranging from 175 to 475 d.u. Mid latitudes are around 45 degrees north, the latitude of the NASA Glenn Research Center flights. The maximum altitude for the flights is about 50 kft. Figure 2 shows the fraction of the total column ozone above 55 kft decreases with increasing total column ozone. The fraction at 55 kft is about 0.87 of the total column ozone when the total column ozone is 175 d.u.; the fraction decreases to about 0.77 at 475 d.u. The fraction is about 0.92 and fairly independent of total column ozone at 40 kft.

The revised AM0 short-circuit current correction method included converting the aircraft altitudes to atmospheric pressure, p . The total column ozone on the day of the flight was obtained and used to select the appropriate TOMS ozone profile in Figure 2. The fraction of the total ozone column $f(p)$ above the aircraft during each of the measurements was calculated. The ozone corrected short-circuit current $I_{scm}(p)$ was calculated for each measurement $I_{sc}(p)$ using:

$$I_{scm}(p) = I_{sc}(p) + f(p)F_o^x T_{oc} \sec\theta \tag{16}$$

The ozone corrected short-circuit currents were plotted as a function of pressure on a Langley plot, instead of a function of air mass. The linear plot was extrapolated to zero pressure to determine the AM0 short-circuit current. Results with the revised method were compared to the one percent method using data for a Si single-junction solar cell. Data collected over two time intervals, namely a short term and long term, were compared. The short-term data were collected on one cell during twenty flights in one year. The long-term data were collected on the same cell during thirteen flights over a period of eight years. Table 1 shows differences in the average AM0 short-circuit currents using the one percent, Av. Isco 1%, and revised ozone correction methods, Av. Isco Revised. The percentage difference in the averages of the currents are 0.52 and 0.54 % for the short and long terms, respectively, showing the percentage differences are essentially the same for the two periods. The percent standard deviation decreases from 0.49 to 0.26 % and 0.72 and 0.48 % for the short and long terms, respectively, showing the importance of the revised ozone correction method in reducing the systematic error in the aircraft method. The percentage differences between the highest and lowest AM0 short-circuit currents decreases from 3.2 to 1.2 % and 2.5 to 1.0 % for the short and long terms, respectively, again showing the improvement of the results with the revised ozone correction method. The relatively larger percentage differences in the highest and lowest AM0 short-circuit currents is due to the fact that the zenith angle ranged between about 48 and 68 degrees during the various flights. Both methods show a decrease in the ozone corrected AM0 short-circuit currents as the zenith angle increases. However, the revised ozone correction method is considerably more effective in correcting for the effect of the zenith angle. Not shown in Table 1 is the percentage difference in the average AM0 short-circuit currents using the revised method for the short and long terms; the difference is 0.26 % which is within the standard deviation for the measurements.

Table 1. Comparison of ozone correction methods for Si, GaAs and InGaP single-junction solar cells [21].

Si Short Term		
Av. Isco Revised - Av. Isco 1%=0.52%		
	1%	Revised
	(%)	(%)
Std. Dev.	0.49	0.26
High-Low	3.2	1.2
Si Long Term		
Av. Isco Revised - Av. Isco 1%=0.54%		
	1%	Revised
	(%)	(%)
Std. Dev.	0.72	0.48
High-Low	2.5	1.0
GaAs Long Term		
Av. Isco Revised - Av. Isco 1%=1.0%		
	1%	Revised
	(%)	(%)
Std. Dev.	0.75	0.47
High-Low	2.6	2
InGaP		
Av. Isco Revised - Av. Isco 1%=2.3%		
	1%	Revised
	(%)	(%)
Std. Dev.	0.45	0.14

Table 1 also shows the differences in the average AM0 short-circuit currents for GaAs and InGaP single-junction solar cells using the 1%, and revised ozone correction methods. The GaAs data were measured in 31 flights over a nine-year period. The InGaP data were collected during seven flights over a few years. The band gap of GaAs is 1.43 eV. The band gap of the InGaP cell is not known because the alloy concentrations were not reported for this particular cell; however, it is expected that it is greater than the band gap of GaAs. The percentage difference in the averages of the currents corrected by the 1% and revised methods are 1.0 and 2.3 % for the GaAs and InGaP

cells, respectively, showing the revised method gives larger currents as the band gap increases. The percent standard deviations are reduced for both the cells as was observed for the Si cell, again confirming the importance of the ozone correction. The differences in the high and low current values are reduced for both cells when the revised method is used. A larger zenith angle results in a larger correction in the AM0 short-circuit currents for both cells. The revised method is more effective in correcting for larger zenith angles as is illustrated by the smaller high-low percentage differences in the AM0 short-circuit currents. However, there is a trend for corrected currents to exhibit a decreasing trend with increasing zenith angle.

Balloon Method

The first balloon method measurements to determine the AM0 short-circuit current of single-junction silicon solar cells was reported by Zoutendyk [24]. A sun tracker weighing about 70 lbs was flown mounted on the top of a balloon, as opposed to in a gondola suspended below the balloon. Mounting the sun tracker on top of the balloon also reduced the effect of sunlight reflections from the balloon on the cell measurement. The top mounting also eliminated anticipated complicating effects of pendulum and torsional motion of the gondola on tracking of the sun. The downlinked data included three solar cell temperatures, fourteen cell short-circuit currents and seven precision standard voltages. The cell short-circuit current was defined at the current through a 1.000 Ω precision resistor that was placed in series with the cell. The weight of the balloon, parachute, sun tracker, batteries, transmitter, data acquisition system and other incidental items was 425 lb; the batteries and transmitter were mounted in a gondola attached to the parachute which is turned was attached to the bottom of the balloon. The maximum volume of the balloon was 175,000 cubic feet and required 7,150 cubic feet of helium to provide an ascent rate of about 1000 feet per minute. It took about two hours for the balloon to reach the 80,000 ft float altitude. The float time for flights was about four hours with two hours of floating time before solar noon and two hours after solar noon. Two vehicles were used in support of flights. One was a bus with communications equipment that maintained a distance of less than 200 miles from the balloon and received the downlinked data. The other vehicle was a chase truck that retrieved the equipment and solar cells. An aircraft was also available to assist if necessary with tracking the balloon.

The solar irradiance at a zero zenith angle and the 80 kft float altitude was estimated to be 95 % of AM0, corresponding to an air mass of 0.05. A reduction of 0.3 % was estimated in the air mass 0.05 cell short-circuit current, as compared to AM0, considering the spectral response of the solar cells. The sun tracker was able to track the sun to within $\pm$ 4 degrees. An error analysis of the measurement system showed a maximum error of about $\pm$ 0.6 %. Three flights were carried out over a period of three months and the results of the calibration of two silicon solar cells were reported. The cell temperatures were 19 $\pm$ 1 ^{o}C during the first flight and 32 $\pm$ 1 ^{o}C during the last two flights. The data were corrected for temperature. AM0 short-circuit currents were reported for the mean earth-sun distance and 28 ^{o}C cell temperature. No corrections were made for ozone absorption. The repeatability in AM0 short-circuit currents for three flights was better than $\pm$ 0.5 % and the accuracy estimated at $\pm$ 0.6 %.

The balloon method has been further developed over the years by Anspaugh and collaborators [25]. It has been used by the NASA Jet Propulsion Laboratory to provide primary standards to the space photovoltaic community. The standards are calibrated at about 120,000 ft, the float altitude of the balloon. Balloon flights are carried out at least once a year during the summer months. The combined weight of the balloon and top and bottom payloads is about 1,400 lb. The main balloon has a volume of about 3.6 E6 cubic feet and requires about 24,000 cubic feet of helium. Launching requires the use of a tow balloon, spool vehicle, launch vehicle and helium tanker. The top payload weighs about 140 lb and consists of the sun tracker, solar panel, transmitters, command receivers, data acquisition electronics, video camera, batteries and miscellaneous items. The bottom payload is tethered in a gondola and includes of batteries, ballast module, flight terminate equipment, pressure transducer, transmitters, GPS receivers, and a variety of supporting electronic systems. The top and bottom payloads have separate parachute and release mechanisms. In excess of 75 cells and modules can be calibrated during a flight. An on-board microprocessor-based system is used for data acquisition and storage during flights. Current-voltage measurements are made over a voltage range from about 100 mV to the cell open-circuit voltage. Cell temperatures are measured both during ascent and at float altitude. Cell temperatures are between 30 and 40 ^{o}C during ascent and about 75 ^{o}C at float altitude. The balloon ascent rate was about 900 ft/min and the time from launch to a 120 kft float altitude was about two

hours; float times ranged between 1.5 to 3.0 hours. Data are downlinked to a base station at the launch site. An aircraft with a two-person crew direct both the termination of the flight and recovery activities. The aircraft crew in retrieving the two payloads directs a chase truck equipped with communications equipment.

Laboratory characterization of solar cells and modules is carried out both before and after balloon flights to insure the cells are not damaged. Cells with a variety of structures have been flown including single and multi-junction cells fabricated from crystalline and amorphous materials. Both thick crystalline and thin-film cells have been calibrated. Only data collected with the tracker pointed to within ± 2 % of the sun are used in characterizing cells. "Wild" data points have been observed in recent years with modifications in the equipment, e.g., adding a video camera and placing some of the transmitters in the top package [26]. The data acquisition system has been programmed to exclude "wild" data points from the data files that were used in determining the cell AM0 characteristics. The cause of the "wild" points was not know but it was suggested that they may be due to water condensation or radio interference.

A module was flown for 41 flights to evaluate both measurement repeatability and the role of position on the solar panel. It was felt that changing the position of the module on solar panel could be used to evaluate the geometric quality of the solar irradiance "with regard to uniformity, shadowing, or reflections" [27]. The standard deviation for 41 flights was 0.46 % and it was concluded that there are no geometric problems. The cell used in the 41 flights was damaged and replaced. It was replaced with a set of nine standard cells and modules to continue checking the repeatability of the balloon method. The nine standard cells and modules were not flown on every flight. Cells and modules were flown between 6 and 26 times. The standard deviations of the AM0 short-circuit currents for the flights range between 0.23 and 1.0 %. The percent differences between the maximum and minimum AM0 short-circuit currents range between 1.3 and 4.4 % for all the standard cells [28]. Two of the silicon single-junction standard cells were flown on the Discovery Shuttle and the AM0 short-circuit current measured in a manner similar to the balloon method. The differences between one measurement on the shuttle flight for each of the two cells, and the average of the AM0 short-circuit currents measured on multiple balloon flights, were 0.21 and 0.11 %, respectively. The agreement is seen as "verifying the accuracy of the calibration procedures used on the balloon flights" [29].

The agreement between shuttle and balloon calibrations for two Si solar cells was 0.21 and 0.11 %, yet the set of standard cells have standard deviations for multiple balloon flights that range between 0.23 and 1.0 %. Moreover, the percentage differences between the maximum and minimum AM0 short-circuit currents range between 1.3 and 4.4 % for the set of nine standard cells [28]. If the agreement between the shuttle and balloon methods is taken as representative of the accuracy of the balloon method for silicon single-junction cells, then the differences in the balloon measurements may be due to either the spectral responses or instabilities in the standard cells. The cell structure and materials are not given for the nine standard cells [28], and for this reason, it is not possible to correlate the differences with cell spectral response. The standard cell with a 1.0 % standard deviation and a 4.4 % difference between the maximum and minimum AM0 short-circuit current was flown on 13 balloon flights. The data may be used to evaluate the role of cell instability on measurements. The first current measurement was 166.83 mA; the current measured on the thirteenth flight was 611.11 mA. Inspection of the measurements for the 13 balloon flights shows the trend is for the cell current to decrease with each successive flight. The data show that the reason for the relatively large cell statistics is a gradual decrease in the cell's current. The behavior suggests the existence of a cell degradation mechanism. It in noteworthy that the cell operates at 75 ^{o}C at the float altitude. The cell will operated at 75 ^{o}C in excess of twenty hours during the 13 flights. It is probable that thermal degradation resulted in the relatively large change in cell current. However, opto-electronic degradation and other sources of instability should also be considered.

SUNTRACKER PROJECT

A joint NASA Glenn Research Center/Wayne State University program called Suntracker is underway to explore the use of weather-balloon and communication technologies to characterize solar cells at elevations up to 120,000 feet [30-32]. The balloon flights are low-cost and can be carried out any time of the year.

The Suntracker scientific package includes a collimator with a cell to be calibrated, two GPS receivers, two transmitters, two separate battery packs, control electronics and a video camera. Figure 3 shows the scientific package. The main body of the package is cylindrical and fabricated from urethane foam; it measures 11" in

Figure 3. Suntracker scientific package developed for characterizing multi-junction solar cells in the stratosphere.

Table 2. Summary of Suntracker Flights

ST	Date	Launch Site	Landing Site	Alt. (ft)	Range (mi)
I	8/29/99	Findlay, OH	Marion, OH	87,000	40
II	9/9/00	Findlay, OH	Aborted due to hardware problems		
III	9/14/02	Findlay, OH	Greenwich, OH	94,256	55
IV	10/12/02	Findlay, OH	Brunswick, OH	87,127	94
V	11/9/02	Portland, IN	Aborted due to surface winds		
VI	12/7/02	Portland, IN	Canton, OH	95,956	186
VII	8/16/03	Findlay, OH	Amlin, OH	99,500	68

diameter and 11” high. The package is about one inch thick and provides thermal insulation for the electronics. Two battery packs are supported 22” from the main body by light carbon composite tubes that are arranged in a “z” configuration. The battery packs are mounted in this fashion to increase the rotational inertia of the package; the 22” length is limited by the interior width of the mobile unit. The two battery packs are enclosed in separate carbon tubes and wrapped in foam insulation to provide thermal insulation. The dimensions of the collimator are 1.25"x1.25"x4.00"; the front aperture is 1.00"X1.00" and the cell area 0.79"x0.79" [x]. The dimensions of the collimator were selected to provide a 1:4 collimation ratio and a one degree pointing accuracy. The collimator prevents light scattered from the balloon, earth, moon or clouds from contributing to solar cell current . Two motors and supporting electronics control the altitude and bearing angles of the collimator during a flight. A video camera is mounted on top of the package and used to observe the operation of the Suntracker as it ascends though low temperatures to the stratosphere. The weight of the payload is about six pounds. Photographs showing the system components inside the scientific package may be viewed on the Suntracker Web site [33].

The scientific package is attached to a parachute that is affixed to a latex balloon. The balloon weighs about three pounds and is inflated with about 250 cubic feet of helium and launched by a three-person team. The Suntracker scientific package is tethered below the balloon and the electronics is programmed to point the collimator at the sun during ascent. The balloon ascends at a rate of about 800 ft/min to a burst altitude ranging between about 87 and 100 kft in about two hours and then parachutes to a landing site. Data are downlinked continuously during the flight on 2 m and 70 cm bands to a mobile unit that is equipped with receivers, computers and tracking software. The three-person team in the mobile unit chases the balloon, records the data and retrieves the scientific package. The data includes cell voltage, cell temperature, electronics module temperature, video, reference voltage, and atmospheric pressure. The short-circuit current is determined from the cell voltage across a 1.000 Ω precision resistor that is in series with the cell.

RESULTS

Seven flights have been attempted with five successful launches. Table 2 shows the launch dates and locations, burst altitudes, landing sites and balloon trajectory ranges. The scientific package was retrieved on the same day for the Suntracker I, III and IV flights. Hardware problems developed during the Suntracker VI and VII flights that resulted in the loss of GPS signals; the package was found within a few days of the launch by individuals and subsequently retrieved. A single-junction silicon solar cell was mounted in the collimator during

the flights. The cell voltage data downlinked during the Suntracker IV and VI flights have been analyzed using Langley plots to determine the AM0 short-circuit current. The Suntracker IV uncorrected short-circuit current versus altitude is shown in Figure 4. Only the maximum currents were selected for use in the Langley plot. The cell current data illustrate the tracking characteristics during the ascent. For the most part the Suntracker was not locked on the sun during the flight. The video data showed the motors slowed down during the ascent as a result of the low atmospheric temperatures. Motor assemblies using lubricant with lower temperature specifications will be evaluated in future flights. Additionally, the stability of the scientific package and the collimator control algorithm will be investigated in order to improve the performance of the Suntracker system.

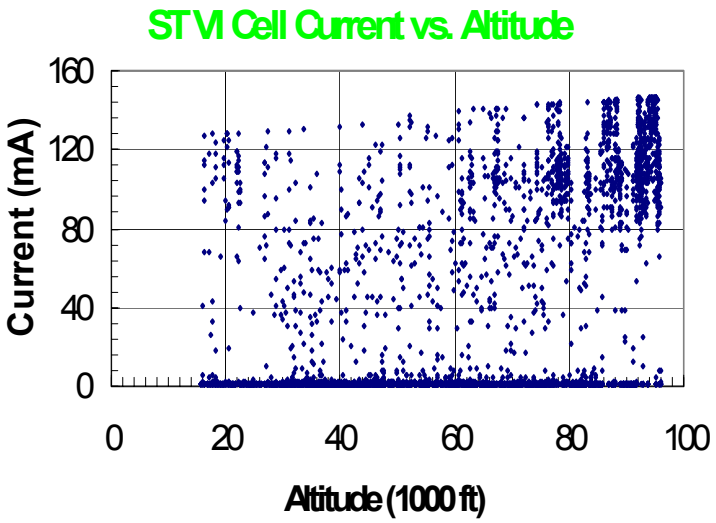

Figure 4. Suntracker VI short-circuit current versus altitude for a single-junction silicon solar cell.

The cell temperature versus altitude during the Suntracker VI flight is shown in Figure 5. Also shown are the radiosonde data reported by the National Weather Service (NWS) on the day of the flight. The effect of solar heating on the cell current is apparent . While the solar cell temperature increased from –10 to about 0 °C as the balloon ascended from 80 to 96 kft, the atmospheric temperature remained at about –45 °C. The dependence of the cell and NWS temperatures in this altitude range suggests that the cell temperature may be higher at higher altitudes. If this is the case, it will be possible to operate cells closer to 25 °C at higher altitudes, and to determine the temperature coefficient of the short-circuit current as the package ascends.

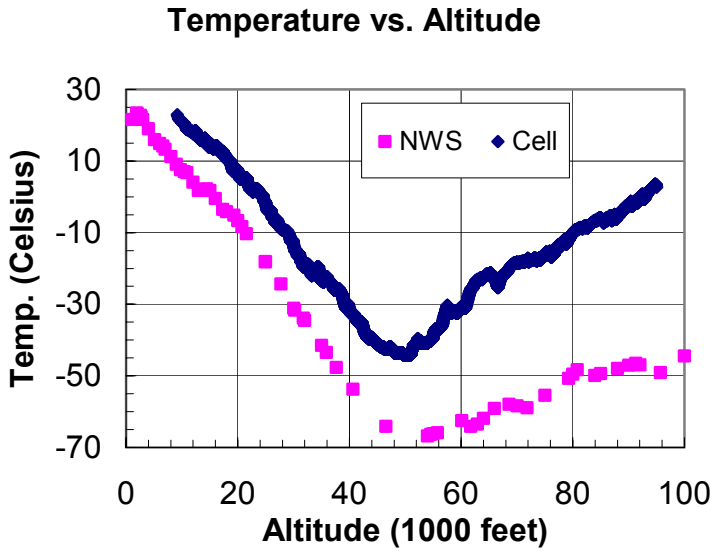

Figure 5. Suntracker VI downlinked solar cell and atmospheric NWS temperatures versus altitude.

Figure 6 is a Langley plot of the data for a single-junction silicon solar cell from the Suntracker IV and VI flights. The optical air masses were calculated using Equation 11. The data have been corrected for the earth-sun distance and cell temperature, and fit with straight lines. The extrapolated AM0 short-circuit currents are 144.32 and 144.38 mA for the Suntracker IV and VI measurements, respectively. The average AM0 short-circuit current is 144.35 mA ± 0.02 %. The resolution of the eight-bit ADC in the Suntracker data acquisition system is ± 0.2 %, showing that the agreement between the two flights is better than the uncertainty in the measurements and probably reflects the statistics of the curve fitting etc. The AM0 short-circuit current of the single-junction silicon solar cell flown on the Suntracker flights was determined using the aircraft method at NASA Glenn Research Center [21]. The AM0 short-circuit current was 144.88 mA and within ± 0.36 % of the Suntracker average value. The results agree to within the statistics

of the two methods, namely about ± 0.2 % for the Suntracker measurements and ± 0.6 % for the aircraft method.

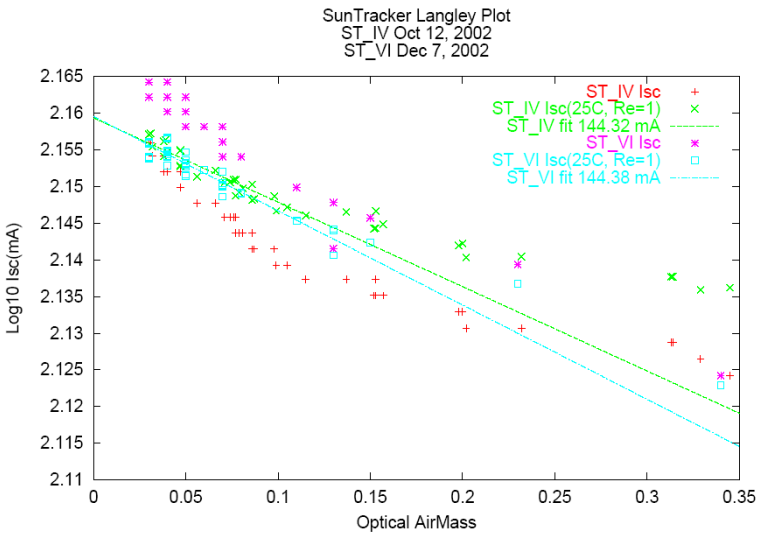

Figure 6. Langley plot of corrected Suntracker IV and VI data for a single-junction silicon solar cell.

It is instructive to determine the atmospheric optical absorption coefficients for the two methods using Equation 9. The slopes of the two straight lines in Figure 6 were analyzed to determine the absorption coefficients; the coefficients are 0.265 and 0.293 per air mass for the Suntracker IV and VI data, respectively. The average value of the atmospheric optical absorption coefficient is 0.280 per air mass ± 5 %. An analysis of the Langley plot produced with aircraft data gives absorption coefficients of 0.125 per air mass. The Suntracker value is somewhat larger than the 0.20 per air mass determined from the earlier aircraft measurements [13] while the absorption coefficients determined with the current aircraft data is considerably less. The reasons for these differences are not understood and will be the subject of future investigations.

CONCLUSIONS

The voltage dependence of the spectral responses of multi-junction solar cells complicates optimization of cell design. The series nature of multi-junction solar cells places more demands on the need for standard cells characterized under AM0 conditions. Cells selected for use as standards should have a history of thermal cycling and light soaking that provides evidence of the level of cell stability. The AM0 short-circuit current of a single-junction silicon solar cell was determined using data collected during two Suntracker flights. The agreement in the two measurements was ± 0.02 %. The agreement in the AM0 short-circuit current of the cell measured with the Suntracker balloon method and NASA Glenn Research Center aircraft method was ± 0.36 %, which is within the uncertainty of the two methods. There is a need to understand the role of ozone and atmospheric optical absorption on the calibration of solar cells in the stratosphere.

REFERENCE

1. James R. Woodyard, “Laboratory Instrumentation and Techniques for Characterizing Multi-Junction Solar Cells,”Proceedings of the Twenty-Fifth Photovoltaic Specialists Conference, page 203, 1996.

2. Geoffrey A. Landis and Shelia G. Bailey, “Photovoltaic Engineering Testbed on International Space Station,” Proceedings of the Second World Conference on Photovoltaic Solar Energy Conversion, page 3564, 1998.

3. John A. Zoutendyk, “A Method for Predicting the Efficiency of Solar Cell Power Systems Outside the Earth’s Atmosphere,” NASA Technical Report No. 32-259 (1962).

4. Moon, P., “Proposed Standard Solar Radiation Curves for Engineering Use,” 1940, J. Franklin inst., 230, 583-617, 1940.

5. National Technical Information Office, ”Standard Atmosphere Model,” Springfield, Virginia (Product Number: ADA-035-6000).

6. Johnson, F. S., “The solar constant,” 1954, Journal of Meteorology, 11, 431-439.

7. D. W. Ritchie, “Development of Photovoltaic Standards for NASA,” Proceedings of the Fourth Photovoltaic Specialists Conference, page C-5-1, 1964.

8. Henry W. Brandhorst, Jr., “Airplane Testing of Solar Cells,” Proceedings of the Fourth Photovoltaic Specialists Conference, page C-2-1, 1964.

9. Henry W. Brandhorst, Jr., and Earle O. Boyer, “Calibration of Solar Cells Using High-Altitude Aircraft,” NASA Technical Note, NASA TN D-2508, February 1665.

10. E. Vigroux, “Contribution to the Experimental Study of the Absorption of Ozone,” Annales de Phys., vol. 8, page 709, 1953.

11. L. A. Biryukova, “Distribution of Energy in the Spectrum of Solar Rays a Various Altitudes,” JPRS 7488, Joint Pub. Res. Service, 1959. C. P. Hadley, Proceedings of the Fourth Photovoltaic Specialists Conference, page C-3-1, 1964.

12. C. P. Hadley, “Comparison of Flight and Terrestrial Solar Measurements on Silicon Cells,” Proceedings of the Fourth Photovoltaic Specialists Conference, page C-3-1, 1964.

13. Henry W. Brandhorst, Jr.,” Calibration of Solar Cells Using High-Altitude Aircraft,” Proceedings of the Fifth Photovoltaic Specialists Conference, page E-1-1, 1965.

14. Henry W. Brandhorst, Jr., “Anomalies in Solar Cell Langley Plots Associated with the Tropopause,” Applied Optics, vol. 7, page 716, 1968.

15. Philip Jenkins, David Brinker, and David Scheiman, “Uncertainty Analysis of High Altitude Aircraft Air Mass Zero Solar Cell Calibration,” Proceedings of the 26th Photovoltaic Specialists Conference, page 857, 1997.

16. David J. Brinker, David A. Scheiman, and Phillip Jenkins, “Calibration of Space Solar Cells Using High Altitude Aircraft,” Proceedings of the 2nd World Conference on Photovoltaic Solar Energy Conversion, page 3654, 1998.

17. http://powerweb.grc.nasa.gov/pvsee/facilities/scel/lear

18. David B. Snyder, David A. Scheiman, Philip P. Jenkins, William J. Rieke and Kurt S. Blankenship, “Ozone Correction for AM0 Calibrated Solar Cells for the Aircraft Method,” Proceedings of the 29th Photovoltaic Specialists Conference, page 832, 2002.

19. http://rredc.nrel.gov/solar/spectra/am0/NewAM0.xls

20. B. Leckner, “The Spectral Distribution of Solar Radiation at the Earth’s Surface – Elements of a Model,” Solar Energy, volume 20, page 143, 1978.

21. David B. Snyder, Philip P. Jenkins and David A. Scheiman, “Historical Precision of an Ozone Correction Procedure for AM0 Solar Cell Calibration,” Proceedings of the Space Photovoltaic Research and Technology Conference, 2003, In Press.

22. Richard D. McPeters, P. K. Bahartia, Arlin J. Krueger, Jay R. Herman, Charles G. Wellemeyer, Colin J. Seftor, Glen Jaross, William Byerly, Steven L. Taylor, Tom Swissler and Richard P. Cebula, “Earth Probe Total Ozone Mapping Spectrometer (TOMS) Data Products User’s Guide,” NASA Technical Publication 1998-206895, page 53, 1998.

23. IBID, page 53.

24. John A. Zoutendyk, “The Space Calibration of Standard Solar Cells Using High Altitude Balloon Flights,” Proceedings of the Fourth Photovoltaic Specialists Conference, page C-4-1, 1964.

25. B. E. Anspaugh and R. L. Mueller, ”Results of the 2002 JPL Balloon Flight Solar Cell Calibration Program,” JPL Publication 02-03, 2002.

26. IBID, page 20.

27. IBID, page 22.

28. IBID, page 26.

29. IBID, page 1.

30. Glenroy A. Bowe, Qianghua Wang, James R. Woodyard, Richard R. Johnston and William J. Brown, “Investigations to Characterize Multi-Junction Solar Cells in the Stratosphere Using Low-Cost Balloon and Communication Technologies,” Proceedings of 16th NASA Space Photovoltaic Research and Technology Conference, August 31-Septermber 2, 1999, page 189.

31. Glenroy A. Bowe, Qianghua Wang and James R. Woodyard, ”Investigations to Characterize Multi-junction Solar Cells in the Stratosphere Using Low-Cost Balloon and Communication Technologies,” Twenty-Eight IEEE Photovoltaic Specialists Conference Proceedings, 2000, page 1328.

32. Ali Mirza, David Sant, James R. Woodyard, Richard R. Johnston and William J. Brown, “Report on Project to Characterize Multi-junction Solar Cells in the Stratosphere Using Low-Cost Balloon and Communication Technologies,” Seventeen Space Photovoltaic Research and Technology Conference, 2001, page 137.

Historical Precision of an Ozone Correction Procedure for AM0 Solar Cell Calibrations

David B. Snyder, NASA Glenn Research Center
Phillip Jenkins, Ohio Aerospace Institute
David Scheiman, Ohio Aerospace Institute

Abstract

In an effort to improve the accuracy of the high altitude aircraft method for calibration of high band-gap solar cells, the ozone correction procedure has been revisited. The new procedure adjusts the measured short circuit current, *Isc*, according to satellite based ozone measurements and a model of the atmospheric ozone profile then extrapolates the measurements to air mass zero, AM0. The purpose of this paper is to assess the precision of the revised procedure by applying it to historical data sets. The average *Isc* of a silicon cell for a flying season increased 0.5% and the standard deviation improved from 0.5% to 0.3%. The 12 year average *Isc* of a GaAs cell increased 1% and the standard deviation improved from 0.8% to 0.5%. The slight increase in measured *Isc* and improvement in standard deviation suggests that the accuracy of the aircraft method may improve from 1% to nearly 0.5%.

Introduction

The NASA GRC High Altitude Aircraft Method has been used to provide the aerospace industry with solar cells calibrated to orbital conditions for nearly 40 years. The method measures the short circuit current, *Isc*, with an accuracy of 1% for setting solar simulators to space conditions during ground-based measurements (ref.1). However, with the increased application of high band-gap and multijunction solar cells in space, it has become necessary to reassess and revise the method in order to continue to provide measurements correctly adjusted to air mass zero, AM0.

Aircraft based measurements are made at the lower edge of the stratospheric ozone layer (figure 1) where the ozone density is increasing with altitude. The Langley Plot method is used to extrapolate flight measurements to AM0. It assumes that the adsorption characteristics of the atmosphere are proportional only to pressure. The extrapolation will therefore be offset due to the non-uniformity of the ozone density. This has been accounted for by increasing the measured *Isc* by 1% based on an estimate of the influence of ozone absorption on silicon solar cells (ref.1). This procedure must now be adjusted for higher band gap solar cells.

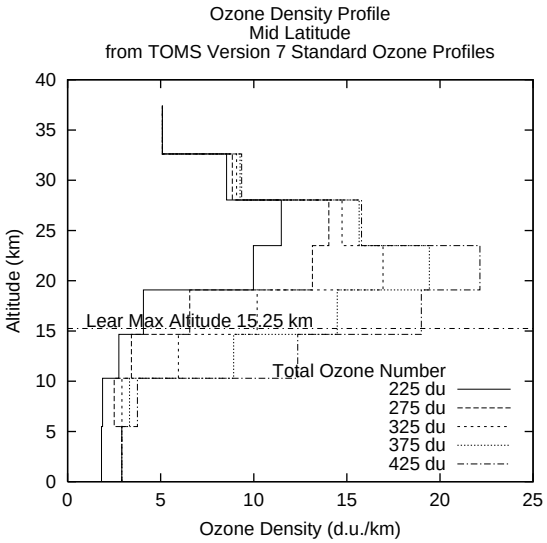

Figure 1. Ozone profiles for various total ozone numbers.

Initial work indicated that it was not sufficient to use the sun angle with the ozone number to calculate a correction factor (ref. 2) Instead correcting the measured Isc according to an ozone profile model, then performing the Langley extrapolation, looked promising. This paper applies the technique to historical data to see how it improves the precision and, presumably, the accuracy of the flight measurements.

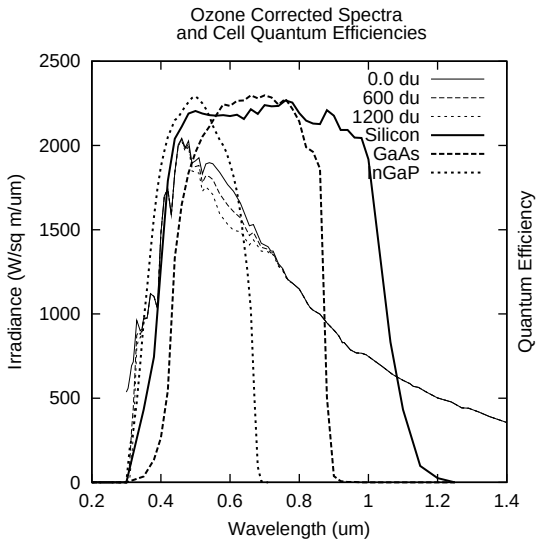

Figure 2. Ozone corrected irradiance and solar cell quantum efficiencies.

Procedure

A new ozone correction procedure has recently been developed (ref 2). The first step in the new procedure is to use spectral response data to calculate an ozone correction factor, *Foz*, for each cell technology. The measured *Isc* is then adjusted by a factor, $1+[O_3]*Foz$, where $[O_3]$ is the Ozone column along the optical path. Examples of *Foz* are shown in Table 1 for various types of solar cells. Next, based on satellite data available the day after a calibration flight, an ozone profile is produced and used to correct the measured *Isc* as a function of air mass and altitude. The corrected *Isc* is then extrapolated via the Langley Plot method to AM0.

Cell type	***Foz (*****du)**
Silicon	29.6×10^{-6}
α Silicon	50.4×10^{-6}
GaAs	42.6×10^{-6}
InGaP top junction	57.2×10^{-6}
GaAs middle junction	26.3×10^{-6}
Ge bottom Junction	2.43×10^{-6}

Table 1. Ozone correction factors for various solar cell types.

The *Foz* calculation is based on the convolution of the ozone absorbed WM0 spectra with the spectral response data for a solar cell type as illustrated in figure 2. The ozone absorption region of the spectra that most affects solar cell performance is from about 500 nm to 800 nm. This means that high band gap cells tent to be affected more than low band gap cells.

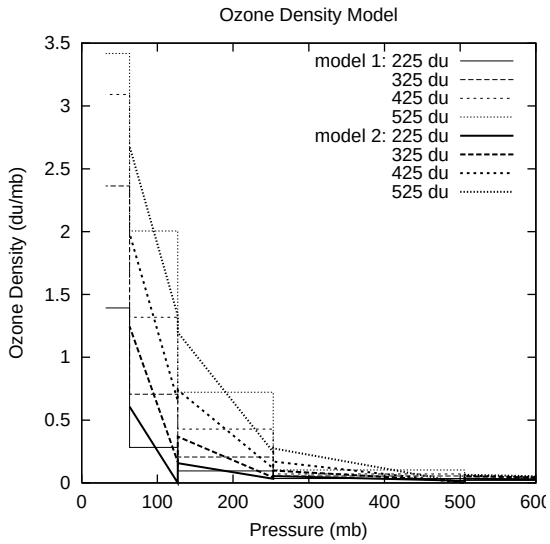

Figure 3. Pressure dependent ozone density model.

Next each *Isc* measurement during the flight is corrected using *Foz* and the ozone along the optical path by a factor of $1+[O_3]Foz$. The total Ozone number, *On*, for the flight date and location is available from the Earth Probe satellite at the web site in reference 3. This is then adjusted by an ozone density model for the altitude, *f(p)*,as given by the pressure of the *Isc* measurement illustrated as Model 2 in figure 3. The ozone density model is based of the TOMS Version 7 Standard Ozone Profile as described in appendix A of reference 4. Finally , the optical path is corrected for the sun altitude, θ, approximately $1/\sin(\theta)$. So, $[O3] = On * f(p)/\sin(\theta)$.

Results

This paper reports on data from three solar cells. First, is a silicon solar cell that has been flown since 1985. It is used for two sets of data, first it a short term set of data set with 20 flights over a single flying season, second is a selection of 13 flights over an eight year period. The second cell examined is a GaAs cell. Selected flight data from 31 flights over ten years are examined. Finally, data from an InGaP top cell which was flown seven times in

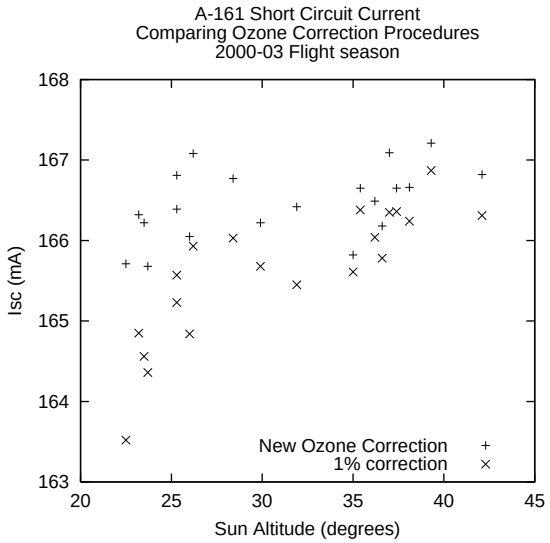

Figure 4. Variation in *Isc*(AM0) of a silicon solar cell as a function of sun angle during a flight season.

recent flight seasons are presented.

Si cell short term

The silicon solar cell A-161 has flown frequently on the Lear 25 as a monitor cell during calibration flights. It flew 20 times during the 2000-2001 flying season. Using the 1% ozone correction method, the short circuit current, *Isc*, measurements averaged 165.60 mA with a standard deviation of 0.81 mA. With the new ozone correction method the average *Isc* was 166.46 mA with a standard deviation of 0.43 mA. Figure 4 shows a comparison of the measurements plotted against sun angle during the measurement. The reduction in *Isc* at lower Sun altitudes using the 1% correction method, is interpreted as due to the increased optical path length through the ozone layer. The new correction method nearly removes this dependence.

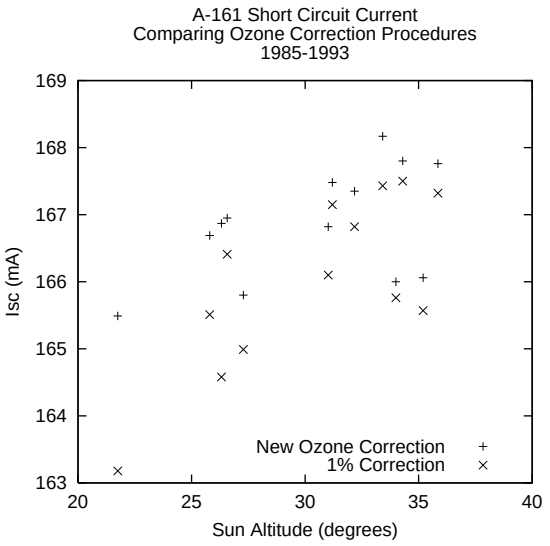

Figure 5. Long term comparison of *Isc*(AM0) of a silicon cell as a function of sun angle.

Si cell long term

Flight data is also available for A-161 since the 1985 flying season. Figure 5 shows some of the data over the interval 1985-1993. The ozone data for this period is available from the Nimbus 7 satellite (ref. 5). *Isc* from 13 flights over that interval averaged 166.0 mA with a standard deviation of 1.2 mA. Using the new procedure *Isc* averaged 166.9 mA with a standard deviation of 0.8 mA.

GaAs cell long term

A-133 is a GaAs cell that has flown frequently. Data was examined that was obtained in the period 1985-1994. Of 31 flights the old procedure gave a average of 110.16 mA with a standard deviation of 0.83 mA. The new ozone correction procedure gives an average of 111.29 mA with a standard deviation of 0.52 mA. A comparison is shown in figure 6.

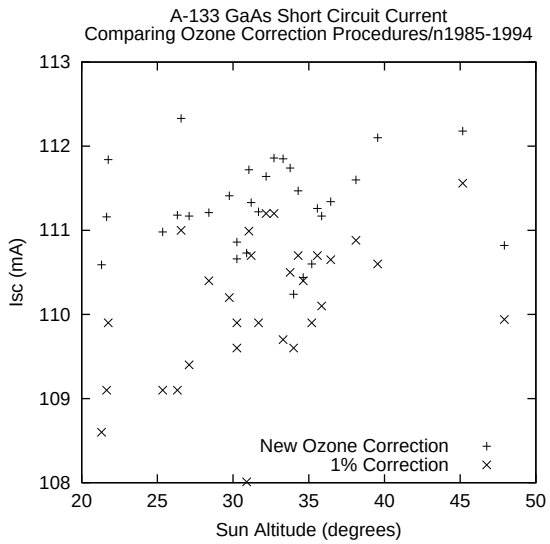

Figure 6. Long term variation in *Isc* measurements of a GaAs solar cell.

InGaP Top Cells

134-5-6 is an InGaP Top Cell, part of a pair of subcells for a dual junction solar cell. It has been flown several times over the past few

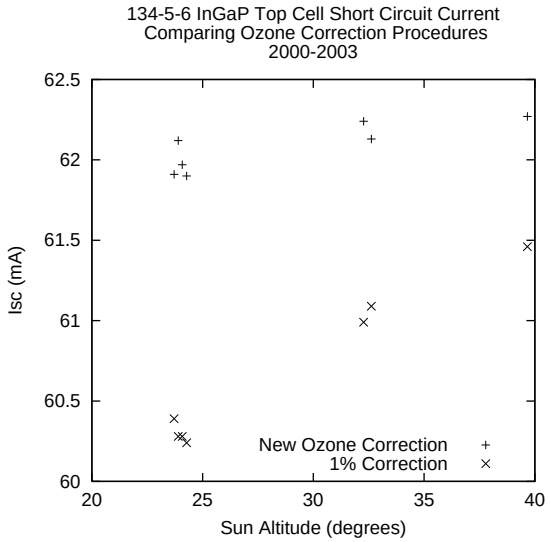

Figure 7. *Isc* of an InGaP cell as a function of sun angle.

years. Figure 7 compares results from seven flights in the 2000-2001 and 2002-2003 seasons. The 1% correction procedure gave an average of 60.68 mA with a standard deviation of 0.46 mA. The new method gives an average of 62.08 mA and a standard deviation of 0.14 mA.

Discussion and Conclusion

This paper has compared an old procedure for correcting Isc measurements for atmospheric ozone with a new one. Table 2 shows the changes due to this method. The slight increase in Isc is expected as the procedure accounts for the increased optical path due to low sun altitude. In addition, the correction increases with band gap.

Cell Type	Isc change	Standard Deviation	
		1%	new
Si short term	0.52%	0.49%	0.26%
Si long term	0.54%	0.72%	0.48%
GaAs long term	1.02%	0.75%	0.47%
InGaP	2.26%	0.76%	0.23%

Table 2. Relative changes is *Isc* measurements.

The standard deviation of each set of measurements also improves by at least one third because the dependence on sun angle is nearly removed. This suggests that the influence of atmospheric ozone has been an important uncertainty in the aircraft based measurements. The new correction procedure appears to produce a significant improvement in measurements. However, in order to have complete confidence in the procedure, results still must be compared to high altitude balloon measurements.

The new procedure has been used at NASA GRC for measurements beginning with the 2002-2003 flight season. It is anticipated that in the 2003-2004 season the capability of making a spectroscopic measurement of the ozone profile will refine these calibration measurements further.

References

[1] P.Jenkins, D. Brinker and D. Scheiman, "Uncertainty Analysis of High Altitude Air Mass Zero Solar Cell Calibration ", 26th IEEE PVSC, V26-206 ,1997, pp.857-860..

[2] D. Snyder, et al, "Ozone Correction for AM0 Calibrated Solar Cells for the Aircraft Method ", 29th IEEE PVSC,2002.

[3] <http://toms.gsfc.nasa.gov/eptoms/ep.html>

[4] McPeters, R.D. et al, Earth Probe Total Ozone Mapping Spectrometer (TOMS) Data Products Users Guide, NASA TP 1998-206895, 1998.

[5] <http://toms.gsfc.nasa.gov/n7toms/nim7toms.html>

EVALUATION OF THIN-FILM SOLAR CELLS FOR SPACE APPLICATIONS

S. H. Liu, E. J. Simburger, J. Matsumoto, A. Garcia III, J. Ross, and J. Nocerino
The Aerospace Corporation, Los Angeles, CA 90009-2957

INTRODUCTION

Photovoltaic devices used on spacecraft have requirements that include high solar-to-electric conversion efficiency with low mass (high specific power), low volume (high specific volume), tolerance of space radiation damage, and stable performance through thermal cycling [1]. Current spacecraft use high-efficiency, single-crystal Si and III-V semiconductor solar cells as the source of power generation. With the development of lightweight flexible thin-film solar cells for terrestrial applications, there is an interest in transitioning this technology to space applications. Thin-film solar cells have many attractive advantages over crystalline solar cells. The low mass of the thin-film solar cells increases the specific power by an order of magnitude from the current level of 65 W/kg [2]. Figure 1 compares specific power versus conversion efficiency for various solar cell technologies. The maximum specific power achievable with crystalline solar cell technology is in the range of 200 W/kg. If thin-film solar cell technology efficiency improves from the current 5%–8% range to a 15%–18% range, the specific power for the array would double from the current 200 W/kg to 400 W/kg.

A part of the process of transitioning thin-film solar cell technology to space applications is to assess the solar cell performance in a simulated space environment. While in geosynchronous orbit, thin-film solar cells will experience extreme temperatures from –160°C to +100°C within a few minutes after eclipse. The manufacturers of thin-film solar cells for terrestrial applications have not measured the temperature coefficient over this temperature range. The impact of the operational temperature on the performance of thin-film solar cells must be taken into account in the design of the spacecraft power system. In this paper, we present the measured temperature-dependent performance data on thin-film solar cells from the following vendors: Iowa Thin-film Technologies (ITFT), Uni-Solar Systems Corp., and MicroSat Systems Inc.

EXPERIMENTAL

The experiment consisted of measuring the I-V characteristic of sample thin-film solar cells at temperatures between 15°C and 100°C. The temperature coefficients of the ITFT thin-film, dual-junctions amorphous silicon (a-Si) on polyimide substrate, Uni-Solar triple-junctions of a-Si and a-Si/Ge on 1-mil stainless-steel substrate, and MicroSat Systems' single junction $CuInGaSe_2$ ($CIGS_2$) on 1-mil stainless-steel substrate solar cells was measured. Measurements were conducted on Uni-Solar and MicroSat Systems solar cells as provided by the manufacturers. Two changes were made to the ITFT cells. First, a high-conductance silver front contact was deposited onto the solar cells by Aerospace rather than a printed ink contact normally applied by ITFT for terrestrial applications. The second change is the use of aluminum instead of stainless steel as a method of bleeding off static charge buildup during the roll-to-roll deposition process at ITFT. The aluminum layer on the back of the solar cell was etched away, exposing the surface of the 2-mil-thick polyimide substrate. Three cells from each manufacturer were used in making these measurements. The dimensions of the Uni-Solar cells are 5 cm $\times$ 26.08 cm with an active area of 130.4 cm^2 (Figure 2). The ITFT hexagon solar cells have an active area of 347 cm^2 (Figure 3). MicroSat Systems solar cell dimensions are 7.25 cm $\times$ 1.65 cm with an active area of 75 cm^2 (Figure 4).

The temperature coefficient measurements of the thin-film solar cells, within the temperatures range of 15°C to 100°C, were conducted inside a Plexiglas box that houses a temperature-controlled vacuum plate. The Plexiglas housing allows purging of the system with dry nitrogen. The vacuum plate ensures maximum thermal contact between the plate and the solar cell, and reduces any thermal gradient in the solar cell. The vacuum plate also serves as a thermal reservoir that maintains temperature stability during the performance evaluation. A temperature bath that uses coolant as a heat exchange source controls the temperature of the vacuum plate.

A Spectrolab X-25 Solar Simulator calibrated for AM0 conditions provided the necessary insolation in performance characterization of the thin-film solar cells. Figure 5 shows the spectra of the sun at AM0, the X-25 Solar Simulator, and X-25 with Plexiglas that houses the vacuum plate.

Table 1. The I-V Characteristics of Thin-Film Solar Cells Provided by ITFT, Uni-Solar, and MicroSat Systems at 25°C.

Sample	Voc (V)	Isc (A)	Pmax (W)	Eff. (%)
ITFT #1	5.1414	0.7139	1.6188	3.45
ITFT #2	4.9329	0.7155	1.4435	3.07
ITFT #3	5.1481	0.7157	1.5906	3.39
Uni-Solar #1	2.2220	1.0249	1.4651	8.30
Uni-Solar #2	2.2153	0.9924	1.4194	8.05
Uni-Solar #3	2.2181	0.9933	1.4028	7.95
MicroSat #1	0.5213	2.3933	0.6512	6.42
MicroSat #2	0.4560	2.5250	0.6356	6.26
MicroSat #3	0.4892	2.2216	0.5937	5.85

RESULTS

Temperature coefficients of the open-circuit voltage (Voc) and short-circuit current (Isc) for each solar cell were determined by averaging three separate measurements. The Voc and Isc temperature coefficients were obtained from the least-square linear regression of the raw data. The conversion efficiency temperature coefficient was determined based on the normalized data. Table 1 shows the I-V characteristics of various solar cells measured at 25°C. The results are grouped according to manufacturer.

Uni-Solar

The temperature dependence of Uni-Solar I-V characteristics is shown in Figures 6–8 and Table 2. Both Voc and Isc showed a linear temperature dependence of –0.0080±0.0002 V/°C and 0.000877±0.00002 A/°C, respectively. The coefficient of efficiencies are –0.14±0.04 %/°C over the temperature range of 20°C–40°C, –0.35±0.01%/°C over the range of 50°C–70°C, and –0.45±0.06 %/°C over the range of 70°C–100°C.

Table 2. Temperature Coefficients of Uni-Solar a-Si Dual-junction Thin-film Solar Cells

I-V Characteristics	Temperature Coefficients
Voc (V)	
15°C–100°C	–0.0080 V/°C
Isc (A)	
15°C–100°C	0.000877 A/°C
Conversion Efficiency (%)	
20°C–40°C	–0.14 %/°C
50°C–70°C	–0.35 %/°C
70°C–100°C	–0.45 %/°C

Iowa Thin-Film Technology

The temperature dependence of Iowa Thin-film Technology a-Si solar cells I-V characteristics is indicated in Figures 9–11 and Table 3. Over the temperature range of 15°C to 100°C, Voc showed an average temperature coefficient of –0.0133±0.0006 V/°C, and Isc showed a linear dependence of 0.00063±0.00003 A/°C. The temperature coefficients of cell efficiency are 0.14±0.01% over the temperature range of 25°C to 45°C, -0.05±0.01%/°C over the temperature range of 45°C to 60°C, and –0.14±0.04%/°C over the temperature range of 60°C to 100°C. Between 15°C and 25°C, measurements of the cell efficiency showed inconsistent results. Two measurements indicated a negative temperature coefficient, but the third one showed otherwise. The cause of this discrepancy is unclear, and it will be further investigated in the future.

Table 3. Temperature Coefficients of Iowa Thin-Film Technology a-Si Dual-Junction Thin-film Solar Cells

I-V Characteristics	Temperature Coefficients
Voc (V)	
15°C–100°C	–0.0133 V/°C
Isc (A)	
15°C–100°C	0.00063 A/°C
Conversion Efficiency (%)	
25°C–45°C	0.14 %/°C
45°C–60°C	–0.05 %/°C
60°C–100°C	–0.14 %/°C

MicroSat Systems

Figures 12–14 and Table 4 present the I-V characteristics of MicroSat $CIGS_2$ solar cell. The I-V characteristics of Voc, Isc, and efficiency showed linear temperature dependence from 15°C to 100°C. Between 15°C and 100°C, the Voc, Isc and efficiency temperature coefficients are –0.0024±0.0001V/°C, –0.00090±0.00006 A/°C, and -0.69±0.03%/°C, respectively.

Table 4. Temperature Coefficients of MicroSat Systems $CIGS_2$ Thin-Film Solar Cells

I-V Characteristics	Temperature Coefficients
Voc (V)	
15°C–100°C	–0.0024 V/°C
Isc (A)	
15°C–100°C	-0.00090 A/°C
Conversion Efficiency (%)	
15°C–100°C	–0.69 %/°C

SUMMARY

Lightweight, flexible, thin-film solar cells present many promising applications in space power systems. Thin-film photovoltaic devices offer attractive advantages in terms of high specific power and high specific volume over traditional crystalline solar cells. The assessment of cell performance must be conducted in simulated space conditions in order to apply commercially available terrestrial thin-film solar cells for space missions. In this paper, we have reported on the experimental measurements of temperature coefficients for Voc, Isc, and conversion efficiency in the temperature range of 15°C to 100°C for three different types of thin-film solar cells. This represents the initial effort in measuring the temperature coefficients of thin-film solar cells I-V characteristics over the extreme temperatures that spacecrafts experience in space. We are in the process of building a vacuum chamber that will allow solar cell temperature to reach as low as –160°C (Figure 15). Results will be presented in future publications. Our effort in characterizing solar cell performance allows assessment of current thin-film solar cell technology for space applications, and provides a basis for spacecraft design.

REFERENCES

1. P. Iles, “Future of Photovoltaics for Space Applications,” Prog. in Photovo.: Res. Appl. 2000; 8:39-51.

2. N. Dhere, S Ghongadi, M. Pandit, A. Jahagirdar, and D. Scheiman, “CIGS2 Thin-Film Solar Cells on Flexible Foils for Space Power,” Prog. in Photovo.: Res. Appl. 2002; 10:407–416.

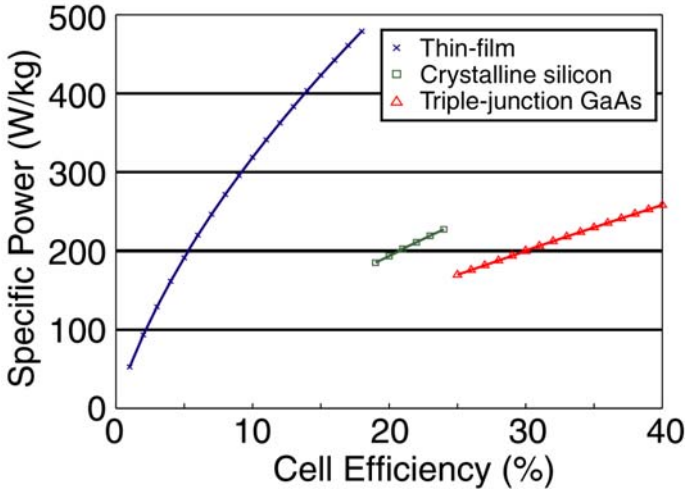

Figure 1. Specific power of lightweight solar array with thin film, thin crystalline silicon, and crystalline GaAs solar cells as a function of solar efficiency.

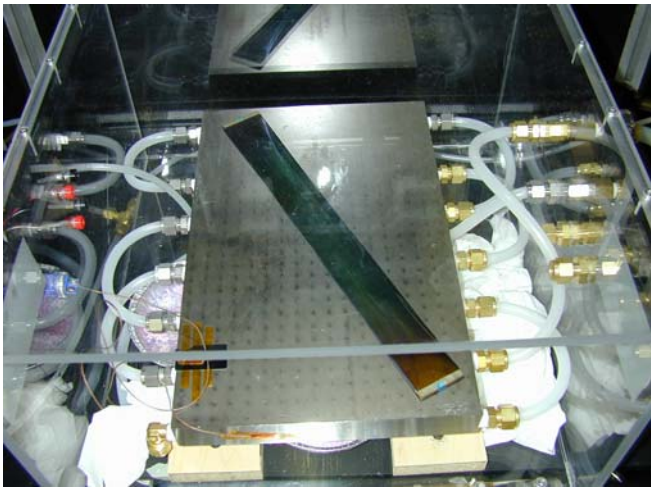

Figure 2. Uni-Solar System Corp. a-Si solar cell.

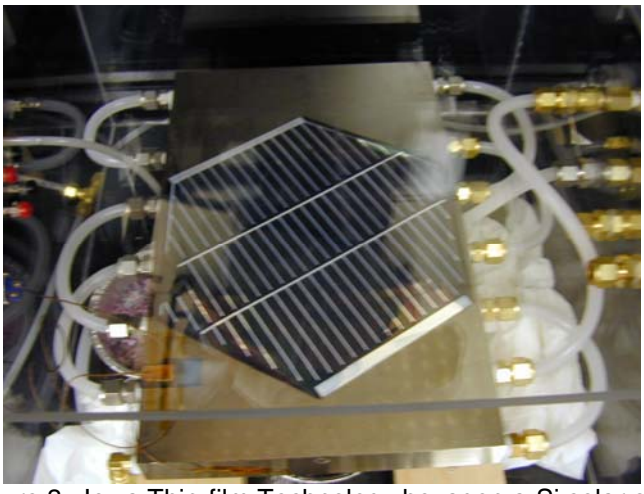

Figure 3. Iowa Thin-film Technology hexagon a-Si solar cell.

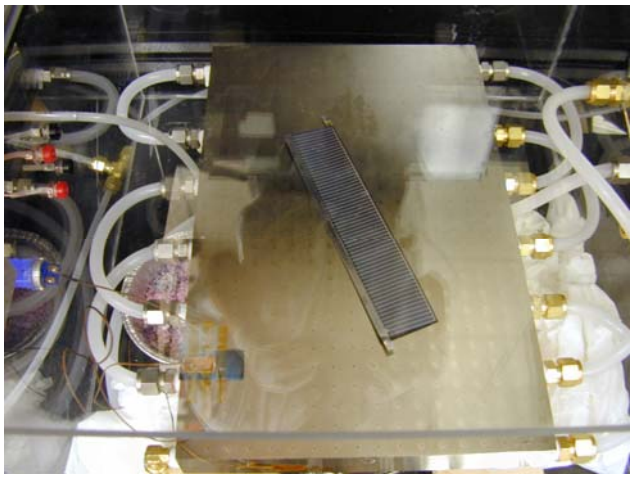

Figure 4. MicroSat Systems Inc. $CIGS_2$ solar cell.

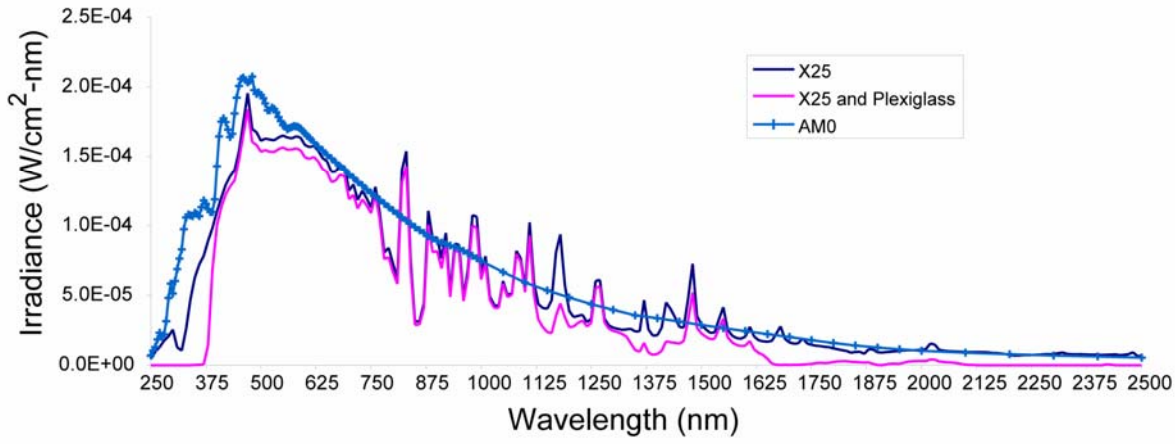

Figure 5. Spectra of sunlight at AM0 condition, X-25 Solar Simulator, and X-25 Solar Simulator with Plexiglas.

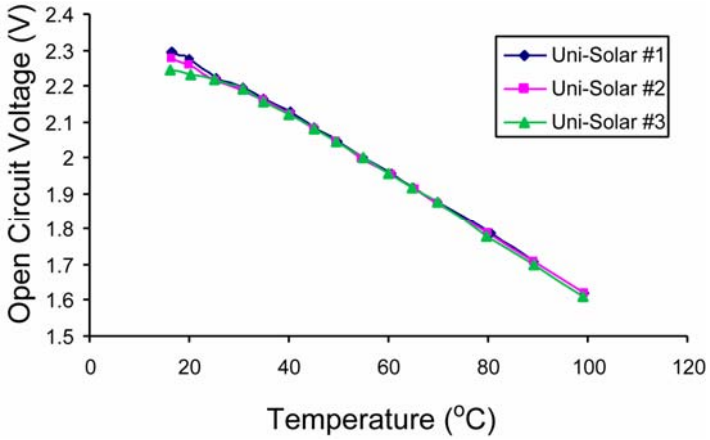

Figure 6. Open-circuit voltage vs. measurement temperature for a-Si triple-junction Uni-Solar thin-film solar cells.

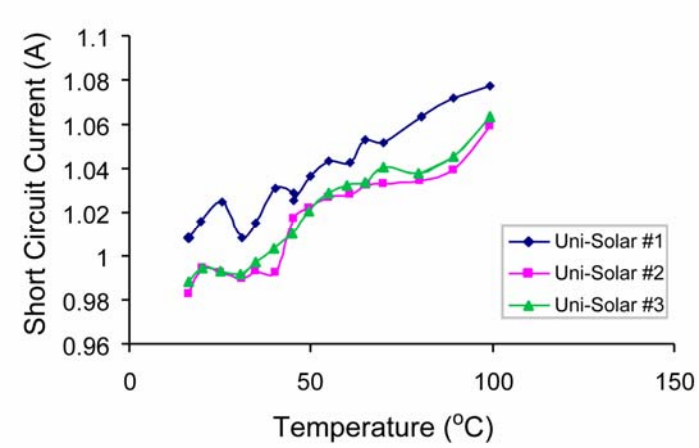

Figure 7. Short-circuit current vs. measurement temperature for a-Si triple-junction Uni-Solar thin-film solar cells.

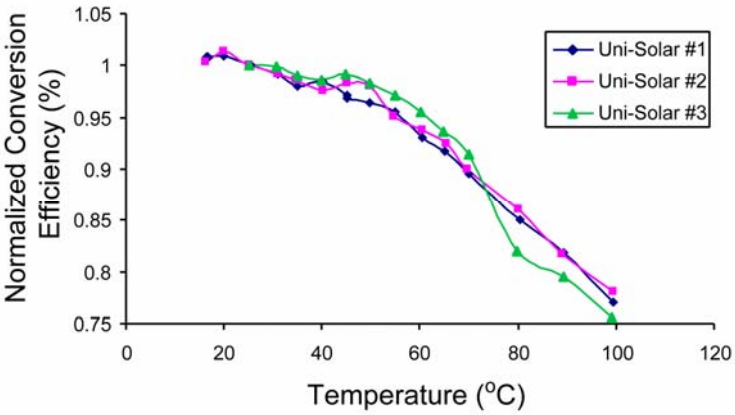

Figure 8. Conversion efficiency vs. measurement temperature for a-Si triple-junction Uni-Solar thin-film solar cells.

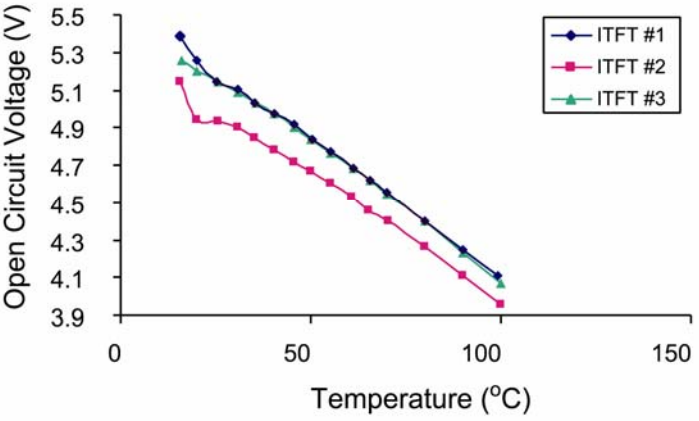

Figure 9. Open circuit voltage vs. measurement temperature for a-Si dual-junction Iowa Thin-film Technology thin-film solar cells.

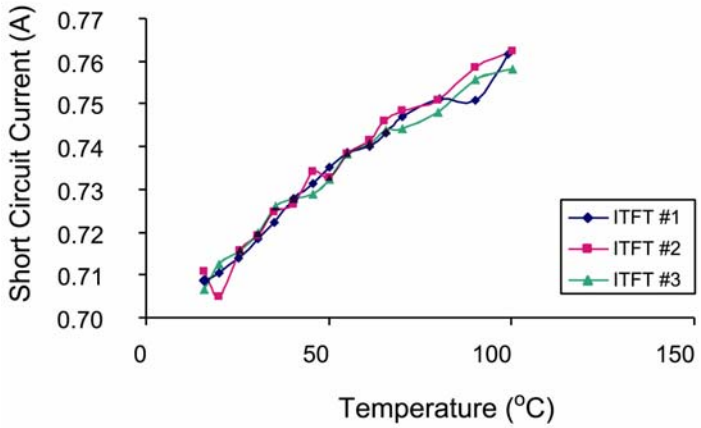

Figure 10. Short-circuit current vs. measurement temperature for a-Si dual-junction Iowa Thin-film Technology thin-film solar cells.

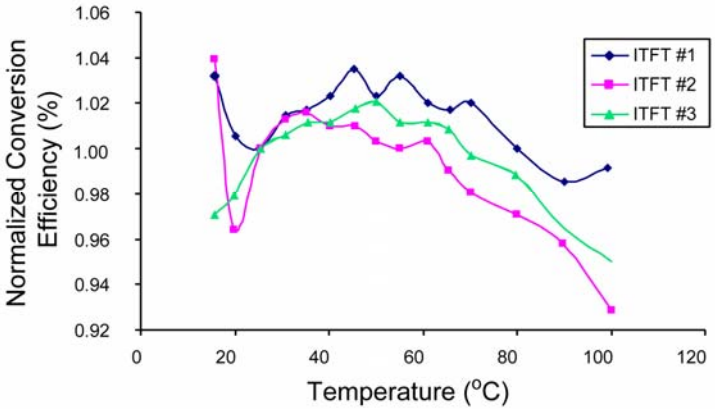

Figure 11. Conversion efficiency vs. measurement temperature for a-Si dual-junction Iowa Thin-film Technology thin-film solar cells.

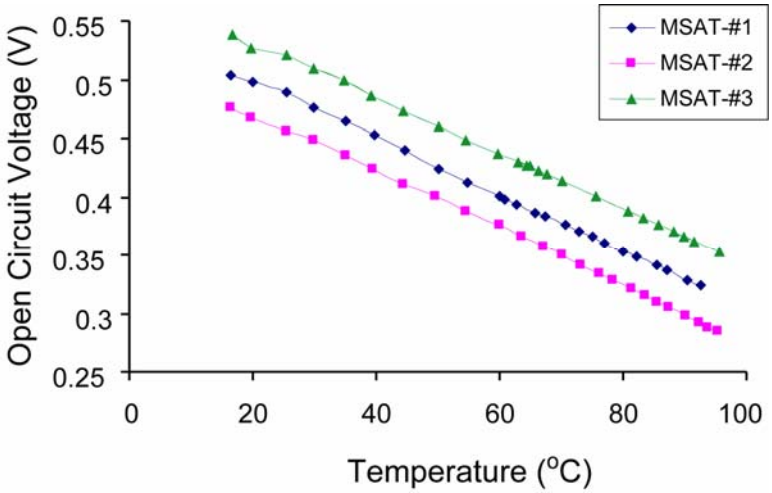

Figure 12. Open circuit voltage vs. measurement temperature for $CIGS_2$ Micro-Sat Systems thin-film solar cells.

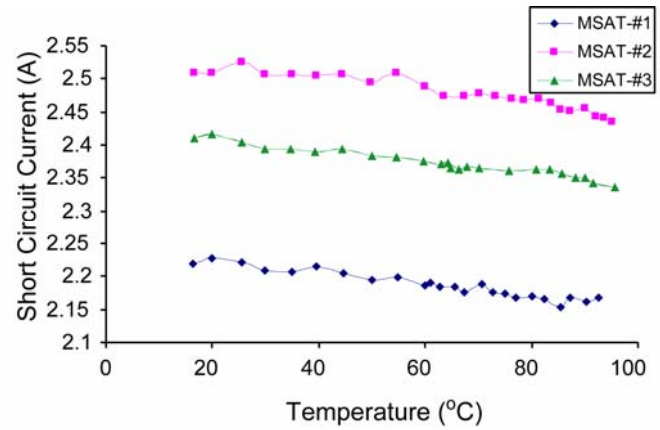

Figure 13. Short circuit current vs. measurement temperature for $CIGS_2$ Micro-Sat Systems thin-film solar cells.

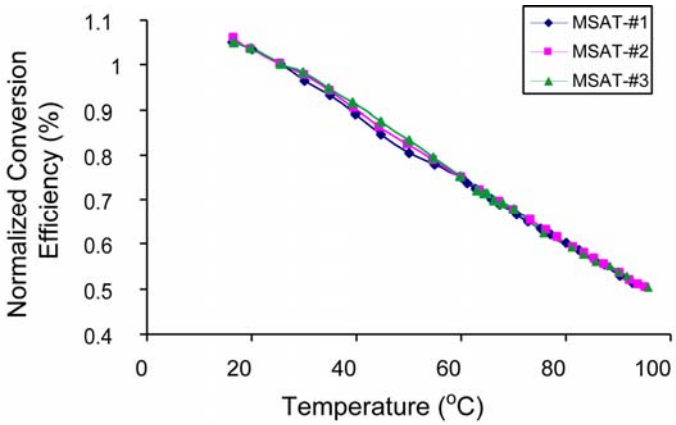

Figure 14. Conversion efficiency vs. measurement temperature for $CIGS_2$ Micro-Sat Systems thin-film solar cells.

Figure 15. New vacuum chamber that will be used in future I-V temperature coefficients measurement.

DEVELOPMENT OF CIGS2 THIN FILMS ON ULTRALIGHTWEIGHT FLEXIBLE LARGE AREA FOIL SUBSTRATES

Neelkanth G. Dhere, Vivek S. Gade, Ankur A. Kadam, Anant H. Jahagirdar, Sachin S. Kulkarni and Sachin M. Bet
Florida Solar Energy Center, Cocoa, FL 32922, U.S.A.

Introduction

The development of thin film solar cells is aimed at reducing the costs for photovoltaic systems [1]. Use of thin film technology and thin foil substrate such as 5-mil thick stainless steel foil or 1-mil thick Ti would result in considerable costs savings. Another important aspect is manufacturing cost. Current single crystal technology for space power can cost more than $ 300 per watt at the array level and weigh more than 1 kg/m^2 equivalent to specific power of ~ 65 W/kg. Thin film material such as $CuIn_{1-x}Ga_xS_2$ (CIGS2), $CuIn_{1-x}Ga_xSe_{2-y}S_y$ (CIGSS) or amorphous hydrogenated silicon (a-Si:H) may be able to reduce both the cost and mass per unit area by an order of magnitude. Manufacturing costs for solar arrays are an important consideration for total spacecraft budget. For a medium sized 5kW satellite for example, the array manufacturing cost alone may exceed $ 2 million. Moving to thin film technology could reduce this expense to less than $ 500K [2]. Earlier publications have demonstrated the potential of achieving higher efficiencies from CIGSS thin film solar cells on 5-mil thick stainless steel foil as well as initial stages of facility augmentation for depositing thin film solar cells on larger (6"x 4") substrates [3]. This paper presents the developmental study of achieving stress free Mo coating; uniform coatings of Mo back contact and metallic precursors. The paper also presents the development of sol gel process, refurbishment of selenization/sulfurization furnace, chemical bath deposition (CBD) for n-type CdS and scrubber for detoxification of H_2S and H_2Se gases.

Sol Gel Process

A new sturdy and robust set up for carrying out sol-gel SiO_2 coating by dip coating method was prepared at FSEC (Figure 1). A structure of adequate height was fabricated for large samples to be raised easily from the container (beaker of capacity 4 liters) holding the sol-gel solution. A DC gear motor of shaft diameter = 0.312"(0.79 cm) with 4 rpm and a pulley assembly for raising and lowering the sample were mounted atop the structure. A 12V DC, 1500 mA power supply was used to control the motion of the DC motor. Special bushings of various dimensions were designed and fabricated for attaching to the motor for variable speeds for carrying out experiments with speeds ranging from 8-16 cm/min. The speed of withdrawal was one of the important factors and attempts were made to optimize the speed for improving the quality of the coating. Weights attached to the bottom of the foil kept it vertical so that the foil enters the sol-gel solution and is withdrawn normal to the sol surface. This prevents the thickness variation during coating. After withdrawal of the foil, it was left hanging to dry for a period of 5 minutes. Later the foil was placed in an Isotemp Muffle Furnace for sintering along with other foils. A batch of four foils could be heat-treated at a time in the furnace in one run. Adequate care was taken to place the foils in a specially prepared fixture without bending or stressing. Samples were sintered in air at a temperature of 450ºC for a period of 1 hour. After cooling for approximately 2 hrs the samples were removed from the furnace, rinsed with deionized water and dried with compressed N_2 gas prior to storing them in a desiccators. Atomic Force Microscopy (AFM) was carried out at National Renewable Energy Laboratory to study the morphology and roughness of the SiO_2 layer on Ti foil substrate at a high resolution. The images were obtained for an area of (100 X 100) μm^2.

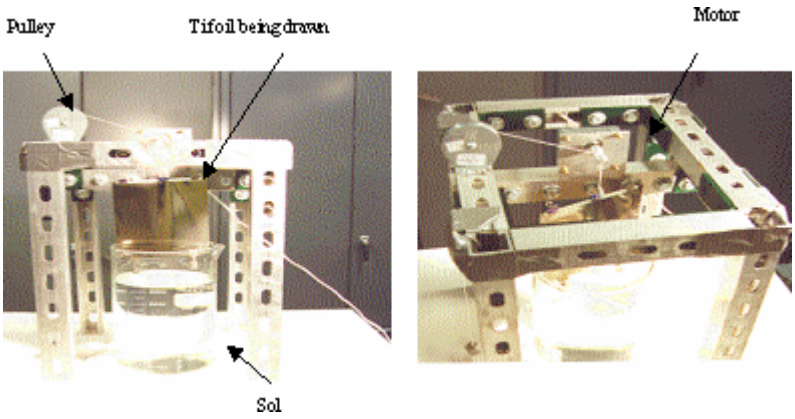

Figure 1. Sol gel setup

AFM images show both the 3-dimensional and normal 2-dimensional images. Figure 2 shows both these images for a plain Ti foil surface without any SiO_2 deposition. The average roughness value obtained was Ra = 543 Å. Figure 3 shows Ti foil coated with SiO_2 where the average roughness value was measured to be 146 Å [4].

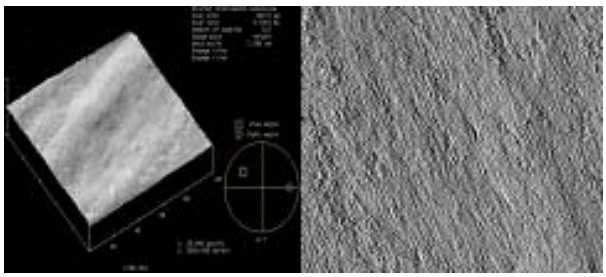

Figure 2: AFM images (100 X 100 μm^2) of plain Ti foil, Ra = 543 Å.

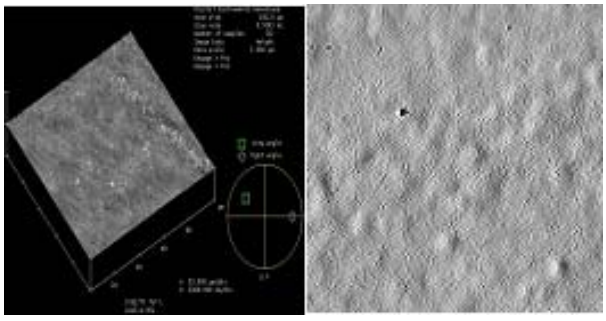

Figure 3: AFM images (100 X 100 μm^2) of Ti foil + 1 thick (0.55 μm) + 2 thin (0.35 μm) SiO_2 layer, Ra = 146 Å.

CIGS2 thin film was deposited on the foil after cleaning in distilled deionized water and drying with compressed N_2 gas. Figure 4 shows a stacked layering sequence for the thin film deposition of CIGS2 on SiO_2 coated titanium foil substrate. Ti was chosen because of its good compromise between cost and physico-chemical properties.

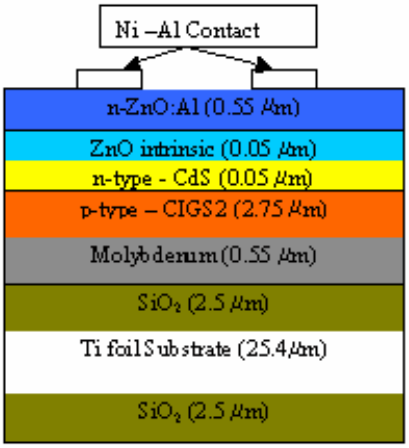

Figure 4: Structure of completed Polycrystalline CIGS2 Thin film Solar Cell.

Mo Back Contact

Depending on the working gas pressure, residual stresses are developed in refractory metal films prepared by magnetron sputtering. Films deposited below transition pressure develop compressive stresses, whereas those deposited above the transition pressure develop tensile stresses. Gross stress may be determined by visual inspection in that highly compressed films tend to buckle up, frequently in zigzag patterns, whereas films under extreme tensile stress develop a system of stress lines that appear like scratches.

Thin flat strips of clean titanium foil of 1cm x 15cm were attached at their ends to a glass substrate prior to deposition (Figure 5) using vacuum compatible tape. It was observed that films deposited at high power of 300W and low argon pressure of 3 x 10^{-4} Torr resulted in compressive stresses. The thin foil deposited under these parameters showed convex bending (Figure 6). On the other hand films deposited at power of 200W and argon pressure of 5 x 10^{-3} Torr resulted in tensile stresses showing concave bending and stress lines (Figures 7-8) [5].

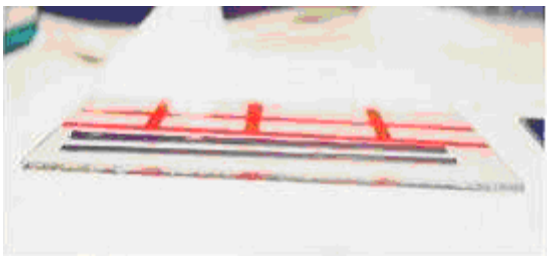

Figure 5: Thin strips of flat foil attached to glass substrate prior to deposition.

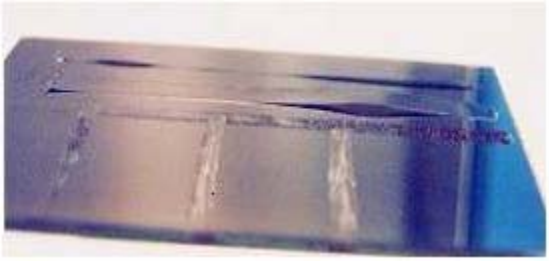

Figure 6: Films deposited at high power of 300W and low argon pressure of 3 x 10^{-4} Torr resulting in compressive stresses leading to lifting of the flat foil.

Figure 7: Films deposited at low power of 200W and high argon pressure of 5 x 10^{-3} Torr resulting in tensile stresses leading to lifting of the inverted deposited foil.

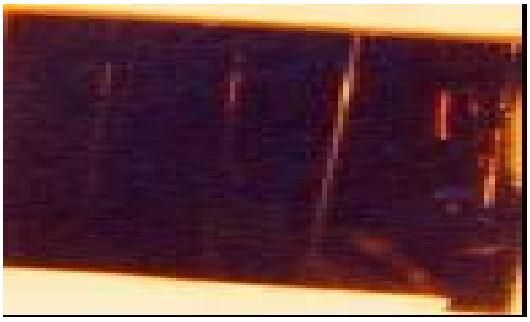

Figure 8: Scratches observed due to tensile stresses on films deposited 200W/ 5 x 10^{-3} Torr.

A simple bending foil technique was used to estimate the magnitude of stress present in the foils. Loads were applied to the concave and convex region of the foil and weight required to make the foil flat similar to its position prior to deposition was measured. The load required and the curvatures in the cycles mentioned above are provided in Table I.

Table I: Loads applied to make foil flat.

Power / Argon Pressure	Height of curvature	Loads applied
300W / 3 x 10^{-4}	0.88 mm	450 mg
200W / 5 x 10^{-3}	0.48 mm	130 mg

The applied loads as well as the curvature of the foil were used for estimating the stress. These samples were sulfurized in 4% H_2S in argon mixture at 475°C for 20 minutes. The reactivity of the molybdenum in sulfur/ selenium atmosphere has been reported to occur at temperatures over 600°C. However, it was observed that the sample under compressive stress peeled off from several regions and turned reddish pink indicating a chemical reaction occurring even at 475°C. On the other hand, the sample under tensile stress remained, mostly as it was with slight change in color from brownish to brownish red.

Foils were deposited with a number of combinations of the cycles of high power/low pressure and low power/high pressure to obtain a very flat foil after deposition. It is reported that such stress reversal is dependent on energetic bombardment by reflected neutral and/or sputtered atoms. At relatively low pressure, the mean free path is high, as a result of which the arriving atoms have higher kinetic energy and the resulting film has dense microstructure thereby experiencing compressive stresses. At higher working pressure the mean free path is reduced resulting in moderate flux of atoms reaching the substrate leaving the film in tensile stress. However, for producing highly efficient 4"x 4" size solar cell, the back contact molybdenum has to be fairly free of residual stresses. Therefore, the deposition started with low power and high pressure to reduce chemical reactivity. Two compressive stress cycles sandwiched between three tensile cycles were deposited in order to lower the stress and to achieve required thickness uniformity.

Thickness Uniformity

Molybdenum back contact and zinc oxide thin films were deposited on large-area glass substrates using optimized parameters of DC or RF sputtering power, working gas pressure, target-to-substrate distance, sputtering time and linear substrate movement parallel to the 4" width of the target.

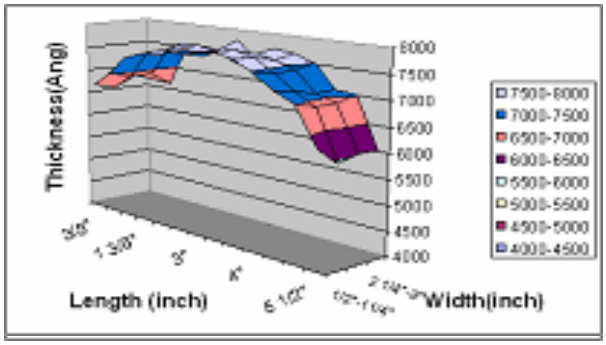

Figure 9. Thickness distribution profile.

After depositions, the grid design initially drawn on the substrates together with the overlaying thin film was removed by ultrasonic cleaning in isopropanol, thus providing a distinct step for measurements with a Dektak[3] thickness profilometer. Thickness variation of ±11% over the central 4"x4" region was observed. Series of experiments were carried out for improving thickness uniformity by empirically modifying the magnetic field distribution. Experiments were carried out using various permutations and combinations of

nickel coated soft iron strips arrangements. The strips were replaced by similar-size rubber strips to maintain the shape integrity. The optimum configuration resulted in a thickness uniformity of ±3% over central 4" x 4" region for molybdenum thin films (Figure 9) while it continued to drop beyond this region [6].

Based on the continued thickness drop beyond 4", it was realized that the magnetic field must be boosted at the extremities to achieve better thickness uniformity. The sputtering sources were also found to produce non-uniform plasma distribution within the racetrack leading to varying plasma intensity glow, again confirming the need to modify magnetic array. In the mean time, the manufacturer had modified the magnetic array with a better magnetic field distribution and stronger magnetic field at the extremities. Two such new magnetron-sputtering sources were procured. The old and new modified magnetic arrays are shown in Figures 10 and 11 respectively.

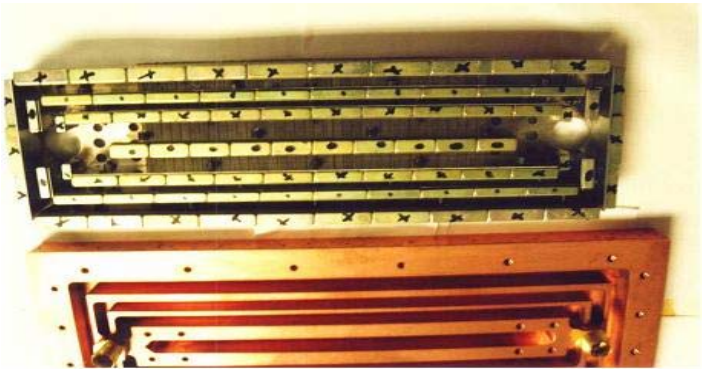

Figure 10: Older Magnetic Array design

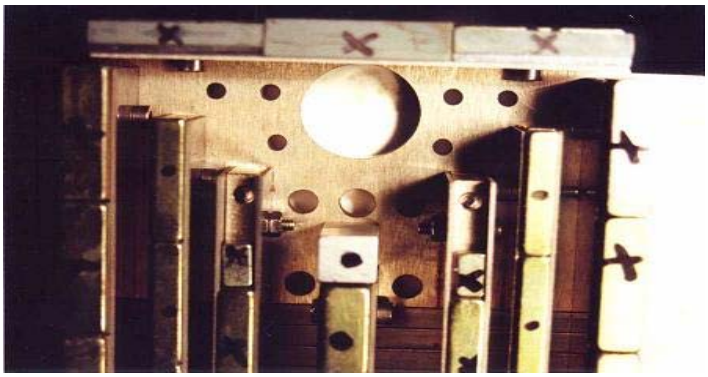

Figure 11: Modified magnetic array.

However, in the absence of specific information of their being substantially different, they were assumed to be similar to the older sources and no thickness profiling experimentation was carried out with them. The new magnetic array design and the necessary additional magnets were obtained from the manufacturer for upgrading the remaining three magnetron-sputtering sources. The design introduced extra magnets at and near the periphery. The copper body holding the magnetic assembly was machined to accommodate the modified assembly. The problem of non-uniform plasma was resolved after modifying magnetic assembly. The initial non-uniform plasma was modified into the dumbbell shape of the racetrack region with the modified magnetic arrays having boosted magnetic field at extremities (Figure 12 a, b).

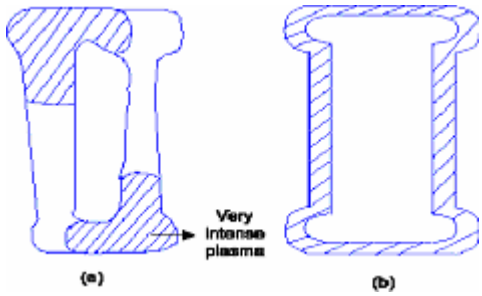

Figure 12. a) Non-uniform plasma b) Uniform plasma.

Figure 13 shows variation of thickness of molybdenum deposited by DC sputtering and zinc oxide by RF magnetron sputtering averaged over 2.75" distances along the linear movement direction with the length parallel to the 12" dimension of sputtering sources. The thickness uniformities over central lengths were: Molybdenum: ±2.24 % over 4", ±2.40% over 5", ±2.95% over 6" and zinc oxide: ±2.46 % over 4", ±3.84% over 5", ±5.60% over 6". Fortunately the thickness uniformity for ZnO/ZnO:Al is slightly less critical. These results pave the way for deposition of large area (6"x4") thin film solar cells.

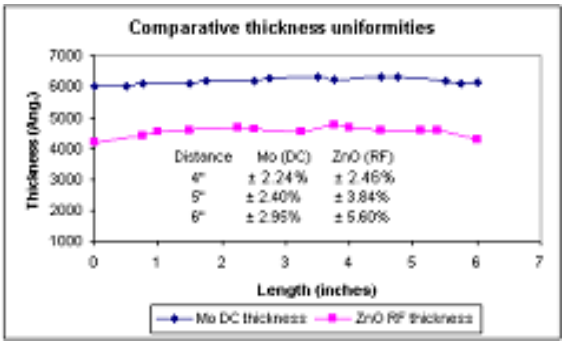

Figure 13. Thickness variation plots Mo (DC sputtering) and ZnO (RF sputtering).

Selenization/Sulfurization Furnace

Deposition of metallic precursors on the substrate is followed by sulfurization to get p-type CIGS2 absorber layer. A furnace was donated by Shell (formerly Siemens) Solar capable of Selenization/Sulfurization of metallic precursors on large 6"x 4" size substrates. The furnace is capable of sulfurizing one hundred 4"x4" or sixty-six of 6"x 4" substrates in a single run. The furnace in as received condition needed upgrade. The major part of upgrade included; the computer, mass flow controllers, valves, thermocouples and cables. The furnace is now fully operational and produces CIGS2 absorber layer on routine basis.

Figure 14. Selenization/Sulfurization furnace

CdS by Chemical bath deposition

Having augmented the substrate size to 4"x 4", next step was to design and construct chemical bath deposition (CBD) setup for four such substrates. The setup was built using teflon sheets of ½" and 1/8" thickness, and a teflon rods of 1/8" diameter. The setup can hold two1/8" thick glass samples and two 1-5 mil thick stainless steel or titanium foil substrates. Holes were drilled in the bottom and top teflon plate to insert 1/8" diameter rods for holding the two top and bottom sheets assembly. 4 5/8" length of the rods allowed 4" clearance between top and bottom plates for placing 4" x 4" substrates. The bottom plate has a central circular hole for the stirrer movement. The top plate had openings for insertion of the thermometers and pH control sensors. The final assembly is shown in the figure 15. Experiments were carried out with the new designed set up, thus scaling up from 1.25" x 1" to 1" x 4" to 4" x 4" as shown in Figure 16. Table 2 provides the bath composition for carrying out deposition on 4"x 4" substrates.

Table II. Chemical bath composition for 4" x 4" substrates

Sr.No.	Type of solution	Concentration	Quantity (milliliters)
1	Distilled and Deionized water	-	1320
2	Ammonium Hydroxide $(NH)_4OH$	28 to 30%	309
3	Cadmium Sulfate $CdSO_4$	0.015 M	181.5
4	Thiourea	1.5 M	90.75

Composition of the bath was chosen so that the substrates would be completely immersed inside the chemical bath. The bath is prepared in a beaker of 3500 ml capacity for the new set up of 4" x 4" substrates to fit snugly [7].

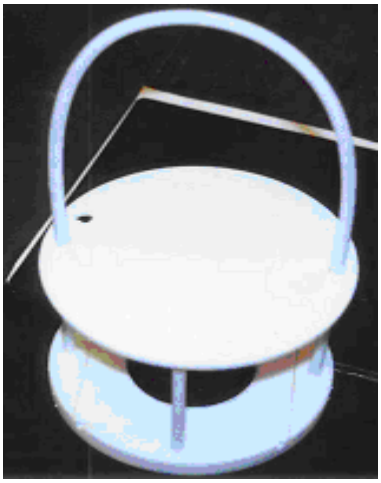

Figure 15. CDS setup for 4”x 4” substrates

Figure 16. Increase in substrate sizes from 1.25” x 1” to 1” x 4” to 4” x 4”

Scrubber

A scrubber was designed and fabricated to detoxify H_2S and H_2Se gases coming out of the furnace reaction tube. Reaction tube having a volume of 15.3 liters is filled with process gas [N_2+H_2S (<4%) or N_2+ H_2Se (<4%)] and heated to 500 ^{0}C in a furnace. A mechanical pump pumped the process gas from the reaction tube through a mass flow controller. The effluent gas was further diluted with nitrogen by factor of 60. The process gas was fed through a venturi that is propelled by nitrogen gas used for dilution. The total flow of diluted hydrogen selenide (666 ppm) or diluted hydrogen sulfide (666 ppm) gas was calculated to be 132 liters/min equivalent to 4.7 scfm. The diluted process gas flows through the first wet scrubber and then through the first packed-bed column. The total height of the packed bed was calculated to be 6.9 feet for H_2S in order to achieve less than 10 ppm at exhaust. The height of the total packed bed was calculated to be 17.14 feet for H_2Se to achieve 50 ppb prior to exhaust according to Occupational Safety and Health Administration (OSHA). The packed-bed column was split in two. The height of the first column was 10.25 feet and the second was 9.25 feet. The extra height was provided to accommodate the packed bed column internals. Prior to entering the second packed-bed column, the gas passes through the second wet scrubber. The effluent gas from the packed-bed column(s) passes

through drums containing activated carbon impregnated with KOH and from there will be exhausted to the atmosphere [8].

The four point CM4 analyzer for H_2Se has been installed, to detect the H_2Se gas concentration at various levels. This CM4 analyzer has been connected to the present building alarm system in FSEC.

Figure 17. Inside (left) and outside (right) scrubber assembly including CM4 connections

Figure 18. Drums containing activated carbon impregnated with KOH and exhaust fans assembly

Conclusion

The paper demonstrates the potential of PV Materials Lab at the Florida Solar Energy Center (FSEC) for carrying out research and development of $CuIn_{1-x}Ga_xSe_{2-y}S_y$ (CIGSS) thin-film solar cells on large area ultralightweight flexible metallic foil for space applications. This facility equipped with large area deposition systems, sulfurization/selenization furnace along with CBD setup for CdS deposition and the scrubber unit is one of its kinds amongst University Labs and could serve as a nucleus of a small pilot plant for CIGSS thin film solar cell fabrication.

Acknowledgements

This work was supported by the NASA Glenn Research Center, Contract # NCC 3712, and the National Renewable Energy Laboratory, contract no. NDJ-2-30630-03.

References

[1] Schock H. W and Pfisterer. F, "Thin Film Solar Cell: The Early Years", 16th European photovoltaic solar energy conference, vol. 1 (2000), pp. 269-274

[2] S. R. Ghongadi, "$CuIn_{1-x}Ga_xS_2$ (CIGS2) Thin Film Solar Cells On Stainless Steel Foil Space Power Application", Master's Thesis (University of Central Florida, Orlando) 2000

[3] N. G. Dhere, S. R. Ghongadi, M. B. Pandit and A. H. Jahagirdar, "CIGS2 Thin Film Solar Cells On Flexible Foils For Space Power", Proc. 17th Space Photovoltaic Research and Technology Conference, Cleveland, OH, Sept. 2001

[4] V. S. Gade, "Development Of Copper Indium Gallium Disulfide $CuIn_{1-x}Ga_xS_2$ (CIGS2) Thin Film Solar Cells On Large Area Ultralightweight Titanium Foils Coated With Sio_2 Barrier Layers", Master's Thesis (University of Central Florida, Orlando) 2002

[5] S. M. Bet, "High Voltage Bias Testing Of Thin Film PV Modules, Adhesional Strength And Surface Analysis For PV Module Durability And Study Of Back Contact Molybdenum For Thin Film CIGS2 Solar Cells", Master's Thesis (University of Central Florida, Orlando) 2003

[6] A. A. Kadam, "Development Of Large Area Copper Indium Gallium Disulfide (CIGS2) Thin Film Solar Cells On Stainless Steel Foil For Space Application", Master's Thesis (University of Central Florida, Orlando) 2002

[7] C. Guillein, M.A. Martinez, J. Herrero "Accurate Control Of Thin Film CdS Growth Process By Adjusting The Chemical Bath Deposition Parameters", Thin Solid Films 335 (1998) 37-42

[8] S. S. Kulkarni, "Development Of Scrubber, Optimization Of Deposition Parameters For Large Area CIGS2 Solar Cells", Master's Thesis (University of Central Florida, Orlando) 2003

$Cu(InGa)Se_2$ SOLAR CELLS ON A FLEXIBLE POLYMER WEB

Robert Birkmire, Erten Eser, Shannon Fields, William Shafarman
Institute of Energy Conversion
University of Delaware, Newark, DE 19716

Introduction

Elemental in-line evaporation on glass substrates has been shown to be a viable process for the large-area manufacture of $CuInSe_2$-based photovoltaics, with demonstrated module efficiencies as high as 12.7% [1]. However, in certain applications such as space power and mobile terrestrial power sources, lightweight, flexible modules are preferable. In addition, flexible substrates allow the thin film to be deposited in a roll-to-roll configuration which may have significant manufacturing advantages. These considerations motivated the use of high-temperature polymer substrates [2], which resulted in a highest efficiency of 12.8% for a laboratory device fabricated by a lift-off process [3]. Unlike metal foils, which are also lightweight and flexible, polymer substrates are (a) electrically insulating, simplifying monolithically-integrated module fabrication, (b) inert in the $Cu(InGa)Se_2$ deposition environment, and (c) are not a source of impurities diffusing into the growing film. However, while possessing these advantages, polymer substrates have a potential disadvantage in their limited maximum operating temperature and their effect on adhesion between the $Cu(InGa)Se_2$ film and the Mo back contact. It should also be mentioned that Na incorporation into the $Cu(InGa)Se_2$ film, which has been shown to increase efficiency [4], would be problematic for both metal foils and polymer substrates. The Institute of Energy Conversion (IEC) has modified its in-line evaporation system [5] from deposition onto glass substrates to roll-to-roll deposition onto polyimide (PI) film. The addition of this capability has allowed the investigation of key issues in the deposition of large-area $Cu(InGa)Se_2$ films on flexible substrates. In particular, this paper gives a brief description of the in-line system and the theoretical model simulating the film growth process and presents experimental results addressing $Cu(InGa)Se_2$ adhesion to the Mo back contact, large-area uniformity, and device performance.

Experimental

$Cu(InGa)Se_2$ films were deposited in a multi-source in-line evaporation system onto a 6-inch wide polyimide/Mo web provided by Global Solar Energy. A detailed description of the system shown in Figure 1 is given in Reference 5. The system consisted of Cu, Ga, and In sources each having two nozzles with Se delivered globally via a sparger. The substrate web was heated from the backside by two sequential platens. The deposition zone was limited to a 5"x15" area defined by an aperture just below the web. Cu and In evaporation were controlled by in-situ atomic absorption spectroscopy (AAS) using the ATOMICAS™ system by Sycon Instruments, while Ga evaporation was controlled by temperature. The internal layout of the system is shown schematically in Figure 2. This configuration where sources are placed sequentially gives, nevertheless,

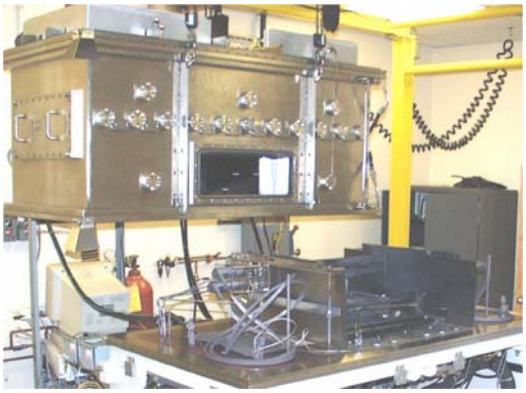

1. Fig. 1. View of the roll-to-roll deposition system.

uniform Cu distribution through the thickness of the film due to the high diffusivity of Cu atoms. The distribution of Ga relative to In, however, will change as the film grows. This results in a band gap gradient in the film that can be engineered, giving another level of control in optimizing the performance of the devices based on these films.

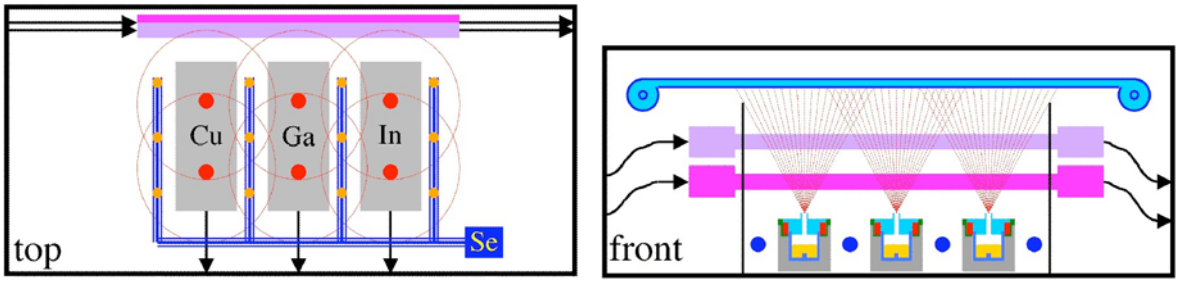

Fig. 2. Schematic layout of the web substrate, sources and AAS beams.

Two growth sequences were used to deposit Cu(InGa)Se_2 films: 1) The web was moved through a Cu-Ga-In source sequence at a web speed of 0.75"/min. at a web temperature between 400 to 450°C. This yielded a 1.8 μm Cu(InGa)Se_2 film in 20 min. (0.09 microns/min). With this source sequence, the Cu(InGa)Se_2 film initially grows Cu-rich, followed by a Cu-deficient growth stage [5]. 2) The web was initially coated with a Ga-In-Se film deposited by moving the web through an In-Ga source sequence at a substrate temperature of approximately 350°C. Then, the Cu(InGa)Se_2 film was deposited as in sequence 1. Typical thickness of the final film was between 1.8 to 2.5 microns.

The composition of the Cu(InGa)Se_2 film was determined by energy dispersive spectroscopy (EDS) at 20 kV accelerating voltage. The structure of the Ga-In-Se precursor and Cu(InGa)Se_2 films were characterized using $\theta/2\theta$ X-ray diffraction (XRD), or glancing incidence XRD, (GIXRD) at an incident angle of 1°. In some cases, composition depth profiles were obtained by auger electron spectroscopy (AES).

Devices were 0.56 cm^2 in area, and were fabricated using a PI/Mo/Cu(InGa)Se_2/CdS/ZnO/ITO/Ni-Al device structure. After initial J-V characterization under 100mW/cm^2 AM1.5 illumination, devices were sometimes heat treated in ambient air at 200°C and re-tested. Heat treatment times ranged from 2 to 150 minutes.

Results

Film Growth Model

The film growth model developed considers only the transport of metal atoms from the sources on to the substrate and assumes unity sticking coefficients and instantaneous chemical reaction on the substrate surface with Se atoms. The problem is then defined, as in Figure 3, by the effusion rate of the metal atoms from the source nozzles and by the arrival flux of these atoms on a unit area of the moving web. Kinetic theory of gases gives for the evaporative effusion rate from the surface of the melt of area A_{surf},

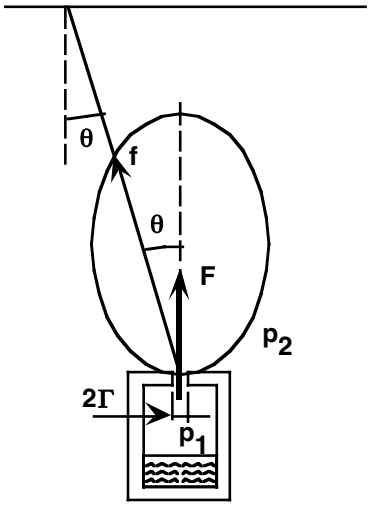

Fig. 3. Geometry of the effusion flux onto a substrate.

$$F = \left[\frac{M}{2\pi RT}\right]^{1/2}\left(p^{sat}(T) - p_1\right)A_{surf} \qquad \text{Eq. 1}$$

The theory of gaseous flow through orifices, in the free molecular regime gives,

$$F = 2\pi\Gamma^2 K\left[\frac{M}{2\pi RT}\right]^{1/2}\left(p_1 - p_2\right) \qquad \text{Eq. 2}$$

for the two nozzle sources used.

These effusion rates are set equal due to the conservation of mass solving for p_1, the internal pressure in the sources. Assuming that flux intensity profile is of the form $a\cos^n\theta$, one finds by setting the integrated flux over a hemispherical surface to be equal to the total effusion that

$$f = \frac{(n+1)F}{2\pi r^2}\cos^{n+1}\theta \qquad \text{Eq. 3}$$

In the present case, the exponent n was determined experimentally by measuring the thickness of Cu films deposited on glass slides located on a hemispherical ring placed right over one of the nozzles. Figure 4 below gives the normalized Cu thickness for a number of effusion rates spanning the range from 0.15 g/hr to 23.2 g/hr from the nozzle. As can be seen, n = 3 gives an acceptable fit to data.

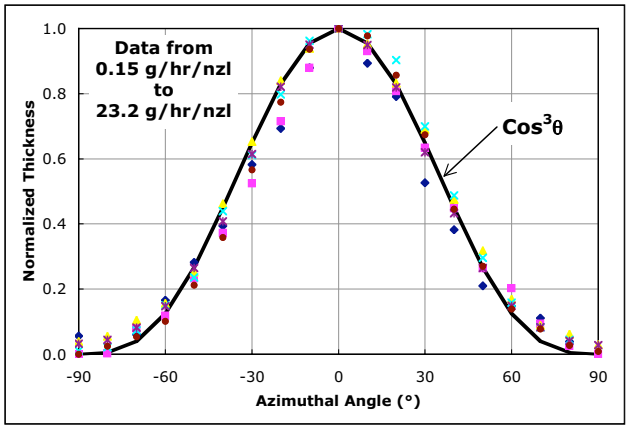

Fig. 4. Flux intensity profile from normalized thickness measurements and $\cos^3\theta$ distribution.

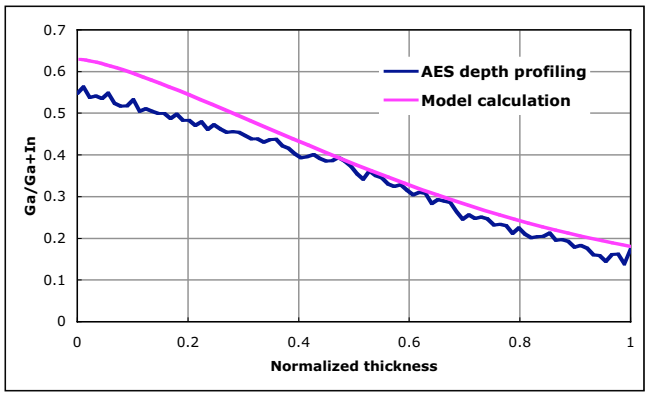

Fig. 5. Ga/Ga+In ratio from Auger depth profiling data and from the film growth model calculation.

The Ga gradient in a typical Cu(InGa)Se_2 film has been measured by AES and is shown in Figure 5, along with the profile calculated from the model. Normalized thickness 0 indicates the Mo/Cu(InGa)Se_2 interface, and 1 indicates the film surface. Although there is some difference between the model and the experimental data at the Mo interface, this difference becomes negligible in the top 60% of the film. Figure 5 also indicates that the Ga gradient in these films is almost linear. For this particular Cu(InGa)Se_2 film Ga ratio changes from 55% at the Mo interface to 18% at the surface corresponding to a band gap variation from 1.33 eV to 1.12 eV [6].

Adhesion and Crystallographic Structure

Cu(InGa)Se_2 films deposited on glass substrates by sequence 1 and characteristics of devices fabricated on them were previously reported [5]. This single-layer deposition process produced well-adherent films with good device efficiencies on Mo-coated glass. Films deposited directly on the polyimide/Mo web using sequence 1, however, delaminated during subsequent handling especially during CdS film growth by the chemical cath deposition method. This situation was resolved by depositing a Ga-In-Se precursor layer prior to Cu(InGa)Se_2 deposition (i.e. sequence 2). These films showed no delamination when subjected to a 40 oz/inch tape test as well as during cell fabrication processes.

XRD measurements show that the Cu(InGa)Se_2 films deposited by sequence 1 had (112) preferred orientation at ~400 °C web temperature and tend to be more randomly oriented at higher web temperatures. The Cu(InGa)Se_2

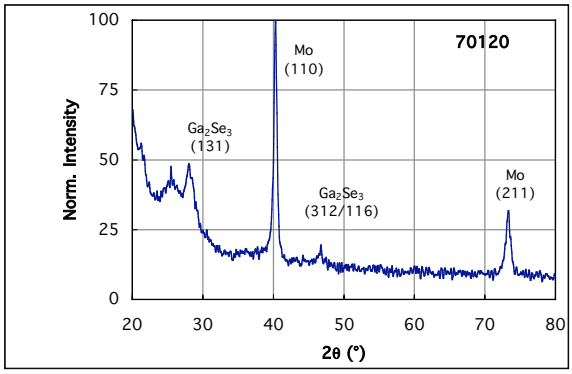

1. Fig. 6. GIXRD spectrum of the precursor layer.

films deposited on the Ga-In-Se layer were randomly oriented independent of web temperature. The structure of the precursor layer was determined by the GIXRD technique and its composition by AES depth profiling. The GIXRD spectrum of Figure 6 shows that the structure is consistent with that of β-Ga_2Se_3 (JCPDS 44-1012) with the peaks shifted to a higher d-spacing due to the presence of indium atoms at substitutional sites in the lattice. AES indicates an Ga/(Ga+In) ratio of 0.8 identifying the precursor layer to be β-$(Ga_{1-x}In_x)_2Se_3$.

Uniformity and Device Performance

The cross web thickness uniformity was evaluated by estimating film thickness from SEM cross-sections and was found to have better than ±3% standard deviation, well within the accuracy of the measurement.

Table I. Film composition over 5 feet x 6" of web.

Position (") X	Y	Cu (at%)	In (at%)	Ga (at%)	Se (at%)	Cu/III	Ga/III
0.0	10	23.3	20.0	7.7	49.0	0.84	0.28
-1.5	25	24.1	19.9	7.8	48.3	0.87	0.28
1.5	25	23.8	19.7	7.7	48.8	0.87	0.28
0.0	30	23.9	19.9	7.2	49.0	0.88	0.26
-1.5	35	23.9	19.7	7.6	48.8	0.88	0.28
0.0	35	23.7	19.8	7.6	48.9	0.86	0.28
1.5	35	24.1	19.6	7.5	48.9	0.89	0.28
0.0	40	24.3	19.6	7.3	48.9	0.90	0.27
0.0	45	23.6	19.6	7.2	49.6	0.88	0.27
-1.5	45	23.8	19.5	7.3	49.3	0.89	0.27
1.5	45	24.2	19.5	7.3	49.1	0.91	0.27
0.0	50	23.9	19.7	7.5	49.0	0.88	0.28
0.0	55	24.2	20.0	7.5	48.3	0.88	0.27
0.0	60	23.6	19.6	8.1	48.8	0.85	0.29
1.5	65	24.5	19.5	8.0	48.0	0.89	0.29
-1.5	65	24.4	19.5	7.6	48.5	0.90	0.28
0.0	65	24.4	19.8	7.5	48.3	0.89	0.27
0.0	70	24.4	19.7	7.6	48.2	0.89	0.28
Average		**24.0**	**19.7**	**7.5**	**48.7**	**0.88**	**0.28**
Stdev (%)		**1.4**	**0.9**	**3.3**	**0.9**	**1.9**	**2.5**

The compositional uniformity was evaluated by an 18-point EDS characterization of a single run of 5 feet in length and the results are summarized in Table I. The standard deviation of about 1% for the atomic concentration and ratios are within the accuracy of the EDS measurement. Composition controllability over 16 consecutive runs had a standard deviation of 0.062 for Cu/(Ga+In) and 0.025 for Ga/(Ga+In). The Cu(InGa)Se_2 composition and film thickness data indicate acceptable uniformity in film properties over the web surface for a given deposition.

Device uniformity for Cu(InGa)Se_2 films in a single run over a 5 foot length of web are shown in Table II for 18 devices fabricated along the centerline of the web. The average V_{oc} was 0.529 V with a standard deviation of only 0.005 V and average efficiency was 10%. For this run the Cu/(Ga+In) ratio was 0.82 and the Ga/(Ga+In) 0.40. Cu(InGa)Se_2 film thickness was measured to be 1.9 μm. A 2-D device efficiency survey of the web is given in Table III where each entry is the average of 4 devices over 1"x1" sample. Device efficiencies averaged 10.0%±0.4% along the centerline of the web, and 8.8%±1.0% and 8.4%±0.9% along either edge. The data show a clear pattern of higher efficiencies along the centerline, and also a trend of improving performance and cross-web uniformity down the web.

Table II. Device uniformity over the centerline of the web.

Position (")	Cell #	Voc (V)	Jsc (mA/cm2)	FF (%)	Eff (%)
20	3	0.517	29.6	56.7	8.7
	4	0.533	30.2	63.0	10.2
30	1	0.527	30.6	60.1	9.7
	2	0.521	31.0	60.1	9.7
	3	0.534	30.2	62.4	10.1
	4	0.532	30.3	60.8	9.8
40	1	0.529	30.7	62.5	10.1
	2	0.528	30.6	62.6	10.1
	3	0.532	30.9	62.6	10.3
	4	0.528	30.8	62.7	10.2
50	1	0.528	31.0	60.5	9.9
	2	0.533	30.9	62.2	10.2
	3	0.529	30.4	60.1	9.7
	4	0.533	30.8	63.0	10.4
60	1	0.529	30.4	61.1	9.8
	2	0.526	31.0	61.6	10.1
	3	0.535	30.4	61.6	10.0
	4	0.531	31.0	62.4	10.3
	Best	**0.533**	**30.8**	**63.0**	**10.4**
	Avg	**0.529**	**30.6**	**61.4**	**10.0**
	Stdev (%)	**0.86**	**1.2**	**2.6**	**3.9**

Figure 7 shows the efficiency of the best device from each run obtained for 21 different depositions of 5 to 6 feet. The run-to-run composition variation observed in the figure suggests that the effusion control technique may require some refinement. However, it should be noted that the sensitivity of device efficiencies, especially after heat treatment, on the Cu/(Ga+In) ratio is quite low, which mitigates deficiencies in the effusion control scheme as currently implemented. In fact the data show that the process is able to produce high-quality material over a wide range of Cu/(Ga+In) ratios from 0.67 to 0.96. The best efficiency was obtained for Cu/(Ga+In) = 0.70 and Ga/(Ga+In) = 0.26. After a 150-minute heat treatment the efficiency was 11.5%, reaching 12.1% with a 1200 Å MgF_2 anti-reflection coating (see Fig. 8).

The device parameters currently limiting performance are open-circuit voltage and fill factor is probably due to the fact that substrate temperature is limited to 400°C to 450°C because of the polyimide substrate. However,

incorporation of Na into the Cu(InGa)Se_2 film, using a separate source, would contribute to improving the performance.

Table III. 2-D efficiency survey of 5' of web.

Location	20”	30”	40”	50”	60”	Cumulative
-1.5”	9.0 ± 0.4		8.2 ± 1.6		9.1 ± 0.3	8.8 ± 1.0
0	9.4 ± 1.1*	9.8 ± 0.2	10.2 ± 0.1	10.0 ± 0.3	10.0 ± 0.2	10.0 ± 0.4
+1.5”	8.2 ± 0.4		8.2 ± 1.5		9.0 ± 0.2	8.4 ± 0.9
Cumulative	8.7 ± 2.1		8.8 ± 1.5		9.4 ± 0.5	9.2 ± 1.0

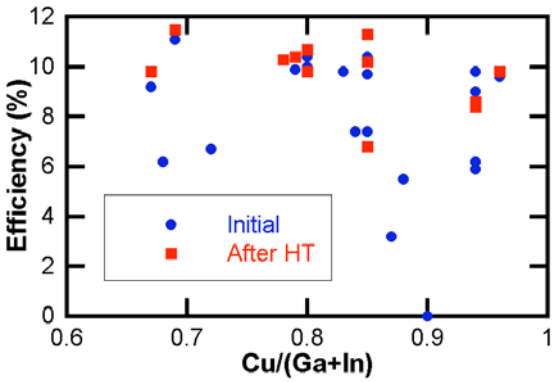

Fig. 7. Best device efficiency as a function of Cu/(Ga+In) ratio over 21 depositions.

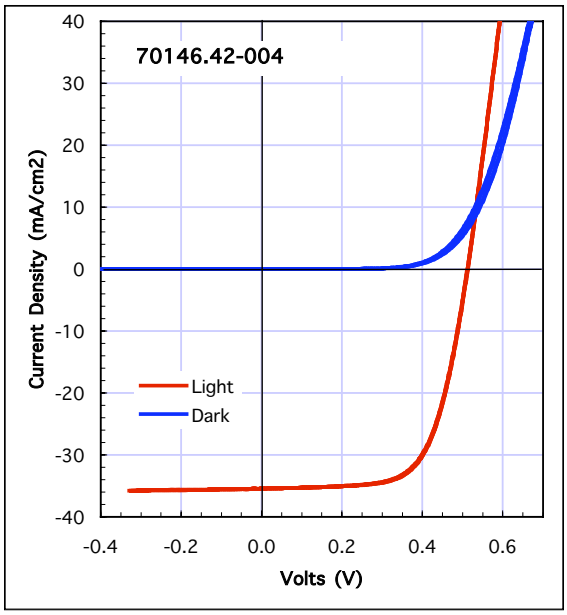

Fig. 8. J-V characteristics of the best device with a MgF_2 anti-reflection coating. J_{sc} = 35.4 mA/cm_2, V_{oc} = 0.512 V, FF = 66.6 %, Eff = 12.1 %.

Conclusion

A pilot process for depositing uniform, adherent Cu(InGa)Se_2 films onto a continuous polyimide/Mo web has been demonstrated. Average device efficiencies are better than 9%, with a highest efficiency of 12.1%. Device uniformity in the range of 10% has been demonstrated. The process also demonstrates a high tolerance to Cu/(Ga+In) variation. In summary, this study lends support to the feasibility of $CuInSe_2$-based photovoltaics on polyimide, and has identified both fundamental and engineering issues to further their realization.

References

1. Powalla, M. and B. Dimmler, Thin Solid Films 361-361, 540 (2000).
2. Basol, B.M., V.K. Kapur, C.R. Leidholm, A. Halani, and K. Gledhill, Solar Energy Materials and Solar Cells 43, 93 (1996).
3. Tiwari, A.N., M. Krejci, F.-J. Haug, and H. Zogg, Progress in Photovoltaics: Research and Application 7, (1999), pp. 393-397.
4. Shafarman, W., Stolt, L., Chapter 13 in Handbook of Photovoltaic Science and Engineering, (A. Luque and S. Hegedus, eds.), Wiley and Sons, Chichester UK, 2003.
5. Hanket, G.M., P.D. Paulson, U. Singh, S.T. Junker, R.W. Birkmire, F.J. Doyle III, E. Eser, and W.N. Shafarman, 28th IEEE Photovoltaic Specialists Conf., 2000.
6. Paulson, P.D., R.W. Birkmire, and W.N. Shafarman, J. Appl. Phys., 94, 879 (2003)

WIDE-BANDGAP CIAS THIN-FILM PHOTOVOLTAICS WITH TRANSPARENT BACK CONTACTS FOR NEXT GENERATION SINGLE AND MULTI-JUNCTION DEVICES

Lawrence M. Woods, Ajay Kalla, Damian Gonzalez and Rosine Ribelin
ITN Energy Systems Inc., Littleton, CO, 80127

INTRODUCTION

Future spacecraft and high-altitude airship (HAA) technologies will require high array specific power (W/kg), which can be met using thin-film photovoltaics (PV) on lightweight and flexible substrates.(1) It has been calculated that the thin-film array technology, including the array support structure, begins to exceed the specific power of crystalline multi-junction arrays when the thin-film device efficiencies begin to exceed 12%.(2) Thin-film PV devices have other advantages in that they are more easily integrated into HAA's, and are projected to be much less costly than their crystalline PV counterparts. Furthermore, it is likely that only thin-film array technology will be able to meet device specific power requirements exceeding 1 kW/kg (photovoltaic and integrated substrate/blanket mass only). Of the various thin-film technologies, single junction and radiation resistant $CuInSe_2$ (CIS) and associated alloys with gallium, aluminum and sulfur have achieved the highest levels of thin-film device performance, with the best efficiency, reaching 19.2% under AM1.5 illumination conditions and on thick glass substrates.(3) Thus, it is anticipated that single- and tandem-junction devices with flexible substrates and based on CIS and related alloys could achieve the highest levels of thin-film space and HAA solar array performance.

ITN Energy Systems, Inc. (ITN) intends to meet the requirements for future high-altitude airship and spacecraft power by developing highly efficient single-junction and two-terminal monolithic tandem (multi-junction) PV cells using low-cost thin-films on lightweight flexible substrates. ITN will achieve this goal using thin-films of high-efficiency and radiation resistant CIS partnered with bandgap-tunable CIS-alloys with Ga (CIGS) and/or Al (CIAS) on novel lightweight and flexible substrates. ITN is currently developing a wide-bandgap CIAS top cell on infra-red transparent back contacts and polyimide substrates to increase the single-junction performance over existing thin-film CIGS on thin metal foil. An illustration of this configuration is given in Figure 1. As a single-junction material, a device using a wide-bandgap CIAS solar absorber offers several performance advantages over standard low-bandgap CIGS devices: it is better tuned to the optimum bandgap for the AM0 solar spectrum; it is better suited for high voltage applications; it undergoes lower resistive losses for cells and modules; it transmits more unused infra-red light for lower temperature operation; and it produces higher power during high-temperature applications due to lower temperature coefficients. A wide-bandgap single junction with transparent back contacts also enables potential backside power generation and is applicable as the top cell and

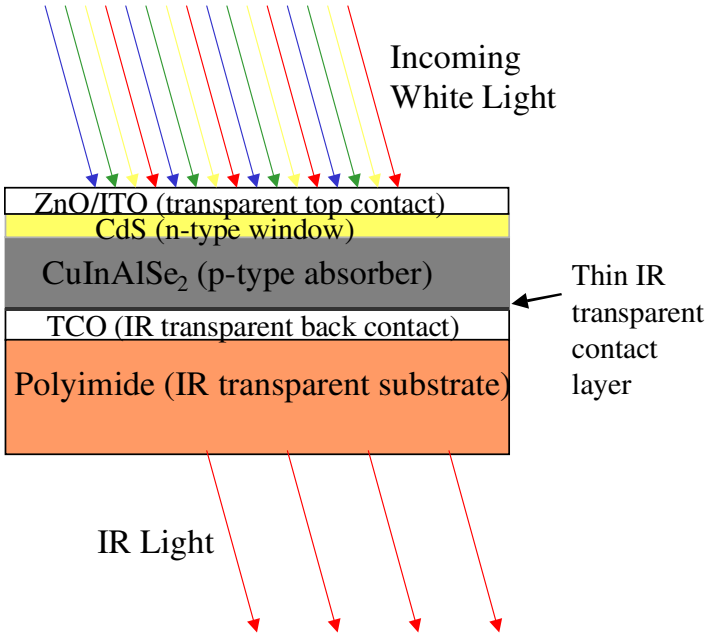

Figure 1 – Cross-sectional (not to scale) illustration of wide-bandgap CIAS device with IR transparent back contacts and substrate.

transparent interconnect components in a monolithic tandem device. This paper discusses the current performance, testing, and problems of the wide-bandgap single junction CIAS device with transparent back contacts.

WIDE-BANDGAP CIAS ALLOY THIN-FILM DEVICES

The electronic quality of the $CuIn_{1-x}Ga_xSe_2$ (CIGS) material has been shown to degrade for x > 0.3, thus the achievement of high-efficiency wide-bandgap CIGS devices is not as easy as simply increasing the Ga alloying in the CIGS material. The best CGS devices (x=1 or bandgap equal to 1.67 eV) were recently fabricated and tested at 9.53% under AM1.5 illumination (Reference: NREL report, "Polycrystalline Thin Film High Performance: NREL In-house Activities," March/April 2003 bimonthly); a good result but far from the 19.2% efficiency of the low-bandgap material. One approach to potentially overcome the bandgap limitations of CIGS devices is to alloy the CIS with aluminum instead of gallium, thus forming thin-film $CuIn_{1-x}Al_xSe_2$ (CIAS). This approach for thin-film photovoltaic devices was initiated by ITN in conjunction with the Institute of Energy Conversion (IEC) nearly four years ago, and is currently under continued development at ITN for large-area (production-like) CIAS depositions. The potential advantage of CIAS is that, for a given wide bandgap, much less Al alloying is needed compared to alloying with Ga,(4) and thus potentially avoiding defect formation associated with higher alloy (Ga or Al) content materials.(5,6) Indeed, recent information about CIAS deep defect density has indicated that Al alloying has more of an effect on the band tail defect distribution, rather than deep defects (Reference: Heath et al., Spring MRS 2003, to be published). R&D CIAS devices with efficiencies of about 11% have been fabricated with bandgap • 1.5 eV (x = 0.5). Furthermore, excellent devices (eff. ≈ 17% under AM1.5) have recently been achieved using small amounts of Al alloying,(7) and with low substrate temperatures (450 ºC) during CIAS co-evaporated deposition.(8) This good performance capability for this material system at the lower substrate temperatures is important for the temperature-limited polyimide substrates and for reducing the stress to the bottom cells in monolithic tandem devices. For CIAS with more top-cell-optimal bandgaps of around 1.65 eV, the best devices to date are 7.8%, but without a performance enhancing anti-reflective top coat, and is thus similar to the CGS performance mentioned above.(8) All these references to CIAS device performance were measured on devices with CIAS deposited without any bandgap tailoring vs. depth, which is typically associated with the highest performance devices. More latitude with bandgap tailoring is available for the wide-bandgap materials using the CIAS alloy system, given its endpoint bandgap of 2.7 eV (CAS), compared to 1.68 eV for CGS in the CIGS alloy system. ITN's CIAS device performance, from the large area and moving substrate deposition system (production like), show similar performance trends with Al content as stated above, and are currently achieving about 2/3^{rds} the efficiency of the best laboratory (small area, stationary substrate) devices. Some light IV curves from a series of CIAS devices with variable Al-content made using the large-area, moving substrate system at ITN are shown in the left side of Figure 2.

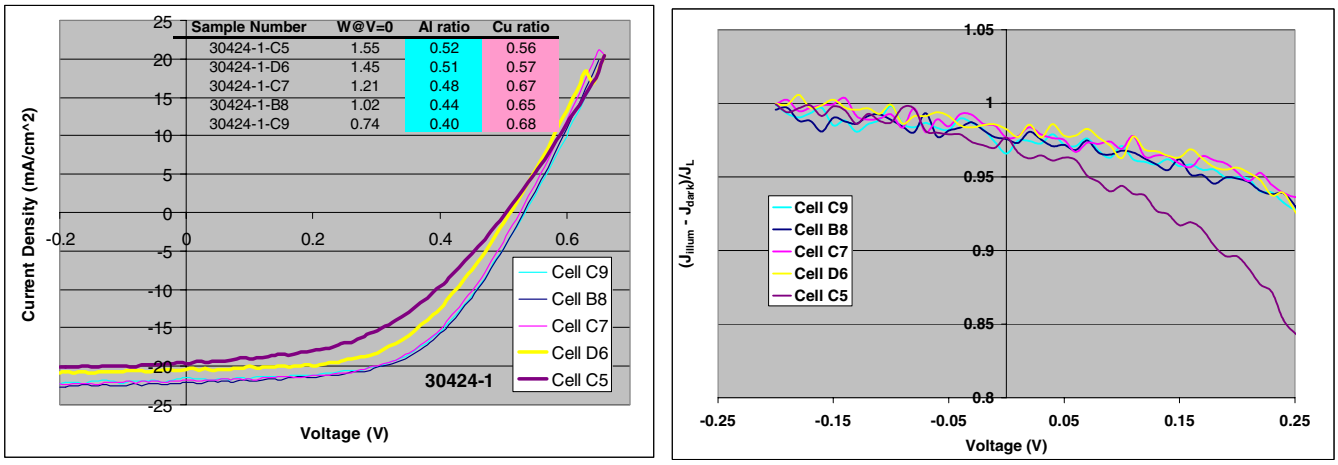

Figure 2 –Light IV curves (left) and voltage dependence of the normalized current difference (right) of small-area (1 cm^2) wide-bandgap CIAS devices from the large-area, moving substrate deposition system. Device composition and zero bias depletion width (W@V=0) are given in the inset tables.

Table 1 - AM1.5 Light IV parameters for small-area (1 cm^2) wide-bandgap CIAS devices shown in Figure 2.

Device	Eff. (%)	Voc (V)	Jsc (mA/cm^2)	Fill Factor	Rs (ohms)	Rsh (ohm-cm)	Diode Factor
30424-1-C5	4.66	0.504	19.71	0.47	4.01	227.00	4.36
30424-1-D6	5.65	0.511	20.45	0.54	3.22	255.00	3.68
30424-1-C7	6.41	0.526	21.81	0.56	3.34	166.00	3.07
30424-1-B8	6.61	0.532	22.15	0.56	3.33	107.00	3.14
30424-1-C9	6.47	0.535	21.51	0.56	3.55	174.00	3.05

The IV curves indicate an apparent high series resistance problem that becomes worse when the Al-ratio exceeds 0.5. Closer examination shows that the series resistance (Rs) as determined using the intercept of a plot of dV/dJ vs J^{-1}, given in Table 1, does not change much with Al content. Furthermore, a plot with the voltage dependence of the normalized current difference (right side of Figure 2) shows significant voltage dependence in all devices, especially in the device with the highest Al-content. Thus, the IV curve features are partially a result of voltage-dependent current collection. In addition, there is a decrease in the open-circuit voltage (Voc) for these higher Al content devices, instead of steadily increasing with increasing Al content. This is accompanied by an increased diode factor (A, in Table 1) and decreasing FF with increasing Al-content. Using the standard solar cell model, the series of measured light IV results can only be fitted by increasing the diode saturation current and diode factor with increasing Al-content, and thus indicates changes in the CIAS electronic properties with Al-content. Indeed, the zero bias depletion widths from Capacitance-Voltage (CV) testing, shown in the figure inset (in units of microns), indicate an increase in the junction depletion width with increasing Al-content. This indicates a decrease in the net doping density near the junction with increasing Al-content. Additional data on the zero bias depletion depth versus CIAS composition are shown in Figure 3, and confirm the correlation with Al content. In this figure the data is color-coded for different Cu-ratio ranges, so that the effect of Cu-ratio on the depletion width can be separated out. For this analysis, the depletion widths were calculated using a composition-dependent dielectric constant, $\varepsilon_r(x)$, which was estimated as linearly decreasing with Al-content between $\varepsilon_r(0)=11.5$ and $\varepsilon_\rho(1)=8.8$, representing the respective CIS and CAS endpoint ternaries. This adjustment works to counteract the apparent trend, thus without it, the depletion width dependence on Al-content would have shown a higher correlation. Similarly, a reduction in depletion width from Cu-ratios around 0.63 is also apparent as shown in Figure 3, but is not as strongly correlated as the Al-ratio. Here also the data is color coded for different Al-ratio ranges, so that the effect of Al-ratio on the depletion width can be separated out.

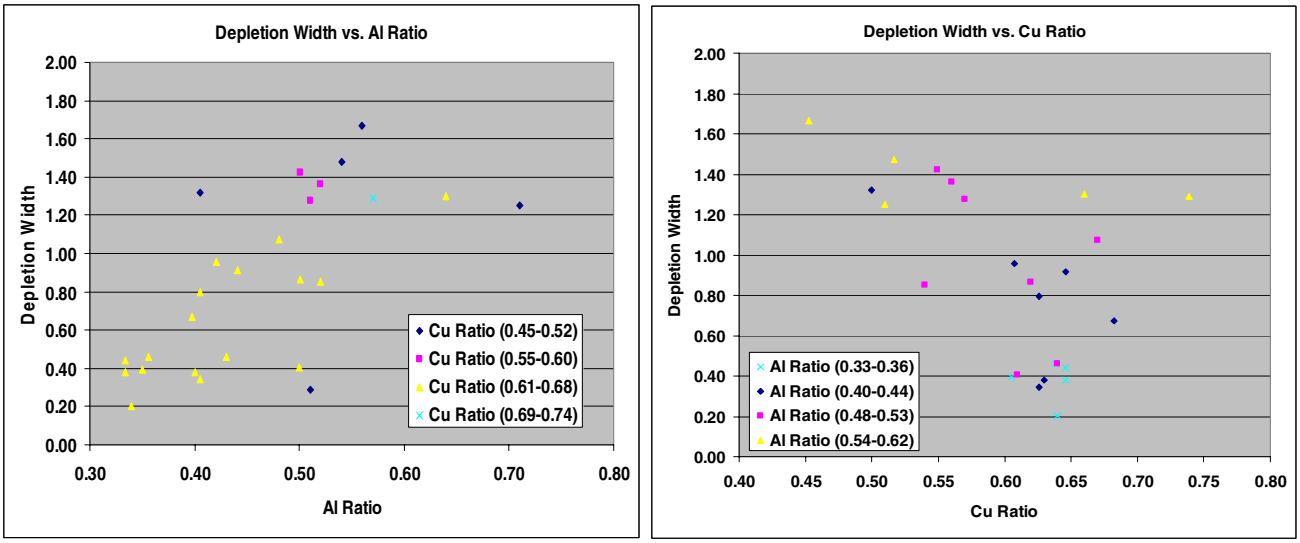

Figure 3 - Zero Bias depletion width versus Al-ratio (left) and Cu-ratio (right) for several devices. Data is adjusted for linearly vary dielectric constant with Al-content and color coded to bracket certain Cu-ratio ranges (left) and Al-ratio ranges (right).

Owing to the lower net doping level in the junction region, the high Al and low Cu content (highly compensated) CIAS devices may have a more severe surface inversion (n-type) layer, a feature now commonly associated with low bandgap CIGS devices. This inversion layer, with an electron barrier at the CdS/inversion layer interface, could lead to the observed voltage dependent current collection and the kink feature sometimes observed in IV curves. A barrier in the conduction band at the CdS/inversion layer interface is possible with increasing conduction band maximum in the CIAS and an n-type inversion layer. This possibility is supported by the high sensitivity of the voltage dependent current collection to air annealing (surface sensitivity), which may reduce the inversion layer thickness and doping in high Al content CIAS devices. An IV curve example of this sensitivity is shown in Figure 4.

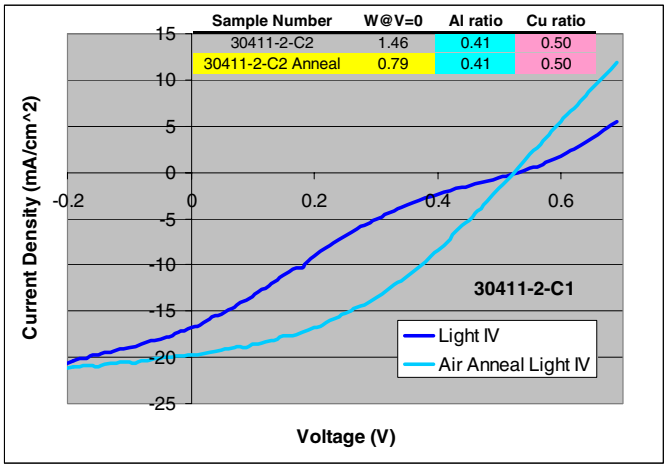

Figure 4 – Example IV's showing the effect of air anneal on high bandgap CIAS devices.

As expected, the short-circuit current (Jsc) decreases with increasing Al-content (bandgap). The quantum efficiency (QE) measurements shown in Figure 5 confirm the increasing bandgap with Al content, as indicated by the decreasing long wavelength cut-off with increasing Al content (left side of Figure 5). The QE measurements also indicate wavelength dependent collection with reduced collection at longer wavelengths and significant sub-bandgap collection. These characteristics worsen with increasing bandgap (Al-content), as does the maximum QE, and is easier to see when the QE curves are aligned near their long-wavelength inflection points as shown in the right side of Figure 5.

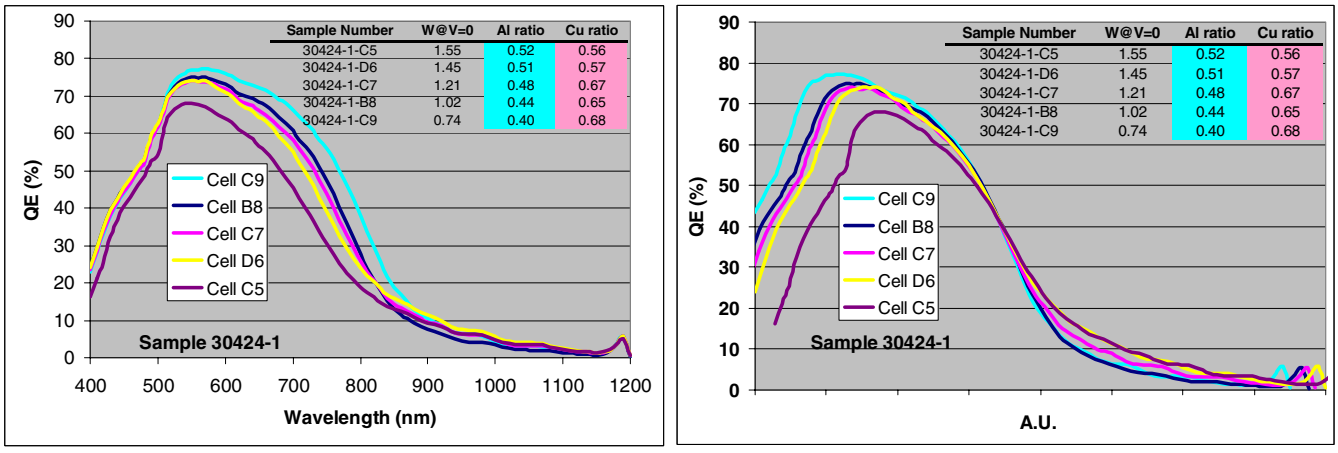

Figure 5 - QE's (right) of small-area (1 cm^2) wide-bandgap CIAS devices from the large-area, moving substrate deposition system. Device composition and zero bias depletion width (W@V=0) are given in the inset tables. QE's on left are the same devices but adjusted to line-up the long wavelength inflection point.

Devices with a depletion width extending almost completely through the CIAS thickness (higher Al content) do not give the expected better long wavelength collection efficiency, and indicate an increase in junction and bulk recombination.

TRANSPARENT BACK CONTACTS

Reverse bias capacitance-voltage profiling (not shown) of CdS/CIAS devices with standard opaque Mo back contacts, reveals that the net bulk doping density is decreasing with increasing Al-content and correlates with the zero bias depletion widths discussed above. The lowest values are measured to be in the low 10^{-15} cm^{-3} range. This could affect the back contact as the native bulk doping level may not be sufficient for a good low resistance contact or to get appreciable majority carrier thermally assisted tunneling and thermionic emission over the back contact Schottky barrier.(9) The majority carrier current is likely to be further impeded by an increasing Schottky barrier energy with increasing Al-content, due to a decreasing CIAS valance band maximum energy.(10) This could be the reason for the high series resistance measured in the devices above. High-efficiency CIGS devices have order of magnitude higher doping levels than those measured on the CIAS devices herein, and high bandgap CGS devices do not show back contact related problems. This is presumably due to increasing net acceptor doping with increasing Ga content, and a valance band maximum energy that does not change much with increasing Ga content. These results lead us to believe that the high series resistance observed in the high Al-content CIAS devices is due in part to the back contact. Thus, the low doping densities in high Al-content CIAS could further complicate the ability to make low resistance transparent back contacts.

Several transparent conducting oxides (TCO's) have been tested as IR transparent replacements to the standard opaque Mo back contacts on high- and low-bandgap CIGS devices. Indium Tin Oxide (ITO) was demonstrated to make good devices with low-bandgap CIGS (low Ga, E_g = 1.1 eV), while additionally showing good durability to the top cell deposition. However, high-bandgap CIGS or CIAS devices (E_g > 1.35 eV) do not make good devices directly on ITO. Other TCO's such as SnO_2 and ZnO did not fair well either, even with the low-bandgap CIGS, indicating that the type of TCO is important to the transparent back contact. Theoretically, this could be due to the decreasing valance band maximum with increasing bandgap, as previously discussed, and a lack of sufficient interface states or mid-gap states in the TCO for tunneling or thermally emitted holes followed by recombination processes. The energy band diagram of the back contact "Schottky" barrier at the p-type CIAS and degenerate n-type TCO interface, and the majority carrier tunneling and recombination process is depicted in Figure 6 below. These results suggest that an interface layer is necessary for wide-bandgap devices using TCO back contacts.

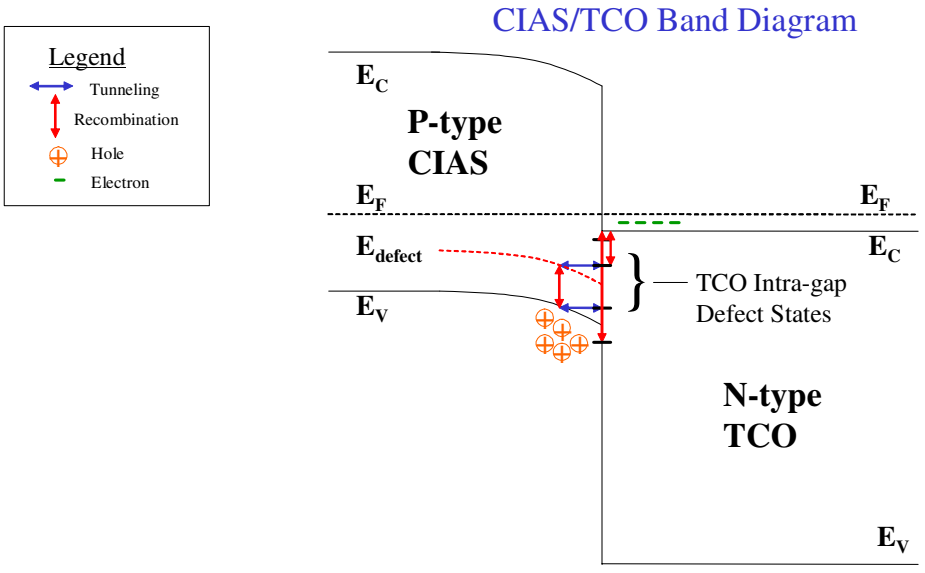

Figure 6 - Energy band diagram of the back contact "Schottky" barrier at the p-type CIAS and degenerate n-type TCO interface, and showing the majority carrier tunneling and recombination process.

Since the earlier CIAS and CIGS device testing with TCO back contacts, ITN has developed an interface layer to the TCO's. The normalized transmission data for this interconnect is shown in Figure 7 below, and was tested to have an average transmission of about 71.5%, weighted to the AM0 solar irradiance in the range of 750 nm to 1300 nm.

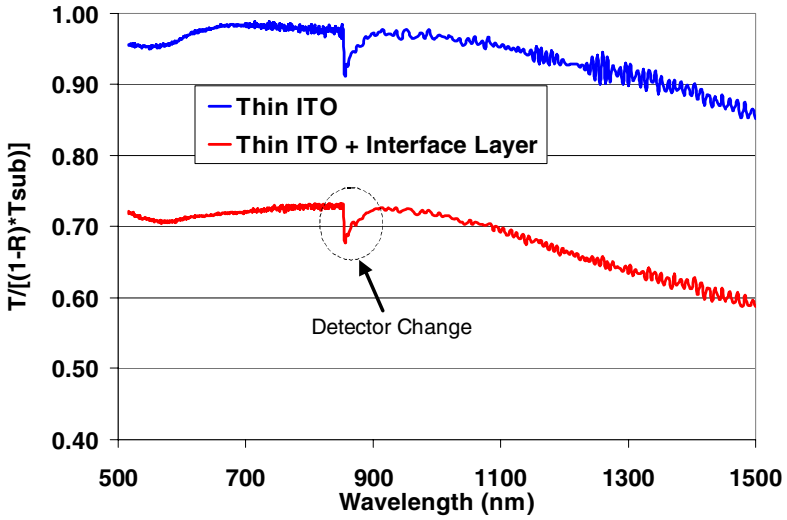

Figure 7 – Normalized Transmission (substrate divided out) of a thin ITO layer, and a thin ITO layer plus a top interface layer.

This level of transmission enables approximately 33% of the useable AM0 solar power to be transmitted to the bottom cell in a tandem configuration when assuming a top cell bandgap of 1.65 eV or 750 nm, or to be transmitted out of the device for lower temperature operation from a wide-bandgap single junction device. In addition, this back contact would enable over 70% transmission of the visible spectrum to pass through, in the event of bifacial illumination.

The same semi-transparent back contact structure was used in the fabrication of CIAS devices (bandgap ≈ 1.35 eV) and efficiencies near 11% were obtained. These efficiencies were comparable to the performance of the controls using the standard opaque molybdenum back contacts. The results are shown in Table 2 below. However, the device results have not yet tested for compatibility with wider-bandgap CIAS (E_g > 1.5 eV).

Table 2 – CIAS device with transparent back contact and Mo controls (Al/[Al+In] = 0.35, Cu/[Al+In] = 0.69, Tsub = 450°C)

Glass Substrate/ Back Contact	V_{oc} (Volts)	J_{sc} (mA/cm^2)	FF (%)	η (%)
SL/Mo	0.58	29.4	63.5	10.9
7059/Mo	0.56	28.8	65.7	10.7
7059/Mo/TCO/Thin TIL*	0.59	27.8	64.9	10.7

* TIL - transparent interface layer

SUMMARY

Significant challenges exist in the development of high-efficiency wide-bandgap devices, but this development is still in its infancy and some possibilities for improvement exist. The wide-bandgap CIAS device performance

without any bandgap tailoring to date has not yet proven to be any better than the CIGS performance at the same bandgap.(8) This equivalence supports some recent theories about deep defects becoming more effective by moving toward mid-gap with increasing bandgap.(11) However, there are enough differences between the two wide-bandgap CIS alloys to suggest the possibility of different mechanisms limiting their respective performance. These include differences in the intra-gap defect distribution, net native doping, and valance and conduction band maximum energies, all of which can have implications for device performance. The test results presented herein suggest that improvements to the CIAS near surface properties could improve the high Al content devices from the large-area, moving substrate deposition system. This could involve modified CIAS deposition near the surface or some post deposition surface treatments. The test results also suggest that a back contact interface layer may be needed to help improve the back contact. Other device test results with $CuGaSe_2$ (E_g = 1.67 eV) solar absorbers show dominant interface recombination, indicating that better matched alternative heterojunction partners or surface treatments may be needed for the wide-bandgap devices.(12)

Finally, the potential for obtaining good transparent back contacts to wide-bandgap devices is promising, with demonstrated IR transparency greater than 60% on some back contact structures and device efficiencies that are comparable to standard Mo back contacts, but there is still much room for improvement.

ACKNOWLEDGEMENTS

ITN would like to acknowledge the Institute of Energy Conversion for collaborative work performed on CIAS on TCO results. The results discussed herein were obtained by work funded by: NIST/Dept. of Commerce, Advanced Technical Program, Contract No. 70NANB8H4070; and NASA, Contract No.'s NAS3-02027 and NAS3-02170.

REFERENCES

[1] S.G. Bailey, A.F. Hepp, and R.P. Raffaelle, "Thin Film Photovoltaics for Space Applications," *Proc. Of the 36th IECEC*, pp. 235-238, (2001).
[2] D. Hoffman, "A Parametric Assessment of the Mission Applicability of Thin-Film Solar Arrays," NASA Technical Memorandum: NASA/TM-2002-211720, (2002).
[3] K. Ramanathan, M.A. Contreras, C.L. Perkins, S. Asher, F. S. Hasoon, J. Keane, D. Young, M. Romero, W. Metzger, R. Noufi, J. Ward, A. Duda, "Properties of 19.2% Efficiency $CuInGaSe_2$ Thin-film Solar Cells", *Progress in Photovoltaics: Research and Applications*, Vol. **11**, pp. 225-230, (2003).
[4] P. Paulson, M. Haimbodi, S. Marsillac, R. Birkmire and W. Shafarman, "$Cu(In_{1-x}Al_x)Se_2$ Thin Films and Solar Cells, *J. Appl. Phys.*, **91**, pg. 10153, (2002).
[5] U. Rau, M. Schmidt, A. Jasenek, G. Hanna, H. Schock, "Electrical Characterization of $Cu(In,Ga)Se_2$ Thin-Film solar Cells and the Role of Defects for the Device Performance," *Sol. Energy Mat. & Sol. Cells*, **67**, pp.137-143, (2001).
[6] J. Heath, J. Cohen, W. Shafarman, and D. Johnson, "Characterization of Deep Defects in $CuIn_{1-x}Ga_xSe_2$ (CIGS) Working Photovoltaic Devices," *Photovoltaics for the 21st Century II*, The Electrochemical Society, Inc., New Jersey, pp. 324-332, (2001).
[7] S. Marsillac, P. Paulson, M. Haimbodi, R. Birkmire, and W. Shafarman, "High-Efficiency Solar Cells Based on $Cu(InAl)Se_2$ Thin Films, *Appl. Phys. Lett.*, **81**,(7), pp. 1350-1352, (2002).
[8] W. Shafarman, S. Marsillac, P. Paulson, M. Haimbodi, T. Minemoto, and R. Birkmire, "Material and Device Characterization of Thin Film $Cu(InAl)Se_2$ Solar Cells, *Proc. of the 29th IEEE PVSC*, pp. 519-522, (2002).
[9] A. Fahrenbruch and R. Bube, "Fundamentals of Solar Cells – Photovoltaic Solar Energy Conversion," Academic Press, London, UK, 1983, pg. 169.
[10] S. B. Zhang, S.H. Wei, and A. Zunger, "A Phenomenological Model for Systematization and Prediction of Doping Limits in II-VI and I-III-VI_2 Compounds," *J. Appl. Phys.*, 83(6), pp. 3192-3196, (1998).
[11] J. Heath, J. Cohen, W. Shafarman, D. Liao, and A. Rockett, "Effect of Ga Content on Defect States in $CuIn_{1-x}GaxSe_2$ Photovoltaic Devices," *Appl. Phys. Lett.*, **80**(24), pp.1-3, (2002).
[12] J. Malmstrom, J. Wennerberg, M. Bodegard, and L. Stolt, "Influence of Ga on the Current Transport in $Cu(In,Ga)Se_2$ Thin Film Solar Cells," *Proc. of the 17th European Photovoltaic Solar Energy Conference and Exhibition*, Munich, Germany, (2001).

DEVELOPMENT OF A THIN FILM SOLAR CELL INTERCONNECT FOR THE POWERSPHERE CONCEPT

Edward J. Simburger, James H. Matsumoto, Thomas W. Giants, Alexander Garcia III, Simon Liu
The Aerospace Corporation, El Segundo, CA 90245

Dr. Suraj P. Rawal, Alan R. Perry, Craig H. Marshall,
Lockheed Martin Corporation, Denver, CO 80125

John K. Lin, Stephen E. Scarborough
ILC Dover Incorporated, Dover, DE 19946

Henry B. Curtis, Thomas W. Kerslake, Todd T. Peterson
NASA Glenn Research Center, Cleveland, OH 44135

Introduction

Dual junction amorphous silicon (a-Si) solar cells produced on polyimide substrate have been selected as the best candidate to produce a lightweight solar array for the PowerSphere program. The PowerSphere concept features a space-inflatable, geodetic solar array approximately 0.6 meters in diameter and capable of generating about 20W of electrical power. Trade studies of various wiring concepts and connection methods led to an interconnect design with a copper contact that wraps around the edge, to the back of the solar cell. Applying Plasma Vapor Deposited (PVD) copper film to both sides and the edge of the solar cell produces the wrap around contact. This procedure results in a contact pad on the back of the solar cell, which is then laser welded to a flex circuit material. The flex circuit is constructed of copper in a custom designed routing pattern, and then sandwiched in a Kapton® insulation layer. The flex circuit then serves as the primary power distribution system between the solar cells and the spacecraft[1,2,3]. Flex circuit material is the best candidate for the wiring harness because it allows for low force deployment of the solar cells by the inflatable hinges on the PowerSphere. An additional frame structure, fabricated and assembled by ILC Dover, will reinforce the wrap around contact-flex blanket connection, thus providing a mechanically robust solar cell interconnect for the PowerSphere multifunctional program[4,5]. The PowerSphere team will use the wraparound contact design approach as the primary solution for solar cell integration and the flex blanket for power distribution.

Use of the wrap around contact will yield three key benefits noted below.

1.) Utilizing the back of the solar cell for PVD copper electrical traces due to the insulation properties of polyimide. This multifunctional benefit reduces mass by removing what would otherwise be additional flex circuit material. Future advancements in this area could result in removal of the entire flex material from Powersphere solar array system creating an integral wiring harness.

2.) The use of the wrap around contact physically locates both the top and bottom contact on the same side of the solar cell. This provides fabrication process simplification by laser welding both contacts of the solar cell to the flex circuit at the same time thus reducing costs.

3.) After the wrap around contact PVD process is complete a protective Tefzel® film is applied over the solar cell and contact. The Tefzel® film is applied to the front of the solar cell to increase the thermal emissivity to 0.8, which limits the peak temperature of the cell from exceeding 80°C. It also improves the robustness of the solar cell and mitigates possible risk of damage from a handling aspect. By utilizing the back of the solar cell as the contact, the protective Tefzel® film will not impede on the laser welding process.

Requirements

Developments of a solar cell interconnect to be used for a Low Earth Orbit (LEO) application was driven by several specific requirements. It must be able to withstand the extreme environmental conditions that are present including Atomic Oxygen (AO), Ultraviolet light (UV) and rapid thermal cycling. Exposure to these conditions will cause degradation of the solar cell interconnect and possibly complete failure of the joint.

Additional requirements that were derived for the interconnect joint are described below.

1.) Mechanically robust in order to survive loads incurred during launch.

2.) Adequate sizing to support electrical loads.

3.) Ability to be scaled to support different sizes of solar cells.

4.) Easily repaired if interconnect is damaged.

Background

Several trade studies were undertaken to investigate the successful fabrication of solar cell interconnect architecture. Various methods of joining the a-Si solar cell to a flexible Kapton® blanket including joint architecture, materials and fabrication methodology were considered.

Prior to starting the trade studies a lap joint configuration was selected as the best candidate to verify all of the requirements to evaluate the robust solar cell interconnect. Also, methods that both electrically and mechanically joined the solar cell to the flex circuit material received the highest priority.

The architecture trade study parameters included the overall geometry, mechanical and electrical configuration of the interconnect joint. Several methods to electrically and mechanically join the materials were considered. Conventional methods such as conductive epoxies, solders and conductive tapes were quickly eliminated due to lack of confidence in the survivability at the temperature extremes. Additional methods that were considered to provide the electrical connection include drilled vias, welded wire or foil and PVD copper film.

Based on the trade studies, PVD copper film was selected as the leading candidate to provide the electrical interface. Pressure Sensitive Adhesive (PSA) was used to mechanically join the solar cell to the flex blanket. The PVD copper film was applied over the lap joint to produce the coupon shown in Figure 1.

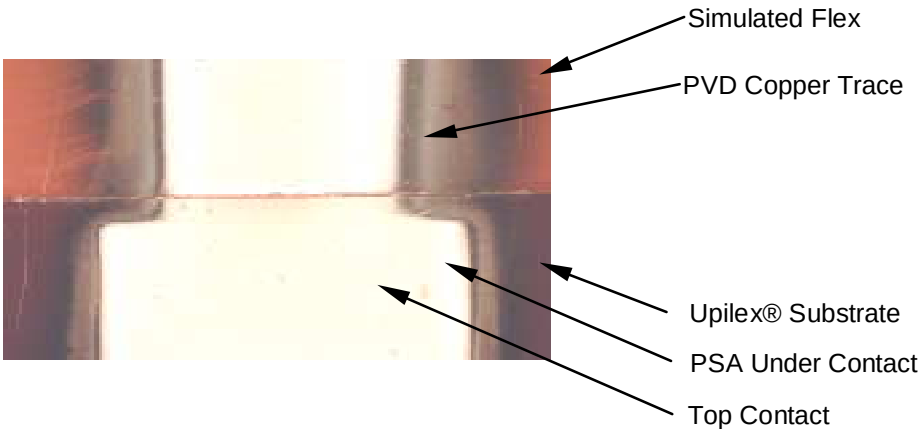

Figure 1- PVD Copper/PSA Coupon

This concept proved to be challenging due to the high out gassing of the adhesive during the vacuum deposition process and relatively large step between the cell and flex circuit. Thermal mismatch between the materials was also a concern and this concept was abandoned.

As a result of the previous coupon preparation an alternate PVD process was considered. This concept utilized the PVD copper film applied to the solar cell contact that was laser welded to the flex circuit. The copper film was applied to the top, edge and bottom of the solar cell thus routing the generated electrical load to the back of the solar cell. This wrap around contact is achievable by sputtering the copper film unlike other deposition

processes that provide line of site application only. Having both contact located on the back of the solar cell provides many benefits that are previously noted. A cross section of wrap around concept is shown in Figure 2. Several coupons were produced using the wrap around design.

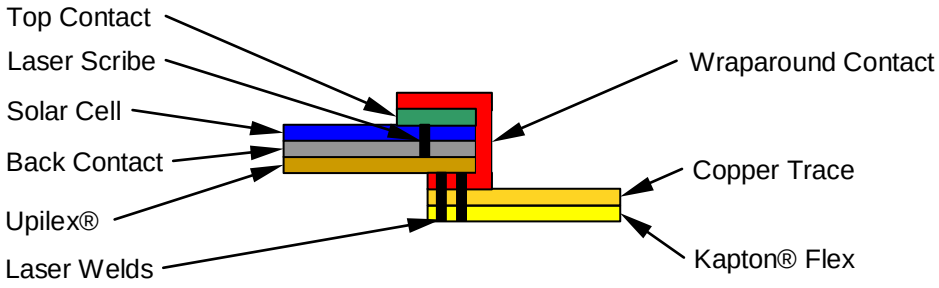

Figure 2- Cross Section of Wrap Around Contact

Figure 3 shows a magnified view of the initial laser welds that were produced indicating a good laser weld between the back contact and the PVD copper film. The picture shows the Kapton® side of the flex circuit where the laser makes first contact.

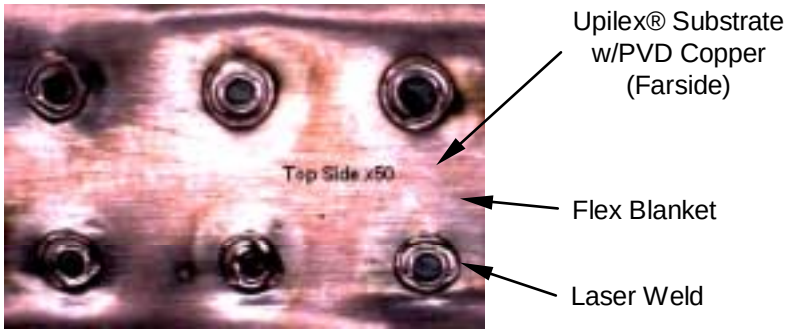

Figure 3- Laser Weld Coupon

Once the fabrication process was established, four coupons were produced using representative materials. Two of the coupons had an additional ILC Dover mock frame installed to simulate actual conditions. The coupons were subjected to rapid thermal cycling at NASA Glenn Research Center to simulate a LEO environment. Pretest and posttest resistance measurements between the simulated flex circuit and solar cell were documented to evaluate the electrical continuity and integrity of the welded coupons. During the thermal cycle testing all but one of the coupons survived with the one failure attributed to material handling. The posttest resistance measurements showed that there was little degradation of the laser-welded solar cell interconnect. Figure 4 shows both types of coupons, with and without the simulated frame.

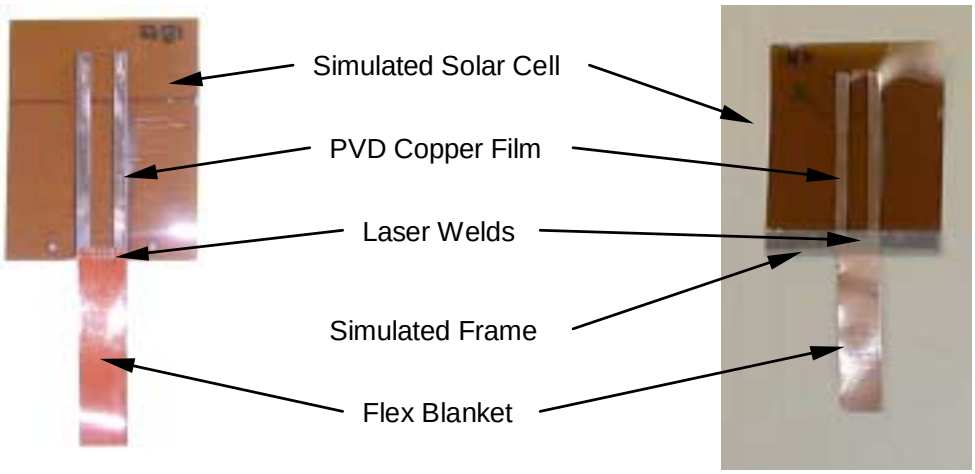

Figure 4- Unframed and Framed Weld Coupons

A thermograph inspection was also performed to verify adequate electrical sizing of the laser welds when subjected to 1 amp of current. The white areas around the laser welds in Figure 5 represent the coolest area and confirmed that the weld sizing was done correctly.

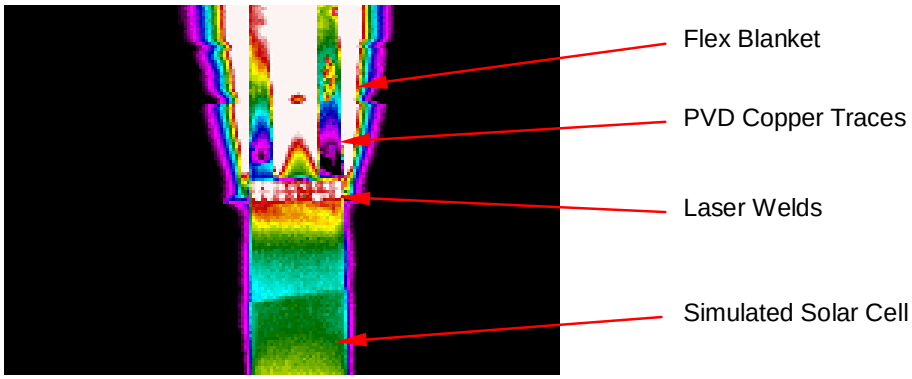

Figure 5-Laser Weld Thermograph

Design Improvements

Once the wrap around concept proved to be a viable approach for fabricating a robust interconnect, five improvements in the weld approach were investigated. The first improvement attempted was to laser weld completely through the flex circuit and solar cell. Visual observation of the plasma exiting the weld was used as initial verification of a successful weld. This can only be accomplished on the edge of the solar cell where the contact pad was isolated from the active solar cell area and eliminate possible shorting of the cell. Testing has shown that this change has significantly improved the quality of the weld.

A second improvement to the design was to decrease the PVD copper thickness on the wrap around contact. This was attempted to reduce the residual stresses in the copper film, which caused the substrate to curl and can potentially cause possible delaminations. However, sufficient copper thickness must be present to provide adequate material for the weld. The PVD copper thickness was optimized to meet all of the previously noted requirements. An analysis of the electrical sizing was also accomplished to verify that the reduction in film thickness was still adequate to carry solar cell power.

The third improvement was to apply a titanium thin film binder layer prior to the PVD copper film. This helped to reduce the delaminations of the copper from the solar cell substrate during the welding process. The delaminations occurred due to localized shrinkage of the weld material. The future binder material will use chromium at the base layer that has previously demonstrated superior properties to that of titanium.

The laser welding process provides both the mechanical and electrical joint, however the mechanical strength of the weld is weak suggesting the need for a adequate structural support such as Kapton® tape. Tape was used to provide the clamping force during the laser welding process. The tape also helped to reinforce the solar cell interconnect to minimize failures due to material handling during the solar cell frame installation. One additional benefit of the tape is that it provides more intimate contact of the copper during the welding process, which produces better welds.

The last improvement that was investigated was to increase the spacing or pitch of the laser welds. This was attempted to reduce some of the localized delaminations of the PVD copper from the substrate in the heat-affected zone of the weld area. By increasing the pitch of the welds the issue of delaminations was eliminated. Decreasing the amount of welds also decreases the amount of current carrying capacity. The electrical load analysis was reevaluated to verify that the amount of welds was adequate to support the electrical loads.

Flight Experiment

Building upon the successful development of the solar cell interconnect a flight experiment will be used to validate the wrap around contact and associated PowerSphere technologies. All of the design improvements were incorporated into the Material International Space Station Experiment 5 (MISSE 5) flight experiment. The experiment consisted of three a-Si solar cells laser welded to a flex circuit and embedded in a composite frame as shown in Figure 6.

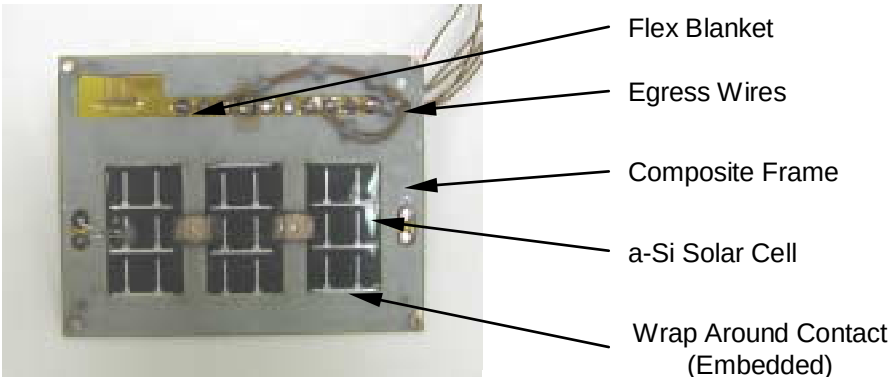

Figure 6- MISSE 5 Flight Experiment

The MISSE 5 experimental coupon will be mounted to the exterior of the International Space Station for an approximately one-year exposure. On orbit IV curves will be generated from the experiment to better understand the overall exposure to a LEO environment. The ability to demonstrate new technologies operating in the actual environmental conditions will prove to be an invaluable tool for future designs. Once the experiment is returned the materials will be evaluated and the effects of the LEO environmental exposure will be documented.

Significant improvements have helped to create a successful design and fabrication process for the PowerSphere solar cell interconnect. Fabrication of the MISSE 5 flight experiment helped to improve upon the initial concept and create an optimized design as shown in Figure 7.

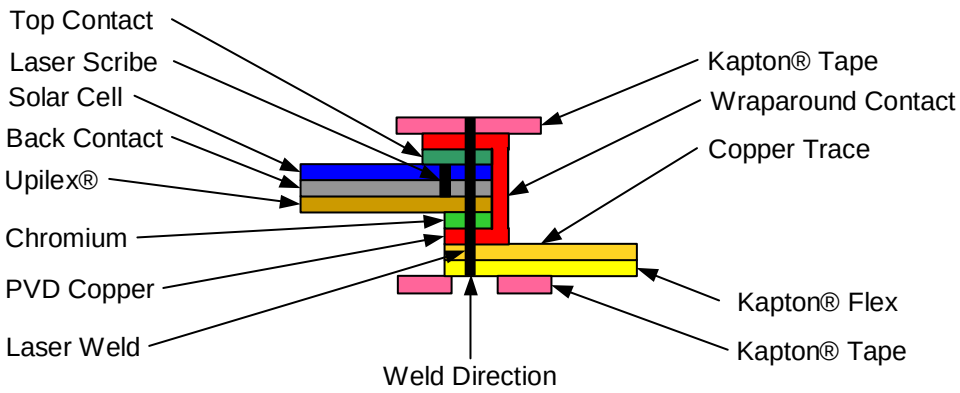

Figure 7- Optimized Interconnect Design Cross Section

In the optimized design the laser first makes contact with the Kapton® and then fully penetrates all layers with the plasma exiting the Kapton® tape on the opposite side. Once the solar cell interconnect has been welded, a frame will encapsulate the weld area and further reinforce the joint. A patent application has been filed with the United States patent office for the solar cell contact design co-developed by Aerospace Corp. and Lockheed Martin Corp.

Summary and Conclusions

The significant advancements in solar cell interconnect design and fabrication has provided a valuable building block for the PowerSphere program. Lessons learned from preliminary concepts, MISSE 5 flight experiment and thermally cycled coupons have provided a robust design. Future testing of the complete engineering design unit assembly will verify that the wrap around design is an effective concept for both electrically and mechanically joining a-Si solar cells to flex circuit.

Acknowledgment

This work was supported by NASA contract NAS3-01115.

References

[1] A. Prater, E.J. Simburger, D.A. Smith, P.J. Carian, and J.H. Matsumoto, The Aerospace Corporation, “Power Management and Distribution Concept for Microsatellites and Nanosatellites,” Proceeding of IECEC, August 1-5, 1999.

[2] D.G. Gilmore, E.J Simburger, M.J. Meshishnek, D.M. Scott, D.A. Smith, A. Prater, J.H. Matsumoto, and M.L. Wasz, The Aerospace Corporation, “Thermal Design Aspects of the PowerSphere Concept,” Proceedings of Micro/Nano Technology for Space Application Conference, April 11-15, 1999.

[3] E.J. Simburger, J.H. Matsumoto, T.W. Giants, M. Tueling, J. Ross, J.K. Lin, C. Knoll, S. Rawal, A.R. Perry, C. Marshall, D.M. Barnett, T.T. Peterson, T.W. Kerslake, and H. Curtis, “Development of Flex Circuit Harness for the PowerSphere Concept,” 29th Photovoltaics Specialist Conference, IEEE, New Orleans, LA, May 20-24, 2002.

[4] E.J. Simburger, J.H. Matsumoto, D.A. Hinkley, D.G. Gilmore, T.W. Giants, and J. Ross, “Multifunctional Structures for PowerSphere Concept,” 42nd AIAA/ASME/ASCE/ASC Structures, Structural Dynamics, and Materials Conference & Exhibit, Seattle, Washington, April 16-19, 2001.

[5] E.J. Simburger, J.H. Matsumoto, J.K. Lin, C.Knoll, S. Rawal, A.R. Perry, D.M. Barnett, T.T. Peterson, T.W. Kerslake, and H. Curtis, “Development of a Multifunctional Inflatable Structure for the PowerSphere Concept,” AIAA-2002-1707 43rd AIAA/ASME/ASCE/ASC Structures, Structural Dynamics, and Materials Conference & Exhibit, Denver, Colorado, April 22-25, 2002.

RESEARCH TRENDS TO ENHANCE THE RADIATION TOLERANCE OF Si SPACE SOLAR CELLS

A. Khan and Al-Khatib
Department of Electrical and Computer Engineering,
University of South Alabama, Mibile, AL 36688

M. Yamaguchi
Toyota Technological Institute, Nagoya, Japan

T. Abe
Shin-Etsu Handotai, Gumma, Japan

M. Imaizumi and S. Matsuda
National Space Development Agency of Japan, Tsukuba, Japan

1. Introduction

Previously, we developed an analytical model [1], which could be adequately used for improving the radiation tolerance of silicon space solar by varying the base carrier concentration [Figure 1]. However, the optimization of the base carrier concentration reduces the pre-radiation minority-carrier diffusion length in the base , therefore there have to compromise between beginning of the life (BOL) and end of the life (EOL) performance of the space solar cell.

The fact remain that achieving still higher radiation tolerance require that use of alternatives approaches. The interaction between vacancies, self-interstitials (Si_i), impurities, and dopants in Si leads to formation of undesirable point defects such as recombination and compensator centers which effect performance of the solar cells in space. In our previous studies [2, 3], the E_C-0.18-0.21eV center is found to especially plays a dominant role in carrier removal, which is related to interstitial-boron and interstitial-oxygen complex (B_i-O_i) [4,5]. This implies that using different dopants and less oxygen crystals such as FZ-grown Si could reduce carrier removal effect. Furthermore, Ga-doped Czochralski (CZ) grown Si solar cells show less light-irradiation degradation as compared to boron-doped CZ-grown cells [6]. This leads to the fact that Ga-doped CZ-grown solar cells may have more potential compared to B-doped CZ grown Si solar cells, In addition, understanding the origins of radiation-induced deep levels in Si, especially interaction of Si interstitials with impurities in Si, is very important to further improve radiation-tolerance of Si space solar cells.

No effort has apparently yet been made to limit the effect of carrier removal by deliberately doping with different dopants in order that the defects generated should be less electrically active In this study, we first present the results of a comparison of radiation-induced defects in n^+-p-p^+ CZ-grown Si diodes doped with gallium or boron ranging in resistivity from 0.33-10 Ω cm. Next, we will

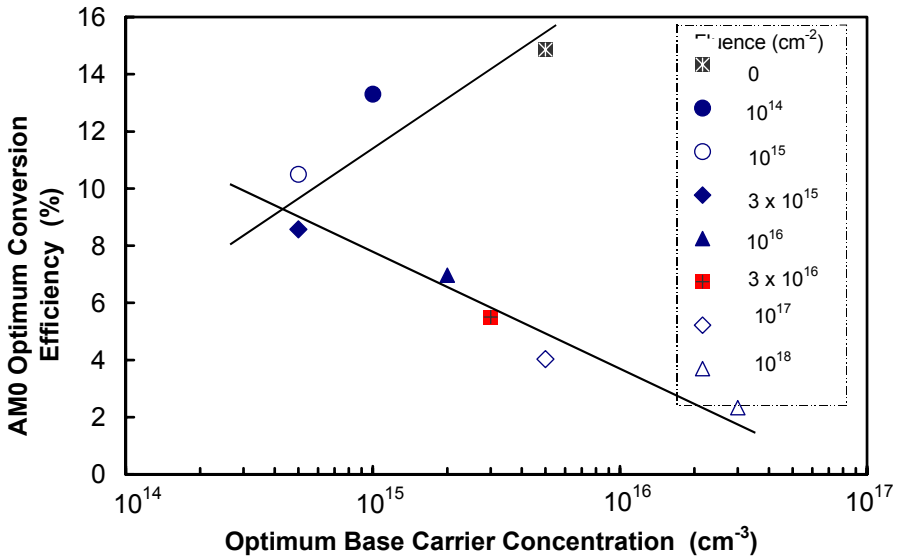

Fig. 1. Variation of the optimum base carrier concentration and efficiency as a function of 1-MeV electron fluence from 10^{14} cm^{-2} to 10^{18} cm^{-2}.

give a detailed account of the impact of impurities, such as gallium, boron, carbon and oxygen on radiation-induced defects (i.e. B_i-O_i, C_i-O_i, V-V) and hierarchy of defect reaction in silicon.

2. Experimental details

The fundament of the current investigation of impurity effects on radiation-induced defects in Si is a set of wafers grown by Shin-Etsu Handoti, Japan. The different types of boron and gallium doped wafers grown either with the Czochralski (CZ), magnetic Czochralski (MCZ) or float zone (FZ) method with doping and oxygen concentrations were used. The $n^+/p/p^+$ solar cells structure was similar to the structure used in previous studies. Area of 2 x 10^{-6} ~ 4 x 10^{-6} m^2 was defined in order to keep the capacitance of the device within the range of the capacitance meter used for C–V measurements. The carrier concentration was also measured using Hall effect measurements at room temperature. The samples were irradiated in the open circuit condition with 1 MeV electrons and 10 MeV protons using a Cockcroft-Walton accelerator and Tandem accelerator, respectively at Japan Atomic Energy Research Institute (JAERI), taking care to avoid sample heating by appropriate control of the beam current and water cooling of the sample mount. Additionally, the electron and proton beam was scanned in order to insure a uniform irradiation over the whole surface of the sample.

3. Results and Discussion

A. Suppression of recombination and compensator centers by Ga impurity

Figure 2 shows a minority-carrier emission (injection pulse) spectra of 9 and 10 Ωcm, B and Ga-doped CZ-grown silicon irradiated to a fluence of 3 x 10^{16} electrons cm^{-2}. Comparison with published data shows that the hole levels E_V+0.36 eV is most probably due to the interstitial-carbon-interstitial-oxygen complex (C_i-O_i) [2, 3, 5]. The electron level E_C-0.18 eV is one of the highest concentration defects that has been commonly observed only in B-doped CZ grown Si samples, while this level is found to be totally absent in Ga-doped CZ-grown samples (Fig. 2). The absence of this level in Ga-doped Si gives support that this center in B-doped Si is related to B_i-O_i [3, 6] complex.

As we have previously demonstrated that the hole center E_V+0.36 eV acts as recombination center and has a dominant role to control lifetime is Si solar cells [2]. It is worth noting that the overall concentration of E_V+0.36 eV is strongly suppressed in Ga-doped samples as compared to B-doped samples, as shown in Fig. 2. This implies that the minority carrier lifetime degradation can be improved by using Ga as the dopant in Si space solar cells.

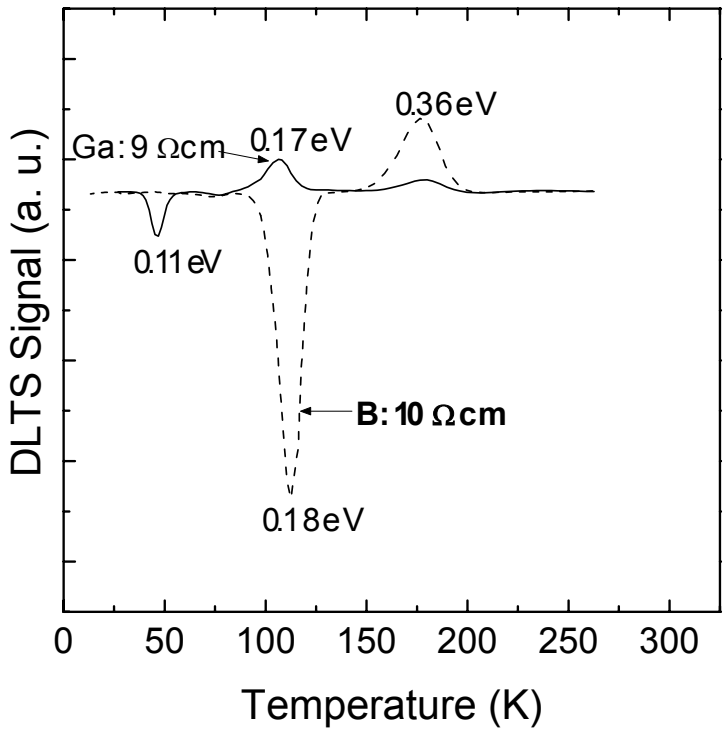

Fig. 2. Comparison of the minority carrier DLTS spectra measured for boron-or gallium –doped CZ-grown Si at same gallium and boron doping levels, irradiated with 1-MeV 3 x 10^{16} electrons/cm^2.

One of the most interesting and technologically important feature of our work is the disappearance of the dominant donor like electron level E_C-0.18 eV in Ga-doped CZ- grown samples. As we have discussed in previous studies [2], this level acts as a compensator center, which is positively charged before electron capture. The concentration of this level is about 60% of the change in carrier concentration after heavy fluences and therefore populous enough to be the dominating influence on device performance. This implies that carrier removal effects can be partially offset by using gallium as dopant instead of boron.

B. Carrier concentration analysis: using different dopants species

Our detailed carrier concentration analysis show that carrier removal effects can be partially offset by using gallium as dopant instead of boron. For low fluences, the change in carrier concentration can be expressed by the following expression:

$$p_0 - p_\phi \approx R_c \phi \qquad (1)$$

Where p_o and p_ϕ are the carrier concentrations before and after irradiation with fluence ϕ of 1 MeV electrons and R_C is the carrier removal rate. However, for high fluences it can be approximated by,

$$p_\phi \approx p_0 \exp\left(\frac{-R_C \phi}{p_0}\right) \qquad (2)$$

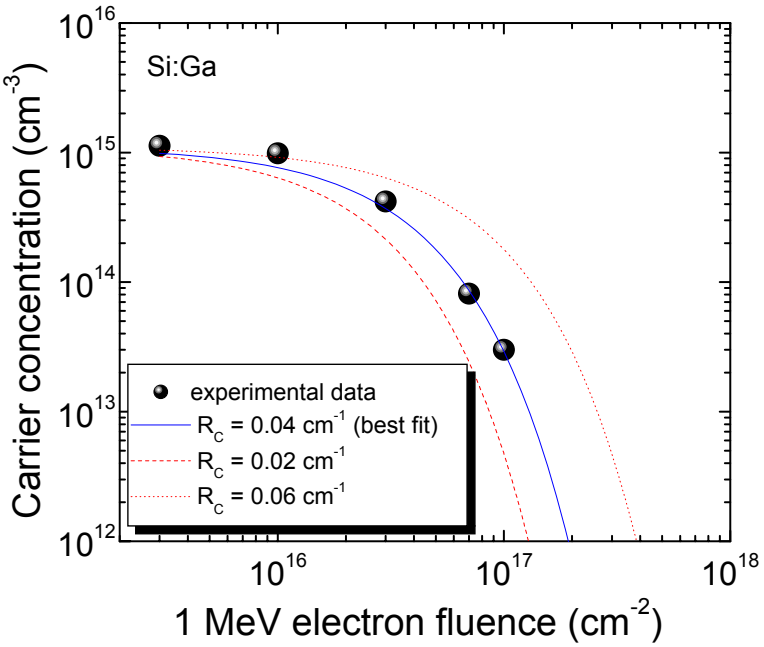

Fig. 3. Calculated and experimental changes in the carrier concentration of p-Si gallium doped crystals with initial carrier concentrations of 1.15 x 10^{15} cm^{-3}, as a function of 1-MeV electron fluence.

Equation (2) is equivalent to Equation (1) in the range of low fluence. The changes in carrier concentration determined from C–V and Hall effect measurements as a function of 1 MeV electron fluence, with pre-irradiation carrier concentration p_0 of 1.15 x 10^{15} cm^{-3} are shown in Fig. 3. Fitting of

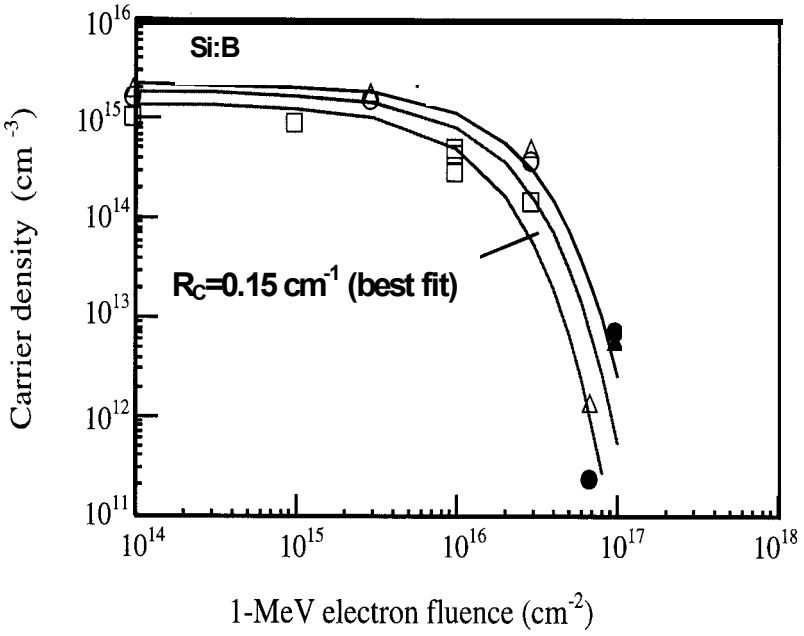

Fig. 4. Calculated and experimental changes in the carrier concentration of p-Si boron doped crystals with initial carrier concentrations of 1.15 x 1015 cm-3, as a function of 1-MeV electron fluence.

Eq. (2) gives the value of R_C = 0.04 cm^{-1} that is almost four times lower than that for boron doped Si (0.15 cm^{-1}), as shown in Fig. 4 with initial carrier concentration of 1.51 x 10^{15} cm^{-3}. This is a highly technologically interesting new result on the properties of the gallium as dopant in Si. Furthermore, this result is consistent with deep level transient spectroscopy (DLTS) analysis (Fig. 2), which showed that introduction of gallium as dopant in Si provides a simple method for selectively bleaching the dominant compensating center (B_i-O_i).

The damage coefficient K_L determined from the spectral response, by fitting the numerical simulation, is 8 x 10^{-11} for 10 Ωcm boron doped Si solar cells and 4 x 10^{-11} for gallium doped Si solar cells. These values are consistent with the degradation behaviors of the solar cells. This is further supporting evidence that gallium doped silicon solar cells showed better radiation tolerance compare to boron doped silicon solar cells.

C. Annealing behavior of radiation-induced defects in Ga-doped Si

Isochronal thermal annealing was performed on gallium doped silicon samples after exposing them with the same fluence of 3 x 10^{16} cm^{-2} 1 MeV electron to investigate (i) the effects, if any, of the presence of gallium as dopant on the thermal stability of the radiation-induced defects (ii) to monitor the evolution of new defect following annealing of first order point defects, such as vacancy-interstitial and their complexes with impurities. These three aspects together would be expected to provide a comprehensive comparative picture of the radiation-induced defects in boron and gallium doped silicon, which can, in turn shed light on the possible formation of their complexes.

Isochronal annealing was performed for 15 minutes in steps of 25-30°C in nitrogen ambient, each followed by DLTS measurements. The concentration data obtained for the various deep levels from these experiments are plotted in Fig. 5 as a function of the isochronal annealing temperature up to 400 °C.

Comparison with the isochronal annealing curve data for the radiation-induced levels in the boron doped samples [3] show that gallium not only strongly suppressed recombination centre (E_V+0.36) eV but also annealing curve are found to show different anneal-out characteristics to that in

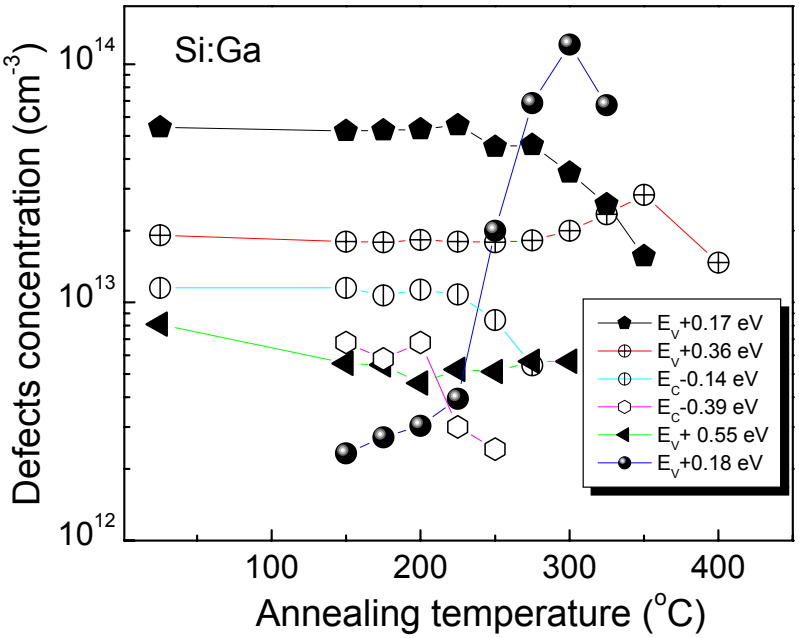

Fig. 5. Concentration of the annealed-out and annealed-in deep levels in 1 MeV (3 x 10^{16} cm^{-2}) electron irradiated Ga-doped Si diodes and space solar cell as a function of isochronal annealing temperature. Each annealing step was 15 min duration.

boron samples. One important difference in the reverse annealing behaviour (300 ^{o}C-350 ^{o}C), which is negligible in gallium doped samples and significant in boron doped samples [3]. This is further supporting evidence to the fact that reverse annealing (an increase in concentration) of C_i-O_i complex (E_V+0.36 eV) in boron doped samples is due to an increase in the concentration of B_i-C_s complex [6] at E_V+0.30 eV following annealing of donor like B_i-O_i center (E_C-0.18 eV), which acts as a minority trap in boron doped silicon. It is worth noting that neither of these levels (B_i-C_s, B_i-O_i) has been observed in gallium-doped samples, consequently reverse annealing [3] is almost absent in gallium-doped samples. The E_V+0.36 eV level both in boron doped samples and gallium doped samples remains almost unchanged up to 400 ^{o}C annealing step as the C_i-O_i complex is the one of the most stable complexes of all the observed interstitials related deep levels in silicon.

The annealing behaviour of E_V+0.17–0.18 eV level which is associated divacancy in gallium-doped samples is found to show almost identical anneal-out (375-400 ^{o}C) characteristics of this level to that in the boron-doped samples, showing that different dopant does not alter its characteristics.

As seen in Fig. 5, the dominant level to anneal in earliest in gallium-doped samples is E_V+0.18 eV. It shows up at 150 ^{o}C and raises two orders of magnitude with the increase in annealing temperature, reaching a maximum in concentration (1 x 10^{14} cm^{-3}) at 325 ^{o}C. Thereafter, it suddenly anneal-out as shown by a sharp decline in its concentration (Fig. 5).

3. Further Discussion

A. tentative identification of the recombination and compensator centers

The identification of the dominant hole level E_V+0.36 eV observed in our electron and proton irradiated samples has been less straightforward. However, our comprehensive study throws new light on the formation mechanism of this defect and fixed its identification as C_i-O_i complex. A summary of the boron concentration dependence of the introduction rates of E_V+0.36 eV defect

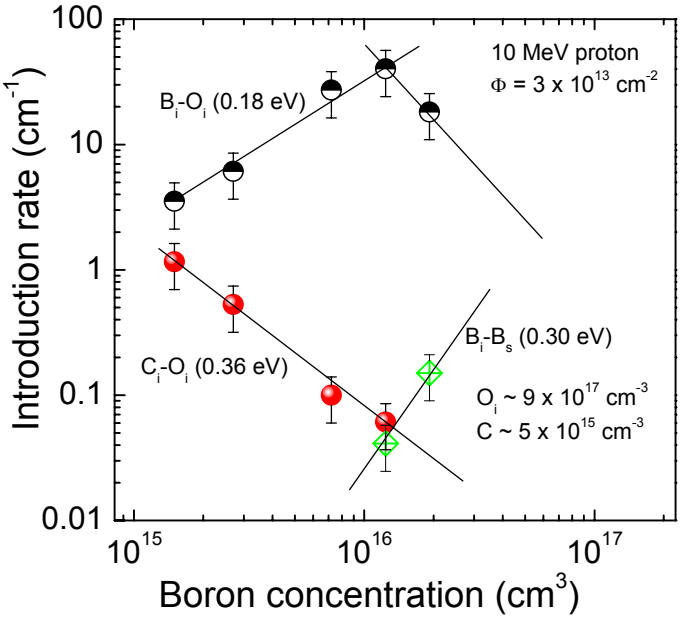

Fig. 6. Variation in the introduction rates of the interstitial related defects in 10 MeV proton irradiated p-Si as a function of background impurity concentration.

together with other room temperature stable defects in 10 MeV proton irradiated p-type silicon is shown in Fig. 6. In all these Czochralski (CZ) grown samples the concentration of interstitial oxygen (O_i) is on the order of ~9 x 10^{17} cm^{-3}.

In the first experiment we investigated the defects introduction rates as a function of boron concentration as shown in Fig. 6. The introduction rate of E_V+0.36 eV defect decrease linearly as the boron concentration (B_s) increases (Fig. 6). It is important to point out here, in this concentration region, the electron level E_C-0.18eV is increasing, being consistent with its identification (B_i-O_i). This implies that E_V+0.36 eV is in direct competition with the production of B_i-O_i. Higher introduction rates of B_i-O_i strongly suppressed the production of the C_i-O_i (E_V+0.36) defect.

In order to provide the additional information about the nature of the defects the influence of interstitial oxygen has been studied quantitively, CZ, FZ, and MCZ grown samples of almost same boron concentration were chosen. The E_V+0.36 eV introduction rate increases with increasing O_i as shown in Fig. 7. The conclusion is clearly justified that oxygen is one of the component of this defect.

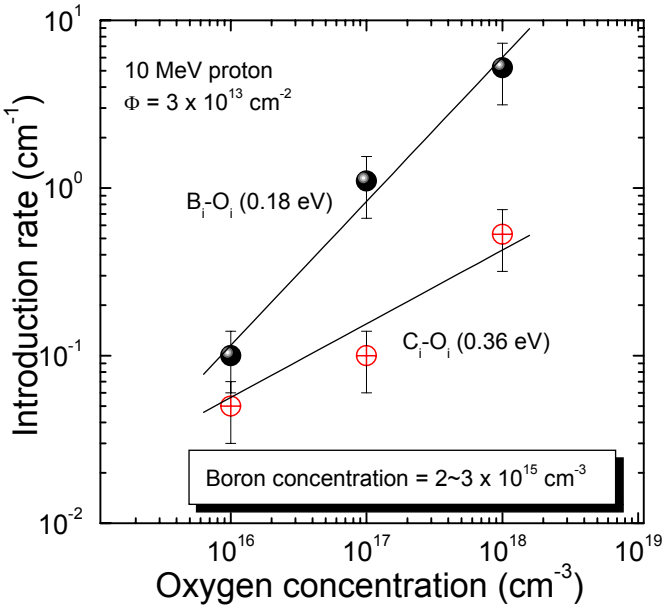

Fig. 7. Variation of the introduction rates in boron-doped silicon (irradiated with 10 MeV proton) as a function of interstitial oxygen concentration.

An analogous investigation was performed for the influence of carbon on the introduction rates of E_V+0.36 eV defect. Now samples with interstitial oxygen concentration between 6.2 to 9.4 x 10^{17} cm^{-3} and boron concentration between 1.2–1.9 x 10^{16} cm^{-3} were selected. There is approximately linear relationship between the E_V+0.36 eV defect and carbon concentration as presented in Fig. 8. These observations that carbon and oxygen are the major components of the E_V+0.36 eV defect in electron and proton irradiated silicon fixed its identification as C_i-O_i complex. It is worth noting that with increasing carbon concentration E_C-0.18 eV (B_i-O_i) is decreasing due to direct competition with the production of C_i-O_i (E_V+0.36) complex.

This defect (E_C-0.18-0.20 eV) was observed to have one of the highest concentrations in our low dose samples up to low/intermediate fluence. As presented in Fig. 6 the introduction rate of minority level (E_C-0.18 eV) for 10 MeV proton irradiated CZ-grown samples in which oxygen content is constant at ~9 x 10^{17} cm^{-3} increases linearly with boron concentration at lower doping level (~10^{16} cm^{-3} Obviously, the boron concentration plays an important role in the formation of this center. Kimirling and Mooney [6, 7] have also observed this phenomenon in 1 MeV electron irradiated samples. At higher boron doping level there is competition between E_C-0.18 eV and B_i-B_s (Fig. 6) and consequently introduction rates of E_C-0.18 eV center decrease following evolution of B_i-B_s [6]. Figure 7 also show that the introduction rates of E_C-0.18 eV also increases linearly with oxygen concentration for intermediate boron level. The linear dependence of the introduction rate on both boron and oxygen firmly justify the hypothesis that boron and oxygen are the major component (B_i-O_i) of this compensator center (E_C-0.18 eV) in silicon. Moreover, the absence of this level in Ga-doped

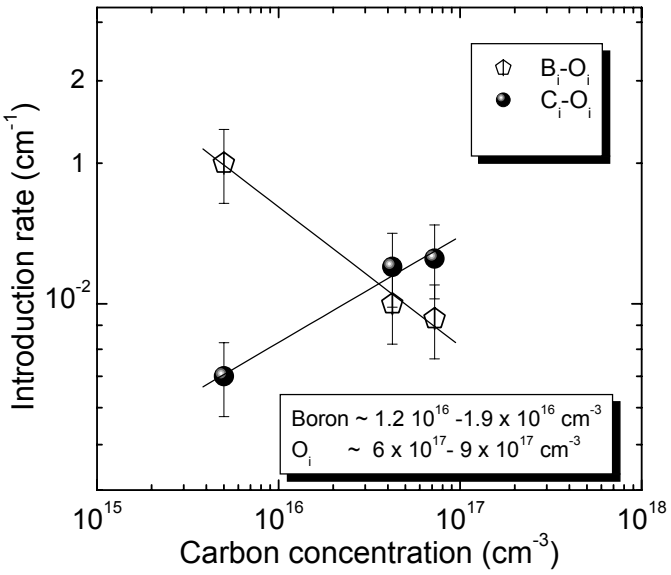

Fig. 8. Influence of carbon concentration on the defects productions in Si samples irradiated with 10 MeV proton.

silicon demonstrates that this center in boron-doped silicon is related to B_i-O_i complex. This identification is consistent with the previous speculations [6, 7] and fixed its identification as B_i-O_i complex.

B. Possible reasons behind the different role of boron and gallium in Si

As we have discussed in previous sections the presence of gallium as dopant in silicon leads to strong suppression of the recombination center E_V+0.36 eV and complete removal of the dominant compensator center E_C-0.18 eV (B_i-O_i). This implies that boron has a strong affinity for pairing with oxygen in p-type silicon like well known reported boron iron complex (B_s-Fe_i) [8]. The possible interpretations for this new observation are discussed below.

It is known that Si self-interstitial (Si_i) produced by radiation interchanges its location with substitutional boron (B_s), carbon (C_s) [9,10] and gallium (Ga_s), results in interstitial B (B_i), C (C_i) and Ga (Ga_i), and forms complex defects such as B_i-O_i, C_i-O_i and Ga_i-O_i by combining with interstitial oxygen (O_i) as follows:

$$Si_i + B_s \rightarrow B_i \rightarrow B_i + O_i \rightarrow B_i - O_i$$

$$Si_i + C_s \rightarrow C_i \rightarrow C_i + O_i \rightarrow C_i - O_i$$

$$Si_i + Ga_s \rightarrow Ga_i \rightarrow Ga_i + O_i \rightarrow Ga_i - O_i$$

The activation energy of replacing Si_i with impurities is thought to be due to atomic size and charge state of impurities. In fact, the size of the tetrahedral covalent radius is different for B (0.088nm), C (0.077nm), Si (0.117nm) and Ga (0.126nm). Therefore, the Ga atom with larger size is thought to produce more lattice stress as compared to B and C, and thus influence on the probability of generation of complex defect such as Ga_i-O_i and the activation energy for generating Ga_i-O_i must be larger than those of B_i-O_i and C_i-O_i.

However, further study is necessary in order to understand the effects of Ga atoms upon generation and annihilation of radiation-induced defects.

5. Summary

The present study fully explored the better radiation tolerance of gallium doped silicon solar cells as compared to conventional boron doped silicon solar cells after heavy fluence of 1 MeV electron and 10 MeV proton irradiation. Analysis of the carrier removal rate *RC* in boron, and gallium doped Si solar cells showed that carrier removal effects can be partially offset by using gallium as dopant instead of boron, which demonstrates the better radiation tolerance of gallium doped Si solar cells as compared to boron doped.

Present study have also drawn a quite complete picture towards the identification of the dominant radiation-induced defects in Si. The radiation-induced defect E_V+0.36 eV has been identified as C_i-O_i complexes. The absence of E_c-0.18 eV complex center in gallium doped samples and linear dependence of its introduction rates on both boron and oxygen content fixed its identification as the B_i-O_i complex in boron doped Si. One of the technologically important results of present study is that the gallium appears to strongly suppress the radiation induced defects, especially hole level E_V+0.36 eV (C_i-O_i), which is thought to act as a recombination center as well as the dominant compensating center at E_C-0.18 eV (B_i-O_i). As a result the effects of lifetime degradation and carrier removal could be partially offset to higher radiation fluences by using Ga as dopant instead of boron in Si space solar cells. These results reveal that gallium, as dopant in Si, is a promising material for next generation radiation hard space solar cells.

6. Reference

1 M. Yamaguchi, A. Khan, S. J. Taylor, M. Imaizumi T. Hisamatsu and S. Matsuda, IEEE Transactions on Electron Devices Vol. 46, No. 10, 2133 (1999).

2 M. Yamaguchi, A. Khan, S. J. Taylor, K. Ando, T. Yamaguchi, S. Matsuda, and T. Aburaya, J. Appl. Phys. 86, 217 (1999).

3 A. Khan, M. Yamaguchi, T. Hisamatsu and S. Matsuda, J. Appl. Phys. 87 2162 (2000).

4 P. M. Mooney, L .J. Cheng, M. Sull, J. D. Gerson, and J. W. Corbett, Phy. Rev. B 15, 3836 (1977).

5 J. M. Trombetta. and G. D. Watkins, Appl. Phys. Lett. 51, 1103 (1987).

6 S. W. Glunz, S. Rein, W. Warta, J. Knobloch and W. Wettling, Tech. Digest PVSEC-11, 549 (1999).

7 L.C. Kimerling, IEEE Trans. Nucl. Sci. Ns-23 1497 (1976).

8 K. Graff and H. Pieper , J. Electrochem. Soc. 128, 660 (1981).

9 J.M. Trombetta and G.D Watkins, Appl. Phys. Lett. 51, 1103 (1987).

10 G.D. Watkins, Phys. Rev. B12, 5824 (1975).

USING SRIM TO CALCULATE THE RELATIVE DAMAGE COEFFICIENTS FOR SOLAR CELLS

Scott R. Messenger
SFA, Inc., Largo, MD 20774

Edward A. Burke
Consultant, SFA, Inc., Largo, MD 20774

Robert J. Walters and Jeffrey H. Warner
Code 6818, Naval Research Laboratory, Washington, DC 20375

Geofffey P. Summers
Code 6818, Naval Research Laboratory, Washington, DC 20375
Department of Physics, UMBC, Baltimore, MD 21250

ABSTRACT

It is shown how the widely available computer code SRIM can be used to calculate proton relative damage coefficients (RDCs) for solar cells. This approach is essential in the case of crystalline Si cells where the incident proton energy is reduced significantly in traversing the active volume of the cell. However, the same approach can be used in other cases such as GaAs-based multi-junction cells where the active region consists of several different material layers. In the case of Si cells analytic calculations of the non-ionizing energy loss (NIEL) are not satisfactory for calculating the energy dependence of the RDCs in contrast to technologies such as single junction GaAs and thin films such as CIGS, for which the NIEL approach has been extremely successful. In the SRIM approach it is assumed that the RDCs are proportional to the number of total vacancies formed. The calculation involves integrating the vacancy.txt files produced by SRIM over the active depth of the cells and normalizing the results to the number of vacancies produced by 10 MeV protons. The RDCs calculated from SRIM are found to agree well with experimentally measured values for both Si and MJ cells. In particular the “double hump” structure in the measured RDCs for several kinds of MJ technologies can be reproduced.

INTRODUCTION

Relative damage Coefficients (RDCs) are needed to estimate solar cell degradation in the complex proton and electron environment found in space. The most straightforward way to determine the RDCs is to measure them directly. In a typical case such an undertaking involves measuring cell degradation curves for various photovoltaic parameters for a range of incident proton and electron energies. Anspaugh [1] produced an excellent data set of this kind for single junction GaAs cells. The RDCs for normal incidence monoenergetic particles can be converted to the corresponding RDCs for an isotropic environment, from which the RDCs for shielded cells can be derived using the widely used approach developed at JPL and described in the Solar Cell Radiation Handbooks and elsewhere [2,3]. The problem with this approach is that acquiring the necessary data is extremely labor intensive and consequently expensive.

In a series of papers over the last decade NRL showed that in many cases the energy dependence of the RDCs could be determined analytically using calculations of the nonionizing energy loss for particular particles and cell materials [4 and references therein]. These calculations have become progressively more sophisticated for electrons and protons, and have been recently extended to incident heavy ions [5]. When the NIEL is multiplied

by a particle fluence a quantity called displacement damage dose is obtained, which plays the same role for displacement damage that ionizing dose plays for ionization effects. When Anspaugh's data for GaAs was converted to displacement damage dose it was found that the curves for E >10keV collapsed to a single characteristic curve. Indeed it was primarily the availability of Anspaugh's excellent data set that enabled the displacement damage dose approach to cell degradation to be developed.

The NIEL approach works well when the particle energy can be assumed to be constant across the active region of the device. This is the case for GaAs-based cells, where the active region can be considered thin for proton energies >~100 keV. In these cases the energy dependence of the NIEL and the relative damage coefficients (RDCs) are similar [4]. However, this is not true for very low energy protons incident on uncovered GaAs cells, and deviations between the energy dependence of the NIEL and the RDCs are observed at proton energies < 100 keV [1]. The reason for the deviation is that protons with these energies slow down significantly or stop in the active region of the cell.

For silicon cells, where the active region in typical cells is 100 times greater than is the case for GaAs, the problem is exacerbated. In GaAs cells, the active region is typically on the order of a few micrometers in depth from the front surface of the cell, as opposed to ~100 μm for crystalline silicon cells. This means that protons with relatively high energy will slow down significantly or reach the end of their tracks in the critical silicon cell regions more so than is the case in GaAs cells. The slowing-down effects complicate the analysis. What is more, experiments show that, for normally incident protons of a given energy, the damage per incident proton is a maximum when the particle track terminates in the active device region. Whereas for GaAs [1,6] the energies where this is a problem exist only for protons below a few hundred keV, it extends to several MeV in the case of silicon [2,3].

RDCs FOR CRYSTALLINE Si CELLS

The observations made above can be quantified by analyzing actual experimental results. Figure 1 shows data for the degradation of Pmax for Si cells taken from the Solar Cell Radiation Handbook [2,3]. Results are shown for incident 100,and 300 keV, and 1 and 9.5 MeV protons. The two most striking features of these data are firstly that the curves are not similar in shape and secondly the curves do not come in any obvious order with increasing

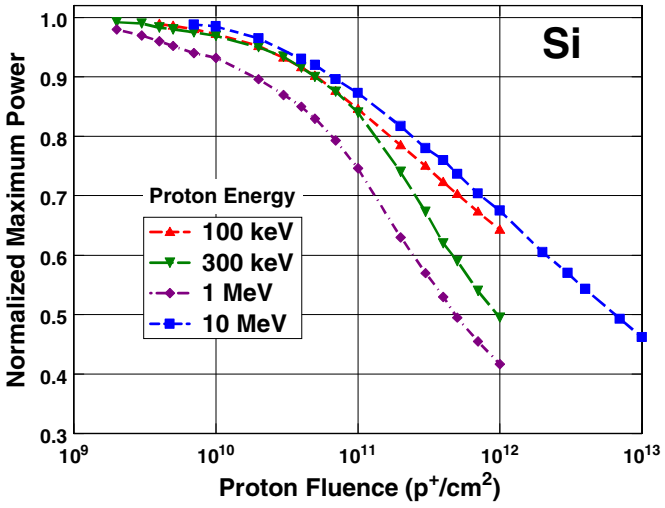

Figure 1. The degradation of the maximum power point of Si cells as a result of proton irradiation [2,3]. The points of the curves are for identification only and are not measured data.

proton energy. The data for Si cells is in contrast to similar data for the degradation of Pmax in GaAs cells taken from Anspaugh and shown in Fig. 2. In this case the curves are similar in shape except for the two lowest energies (50 and 100 keV) and there is a clear trend with energy, with the lowest energy protons causing the most damage as would be expected from the interaction cross sections. It is the behavior of the 50 and 100 keV curves in Fig. 2 that suggests the cause of the results shown in Fig. 1. As noted above 50 and 100 keV protons do not completely traverse the active region of single junction GaAs cells so that the damage is done in these cases differently than for higher energies. Once the proton energy is > ~200 keV the damage is done uniformly and the degradation curves become similar in shape. For the data shown in Fig. 1 only in the case of the 9.5 MeV curve do the incident protons traverse the active region of the Si cell. For the other energies the protons stop in different parts of the active region.

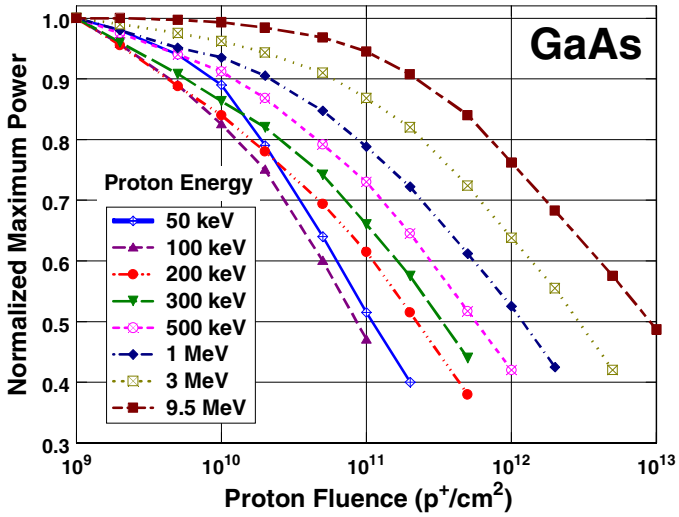

Figure 2. The degradation of the maximum power point of GaAs cells due to proton irradiation [1]. The points on the curves are for identification only and are not measured data.

There is an added complication that arises when the degradation curves are not similar in shape and that is in the determination of the RDCs. In the JPL approach, the RDCs are determined by comparing the fluences of different energy protons that cause the same relative damage. Typically the 75% degradation point is used. If the curves are not parallel obviously the RDCs will vary if a different degradation point is chosen.

Figure 3 shows the RDCs for Si cells determined from the kind of data shown in Fig .1. For comparison the energy dependence of the calculated NIEL for protons in Si is also plotted on the figure [7], with the two curves normalized at 10 MeV. It is clear that the NIEL only tracks the measured RDCs for energies where the slowed down energy in the active region Eso is comparable to the incident energy (Einc).

It is reasonable to assume that the active region of the cells that produced the data shown in Fig. 1 ranged from ~0.8 – 80 μm from the front of the cell. SRIM [8] runs then put the discussion above on a more quantitative basis as can be seen in Fig. 4. Figure 4 was obtained from the vacancy.txt output of SRIM, which has been converted to NIEL using the Kinchin-Pease approximation. The SRIM studies show that at energies below about 3 MeV the proton stops within the active region.

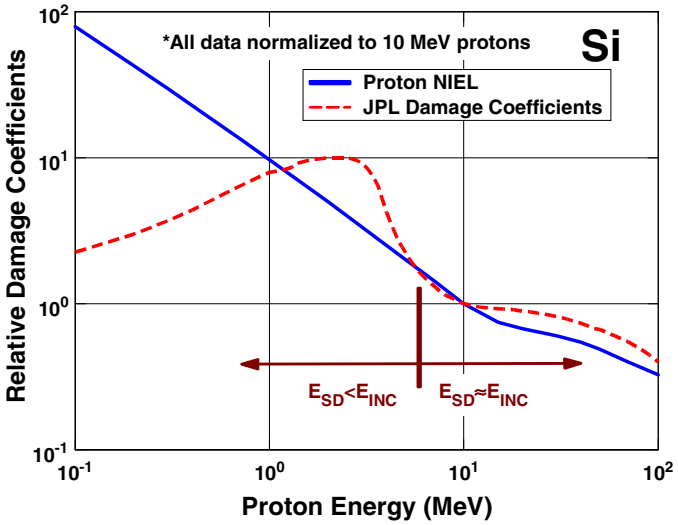

Figure 3. Comparison of the calculated NIEL for protons in Si [7] with the measured RDCs for maximum power degradation [2,3]. In the figure, E_{inc} refers to the incident proton energy and E_{so} refers to the slowed down energy.

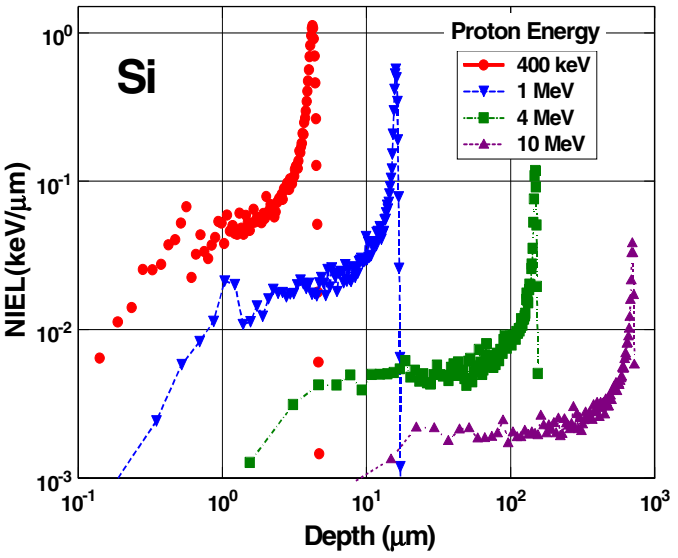

Figure 4. SRIM derived NIEL as a function of the depth for an incident proton in Si [8] .

The simplest approach to quantitatively account for the spatial nature of the damage is to assume that the RDC changes in direct proportion to the total damage produced within a minority carrier diffusion length of the junction. The energy deposited to displacements at low energies can be estimated by numerically integrating the SRIM-derived NIEL over the particle track. The adjusted NIEL is then calculated by dividing the total deposited energy

by the width of the active region (80 μm). At high energies, where the protons traverse the cell with little change in energy, the damage factor is assumed to be proportional to the displacement damage energy deposited. This is given by the product of NIEL and the width (approximately 80 μm). The NIEL for 10 MeV protons in silicon is 7.885×10^{-3} MeVcm^2/g [5]. This can be expressed as 1.829×10^{-3} keV/mm or 3.33×10^{-2} vacancies/mm [5]. The latter units are convenient for direct comparison to SRIM results, which are usually expressed as vacancies/mm The low-depth tail of the 10 MeV SRIM-derived NIEL indeed agrees with the analytical value obtained in [7].

The results obtained by applying this procedure (and normalizing at 10 MeV) are given in Fig. 5 and are compared with the data given in [3]. Inspection of Fig. 5 shows reasonable agreement between the calculated and the experimentally determined RDCs. The general shape of the calculated curve is not very sensitive to the exact value used for the diffusion length. As shown in the Fig. 5, an active depth value of 100 μm does not alter the shape or the curve significantly.

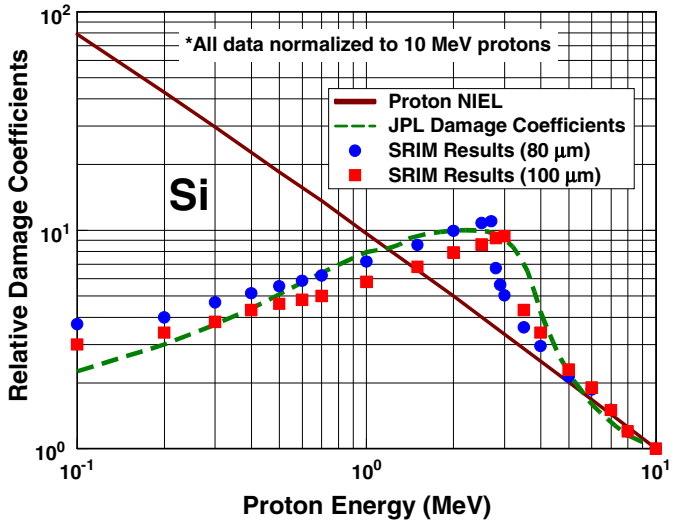

Figure 5. Comparison of the SRIM-derived RDCs for Si cells and the experimentally determined values, (see Fig. 3). 100 μm and 80 μm refer to the active depth assumed in the calculation.

.

RDCs FOR MULTI-JUNCTION CELLS

A similar analysis can be performed for the case of multi-junction cells. In this case the added complexity comes from the fact that the active region of the cells extends over several different materials; InGaP, GaAs and Ge. Figure 6 shows the degradation curves for Pmax for a three junction InGaP/GaAs/Ge cell technology [ ]. It can be seen that for E >400 keV the curves have similar shapes and follow the expected variation with energy. For lower energies the curves show the familiar variation that occurs when the incident protons slow down or stop in there active volume of the cells. Figure 7 shows experimentally determined [10,11] RDCs for Pmax degradation for several kinds of MJ cells compared to calculations of the NIEL for protons in GaAs. It should be noted that the energy dependence of the NIEL for GaAs is almost identical to that for Ge, and very close to that for InGaP. An obvious feature of the experimental data is the double hump structure seen ~0.1 MeV where the data starts to fall below the NIEL. At higher energies there is good agreement between the experimental data and the calculated NIEL.

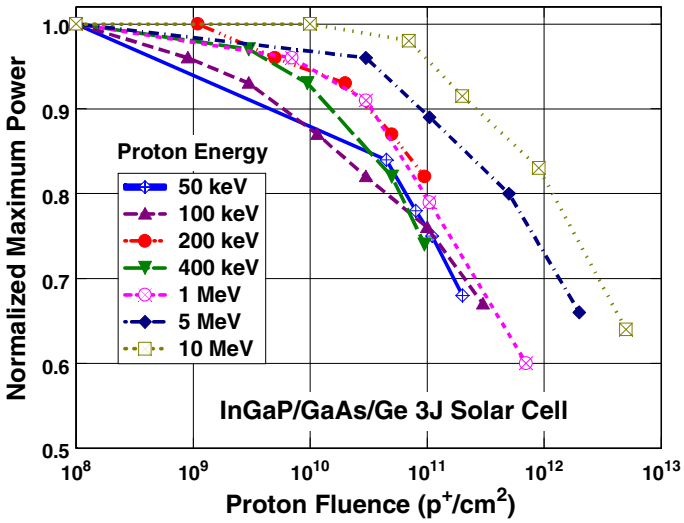

Figure 6. The degradation of the maximum power point of InGaP/GaAs/Ge triple junction cells due to proton irradiation [ ].

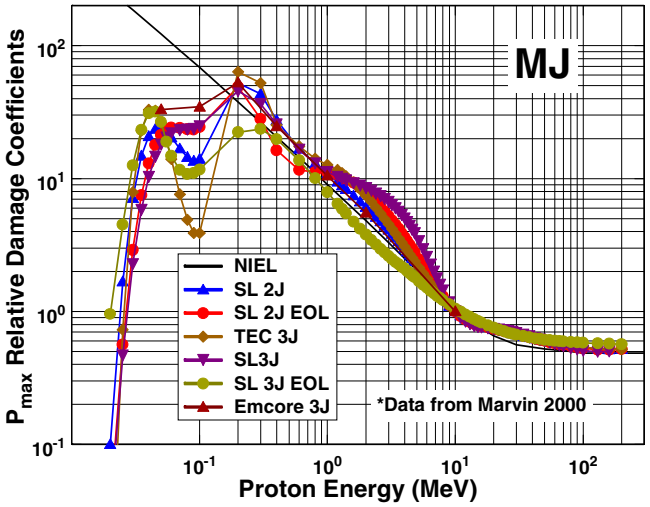

Figure 7. Comparison of the calculated NIEL for protons in GaAs with the experimentally determined RDCs for several multijunction InGaP/GaAs/(Ge) cell technologies [9,10,11].

It is reasonable to assume in light of the discussion above for Si cells, that the deviation of the experimental data from the NIEL in the double hump region in Fig. 7 is due to slowing down of the incident protons in the active volume of the cell. This is confirmed by SRIM runs as shown in Fig. 8. The analysis that follows is aimed at using these SRIM runs to try to reproduce the double hump structure in the energy dependence of the RDCs as shown in Fig.7.

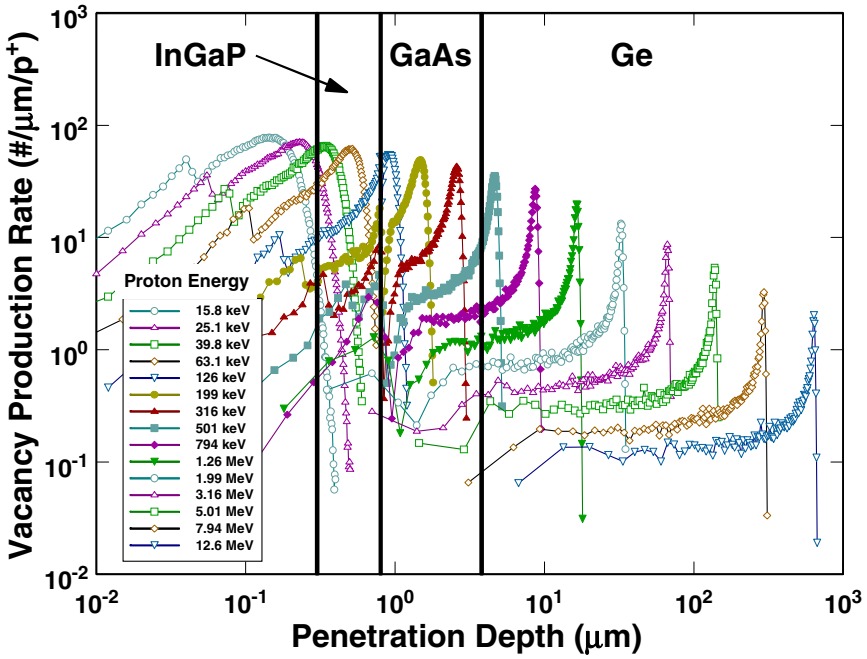

Figure 8. SRIM-derived vacancy introduction rates for protons on an InGaP/GaAs/Ge triple junction cell.

In the case of a cell technology consisting of one material such as Si, it was shown above that a good representation of the energy dependence of the RDCs could be found by determining the total number of vacancies produced over the active volume. When the cell consists of several different materials it is necessary to take into account the fact that incident protons will usually affect the electrical properties of the junctions differently. For example InGaP cells are more radiation resistant than GaAs cells. The different radiation resistance could be due to a greater level of defect annealing in InGaP than in GaAs, for example, or it might be due to the different electrical properties of the defects produced. The result in InGaP/GaAs cells is that the degradation of the overall cell is largely determined by the softer GaAs subcell. This result is confirmed by measurements of the quantum efficiency (QE) of each of the junctions following irradiation with the same fluence of protons of different energies. A fluence of 1 x 10^{12}/cm^2 of 50 keV protons, which stop in the top surface of the InGaP region, decrease only the blue part of the QE of the InGaP junction, whereas 100 keV protons, which stop in the back region of the InGaP junction decrease the QE of the red part of the InGaP junction. In both cases the change in the QE measured was quite small. However, the same fluence of 400 keV protons, which stop in the GaAs junction, produces a large drop in the GaAs QE even though 400 keV protons are less damaging than 100 keV protons

In light of these results the following approach was taken. Using the SRIM results in Fig. 8, the vacancy.txt files for energies up to 126 keV were used to calculate the total number of defects produced in InGaP over the whole range of the slowed down protons. These results were normalized to the total number of vacancies produced by 10 MeV protons. For energies >126 keV only the defects produced in the GaAs layer were counted since these appear to be much more effective in degrading the operation of the cell than those in either the InGaP or Ge layers. The results of this analysis can be seen in Fig. 9 where the SRIM-derived RDCs are compared to the experimentally determined values. It can be seen in Fig. 9 that the SRIM analysis produces the double hump structure seen in the experimental data, although the calculated RDCs in this energy region are slightly higher than the measured values. It should be noted that SRIM does not include contributions from inelastic proton interactions, which are responsible for the flattening out of the total NIEL for protons in GaAs at E > 10 MeV. The SRIM-derived RDCs are therefore expected to fall below the experimental determined values at these higher energies.

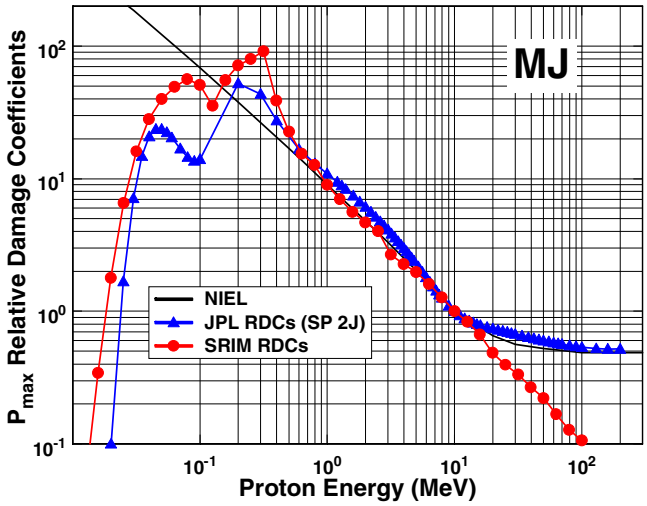

Figure 9. Comparison of SRIM-derived RDCs, experimentally determined values [10], and the calculated NIEL for protons [7] in GaAs, normalized at 10 MeV.

CONCLUSIONS

It has been shown that calculations of the total number of vacancies formed in active regions of solar cells using the Monte Carlo code SRIM can be used to calculate proton RDCs, which agree quite well with experimentally determined values. The approach is particularly useful in two cases. Firstly, in crystalline Si cells where because of the large active region of the cell protons in the MeV range slow down significantly or stop. Secondly, in multijunction cells such as InGaP/GaAs/Ge where the active volume consists of several monolithic layers of different materials. The ability to reproduce RDCs in this way is very useful because. from this basic curve for unidirectional, monoenergetic incident proton beams a family of RDC curves can be generated for isotropic protons traversing different amounts of shielding using the approach described in detail in references [3]-[6]. The performance of Si or multijunction solar cells can then be predicted for any defined space radiation environment. Comparison of predictions made for specific space missions using SRIM-derived RDCs and those experimentally determined are found to agree closely. This gives confidence in the reliability of SRIM-derived RDCs for developmental cells where experimental values are not yet available.

REFERENCES

[1] B.E. Anspaugh, Proc. 22nd IEEE Photovoltaic Specialists Conf., Las Vegas, NE, 1593, (1991).

[2] Y. Tada, J.R. Carter, Jr., B.E. Anspaugh and R.G. Downing, Solar Cell Radiation Handbook, 3rd Edition JPL Publication 82-69, 1982.

[3] B.E. Anspaugh and R.G. Downing, Radiation Effects in Si and GaAs Solar Cells Using Isotropic and Normally Incident Radiation, JPL Publication 84-61, 1984.

[4] S.R. Messenger, G.P. Summers, E.A. Burke, R.J. Walters, and M.A. Xapsos, Prog. Photovolt.: Res. Appl., 9, 103-121 (2001).

[5] S.R. Messenger, G.P. Summers, E.A. Burke, M.A. Xapsos, R.J. Walters, E.M. Jackson, and B.D. Weaver, IEEE Trans. Nucl. Sci., 46-6, 1595-1602 (1999).

[6] B.E. Anspaugh, GaAs Solar Cell Radiation Handbook, JPL Publication 96-9, 1996.

[7] G.P. Summers, E.A. Burke, P. Shapiro, S.R. Messenger and R.J. Walters, IEEE Trans. Nucl. Sci. 40, 1372 (1993).

[8] J.F. Ziegler, J.P. Biersack, and U. Littmark, *The Stopping and Range of Ions in Solids*, Volume I, New York: Pergammon Press, 1985. (SRIM is freely available at http://www.srim.org.)

[9] D.C. Marvin and J.C. Nocerino, Proc. 26th IEEE Photovoltaic Specialists Conf., Anchorage, AK, 1102 - 1105 (2000).

[10] D.C. Marvin, Aerospace Report TOR-2000(1210)-1.

[11] P.R. Sharps, D.J. Aiken, C.H. Thang, and N.S. Fatemi, Proc. 17th EUPVSEC, Munich, Germany, (2001).

Physics of Quantum Structures in Photovoltaic Devices

Ryne P. Raffaelle and John D. Andersen
Physics Department, Rochester Institute of Technology
Rochester, NY 14623

Abstract

There has been considerable activity recently regarding the possibilities of using various nanostructures and nanomaterials to improve photovoltaic conversion of solar energy. Recent theoretical results indicate that dramatic improvements in device efficiency may be attainable through the use of three-dimensional arrays of zero-dimensional conductors (i.e., quantum dots) in an ordinary p-i-n solar cell structure. Quantum dots and other nanostructured materials may also prove to have some benefits in terms of temperature coefficients and radiation degradation associated with space solar cells. Two-dimensional semiconductor superlattices have already demonstrated some advantages in this regard. It has also recently been demonstrated that semiconducting quantum dots can also be used to improve conversion efficiencies in polymeric thin film solar cells. Improvement in thin film cells utilizing conjugated polymers has also be achieved through the use of one-dimensional quantum structures such as carbon nanotubes. It is believed that carbon nanotubes may contribute to both the disassociation as well as the carrier transport in the conjugated polymers used in certain thin film photovoltaic cells. In this paper we will review the underlying physics governing some of the new photovoltaic nanostructures being pursued, as well as the the current methods being employed to produce III-V, II-VI, and even chalcopyrite-based nanomaterials and nanostructures for solar cells.

Introduction

The underlying physics providing the impetus for the use of nanostructures in solar cells can be understood through elementary quantum mechanics. One of the first lessons learned in an introduction to the field is that electron motion is governed by Schroedinger's Equation and the potential V(r)

$$\frac{-\hbar^2}{2m}\nabla^2\Psi(r)+V(r)\Psi(r)=E\Psi(r) \tag{1}$$

If V(r) = 0, the solution is a simple plane-wave. In regions where V is non-zero, and the electron has enough energy to pass over of tunnel through, we will have a modified plane-wave solution (scattering states). However, where V(r) is negative we will have bound (negative energy) states. Although scattering and bound states differ in many ways, of particular interest is the fact that scattering states are continuous function of the electrons energy, whereas bound states are possible only for particular values of the energy. That is, bound states only occur for discrete values of energy (i.e., they are "quantized"). If two identical atoms are brought together, with an electron is the same quantum state, the energy levels must split due to the Pauli Exclusion Principle.

Solutions to Schroedinger's equation for electrons in a crystalline solid are called Bloch wavefuntions. Fourier's theorem shows that the functions are simply a plane-wave solution multiplied by a periodic function whose periodicity matches that of the potential in the crystal.

$$\Psi(r)=u(r)e^{ik\cdot r} \tag{2}$$

Confining Bloch electrons to a thin plane by providing a rectangular potential well perpendicular to the plane will also produce a discrete bound state spectrum. Such a system is an example of a Quantum Well (QW). If the electron is completely confined to the plane, due to an infinitely deep potential well of width a_Z, the bound state energies are

$$E = \left(\frac{\hbar^2}{2m}\right)\left(k_x{}^2 + k_y{}^2\right) + \left(\frac{\hbar^2}{2m}\right)\left(\frac{\pi n_z}{a_z}\right)^2 \tag{3}$$

Similarily, if constrained in two dimensions we have a quantum wire with energy levels given by

$$E = \left(\frac{\hbar^2}{2m}\right)k_x{}^2 + \left(\frac{\hbar^2}{2m}\right)\left[\left(\frac{\pi n_y}{a_y}\right)^2 + \left(\frac{\pi n_z}{a_z}\right)^2\right] \tag{4}$$

and if constrained in three dimension we have a quantum dot with energy levels given by

$$E = \left(\frac{\hbar^2}{2m}\right)\left[\left(\frac{\pi n_x}{a_x}\right)^2 + \left(\frac{\pi n_y}{a_y}\right)^2 + \left(\frac{\pi n_z}{a_z}\right)^2\right] \tag{5}$$

In the same way that bringing a number of atoms together in a solid results in “energy bands,” bringing a number of quantum structures together (i.e., multiple quantum wells, ordered arrays of quantum wires or quantum dots) will also result in bands. If these collections of quantum structures reside within a host semiconductor we will have what are called “minibands” (see Figure 1) Electronic States in “wells” are “quantized” and therefore have discrete-like energy levels. The mini-band levels depend on the width of the wells. These size dependent mini-bands levels afford photovoltaic designers the flexibility to tune the absorption spectrum of devices beyond what is available through the normal array of bulk semiconductor bandgaps. In addition to adjusting the absorption specturm of the device, these minibands also provide the possibility to take advantage of such things as two-photon processes and slow-cooling effects.

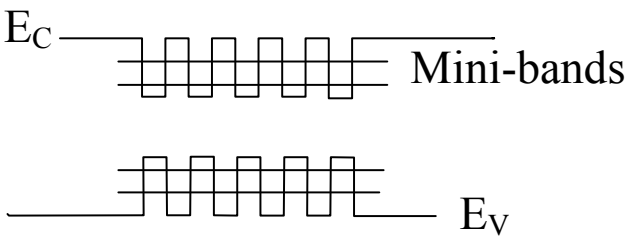

Figure 1. Idealized energy band diagram of a multiple quantum well structure showing electronic "mini-bands".

To a first order approximion the effective bandgap of a semiconducting quantum dot can be calculated using

$$\hbar\omega = E_g + \frac{\hbar^2}{2m_e^* r^2}\pi^2 \tag{6}$$

Thus, for a real material the appropriate size to achieve mid-gap state in a suitable device structure can be determined. Figure 2. shows a atomic force micscopy image of InAs quantum dots grown by metal organic chemical vapor deposition on InGaAs at Essential Research Incorporated and imaged in the NanoPower Research labs at Rochester Institute of technology.

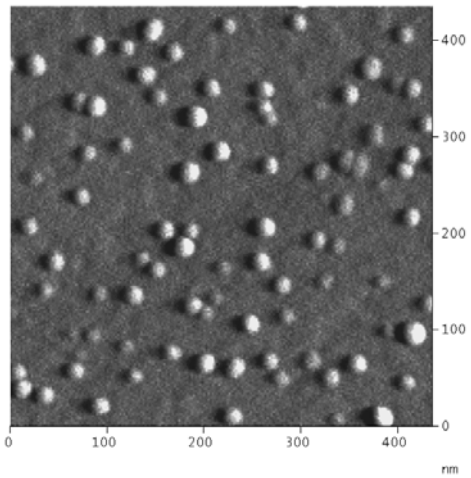

Figure 2. Atomic force micrograph of InAs quantum dots grown on InGaAs.

Historical Developments

An antecedent to the use of nanostructures for photovoltaics lies in what has been referred to as the "impurity photovoltaic effect (IPV)"[1]. M. Wolf suggested in 1960 that impurities could be added in such a way to a conventional *p-n* junction solar cell that they would create available electronic states within the bandgap (see Figure 3). These states could then participate in sub-bandgap absorption and act to raise the overall efficiency of a solar cell. However Schockley and Queisser, early modelers of single junction photovoltaic, argued against the IPV by cited that the recombination losses, which would result from the introduction of the impurities would make IPV devices impractical [2].

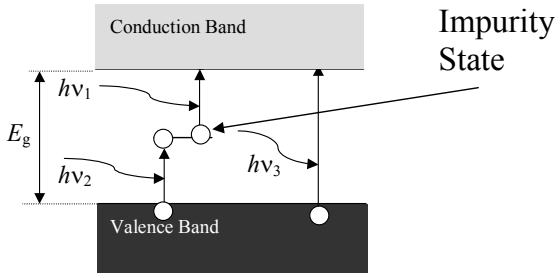

Figure 2. Idealized energy band diagram outlining the impurity photovoltaic effect.

Photovoltaics designers were able to finally overcome the single junction Shockley - Quiesser model limit through the use of tandem cells. Even multijunction solar cells have their theoretical limitations imposed by such things as current matching of the junctions and the actual materials issues imposed by non-idealized or real materials. Theoretically, at least, designers could envision solar cell efficiencies that dwarfed the single-junction limit by the use of an ever-increasing number of junctions.

In 1990, a new approach to the possible design of solar cells was put forth in a seminal paper by Barnham and Duggen (see Figure 4) [3]. They proposed that the limits imposed on a tandem cell could be eliminated through the use of multiple quantum wells (MQW). This work was followed by suggestions that the use of these and similar nanostructured approaches could yield other benefits such as inverse Auger mechanisms with quantum efficiencies greater than one [4-5]. Luque and Marti showed that a quantum dot array incorporated in a *p-i-n* junction solar cell could dramatically exceed the Shockley - Quissier limit and even that of an ideal tandem cell (see Figure 5) [6]. The proposed use of quantum dots for spectral shifting and concentrator applications has also generated interest [7]. However, the largest impact in the development of photovoltaics from quantum dots has been their use as additives in thin film polymeric solar cell development [8]. It has been demonstrated that these quantized nanostructured materials will act as disassociation centers for the excitons created in the conjuated poymeric absorbers and can help facilitate carrier transport through these devices.

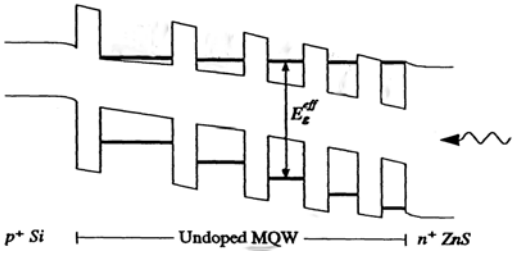

Figure 4. Idealized band diagram of a multiple quantum well (MQW) solar cell. Electronic States in “wells” are “quantized” and therefore have discrete-like energy levels. The mini-band levels depend on the width of the well. K.W.J. Barnham and G. Duggan, *J. Appl. Phys*., **67**, 7, 1990.

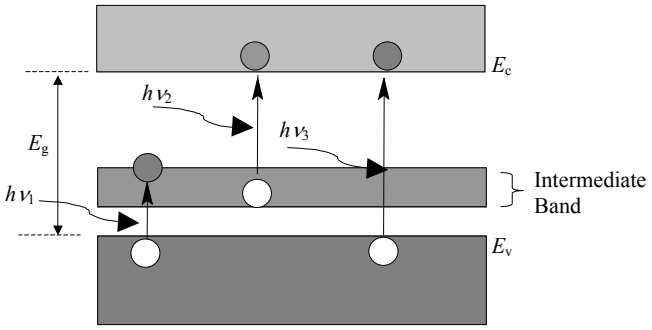

Figure 5. Idealized energy band diagram of an intermediate band quantum dot solar cell (A. Luque and A. Marti, *Phys. Rev Lett.* **78**, 5014 (1997).

Solar Cell Enhancement with Nanostructures

The question which normally arises from a discussion of quantum structures and solar cells is "can these quantum structures truly be used to enhance solar cell performance? " In order to address such a question we must first define what is meant by enhancement. In terms of the theoretical analysis of photovoltaic structures, one normally speaks of either a global or relative efficiency enhancement. For a global enhancement the question that must be answered is "can the efficiency of a nanostructured solar cell under solar illumination be greater than the optimum single-gap cell?" These comparisons normally involve many theoretical idealizations used in calculating limiting efficiencies. In contrast a relative efficiency enhancement refers to

whether in principle and practice a nanostructured solar cell can be more efficient under solar illumination than corresponding single-gap baseline cells for at least some range of baseline cell bandgaps. Finally, there can also be ancillary enhancements, other than just overall devices efficiency, whereby in practive a nanostructured solar cell can offer various advantages over single-gap cells under useful illumination and operating conditions. Several of these advantages that could be especially relevant in terms of space solar power development. For example, it has been demonstrated that a multiple quantum well structured can be more radiation resistant than a non-nanostructured counterpart [9]. Also, these structures can be used to tailor the thermal characteristics of cell to improve cell performance in thermophotovoltaic applications [10].

The question of relative efficiency enhancement was recently addressed when it was demonstrated that GaAs wells in AlGaAs increased efficiency and photocurrent under broadband illumination [11]. However, the observed open circuit voltage drop was inconsistent with original hypothesis and this coupled with larger than optimum Eg of AlGaAs left open the possibility that the wells merely provided bandgap tuning. The case of global efficiency enhancement is even much less clear than that of relative efficiency enhancement and has generated a considerable amount of debate. It was argued that the use of a MQW could be used to extend the spectral response of a solar cell without sacrificing photovoltage [12]. However, shortly thereafter a detailed balance equation calculation was published which showed that the efficiency of a MQW cell was the same as that of an ideal single-gap cell [13]. The assumptions used in this calculation were immediately challenged and a similar calculation with numerical estimates based on real wells actually showed a small global enhancement [14]. However, this result has also been criticized because the absorptivity and emissivity of the structure was treated differently [15]. There have been other models which use more realistic features and may be better suited to real MQW solar cells [16].

The differences in the results of these models could be rectified if it was conclusively know whether or not one should assume uniform quasi-Fermi levels (QFLs) across a MQW solar cell. If not, then then the criticisms of the detailed balance analyses would no longer be valid. Several groups have explored the consequences of non-uniform QFLs, most notably in incomplete thermalization [17]. There has been considerable Experimental support for this hypothesis [18].

Detailed balance efficiency limits in QWSCs with non-uniform QFLs, which include two-photon processes, has been calculated to be 63% [19]. (Ironically this is the same exact value that is obtained by Luque and Marti for their intermediate band solar cell (IBSC) utilized quantum dots). In addition, if one allows for reduced carrier transport through hot electron transport, limiting efficiencies could exceed even the 63% mark. Luque, Marti, and Quadra have studied various multiband models thermodynamically and have concluded that if photon-assisted escape is possible then global efficiency improvements are possible [20]. Also, if one neglects hot-electron transport, then the thermodynamic model also predicts 63%. However, Luque, Marti, and Quadra actually argue against non-uniform QFLs citing it would violate the second law of thermodynamics.

It is well accepted that the maximum thermodynamic limit for a single junction conversion of solar irradiance into electrical free energy in the radiative limit using detailed balance is 31% [21]. Therefore, one may view the use of a multi-junction cell approach is actually a means of reducing thermalization losses. (The limit of an infinite number of junctions perfectly matched to a one-sun solar spectrum being 66%). It can thus be argued that quantum structures can exhibit global efficiency improvements by reducing thermal losses. Several approaches to accomplishing this in practice have been outlined [22-24]. However, it must be noted in order to accomplish this the rates of photogeneration of carriers, transport, and interfacial transfer to the contacts must be comparable to the rate of carrier cooling. It has been predicted and experimentally shown that relaxation dynamics can be dramatically altered by quantization (nanostructures, quantum wells, superlattices, quantum wires, and dots). When carriers are confined in potential regions whose dimension is comparable to their deBroglie wavelength or Bohr exciton radius in the semiconductor bulk, their relaxation dynamics are dramatically altered (i.e., hot carrier extraction rates can be comparable to the rate of carrier cooling).

Nanostructured Solar Cell Fabrication

The vast majority of nanostructured photovoltaics have been produced using epitaxial growth involving either molecular beam epitaxy (MBE) or metal organic chemical vapor deposition (MOCVD), which is sometimes referred to as metal organic vapor phase epitaxy (MOVPE). Groups such as the K. Barnham group at Imperial College in London and the A. Zunger group in the Space Vacuum Epitaxy Center or the University of Houston have been leaders in the use of nanostructure growth for photovoltaics. Recently there has been considerable effort in using these similar synthesis techniques to produce photovoltaic structure that incorporates quantum dots as opposed to the quantum wells. These attempts use what is referred to as Stranski-Krastanow growth. This growth technique utilizes lattice strain to produce "islands" of material on a semiconductor surface, and this process can be repeated with alternating complete layers of quantum dots to produce self-organized columnar arrangement of dots (see Figure 6).

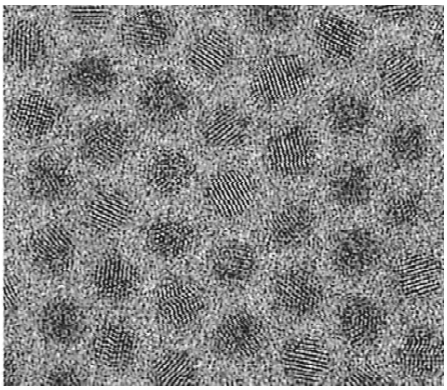

Figure 6. Transmission electron micrograph of self-organized quantum dots (Talapin et. al. *Nanoletters* **2001**, *1*, 207 - 211).

The most widely investigated nanomaterials for polymeric solar cells have been semiconducting nanocrystals, fullerenes, and single wall carbon nanotubes (SWNTs) [28-33]. In particular, CdSe quantum dots (QDs), nanorods, and tetrapods have all shown to improve the performance of solar cells utilizing conjugated polmers. This work has attracted the attention of the space power community for the simple reason that these cells could someday provide specific powers that would be unimaginable for their crystalline counterparts. To date the efficiencies are still in the single digits and the question of stability in a space environment has yet to be addressed.

Conclusions

Ancillary improvements via quantum structures are probably more important to space photovoltaics than any other solar cell application. This is due to the potential they hold for better temperature coefficients, radiation resistance, and spectral shifting. The bandgap tuning available through the use of nanostructures could potentially be integrated into a multi-junction solar cell to add another means to improve current matching. Spectrum shifting through up- and down-conversion could be combined with almost any cell to improve performance. Quantum dots appear to be ideally suited for this application. These nanomaterials and other nanostructures should prove quite useful in new concentrator designs. Nanostructured materials may also hold the key by which polymeric-based cells reach viable efficiencies and become a contender for space solar power applications.

Acknowledgements

The authors wish to thank the NASA Glenn Research Center Strategic Research Fund, NASA Cooperative Agreements NCC3-710, NCC3-563, National Science Foundation, and First-in-Class program of Rochester Institute of Technology.

References

1. M. Wolf, *Proc. of IRE* **48**, 1246 (1960).
2. W. Shockley and H. Queisser, *J. Appl. Phys.* **32**, 510 (1961).
3. K. Barnham and G. Duggan, *J. Appl. Phys.* **67**, 3490 (1990).
4. M. Keevers and M. Green, *J. Appl Phys.* **75**, 4022 (1994).
5. J. Werner, et. Al. *Phys. Rev. Lett.* **72**, 3851 (1994).
6. A. Luque and A. Marti, *Phys. Rev Lett.* **78**, 5014 (1997).
7. K. Barnham, et. al., *Appl. Phys. Lett.* **76**, 1197 (2000).
8. W.U. Huynh, X. Peng, and A.P. Alivisatos, *Adv. Mat.* **11**, 923 (1999).
9. R.J. Walters, G.P. Summers, S.R. Messenger, A. Freundlich, C. Monier, F. Newman, *Prog. In Photovolt.: Res. Appl.* **8** (2000) 349; N.A. Sobolev et al. *Phys. Stat. Sol B* 224 (2001) 93.
10. P. Griffin, I. Ballard, K. Barnham, J. Nelson, A. Zachariou, J. Epler, G. Hill, C. Button, M. Pate, *Sol. Energy Mater. Sol. Cells*, 50 (1998) 213.
11. K.W.J. Barnham, B. Braun, J. Nelson, M. Paxman, *Appl. Phys. Lett.* 59 (1991) 135.
12. K.W.J. Barnham, G. Duggan, *J. Appl. Phys.* 67 (1990) 3490.
13. G.L. Araujo and A. Marti, *Sol. Energy Mater. Sol. Cells* 33 (1994) 213.
14. R. Corkish and M. Green, *Proceedings of the 23rd IEEE Photovolt. Specialists Conference* (1993) 675; N.G. Anderson *J. Appl. Phys.* 78 (1995) 1850.
15. G.L. Araujo, A. Marti, *Appl. Phys. Lett.* 66 (1995) 894.
16. N.G. Anderson and S.J. Wojtczuk, *J. Appl. Phys.* 79 (1996) 1973.
17. S. Kettemann, J.F. Guillemoles, *Proc. of the 13th Europeand Photovolt. Spec. Conf.* (1995) 119.
18. E. Tsui, et. al. *J. Appl. Phys*. 80 (1996) 4599; J. Nelson, et. al. 82 (1997) 6240; N.J. Ekins-Daukes, et. al. *Physica E*, (1998) 171; K.W.J. Barnham, et. al., *J. Mater. Sci.: Mater. Electron.* 11 (2000) 531; B. Kluftinger, et. al. *Sol. Energy Mater. Sol. Cells*, 66 (2001) 501; K Barnham, et. al., *Physica E* 14 (2002) 27.
19. S.P. Bremmer, R. Corkish, and C.B. Honsberg, *IEEE Trans. Electron. Devices* 46 (1999) 1932.
20. A. Luque, A. Marti, L. Cuadra, *IEEE Trans. Electron. Devices* 48 (2001) 2118; A. Luque, *Physica E*, 14 (2002) 107.
21. W. Shockley and H.J. Queisser, J. Appl. Phys. 32 (1961) 510.
22. D.S. Boudreaux, F. Williams, A.J. Nozik, J. Appl. Phys. 51 (1980) 2158; A.J. Nozik, *Ann. Rev. Chem. Phys*. 52 (2001) 193.
23. P.T. Landsberg, H. Nussbaumer, G. Willeke, *J. Appl. Phys.* 74 (1993) 1451; S. Kolodinski, J.H. Werner, T. Wittchen, H.J. Quiesser, *Appl. Phys. Lett.* 63 (1993) 2405.
24. A. Luque and A. Marti, *Phys. Rev. Lett.* 78 (1997) 5014.
25. F.E. Williams, A.J. Nozik, *Nature* 311 (1984) 21.
26. F. Williams, A.J. Nozik *Nature* 271 (1978) 137.
27. D.S. Ginger and N.C. Greenham, *J. of Appl. Phys.* 87, 3 (2000) 1361.
28. V. Dyakonov, Thin Solid Films 451-452 (2004) 493-497.
29. W.U. Huynh, J.J. Dittmer, A.P. Alivisatos, Science 295 (2002) 2425-2427.
30. E. Kymakis, G.A.J. Amaratunga, Appl. Phys. Lett. 80 (2002) 112-114.
31. S.E. Shaheen, C.J. Brabec, N.S. Sariciftci, F. Padinger, T. Fromherz, J.C. Hummelen, Appl. Phys. Lett. 78 (2001) 841-843.
32. B. Sun, E. Marx, N.C. Greenham, Nano Lett. 3 (2003) 961-963.
33. G. Yu, J. Gao, J.C. Hummelen, F. Wudl, A.J. Heeger, Science 270 (1995) 1789-1791.

SINGLE WALL CARBON NANOTUBE-POLYMER SOLAR CELLS

Sheila G. Bailey
NASA Glenn Research Center, Cleveland, OH 44135, USA

Stephanie L. Castro
Ohio Aerospace Institute, Brookpark, OH 44142, USA

Brian J. Landi, Thomas Gennett, and Ryne P. Raffaelle
NanoPower Research Laboratories, Rochester Institute of Technology, Rochester, NY 14623, USA

Investigation of single wall carbon nanotube (SWNT)-polymer solar cells has been conducted towards developing alternative lightweight, flexible devices for space power applications. Photovoltaic devices were constructed with regioregular poly(3-octylthiophene)-(P3OT) and purified, >95% w/w, laser-generated SWNTs. The P3OT composites were deposited on ITO-coated polyethylene terapthalate (PET) and I-V characterization was performed under simulated AM0 illumination. Fabricated devices for the 1.0% w/w SWNT-P3OT composites showed a photoresponse with an open-circuit voltage (V_{oc}) of 0.98 V and a short-circuit current density (I_{sc}) of 0.12 mA/cm^2. Optimization of carrier transport within these novel photovoltaic systems is proposed, specifically development of nanostructure-SWNT complexes to enhance exciton dissociation.

INTRODUCTION

The lure of large area, inexpensive, and environmentally benign solar cells has attracted many researchers over the past four decades or so. Since the early 1990's, considerable attention has turned to lightweight, flexible organic thin-film photovoltaics based on soluble conducting polymers.[1] This new class of devices relies upon the interaction between a nanomaterial and a conjugated polymer.[2] In addition to enhancing photovoltaic conversion efficiency, the incorporation of nanomaterials can potentially improve photochemical, mechanical, and environmental stability.

Photon absorption in the organic based composites produces bound-state excitons. Dissociation of these charge pairs can be accomplished by the potential difference across a polymer-metal junction provided the excitons are near the interface. However, the dissociation can also be accomplished via electron accepting impurities.[2] Thus, under illumination a preferential transfer of electrons to the acceptors will leave holes to be preferentially transported through the conjugated polymer. This process is known as photoinduced charge transfer. Since the discovery of photoinduced charge transfer, a variety of acceptor materials have been introduced into donating conjugated polymers to produce photovoltaic devices (i.e., Buckminster fullerenes,[3,4] CdSe quantum dots and nanorods,[5] and single wall carbon nanotubes[6]). Typical devices are produced by placing the doped polymeric films between a transparent conductive oxide (TCO) top contact and a metallic back contact.

The use of SWNTS in this type of device is a particularly attractive approach for several reasons. The extremely high surface area, ~1600 m^2/g reported for purified SWNTs,[7] offers a tremendous opportunity for exciton dissociation. Since SWNTs have diameters of ~1 nm and lengths on the order of microns, these materials exhibit significantly large aspect ratios (>10^3). At low doping levels, percolation pathways are established providing the means for a high carrier mobility and efficient charge transfer. This has been a problem in the majority of polymer solar cells developed to date, even with the advent of semiconductor nanorods. Since the diffusion distances for excitons in conducting polymers, poly(phenylenevinylene) for example, have been reported at <10 nm,[4] the requirement for a sufficient percolation network of electron-accepting dopants in the polymer composite is substantiated. Electrical conductivity data has validated that SWNT-doped polymer composites demonstrate this extremely low

percolation threshold. For SWNT-epoxy composites, the electrical conductivity has been claimed to rise by nearly 10^5 S/cm between 0.1 and 0.2% w/w loading.[8]

Other beneficial properties of SWNTs relevant to polymeric photovoltaic development include composite reinforcement and thermal management. Single wall carbon nanotubes have shown promise in the development of polymer composites with enhanced mechanical strength by load transfer from the polymer matrix to the dopant.[9] Tensile strengths for SWNTs have been estimated to equal ~20 GPa,[10] while the Young's modulus measured by atomic force microscopy is ~1 TPa.[11] This high Young's modulus and strength-to-weight ratio could help provide much needed mechanical stability to large area thin-film arrays. Single wall carbon nanotubes may also provide assistance in thermal management for such arrays. The thermal conductivity of an isolated (10, 10) SWNT has been theoretically predicted to be as high as 6600 W/mK.[12] Polymer composites doped with as little as 1% w/w SWNTs have shown a 70% increase in the thermal conductivity at 40 K.[8]

The viability of incorporating SWNTs into a conducting polymer for photovoltaic devices was established in 2002, utilizing arc-generated SWNT- poly(3-octylthiophene)-(P3OT) composites.[6] Their results showed a diode response for devices constructed in the sandwich formation, containing the composite film between an indium-tin-oxide (ITO) front contact and aluminum back contact. There was a photoresponse under AM1.5 illumination for both the pristine P3OT device and a 1% SWNT-P3OT composite blend, albeit the composite exhibits current densities several orders of magnitude higher. The photoresponse for a 1% w/w doped SWNT-P3OT composite was reported to have an open-circuit voltage (V_{oc}) of 0.75 V and a short-circuit current density (I_{sc}) of 0.12 mA/cm^2, in comparison to a V_{oc}= 0.35 V and I_{sc}= 0.7 μA/cm^2, for the pristine P3OT device.[6]

Originally, the SWNT-P3OT cells were described using the metal-insulator-metal (MIM) model for determining the V_{oc} based on a work function differential between the two metal electrodes. In the reported case, the maximum V_{oc} would be ~0.4 V based on values of 4.3 eV for Al and 4.7 eV for ITO,[6] although work has been done to show some variability in the work function of ITO dependent on processing and oxygen content.[13] Recent work has shown that investigation of differing work function metal electrodes that the MIM model is not applicable for SWNT-P3OT systems, due to a consistent V_{oc} of 0.75V. Rather, they propose that internal SWNT/polymer junctions based on the highest occupied molecular orbital (HOMO)-lowest unoccupied molecular orbital (LUMO) of the respective materials leads to enhanced charge separation and collection, providing the higher observed V_{oc} value.[14] In principle, control over these junctions may be garnered by reducing defect sites, altering the diameter distributions (which is inversely related to the bandgap in semiconducting types), or varying the concentration ratio of metallic to semiconducting for the SWNTs prior to dispersion. Such processing control offered by alternative synthesis conditions and purification strategies may further improve the V_{oc} and in turn produce more efficient SWNT-polymer solar cells.

EXPERIMENTAL

Single wall carbon nanotubes used for this study were synthesized using the pulse laser vaporization technique, employing an Alexandrite laser (755 nm) which pulsed the surface of a 0.6 at.% Ni/Co doped graphite target at a power density of 20 - 150 W/cm^2. The reaction furnace temperature was held at 1150°C, while the chamber was at a pressure of 400 torr with 100 sccm flowing $Ar_{(g)}$.[15] The as-produced SWNTs were collected from the condensed region on the quartz tube outside the furnace and purified by modification of the previously reported procedure.[16] In short, ~50 mg of as-produced SWNTs were refluxed in 3M nitric acid for 16 hours, and then filtered over a 0.2 μm PTFE membrane filter with copious amounts of de-ionized water. After drying the membrane filter at 70°C in vacuo to remove the SWNT paper, thermal oxidation proceeded in air at 500°C for one hour in a muffle furnace. Use of a 6M Hydrochloric acid wash for one hour in a water bath sonicator was at times necessary to remove any remaining metal catalyst impurities, with similar filtering steps. Finally, thermal oxidation at 550°C in air for one hour completed the purification. Raman spectroscopy, surface area analysis, scanning electron microscopy (SEM), optical absorption spectroscopy, and thermal gravimetric analysis (TGA) were utilized to fully characterize all raw soot and purified materials.

Preparation of the SWNT-P3OT composite solutions was performed using a series of mixing and sonication steps as previously demonstrated for other SWNT-polymer systems.[17] The necessary amount of regioregular P3OT, supplied by Aldrich, was dissolved in chloroform using water bath sonication to achieve the pristine 15 mg/mL solution. Composite dispersion was performed by

combining the appropriate mass of purified SWNTs to the pristine solution at desired doping levels. The composite solution was then placed in a water bath sonicator for five minutes prior to high speed stirring at room temperature for 72 hours. Aliquots of this dispersed solution were cast on Teflon substrates at room temperature to produce desired thin films required for optical absorption spectroscopy.

Device fabrication involved the use of commercially-obtained, high quality (i.e., < 10 Ω/sq.) ITO-coated polyethylene terapthalate (PET) substrates. The required cleaning of the ITO substrate prior to deposition was performed by sonication and rinsing of cut samples (1 inch x 1.5 inches) in de-ionized water, acetone, and methanol. Initially, an intrinsic layer of pristine P3OT is spray deposited (~1-2 mL of the 15 mg/mL solution) onto the masked, 1 $in.^2$ active area of the substrate. This is followed with spray deposition of the SWNT-P3OT composite solutions at similar volumes. As seen in Figure 1, completion of the solar cell occurs when aluminum contacts (typical thicknesses of 1000Å) are applied to the ITO and SWNT-P3OT composite film layers. This is accomplished using thermal evaporation under vacuum at pressures $<10^{-6}$ mbar with a standard shadow mask.

Solar cell testing was performed in an isolated black box configuration to assure standard calibration and reproducibility of results. Thin film SWNT-P3OT cells were placed on a temperature-controlled stage, held at 20ºC, during analysis. The I-V characteristics were monitored using a Keithley 237 source measurement unit. Simulated AM0 illumination was achieved by calibration of ELH lamps with a NASA certified Si standard cell.

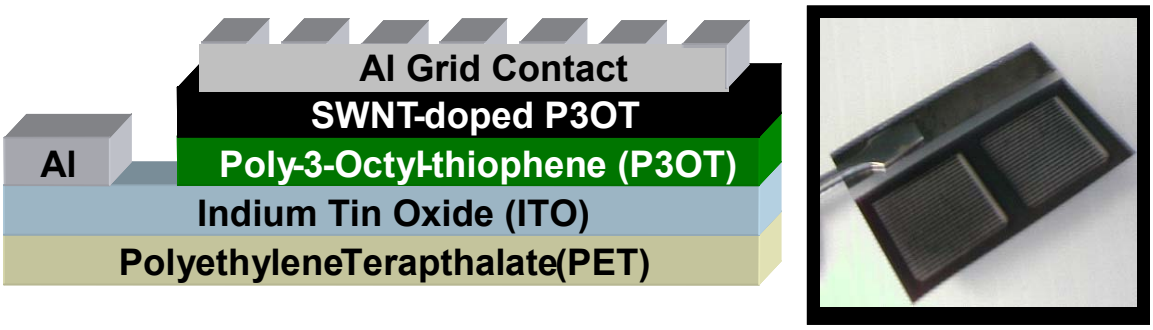

(a) (b)

Figure 1. (a) Schematic representation and (b) image depicting the composition of fabricated SWNT-P3OT flexible solar cells

RESULTS

The ability to elicit control over as-produced SWNTs is a major advantage for using pulse laser vaporization synthesis techniques. Such parameters as diameter distribution, defect density, and metallic to semiconducting ratios can be altered based on the synthesis conditions.[15,16,18] The as-produced SWNTs used in this study were synthesized and purified under typical conditions, where substantial yields and minimal defects have been observed. Shown in Figure 2 is a representative (a) SEM image of purified, >95% w/w SWNTs, and (b) an overlay of the Raman spectra for the radial breathing mode (RBM) of this sample for incident laser energies of 1.96 and 2.55 eV. The SEM image shows an entangled "mat" of SWNTs with no significant metal catalyst impurities or amorphous carbon coatings. The high purity SWNTs will "bundle" due to the Van der Waals interaction between the individual tubes. Control over the influence of bundling can potentially be addressed through polymeric interaction. Previous work has suggested a "debundling" effect with SWNT-Nafion composites, observed by SEM, that was proposed to reduce the necessary doping level for a percolation threshold.[17] Dispersions of SWNTs in P3OT may follow similar results, although full evaluation of this has not yet been performed. In addition, Raman spectroscopy can be used to determine the diameter distribution, chirality, and defect density of the as-produced and purified SWNTs. The RBM is routinely used to

calculate the diameter distribution.[19] Using two incident laser energies during analysis allows for the determination of SWNT type, i.e. semiconducting vs. metallic.[20,21] For this diameter range, the 1.96 eV laser resonantly enhances predominantly metallic SWNTs which correspond to ~1.2-1.4 nm in diameter.[19] Similarly, the 2.55 eV laser probes the semiconducting type, also shown to contain equivalent diameters for the purified sample.

The homogeneous distribution of SWNTs in a polymer matrix is dependent upon the ability of the polymer chain to associate with the SWNT superstructure. Stable composite dispersions of 0.1% and 1.0% w/w SWNTs in P3OT were produced and analyzed in this study. Optical spectroscopy was conducted to observe the SWNT doping level effects on the absorption properties and infer potential electronic interactions between dopant and polymer.

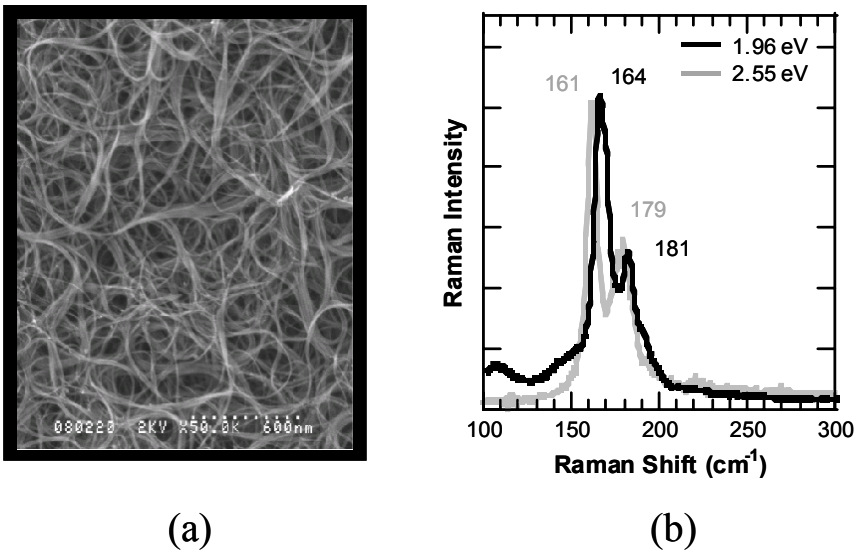

Figure 2. (a) SEM image of purified, >95% w/w SWNTs, and (b) overlay of Raman spectrum for the RBM of (a) at incident laser energies of 1.96 and 2.55 eV. The labeled peaks correspond to a diameter distribution between 1.2-1.4 nm for both metallic and semiconducting SWNTs.

Shown in Figure 3 is an overlay of these spectra where the pristine P3OT shows strong optical absorption at energies >2 eV. As expected, variation in absorption properties for the SWNT-P3OT composites is observed as the doping level increases. Through modification of the SWNT doping level in the polymer, it is possible to alter the absorption pattern of these composite materials. In fact, at these relatively low doping levels, the P3OT shows a significant enhancement in absorption through the near-IR and visible regions. The gray curve for purified SWNTs is offset from the other three for clarity, but indicates the typical complex pattern observed for this spectral range. The two lowest energy peaks for SWNTs (~0.7 eV and ~1.3 eV) are representative of the energy transitions corresponding to the 1st and 2nd Van Hove (VH) singularities for semiconducting types, respectively.[22] The SWNT-P3OT composites display a relative quenching of the 1st VH compared to the 2nd VH, which is typical of doping effects on the SWNTs.[23,24] Therefore, an apparent doping of the semiconducting SWNTs by the polymer is present. However, due to the higher intensity at larger energies, typical of absorption for the metallic SWNTs (~1.8 eV), any interaction between these SWNT types and the polymer is presently unavailable.

Application of SWNT-P3OT composite solutions to the constructed devices was performed using a solution-spray technique onto the ITO/PET substrates. The unique approach to deposit these photoactive composites on polymer substrates demonstrates the inherent advantages of thin film polymeric solar cells, namely low structural weight and flexibility. These novel polymeric solar cells were constructed for pristine P3OT, 0.1% w/w, and 1.0% w/w SWNTs in P3OT, and tested under simulated AM0 illumination to determine the respective I-V characteristics. The typical photoresponse observed for pristine P3OT and 1% w/w SWNT-P3OT cells is shown in Figure 4. Although each overlay

shows significant enhancement in both I_{sc} and V_{oc} upon illumination, there is an absense of the typical diode "knee" for both cases. The cause of the larger than expected reverse bias currents is presently not understood. This effect may be attributed to long-lived energy states for the SWNTs and P3OT or the presense of carrier traps which reduces the I_{sc}.

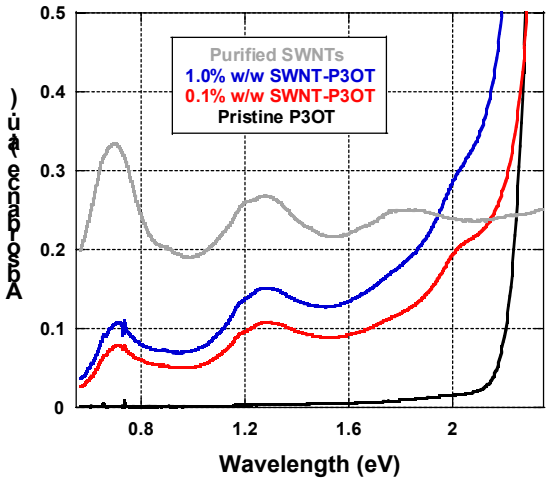

Figure 3. Optical absorption overlay for thin films of pristine P3OT (black), 0.1% w/w SWNT-P3OT composite (red), 1.0% w/w SWNT-P3OT composite (blue), and purified SWNTs (gray). Enhancement in absorption for the composites relative to the pristine P3OT is clearly observed

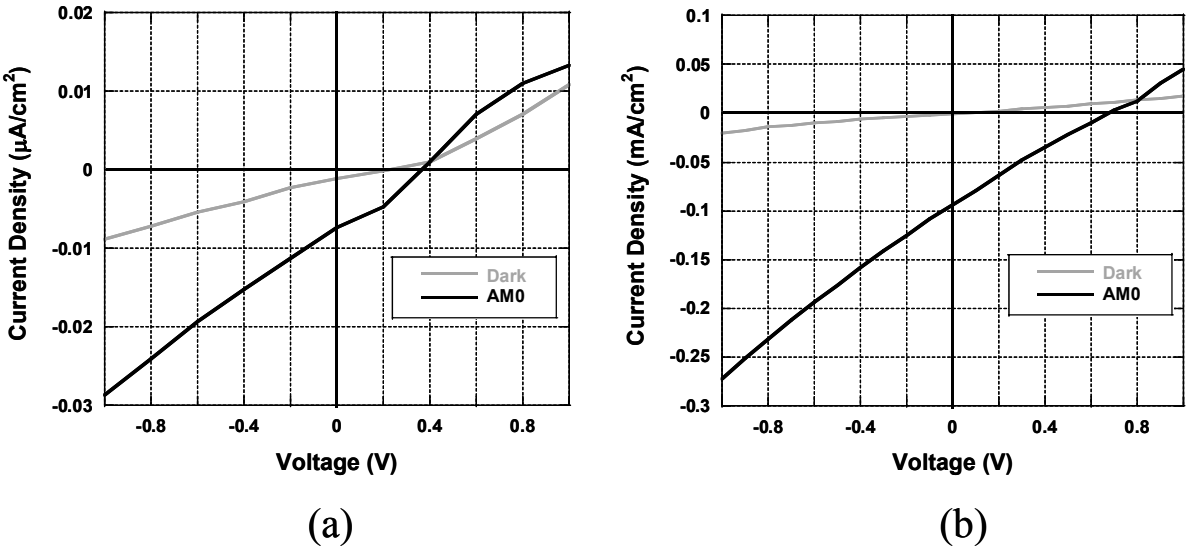

Figure 4. Characteristic I-V plots in the dark (gray) and under simulated AM0 illumination (black), displaying the photoresponse for (a) pristine P3OT and (b) 1% w/w SWNT-P3OT composite solar cells

Further characterization of the composite cells showed a corresponding increase in the I_{sc} as the doping level of SWNTs increased in the P3OT. Figure 5 shows an I-V overlay under the simulated AM0 illumination for the pristine P3OT, 0.1%, and 1.0 % w/w SWNT-P3OT cells in the region of forward bias. Clearly evident is an order of magnitude increase in the I_{sc} from the pristine P3OT to the 0.1% w/w SWNT-P3OT composite cell. An additional increase of ~50% is observed when the doping level reaches 1.0% w/w, with an I_{sc} equal to 0.12 mA/cm^2 for the cell. This result indicates that there is an apparent conductivity effect on the I_{sc} in the composite films which can be controlled by SWNT doping. Optimization of the doping level for maximum current density is a necessary step at improving the overall efficiency of these cells. Similarly, the V_{oc} more than doubled for both SWNT-doped cells,

although the 0.1% w/w composite has a slightly higher value than the 1.0 % w/w composite. Interestingly, the measured V_{oc} of 0.98 V is signficantly higher than the recent report, where they postulated that the energy difference in the HOMO-LUMO levels of the SWNT/polymer junction is responsible for the open-circuit-voltage.[14] An explanation of this current result may reside in the purity and defect density of the SWNTs. This is an important variable to consider since the interaction between SWNTs and the polymer can directly affect the junction by which exciton dissociation occurs. Other variables to evaluate for SWNT-polymer solar cells are the diameter distributions and metallic to semiconducting ratios of the dopant. If the SWNTs are primarily acting as a conductive network, then the presence of metallic types would be the preferential dopant. However, the possibility exists that semiconducting SWNTs are participating in the photoconversion process since a recent report has shown certain photoconductivity effects exist for SWNTs.[25] In either case, selective dispersion of one type could lead to higher SWNT-P3OT solar cell efficiencies. Above all though, the ability to dissociate and extract the generated carriers upon illumination in these conducting polymer solar cells is the foremost concern to augment the overall efficiency.

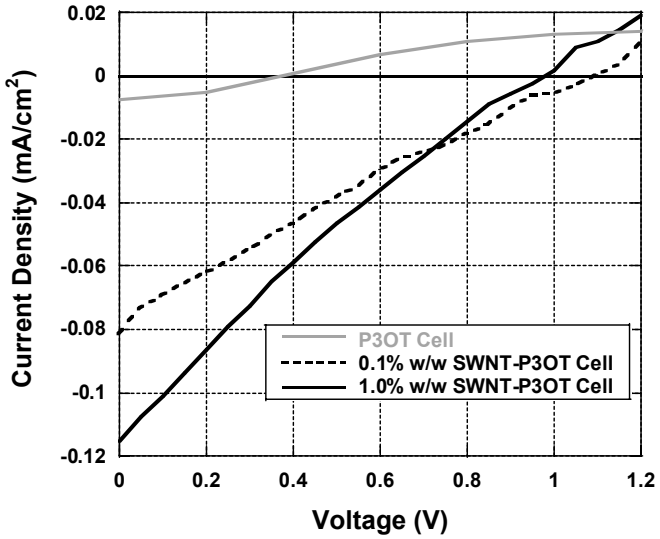

Figure 5. Overlay of the I-V relationship under simulated AM0 illumination for pristine P3OT (gray), 0.1% w/w SWNT-P3OT composite (black dashed), and 1.0% w/w SWNT-P3OT composite (black line) solar cells.

A next-generation approach to maximizing the charge separation and carrier transport in SWNT-doped P3OT cells may be through attachment of nanostructured components to the SWNTs (see Figure 6a). Such versatility enables tuning of the optoelectronic properties of the dopant in the polymer cell to match the energy bands between components and conducting polymer HOMO/LUMO levels. Our approach to improve device efficiency is through covalent attachment of semiconducting quantum dots to SWNTs. It is expected that conjugation of SWNTs and quantum dots prior to dispersion will facilitate charge dissociation and transport in the polymer solar cells. Our initial attempt at establishing the necessary chemistry has been successful with attachment of CdSe quantum dots to functionalized SWNTs through an ethylenediamine (en) linker, similar to the reported procedures.[26,27] Shown in Figure 6b is a tapping-mode atomic force micrograph (AFM) of our resulting CdSe-en-SWNT complexed sample. Incorporation of this material into similar P3OT composite solar cells as described here, is currently under investigation.

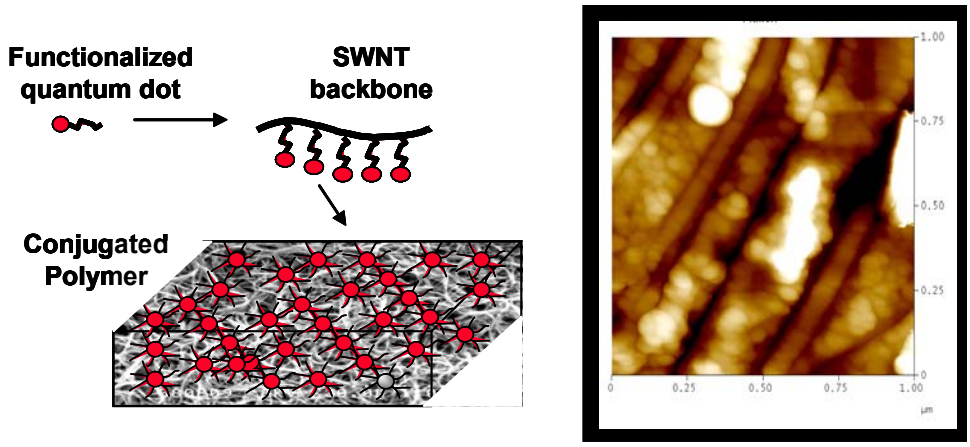

(a) (b)

Figure 6. (a) Schematic representation of the approach to conjugate quantum dots with SWNTs prior to dispersion in the conducting polymer; (b) AFM image of CdSe-en-SWNTs to be used as dopant in future SWNT-P3OT solar cells.

CONCLUSIONS

The ability to construct flexible solar cells containing SWNT doped polymer composites has been demonstrated. Devices containing 1% w/w SWNTs in P3OT have shown a photoresponse with low current densities but relatively high open-circuit voltages (~1 V). Attempts to improve the exciton dissociation and carrier transport in these systems may rely upon controlled processing of SWNTs for appropriate material properties. Ultimately, the ability to covalently attach other nanomaterials to the SWNTs could result in higher polymer solar cell efficiencies.

ACKNOWLEDGEMENTS

This work was supported by NASA Glenn Research Center through grant NAG3-2595 and the National Science Foundation through grant ECS 0233776. The authors wish to thank Stephen Fahey for obtaining the AFM images.

REFERENCES

(1) Yu, G.; Gao, J.; Hummelen, J. C.; Wudl, F.; Heeger, A. J. *Science* **1995**, *270*, 1789-1791.
(2) Granstrom, M.; Petritsch, K.; Arias, A. C.; Lux, A.; Andersson, M. R.; Friend, R. H. *Nature* **1998**, *395*, 257-360.
(3) Camaioni, N.; Ridolfi, G.; Casalbore-Miceli, G.; Possamai, G.; Garlaschelli, L.; Maggini, M. *Solar Energy Materials & Solar Cells* **2002**.
(4) Halls, J. J. M.; Pichler, K.; Friend, R. H.; Moratti, S. C.; Holmes, A. B. *Appl. Phys. Lett.* **1996**, *68*, 3120-3122.
(5) Huynh, W. U.; Dittmer, J. J.; Alivisatos, A. P. *Science* **2002**, *295*, 2425-2427.
(6) Kymakis, E.; Amaratunga, G. A. J. *Appl. Phys. Lett.* **2002**, *80*, 112-114.
(7) Cinke, M.; Li, J.; Chen, B.; Cassell, A.; Delzeit, L.; Han, J.; Meyyappan, M. *Chem. Phys. Lett.* **2002**, *365*, 69.
(8) Biercuk, M. J., Llaguno, M.C., Radosavljevic, M., Hyun, J.K., Johnson, A.T., Fischer, J.E. *Appl. Phys. Lett.* **2002**, *80*, 2767-2769.
(9) Schadler, L. S.; Giannaris, S. C.; Ajayan, P. M. *Appl. Phys. Lett.* **1998**, *73*, 3842.
(10) Li, F., Cheng, H.M.; Bai, S.; Su, G.; Dresselhaus, M.S. *Appl. Phys. Lett.* **2000**, *77*, 3161-3163.
(11) Salvetat, J.; Briggs, G. A. D.; Bonard, J.; Bacsa, R. R.; Kulik, A. J.; Stockli, T.; Burnham, N. A.; Forro, L. *Phys. Rev. Lett.* **1999**, *82*, 944.

(12) Berber, S.; Kwon, Y.; Tomanek, D. *Phys. Rev. Lett.* **2000**, *84*, 4613.
(13) Sugiyama, K.; Ishii, H.; Ouchi, Y.; Seki, K. *J. Appl. Phys.* **2000**, *87*, 295.
(14) Kymakis, E.; Alexandrou, I.; Amaratunga, G. A. J. *J. Appl. Phys.* **2003**, *93*, 1764.
(15) Gennett, T.; Dillon, A. C.; Alleman, J. L.; Jones, K. M.; Parilla, P. A.; Heben, M. J. *Mat. Res. Soc. Symp. Proc.* **2001**, *633*, A2.3.1.
(16) Dillon, A. C.; Gennett, T.; Jones, K. M.; Alleman, J. L.; Parilla, P. A.; Heben, M. J. *Adv. Mater.* **1999**, *11*, 1354.
(17) Landi, B. J.; Raffaelle, R. P.; Heben, M. J.; Alleman, J. L.; VanDerveer, W.; Gennett, T. *Nano Lett.* **2002**, *2*, 1329.
(18) Dillon, A. C.; Parilla, P. A.; Alleman, J. L.; Perkins, J. D.; Heben, M. J. *Chem. Phys. Lett.* **2000**, *316*, 13.
(19) Rao, A. M.; Chen, J.; Richter, E.; Schlecht, U.; Eklund, P. C.; Haddon, R. C.; Venkateswaran, U. D.; Kwon, Y. K.; Tomanek, D. *Phys. Rev. Lett.* **2001**, *86*, 3895.
(20) Alvarez, L.; Righi, A.; Guillard, T.; Rols, S.; Anglaret, E.; Laplaze, D.; Sauvajol, J. L. *Chem. Phys. Lett.* **2000**, *316*, 186.
(21) Dresselhaus, M. S.; Dresselhaus, G.; Jorio, A.; Souza Filho, A. G.; Saito, R. *Carbon* **2002**, *40*, 2043.
(22) Kataura, H.; Kumazawa, Y.; Maniwa, Y.; Umezu, I.; Suzuki, S.; Ohtsuka, Y.; Achiba, Y. *Synth. Met.* **1999**, *103*, 2555.
(23) Minami, N.; Kazaoui, S.; Jacquemin, R.; Yamawaki, H.; Aoki, K.; Kataura, H.; Achiba, Y. *Synth. Met.* **2001**, *116*, 405.
(24) Kazaoui, S.; Minami, N.; Kataura, H.; Achiba, Y. *Synth. Met.* **2001**, *121*, 1201.
(25) Freitag, M.; Martin, Y.; Misewich, J. A.; Martel, R.; Avouris, P. *Nano Lett.* **2003**, *3*, 1067.
(26) Banerjee, S.; Wong, S. S. *Nano Lett.* **2002**, *2*, 195-200.
(27) Haremza, J. M.; Hahn, M. A.; Krauss, T. D.; Chen, S.; Calcines, J. *Nano Lett.* **2002**, *2*, 1253.

High-Temperature Solar Cell Development

Geoffrey A. Landis,
NASA John Glenn Research Center
21000 Brookpark Road, Cleveland, OH 44135

Danielle Merritt and Ryne P. Raffaelle
Rochester Institute of Technology
Rochester, NY

David Scheiman
Ohio Aerospace Institute
Brook Park, OH 44142

Missions for High Temperature Solar Cells

The vast majority of space probes to date have relied upon photovoltaic power generation. If future missions designed to probe environments close to the sun (Figure 1) will be able to use such power generation, solar cells that can function at high temperatures, under high light intensity, and high radiation conditions must be developed. The significant problem is that solar cells lose performance at high temperatures.

Approaches to solar arrays for near-sun missions include:

- High epsilon/low alpha coatings
- Array off-pointing: array points at angle to sun
- Partially-populated array (with missing cells replaced with mirrors)
- Reflective coatings
- Solar cells designed to operate at high temperature

Active cooling techniques, such as use of solid-state refrigerators, in general require more power to operate than the resultant gain in efficiency.

For example, current plans for Mercury missions reflect away most of the incident solar energy to limit the operating temperature and avoid destroying the array (figure 2). While this is one solution to the problem, this does not optimally use the solar energy, and it would be desirable to develop solar cells that can perform well at high temperatures, rather than developing techniques to reduce the temperature at the price of reduced performance.

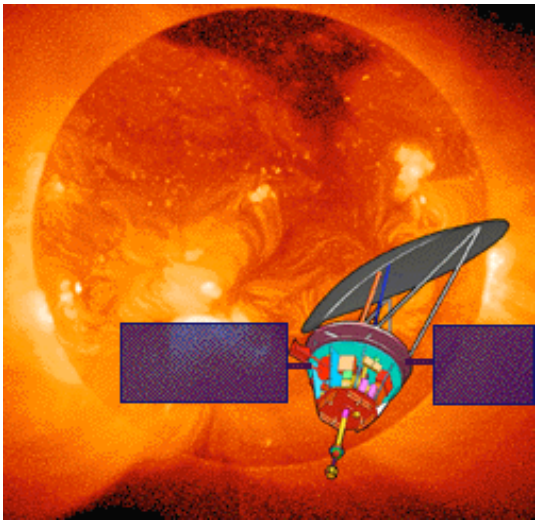

Figure 1: Artist's concept of the Solar Probe mission, proposed to reach a distance of 4 solar radii from the sun.

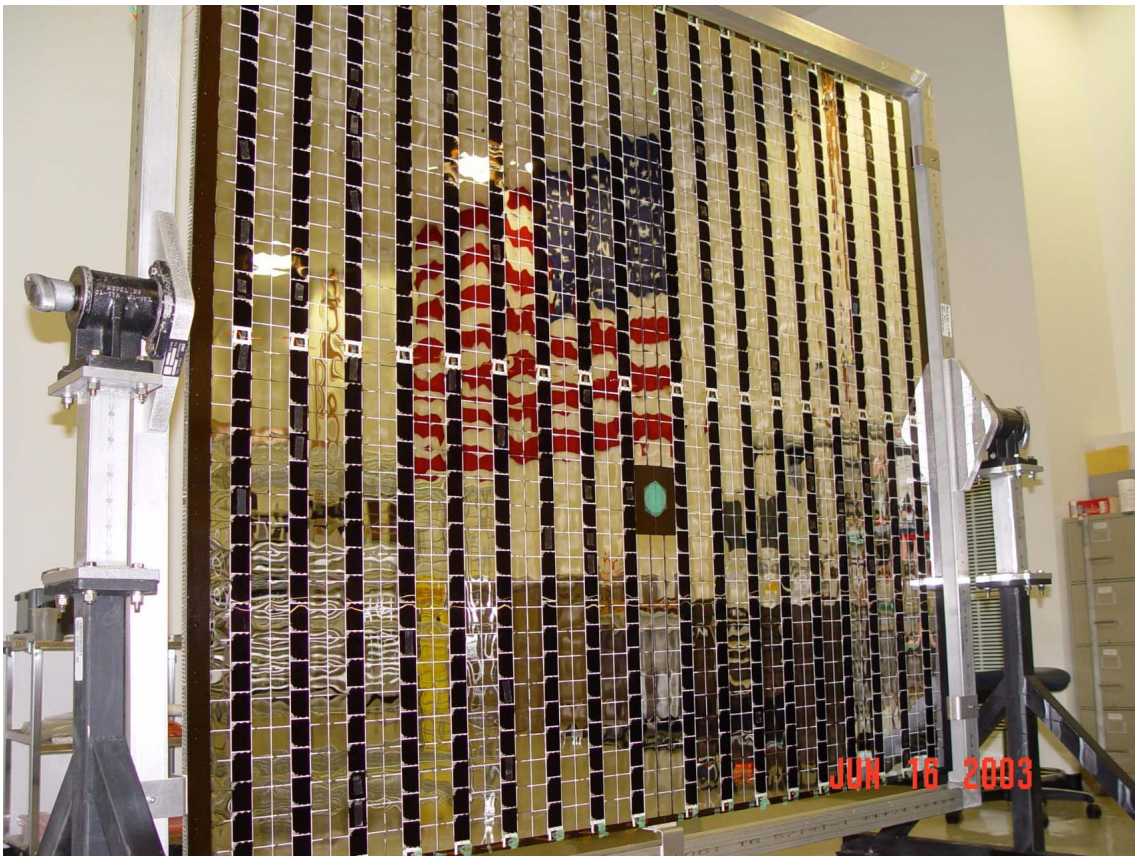

Figure 2: Solar array for the MESSENGER mission to Mercury (Johns Hopkins Applied Physics Laboratories). The majority of the sun-facing surface consists of mirrors to reflect the incident solar radiation and limit temperature.

NASA requirements for solar power systems for high temperature near-sun operation has the goals [1]:

Improved efficiency at high temperature

Improved lifetime at high temperature

Solar cells are desirable for elevated operating temperatures ranging from the Mercury orbiter, in which the solar array equilibrium temperature (assuming a sun-facing array with no reflectors) would be 450 C, to the proposed Solar Probe mission [2], for which, at 4 solar-radii, a sun-facing array with no reflectors would reach an equilibrium temperature of approximately 2300 C. Solar cells made from wide bandgap compound semiconductors are an obvious choice for such an application, since the higher voltage of wide bandgap solar cells results in less degradation [3,4]. For example, silicon solar cells (1.1 eV) lose about 0.45% of their power per degree C increase in operating temperature. GaAs cells (1.4 eV) lose about 0.21% per degree C [5].

The normalized temperature coefficient ($1/\eta\ d\eta/dT$) can be resolved into the sum of the variations of the open circuit voltage, Voc, the short circuit current, Jsc, and the fill factor, FF:

$$1/\eta\ d\eta/dT = 1/Voc\ dVoc/dT + 1/Jsc\ dJsc/dT + 1/FF\ dFF/dT \qquad (2)$$

The Voc variation contributes the majority of the change in efficiency. Fill factor variation in general tracks the open circuit variation. Variation of short circuit current with temperature is primarily due to the change in bandgap energy with temperature. As the cell heats up, the bandgap decreases, and hence the cell responds to longer wavelength portions of the spectrum, and therefore the short circuit current actually increases with temperature. Hence, the Jsc variation term is roughly proportional to the incident spectral intensity at wavelengths near the band edge [5].

Since the Voc variation with temperature is roughly the same for cells of different bandgap, while the actual Voc increases with bandgap, the normalized temperature coefficient, $1/\eta\ d\eta/dT$ increases directly with bandgap. However, since the photon flux from the sun decreases at high photon energies, an optimum bandgap exists for each temperature.

To verify the efficiency of wide bandgap solar cells at high temperatures, we measured a GaInP solar cell (1.6) as a function of temperature from room temperature up to 400 C. As shown in figure 3, open circuit voltage and fill factor decrease with temperature, while the short circuit current shows a slight increase. Power loss [1/P dP/dT] is about 0.177% per degree, with irreversible degradation due to shunting occurring slightly above 350C.

The theoretical performance of solar cells as a function of bandgap and temperature is shown in figure 4. As can be seen, the optimum bandgap shifts from about 1.4 volts at room temperature (27C) to about 2.3 volts at 900C.

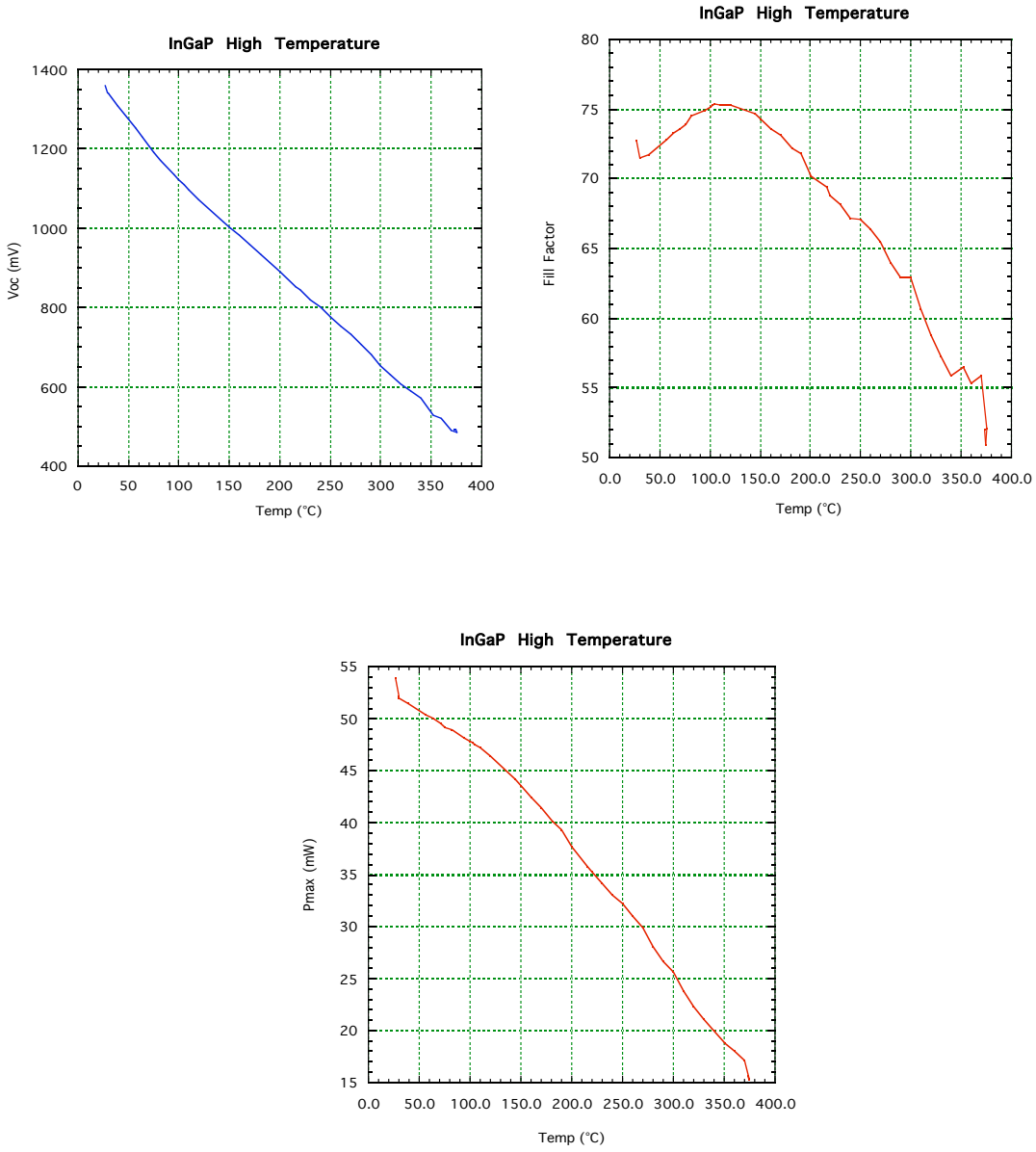

Figure 3: Open circuit current, fill factor, and efficiency of a GaInP solar cell measured as a function of temperature, from 0 to 400 C.

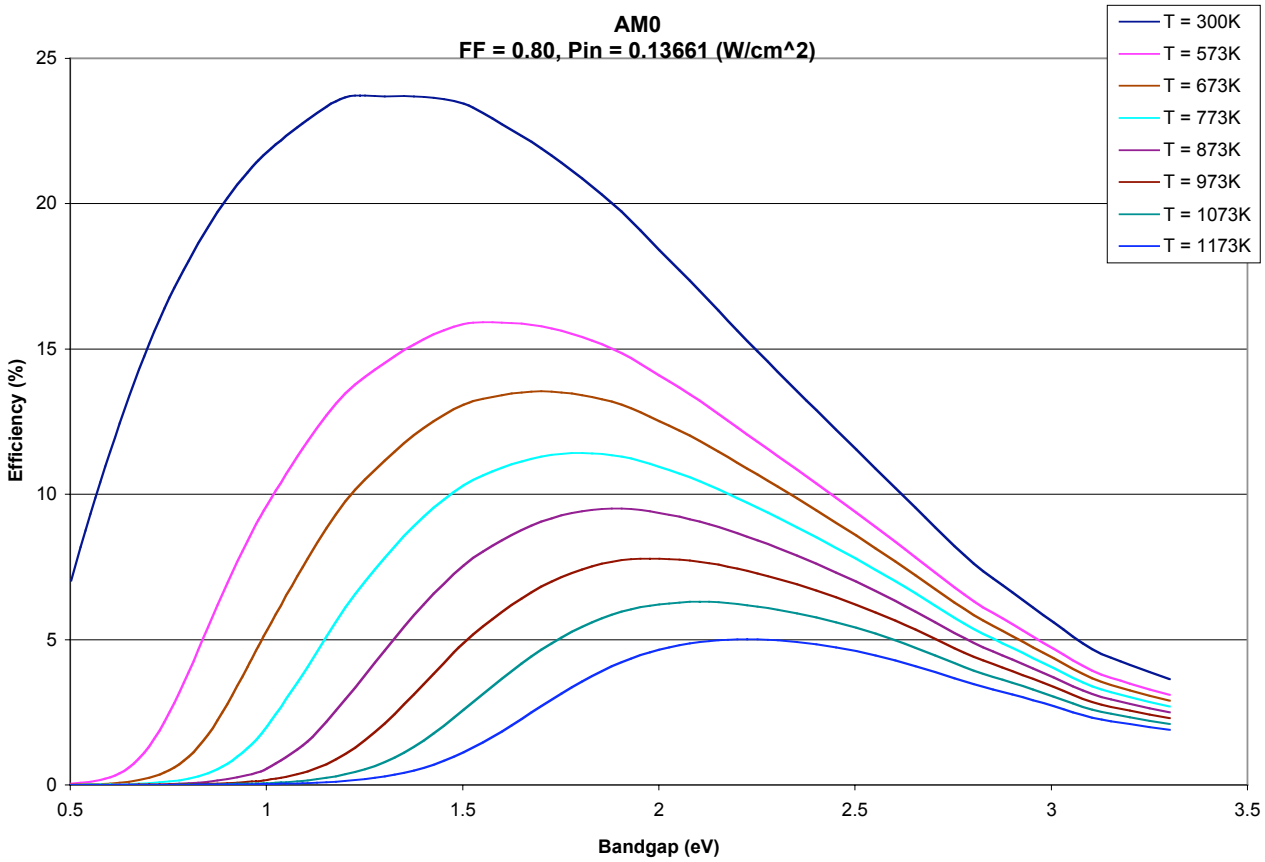

Figure 4: Theoretical efficiency of a solar cell as a function of bandgap, showing the shift of optimum bandgap from about 1.4 volts at room temperature (27C) to about 2.3 volts at 900C.

In order develop solar cells for such applications, we have initiated a program to manufacture and measure the photovoltaic performance of wide bandgap solar cells, including cells from GaInP, GaP [6], GaN, and SiC [7]. Figure 5 shows a SiC solar cell developed at NASA Glenn in collaboration with the Rochester Institute of Technology and Cree Semiconductors [8].

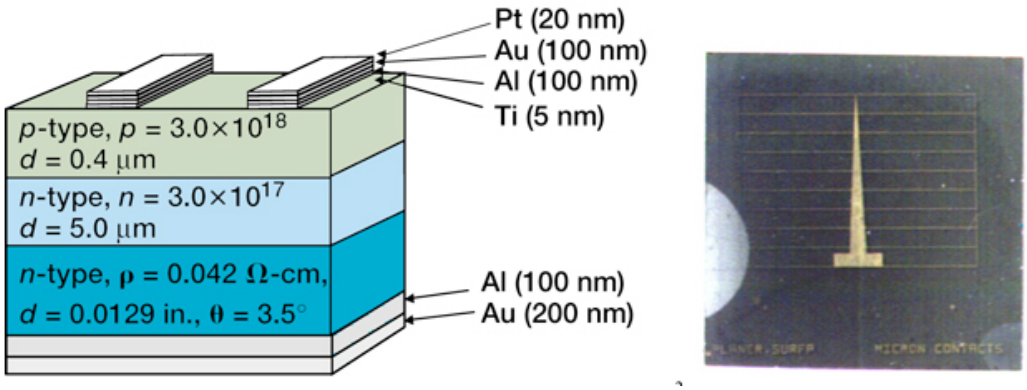

Figure 5: SiC solar cell. Left: schematic cross section. Right: photo of cell.

In addition to the reversible loss of theoretical performance with temperature, solar array operation at high temperature needs to avoid irreversible degradation leading to destruction of the arrays. Effects that produce irreversible performance loss include:

- Ohmic contact degradation [9, 10]
- Dopant diffusion
- Compound semiconductor degradation
- Interconnect-related failure
- Coverglass debonding [11]
- Array structural degradation.

Technologies to deal with these problems have been developed under other programs [9, 10, 11].

Conclusions

High-temperature operation of solar cells is of interest to future NASA missions. Technology solutions such as off-pointing can reduce operating temperature, but also reduce power from the array. New solar cells that can operate at high temperature are desirable; this requires development of high bandgap semiconductors. A program to develop cells for high temperature operation, including GaInP, GaN, SiC and GaP cells, is in progress.

Achieving satisfactory operating lifetime at high temperature is an issue that has not yet been addressed in detail.

References

1. G. Landis and S. Bailey, "Photovoltaic Power for Future NASA Missions," paper AIAA-2002-0718, AIAA 40th Aerospace Sciences Meeting, Reno NV, January 14-17 2002.
2. S. Kerridge, *et al.* "Cost Effective Mission Design for a Small Solar Probe," *Acta Astronautica, Vol. 35, Suppl.,* pp. 257-266 (1995).
3. D. Scheiman, G. Landis, and V. Weizer, "High-Bandgap Solar Cells for Near-Sun Missions," presented at Space Technology & Applications International Forum (STAIF-99), Conf. on Global Virtual Presence, Albuquerque NM, 30 Jan.- 4 Feb. 1999; AIP Conference Proc. 458, 616-620.
4. J. Fan, "Theoretical Temperature Dependence of Solar Cell Parameters," *Solar Cells 17*, pp. 309-315 (1986).
5. G. Landis, "Review of Solar Cell Temperature Coefficients for Space," Proc. XIII Space Photovoltaic Research and Technology Conference, NASA CP-3278, NASA Lewis Research Center, June 1994, 385-400.

6. O. Sulima et al., “High Temperature AlGaP/GaP Solar Cells for NASA Space Missions,” presented at the 3rd World Conference on Photovoltaic Energy Conversion, Osaka Japan, May 11-18 2003.
7. R. Raffaelle, S. Bailey, P. Neudeck, R. Okojie, C. Schanabel, M. Tabib-Azar, D. Scheiman, P. Jenkins, and S. Hubbard, "Optical and Electrical Characterization of SiC Devices, *Proc. 28th IEEE Photovoltaic Specialists Conf.,* pp. 1257-1260 (2000).
8. S. Bailey and R. Rafaelle, "Silicon Carbide Solar Cells Investigated," *Research & Technology 2001,* NASA Technical Memorandum (2002),
9. S. P. Tobin *et al.* “Advanced Metallization for Highly Efficient Solar Cells,” *Proc. 19th IEEE Photovoltaic Specialists Conf.*, pp. 70-75 (1987).
10. M. B Spitzer., *et al.* "Gallium Arsenide Concentrator Solar Cells with Highly Stable Metallization,” *Proc. 20th IEEE Photovoltaic Specialists Conference*, pp. 930-933 (1988).
11. P. Younger, G. Landis and R.G. Tobin, "Integral Glass Covering of Spacecraft Solar Cells by Electrostatic Bonding," *Proceedings of the 14th IEEE Photovoltaic Specialists Conference,* San Diego, CA; 1240-1245 (1980).

Integrated Phase Array Antenna/Solar Cell System For Flexible Access Communications (IA/SAC)

E.B. Clark, R.Q. Lee, A.T. Pal, D.M. Wilt, and B.D. McElroy
NASA Glenn Research Center
Cleveland, OH 44135

C.H. Mueller
Analex Corporation
Cleveland, OH 44135

Abstract

This paper describes recent efforts to integrate advanced solar cells with printed planar antennas. Several previous attempts have been reported in the literature, but this effort is unique in several ways. It uses Gallium Arsenide (GaAs) multi-junction solar cell technology. The solar cells and antennas will be integrated onto a common GaAs substrate. When fully implemented, IA/SAC will be capable of dynamic beam steering. In addition, this program targets the X-band (8 – 12 GHz) and higher frequencies, as compared to the 2.2 – 2.9 GHz arrays targeted by other organizations. These higher operating frequencies enable a greater bandwidth and thus higher data transfer rates. The first phase of the effort involves the development of 2 x 2 cm GaAs Monolithically Integrated Modules (MIM) with integrated patch antennas on the opposite side of the substrate. Subsequent work will involve the design and development of devices having the GaAs MIMs and the antennas on the same side of the substrate. Results from the phase one efforts will be presented.

Introduction

Recently, several attempts to integrate printed planar antennas onto solar cells have been reported in the literature. The first work reported in 1995 involved attaching solar cells to the surface of a single micro-strip antenna for a micro-satellite application [1]. Measured data from this study showed very good antenna performance with the solar cells having very little impact on the radiation pattern and return loss at S-band. In 1999, JPL attempted to combine antenna and solar cells for a Mars rover application at 400 MHz [2]. These early works attempted to demonstrate feasibility using commercial solar cells and a single antenna. Integrating multiple antenna elements and solar cells on the same surface, was first reported by a group in Europe [3-4]. Two small antenna arrays integrated with solar cells were demonstrated. The first was an 8-

element (4x2) array with 9 solar cells strips connected in series and superimposed on the antenna elements. The second was a 4x4 array of circularly polarized slot dipoles co-located on the same surface of the solar cells array. Amorphous silicon solar cells with about 5-12% efficiency were used in both demonstrations.

Compared to prior work, the GRC proposed integrated phased array/solar array cell (IA/SAC) concept is technologically more advanced, and is unique in several ways. As stated previously, the earlier work used silicon cells with a maximum efficiency of about 15%. This effort uses GaAs based monolithically integrated module (MIM) technology, which has a greater efficiency and can be easily tailored to produce a desired voltage. In addition, IA/SAC modules will be integrated on a common substrate as opposed to the previous efforts that developed the components on separate surfaces then combined them post processing. Finally, when fully implemented, IA/SAC arrays will be capable of dynamic beam steering in the X-band (8-12 GHz) or higher frequencies. To the best of our knowledge, in all prior developmental efforts, the antennas are passive arrays capable of only fixed point-to-point communications operating in the 2.2 – 2.9 GHz range.

Experimental Procedure

In the first phase of the project, we designed and developed single junction 2x2cm GaAs MIM devices. MIM devices are grown on semi-insulating substrates and have both the positive and negative contacts on the top-side of the device (figure 1). Elimination of the contacts on the back surface allows the semi-insulating substrate to act as the dielectric layer between the ground plane and radiating elements of the antenna.

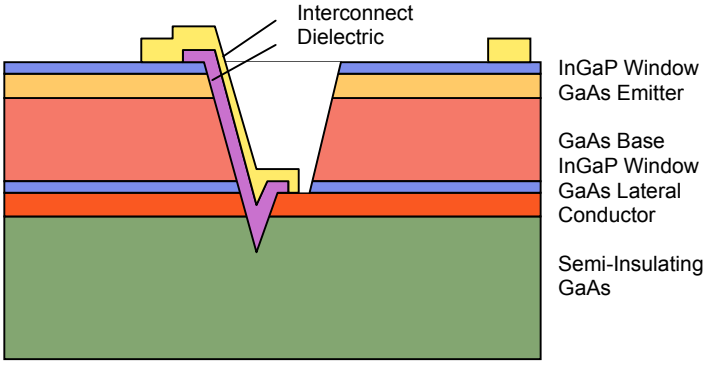

Figure 1. Diagram of a GaAs MIM device showing the device layers and interconnect.

The use of MIM technology was a crucial step towards the ability to integrate the solar cell and antenna on a common substrate. The Photovoltaic and Space Environments (PVSE) Branch of NASA Glenn originally developed the MIM concept for thermophotovoltaic (TPV) energy conversion. This device has been the focus of a multi-million dollar, multi-year development by Bechtel Bettis, Inc [5, 6, 7]. One of the main goals in the first phase of this effort was to increase the size of the GaAs MIMs to 2cm x 2cm. This is significantly larger than previous devices and it is anticipated that these MIM devices will have a conversion efficiency comparable to GRC produced GaAs solar cells (~20% efficiency). The initial devices will have a structure similar to figure 2 but will be optimized for the IA/SAC project.

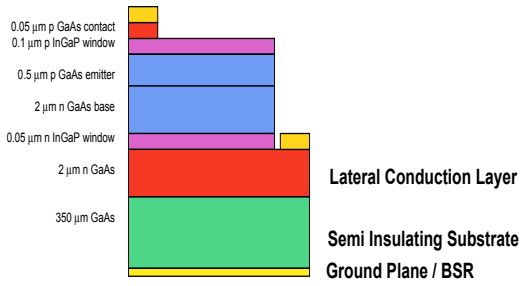

Figure 2. GaAs single junction IA/SAC MIM device structure.

The GaAs MIMs were grown on 2 inch, double side polished GaAs wafers by Organometalic Vapor Phase Epitaxy (OMVPE) at 620^0c and 190 torr. The specular films were then processed into 1cm x 1cm MIMs. After AM0 current-voltage (IV) measurements were taken, patch antennas were deposited on the opposite side of the wafer by E-beam evaporation. After deposition of the antenna, AMO IV measurements were repeated to determine whether there was any degradation to the solar cells.

Results and Analysis

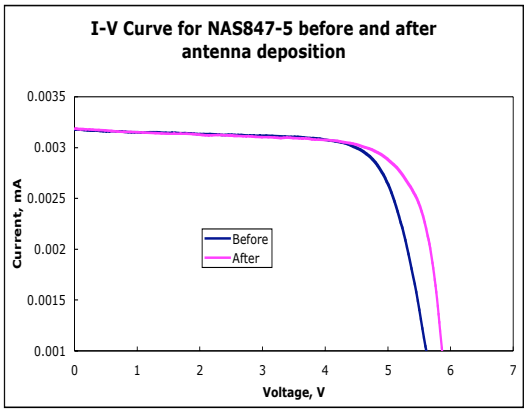

Figure 3. Pre- and Post antenna deposition AM0 IV measurements.

The IV measurements in figure 3 show that there was no degradation in the performance of the solar cells due to the deposition of the antenna. In fact, an increase in the cells performance is noted. This is most likely due to additional contact annealing that occurs during the deposition of the antenna. At the time of this writing, the results of the testing performed in the Microwave Antenna Range at NASA GRC were unavailable.

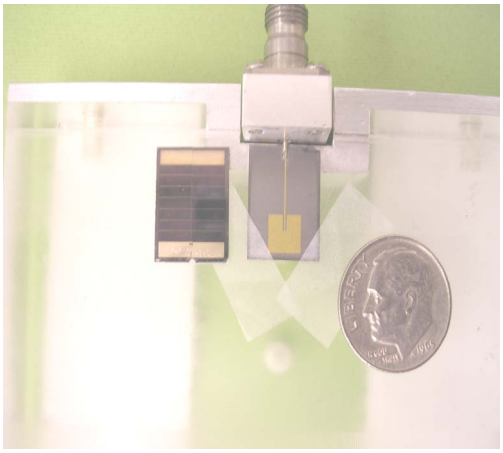

Figure 4. IA/SAC module being mounted for testing in antenna range.

Conclusion

We have demonstrated the feasibility of combining advanced solar cells with RF antenna technology on a common substrate with no degradation to the solar cells. Future phase one work will focus on characterizing the antenna and increasing the size of the MIM to 2cm x 2cm.

References

1. M. Tanaka, Y. Suzuki, K. Araki and R. Suzuki, "Microstrip antennas with solar cells for microsatellites," Electronics Letters, Vol. 31, 1996, pp. 263-266.

2. J. Huang, "Mars rover antenna for solar-array integration,' JPL TMO Progress Report 42-136, Feb. 15, 1999.

3. S. Vaccaro, P. Torres, J.R. Mosig, A. Shah, J.F. Zurcher, A.K. Skrivervik, F. Gardiol, P. de Maagt and L. Gerlach, "Integrated solar panel antennas'" Electronics Letters, vol. 36, No. 5, 2000.

4. S. Vaccaro, P. Torres, J.R. Mosig, A. Shah, A.K. Skrivervil, J.F. Zurcher, P. de Maagt, and L. Gerlach, "Combination of antennas and solar cells for satellite communications," Microwave and Optical Technology Letters, Vol. 29, No. 1, April 2001, pp. 11-16.

5. D.M. Wilt, et al., "Monolithic Interconnected Modules (MIMs) for Thermophotovoltaic Energy Conversion," Journal of Semiconductor Science and Technology, accepted for publication in 2003.

6. D.M. Wilt, D. L. Chubb, "Thermophotovoltaic Energy Conversion Technology Development at NASA Glenn Research Center," Proc. 16th European PV Conf, Glasgow, Scotland, May 2000.

7. D.M. Wilt, et al., "0.55eV n/p/n MIM TPV Cell Development," Proc. 28th PVSC, Anchorage, Alaska, 2000.

ELECTROSTATIC CHARGING OF MIRRORS IN SPACE: A PLAUSIBLE CAUSE OF SOLAR PANEL ANOMALIES ON SATELLITES

Shu T. Lai
Space Vehicles Directorate
Air Force Research Laboratory
Hanscom AFB., MA 01731

ABSTRACT

The entire fleet of Boeing Model 702 geosynchronous satellites has suffered from a similar fate: degradation of the solar cell panels. Mirrors flank both sides of the solar cell panels. Degradation, sometimes sudden and stepwise, shortens the lifetime of the solar cells. We suggest that space environment effects play an important role in damaging the solar cells. As a cornerstone in this idea, we expound a theorem that high reflectivity reduces photoemission. With little or no photoemission, mirrors often charge to minus kilovolts in eclipse as well as in sunlight, whenever the space plasma is hot enough. Since the rest of the solar panel does not have this mirror property, differential charging between the mirrors and the rest of the solar panel occurs during eclipse exits. We show the charging data obtained during an eclipse exit on LANL-97A satellite for supporting the idea of differential charging. Finally, we recommend this important mirror charging property to be taken in account in future solar panel designs and in commercial products of spacecraft charging computer codes.

INTRODUCTION

This work is motivated by the news [1] that all Boeing "Model 702" geosynchronous satellites have suffered from fast degradation of their solar cells. In particular, PanAm's PAS-7, with solar panels of the same design, suffered from a 25% degradation of its solar cell efficiency, when the satellite came out of its eclipse, Sept 6, 2001 [2]. These satellites feature long solar panels flanked by reflectors (mirrors) on both sides [Figure 1]. The purpose of using the mirrors is to enhance the efficiency of sunlight collection on the solar cells. Boeing has now decided to withdraw the mirrors from all future 702 satellites. Motivated by this news, we wish to offer a plausible cause. The cause is built on a cornerstone, which we call mirror charging. We will build this cornerstone in this paper. While the engineering details of the 702 satellites are unknown, we do not attempt to justify our theory with the actual cases. The true cause may never be known.

Figure 1. Boeing model 702 satellite with solar panels flanked by mirrors [3]

PHOTOEMISSION FROM MIRRORS

Photoelectrons from surfaces are generated by photons impacting the surface. According to Einstein, a photon can generate a photoelectron of energy *E*, only if the photon energy $h\nu$ exceeds the work function *W*.

$$h\nu = E + W \tag{1}$$

With a high reflectance surface, the reflected photons are almost as intense as the incoming ones, implying little energy is lost in the reflection. As a result, little energy is imparted to the surface material for generating photoelectrons. The most important spectral line in sunlight is the Lyman α, which has $h\nu$ =10.2 eV [4]. The work function of typical spacecraft surfaces is about *W* = 5 eV [5]. If, for example, only 48% of the sunlight photon energy $h\nu$ is available, there would not be enough energy to generate photoelectrons. The photoelectron yield *Y* per unit incident photon is related to the photoelectron yield γ per unit absorbed photon by the relation [6,7]:

$$Y = \gamma(1-R) \tag{2}$$

where *R* is the reflectance. The depth of reflectance is shallower than the depths of ionization, photoemission and attenuation [8].

Modern mirrors in space are made of aluminum. The reflectance R of highly polished aluminum surfaces is about 90% in the Lyman α wavelength region [4]. With a commercial space mirror coating [9], the reflectance R is in the upper 80%. In view of such high reflectance R, we conjecture that only little photoemission is generated from high reflectance surfaces in space.

MIRROR CHARGING

Surfaces often charge to high voltages (up to hundreds or thousands of negative Volts) in hot plasmas at geosynchronous altitudes in eclipse. Charging occurs if the space plasma electron temperature exceeds a critical temperature [10]. The exact potential is controlled by a current balance equation [11]:

$$I_e(\phi)\left[1 - I_s(\phi) - I_b(\phi)\right] - I_i(\phi) = I_{ph}(\phi) \tag{3}$$

where I_e is the incoming electron current, I_s is the secondary electron current, I_b the backscattered electron current, I_{ph} the outgoing photoelectron current, and ϕ the surface potential.

The photoemission current I_{ph} from most surfaces usually exceeds the incoming plasma electron current I_e. Therefore, no charging to negative potentials is expected in sunlight for most surfaces. Charging of conducting surfaces in sunlight is usually to a few positive Volts only because photoelectrons have only a few eV in energy *E* [12].

However, there is only little photoemission from mirrors. A mirror behaves in sunlight as if it is almost in eclipse, as far as charging is concerned. Therefore, we conjecture that, mirrors charge to negative potentials no matter if they are in sunlight or in eclipse.

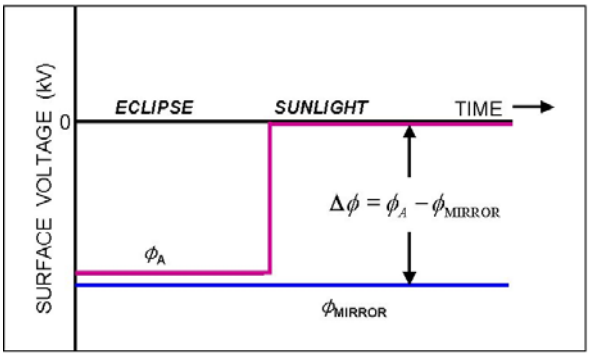

Figure 2. Development of differential charging.

As an example, suppose we consider two surfaces side by side on a geosynchronous spacecraft. Suppose they have about the same surface properties except one (A) is a mirror while the other (B) is not. During eclipse passage, there is no photoemission and therefore both behave similarly, viz., charging to negative kilovolts. Upon eclipse exit, sunlight shines, surface A continues to charge to high negative volts because A emits little or no photoemission, and surface B charges to a few positive Volts as a result of photoemission. The situation becomes one of differential charging [Figure 2].

Furthermore, it is well known that hot electrons of the space plasma at the geosynchronous midnight region convect eastwards to the morning sector as a result of cross-geomagnetic tail electric field and curvature drift by the Earth's magnetic field. A geosynchronous satellite orbits the Earth in the same direction of the Earth's rotation, viz., eastwards. Therefore, upon eclipse exit, the satellite may encounter hot electrons. Spacecraft charging occurs if the plasma electrons are hotter than a critical temperature, typically 1 to 3 keV depending on the surface material [10]. Indeed, statistics show that spacecraft charging to high negative voltages is more likely in the morning sector.

SPACE HAZARD

Differential charging may cause adverse effects. Sudden development of differential charging is potentially hazardous. Suppose two neighboring surfaces (a mirror and a non-mirror) develop a potential difference of about a kilovolt. There can be two adverse effects; (1) a discharge between them may suddenly occur, and (2) sputtering may cause slow degradation of the mirror, reducing its efficiency. A discharge can cause a sudden and stepwise degradation to the solar panel system. Sputtering may pose a long term effect, viz., slow degradation of the system, resulting in shortening the expected lifetime of the solar panel system.

The PAS-7 satellite did not have instruments onboard to measure charging or the hot electrons. The nearest satellite that had this capability was the Los Alamos National Laboratory satellite LANL-97A. Indeed, LANL-07A showed charging to $\phi = -3$ kV during the entire eclipse passage in early morning of Sep 6, 2001 [Figure 3]. The charging level ϕ dropped to $\phi = 0$ abruptly upon eclipse exit. Although PAS-7 had no such measurement capabilities, we infer that PAS-7 might behave likewise, viz,., charging to about $\phi = -3$ kV during the eclipse passage. Upon the PAS-7 eclipse exit, ϕ might drop to 0 abruptly. However, the PAS-7 mirrors probably continued to behave almost as if in eclipse, because they emitted little or no photoelectron current no matter if in eclipse or in sunlight. As a result, differential charging of the order of kV might emerged abruptly upon eclipse exit in the morning sector.

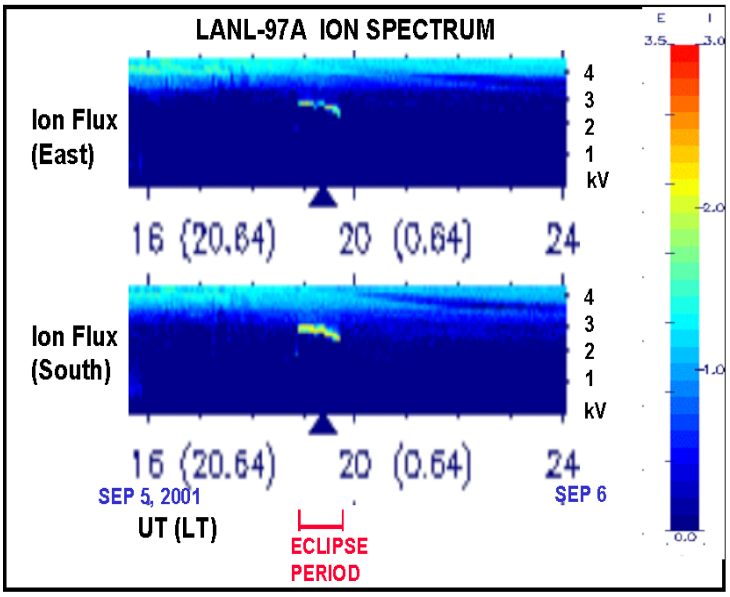

Figure 3. Eclipse charging of LANL 97-A satellite to –3 kV.

CONCLUSION

All Boeing model 702 satellite solar panels flanked by mirrors have experienced gradual or sudden degradations. The true cause is unknown and Boeing has ceased to use this design. We have offered a new concept – mirror charging. We conjecture that mirrors do not generate much photoemission. Accordingly, they charge to high negative voltages no matter if in eclipse or in sunlight. When a mirror and a neighboring non-mirror surface come out from eclipse, differential charging up to kV may occur, depending on the temperature of the space plasma. The effects of differential charging are potential hazards of discharges between surfaces and gradual degradation of the solar panel system due to sputtering by keV ions.

We suggest that the concept of mirror charging be studied in the laboratory and in space. In laboratory studies, care must be taken to separate the photoemissions from mirror samples and from the vacuum chamber walls. In space studies, measurements on differential charging should be made. Finally, we suggest that mirror charging be incorporated into commercial codes of spacecraft charging.

ACKNOWLEDGMENT

The Los Alamos Magnetospheric Plasma Analyzer (MPA) measurements were obtained from the CDAWeb data service at NASA Goddard Space Flight Center. We thank Michelle Thomsen for permission to use the MPA data.

REFERENCES

[1] *Space News*, p.20, Oct 1, 2001.
[2] http://sat-nd.com/failures/timeline.html
[3] http://www.hughespace.com/factsheets/702/
[4] Hinteregger, H.E., K.R. Damson and L.A. Hall, Analysis of photoelectrons from solar extreme ultraviolet, *J. Geophys. Res.*, Vol.64, 961-964, 1959.
[5] CDC Handbook of Physics and Chemistry, CDC Press, 2002.
[6] Highes, A.L. and L.A. Dubridge, *Photoelectric Phenomena*, McGraw-Hill, New York, 1932.
[7] Samson, J.A.R., *Techniques of Ultraviolet Spectroscopy*, John Wiley, New York, 1967.
[8] Spicer, W.E., Photoelectric emission, in *Optical Properties of Solids*, F. Abelés (ed.), pp.755-858, North-Holland Publishing Co., Amsterdam and London, 1972.
[9] http://www.oriel.com/down/pdf/12010.pdf.
[10] Lai, S.T. and D. Della-Rose, Spacecraft charging at geosynchronous altitudes: New evidence of the existence of critical temperature, *J. Spacecraft & Rockets*, vol.38, No.6, 922-928, 2001.
[11] Hastings, D. and H. B. Garrett, Spacecraft Environment Interactions, Cambridge University Press, Cambridge, UK, 1996.
[12] Lai, S.T., H.A. Cohen, T.L. Aggson, and W.J. McNeil, Boom potential on a rotating satellite in sunlight, *J. Geophys. Res.*, vol.91, No.A11, pp.12137-12141, 1986.

EXPERIMENTAL STUDY OF ARCING ON HIGH-VOLTAGE SOLAR ARRAYS

Boris Vayner,
Ohio Aerospace Institute, Brook Park, Ohio 44142

Joel Galofaro, and Dale Ferguson
NASA Glenn Research Center, Cleveland, Ohio 44135

1. Introduction

The main obstacle to the implementation of a high-voltage solar array in space is arcing on the conductor-dielectric junctions exposed to the surrounding plasma. One obvious solution to this problem would be the installation of fully encapsulated solar arrays which were not having exposed conductors at all. However, there are many technological difficulties that must be overcome before the employment of fully encapsulated arrays will turn into reality. An alternative solution to raise arc threshold by modifications of conventionally designed solar arrays looks more appealing, at least in the nearest future. A comprehensive study of arc inception mechanism [1-4] suggests that such modifications can be done in the following directions: i) to insulate conductor-dielectric junction from a plasma environment (wrapthrough interconnects); ii) to change a coverglass geometry (overhang); iii) to increase a coverglass thickness; iiii) to outgas areas of conductor-dielectric junctions. The operation of high-voltage array in LEO produces also the parasitic current power drain on the electrical system. Moreover, the current collected from space plasma by solar arrays determines the spacecraft floating potential that is very important for the design of spacecraft and its scientific apparatus. In order to verify the validity of suggested modifications and to measure current collection five different solar array samples have been tested in large vacuum chamber. Each sample (36 silicon based cells) consists of three strings containing 12 cells connected in series. Thus, arc rate and current collection can be measured on every string independently, or on a whole sample when strings are connected in parallel. The heater installed in the chamber provides the possibility to test samples under temperature as high as 80 C that simulates the LEO operational temperature. The experimental setup is described below.

2.Experimental setup

Low Earth Orbit (LEO) plasma environment was simulated in two different vacuum vessels: 1) horizontal vacuum chamber (1.8 m diameter and 2.5 m long) equipped with cryogenic pump; 2) large vacuum tank (1.8 m diameter and 3 m height) with four diffusion pumps. The vacuum equipment provided pressure as low as 0.5 μTorr. The essential difference between these two tanks is that the residual water vapor partial pressure in horizontal chamber is five times lower than in vertical tank. Each vessel has one Kaufman plasma source that generates xenon (or argon) plasma with electron density $n_e=(0.1\text{-}10)\cdot10^5$ cm^{-3} , temperature T_e=0.6-1.2 eV, and neutral gas pressure $p=(0.7\text{-}7)\cdot10^{-5}$ Torr which can be kept steady during the experiment. To measure plasma parameters, Langmuir probes with diameter 2 cm were employed (two in each tank). To determine an ion distribution function and to improve measurements of electron temperature one retarding potential analyzer (RPA) was mounted on the bottom of vertical tank. It was found that the ion (xenon) thermal flux in the experiment is about three times lower than ram ion flux in LEO, and the electron temperature is 5-10 times higher than in ionosphere. However, the number densities are simulated with a quite high accuracy, and one can believe that the results of high-voltage experiments in vacuum chambers are fairly adequate to the outcomes of processes in LEO plasma.

To control plasma chemical composition (particularly, water vapor and oil partial pressures) a quadruple mass spectrometer was installed in each tank.

The sample (or set of samples) is vertically mounted in the middle of the chamber, and it is biased to a voltage power supply through a capacitor and a 10 kΩ resistor network back to ground. An additional power supply (Solar Array Simulator-SAS) is used to generate electrical field perpendicular to the dielectric side surface for investigating arc inception on semiconductor-dielectric junction and inception of sustained discharges between adjacent strings. Diagnostic equipment includes two current probes to measure discharge current and SAS current, and one voltage probe that allows us to register voltage pulse on the sample during the discharge (Fig.1). To measure optical spectra of arc plasma an intensified CCD (1024x512 pixel) camera with optical spectrometer is installed (Fig.2). The arc sites are determined by employing a video camera and VCR. Most experiments were performed at room temperature (15C), but some tests had been done at the temperature +80 C simulating the exposure of solar array to full sun in LEO.

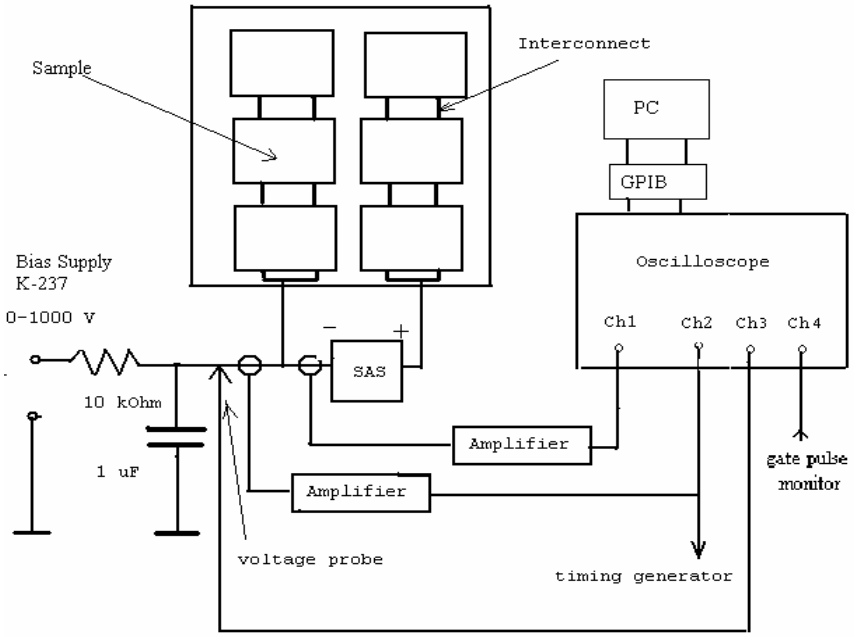

Fig.1. Circuitry diagram for arc inception study.

3. Arc spectra

Previous experimental data and theoretical analysis have demonstrated that water molecules absorbed on the side surface of dielectric (coverglass+adhesive) can play a decisive role in the process of arc inception [5-7]. It is known that spectra of vacuum arcs consist of cathode metal lines only [8] but adding air in vacuum chamber (10^{-4} Torr) results in appearance of hydrogen and hydroxyl lines [9]. Partial pressure of water vapor and nitrogen is always below 10^{-5} Torr for the current experiment. Thus, the presence of hydrogen and hydroxyl in the arc plasma would be a good indicator of water ions dissociative recombination. The presence of other species in arc plasma may reveal other important processes in the discharge development. To elucidate all these problems the measurements of optical spectra have been performed for silicon solar array sample (Fig.3). All dielectric-conductor junctions besides one interconnect area were insulated by

tape to exclude spectra from arcs between cells. The spectral resolution was determined as 0.12 nm/pixel by using standard calibration lamps. To increase the arc luminosity an additional

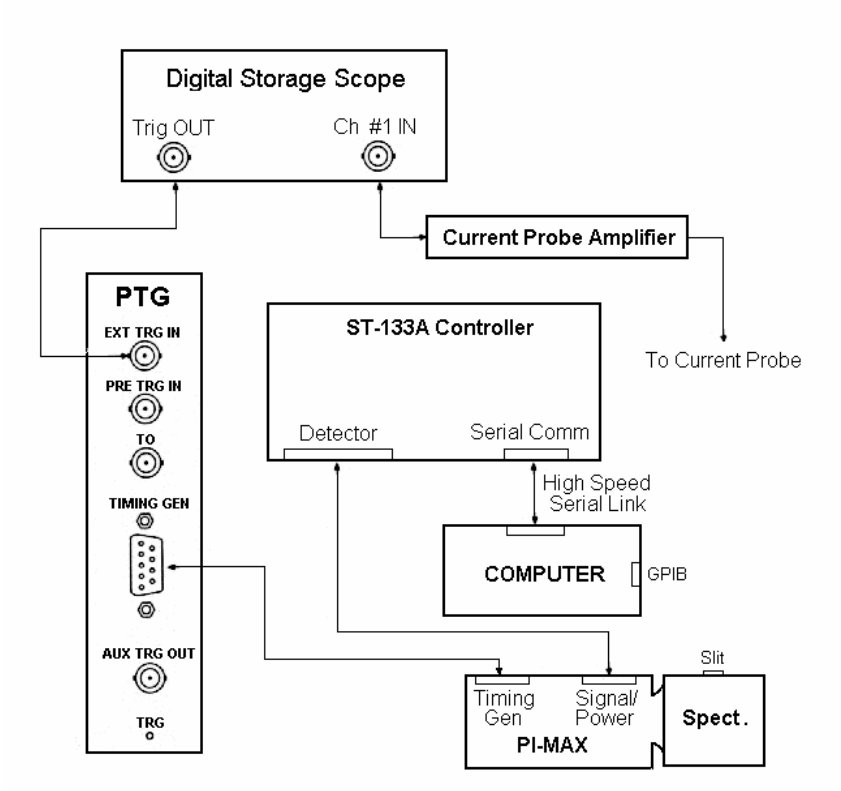

Fig.2. Setup of optical spectra measurements.

capacitor (usually 1 μF) was installed between negatively biased electrode and ground. Gate pulse generator (Fig.2) provided varying both gate pulse width and time delay; thus, it was possible to measure the intensities of spectral lines on different stages of a discharge development. One example of the time sequence of discharge current pulse and gate pulse is shown in Fig.4. In addition to hydrogen (*H*), hydroxyl (*OH*), and metal lines (*Ag*) arcing on the sample revealed also some molecular radicals identified according to Ref. 10 (Fig.5).

The results of spectral measurements, observation of decreasing arc rate with number of arcs (conditioning), and theoretical estimates [11] are very strong argument in favor of the idea that in order to raise arc threshold solar array surfaces must be thoroughly outgassed. The validity of this hypothesis has been confirmed by ground tests described in Sec. 5 below.

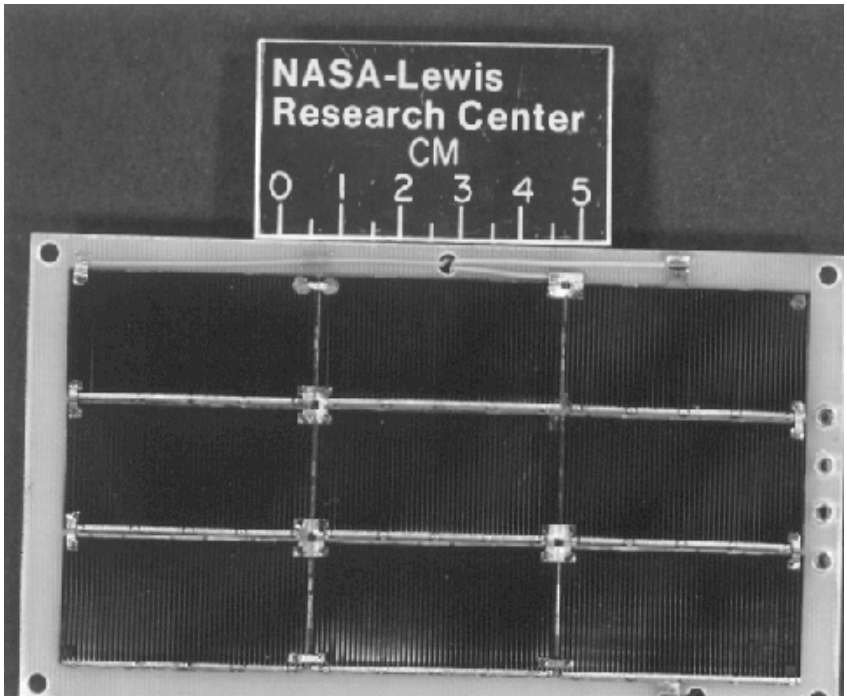

Fig.3. Silicon solar array sample used for measurements of arc spectra.

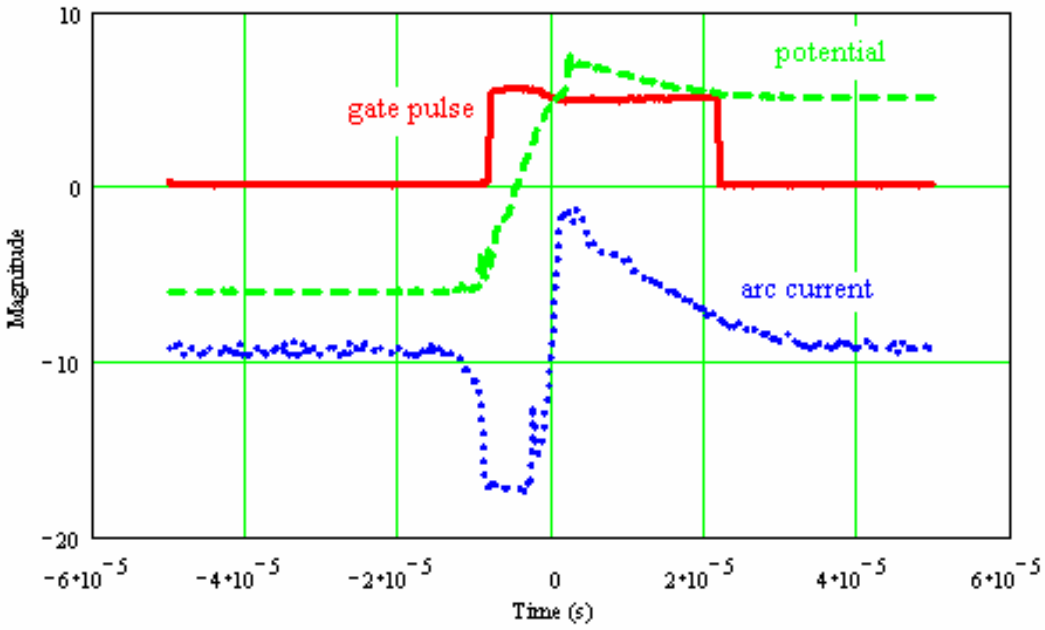

Fig.4. One example of pulses time sequence applied for spectral measurements.

Arc spectrum (Ag lines)

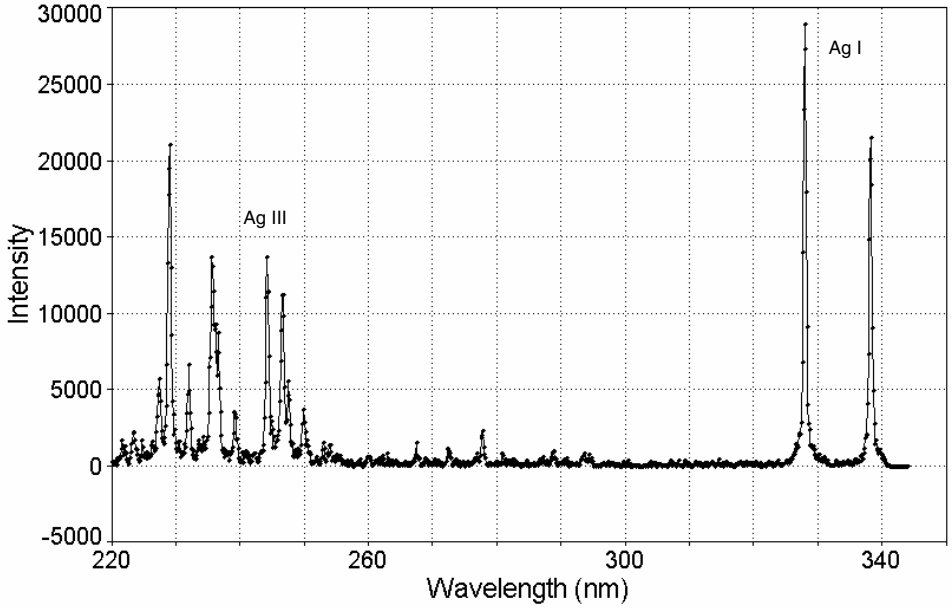

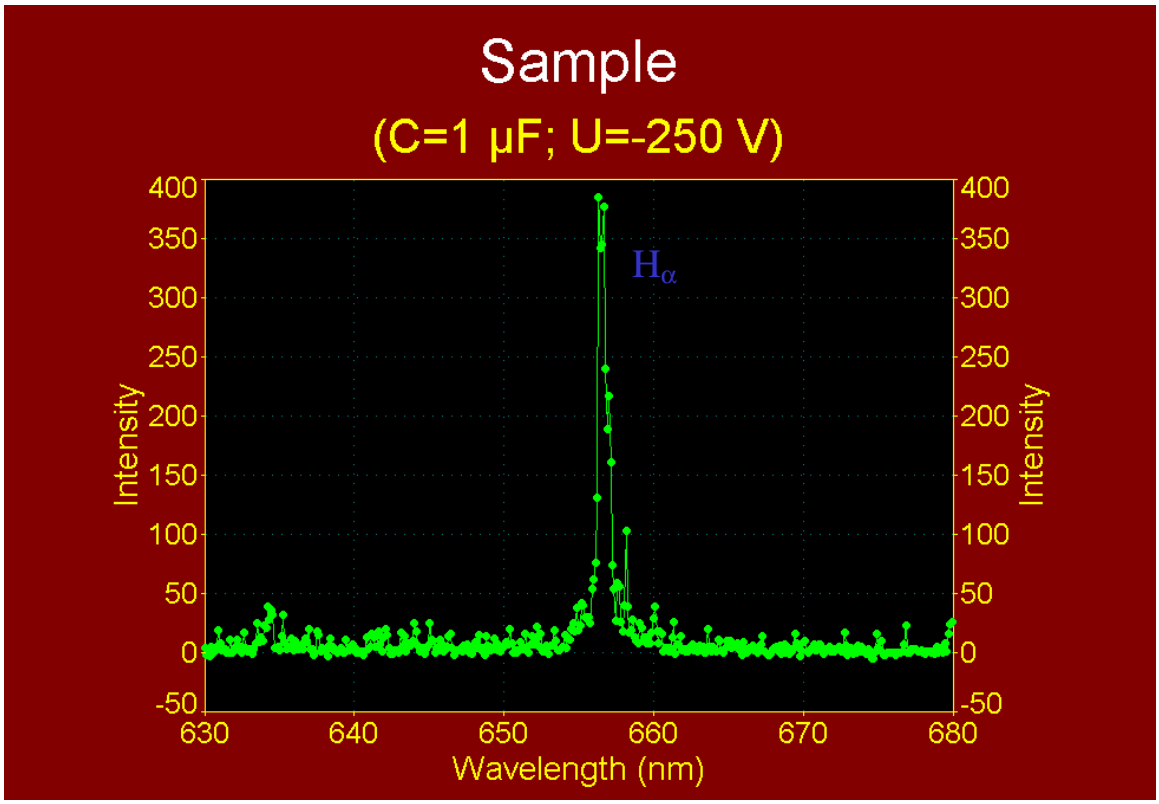

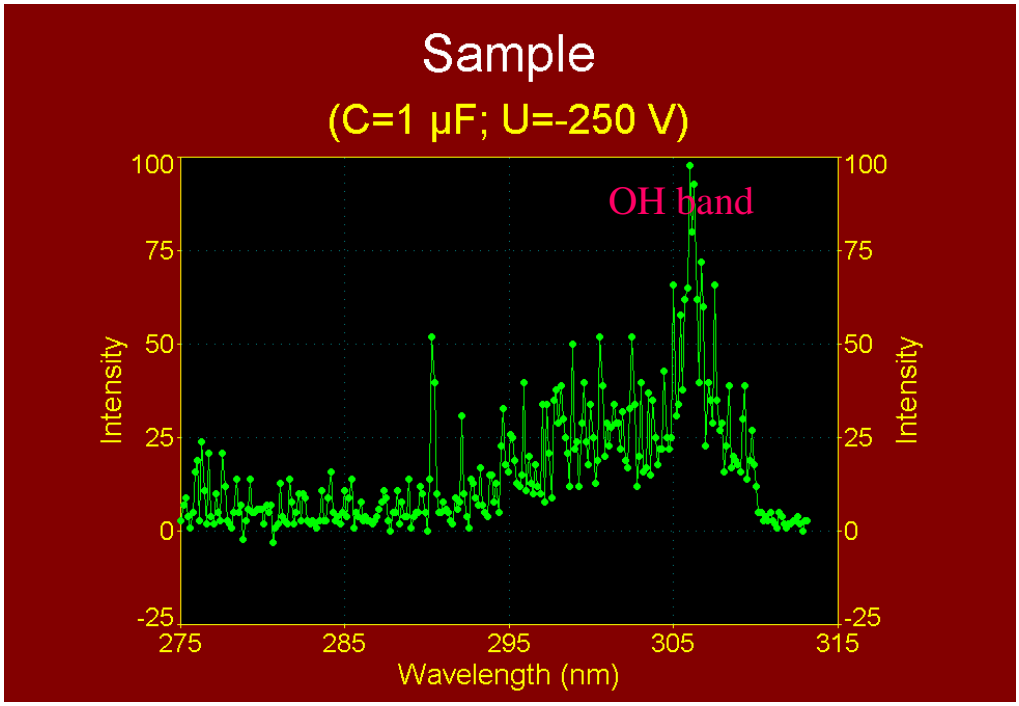

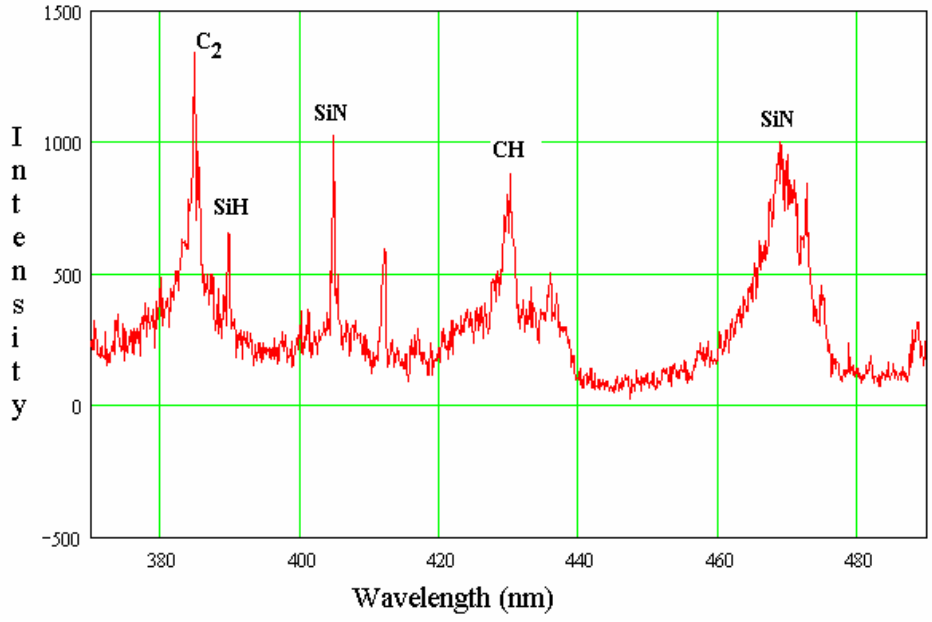

Fig.5. One example of emission spectrum of arc plasma.

4. Contamination of plasma environment

When spacecraft is coming out of eclipse, solar array temperature is rising due to exposure to Sun radiation. Operational temperature of an array in LEO conditions is approximately 80-100 C. It is believed that the adsorbed contaminants from the array surface are evaporating at a high rate due to heating. On another hand, when solar array sample is installed in a vacuum chamber its surface is contaminated not only by “natural” species (adsorbed water, atmospheric gases, and products of a technological process) but also other contaminants. The most abundant of these contaminants is vacuum pump oil. To measure chemical composition of background vacuum and to determine plasma contamination due to heating, the quadruple mass-spectrometer is installed in large chamber. Two solar array samples consisting of 36 cells (4x6 cm) each are mounted on an aluminum sheet with electrical heater placed on the back (Fig.6). This heater provides enough power to radiately heat sample from 15 C to 80 C for about 50 minutes (Fig.7). It is seen that the increase in water vapor partial pressure is considerably higher than the plain isochoric increase $\frac{\Delta p}{p_0} = \frac{\Delta T}{T_0}$, and this observation confirms the presence of water absorbed on solar array surface.

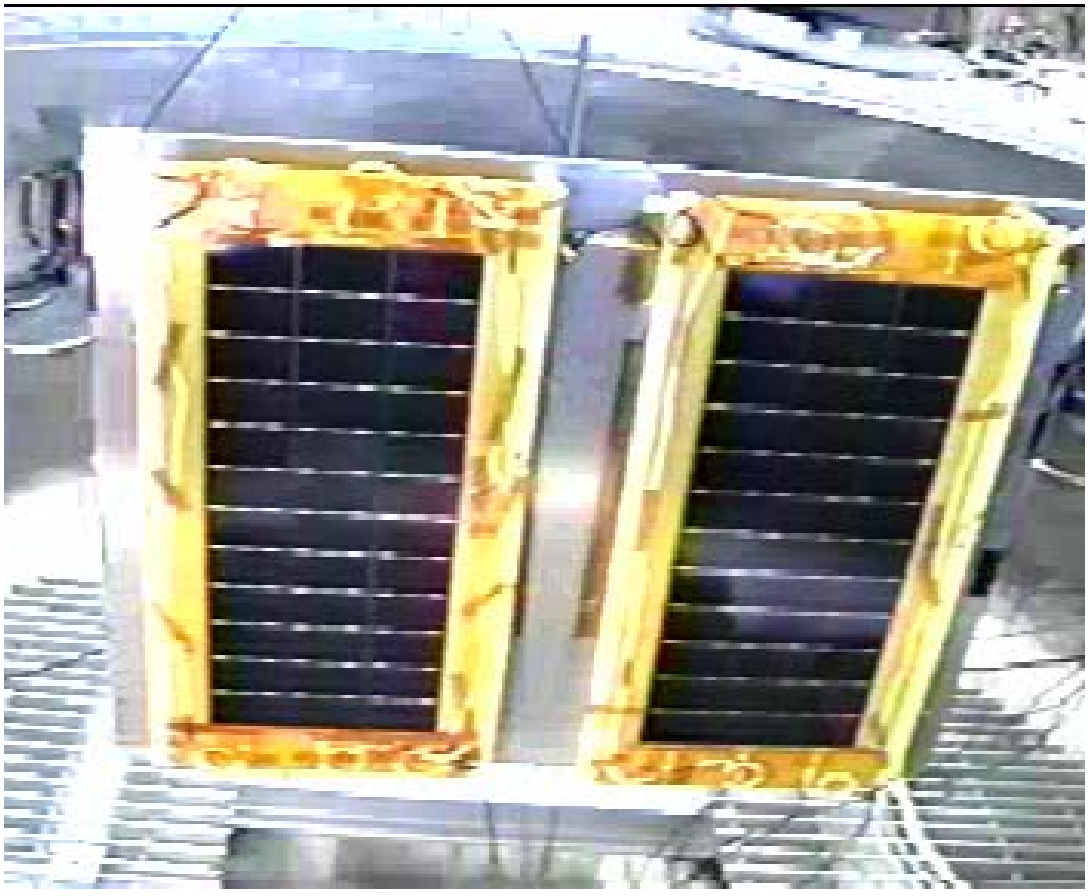

Fig.6. Solar array samples installed in vacuum chamber.

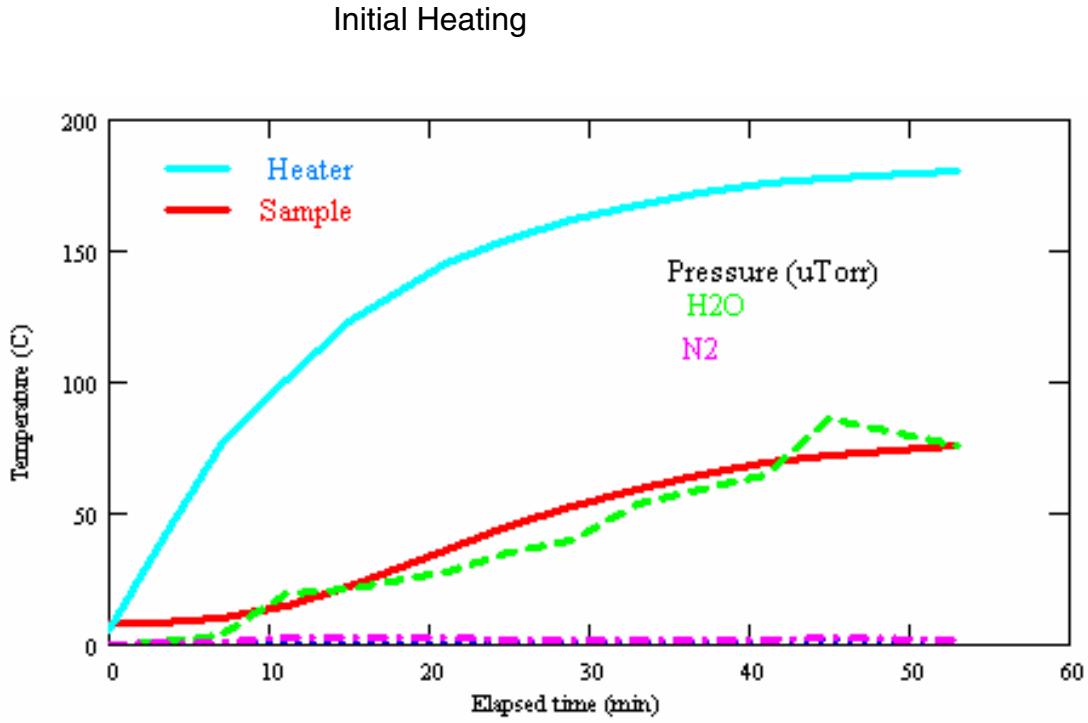

Fig.7. Increase of water vapor pressure is considerably higher than plain isochoric increase.

Five cycles of heating-cooling sample in vacuum chamber resulted in significant drop of residual water vapor pressure (Fig.8).

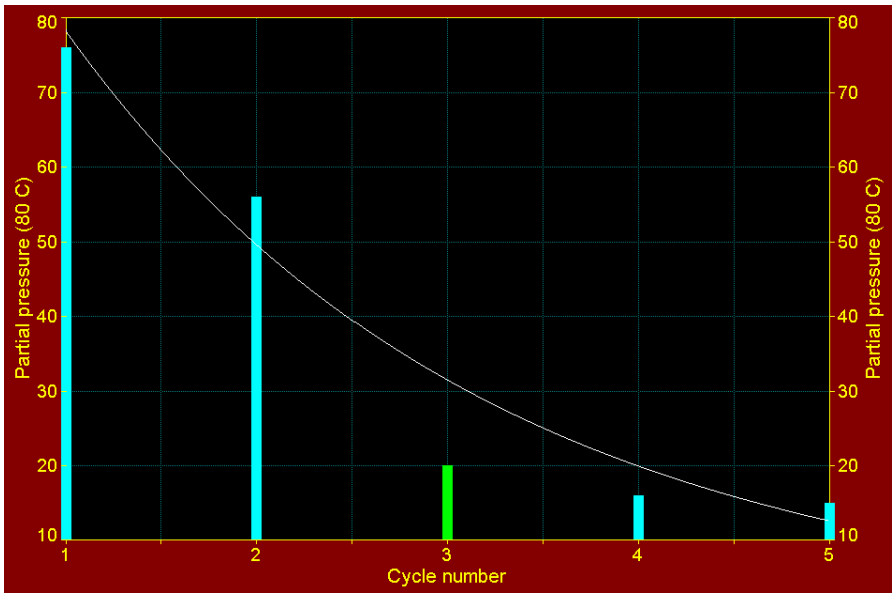

Fig.8. Water vapor partial pressure in course of thermal cycling (rel. units).

5.Arcing in plasma

Five types of tested solar arrays are shown in Table 1. Each string (12 cells in series) is tested separately to measure arc inception voltage and arc rate. Measurements reveal significant differences in these parameters even for strings belonging to one sample. There are two reasons explaining such observations: manufacturing process peculiarities and geometrical design of a sample. In fact, the middle string is separated from neighboring strings by narrow gaps (0.8 mm) covered with a thin RTV layer while two other strings have edges with underlying semiconductor and dielectric exposed to the plasma. Manufacturing peculiarities demonstrate themselves when one compares arc parameters for two outer strings and finds considerable differences. And arc sites are located mostly on interconnects for middle string while great part of arcs on outer strings has been observed on cell edges. To preserve the homogeneity of collected data one common experimental procedure is used for all measurements of arc inception voltages and arc rates: 1) string is initially biased to voltage well below an expected arcing threshold; 2) 15-30 minute time interval is allowed to register (or to not register) an arc; 3) voltage is increased on 10-20 V; 4) arc rate is defined as an average over a respective time span.

Table1. Five types of solar array samples tested in the large chambers.

Sample.: No	Coverglass : Thickness (μm):	Material :	Overhang : (μm)	Cell size : (cm)	Interconnect
1	300	UVR	0	4x6	exposed
2	150	UVR	0	4x6	exposed
3	150	CMX UVR	0	4x6	exposed
4	150	UVR	250	4x6	exposed
5	150	UVR	0	8x8	wrapthrough

On the first stage of the test, two samples (#1 and #2 in Table 1) are mounted on the heater plate and installed in chamber. The results of measurements for middle strings at the room temperature are shown in Fig.9. Obviously, arc inception voltage is lower for the panel with thinner coverglass, and arc rates differ significantly. Arc rates have been also determined at high temperature (Fig.10). Arc rates are widely scattered over a range of voltages 280-380 V. In general, the temperature rise to 80 C results in significant increase of arc inception voltage (40-60 V). In particular, inner strings are not arcing below 300 V. It is worth noting that measurements shown above have been done at comparatively high water vapor partial pressures: 4 μTorr at 15 and 15-30 μTorr at 80 C. These values are much higher than one can anticipate in LEO conditions.

The decrease of an arc rate during the process of continuing arcing (conditioning) has been measured by biasing the whole sample #2 to -400 V and measuring average arc rate for every four minutes. Additional capacitance is increased from 0.22 μF to 1μF to accelerate conditioning. After about 70 arcs, arc rate drops from 3.25 arc/min to the magnitude of 1 arc/min and stays practically steady for the next 30 arcs. To verify the influence of plasma density on arc rate this parameter has been increased by factor 1.5, and arc rate was measured for the next 100 arcs. Finally, arc rate has decreased to 0.25 arc/min after about 200 arcs. Thus, the influence of conditioning on previous measurements of arc rates for separate strings belonging to different samples is insignificant, particularly because of low capacitance (0.22 μF) used in these tests.

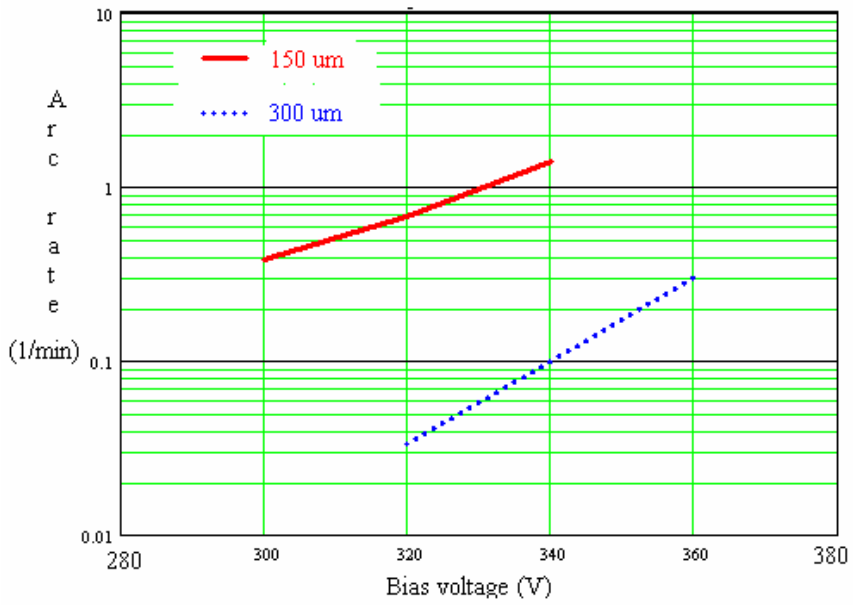

Fig.9. Arc rate on the middle strings (samples #1 and #2).

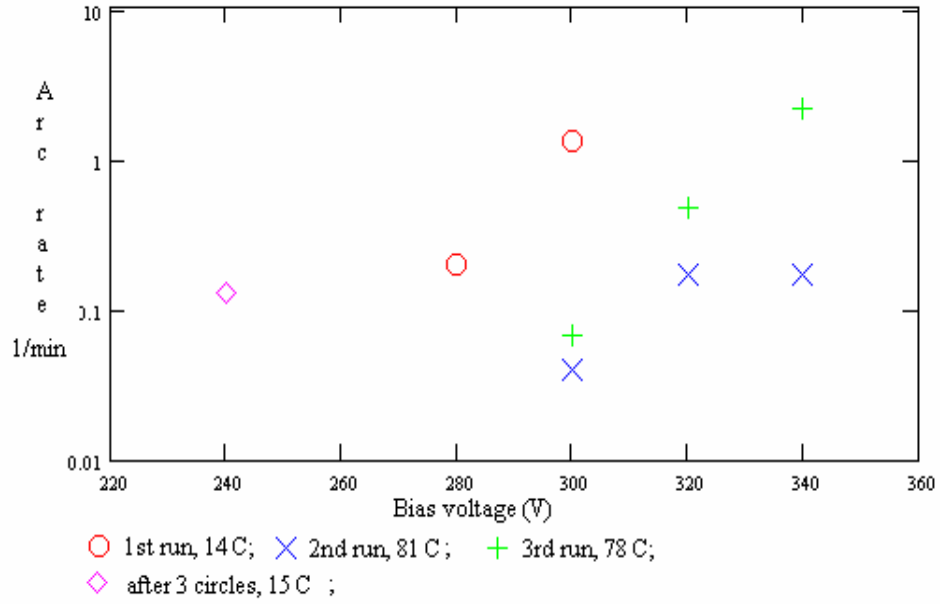

Fig.10. Arc rate on the middle string of sample #2.

To test the possibility of outgassing of the whole sample by heating it to 80 C and pumping out an excess of water vapor the sample #2 has been undergone to five thermal cycles (see Fig.8). Arc rates are measured for all three strings connected in parallel at room temperature before the first cycle and after the fifth cycle. The results are shown in Fig.11.

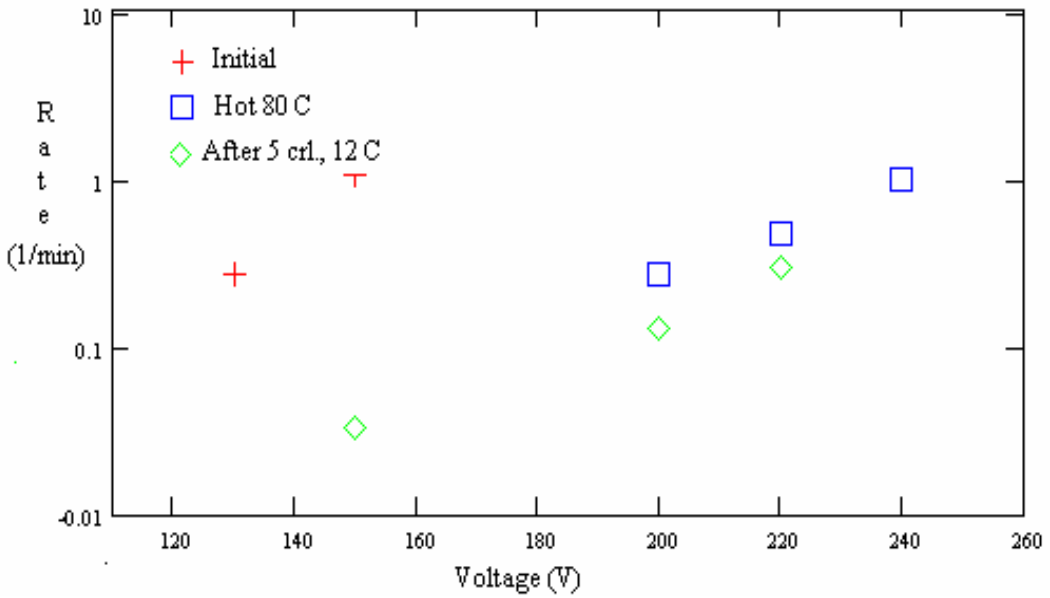

Fig.11. Arc rate on sample #2 (three strings in parallel).

It is seen in Fig.11 that arc rate decreases about 30 times and arc threshold increases approximately 30 V due to outgassing. It should be noted that minimum partial pressure of water vapor in xenon plasma reached in these experiments was 1.4 μTorr that seems not low enough to outgas sample surfaces to the degree expected in LEO.

Arcing on the sample #3 (CMX UVR coverglass) does not show any measurable differences comparatively to arcing on sample #2. Arc inception voltage for the middle string is 300 V, and two other strings are arcing at lower voltages due to considerable percentage of arcs on the cell edges. On the contrary, the test results for the sample #4 (250 μm overhang) look much more prospective. Arc inception voltage is 80-100 V higher, and arc rate is lower for the middle string. Two other strings have also demonstrated the decrease of arc rate in spite of arcing on cell edges. The increase of arc inception voltage to 480 V for the hot sample is particularly important. It seems that the array with coverglass overhang and additional insulation of cell edges can operate at 400 V in LEO conditions.

According to existing model of arc inception [12,13] the most probable arc site on an array surface is a conductor-dielectric junction exposed to the plasma. Thus, if all interconnects are insulated from the surrounding plasma the probability of a discharge decreases significantly. One of the possible realizations of this idea is the array design with wrapthrough interconnects (sample #5, Fig.12). Such design cannot prevent arcing at very high negative potential because edge of semiconductor (silicon, germanium, or other) stays exposed to the plasma, and many tests (including ones described in this paper) have demonstrated intensive arcing on cell edges. However, considerable increase of arc inception voltage can be expected, particularly for the middle string. Test results confirm these expectations (Fig.13). The inception of arc is observed on the middle string at bias voltage 440 V that is 60 V higher than arc inception voltage for the

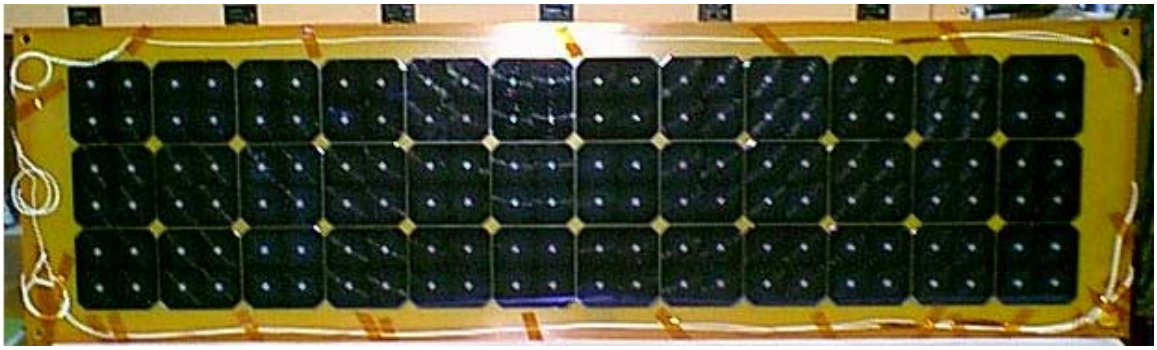

Fig.12. Solar array sample with wrapthrough interconnects.

string with coverglass overhang. Arc sites are located between adjacent cells belonging as to middle string as to neighboring strings. Two other strings demonstrate much lower arc inception voltages due to arcing on edges. Unfortunately, experimental setup has not provided a possibility to heat this sample above room temperature but even the results obtained to date show that this kind of solar array can be used in LEO to generate power at voltage 450 V if array edges are electrically insulated.

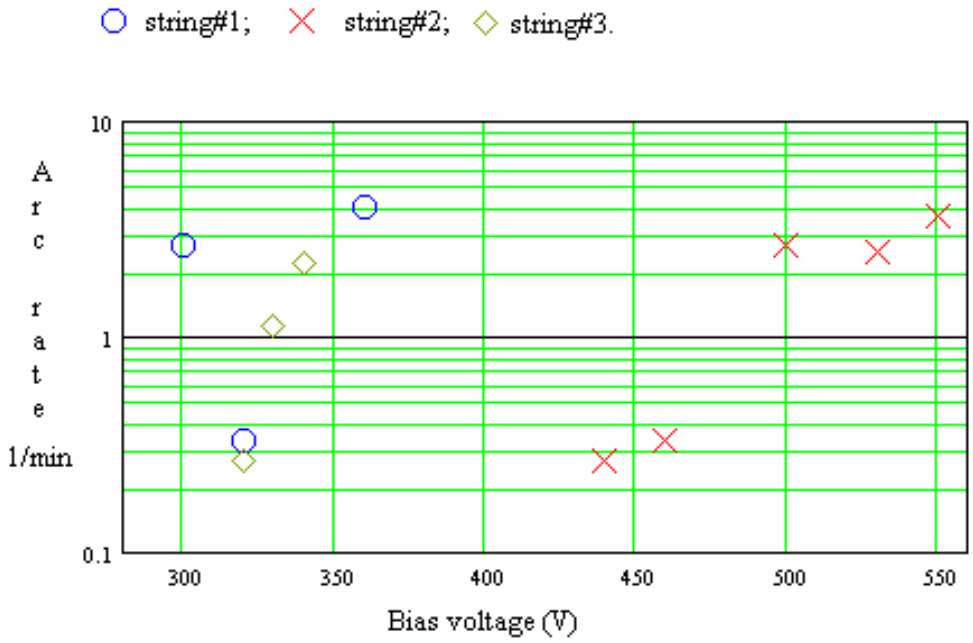

Fig.13. Arc rate on sample #5.

Short electrostatic discharges studied above are certainly undesirable events that must be prevented for reliable operation of the spacecraft. However, this kind of transients are not damaging solar array irreversibly, at least in cases of low additional capacitances used in current experiments. Sustained discharges initiated between adjacent cells with a few tens volt potential difference are much more dangerous [14,15] because they can destroy cells and underlying substrate that results in considerable loss of power. Samples #1, #2, and #4 have been tested against an inception of sustained arc between two strings. The circuitry diagram for the test is shown in Fig.1. Test starts with lower limits on SAS voltage and current. After the registration of 5-10 arcs these parameters are gradually changed and more arcs are generated until initial sign

of sustained discharge is seen on the oscilloscope. This sign represents the SAS current pulse that continues much longer than original arc. The corresponding SAS voltage and current are considered as threshold parameters because even a small increase of them (10 V and 0.25 A) results in spectacular event shown in Fig. 14. In this case the sustained discharge has been quenched after 20 s by turning SAS off. Damaged part of the sample is shown in Fig.15. Threshold parameters depend on solar array design: they are 40 V and 1 A for sample #1, 60 V and 2 A for sample #2, and 80V and 1.6 A for sample #4.

Fig.14. Sustained arc between adjacent strings on sample #2.

5. Scaling of arc parameters

Even short transients are detrimental for spacecraft, and the degree of damage increases with the increase of arc current amplitude and pulse width. These two parameters depend on the amount of electrical charge leaking into surrounding plasma during the discharge time. There are currently two theoretical models that allow estimating lost electrical charge and its dependence on the array capacitance. First model[7] is based on the suggestion that the discharge generates an expanding plasma sheath neutralizing positive charge on top of coverglass. If plasma expends with a constant speed the discharge time is proportional to the array linear dimensions, or, in another terms, to the square root of an array capacitance. This dependence has been proved in many experiments [16,17]. However, the distance that plasma can expand on is limited to about 1 m in simulated LEO conditions [18]. Thus, according to the first model the upper limit for the effective capacitance is the capacitance of the part of solar array with area approximately 1 m^2. The second model also envisages that both arc current amplitude and pulse width are proportional to the square root of a capacitance but this prediction is based on the dynamics of ionization-recombination processes in the discharge plasma [6]. If the second model is correct the effective capacitance is only two-three times less than the capacitance of a whole solar array. A simple experiment has been performed to verify the validity of the second model. Two solar array

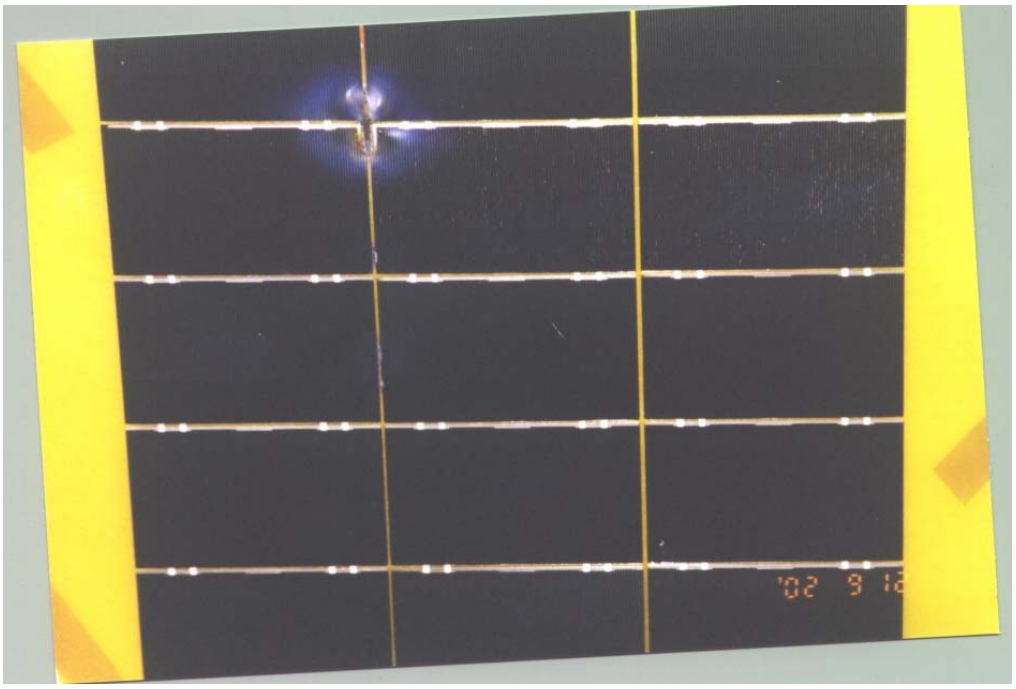

Fig.15. Damage induced by sustained arc.

samples (sample #2) are mounted on aluminum panel with grounded aluminum plate installed between samples. The height of the plate is 7.5 cm bigger than the distance between aluminum panel and top of the sample. Such arrangement prevents the expansion of plasma sheath from one sample to another. The additional capacitor of 1000 pF is used in this particular experiment.

The capacitance of one cell can be calculated as

$$C_1 = \frac{\varepsilon_0 \varepsilon_1 S_1}{d_1}\left(1 + \frac{\varepsilon_1 d_2}{\varepsilon_2 d_1}\right)^{-1} \qquad (1)$$

where $\varepsilon_{1,2}$ are dielectric constants of coverglass and adhesive, $d_{1,2}$ are their thicknesses, and S_1 is a cell area.

Dielectric constants are: for borosilicate coverglass ε_1=6.7, and for epoxy ε_2=3.6. Thus, a quite reliable estimate can be obtained: C_1=590 pF/cell. Moreover, the scaling does not practically depend on exact numbers for largest capacitances. Ten measurements of arc current pulse widths for each configuration have been done by biasing one string, three strings, and six strings in parallel. The results are shown in Fig.16. The scaling is confirmed with a very high accuracy, which means that adequate ground simulations of arcing on spacecraft surfaces have to be performed with a very large additional capacitance (for instance, about 1000 μF for ISS).

7.Current collection

One solar cell provides current of 1 A in order of magnitude while collected current is scaled in hundred microamps. Thus, the role of collected current in a parasitic power drain is certainly negligible. However, the floating potential of the spacecraft strongly depends on the current collected by the solar array [19]. There are three main factors that influence the magnitude of collected current: i) solar array design; ii) solar array temperature; iii) parameters of surrounding

plasma. Obviously, the design with coverglass overhang and with wrapthrough interconnects offers arrays with considerably decreased collected currents. Electron number density and electron temperature also influence on current collection. Ground tests that simulate an electron component of LEO plasma quite reasonably provide reliable data for current collection by cells with positive potentials with respect to surrounding plasma. Test data containing measurements of collected current for negatively biased cells are applicable to the analysis of spacecraft floating potential not better than in order of magnitude because the characteristics of ion component are different in ground tests and in LEO.

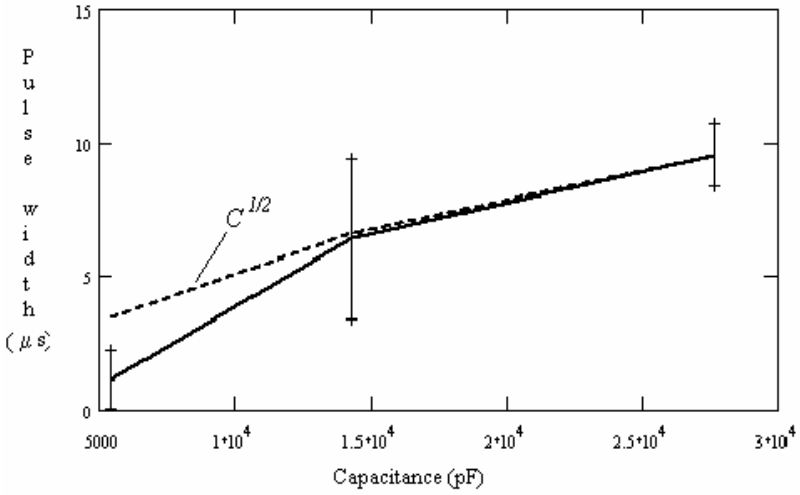

Fig.16. Pulse width scaling measured by biasing to -340 V one, three, and six strings of sample #2. Error bars (±1) are calculated from ten measurements for each point.

A few examples of the dependence of electron current collection on bias voltage are shown in Fig.17. It is seen than the increase of electron number density results in the almost proportional increase in current collection. But the dominant factor in the current collection is an array temperature. The magnitude of collected current grows more than three times when array temperature reaches 79 C. This observation must be taken into account for the computations of spacecraft floating potentials. Ion currents are measured by biasing separate strings up to 100 V negative, and these currents do not exceed 1 μA for all situations studied even though the same effect of significant increase due to heating is also found.

Measurements of collected currents for the sample with coverglass overhang have demonstrated the decrease in magnitude close to the factor 2 comparatively to sample with a standard design. Cell with wrapthrough interconnects collects not much less current than cell with coverglass overhang but it generates three times higher power. It seems that tests in simulated plasma environment are suitable for creation a data base for further computations of the spacecraft floating potentials in LEO.

8. Conclusions

Comprehensive tests of five different types of solar array samples in simulated LEO plasma environment have demonstrated that the highest arc threshold (440 V) can be achieved for an array with wrapthrough interconnects if edges of strings are not exposed to the plasma. This design is also effective in decreasing of an array current collection. The design with exposed interconnects but with coverglass overhang also provides significant improvement comparatively to the conventional design. Particularly, arcing on the sample cannot be initiated at potentials below 300 V even under room temperature, and arc threshold increases to 420 V under

temperature 72 C. The increase of coverglass thickness also results in some improving of array parameters. Thorough outgassing of solar array surfaces may result in significant decrease of arc rate for a conventionally designed solar array.

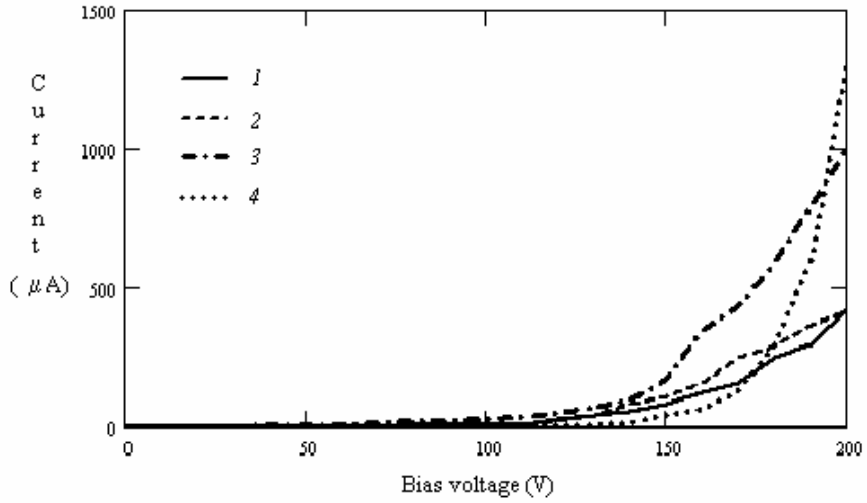

a)

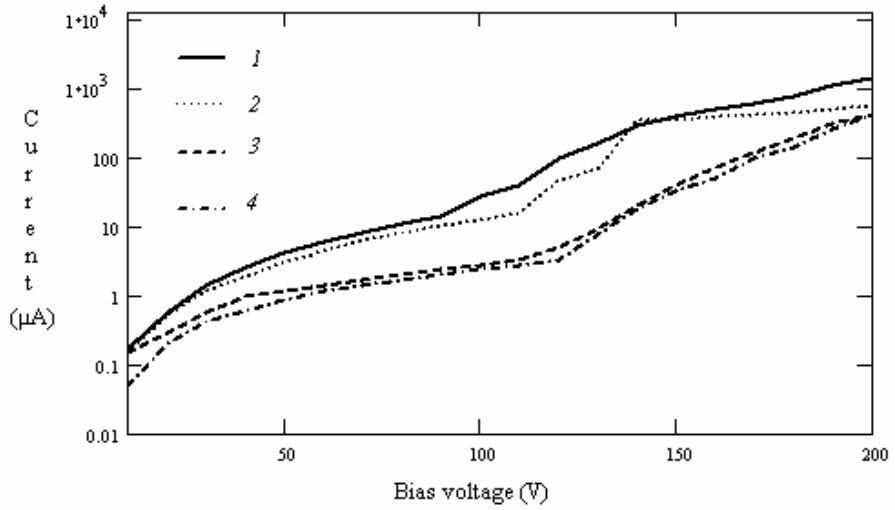

b)

Fig.17. Electron current collection: a) *1*-sample #2, str.2, n_e=2*10^5 cm^{-3},15 C; *2*-sample #1, str.1, n_e=7*10^5 cm^{-3},15 C; *3*-sample #1, str.2, n_e=2*10^6 cm^{-3},15 C; *4*-sample #2, str.1, n_e=5*10^5 cm^{-3}, 79 C. b) *1*-sample #3, str.2, n_e=1*10^6 cm^{-3}; *2*- sample #4, str.2, n_e=1*10^6 cm^{-3}; *3* and *4*-sample #5, str.1 and 2 respectively, n_e=3.5*10^5 cm^{-3}, temp. 15 C.

References

1.Stevens, N.J. "Interactions Between Spacecraft and the Charge-Particle Environment", Proc. Spacecraft Charging Technology Conference, NASA CP-2071, 1978, p.268-294.

2.Ferguson, D.C. "Solar Array Arcing in Plasmas", NASA CP-3059, 1989, p. 509.

3.Hastings, D.E. "A Review of Plasma Interactions With Spacecraft in Low Earth Orbit",

Journal of Geophys. Research, Vol.100, No.A8, 1995, pp.14,457-14,483.

4.Parks,E.D.,Jongeward,G.,Katz,I., and Davis, V.A. “Threshold-Determining Mechanisms for Discharges in High Voltage Solar Arrays”, Journal of Spacecraft and Rockets, Vol.24, No.4, 1987, pp.367-371.

5. Upschulte, B.L., Marinelli, W.J., Carleton, K.L., Weyl, G., Aifer, E., and Hastings, D.E. “Arcing on Negatively Biased Solar Cells in a Plasma Environment”, Journal of Spacecraft and Rockets, Vol.31, No.3, 1994, pp.493-501.

6.Vayner, B., Galofaro, J., Ferguson, D., and Degroot, W. “Electrostatic Discharge Inception on a High-Voltage Solar Array”, AIAA Paper 2002-0631, Jan.2002.

7. Galofaro, J., Vayner, B., Ferguson, D., and Degroot, W. “A Desorbed Gas Molecular Ionization Mechanism for Arcing Onset in Solar Arrays Immersed in a Low-Density Plasma”, AIAA Paper 2002-2262, May 2002.

8. Anders, A., and Anders, S. “Emission Spectroscopy of Low-Current Vacuum Arcs”, Journal of Physics D:Appl.Phys., Vol.24, 1991, pp.1986-1992.

9.Yotsombat, B., Davydov, S., Poolcharuansin, P., Vilaithong, T., and Brown, I.G. “Optical Emission Spectra of a Copper Plasma Produced by a Metal Vapor Vacuum Arc Plasma Source”, Journal of Physics D: Appl.Phys., Vol.34, 2001, pp.1928-1932.

10. Pearse, R.W.B., and Gaydon, A.G. “The Identification of Molecular Spectra”, 3rd edition, Chapman&Hall LTD, London, UK, 1963, 347p.

11 Vayner, B.V., Galofaro, J.T., and Ferguson, D.C. “The Neutral Gas Desorption and Breakdown on a Metal-Dielectric Junction Immersed in a Plasma”, AIAA Paper 2002-2244, May 2002

12.Cho,M., and Hastings, D.E. “Computer Particle Simulation on High-Voltage Solar Array Arcing Onset”, Journal of Spacecraft and Rockets, Vol.30, No.2, 1993, pp.189-205.

13.Hastings,D.E., Weyl,G., and Kaufman, D. “Threshold Voltage for Arcing on Negatively Biased Solar Arrays”, Journal of Spacecraft and Rockets, Vol.27, No.5, 1990, p.539-544.

14.Hoeber, C.F., Robertson, E.A., Katz, I., Davis, V.A., and Snyder, D.B. “Solar Array Augmented Electrostatic Discharge in GEO”, AIAA Paper 98-1401, Jan. 1998.

15. Snyder, D.B., Ferguson, D.C., Vayner, B.V., and Galofaro, J.T. ”New Spacecraft-Charging Solar Array Failure Mechanism” 6th Spacecraft Charging Technology Conference, Nov. 2-6, 1998, Air Force Res. Lab., Hanscom AFB, MA, USA, pp.297-301.

16. Balmain, K. G., and Dubois, G. R. “Surface Discharges on Teflon, Mylar and Kapton”, IEEE Transactions on Nuclear Science, Vol. 26, No.12, 1979, pp.5146-5151.

17. Snyder, D.B. “Characteristics of Arc Currents on a Solar Cell Array in a Plasma”, IEEE Transactions on Nuclear Science, Vol.31, No.4, 1984, pp.1584-1587.

18.Cho, M., Ramasamy, R., Hikita, M., Tanaka, K., and Sasaki, S. “Plasma Response to Arcing in Ionospheric Plasma Environment: Laboratory Experiments”, Journal of Spacecraft and Rockets, Vol.39, No.3, 2002, pp.392-408.

19. Ferguson, D.C., and Hillard, G.B. “In-Space Measurements of Electron Current Collection by Space Station Solar Arrays”, AIAA Paper 95-0486, Jan. 1995.

LIQUID PHASE DEPOSITION OF SINGLE-PHASE ALPHA-COPPER-INDIUM-DISELENIDE

J. Cowen
Case Western Reserve University, Cleveland, Ohio

L. Lucas
Case Western Reserve University, Cleveland, Ohio

F. Ernst
Case Western Reserve University, Cleveland, Ohio

P. Pirouz
Case Western Reserve University, Cleveland, Ohio

A. Hepp
National Aeronautics and Space Administration, Cleveland, Ohio

S. Bailey
National Aeronautics and Space Administration, Cleveland, Ohio

Introduction

The success of exploratory missions in outer space often depends on a highly efficient renewable energy supply, as provided by solar cells. Figure 1 shows a well-known example: The robotic vehicle "Rover," constructed for NASA's "Mars Pathfinder" mission. The solar cells for such applications not only need to have high conversion efficiency, but must possess a high *specific* power, thus a high power output per unit mass. Since future missions will demand for large aggregates of solar cells and space flights are expensive, the solar cells must furthermore be available at low costs (per unit power output) and – very important in outer space – have a long lifetime and a high resistance against structural damage introduced by irradiation with high-energy electrons and protons.

The photovoltaic materials that are presently available only partly fulfill all these requirements. Therefore, we propose to explore a new method for fabricating thin-films for cost-efficient solar cells with very high specific power, high irradiation resistance, and long lifetime, based on the α-phase of the Cu–In–Se system, "α-CIS."

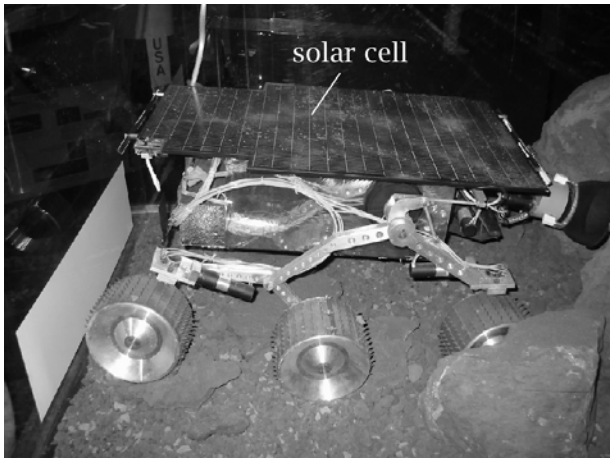

Fig. 1: The robotic vehicle "Rover," which NASA sent to the surface of planet Mars (exhibit at NASA Glenn Research Center, Cleveland).

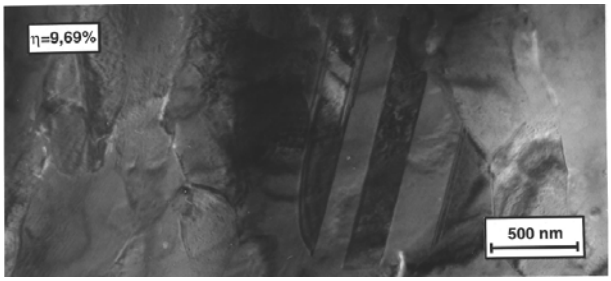

Fig. 2: Cross-sectional TEM image of a CIS film grown at 460 to 520 °C by PVD. Cu:In:Se ratio in the vapor: 1:1:2. Composition measured by XEDS: $Cu_{25.5}In_{24.8}Se_{49.8}$.

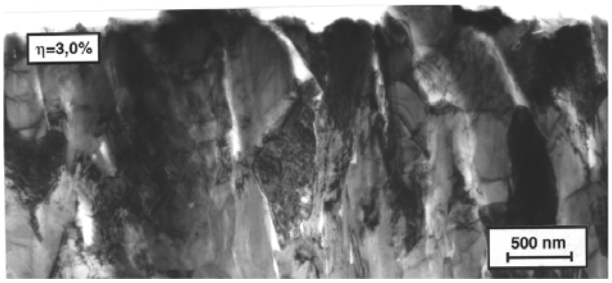

Fig. 3: Cross-sectional TEM image of a CIS film grown at 460 to 520 °C by PVD. Cu:In:Se ratio in the vapor: 1:3:5. Composition measured by XEDS: $Cu_{24.0}In_{25.9}Se_{50.2}$.

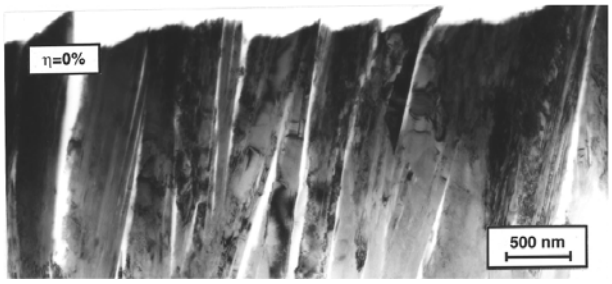

Fig. 4: Cross-sectional TEM image of a CIS film grown at 430 °C by PVD. Cu:In:Se ratio in the vapor: 1:2:3.5. Composition measured by XEDS: $Cu_{16.6}In_{32.2}Se_{51.2}$.

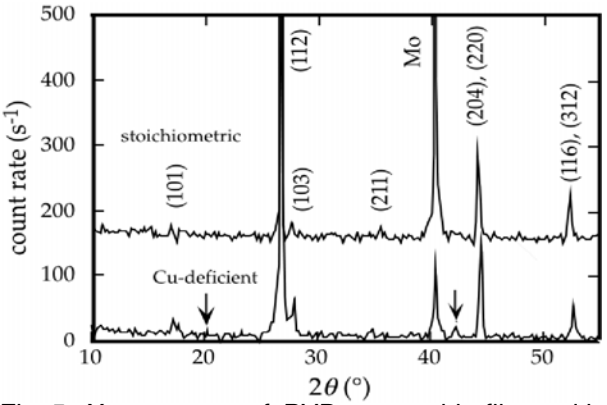

Fig. 5: X-ray scans of PVD-grown thin-films with stoichiometric ($CuInSe_2$) and with Cu-deficient composition.

The stoichiometric composition of α–CIS corresponds to $CuInSe_2$. It has long been known that this compound possesses outstanding properties for thin-film solar cells. So far, however, one cannot fully exploit the advantages of this material, because it is not possible to make α-CIS layers with a sufficiently low concentration of structural and, consequently, electronic defects. In this paper, we describe a research program to overcome these limitations and to optimize the fabrication of α-CIS thin-films for solar cell applications in outer space.

Presently, the CIS films with the best photovoltaic performance are grown by physical vapor deposition (PVD). However, such films contain high concentrations of structural defects, which degrade their efficiency in photovoltaic devices: point defects, dislocations, large-angle grain boundaries, pores, anti-phase boundaries, cracks, or inclusions of other phases and, correspondingly, interphase interfaces [1].

Figures 2, 3, and 4 present cross-sectional TEM (transmission electron microscopy) bright-field images revealing these kinds of defects in CIS thin-films grown under a variety of different conditions by the group of H.-W. Schock at the Institut für Physikalische Elektronik, University of Stuttgart, Germany. The microcharacterization, including TEM, was carried out as part of the Ph. D. project of T. Haalboom at the Max-Planck-Institut für Metallforschung (*Materials Science*) in Stuttgart, Germany, under the supervision of F. Ernst.

As apparent from the micrographs, the microstructure sensitively depends on the processing conditions. For a Cu:In:Se ratio of 1:1:2 in the vapor, high temperatures (between 460 and 520 °C) lead to relatively large grains. Low temperatures (430 °C), in contrast, lead to the formation of extended, plate-like crystallites.

In addition to the defects mentioned before, thin-films grown with a Cu:In:Se ratio near 1:1:2 in the vapor always exhibit a high density of stacking faults and twin boundaries.

Another problem of PVD, apart from the high defect density in the films, is to control the chemical composition. Analysis of the films in Figs. 2, 3, and 4 by XEDS (X-ray energy-dispersive spectroscopy) revealed that the actual, local chemical composition of the thin-films may substantially differ from the nominal composition of the vapor (indicated in the figure captions). As demonstrated by the X-ray scans in Fig. 5, even slight deviations from the ideal composition $CuInSe_2$ lead to the formation of secondary phases. The two X-ray scans were obtained from stoichiometric and Cu-deficient CIS films. Both diffraction patterns exhibit reflections of the (desired) α-$CuInSe_2$ phase [2] and Mo-reflections of the substrate. Additional reflections at 2θ=

21.8° and 42.6°, however, indicate the presence of a second phase (defect phase β [3]) in the Cu-deficient material. Since the presence of second phases has a particularly adverse effect on the conversion efficiency [4], this material is not suitable for photovoltaic devices.

The present record of conversion efficiency with PVD α-CIS thin-films is at 18.8 % [5]. While this number is impressive, the theoretical conversion efficiency is still 30% higher (24%) [6]. Moreover, the efficiency of standard PVD material is way below 18%. There is no doubt that the high concentration of grain boundaries and phase boundaries encountered in PVD-grown material accounts for the major part of the discrepancy between actual an theoretical conversion efficiency [4]. Annealing can somewhat improve the structural properties, but usually of the film composition (particularly the Se content) and causes segregation [7-10].

The conversion efficiency of PVD-grown α-CIS thin-films is limited by structural defects, which form because these films grow far from thermodynamic equilibrium, under high driving forces, but with small atomic mobility. A promising approach for improving the structural quality of α-CIS, therefore, is by growing it from the melt, close to thermodynamic equilibrium.

CIS Growth from the Melt

Near-equilibrium growth from the melt will not only allow the fabrication of *single-phase*, pure α-CIS, but should also enable the growth of macroscopic α-CIS single crystals. Single crystals of α-CIS are valuable for studying the *intrinsic* properties of α-CIS, and to find out how much room there really is for improving the conversion efficiency of α-CIS thin-film solar cells by improving the structural quality of the material.

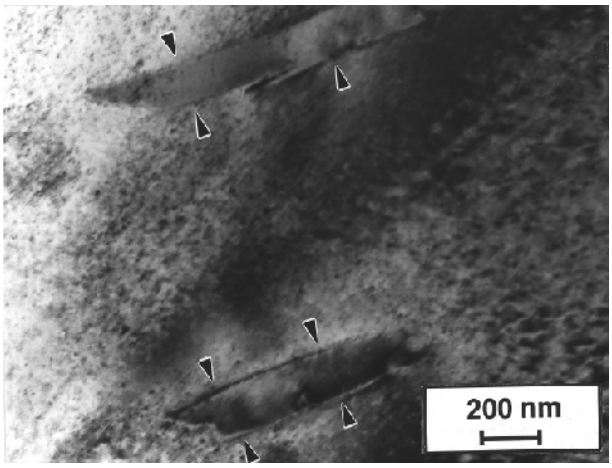

Fig. 6: TEM image revealing the presence of a second phase ("β", arrowed regions) in a "single crystal" of $Cu_{23.6}In_{25.9}Se_{50.5}$.

Following this idea, C. R. Schwerdtfeger at the National Renewable Energy Laboratory (NREL) employed high-pressure, liquid-encapsulated directional solidification to grow (Cu-deficient) α-CIS single crystals and obtained apparently coarse-grained macroscopic crystals [11, 12]. However, no study of the microstructure of this material has been published. More recent attempts of M. Hornung to grow α-CIS single-crystals from the melt by the vertical gradient freeze method also failed [13]. SEM (scanning electron microscopy) and TEM studies on the largest grains of these "single crystals" revealed that they were never even single-phase α-CIS, but always contained a second phase (β) and an enormous density of α/β phase boundaries [14]. Fig. 6 presents an example from this material: a TEM image revealing particles of the β-phase in an α-CIS "single crystal". Note that the β particles did not form because the solidified material had the incorrect composition. Careful analysis of chemical composition by XRF (X-ray fluorescence analysis) and ICP-OES (inductively-coupled plasma optical emission spectroscopy) confirmed that the composition of this material was $Cu_{23.6}In_{25.9}Se_{50.5}$, thus sufficiently close to the stoichiometric composition of α-CIS for obtaining a single-phase material. The latest reports on α-CIS single crystals are by Cahen *et al.* [15], but again no detailed microstructural studies were published.

Cu–In–Se Phase Equilibria

To understand these drawbacks, we have recently investigated all phase equilibria of the entire Cu–In–Se system and determined the first complete and correct ternary phase diagram [16-18].

The new phase diagram, which constitutes one of the most complicated ternary phase diagrams known so far, explains why it is difficult (if not impossible) to grow single-phase α-CIS from a melt with the composition equal to or close to $CuInSe_2$. Consider the Cu_2Se–In_2Se_3 isopleth of Fig. 7, for which we have proven that it actually constitutes a *quasi*-binary vertical section of the Cu–In–Se phase diagram. On cooling a melt with the composition $CuInSe_2$, the first solid phase is not α-CIS, but a high-temperature phase we denote as δ_H. On further cooling, α-CIS should then form from δ_H via a phase transformation. However, the melting point maximum of the δ_H phase field lies at a Cu content of 23.5 %, thus considerably off (on the left hand side of α-CIS in Fig. 7) the 25.0% composition required for stoichiometric α-CIS ($CuInSe_2$). Therefore, if one tries to grow single-phase α-CIS by cooling down a melt with a composition in the vicinity of the stoichiometric composition $CuInSe_2$, one first obtains the phase δ_H, which has the "incorrect" composition $Cu_{23.5}In_{26.0}Se_{50.5}$, surrounded by more Cu-rich material. On further cooling, this material cannot perfectly transform to α-CIS, owing to the limited kinetics. Instead, it will transform to $\alpha + \delta_R$. Consequently, one obtains a high density of phase boundaries.

Starting out from a composition not equal to but in the vicinity of $CuInSe_2$ does not yield single-phase material, either. As revealed in isothermal sections of the Cu–In–Se phase diagram [16-18], α-CIS establishes two-phase and three-phase equilibria with *nine* different phases! This variety of phase equilibria explains the difficulties other researchers have encountered when attempting to grow $CuInSe_2$ single crystals.

1.1 How to Solve the Problem

Figure 8, taken from [18], represents the most important data for our project: the projection of the *liquidus surface* of the Cu–In–Se phase diagram onto the composition triangle. (The liquidus surface separates liquid and solid phases in the ternary phase diagram. Figure 8 constitutes a topographical map of the liquidus surface, where contour lines indicate the temperature.) Figure 8 confirms in a more comprehensive (three-dimensional) way than the isopleth of Fig. 7 that a melt with the composition $CuInSe_2$ does *not* precipitate α-CIS, but the phase δ_H – and this is the reason why previous attempts to grow single-phase α–CIS from the melt have failed. On the other hand, the liquidus surface exhibits four different faces that *do* enable *direct*, "primary crystallization" of α-CIS from the melt (shaded regions in Fig. 8). However, the corresponding compositions are far away from the composition $CuInSe_2$. This explains that direct precipitation of α-CIS from the melt was not discovered "accidentally."

Summarizing, the new phase diagram explains the difficulties associated with growing single-phase α-CIS from a melt with the composition near $CuInSe_2$, but also suggests melt compositions that do precipitate single-phase α-CIS *directly*, without causing any phase transformation such as $\delta_H \rightarrow \alpha$.

Liquid-Phase Deposition of α-CIS

According to Fig. 8, it should be possible to grow single-phase α-CIS thin-films by *liquid-phase deposition* (LPD) – by casting a melt with a composition within one of the shaded fields of Fig. 8 over a substrate, and cooling it slowly to a temperature somewhat below the liquidus temperature. According to Fig. 8, the melt will then *directly* precipitate a film of α-CIS onto the substrate, without further phase transformations. After the film has reached the desired thickness, the melt is removed from the substrate. Subsequently, the system is cooled to room temperature.

Since the material grown from the melt will be pure α-CIS and solidifies under near-equilibrium conditions, we anticipate substantially lower concentrations of structural defects than in PVD layers, and thus major advantages in photovoltaic efficiency (by definition, defects are non-equilibrium features). Indeed, the TEM image of Fig. 9, recently obtained from α-CIS material produced during the experiments carried out to determine the new phase diagram, reveals coarse-grained, pure α-CIS with a *much* lower concentration of defects than Figs. 2, 3, and 4.

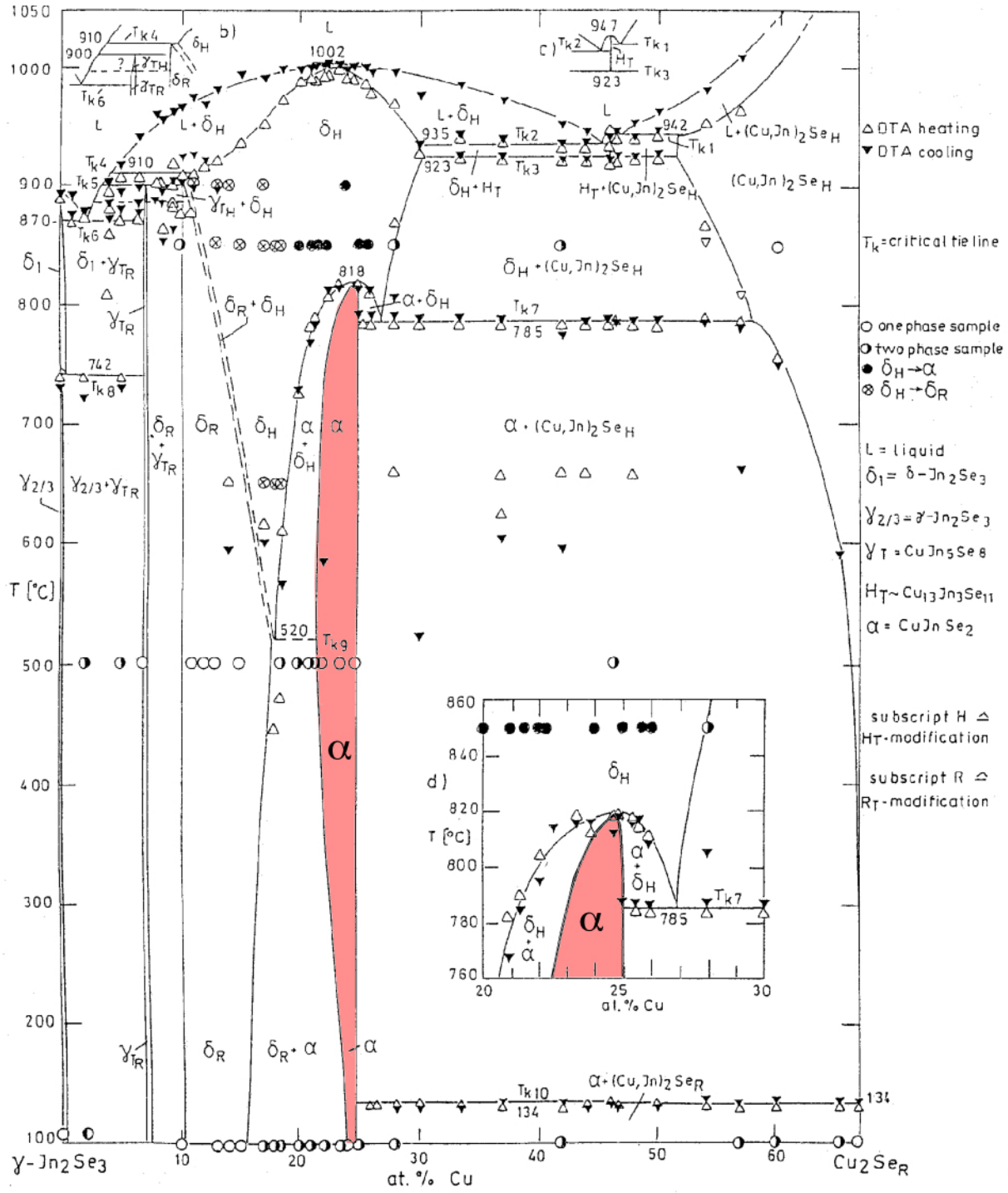

Fig. 7: The Cu_2Se–In_2Se_3 isopleth, a *quasi-binary* vertical section of the new phase diagram.

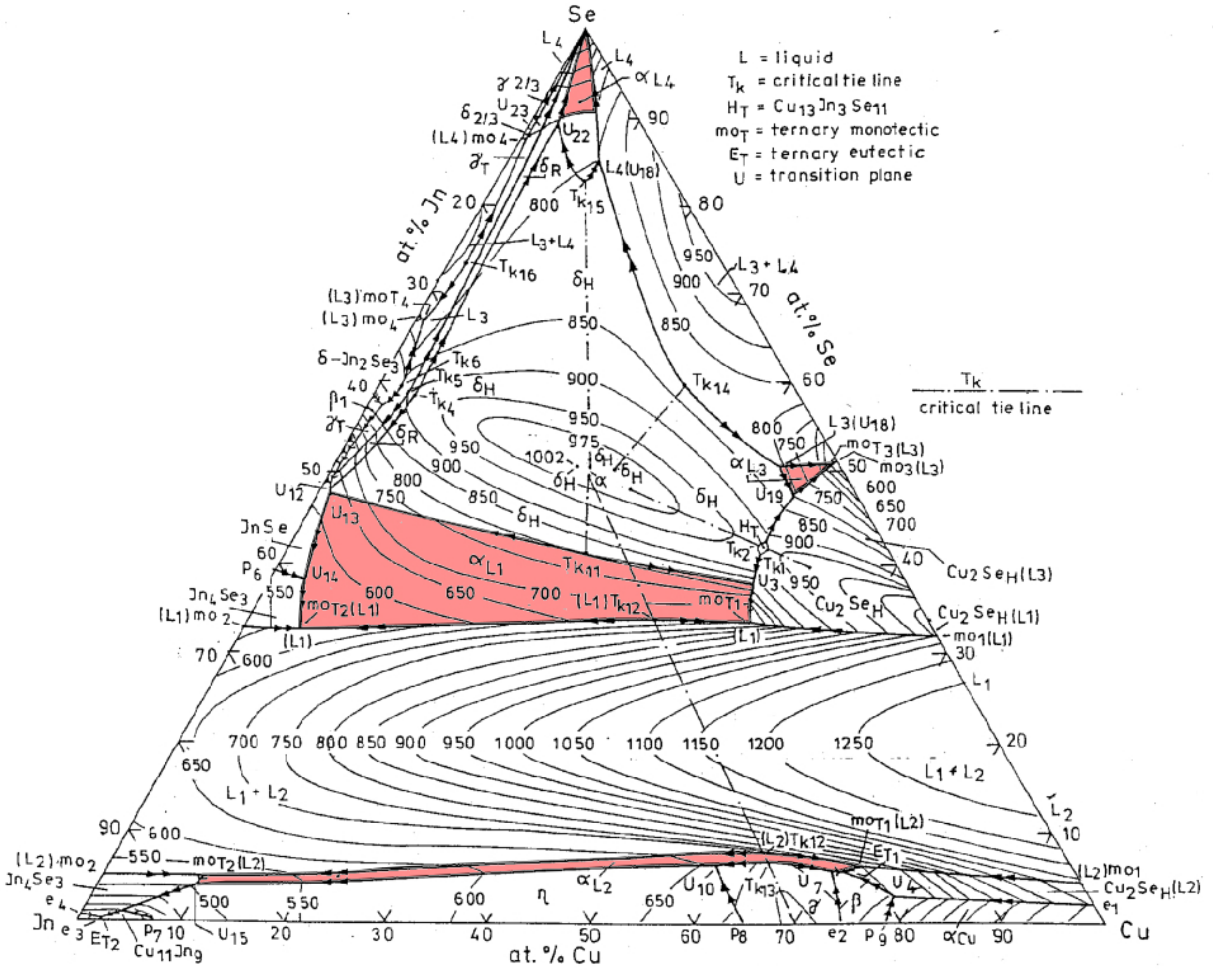

Fig. 8: Projection of the liquidus surface of the Cu–In–Se phase diagram onto the composition triangle. The four shaded areas indicate surfaces of primary crystallization of α-CIS – thus melt compositions from which α-CIS precipitates *directly*, with no further phase transformations.

Contrary to the typical PVD-grown material, moreover, LPD-grown α-CIS will be (nearly) *thermodynamically stable*. Since it is single-phase α–CIS, its lifetime in a solar cell will not be limited by ongoing diffusional phase transformations. Note that at low temperatures, the phase field of α-CIS, shaded in Fig. 7, becomes very narrow. A material outside of this narrow compositional range, as typically encountered in PVD-deposited thin-films, is not thermodynamically stable and will undergo diffusional phase transformations that may limit its lifetime in a solar cell. This issue is even more important in outer space than on the ground, because the cosmic radiation (vacancies by knock-on events) [19] and higher operating temperature owing to lack of heat convective heat release (no air) promote diffusion.

According to the isopleth in Fig. 10, it should be possible to precipitate α-CIS at temperatures below 400 °C. This opens the perspective to deposit α-CIS thin-films onto temperature-resistant polymer films, enabling the fabrication of solar cells with very high-specific-power (power output per unit mass). Moreover, LPD will allow the fabrication of larger modules than PVD and can decrease the fabrication costs of α-CIS photovoltaic devices, because the deposition rate of LPD is much higher than for PVD, and LPD does not require UHV chambers, which are costly to set up and costly to maintain. Experiments of the Liquid-Phase Epitaxy Group at the Max-Planck-Institut für Festkörperforschung have shown that large (Ø=4in) wafers can be efficiently coated by *centrifuging* the melt by rotating the substrate.

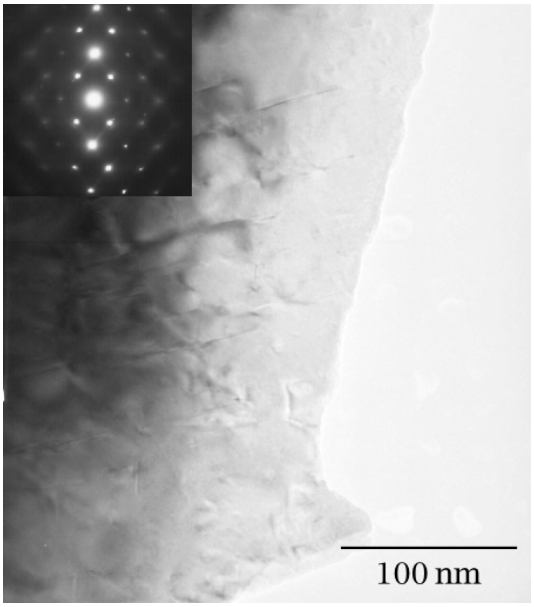

Fig. 9: TEM image of α-CIS produced during the experiments we carried out to determine the new phase diagram. The diffraction pattern (inset) confirms that the region imaged here is a large grain of single-phase α–CIS.

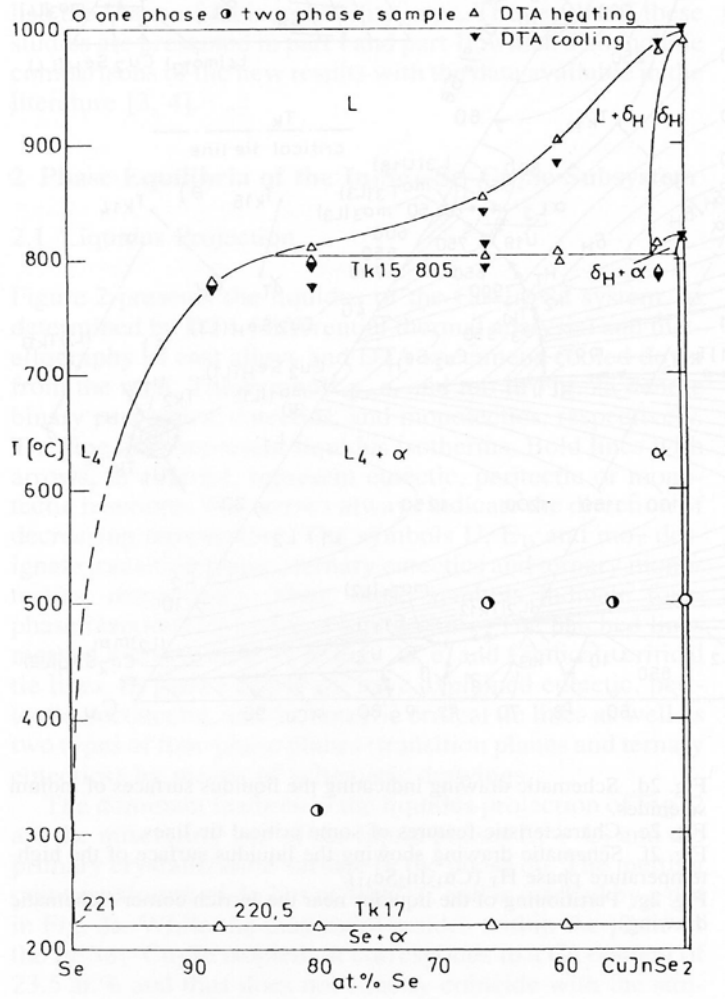

Fig. 10: Se–$CuInSe_2$ isopleth of the Cu–In–Se phase diagram [16-18].

Experimental

For the experimental technique of depositing a solid thin-film from a ternary liquid phase we will draw on the experience that has been gained with the deposition of Si_xGe_{1-x} thin-films from a Si–Ge–Bi melt in the Liquid-Phase Epitaxy Group at the Max-Planck-Institut für Festkörperforschung [20-22].

Fig. 11 presents a schematic cross-sectional view of a first, basic experimental setup we have installed for LPD of α-CIS. The experimental procedure is very similar to the one we have successfully applied for DTA (differential thermal analysis) in our study of phase equilibria of the Cu–In–Se system [16-18]. The material for the melt, a few grams of high-purity Cu, In, and Se, are encapsulated in a quartz tube. After evacuating the tube, it is flushed with Ar at 820 mbar. Encapsulating the material in quartz tubes allows us to observe the changes occurring during processing. In particular, by observing the diffusion zone at Cu stripes protruding from the Se or In melt we can carefully control the temperature. Owing to the large heat of formation and the high vapor pressure of Se, fusion of Cu–In–Se alloys normally causes excessive agitation of the components. The Ar-filling of the tubes, however, solves this problem [13].

After fusing the metal pellets, the newly formed solid solution is annealed in a muffle furnace for up to one hour at 950 °C. To improve the homogeneity of the temperature distribution during this treatment, the silica tube is embedded in a large body of heat-resistant steel. Subsequently, the tube is cooled in air and the ingot inspected. By mechanical agitation, we detach the newly formed material and any left-over of the ingot from the tube walls, put the tube back into the muffle furnace and melt it a second time. Depending on the composition, the melting point may vary between 950 and 1020 °C. After the fusing the ingot in an induction furnace, the ingot material is removed from the quartz tubes and broken up into smaller sizes, each weighing approximately 250 mg. To confirm the homogeneity of the ingots, three separate pieces of the ingot taken from different regions of the ingot are prepared for XRD, DTA and XEDS analysis. By performing XEDS measurements the stoichiometry of the ingots are confirmed not only locally within the ingot but throughout. DTA confirms the liquidus projection, shown in Fig. 8, for any given composition.

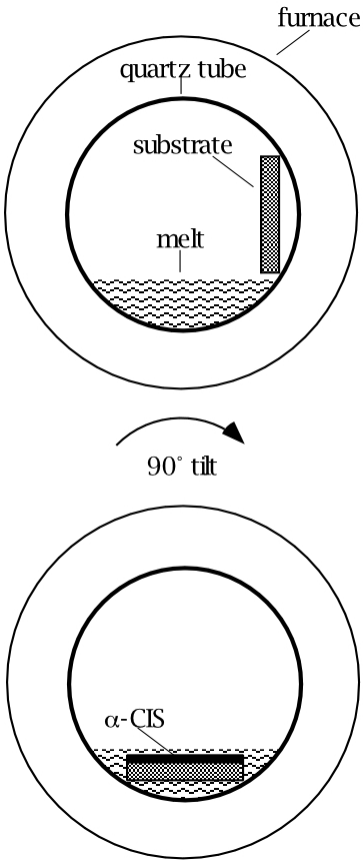

Fig. 11: Schematic cross-sectional view of the setup for liquid-phase deposition of α-CIS.

A commercial tube furnace, equipped with a large-diameter (10 cm) quartz tube and a good temperature control (± 0.5 K), serves for the actual LPD experiments. After the liquidus temperature and the composition of the ingot are confirmed, a piece of ingot, •250 mg, is loaded (along with the substrate) into another quartz tube, where the actual LPD experiment takes place (Fig. 11b). By slowly heating the furnace to a temperature between 550 °C and 1020 °C (depending on the composition of the ingot), a homogeneous melt results. Then the quartz tube is tilted by 90°, such that the melt wets the substrate. By means of an electronic temperature control, we cool the melt to a well-defined temperature somewhat (ideally about 1°) below the temperature of the liquidus surface. Accordingly, the melt will begin to precipitate α-CIS.

In the presence of the substrate, nucleation of α-CIS does not begin homogeneously, in the melt, but heterogeneously, at the surface of the substrate. Subsequently, a closed layer of α-CIS grows and

covers the substrate. After the layer has grown to the desired thickness, the quartz tube is tilted back to the original position (Fig. 11b) and the system cooled down to room temperature.

If we choose the composition of the ingot in one of the four regions of the composition triangle where Fig. 8 indicates primary crystallization of α-CIS, the above procedure should produce a thin-film of single-phase α-CIS on the substrate.

First Results

Ingots were prepared from all primary phase fields represented on the liquidus projection of the Cu-In-Se system (shown in Fig. 8). Many initial attempts to produce thin-film α-CIS failed due to the inability of the melt to wet the substrate. For this reason, we used quartz substrates sputter-coated with 1 µm of Mo, followed by 100 nm of Cu. The intention was to increase the surface energy of the Mo layer. The Cu layer, deposited after the Mo layer without breaking vacuum to the chamber, served to inhibit surface contamination on the Mo. During the liquid-phase deposition process, the Cu layer diffused into the ingot material without altering the ingot composition to any significant extent, revealing a contaminant-free Mo layer. With the incorporation of these Cu coated substrates, we were able to deposit films from all four composition fields suitable for primary precipitation of α-CIS, as indicated in Fig. 8.

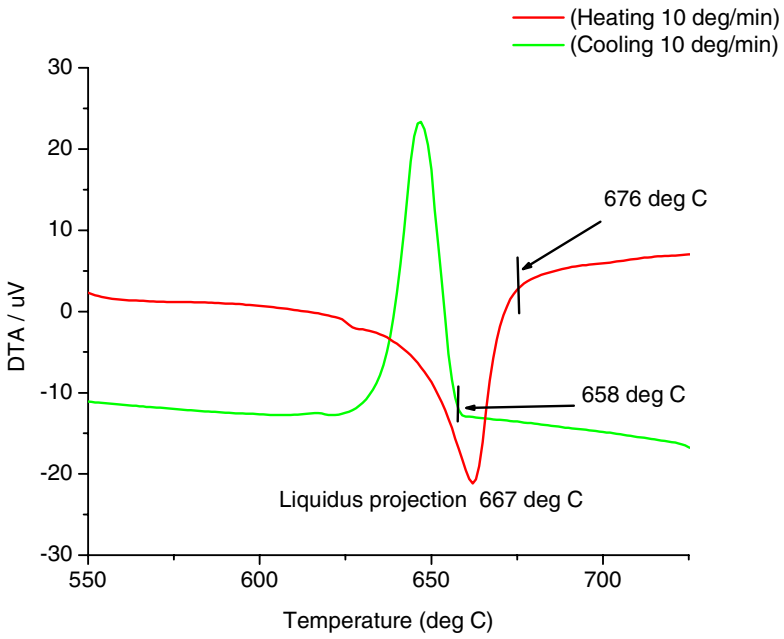

Fig. 12 DTA of ingot I1b revealing a liquidus projection of 667°C.

The liquidus projection of Fig. 8 gave us the temperature in which nucleation of α-CIS would occur. However, to confirm the exact liquidus temperature of the ingots that were fused together, DTA was employed. Fig. 12 shows the DTA plot for ingot designated I1b. From Fig. 12 the liquidus projection is found to be 667 °C. This is in good agreement with the projection given in Fig. 8. A small deviation results from making a composition up which lies slightly off one of the 700 °C contour lines.

Films from all primary phase fields of the liquidus projection were deposited. Several of the deposited films simply exhibited the composition of the ingot material – especially those from the uppermost, Se-rich composition field. The fact that no change in composition was observed indicates that the precipitation of single-phase α-CIS was not successful with these particular fields. However, several deposited films contained compositions that did reflect considerable compositional changes, indicating the precipitation of a thermodynamically stable phase. A summary of compositions of the ingots made (measured by an analytical balance and confirmed by XEDS) and the films (also measured by XEDS) are given in Table 1. From Table 1, the ingot designated I1b initially had a composition corresponding to 1:1:1 Cu:In:Se and resulted in the deposition of a film with a stoichiometry of 1:1:2.

To verify that that the stoichiometry of the film made from ingot I1b did correspond to the α-CIS phase, and not to a sum of several phases adding up to a 1:1:2 composition, XRD was utilized. Figure 13 is an XRD pattern from one of the films grown from the I1b ingot. The presence of a dominant peak at 26.6° confirms the presence of the (112) plane. This peak is the dominant peak within the spectrum as it is

Ingot	Ingot (weighed) Atomic %	Ingot Measured (EDS) Atomic %	Film Measured (EDS) Atomic %
I1a	Cu 12.0 In 47.5 Se 40.5	Cu 8.7 In 41.4 Se 49.9	Cu 4.19 In 52.69 Se 43.12
I1b	Cu 32.5 In 32.5 Se 35.0	-	Cu 24.76 In 27.10 Se 48.14
I1c	Cu 46.0 In 18.0 Se 36.0	-	Cu 59.50 In 15.58 Se 24.92
I2	Cu 55.0 In 38.5 Se 6.5	-	Cu 16.46 In 41.47 Se 42.08
I3	Cu 46.0 In 4.0 Se 50.0	Cu 45.40 In 2.66 Se 51.94	Cu 7.90 In 1.33 Se 90.77
I4	Cu 2.85 In 3.55 Se 93.6	Cu 4.46 In 2.81 Se 92.73	Cu 5.74 In 0.80 Se 93.46

Table 1 is a compilation of compositions,

given in atomic percentages, for all ingots and films.

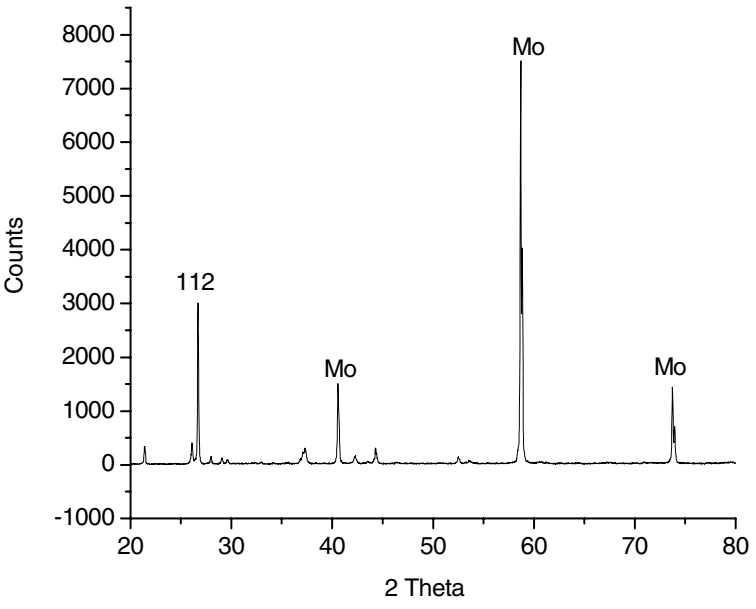

Fig. 13 XRD pattern of the LPD α-CIS from

Ingot I1b.

one the two preferred growth planes of α-CIS along with the (220) plane (not predominately present).

Conclusion

Based on the results described in the previous section, we believe that it is possible to fabricate single-phase α-$CuInSe_2$ layers with high structural and electronic quality by liquid-phase deposition (LPD). Some experimental problems of this method have been identified, such as insufficient wetting of the substrate, high viscosity of the melt below the liquidus temperature, and the necessity of a very precise temperature control. However it seems that these problems can be overcome. As the experimental techniques are further developed, we hope that LPD will become an attractive method for fabricating high-quality α-$CuInSe_2$ thin films at low cost.

References

1. A. Rockett, F. Abou-Elfotouh, D. Albin, M. Bode, J. Ermer, R. Klenk, T. Lommasson, T. W. F. Russell, R. D. Tomlinson, J. Tuttle, L. Stolt, T. Walter and T. M. Peterson: *Structure and chemistry of $CuInSe_2$ for solar cell technology: current understanding and recommendations*, Thin Solid Films 237 (1994) 1-11.

2. D. Suri, K. Nagpal and G. Chadha, J. Appl. Cryst. 22 (1989) 578-583.

3. W. Hönle, G. Kühn and U.-C. Boehnke, Cryst. Res. Technol. 23 (1988) 1347-1354.

4. J. R. Sites, J. E. Granata and J. F. Hiltner: *Losses due to polycrystallinity in thin-film solar cells*, Solar Energy Materials and Solar Cells 55 (1998) 43-50

5. NREL, www.nrel.gov.

6. J. R. Sites: *Separation of voltage loss mechanisms in polycrystalline solar cells,* in: *IEEE Photovoltaic Specialists Conference* 06160-8371 (1988), IEEE, USA, p. 1604-1607.

7. I. Dirnstorfer, W. Burkhardt, W. Kriegseis, I. Osterreicher, H. Alves, D. M. Hofmann, O. Ka, A. Polity, B. K. Meyer and D. Braunger: *Annealing studies on CuIn(Ga)Se2: the influence of gallium*, Thin Solid Films 361-362 (2000) 400-405.

8. S. Kuranouchi and A. Yoshida: *Annealing effects of CuInSe2 films prepared by pulsed laser deposition*, Thin Solid Films 343-344 (1999) 123-126.

9. S. Kuranouchi and A. Yoshida: *Annealing effects of CuInSe2 films prepared by pulsed laser deposition*, Thin Solid Films 343-344 (1999) 123-126.

10. S. Niki, I. Kim, P. J. Fons, H. Shibata, A. Yamada, H. Oyanagi, T. Kurafuji, S. Chichibu and H. Nakanishi: *Effects of annealing on CuInSe2 films grown by molecular beam epitaxy*, Solar Energy Materials and Solar Cells 49 (1997) 319-326.

11. C. R. Schwerdtfeger, T. F. Ciszek and R. Noufi, 1995, *High-Pressure, Liquid-Encapsulated Directional Solidification of Copper-Deficient Copper Indium Selenides*. Crystal Growth of Novel Electronic Materials: Proceedings of the 97th Annual Meeting of the American Ceramic Society (Cincinnati, Ohio: American Ceramic Society), p. 95-103.

12. C. R. Schwerdtfeger: *Crystal Growth of Copper-Deficient Copper-Indium-Selenides Using Computer-Controlled High-Pressure Liquid-Encapsulated Directional Solidification*, Ph. D. Thesis, National Renewable Energy Laboratory (1995).

13. M. Hornung: *Züchtung von Kristallen im System Cu–In–Se und deren mikrostrukturelle Charakterisierung*, Dissertation, Universität Freiburg (1996).

14. T. Haalboom: *Mikrostruktur und Konstitution von Kupfer-Indium-Selen-Mischkristallen für Solarzellen (Microstructure and phase equilibria of copper-indium-selenium solid solutions for solar cells)*, Doctoral Thesis, Universität Stuttgart (1999).

15. V. Lyahovitskaya, S. Richter, F. Frolow, L. Kaplan, Y. Manassen, K. Gartsman and D. Cahen: *Growth of single $CuInSe_2$ crystals by the traveling heater method and their characterization*, Journal of Crystal Growth 197 (1999) 177–185.

16. T. Gödecke, T. Haalboom and F. Ernst: *Phase Equilibria of Cu-In-Se. I. Stable States and Non-Equilibrium States of the In2Se3–Cu2Se Subsystem*, Zeitschrift für Metallkunde 91 (2000) 622-634.

17. T. Gödecke, T. Haalboom and F. Ernst: *Phase Equilibria of Cu-In-Se. II. The Cu–Cu2Se–In2Se3–In Subsystem*, Zeitschrift für Metallkunde 91 (2000) 635-650.

18. T. Gödecke, T. Haalboom and F. Ernst: *Phase Equilibria of Cu-In-Se. III. The In2Se3–Se–Cu2Se Subsystem*, Zeitschrift für Metallkunde 91 (2000) 651-662.

19. A. F. W. Willoughby: *The control of radiation resistance in space solar cells*, International Journal of Electronics 76 (1994) 865-882

20. H.-P. Trah: *Flüssigphasen-Heteroepitaxie auf Silizium-Substraten*, Ph. D. Thesis, Universität Freiburg (1988).

21. V. I. Tagirov, N. F. Gakhramanov, A. G. Guseinov, F. M. Aliev and G. G. Guseinov, Soviet Journal of Physics and Crystallography 25 (1980) 237-239.

22. H.-P. Trah: *Liquid phase epitaxy in the ternary system Si-Ge-Bi*, Journal of Crystal Growth 102 (1990) 175-182.

RECENT PROGRESS IN $CuInS_2$ THIN FILM SOLAR CELL RESEARCH AT NASA GLENN

M. H.-C. Jin, K. K. Banger, and C. V. Kelly
Ohio Aerospace Institute, Brook Park, OH 44142

J. H. Scofield
Oberlin College, Oberlin, OH 44074

J. S. McNatt, J. E. Dickman, and A. F. Hepp
NASA Glenn Research Center, Cleveland, OH 44135

INTRODUCTION

The National Aeronautics and Space Administration (NASA) is interested in developing low-cost highly efficient solar cells on light-weight flexible substrates, which will ultimately lower the mass-specific power (W/kg) of the cell allowing extra payload for missions in space as well as cost reduction (1). In addition, thin film cells are anticipated to have greater resistance to radiation damage in space, prolonging their lifetime (2). The flexibility of the substrate has the added benefit of enabling roll-to-roll processing (3).

The first major thin film solar cell was the "CdS solar cell" – a heterojunction between p-type Cu_xS and n-type CdS (4). The research on CdS cells started in the late 1950s and the efficiency in the laboratory was up to about 10 % in the 1980s (5). Today, three different thin film materials are leading the field. They include amorphous Si, CdTe, and $Cu(In,Ga)Se_2$ (CIGS) (6). The best thin film solar cell efficiency of 19.2 % was recently set by CIGS on glass (7). Typical module efficiencies, however, remain below 15 % (8).

Several groups have attempted to fabricate thin film solar cells on metal foils and polymers. Efficiencies up to 12.8 % on polyimide (9) and 17.1 % on stainless steel (10) have been reported. Polymer substrates cannot tolerate temperatures as high as those allowed by metal foils. Cell fabrication and absorber layer synthesis on polymer substrates must be accomplished at temperatures below 450 °C (11). This low-temperature constraint introduces challenges for achieving high-quality absorber layers and high-efficiency solar cells. To facilitate low temperature deposition, single-source organometallic precursors with low decomposition temperatures (< 250 °C) were synthesized and used in an aerosol-assisted chemical vapor deposition (AACVD) setup to create chalcopyrite thin films (12,13). This paper gives a brief description of the first systematic effort at NASA Glenn Research Center (GRC) to fabricate $CuInS_2$ thin film solar cells.

EXPERIMENTAL

As previously reported, $CuInS_2$ SSP, $(PPh_3)_2CuIn(SEt)_4$ was synthesized following a modified version (12) of the procedure reported by Kanatzidis (14). Because of their sensitivity to O_2 and H_2O, all reagents were handled in an argon-filled glove box. The precursor was dissolved in toluene and the solution was delivered to the heated substrate in the form of sprayed aerosol in a horizontal, atmospheric-pressure, hot-wall AACVD reactor equipped with a plate-type ultrasonic nebulizer (Sonaer Ultrasonics, 2.5 MHz). A detailed description of the film growth process with a schematic of the reactor can be found elsewhere (13,15). For this study, (112)-oriented $CuInS_2$ films were deposited using 0.01 M precursor solution under 4 L/min of Ar flow. The evaporation and hot zone temperatures were 120 °C and 395 °C respectively. Typical film thickness was around 0.7 μm and Cu/In ratio was 1.0 ± 0.1. The detailed characterizations of the films were reported previously (13,16).

The solar cell structure used in this study was Al/ZnO:F/CdS/$CuInS_2$/Mo/glass. Prior to $CuInS_2$ film growth, molybdenum (bottom metal contact) was deposited on glass substrates (Fisher catalogue no. 12-550A) at room temperature using radio-frequency (RF) magnetron sputtering. After $CuInS_2$ film was grown by AACVD, the film

was etched in 1.5 M KCN solution for 1 min at room temperature prior to the CdS chemical bath deposition (CBD). CBD was performed with a solution consisting of 0.001M $CdSO_4$, 1.5M NH_4OH, and 0.0075M thiourea. The bath was heated to 70 °C then the sample was immersed. After the CBD, the particulates on the surface of the sample were removed in an ultrasonic bath. Subsequently a ZnO:F layer was deposited from a 6.5" (16.5 cm)-diameter F-doped ZnO target in an RF sputter system. The sputter gas was pure Ar for both Mo and ZnO:F deposition. Following ZnO:F growth, a 0.2 μm thick Al top metal contact was deposited by thermal evaporation through a shadow mask. The cell area was defined by mechanical scribing after Al deposition with a typical cell area of 0.4 cm^2. A solar simulator at GRC (Spectrolab X-25 Mark II) was used to characterize the solar cells under AM0 radiation, calibrated using either a standard GaAs single-junction cell or a Si single-junction cell.

In order to validate the fabrication procedure, a chalcopyrite thin film deposited by physical vapor deposition (PVD) on Mo-coated glass substrate was acquired and a solar cell was fabricated through the same procedure described. In an effort to improve the cell performance, GRC collaborated with Oberlin College to try a double window layer scheme (n-type ZnO/intrinsic ZnO) after CdS deposition. In addition, a Ni/Al double metal top contact was also used instead of a single Al contact. The intrinsic and the Al-doped ZnO layers were deposited using a reactive DC magnetron sputter process (Sloan) in a mixture of O_2 and Ar gases. The Ni was evaporated from an alumina-coated tungsten boat and the Al from a single-hearth e-gun (Sloan) mounted in a 24-in. diffusion-pumped bell jar. The GRC and Oberlin cell structures are illustrated in Figure 1.

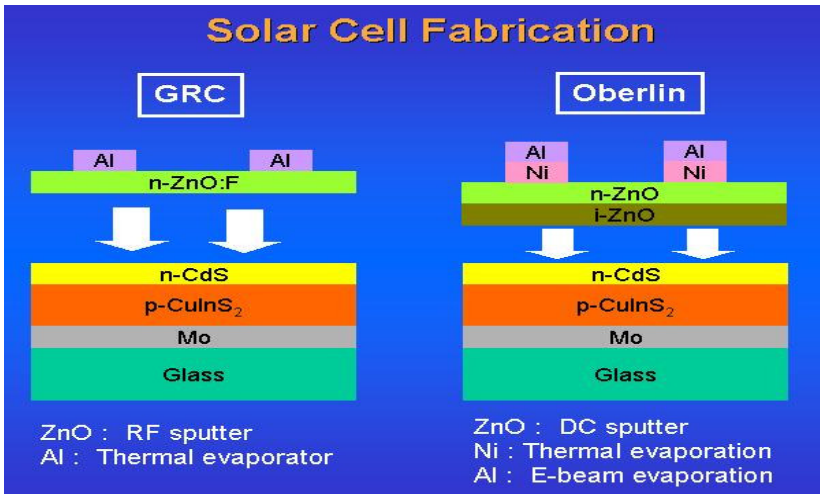

Figure 1. Schematic of the solar cell structures made at GRC and Oberlin College.

The film thickness was determined using a profiler (Sloan Dektak IIA) and the optical transmittance was measured by a UV/VIS spectrophotometer (Perkin-Elmer Lamda-19). The electrical measurements were performed with a four-point probe system (Bio-Rad HL5500PC) operated in the Van der Pauw configuration. For the CdS film, X-ray diffraction (XRD) (PANalytical X'Pert Pro) was used to identify phases and glancing-angle X-ray diffraction (GAXRD) was further performed to probe phases in the film and on the surface of the film separately.

RESULTS AND DISCUSSION

The surface resistance of Mo bottom contact was about 0.5 ohm/sq. with a typical thickness of 0.7 μm. XRD confirmed that the Mo had a body-centered cubic phase with a (110) texture showing the strongest diffraction at $2\theta = 40.5°$. The optical transmittance of CBD-grown CdS was 65 % at a photon energy of 1.5 eV and it had a strong signature of cubic phase with CdO as an impurity phase (Figure 2). GAXRD confirmed that the CdO phase was present both in the bulk and the surface of the film (not shown). There have been many reports regarding secondary phase formation including CdO in the CdS CBD (17,18), but no XRD was reported to support the CdO formation in as-deposited CdS prepared by CBD. A typical 1 μm-thick GRC n-type ZnO:F layer had a sheet resistance of about 200 ohm/sq and a transmittance of 85 % at a photon energy of 1.5 eV. In comparison, a 560 nm thick n-type ZnO layer deposited at Oberlin College had a sheet resistance of about 46 ohm/sq. with a transmittance of about 70 % at a photon energy of 1.5 eV. The transmittance of the 70 nm thick intrinsic ZnO was

over 90 % at photon energy of 1.5 eV and the sheet resistance of the double window layer, n-ZnO/i-ZnO was about 200 ohm/sq. Typical thickness of single Al top contact deposited at GRC was about 700 nm and the sheet resistance of the double top contact layer (2 µm Al/50 nm Ni) made was about 0.18 ohm/sq.

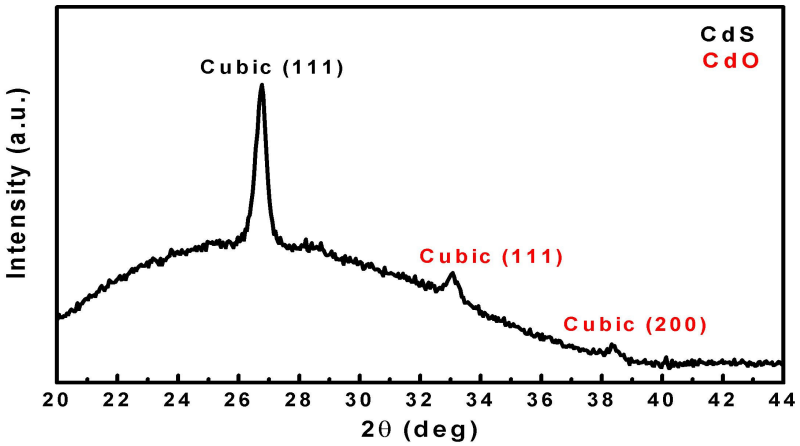

Figure 2. XRD of CdS film deposited by chemical bath deposition.

Figure 3 shows the characteristics of the reference solar cells completed with both the GRC and Oberlin College window/contact layers. The chalopyrite absorber layer deposited by PVD was used for this validation process of the device fabrication at GRC. The AM0 efficiencies of 5.3 % and 6.7 % were obtained with minimum device optimization. The use of intrinsic ZnO and Ni/Al top contact layers, which is known to improve the quality of this type of solar cell (6), lowered the series resistance and improved the fill factor (FF) as shown in the Figure 3. Although the short circuit current (I_{sc}) was comparable to that of any other reported chalcopyrite solar cells (7,8), open circuit voltage (V_{oc}) and FF have to be further improved. Further optimization of the fabrication process will be performed in the future.

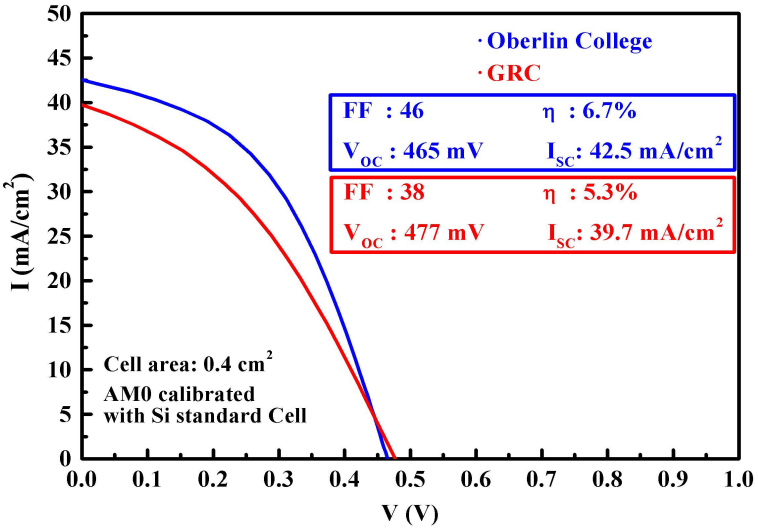

Figure 3. Characteristics of the reference solar cells made at GRC and Oberlin College.

A solar cell with a structure of Al/ZnO:F/CdS/$CuInS_2$/Mo/glass was fabricated with a $CuInS_2$ thin film deposited by AACVD at GRC and its output characteristics were shown in Figure 4. The cell had both low shunt resistance and high series resistance. The intrinsic ZnO and Ni/Al top contact will be incorporated for further improvement in the future. In addition, further increase of $CuInS_2$ film thickness from 0.7 µm should minimize the optical loss. It should be noted that the best efficiency reported for a solar cell prepared from AACVD-made $CuInS_2$ was 2.66 % (20). However, the cell had a superstrate structure – Cd(Zn)S was deposited on the glass substrate first and light

passes through from the glass side - and there was no report of a working device with a typical chalcopyrite solar cell structure, CdS/$CuInS_2$ except for the authors' previous results (13).

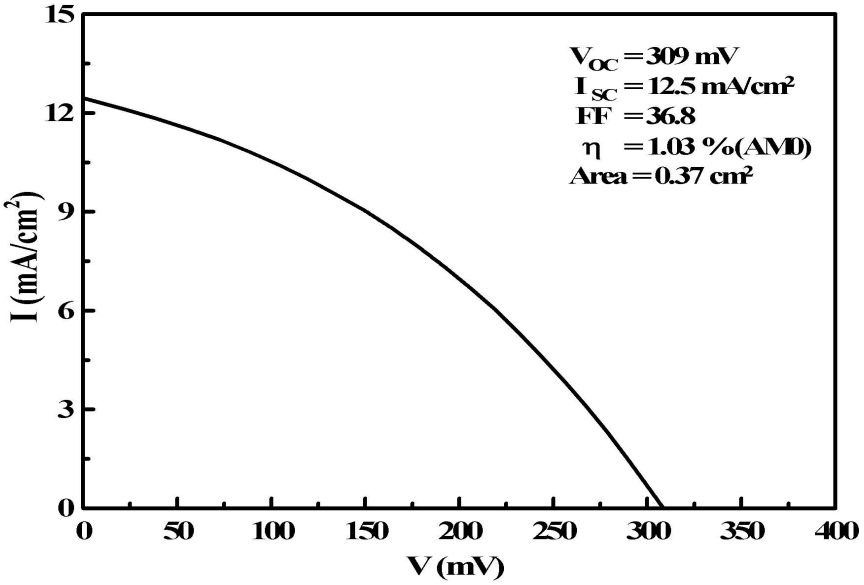

Figure 4. Characteristics of the $CuInS_2$ solar cell made at NASA GRC.

CONCLUSION

Chalcopyrite solar cell fabrication process has been established at NASA GRC. A reference solar cell with a cell structure of Al/ZnO:F/CdS/$CuInS_2$/Mo/glass was fabricated and an efficiency of 5.3 % under AM0 illumination was achieved. Further improvement was made by incorporating an intrinsic ZnO layer and Al/Ni top metal contact at Oberlin College, increasing the efficiency up to 6.7 %. The series resistance and fill factor were clearly improved. In addition, GRC has fabricated $CuInS_2$ thin films solar cells prepared from AACVD using the single source precursor, $(PPh_3)_2CuIn(SEt)_4$. Although the solar cell performance still needs to be improved, I_{sc} and FF were better than results reported previously (13). The major loss was due to the low V_{oc} and it remains as a challenge, which has been observed in solar cells prepared with AACVD deposited films (19,20).

REFERENCES

(1) D. J. Hoffman, T. W. Kerslake, A. F. Hepp, M. K. Jacobs, and D. Ponnusamy, "Thin-Film Photovoltaic Solar Array Parametric Assessment," *Proc. of the AIAA 35th Intersociety Energy Conversion Engineering Conference*, pp. 670-680, Las Vegas, NV, 2000.

(2) V. K. Kapur, M. Fisher, and R. Roe, "Fabrication of Light Weight Flexible CIGS Solar Cells for Space Power Applications," *Mat. Res. Soc. Symp. Proc.*, **668**, pp. H3.5.1-H3.5.6, 2001.

(3) G. M. Hanket, U. P. Singh, E. Eser, W. N. Shafaran, and R. W. Birkmire, "Pilot-scale Manufacture of Cu(InGa)Se_2 Films on a Flexible Polymer Substrate," *Proc. of the 29th IEEE Photovoltaic Specialists Conference*, pp. 567-570, New Orleans, LA, 2002.

(4) A. Rothwarf and A. M. Barnett, "Design analysis of the thin-film CdS-Cu_2S solar cell,"*IEEE Trans. Electron Devices*, **ED-24**, pp. 381-387, 1977.

(5) R. B. Hall, R. W. Birkmire, J. E. Phillips, and J. D. Meakin, "Thin-film polycrystalline $Cu_2S/Cd_{1-x}Zn_xS$ solar cells of 10% efficiency," *Appl. Phys. Lett.*, **38**, pp. 925-926, 1981.

(6) M. D. Archer and R. Hill, "Clean Electricity from Photovoltaics," Imperial College Press, London, 2001.

(7) K. Ramanathan, M. A. Contreras, C. L. Perkins, S. Asher, F. S. Hasoon, J. Keane, D. Young, M. Romero, W. Metzger, R. Noufi, J. Ward, and A. Duda, "Properties of 19.2% Efficiency ZnO/CdS/$CuInGaSe_2$ Thin-film Solar Cells," *Prog. Photovolt: Res. Appl.*, **11**, pp. 225-230, 2003.

(8) K. Kushiya, "Progress in Large-area Cu(InGa)Se2-based Thin-film Modules with the Efficiency of over 13%," *Proc. of the 3rd World Conference on Photovoltaic Energy Conversion*, 2PL-C1-02, Osaka, Japan, 2003.

(9) A. N. Tiwari, M. Krejci, F. J. Haug, and H. Zogg, "12.8% Efficiency Cu(In,Ga)Se_2 solar cell on a flexible polymer sheet," *Prog. Photovolt: Res. Appl.*, **7**, pp. 393-397, 1999.
(10) M. Contreras, B. Egas, K. Ramanatan, J. Hiltner, F. Hasoon, and R. Noufi, "Progress toward 20% efficiency in Cu(In,Ga)Se_2 polycrystalline thin-film solar cells," *Prog. Photovolt: Res. Appl.*, **7**, pp. 311-316, 1999.
(11) F. Kessler, K. Herz, M. Powalla, M. Hartmann, M. Schmidt, A. Jasenek, and H. W. Schock, "Flexible and monolithically integrated CIGS-Modules," *Mat. Res. Soc. Symp. Proc.*, **668**, pp. H3.6.1-H3.6.6, 2001.
(12) K. K. Banger, J. Cowen, and A. F. Hepp, "Synthesis and Characterization of the First Liquid Single-Source Precursors for the Deposition of Ternary Chalcopyrite ($CuInS_2$) Thin Film Materials" *Chem. Mater.*, **13**, pp. 3827-3829, 2001.
(13) J. D. Harris, K. K. Banger, D. A. Scheiman, M. A. Smith, M. H.-C. Jin, and A. F. Hepp, "Characterization of $CuInS_2$ films prepared by atmospheric pressure spray chemical vapor deposition," *Mat. Sci. & Engr.*, **B98**, pp. 150-155, 2003.
(14) W. Hirpo, S. Dhingra, A. C. Sutorik, and M. G. Kanatzidis, "Synthesis of Mixed Copper-Indium Chalcogenolates. Single Source Precursors for the Photovoltaic Materials $CuInQ_2$ (Q = S, Se)," *J. Am. Chem. Soc.*, **115**, pp. 1597-1599, 1993.
(15) J. A. Hollingsworth, K. K. Banger, M. H.-C. Jin, J. D. Harris, J. E. Cowen, E. W. Bohannan, J. A. Switzer, W. E. Buhro, and A. F. Hepp, "Single source precursors for fabrication of I-III-VI_2 thin-film solar cells via spray CVD," *Thin Solid Films*, **431-432**, pp. 63-67, 1993.
(16) M. H.-C. Jin, K. K. Banger, J. D. Harris, and A. F. Hepp, "The Effect of Film Composition on the Texture and Grain Size of $CuInS_2$ Prepared by Chemical Spray Pyrolysis," *Mat. Res. Soc. Symp. Proc.*, **763**, pp. B8.23.1-B8.23.6, 2003.
(17) P. J. Sebastian and H. Hu, "Identification of the Impurity Phase in Chemically Deposited CdS Thin Films," *Adv. Mater. Opt. Electron.*, **4**, pp. 407-412, 1994.
(18) T. Nakada, H. Fukuda, A. Kunioka, and S.Niki, "XPS analysis of chemically deposited CdS films on polycrystalline CIS surface and glass substrates," *Proc. of the 13th European Photovoltaic Solar Energy Conference*, pp.1597-1600, Nice, France, 1995.
(19) P. R. Ram, R. Thangaraj, A. K. Sharma, and O. P. Agnihotri, "Totally sprayed $CuInSe_2$/Cd(Zn)S and $CuInS_2$/Cd(Zn)S solar cells," *Solar Cells*, **14**, pp. 123-131, 1985.
(20) O. Kijatkina, M. Krunks, A. Mere, B. Mahrov, and L. Dloczik, "CuInS2 sprayed films on different metal oxide underlayers," *Thin Solid Films*, **431-432**, pp. 105-109, 2003.

A SILICONE/POSS COATING FOR THIN FILM SOLAR CELLS AND CONCENTRATORS

Henry W. Brandhorst[1], Mark J. O'Neill[2] and Joseph D. Lichtenhan[3]
[1]Space Research Institute, Auburn University, [2]ENTECH, Inc., [3]Hybrid Plastics, Inc.

Introduction:

Significant effort has been devoted to the development of thin film solar cells for use in space. One of the reasons for this enthusiasm is based their exceptional resistance to bombardment by electrons and protons of various energies in the laboratory. This resistance is due in part to their structure and in part to their inherent performance mechanisms. Unfortunately, laboratory testing is limited to a few energies of both electrons and protons. The energies and doses do not correspond well to those found in space. In space of course there is a spectrum of particle energy of both protons and electrons as well as a wide range of fluences as functions of particle and energy. In general, the test results to date do not include very low energy protons due to facility limitations. Because all solar cells including thin film cells are seriously affected by ionizing radiation that is absorbed in their junction region it is important to shield against these highly damaging particles. The protons are the most damaging due to their greater mass and they leave a large ionization trail.

In the past, many have believed that the antireflection coating and/or the transparent conducting oxide layers on the surface of thin film cells would provide protection against this spectrum of ionizing radiation. However, from many laboratory tests using very low energy particles and from the earliest tests of unshielded GaAs cells in space, it is clear that additional protection will be needed if thin film cells are to withstand the rigors of the earth orbital environment. The potential solution of using the traditional rigid cover glass is not desirable for at least two reasons: they are heavy and they are not flexible. Both these factors will reduce or eliminate the advantage of thin film cells in space compared to crystalline cells. The desired coating must be flexible, it must be resistant to atomic oxygen for low earth orbits below about 700 km and it must be resistant to ultraviolet radiation for all earth and near-sun orbits and, of course, it must withstand the damaging effects of space radiation.

These same attributes of the protective layer are directly applicable to the Stretched Lens Array (SLA) developed by ENTECH, Inc. and Able Engineering. The SLA has demonstrated array specific masses of 180 W/kg for arrays sized to 7 kW and the potential exists to increase that impressive value by at least twofold. Because it is a concentrator system, the cells can be protected against radiation with a cover glass. However, the stretched lens must also be flexible and still survive the damaging effects of ultraviolet light, atomic oxygen and space radiation. The lens is made from DC 93-500 silicone material which is also used to secure cover glasses to the cells.

Building on this experience, one material that has many of the desired attributes of a universal protective coating is the Dow Corning silicone resin DC 93-500. Of all the potential optical plastics, it appears to be the most suitable for use in space. As noted above, DC 93-500 has been extensively used to attach cover glasses to crystalline solar cells and has worked exceptionally well over the years. It is flexible and generally resistant to electrons, protons and ultraviolet (UV and VUV) radiation; although a VUV-rejection coating or VUV-absorbing ceria-doped cover glass may be required for long mission durations. It can also be applied in a thin coating (< 25 μm) by conventional liquid coating processes.

Unfortunately, when exposed to atomic oxygen (AO) DC 93-500 tends to develop a frosty surface. Such frosting can lead to a loss of light transmitted into the cells and destroy the essential clarity needed for a concentrator. The damage also erodes the surface and hence to an ultimate failure as a radiation protective coating. This

frosting would be exceptionally harmful for lenses used in a concentrator application. Therefore, solving the protection problem for thin film solar cells may also provide the solution for the stretched lens and vice versa.

A New Option:

A new class of materials has recently been discovered during the search for improvements in optical plastics. This class of materials may eliminate the limitation of DC 93-500. These new polymeric building block materials are called "polyhedral oligomeric silsequioxalanes" and were developed by the Air Force Research Laboratories at Edwards Air Force Base in 1998. The technology is exclusively manufactured by Hybrid Plastics Inc. (Fountain Valley, CA) and is being marketed under the name of POSS® nanocomposites. This technology has several significant advantages that are relevant to solar cell use. The glass-like composition of POSS provides excellent resistance to UV and much reduces or eliminates degradation by atomic oxygen. POSS nanobuilding blocks can be incorporated into all known plastics using conventional polymerization or compounding techniques to afford tailorable optically transparent materials with and entirely new performance levels.

POSS® building blocks contain hybrid (organic-inorganic) compositions in which the internal frameworks are comprised primarily of inorganic silicon-oxygen bonds. As shown in figure 1, the exterior of the nanostructure is covered by both reactive and non-reactive organic functionalities (–R) which ensure both compatibility and tailorability of the nanostructure with organic polymers. The resulting nanoscopic chemicals have low density, range in diameter from 0.5 to 3 nm and can be tailored through variation in the –R groups and the size of the nanocage reported by Gilman[1] and more extensively by Gonzalez[2], the molecularly dispersed POSS readily forms a passivating silica layer when attacked by atomic oxygen. This layer in turn protects the virgin material from degradation. Furthermore, the silica-like composition of POSS provides enhanced UV and VUV resistance. The UV and VUV resistance provided by POSS can even be enhanced further through replacement of metals like Ce for the silicon atoms at the vertices in the nanocage.

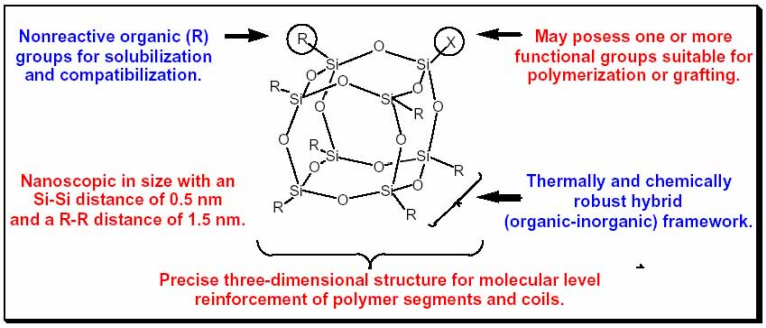

Figure 1: Anatomy of a POSS® nanostructured® chemical

Previous Experimental Results:

Siloxanes (e.g. DC 93-500) are generally considered stable under photo-aging or photo-oxidation conditions. Although they can protect underlying material from oxidation, they do not significantly absorb incident UV radiation, especially if they are alkyl-substituted siloxanes. A related class of materials that are more highly oxidized and thereby more stable to oxidation and UV are silsesquioxanes. Previous research has shown that chemical manipulation of the organic groups surrounding the POSS cage enables dispersion of POSS nanostructures throughout the a polymer matrix at high POSS loadings via blending and co-polymerization techniques.[3] The 1nm level of dispersion attainable with POSS is controlled by the free energy of mixing equation $\Delta G = \Delta H - T\Delta S$.[4] Where the enthalpic ΔH term for POSS dispersion is controlled by the chemical compatibility of the R groups on the POSS nanostructure with the resin along with associated polymer-POSS interactions. The entropic ΔS term for POSS dispersion is always favorable for dispersion because of the monodisperse cage size of POSS. Note this is not the case for the dispersion of a polymeric resin because it is already a dispersion of molecules.

POSS based siloxane copolymers have been explored for use as LEO-resistant coatings (Figure 2).

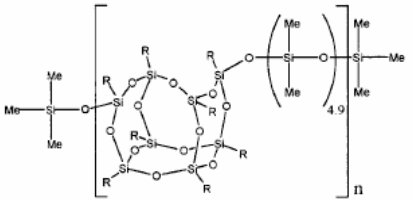

Figure 2: POSS-siloxane copolymers.

Evaluation of the resistance of the POSS-siloxane copolymer to a simulated LEO environment was conducted under exposure to atomic oxygen with and without far-UV radiation. XPS analysis revealed that the surface of the copolymer samples became silicon- and oxygen-rich after exposure to atomic oxygen with and without far-UV radiation. The results shown in Table 1 indicate that the POSS-siloxane copolymer has excellent resistance to the simulated LEO environment and actually gained weight during the exposures. The slight increase of weight is attributed to the loss of surface organics and formation of a passivating silica surface layer. Combining far-UV radiation with atomic oxygen does not appear to significantly change the results.

Table 1: Exposure conditions and mass changes before and after exposure

Exposure Conditions	Far-UV Intensity (mW/cm^2)	Total Fluence ($0\ atom/cm^2$)	Net Mass Change (mg/cm^2)
Atomic oxygen	0	4.3×10^{21}	+ 0.01
Atomic oxygen and far-UV	15 (7 earth suns)	4.3×10^{21}	+ 0.02

A comparative SEM analysis of the exposed and unexposed POSS-siloxane copolymer samples, shown in Figure 3, reveals an interesting change in the surface morphology. The surface defects or microcracks in Figure 4(a), resulting from sample preparation, were completely "healed" by exposure to the atomic oxygen beam [Fig. 4 (b) 1. This is in contrast to the results from the Long Duration Exposure Facility (LDEF) experiment where all siloxane-coating samples showed extensive microcracking, frosting, and oxidation of underlying organic polymeric material due to penetration of A0 through the microcracked coating. We believe that this self-healing nature is a direct result of POSS compatibility and dispersion throughout the polymer matrix. This annealing phenomenon may be from surface heating, both from the heat of reactions and from absorption of the kinetic energy (2-3 eV) of the atomic oxygen. Such behavior provides a significant advantage for these materials since microcracking exposes a coated surface to the LEO environment and to accelerated degradation and contributes to loss of long-term durability for composites used in space. If the glassy silica layer erodes or suffers a microdefect, it would quickly reform due to the uniform POSS dispersion. Furthermore retaining optical characteristics is a great advantage – even a necessity – for solar arrays.

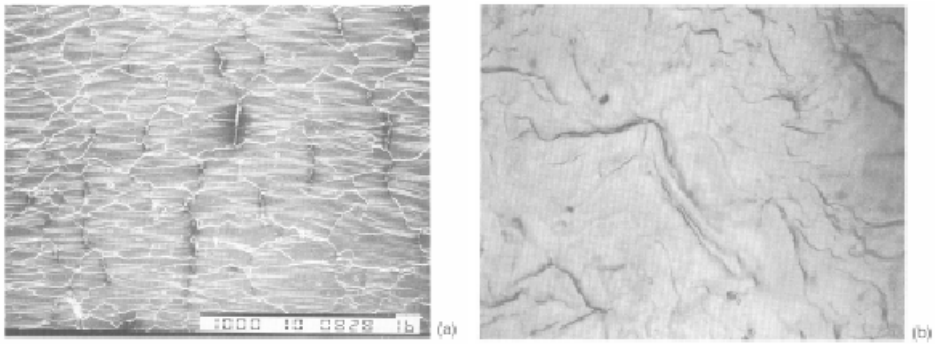

Figure 3: SEM of (a) unexposed and (b) exposed POSS siloxane copolymer surfaces. The simulated LEO exposure has "healed" the microcracks present initially in the POSS-siloxane sample.

Approach:

In this new effort, we plan to improve the UV/VUV and AO resistance of DC 93-500 for both thin film solar cell and concentrator applications using two approaches. First we will incorporate an all-silicon containing POSS material to confirm a modest improvement in UV, VUV, and AO resistance with adequate flexibility and secondly, we will incorporate a Ce-containing POSS to confirm leapfrog-type advancements in VUV and UV stability. The above approaches will maintain the current manufacturing protocols used for DC 93-500. Typical materials are shown in Figure 4.

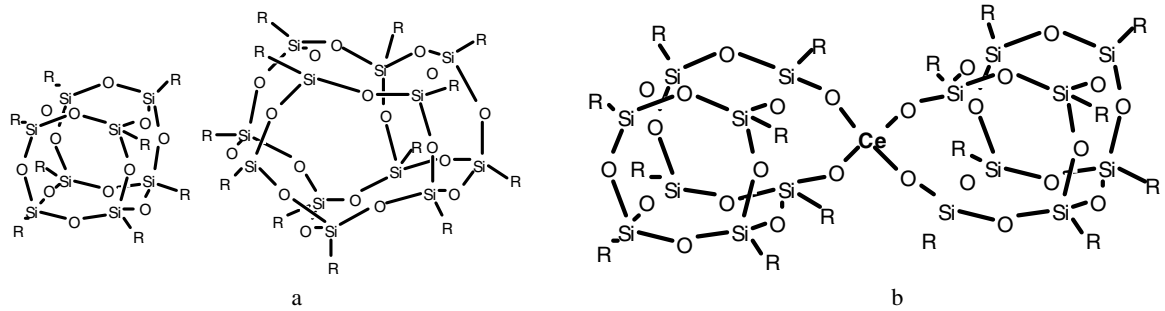

Figure 4: (a) 1.5nm diameter ocatmeric and dodecameric all Silicon POSS additives bearing aromatic R groups suitable for UV absorption (b) A Cerium containing POSS additives for maximum UV absorption.

Incorporating POSS into DC 93-500 will be conducted using a narrow range of POSS systems that show particular promise and compatibility with this resin. Both silicon-only and Ce-containing POSS systems will be explored. In this effort, ENTECH, Inc. will conduct all molding, and testing work to determine the suitability of these materials for use in the SLA concentrator lens materials. Hybrid Plastics, Inc. will conduct all formulation development and fundamental materials characterization. The Space Research Institute will evaluate the use as coatings as thin films.

Variables to be included in the compounding approach will be the composition and the loading level for the POSS systems. These will be evaluated in DC 93-500 in the form of films, test plaques or bars or other appropriately sized specimens for screening and characterization relative to the baseline resins. Specific characterization testing will be conducted relative to clarity, thermal transition heat distortion, abrasion resistance and moldability. Initial screening will be based on optical transparency. A down-select to at least three baseline formulations will be conducted and these will be evaluated with respect to the remaining criteria.

Conclusions:

We are embarking on an entirely new approach for protecting solar cell arrays against UV and VUV radiation and atomic oxygen. If successful, this will lead to a major change in the solar array industry.

References:

1. J.W. Gilman, D.S. Schlitzer and J.D. Lichtenhan, *"Low Earth Orbit Resistant Siloxane Copolymers"*, J. Appl. Polymer Sci. 60, 591-596 (1996)
2. R.I. Gonzalez S.H. Phillips and G.B. Holland, *"In Situ Oxygen-Atom Erosion Study of Polyhedral Oligomeric Silsesquioxane-Siloxane Copolymer"*, J. Spacecraft and Rockets, 37, #4, 463-467, (2000)
3. J. D. Lichtenhan, J. J. Schwab, W. A. Reinerth *"Nanostructured Chemicals: A New Era in Chemical Technology,"* Chemical Innovation January 2001 pp 3-5. (http://pubs.acs.org/subscribe/journals/ci/31/special/0101lead.html)
4. W. Zhang, B. X. Fu, Y. Seo, E. Schrag, B. Hsiao, P. T. Mather, N-L. Yang, D. Xu, H. Ade, M. Rafailovich, and J. Sokolov **"**Effect of Methyl Methacrylate/Polyhedral Oligomeric Silsesquioxane Random Copolymers in Compatibilization of Polystyrene and Poly(methyl methacrylate) Blends", *Macromolecules* 35*,* 8029-8038 (2002).

Future Directions for Thin Films in Space Workshop at SPRAT XVIII

Aloysius F. Hepp and John E. Dickman
NASA Glenn Research Center
Photovoltaic and Space Environments Branch
Cleveland, OH 44135

Overview

For approximately ten years, the SPRAT conference series at NASA Glenn (formerly Lewis) Research Center has devoted a workshop to the topic of thin-film solar cell technology and its potential for space applications. While thin-film materials have been investigated for a number of years, including copper sulfide research at NASA in the 1960's, there has been a re-birth of interest in this class of materials for space applications in the past dozen years or so. There are several reasons for this renaissance. An important contributor is efficiency improvements beyond ten percent. Another contributor is the increase in interest represented by funding opportunities by NASA and several agencies in the U.S. Department of Defense (Missile Defense Agency, Air Force, and DARPA). Finally, there have been several intriguing missions identified through various means, these include: station-keeping for high-altitude airships, space solar power, planetary surface power, and solar electric propulsion. To aid in leading the discussion for this workshop, a series of seven questions were posed. These are reproduced below as well as a summary of key points and conclusions from the workshop as well as an attendees list and results of an informal poll related to long-term potential of thin films for space.

Workshop Discussion Questions

1 – Will thin film PV (for space) always be the technology of the future?

2 – Polycrystalline thin film materials co-exist with polymer? Quantum dots? Poly III-V?

3 – How do metal and polymer substrates compare for I-III-VI_2 arrays? Array interconnects?

4 – Effect of operating temperatures (space environment) on TFPV? Self-annealing?

5 – How far can we push polymers? Are there inherent efficiency limiters? Sodium? Deposition/processing temperature? Do we need new balance of system technologies?

6 – Optimal deposition methods? Important device components? Multi-junction structures?

7 – Specific missions for TFPV? Large area? Surface operations? Integrated power? DOD-related missions? Air Force? Commercial?

Issues Raised During Discussions

- Four space PV companies (Sharp; RWE; Emcore; and Spectrolab) but none that focus on TF cells
- Only TF cells (not arrays) have been flown; TF cells shown to be radiation hard
- Question: is radiation hardness a function of low efficiency? Or is it the fact that there is not very much material for reactions to take place
- Difficult to find suppliers for polymer substrates (low volume for applications) most likely will be a small company
- TF development can't rely on literature and research foundation like Si and III-V materials; the basic physics has not yet been developed
- Thin-film development will most likely require government funding; IRAD will not be sufficient for long-term development

Key Conclusion(s) Derived from Discussions

- The prevailing view is that CI(G)S must be deposited on polymer substrates to be a competitive technology
- Thin film on polymer must have an efficiency of at least eight percent AM0 for a large area
- Array technology that is developed must be revolutionary and developed in parallel with cell technology

Acknowledgements

We would like to acknowledge the excellent support of our peerless administrative assistant, Mrs. Barbara Madej, during SPRAT XVIII and the follow-on *Third Conference on Thin Film and Nano- Materials for Energy Conversion and Storage*. Her cheerful disposition, efficiency, and professionalism turned a burdensome commitment into a pleasant undertaking!

Informal Survey

- The workshop attendees were asked an unscientific survey question: **Are you optimistic about the long-term prospects for thin-film technology for space power?**

- **Results:** Yes – 58% No – 21% Uncertain – 21%

SPRAT Workshop: Nanostructures for Solar Cells
Ryne P. Raffaelle, Chair

The workshop on nanostructures for solar cells focused on a discussion of a few of the general features associated with 0-dimension (quantum dots), 1-d (quantum wires), and 2-d (multiple quantum wells) approaches to photovoltaics developments. A particular focus of the discussion was directed toward the features of these quantum confined structures which may be particularly useful in the development of space photovoltaics. After the identification of general features, their examination, and discussion of their utility the next phase of the workshop was to try and identify the best prospects for near, mid, and far term developmental efforts.

The general features associated with nanostructured solar cells which were discussed are listed below.

General Features
Spectrum Shifting Applications
Minibands/Hot Carrier Transport
Multi-Photon Processes
Exciton Disassociation in Polymers

During the discussion of these general features there were several important considerations and possible advantages identified. In addition to the sub-gap absorption in the well region of a MQW solar cell, the increase in oscillator strengths really allow the I region of the cell to do most of the necessary absorption. This allows the host layers to be very thin to improve radiation tolerance. This was considered to potentially a very important advantage in developing future space solar cells. In addition, they can be more heavily doped to assist in collection and photovoltage.

The problems associated with transport in nanostructured solar cells received quite a lot of discussion. The consensus was that fast carrier extraction and long-lived states would be extremely important in order to avoid the deleterious the recombination and photoluminescence. A strong field across the MWQ region would be essential.

The discussion over the fundamental aspects of nanostructured cells brought up some of the controversy surrounding the reported global efficiencies of various nanotechnological approaches to photovoltaic development. The debate over global efficiency improvements with nanostructures involves much in the way of theory and conjecture and some of the finer points aren't necessary to analyze real cells, and have little to do with relative performance enhancement or ancillary advantages of using nanostructures. Therefore the discussion at the workshop focused on pragmatic approaches and relative improvements with once again a particular focus on ancillary advantages for space usage.

A comparison was made between a QD approach as opposed to a MQW approach to cell development. It was agreed that at this point it is clear that especially in terms of solar cells, MQWs are a much more mature technology that QDs. The possible decrease in

thermalization due to more confinement and two-photon processes which are theoretically possible in the QD approach have not yet been established to the extent that bandgap shifting and transport in MQWs has. The absorption hit that the quantum dot approach will take needs to be overcome by these other positive attributes before relative improvements are established.

After discussing many of the salient features of nanostructured solar cells, attention was focused of realistic implementation schemes and timeframes under which these schemes could be accomplished. Based on this discussion several near, mid, and far term prospects were identified and the workshop was concluded. The prospects for nanostructured solar cells development resulting from the workshop are summarized below.

Near Term

MQW solar cells already can be made thinner than their single junction counterparts due to their enhanced absorption (less weight) and are more radiation tolerant and defect tolerant in general. Temperature coefficients are also better due to decreased thermalization and hot-carrier transport.

Nanostructures have already been shown to expand the crystal growers palette (i.e., 0.1 to 0.2 eV shift in absorption edge in a strain-balance MQW for III-Vs). This technology is ready for integration into multi-junction cells for improving the current limiting junction. This approach can provide a rather large photocurrent increase with only a small photovoltage penalty.

Significant improvement in polymeric solar cell efficiency is possible through the introduction of nanomaterials.

Mid Term

Use of quantum dots as up-converts could improve conversion efficiency in a wide variety of devices and concentrators. Amorphous silicon multi-junction is a technology that could potentially reap much benefit from this approach. The available materials systems need to be expanded. Some narrow gap and high electron affinity material system would be attractive. In addition, the two-photon processes need to be critically examined.

Far Term

Single junction intermediate band solar cells (IBSC) with efficiency which can exceed even the best triple-junction cells of today.

Advanced Solar Cell Testing and Characterization

SPRAT Workshop Summary

Chaired by:
Sheila Bailey, Henry Curtis
and Michael Piszczor

The topic for this workshop stems from an ongoing effort by the photovoltaic community and U.S. government to address issues and recent problems associated with solar cells and arrays experienced by a number of different space systems. In April 2003, a workshop session was held at the Aerospace Space Power Workshop to discuss an effort by the Air Force to update and standardize solar cell and array qualification test procedures in an effort to ameliorate some of these problems. The organizers of that workshop session thought it was important to continue these discussions and present this information to the entire photovoltaic community. Thus, it was decided to include this topic as a workshop at the following SPRAT conference.

The Advanced Solar Cell Testing and Characterization Workshop was divided into two areas of discussion. The first topic focused on the Air Force effort to standardize qualification and testing procedures. Brad Reed from the Aerospace Corporation has led the Air Force effort and was invited to lead that portion of the workshop. After that discussion, Sheila Bailey discussed recent progress in test procedure guidelines at the international level.

Brad Reed started the first part of the workshop with a short talk on the rationale behind the Air Force push to establish standardized test procedures. He noted that the Aerospace Corporation, under direction from the Air Force, is engaged in a project to create military-specifications for inclusion in future Air Force RFPs. He explained that this initiative was borne out of an investigation of recent on-orbit and ground performance problems with military and commercial "space-qualified" solar arrays.

In support of this project, Aerospace is submitting a proposed set of qualification tests to the industry for comment. A preliminary version of these proposed tests were discussed during the workshop and are included in the following three tables. The tables address two primary areas: 1) combined effects testing for solar cell and/or solar panel coupons and 2) accelerated life testing for solar cells for the purpose of determining reliability.
The discussion during the workshop session proceeded to address the individual points in the tables, with a focus on soliciting comments/improvements to the proposed guidelines from the workshop participants. Specifically, input was being sought on:

1. Appropriateness of the tests.
2. Acceptability of the test procedures and standards to the space photovoltaic community.
3. Suggestions for new tests that would enhance the qualification process.
4. Data that could be included by the solar cell manufacturers to enhance the design process.

Brad concluded the discussion by noting that further input from the community would be solicited and this process would continue.

Solar Cell Qualification Test

Environment/Reason	Level	Test Procedure	Test Condition	Criteria/Report
1. Weld or Solder Joint Qualification	Cell	Forward and Reverse Dark Electrical Characterization	28C, sample size determined by TBD	Build Cell to manufacturer's specification and record process
		Weld or Solder Interconnect		Per Manufacturer's Weld or Solder Schedule
		Forward and Reverse Dark Electrical Characterization	28C	Measure 10x
		Reverse Bias	Dark Reverse Bias @ 2.0 V for 10 Seconds @ 80C	
		Forward and Reverse Dark Electrical Characterization	28C	Measure 10x
		NDE of Weld or Solder Joints		
		Pull Test	Pull at 45 degrees	
		100% DPA		Evaluate weld or solder interface micro structure
2. Pre-Launch and On-Orbit Degradation or Failure	2 Coupons with Bypass Diodes	Hotbox Electrical Characterization/Visual Inspection	AM0 @ 1353 w/m2 as characterized by JPL Balloon Flight @ 80C, coupon size TBD. Visual inspect at 1x at 1 foot.	Build Coupons with Composite Substrate and Aluminum core, Standard Interconnect, and 6 mil Ceria-doped microsheet Coverglass, using standard production processes
		Humidity Exposure	90 days @ 95+/- 4% Relative Humidity @ 45C	
		Hotbox Electrical Characterization/Visual Inspection	AM0 @ 1353 w/m2, characterized by JPL Balloon Flight, 80C. Inspect with 1x eyeball at 1 foot.	
		Combined Effects Test	Thermal Cycle first coupon between -180 to +80 for 15,000 cycles. Thermal cycle second coupon between -95 and +110 C for 5000 cycles. In hot cycle either (1) illuminate at AMO under load, or (2) dark forward bias.	
		Hotbox Electrical Characterization	AM0 @ 1353 w/m2, characterized by JPL Balloon Flight @ 80C. Visual inspect 1x at 1 foot.	< 2% Maxiumum Power Degradation
		NDE of Weld or Solder Joints		
		Pull Test	Pull strength at 45 degrees	
		100% DPA	TBD	
3. Stack Reliability Measurement, Verify Ohmic Contacts, Verify Tunnel Junction performance	Bare Cells	X-25 Electrical Characterization	AM0 @ 1353 w/m2 as characterized by JPL Balloon Flight, 28C,	
		Accelerated Life Test	TBD	
		X-25 Electrical Characterization	AM0 @ 1353 w/m2, characterized by JPL Balloon Flight, 28C	
		DPA		

Solar Cell Characterization				
Environment/Reason	Level	Test Procedure	Test Condition	Criteria/Report
1. Electron Radiation Effects	Bare Cell with n-interconnect, p-interconnect, diode interconnects	X-25 Electrical Characterization	AM0 @ 1353 w/m2 as characterized by JPL Balloon Flight Calibration Cell, 28C and 80C, sample size TBD	Baseline Test - Cell group shall not exceed 5% spread at Pmax
		Electron Radiation	Radiation energies of .6, 1.0, and 12 MeV at Fluences of 1e14, 3e14, 1e15, 3e15, 1e16	
		X-25 Electrical Characterization after each Radiation Fluence	AM0 @ 1353 w/m2 as characterized by JPL Balloon Flight Calibration Cell, 28C and 80C, sample size TBD	Cell group shall not exceed 5% spread at Pmax
		Reverse Bias Characterization	Dark Reverse Bias @ 2.0 V for 10 Seconds @ 80C after each fluence	Perform Reverse Bias/Electrical Characterization for maximum of 10 times
		X-25 Electrical Characterization	AM0 @ 1353 w/m2 as characterized by JPL Balloon Flight Calibration Cell, 28C	< 2% Average Efficiency Degradation from Baseline and < 3.5% for any Individual Cell
		100% DPA	TBD	
2. Proton Radiation Effects	Bare Cell with n-interconnect, p-interconnect, diode interconnects	X-25 Electrical Characterization	AM0 @ 1353 w/m2 as characterized by JPL Balloon Flight Calibration Cell, 28C and 80C, sample size TBD	Baseline Test - Cell group shall not exceed 5% spread at Pmax
		Proton Radiation	Radiation energies of 20 KeV, 50 KeV, 100 KeV, 300 KeV, 1MeV, 3MeV, and 10 MeV at Maximum Fluences of TBD	
		X-25 Electrical Characterization after each Radiation Fluence	AM0 @ 1353 w/m2 as characterized by JPL Balloon Flight Calibration Cell, 28C	Cell group shall not exceed 5% spread at Pmax
		Reverse Bias Characterization	Dark Reverse Bias @ 2.0 V for 10 Seconds @ 80C after each fluence	Perform Reverse Bias/Electrical Characterization for maximum of 10 times
		X-25 Electrical Characterization	AM0 @ 1353 w/m2 as characterized by JPL Balloon Flight Calibration Cell, 28C	< 2% Average Efficiency Degradation from Baseline and < 3.5% for any Individual Cell
		100% DPA	TBD	
3. UV Radiation Effects	CIC	X-25 Electrical Characterization	AM0 @ 1353 w/m2 as characterized by JPL Balloon Flight Calibration Cell, 28C, sample size TBD	
		UV Soak	TBD Hours at 200 nm irradiation in a Vaccuum of 10-5 torr until electrical degradation plateaus < 1% per hour. Exposure for another TBD2 Sun-Hours	Report TBD1 hours, and TBD2 % degradation
		X-25 Electrical Characterization	AM0 @ 1353 w/m2 as characterized by JPL Balloon Flight Calibration Cell, 28C	< 2% Average Efficiency Degradation from Baseline and < 3.5% for any Individual Cell
4. Peeling Gridlines after thermal cycle	Cell	Tape Peel Test	Pull with 3M type 600 cellulose tape to Evaluate Contact Adhesion. Visual inspection at 10x under fluorescent illumination	<1% AR and <1% metal peeling
5. Humidity in Storage	Cell	X-25 Electrical Characterization	AM0 @ 1353 w/m2 as characterized by JPL Balloon Flight Calibration Cell, 28C, sample size TBD	
		Humidity Test	30 days @95% RH @ 45C	
		X-25 Electrical Characterization	AM0 @ 1353 w/m2 as characterized by JPL Balloon Flight Calibration Cell, 28C	Average efficiency degradation of < 1.5% from baseline and no individual cell >2.5%
		Visual Inspection	1x at 1 foot distance	no obvious anomalies
6. Breakage of Cells on Curved Array	CIC	Bend Test	multiple radius bend test	measure bend radius up to cell fracture
7. Mechanical Strength - Handling Issues	Cell	Yield Test as per ASTM E 855-90 (2000), Test Method C	TBD samples	yield strength distribution curve
8. Photogeneration Response vs. Wavelength	Cell	Internal or External Quantum Efficiency	Spectral Response from 250 to 2000 nm for TBD energies after electrical radiation fluences of 1e14, 3e14, 1e15, 3e15, 1e16	
9. Off-Normal Electrical Response to Pointing Angle	Cell	Vary Angle of Incidence and provide X-25 Electrical Characterization	Measure response at 5, 10, 20, 30, 40, 50, 60, 70, 80, 85, 90 degrees. Measure cells at AM0 @ 1353 w/m2 as characterized by JPL Balloon Flight Calibration Cell, 28C	
10. Temperature Coefficient	Cell	Vary Temperature and Provide X-25 Electrical Characterization	Measure I-V curve to include Isc, Voc, Imp, Vmp between -180 and 150 C in 10 degree increments on cells with no fluence, and after fluences of e14, e15, e16. Provide AM0 @ 1353 w/m2 as characterized by JPL Balloon Flight Calibration Cell, 28C.	
11. Thermal Design	CIC	Hemispherical Emissivity	from 5 to 50 um	
12. Thermal Design	CIC	Solar Absorptance	from 250 to 2500 nm	
13. Electrical Characterization	Cell	Dark I-V characterization between I = Isc to - Isc at 28C		
14. Electrical Characterization	Bypass Diode	As per Mil-S-19000		

Solar Panel Qualification Test

Environment/Reason	Level	Test Procedure	Test Condition	Criteria/Report
1. Problems During Storage at Launch; Problems On-Orbit	Coupon	Electrical Characterization	AM0 @ 1353 w/m2 as characterized by JPL Balloon Flight, 28C, coupon size determined by TBD	Build Coupon with parts and processes to be used in flight
		Humidity Exposure	30 days @ 95+/- 4% Relative Humidity @ 45C	
		Electrical Characterization	AM0 @ 1353 w/m2, characterized by JPL Balloon Flight, 28C	< 2% Average Efficiency Degradation
		Visual Inspection	TBD	TBD
		Acoustic Test	TBD	
		Electrical Characterization	AM0 @ 1353 w/m2, characterized by JPL Balloon Flight, 28C	< 2% Average Efficiency Degradation
		Combined Effects Test	Thermal Cycle between predicted low non-operational temperature -16C and predicted high non-operational +16C at 1.5 x mission cycles. In hot cycle either (1) illuminate AM0 under load, or (2) dark forward bias. Reverse bias TBD directly after forward bias.	
		Electrical Characterization	AM0 @ 1353 w/m2, characterized by JPL Balloon Flight, 28C	< 2% Average Efficiency Degradation
2. Panel-Level VCM	Panel	Electrical Characterization	AM0 @ 1353 w/m2 as characterized by JPL Balloon Flight, 28C, coupon size determined by TBD	Build Coupon with parts and processes to be used in flight
		Measure VCM on cold surface	Thermal Soak predicted high non-operational temperature + 16C.	Measure as per ASTM 595. Input VCM results to vehicle contamination analysis.
		Electrical Characterization	AM0 @ 1353 w/m2, characterized by JPL Balloon Flight, 28C	< 2% Average Efficiency Degradation

Irving Weinberg Award
Presented by Dr. Sheila Bailey

The Irving Weinberg Award, in memory of Dr. Irving Weinberg (1919–1995), a leading contributor to the field of space photovoltaic research and development for most of his professional career, was established at the 14th Space Photovoltaic Research and Technology (SPRAT) conference in 1995. This award is to be given at every SPRAT meeting to persons who have made significant contributions to the field of space photovoltaics. This award is meant to be inclusive of all aspects of space photovoltaic research and technology, from fundamental investigations of semiconductor materials, to device improvements, and finally to innovations in hardware for actual mission applications. The recipients are

14th SPRAT, October 24 to 26, 1995, Dr. Chandra Goradia
15th SPRAT, June 10 to 12, 1997, Dr. Masafumi Yamaguchi
16th SPRAT, August 31 to September 2, 1999, Dr. Dennis Flood
17th SPRAT, September 11 to 13, 2001, Henry Curtis
18th SPRAT, September 16 to 18, 2003, Dr. Bruce Anspaugh

Irv would have been particularly pleased with the selection of Dr. Bruce Anspaugh.

Bruce received his Ph.D. from the University of Nebraska and started work for the Jet Propulsion Laboratory (JPL), all in 1964. He has spent his whole career trying to damage things, starting with the electronics and solar cells onboard the Mariner IV spacecraft. This early work led to his involvement with the Solar Array group in 1968. His career has been particularly colorful beginning with a review of the very first addition of a Solar Cell Radiation Handbook written more for scientists than panel engineers, followed by in 1973 a “Black” handbook (chosen for the color of the textured surface solar cells developed in that time period); a “Purple” revised handbook was next in 1977 (chosen for the “Violet cells” developed by a Comsat group); next was the “Green” handbook in 1982 that contained the first computer models (I’ve been letting my imagination run wild and believe that green was how he felt after punching all those computer cards), and finally the “Blue” GaAs radiation damage handbook in 1996 (here I’m thinking the space community was singing the blues wondering if this would be the last book). Amidst developing these essential industry standards, Bruce had begged a Dynamitron from the Fission Physics Group at JPL and has spent the last 30 years or so keeping it all together and working. I think he really became interested in the balloon calibrations because of his love of flying. After all, you get to chase the balloon package across the Texas countryside after calibration via a homing beacon. Needless to say, those JPL balloon standards are the foundation for all simulator measurements. The Space community will long remember the remarkable contributions of Dr. Bruce Anspaugh. You will be missed when you retire in November.

REPORT DOCUMENTATION PAGE

Form Approved
OMB No. 0704-0188

1. AGENCY USE ONLY (*Leave blank*)	2. REPORT DATE	3. REPORT TYPE AND DATES COVERED
	April 2005	Conference Publication

4. TITLE AND SUBTITLE

18th Space Photovoltaic Research and Technology Conference

5. FUNDING NUMBERS

WBS–22–103–06–10

6. AUTHOR(S)

Thomas L. Morton, compiler

7. PERFORMING ORGANIZATION NAME(S) AND ADDRESS(ES)

National Aeronautics and Space Administration
John H. Glenn Research Center at Lewis Field
Cleveland, Ohio 44135–3191

8. PERFORMING ORGANIZATION REPORT NUMBER

E–14965

9. SPONSORING/MONITORING AGENCY NAME(S) AND ADDRESS(ES)

National Aeronautics and Space Administration
Washington, DC 20546–0001

10. SPONSORING/MONITORING AGENCY REPORT NUMBER

NASA CP—2005–213431

11. SUPPLEMENTARY NOTES

Proceedings of a conference held at Ohio Aerospace Institute and sponsored by NASA Glenn Research Center in Cleveland, Ohio, September 16–18, 2003. Responsible person, Thomas L. Morton, organization code RPV, 216–433–6287.

12a. DISTRIBUTION/AVAILABILITY STATEMENT

Unclassified - Unlimited
Subject Category: 20 Distribution: Nonstandard

Available electronically at http://gltrs.grc.nasa.gov

This publication is available from the NASA Center for AeroSpace Information, 301–621–0390.

12b. DISTRIBUTION CODE

13. ABSTRACT ***(Maximum 200 words)***

The 18th Space Photovoltaic Research and Technology (SPRAT XVIII) Conference was held September 16 to 18, 2003, at the Ohio Aerospace Institute (OAI) in Brook Park, Ohio. The SPRAT conference, hosted by the Photovoltaic and Space Environments Branch of the NASA Glenn Research Center, brought together representatives of the space photovoltaic community from around the world to share the latest advances in space solar cell technology. This year's conference continued to build on many of the trends shown in SPRAT XVII—the continued advances of thin-film and multijunction solar cell technologies and the new issues required to qualify those types of cells for space applications.

14. SUBJECT TERMS

Solar cell; Photovoltaics power; Radiation damage; Space environment effects

15. NUMBER OF PAGES

310

16. PRICE CODE

17. SECURITY CLASSIFICATION OF REPORT	18. SECURITY CLASSIFICATION OF THIS PAGE	19. SECURITY CLASSIFICATION OF ABSTRACT	20. LIMITATION OF ABSTRACT
Unclassified	Unclassified	Unclassified	